The Interactions of Streamwise, Co-rotating and Counter-rotating Vortices

Kyle Forster

University of New South Wales

School of Mechanical and Manufacturing Engineering

A thesis presented for the degree of

Doctor of Philosophy

January 2018

PLEASE TYPE

THE UNIVERSITY OF NEW SOUTH WALES
Thesis/Dissertation Sheet

Surname or Family name: Forster

First name: Kyle Other name/s: James

Abbreviation for degree as given in the University calendar: PhD

School: Mechanical and Manufacturing Engineering Faculty: Engineering

Title: The Interactions of Streamwise, Co-rotating and Counter-rotating Vortices

Abstract 350 words maximum: (PLEASE TYPE)

The successful control of vortex structures is critical in the field of modern aerodynamics, with automotive and aerospace applications becoming increasingly reliant on vortices to improve aerodynamic efficiency. Knowledge of how streamwise vortex interactions behave as they propagate downstream is essential to designing systems to control these flow structures.

The flow around two NACA0012 vanes at various lateral offsets was investigated by a combination of experimental and numerical means to observe the interactions between two streamwise vortices. The vanes were separated in the streamwise direction, allowing the upstream vortex to impact on the downstream geometry. Initial investigations were performed using water tunnel dye visualisation and Reynolds-Averaged Navier-Stokes analysis, with more detailed Large Eddy Simulations and Particle Image Velocimetry used for quantitative assessment of vortex energies and paths.

Circulation enhancement of the upstream vortex occurred at all offsets for the co-rotating case. The counter-rotating condition was considerably more sensitive to offset, with far offsets causing vortex enhancement and near offsets causing vortex destruction. The presence of the upstream vortex was found to increase the production strength of the downstream vortex in the counter-rotating condition, and decrease it in the co-rotating condition. However, the counter rotating condition was found to have more rapid energy loss than the co-rotating condition, which did not significantly lose circulation across the domain.

In all co-rotating conditions the vortices were seen to tend to an asymmetric merger, however the merging distance was found to be statistical rather than deterministic. Meandering was found to occur in both vortices of the co-rotating pair, with the downstream vortex experiencing a faster growth rate and the oscillations equalising between the vortices. The oscillation was determined to be responsible for the variation in merging location, with variation in vortex separation causing the state at a single plane to merge and unmerge. In the counter-rotating condition oscillations were found to be larger, with higher growth, but less uniform periodicity.

Ultimately it was found that, under certain circumstances, interaction with a counter-rotating downstream vortex could successfully destroy an existing upstream vortex, while a co-rotating downstream vortex would re-energise the existing vortex in all conditions.

Declaration relating to disposition of project thesis/dissertation

…… …… ……

Signature Witness Signature Date

FOR OFFICE USE ONLY Date of completion of requirements for Award:

Certificate of Originality

Copyright Statement

I hereby grant the University of New South Wales or its agents the right to archive and to make available my thesis or dissertation in whole or part in the University libraries in all forms of media, now or here after known, subject to the provisions of the Copyright Act 1968. I retain all proprietary rights, such as patent rights. I also retain the right to use in future works (such as articles or books) all or part of this thesis or dissertation.

I also authorise University Microfilms to use the 350 word abstract of my thesis in Dissertation Abstract International (this is applicable to doctoral theses only).

I have either used no substantial portions of copyright material in my thesis or I have obtained permission to use copyright material; where permission has not been granted I have applied/will apply for a partial restriction of the digital copy of my thesis or dissertation.

Authenticity Statement

I certify that the Library deposit digital copy is a direct equivalent of the final officially approved version of my thesis. No emendation of content has occurred and if there are any minor variations in formatting, they are the result of the conversion to digital format.

Originality Statement

I hereby declare that this submission is my own work and to the best of my knowledge it contains no materials previously published or written by another person, or substantial proportions of material which have been accepted for the award of any other degree or diploma at UNSW or any other educational institution, except where due acknowledgement is made in the thesis. Any contribution made to the research by others, with whom I have worked at UNSW or elsewhere, is explicitly acknowledged in the thesis. I also declare that the intellectual content of this thesis is the product of my own work, except to the extent that assistance from others in the project's design and conception or in style, presentation and linguistic expression is acknowledged.

Signed: Date: January 17, 2018

Abstract

The successful control of vortex structures is critical in the field of modern aerodynamics, with automotive and aerospace applications becoming increasingly reliant on vortices to improve aerodynamic efficiency. Knowledge of how streamwise vortex interactions behave as they propagate downstream is essential to designing systems to control these flow structures.

The flow around two NACA0012 vanes at various lateral offsets was investigated by a combination of experimental and numerical means to observe the interactions between two streamwise vortices. The vanes were separated in the streamwise direction, allowing the upstream vortex to impact on the downstream geometry. Initial investigations were performed using water tunnel dye visualisation and Reynolds-Averaged Navier-Stokes analysis, with more detailed Large Eddy Simulations and Particle Image Velocimetry used for quantitative assessment of vortex energies and paths.

Circulation enhancement of the upstream vortex occurred at all offsets for the co-rotating case. The counter-rotating condition was considerably more sensitive to offset, with far offsets causing vortex enhancement and near offsets causing vortex destruction. The presence of the upstream vortex was found to increase the production strength of the downstream vortex in the counter-rotating condition, and decrease it in the co-rotating condition. However, the counter rotating condition was found to have more rapid energy loss than the co-rotating condition, which did not significantly lose circulation across the domain.

In all co-rotating conditions the vortices were seen to tend to an asymmetric merger, however the merging distance was found to be chaotic rather than static. Meandering was found to occur in both vortices of the co-rotating pair, with the downstream vortex experiencing a faster growth rate and the

oscillations equalising between the vortices. The oscillation was determined to be responsible for the variation in merging location, with variation in vortex separation causing the state at a single plane to merge and unmerge. In the counter-rotating condition oscillations were found to be larger, with higher growth, but less uniform periodicity.

Ultimately it was found that, under certain circumstances, interaction with a counter-rotating downstream vortex could successfully destroy an existing upstream vortex, while a co-rotating downstream vortex would re-energise the existing vortex in all conditions.

Acknowledgements

Completing a project of this magnitude would never have been possible without the help and support of a great number of people. Firstly I'd like to thank my supervisors Assoc. Prof. Tracie Barber, Dr Sammy Diasinos and Dr Graham Doig. Without your careful guidance, direction and knowledge the project would never have been what it is today. You all helped in your own ways, Graham by letting me stay over at your university and fixing my figures relentlessly, Sammy for donating your entire wind tunnel to me for months at a time, and Tracie for always being available right next to my desk for any question I had. We may have had our differences and arguments along the way, but I'd like to think at the end of this that I all consider you not just mentors but also friends.

A lot of my early aerodynamic development drive couldn't have happened without the help of a number of friends and colleagues around the office who helped me out and put me on the right path. Dr Dave Fulker, my colour schemes and figures wouldn't have been the same without you. Dr Reza "Kramer" Keshavarzi who took the time to discuss both CFD modelling and car washing techniques. Dr Pujith "PJ" Vijayaratnam for sharing in the PhD submission time banter, and Lewis, Bryce, Ash and Josh for keeping my lunchtimes fun. Also to Tracie's whole extended research group, John, Eamonn and Azi, you guys all made this a very memorable experience that I will cherish for the years to come. And of course Dr James Keogh, who not only let me work on his crazy cornering wind tunnel, but also provided endless and deep discussion on aerodynamics, cars, and Reynolds number adaptive wakeboards.

A big thanks to Joshua Simmons, apart from being my loyal housemate for half of my PhD (who would've thought any mere mortal could deal with me for that long?), his constant online banter kept me sane and enjoying the later parts of my PhD. And at some point I believe he proofed half my figures as well. And to my whole out-of-uni friendship group, it's probably getting a bit long to list all of you here, but you know who you are, thankyou for making sure I didn't descend back into the insanity of my undergraduate studies.

Conducting an experimental and numerical program of this scale is no small task, especially when the majority of your facilities were untested. For this, I had exceptional support from a wide variety of technical staff, whom I am extremely

grateful for their support. Wendy and Mynga over at Macquarie university were always on call and ready to help out with any wind tunnel help I needed, whether it was as simple as finding me a ruler, or as ridiculous as allowing me to flood the whole building with particles to test the fire alarm response. All the tech staff at UNSW, Ian Cassapi, Andy Higley, Jarred Dawson and Zebb Prime , who were all great assets for getting the rig up and running along with my shiny new wind tunnel. John "Jay-Z" Zaitseff (catchy name eh?) was always quick to respond to my cluster questions, and John Reizes, well, there's no other Professor quite like him, and I wouldn't have it any other way. One day I hope I can match up to one tenth of his comedic ability, and perhaps a smaller percentage of his broad intelligence.

Finally, I would like to thank my family. Not having to worry about food or shelter is an enormous boost in your ability to get a huge amount of things done, and without my parents constantly looking after me I probably would have been rapidly consumed by my metabolism. And to my girlfriend Cassidy Warner for keeping me watered and fed "like a pot plant", thankyou for keeping me from being consumed with work and helping me tone down my extra curricular activities so I actually had time to sleep.

List of Publications

Journal Papers

Kyle Forster, Tracie Barber, Sammy Diasinos, and Graham Doig. LES analysis of transient upstream/downstream vortex interactions. **Submitted to Journal of Fluid Mechanics on 14/09/2017**

Kyle Forster, Tracie Barber, Sammy Diasinos, and Graham Doig. Interactions of a co-rotating vortex pair at multiple offsets. *Physics of Fluids*, 29(5):057102, 2017

Kyle Forster, Tracie Barber, Sammy Diasinos, and Graham Doig. Interactions of a counter-rotating vortex pair at multiple offsets. *Experimental Thermal and Fluid Science*, 86:63-74, 2017

Conference Papers

Kyle Forster, Tracie Barber, Sammy Diasinos, and Graham Doig. The Variation in Co and Counter-Rotating Upstream-Downstream Vortex Interactions. *47th AIAA Fluid Dynamics Conference*, 3305, 2017

Kyle Forster, Sammy Diasinos, Tracie Barber, and Graham Doig. Numerical investigation of streamwise vortex interaction. *SAE Technical Paper*, 2015-01-2573, 2015

Contents

List of Figures

List of Tables

Nomenclature

Roman Symbols

a	Theoretical vortex model core radius
$A_{0.1}$	Area of vortex at 0.1 peak vorticity threshold (C^2)
$A_{0.3}$	Area of vortex at 0.3 peak vorticity threshold (C^2)
AR	Aspect ratio
B_v	Vortex separation (C)
C	Chord length
C_{L2D}	Two dimensional lift coefficient
C_{L3D}	Three dimensional lift coefficient
C_p	Pressure coefficient $p/(1/2 * \rho * v^2)$
C_{pt}	Total pressure coefficient $p_t/(1/2 * \rho * v^2)$
p	Static pressure (Pa)
p_t	Total pressure ($p + 1/2 * \rho * \sqrt{u^2 + v^2 + w^2}$, Pa)
r	Vortex core radius
$R_{0.1}$	Average radius of vortex at 0.1 peak vorticity threshold (C)
$R_{0.3}$	Average radius of vortex at 0.3 peak vorticity threshold (C)
R_e	Reynolds number, based off chord length
S_{tk}	Stokes number
Str	Strouhal number $f * C/U_\infty$
T	Time (s)
u	x-velocity (ms^{-1})
U_∞	Freestream velocity (ms^{-1})
v	y-velocity (ms^{-1})
w	z-velocity (ms^{-1})
X_c	x core location (C)
Y_c	y core location (C)
y^+	Non-dimensional wall distance

Greek Symbols

Γ	Circulation (m^2s^{-1})
Ω	Vorticity (s^{-1})
Ω_x	x-vorticity (s^{-1})
μ_g	Dynamic viscosity of air (kg/ms)

Abbreviations

CFD	Computational Fluid Dynamics
DEHS	Di-Ethyl-Hexyl-Sebacat
LES	Large Eddy Simulation
LDA	Laser Doppler Anemometry
PIV	Particle Image Velocimetry
RANS	Reynolds-Averaged Navier-Stokes
WALE	Wall Adapting Local Eddy Viscosity

Chapter 1

Introduction

Turbomachinery blade interactions, aircraft taking off in succession, wind turbines and vortex generators can all produce vortex interactions with multiple streamwise vortices in close proximity to each other [1–5]. These vortices may be desirable (flow control, heat transfer) or undesirable (aircraft wake vortices). Streamwise vortex/structure interactions have been studied considerably less than either parallel or normal vortex/structure interactions [6], particularly relating to the effects of the upstream vortex migration. In previous work both vortices of a vortex pair have been typically two dimensional or deployed from the same streamwise location [7, 8], limiting the study of their interactions at extremely close core spacings. The studies that have deployed vortices from an upstream location have either focussed on the flow characteristics on the downstream wing itself, and/or have been limited in the number of vortex positions run, making trend analysis difficult. These close interactions are important conditions to understand in order to provide a knowledge base for practical vortex applications, where upstream vortices may move in locations on either side of a vortex producing obstacle, such as a wing or vane.

The successful control of vortex structures is critical for success in the field of modern aerodynamics, with automotive and aerospace applications becoming increasingly reliant on vortices to improve aerodynamic efficiency [9]. Of great importance to these fields is an understanding of how to maximise vortex length on desirable vortices, and rapidly destroy undesirable vortices. This inherently requires knowledge of what vortex interactions conditions produce what strength vortices at a given distance downstream, and what geometries can provide these

initial conditions.

This research aims to better understand the properties of interacting vortices, and how the manipulation of parameters such as vortex rotation direction and proximity affects the downstream vortical structures. More specifically, this research looks at seeing if downstream vortices can be used to re-energise or prematurely destroy existing vortices, and what conditions are desirable to achieve either of these scenarios. By inspecting the circulation and position of the vortices, then studying the links to transient characteristics and pressure fields, this thesis aims to facilitate a better understanding of not just the properties of these vortex systems, but the fundamental mechanisms causing them. This is being investigated through the analysis of two vanes in a streamwise line, with the forward vane producing the initial vortex and the rearward vane producing the vortex which interacts with the primary. The rear vane position is evaluated in multiple lateral positions to vary vortex proximity. This arrangement is evaluated using both computational and experimental methods.

Chapter 2 of this thesis will discuss the existing literature surrounding the fundamentals of vortex flows and vortex interactions. The experimental facilities and setup used for both the low and high Reynolds number testing will be discussed in Chapter 3, along with an explanation of the computational methods used to analyse these results. This will also include the design logic behind components and the specifics of the wind and water tunnels used. Chapter 4 will look at the numerical methods used for the computational analysis of the vanes, with a discussion of vortex metrics used for the computational analysis. The subsequent chapters will discuss the results and conclusions of these experiments, with Chapter 5 detailing the initial flow characteristics used for the construction of further studies, Chapter 6 exploring the more detailed wind tunnel work and Chapter 7 looking at the transient LES numerical studies. Chapter 8 will then compare the co-rotating and counter-rotating vortex scenarios. Appendix A provides a more comprehensive description of the experimental facilities, with additional photographs and drawings.

Chapter 2

Literature Review

2.1 Vortex Modelling

One of the most significant issues regarding current vortex study is the lack of an agreed definition of what constitutes a vortex. Authors such as Lught [10], Haller [11], Roth [12] and Jeong and Hussain [13] all identified the limitations in the various methods of defining and locating vortices and vortex cores. Early definitions of vortices located the core at a region of high vorticity, however as Haller [11] identified; "there is no universal threshold over which vorticity is to be considered high". Vorticity may also be present in flow fields in which no vortices occur, such as shear flows, as well as being absent in some vortical structures such as irrotational vortices. Globus et. al. [14] proposed streamline and pathline methods which track the flow structure, however as Lught [10] pointed out, the circulation of a streamline in an instantaneous frame of reference is no guarantee of the rotation of a group of particles around a singular axis, and thus the method is largely invalid. In addition to this, streamlines structures change during velocity based transformations, making them not useful for accelerating or rotating bodies.

To provide a basis for computational and theoretical investigations, a number of analytical vortex profiles have been proposed. Of these, the most popular are the Rankine, exponential, Hall and Lamb Oseen Vortex [15–20]. The formulations for these vortices are given below in eqs. (2.1) to (2.4). Often the Rankine vortex is used for convenience, as its simplicity facilitates more rapid analysis whilst still

capturing many features of a realistic vortex.

$$\text{Rankine: } \omega = \begin{cases} \Gamma/(\pi a^2), & r \leq a \\ 0, & r > a \end{cases}, v_\theta = \begin{cases} \Gamma r/(2\pi a^2), & r \leq a \\ \Gamma/(2\pi r), & r > a \end{cases} \tag{2.1}$$

$$\text{Hall: } u = \Delta v(G - 1/2 \ln z), v = -1/2 \Delta v(z)^{-1/2}, w = \Delta v(G + 1/2 - 1/2 \ln z)^{1/2} \tag{2.2}$$

$$\text{Exponential: } u = constant, w = \Gamma_\infty / 2\pi r(1 - e^{-z}) \tag{2.3}$$

$$\text{Lamb-Oseen: } \omega = \frac{\Gamma}{\pi a^2} e^{-r^2/a^2}, v_\theta = \frac{\Gamma}{2\pi r}(1 - e^{-r^2/a^2}) \tag{2.4}$$

$$\text{Time Dependent Lamb-Oseen: } v_\theta = \frac{\Gamma}{2\pi r}(1 - e^{-r^2/4vt}) \tag{2.5}$$

A more practical vortex field is provided in the form of the Lamb-Oseen vortex, which is a line vortex model derived directly from the Navier-Stokes equations [21]. It takes into account viscosity, however its specified pressure field is provided purely to ensure an even circumferential manner by effectively providing a centripetal force.

Another practical vortex profile exists in the form of the Batchelor vortex, presented by George Batchelor in 1964 [22]. This model has been applied in determining aircraft wake vortex breakdown lengths, and considers axial and azimuthal velocities. The model is also derived from the Navier-Stokes equations using a boundary layer approximation, and if the axial velocity component is reduced to zero it simplifies to the formulation for the Lamb-Oseen Vortex. These formulations are often used in more recent analytical work due to their improved accuracy and realism over a Rankine vortex and the increased computational power available for analysis. Lamb-Oseen Vortices with Gaussian axial velocity profiles typically have good correlation with experiment [23]. These profiles can be seen graphically in Figure 2.1.

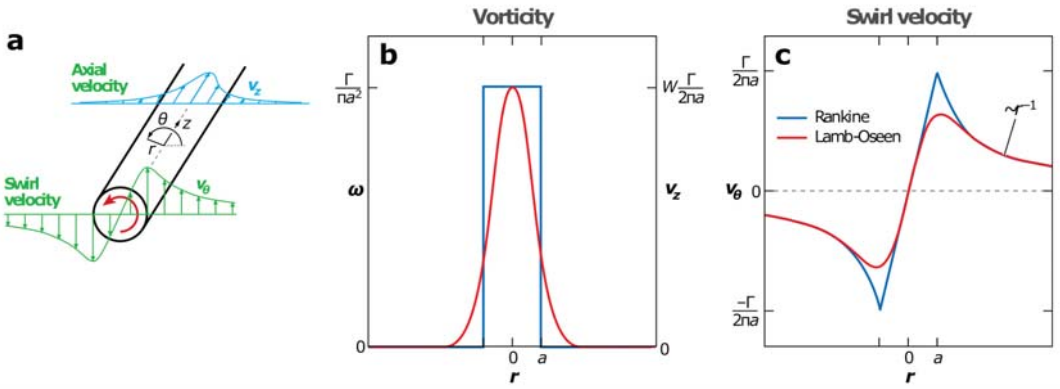

Figure 2.1: Vorticity and velocity profiles for Rankine (blue) and Lamb-Oseen (red) vortices, with axial velocity profile for a Batchelor vortex indicated in a. Reproduced with permission from Leweke et.al. [23]

In addition to the more complicated vortex models used for singular vortices, occasionally it is simpler to approximate vortex pairs as two point vortices with a characteristic radius of vorticity, as defined by Ting & Tung [24]. This facilitates more rapid analytical analysis of vortex pairs.

The total circulation of a vortex can be calculated as either the line integral of vorticity along a closed path, or as the integral of its vorticity across a plane [23, 25], while the Reynolds number is the circulation divided by the kinematic viscosity of the fluid. While it has previously been found that the line integral is more accurate than a vorticity integration [26], for experimental results and coarse grids it is more practical and effective to use the vorticity integration [1]. The vortex centre within a plane is defined as the integral of the vorticity multiplied by the displacement, divided by the circulation [23]. These can be seen in eqs. (2.6) to (2.8).

$$\Gamma = \int \omega dS \tag{2.6}$$

$$X_c = \frac{1}{\Gamma} \int X \omega dS \tag{2.7}$$

$$Y_c = \frac{1}{\Gamma} \int Y \omega dS \tag{2.8}$$

2.2 Singular Vortices

In order to understand the fundamentals of vortex structure and breakdown, it is easiest to isolate the flowfield to a singular vortex. Numerous studies have been performed on isolated vortices acting without the influence of other bodies or vortices to determine what fundamentally causes their breakdown, as well as the vortex structure post-breakdown. Of these, the majority are experimental, however a number of computational studies have also been performed.

2.2.1 Experimental Studies

One of the biggest issues in studying experimentally produced vortices is the need to form a singular, pure vortex structure with no secondary vortices. This is a considerably difficult problem, as geometries such as vanes and ramps produce significant flow deflections, as well as producing a velocity deficit [27]. Other geometries, such as cubes and cylinders, as identified by Jacobi [28] , do not produce flow deflection, however they produce highly turbulent and noisy flowfields that do not serve useful purposes for singular vortex investigations. Two types of generator have been designed to form pure vortices; the tangential slot-entry swirl generator and the swirl vane vortex generator, with schematics for each type shown inFigure 2.2.

Another design, used by Leweke and Williamson [30] and Harris and Williamson [31] is of two flat plates which close together with a jet. This forms a vortex pair with no axial flow, and can be used to study the dynamics of a Lamb Oseen vortex pair experimentally. Such a configuration is shown in Figure 2.3. For many studies attempting to emulate realistic vortex flows with axial pressure gradients and velocity deficits, vanes are used to create wingtip vortices [8, 32–34]. These may be in the form of aerofoils or flat plates, and are most typically of square planform, however elliptical profiles have been used by some [32].

Due to the swirling nature of vortices, they act as pressure gradient amplifiers in the sense that an induced gradient in the freestream will be substantially increased at the vortex core [15]. As such the use of measurement probes which intrude into the flow is not an option for singular pure vortices, as it will significantly affect the result [35]. Cassidy and Falvey [35] found that a probe

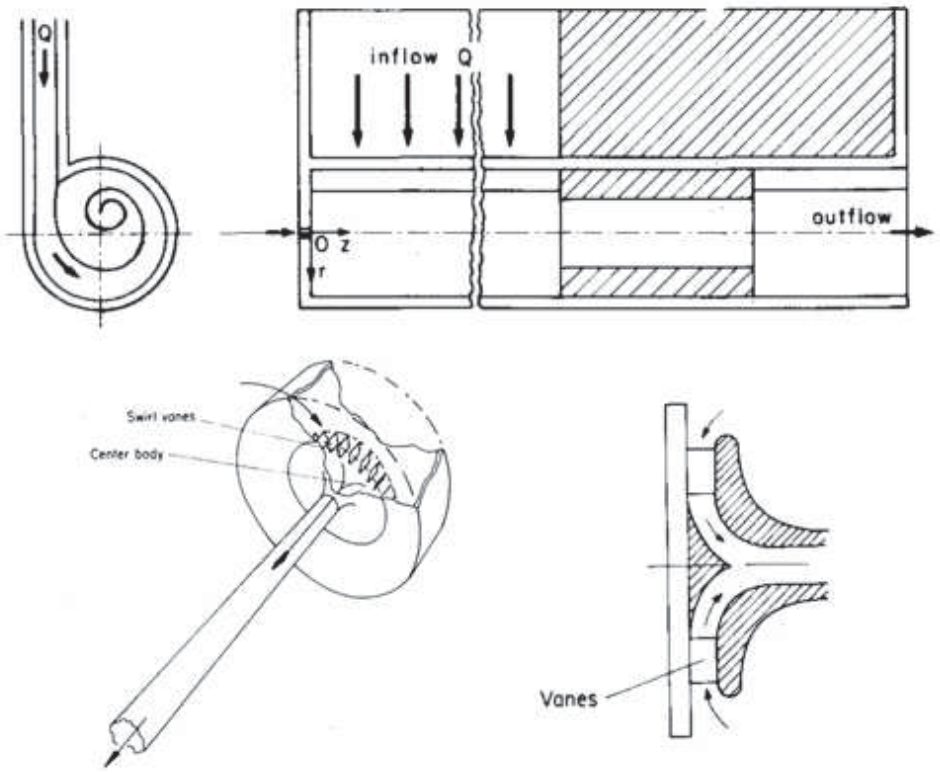

Figure 2.2: Vortex generator types from Leibovich, with tangential slot type top, and swirl vane bottom, reproduced with permission from Leibovich [29]

placed near a pure vortex caused a substantial upstream migration of the breakdown location. Consequently, the primary measurement techniques used for vortex studies are dye and particle filtration, as well as Laser Doppler Anemometry (LDA). The primary downside to this is pressure measurements of the vortex cannot be taken directly experimentally. Another issue with respect to experimental vortex analyses as identified by Lucca-Negro and O'Doherty [19] is the ambiguity of Reynolds numbers used in studies. Some studies define the Reynolds number from core diameter, while others use a geometrical value such as pipe diameter, making comparison difficult. To further complicate matters, of those using core diameter, some use the diameter as a location at a threshold value of vorticity, while others use the point of peak azimuthal velocity.

Seven types of vortex breakdown falling under 3 primary categories have been identified, as classified by Lucca-Negro and O'Doherty [19]. The primary causes of these breakdowns, such as adverse pressure gradients and vortex instabilities, will be discussed later in this chapter, as well as methods of modelling and

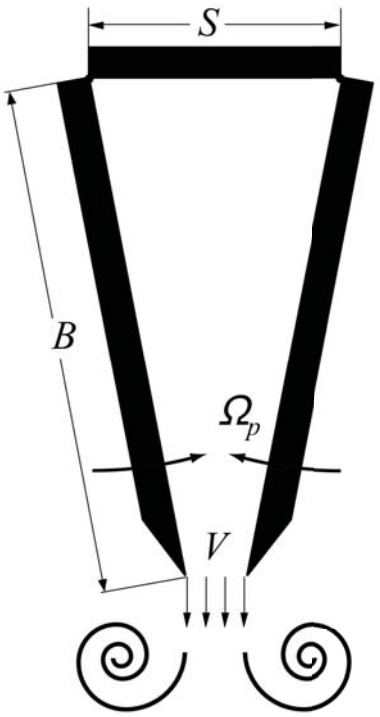

Figure 2.3: Vortex generator used by Leweke and Williamson [30], reproduced with permission.

calculating breakdown location. The three primary modes are bubble type, spiral type and helical breakdown, with the other modes typically being combinations of these (for example a bubble breakdown with a spiral tail as seen in Figure 2.4). Of the primary modes, helical is the most uncommon as it manifests under low Reynolds number conditions [36]. Bubble and spiral modes are common and the flow may switch between the two under the same conditions, as can be seen by the presence of both modes occurring on a single wing in Figure 2.5.

The bubble breakdown consists of a large, externally axisymmetric expansion of the core that leaves a wake similar to a bluff body behind it [29, 37]. It can be classified into two rings as identified by Escudier [17], an approximately symmetric outer ring and an asymmetric inner ring, as can be seen in Figure 2.6. The spiral breakdown does not result in immediate core expansion as seen in the bubble breakdown, but instead a severe kink occurs with the flow turning through 90 degrees at a stagnation point [19]. This forms the core into a corkscrew shape, which continues for 1-2 turns before dissipating.

There are a number of parameters used to characterise vortices, with the most prominently investigated one being the Swirl number, which is the ratio of

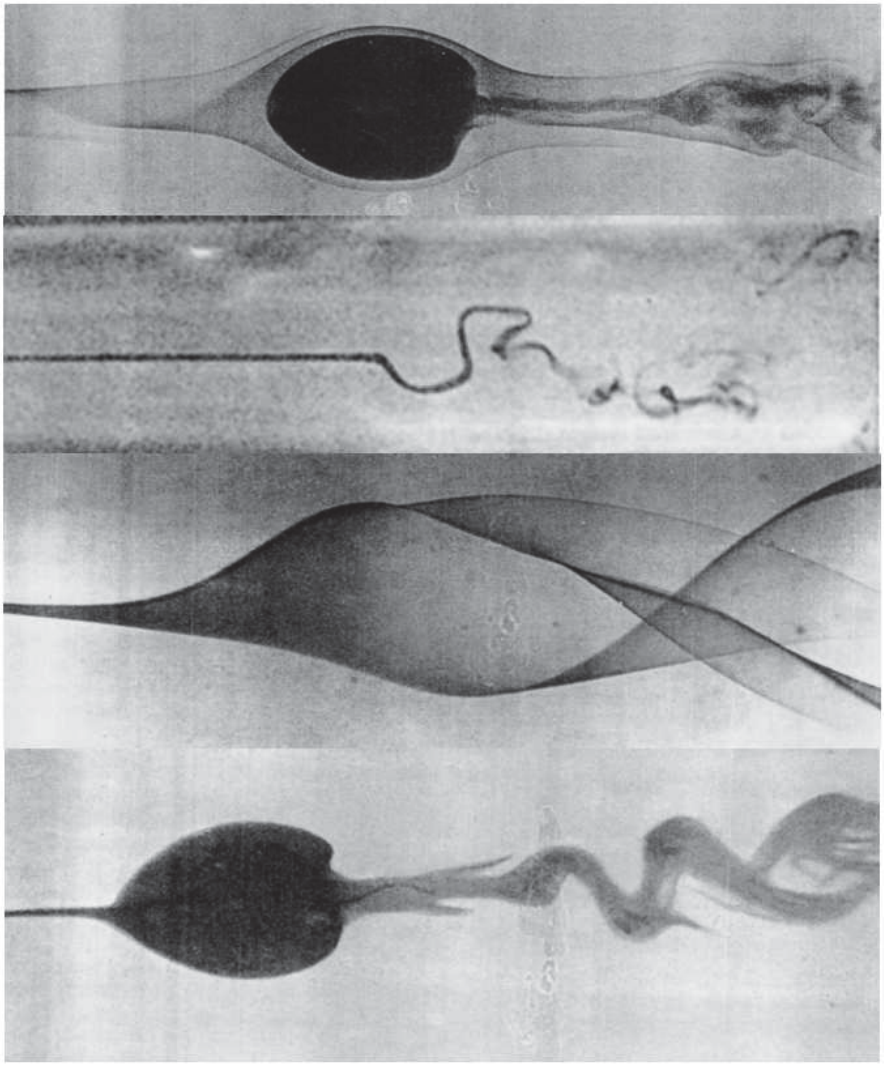

Figure 2.4: Vortex breakdowns, from top to bottom; bubble, spiral, double helix and bubble with a spiral tail, reproduced with permission from Lucca-Negro and O'Doherty [19]

maximum azimuthal velocity to axial velocity within the core [36]. Swirl number has also been used to describe the ratio of circulation to axial velocity [38]. Leibovich [36] found that increasing this swirl number in a spiral breakdown case would cause the breakdown to transition to bubble type. It was also found that bubble type breakdown will always occur upstream of a spiral breakdown for a given vortex. Further increasing the swirl number as tested by Escudier and Zehnder [38] stabilised the shape of the breakdown bubble and moved it upstream until it was out of range of the test equipment. As such, higher swirl numbers of vortices increase their sensitivity to breakdown.

Reynolds number sensitivities of pure vortices have been analysed by various

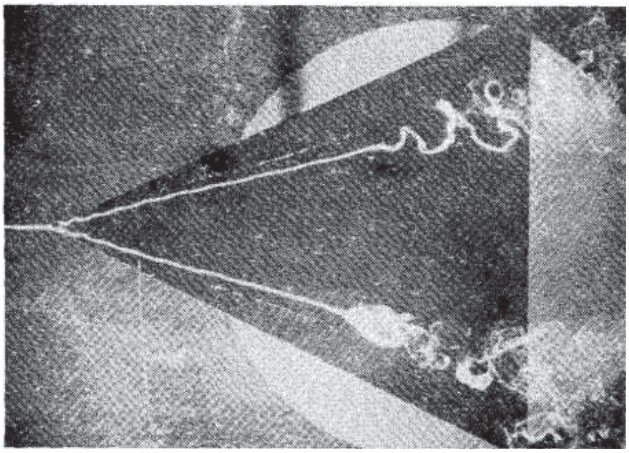

Figure 2.5: Breakdown over a delta wing, showing two different breakdown modes occurring on the same geometry, reproduced with permission from Leibovich [29]

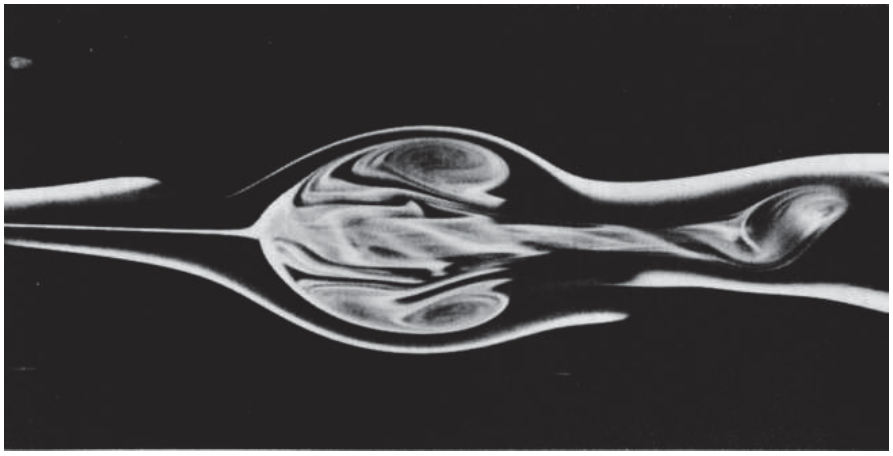

Figure 2.6: Cross section of a breakdown bubble, showing asymmetric centre section, reproduced with permission from Escudier [17]

studies. Chanaud [39, 40] noted that at low Reynolds numbers (less than 300 based off test tube diameter) the vortex motion was steady, however as the Reynolds number increased the flow began a periodic oscillation. As Re was further increased this periodic motion increased in amplitude until a structure representing a spiral was formed. The findings of Cassidy and Falvey [35] were consistent with this observation, with the wake structure behind the vortex breakdown being steady at lower Reynolds numbers, however becoming progressively more unsteady as Re increased. Sarpkaya [41] tested vortices at varying Re and circulation numbers, finding that decreasing both the circulation and Re resulted in a longer distance before vortex breakdown, as can be seen in Figure 2.7. This is an interesting result as increasing the axial velocity increases the breakdown length as noted below, however it also

increases the Reynolds number, which decreases the breakdown length. As such, it can be seen that vortices are more sensitive to total velocity effects than Reynolds number sensitivities.

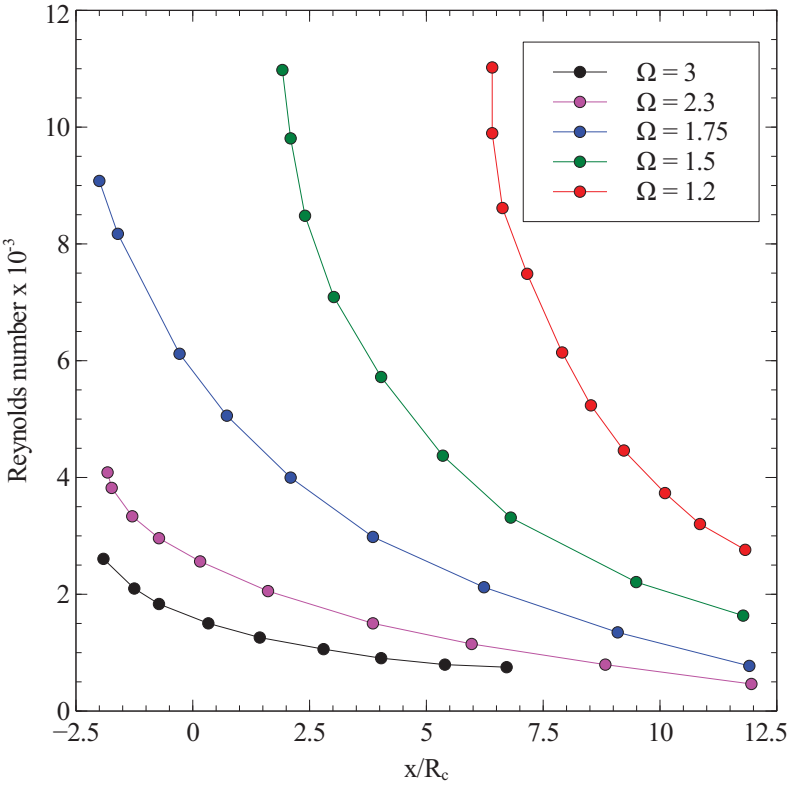

Figure 2.7: Relationship between Reynolds number, circulation and breakdown position, adapted from Sarpkaya et.al [41]. Ω is swirl number, x is taken from a point of expansion in the test section.

The response of singular vortices to adverse axial pressure gradients has also been tested by Sarpkaya [42], who found that by applying blockages at the end of his testing volume he could move the vortex breakdown location upstream. This is consistent with work performed by Lowson [43], who found that the breakdown location of a delta wing vortex was directly related to the degree of pressure recovery along the trailing edge. Approaching the same issue of adverse pressure gradient from a theoretical view, Krause [44] found that for any vortex with core growth, breakdown must eventually occur. By rearranging the momentum equations for a vortex and substituting analytical vortex models, he determined that increasing the freestream velocity and decreasing the radial velocity would delay vortex breakdown. This is consistent with the above mentioned experimental work which found the vortex breakdown was highly dependent on swirl number.

2.2.2 Computational and Numerical Studies

While the bulk of singular vortex studies have been experimental, there are still a considerable number of computational studies focussing on mechanisms that are difficult to simulate experimentally. Initial numerical studies on vortex breakdown used the quasi-cylindrical approximation (QCA), a solution of linearized Navier-Stokes equations in a polar co-ordinate system with the flow outside the vortex modelled as uniform [45]. This approach utilises a downstream step by step approach in conjunction with the initial velocity conditions to determine where breakdown will occur [46]. The method functions in a similar way to the analytical calculation of two-dimensional boundary layers in that the failure of the approximation corresponds to the transition of the flow. In this case, if the flow reaches a step whereby the values violate the QCA, vortex breakdown will occur. QCA tests conducted by Hall [15] and Krause [44] concurred with experimental data on the importance of the external pressure field on vortex breakdown. However, Krause found that for inviscid cases breakdown could not be initiated without some sort of adverse pressure gradient, while for viscous cases the core naturally increased in size, forcing a breakdown to eventually occur.

While the QCA proved very accurate at determining breakdown locations in good correlation with the experimental data, it is limited in its ability to deal with practical engineering flows due to its requirement for slender vortices and inability to predict the resultant flowfield. As such, Navier-Stokes based solutions were required. Moet et al. [47] investigated the wave nature of vortices and their subsequent breakdown. They found that a merging of two induced pressure waves within a vortex core resulted in a decrease in local core velocity, with a helical instability forming. Using large eddy simulation (LES) and direct numerical simulation (DNS), they enforced an abrupt increase of the vortex core size for a length half that of the vortex radius at the computational inlet. It was found that the increase in vortex size was associated with a change in pressure drop within the core, with a larger radius increase further dropping the pressure. The variation in radius also changed the propagation speed, with larger radius differences resulting in faster moving pressure waves. These pressure waves manifested themselves in the form of a toroidal region of increased vorticity, with a minimum increase in core radius at peak tangential velocity of 30% and a reduction of peak tangential velocity of approximately

20%. This structure can be seen in Figure 2.8.

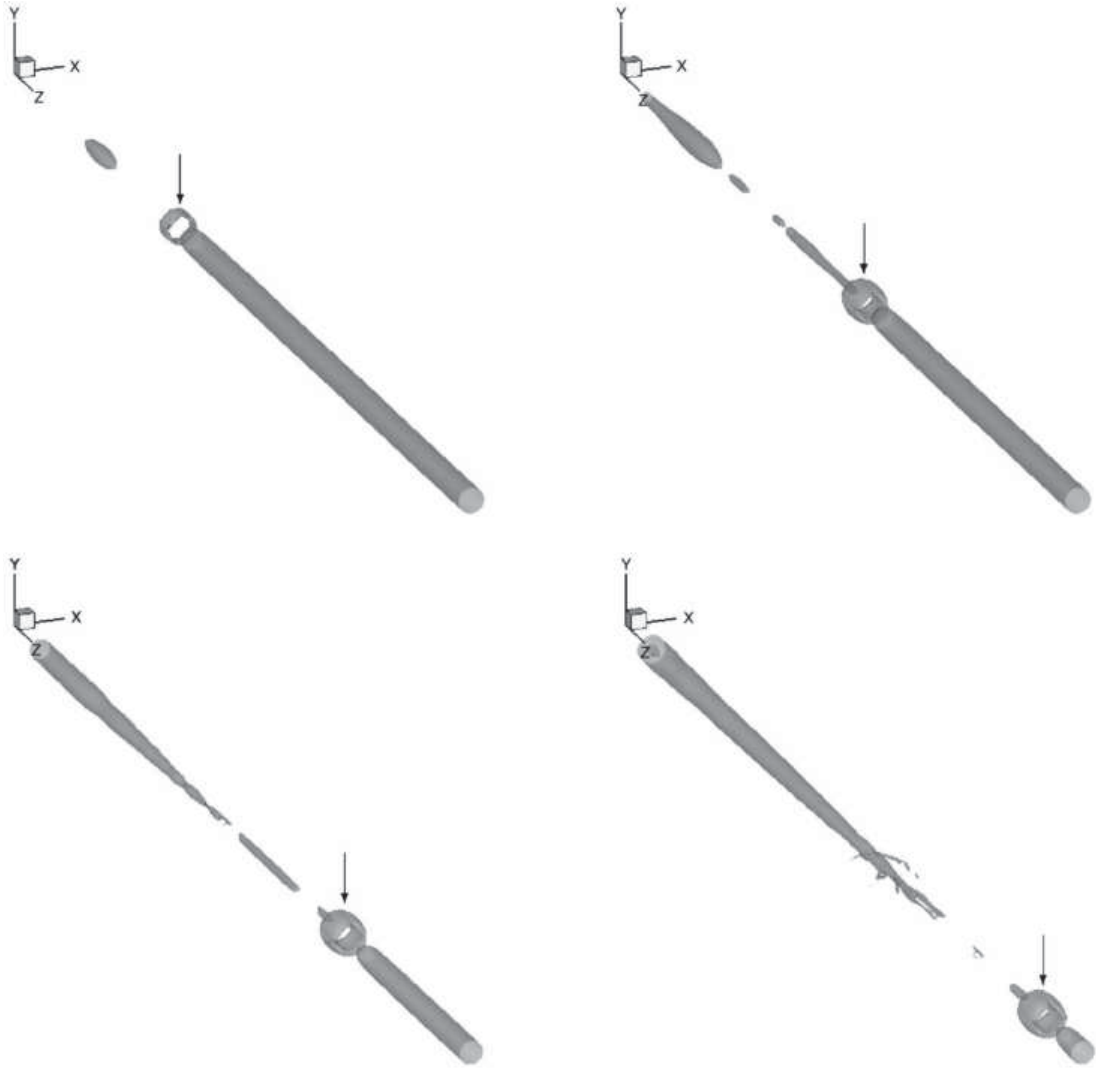

Figure 2.8: Progression of toroidal vortex bubble as found by Moet [47], reproduced with permission.

A second round of simulations were performed by Moet with random white noise in the initialisation to provoke helical instability modes. It was found that the toroidal region formed by the pressure wave was very similar to the axisymmetric vortex expansion found in bubble type breakdown when viewed in a moving reference frame, and as such was likely the mechanism responsible for this type of vortex breakdown.

Singular vortex breakdown has also been used to improve efficiency in combustion chambers, with the breakdown being used to stabilise the flame and improve emissions [48]. Chukwueloka [49] used transient RANS modelling and experimental data to determine the validity of existing theoretical predictions in

vortices produced by a stepped tube structure. They compared their results to the theoretical swirl model developed by Wang and Rusak [50] and found good correlation for breakdown locations on pure pipe flows. However, this model is only well suited to pipe flows where breakdown can be characterised by a critical level of swirl in a columnar vortex.

Iudiciani and Duwig [51] investigated a similar scenario, however used LES methods instead of RANS. While their study largely focused on the flame and combustion effects, some notable findings regarding the vortex structure at the combustor exit were found. By forcing the axial flow at different frequencies, they were able to alter the shape and location of the vortex breakdown. It was observed that at frequencies lower than the vortex core's precession, the vortex breakdown remained constant and axisymmetric as if no disturbance had been applied. As the frequency was increased to significantly higher levels, the vortex breakdown was significantly altered, developing into multiple, smaller counter-rotating vortex cores. This demonstrated a link between the oscillation of the input flow and the breakdown mode of the vortex, which may still be applicable to non-combustor based studies.

2.3 Counter-rotating Vortex Interactions

Vortices in realistic flows will inevitably end up interacting with other vortices and structures present in the flow. These interactions can occur in several ways, however the interactions of streamwise vortices will be the focus of this thesis. This can occur in two manners; if two vortices interacting are of the same sign then the interaction is a co-rotating interaction, and if they are of different sign it is counter-rotating. Multiple combinations of co-rotating and counter-rotating pairs may interact in more complex interactions, however this review will largely focus on the two main types, with the counter-rotating configuration being considered in this section.

2.3.1 Structure

In the case of a two dimensional counter-rotating vortex pair the flow structure produced is symmetrical while the vortices are of equal strength. As identified

by Leweke et. al. [23], when inspected in the co-moving reference frame the structure forms an inner region of flow recirculation around the vortex cores, and an outer region of flow migration along the direction of the axis of symmetry, as can be seen in Figure 2.9.

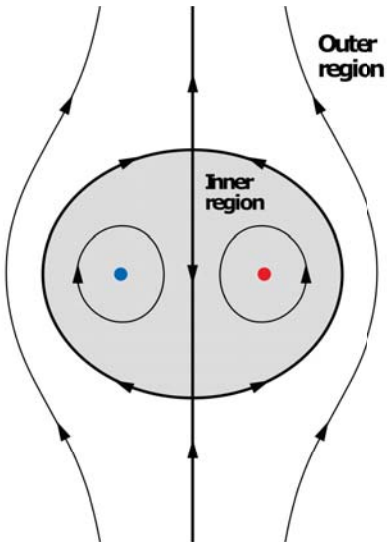

Figure 2.9: Structure of a counter-rotating vortex pair, reproduced with permission from Leweke et.al. [23]

These structures will shift from symmetrical structures into an asymmetric mode as a result of the strain field imposed upon them through interaction with the other vortex [52–54]. As a result the vortices will stretch such that they are longer along the axis of symmetry and shorter on the other axis. The deformation of the vortex cores and the action of the vorticity field increases the strain further within the vortex core [23].

2.3.2 Migration Trends

2.3.2.1 Free Flow Regions

For free flow (unbounded) inviscid cases any vortex pair will maintain a constant core separation distance due to the conservation of angular momentum. For a symmetric (equal circulation), counter-rotating case, this will mean that the pair will translate along the axis of symmetry, while for a case with unequal circulations there will be an orbital motion [55, 56]. This can be interpreted as the outer region streamlines from Figure 2.9 being near stationary and the inner region translating. These migrations can be seen in Figure 2.10.

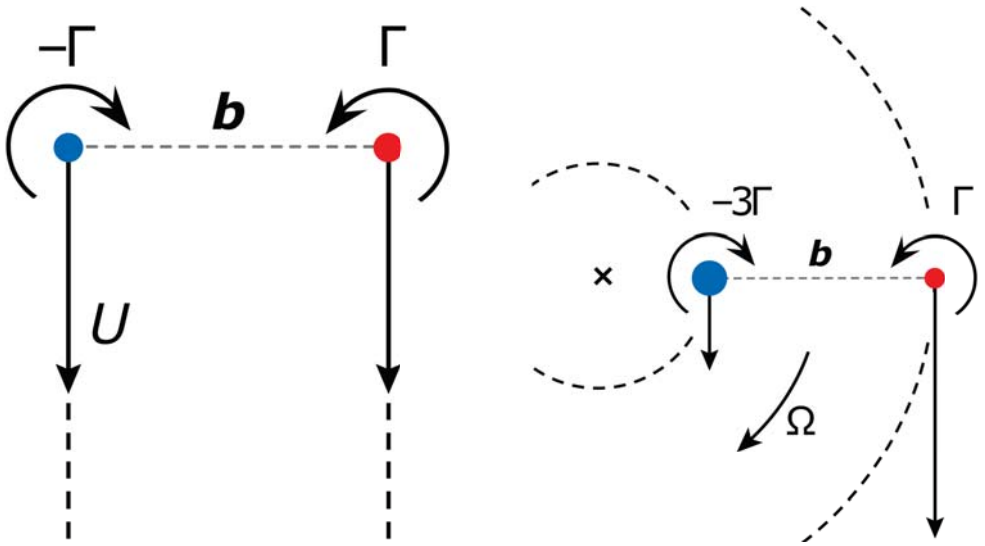

Figure 2.10: Migration trends of a counter-rotating vortex pair, reproduced with permission from Leweke et.al. [23]

These migrations can be seen in the water tunnel testing of Rokhsaz and Rebours [57], where dye marker injected into the cores of a pair of counter-rotating vortices showed a near linear trend in downwards motion of an equal strength pair. This motion increased in magnitude as vortex swirl was increased through varying the angle of attack of the vortex generation blades, while the horizontal displacement of the vortices did not vary significantly. This study also showed an increased magnitude of vortex wandering further downstream in a manner similar to the Crow instability [58], which shall be discussed later.

2.3.2.2 Wall Bounded Regions

When a wall is introduced in proximity to a vortex pair, the direction of migration will notably change. Early inviscid analyses [59] found that a counter-rotating pair will simply move apart as it approaches a wall, however later experimental studies [60] found that the vortex pair rebounded from the surface. Further studies of this phenomenon [61, 62] found that the vortex swirl induced a lateral boundary layer at the wall below the vortices, causing localised separation. This results in the formation of a secondary vortex of opposite sign located above the primary vortex, forcing the original vortex upwards and thus causing the rebound. Such a trajectory can be seen in Figure 2.11, with the separation profile and secondary vortex seen in Figure 2.12.

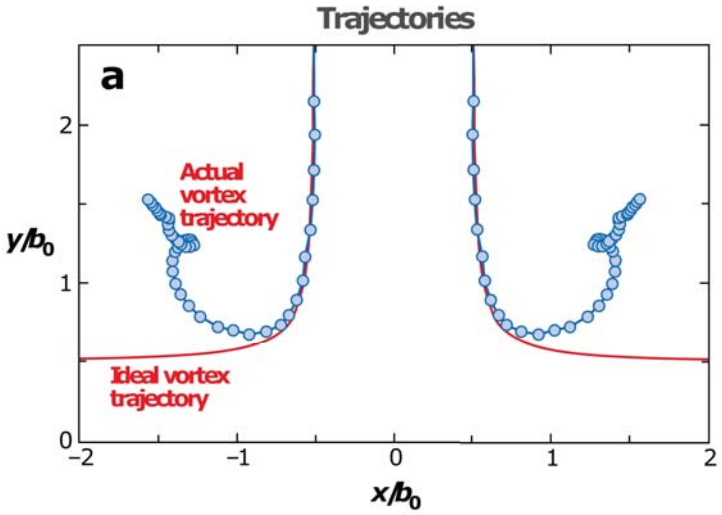

Figure 2.11: Migration trends of a counter-rotating vortex pair, reproduced with permission from Leweke et.al. [23]

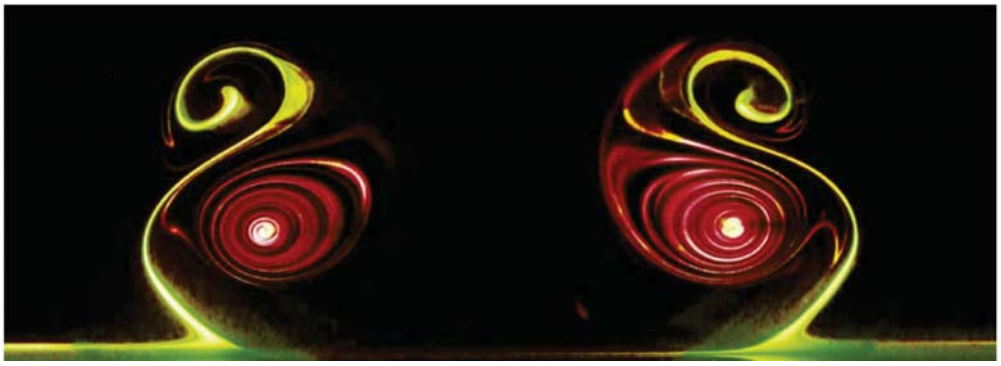

Figure 2.12: Dye visualisation of primary vortices (red) and secondary vortices (green) associated with the boundary layer separation, reproduced with permission from Harris et.al. [31]

In addition to the vertical motion induced by vortex rebound, a pair of counter-rotating vortices will also spread or contract as a result of the rotational shear against the wall face itself. Kliment and Rokhsaz [63] tested vortices produced by flat plates placed in close proximity to a ground plane. They observed a significant lateral deviation in vortex core location resulting from the interaction with the ground plane. In addition to this they found that the migration patterns were relatively insensitive to roughness of the ground, as well as their amplitudes of motion. The presence of the wall also significantly increases the decay rate of the vortices, with a higher level of diffusion and vorticity cancellation resulting from shear against the wall [64, 65].

2.3.3 Instabilities

2.3.3.1 Long Wave

Instabilities of vortices occur in two primary forms, the first is instabilities of the vortex as a whole, with large wavelengths compared to core radius, known as long-wave instabilities. The second is the short wave instabilities, resulting from changes in the core structure from external straining. Within counter-rotating pairs the most common long wave instability is the Crow instability. This is a manifestation of the vortex pressure amplification in which small wave disturbances occurring in one vortex are amplified by the other, causing significant wave displacements to form in the vortex pair. Crow [58] studied the wakes of a variety of aircraft and used a solution to a linear wave system to create formulas capable of describing the deviations. It was found that once the vortex cores reached a certain proximity or cut-off distance the two wakes would unify into vortex rings and rapidly breakdown. Crow's theory was found to be successful in predicting vortex breakdown in counter-rotating cases that are not dominated by singular vortex breakdown. Vortices that rapidly break down or dissipate do not have a long enough duration for waves to form, and as such are not subject to the Crow instability. The sinusoidal deviations of the Crow instability are symmetrically displaced between the two vortices, approximately inclined at 45 degrees to the plane of symmetry. This configuration can be seen in Figure 2.13.

Crow's theory was further expanded by Widnall et. al [66, 67], who considered the addition of axial velocity components, similar to realistic wingtip vortices. Widnall also introduced the concept of an equivalent Rankine Vortex size for non Rankine vortices, allowing the analysis of more realistic velocity distributions such as Batchelor vortices. This was a considerable advancement over Crow, who only considered Rankine vortices. Using these models, Klein et al [68] and Fabre [69] found that all counter-rotating pairs are inherently unstable regarding the long wave Crow instability. The most sensitive wavelengths to the instability are those that are between 6-10 times the separation distance between the two vortices. Rossow [70] found through inviscid vortex filament calculations that inducing out of phase sinusoidal perturbations in the vortices resulted in longer distances before breakdown, with the filaments having less instability growth at closer proximities. However, inducing in-phase instabilities accelerated the

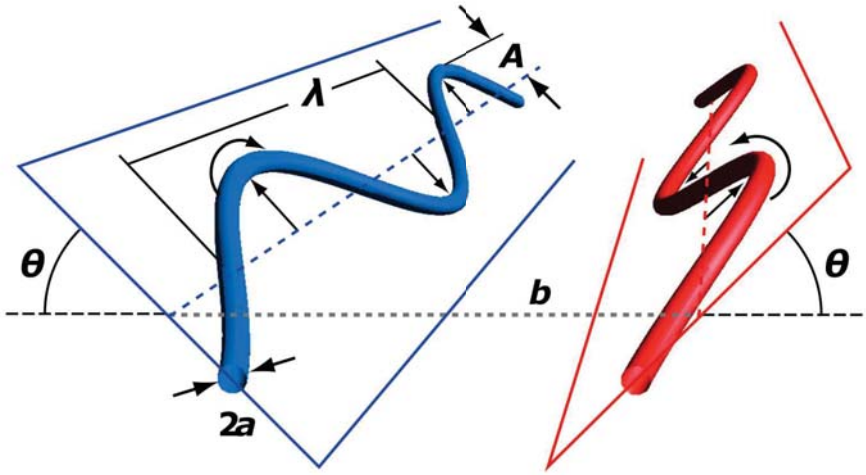

Figure 2.13: Graphical representation of the Crow instability, reproduced with permission from Leweke et.al. [23]

growth of the Crow instability, ultimately shortening vortex wake length by a factor of 4 or more.

Moet et al. [47] continued their study on wave based vortex breakdown on to the effects of breakdown once the Crow instability had manifested. By placing a counter-rotating pair in a stationary frame of reference it was found that the sinusoidal deviations of the vortex cores fed each other, eventually resulting in the connection of the vortex pairs. This produced multiple pressure waves from different ends of the linked pairs, resulting in vortex breakdown at the intersections of these waves as per previous findings on single vortex cores [47]. This is consistent with the findings of Kida & Takaoka [71] and Dhanak & De Bernardinis [72] who found that the connection of the vortex pairs once the oscillations became sufficiently large resulted in the creation of three-dimensional vortex rings. Leweke and Williamson [30] further studied this through water tunnel testing and found that at low Reynolds numbers the vortex rings reformed through the connection of sections into larger vortex loops. They theorised that given an instability of perfect periodicity, this should eventually lead to the reformation of two counter-rotating vortex pairs, however did not observe this due to inherent imperfections in their experimental setup. The evolution of the crow instability can be seen in Figure 2.14.

For unequal strength vortices, the Crow instability can manifest itself at much shorter wavelengths than for an equal strength case. Chatelain et al. [73]

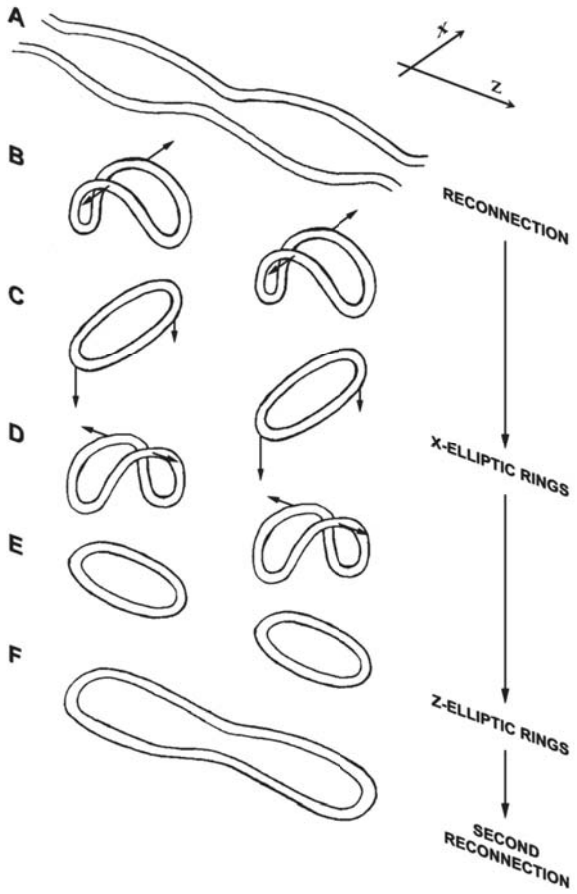

Figure 2.14: Evolution of the Crow instability, reproduced with permission from Leweke et.al. [30]

simulated such a scenario numerically and found a medium length instability present where the weaker vortex was drawn around the primary vortex. The simulations used a vortex particle method with one billion particles, allowing for very high fidelity observations of the vortex interactions through DNS at an Re of 6000. The flow structure can be seen in Figure 2.15. Ortega et al [74] experimentally investigated the same scenario in a tow tank, finding that the weaker vortex formed loops around the stronger vortex, before the loop detached and formed vortex rings. This made quasi steady vortex wakes in the equal strength case unstable within 300 to 600 chord lengths downstream.

Detailed studies of the Crow Instability in ground effect have been more limited, however it has been found that the presence of a ground plane restricts the amplitude of the Crow instability, preventing connection occurring between the two vortices [75].

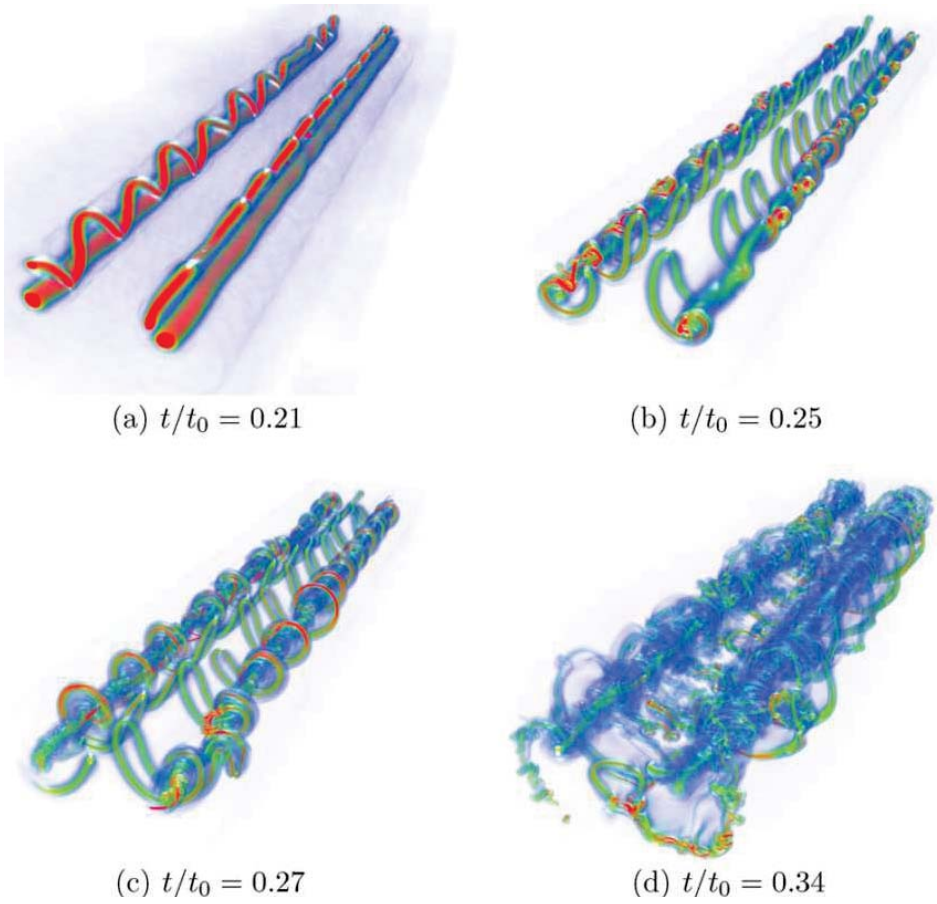

(a) $t/t_0 = 0.21$ (b) $t/t_0 = 0.25$

(c) $t/t_0 = 0.27$ (d) $t/t_0 = 0.34$

Figure 2.15: Evolution of unequal vortex Crow instability, reproduced with permission from Chatelain et.al. [73]

2.3.3.2 Short Wave

The short wave (elliptic) instability is identified in counter and co-rotating pairs by a streamtube in the core of the vortex with a diameter approximately half that of the instabilities wavelength. Such a configuration can be graphically seen in Figure 2.16. The instability is fundamentally caused by a resonance of two Kelvin waves (a sinusoidal deformation) within the vortex core as driven by the strain field induced by the other vortex [76, 77].

When axial flow is present within a vortex, as is indicative of a wingtip vortex [22], the elliptic instability is modified. By performing an analytic small strain analysis a Gaussian axial velocity profile imposed over a Rankine Vortex, Lacaze et. al. [80] found that the typical modes of the Kelvin waves within the core were disrupted. This method was then applied to a Lamb-Oseen vortex [81], thus evaluating a more realistic scenario. From this, it was found that the presence of

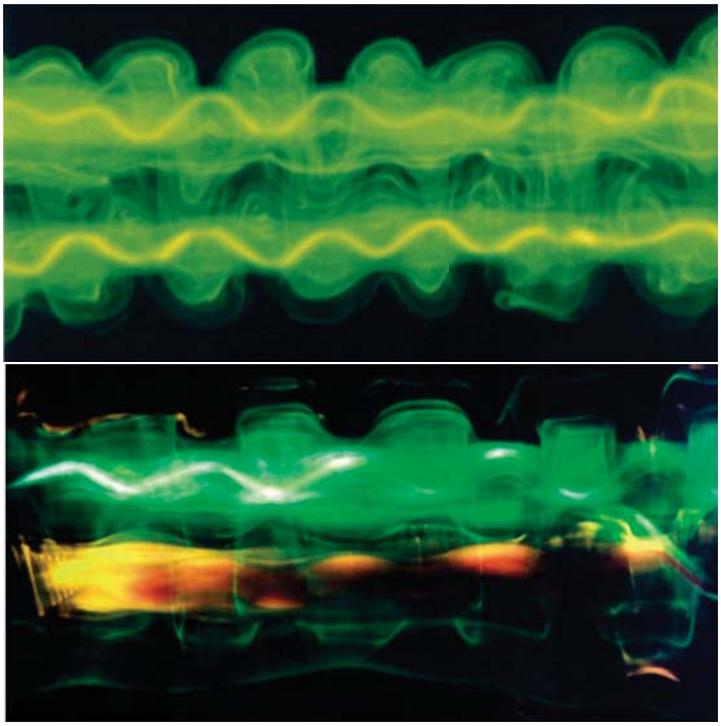

Figure 2.16: Elliptic instability in counter-rotating vortex pair (top, from Leweke et.al. [78]) and co-rotating vortex pair (bottom, from Meunier et. al. [79])

an axial flow in a Batchelor vortex was responsible for damping the Kelvin modes m=-1 and m=1, where m is the azimuthal wavenumber [25], as in the Rankine case. This was due to the axial flow breaking the symmetry of the vortex, causing resonances between modes m=0 and m=-2 to become stronger, and transitioning to modes m=-1 and m=-3 and so on as the axial component increased. These findings have been further confirmed by the numerical investigations of Ryan and Sheard [82] and the water tunnel testing of Roy et. al. [83], who observed the (-2, 0, 1) mode. As such, the dominant mode‘s identified for the elliptic instability are the bending mode (-1, 1, 1) for no axial core velocity, and the double-helix mode (-2, 0, 1) for vortices with axial flow. These modes can be seen in Figure 2.17. It should be noted that as the swirl decreases, the instabilities will shift from a vortex instability to a swirling jet instability, as this has a much faster growth than elliptic instabilities [84].

2.3.3.3 Combined

Counter-rotating pairs may exhibit combinations of both the Crow instability and elliptic instability. Due to the elliptic instability being driven by the strain

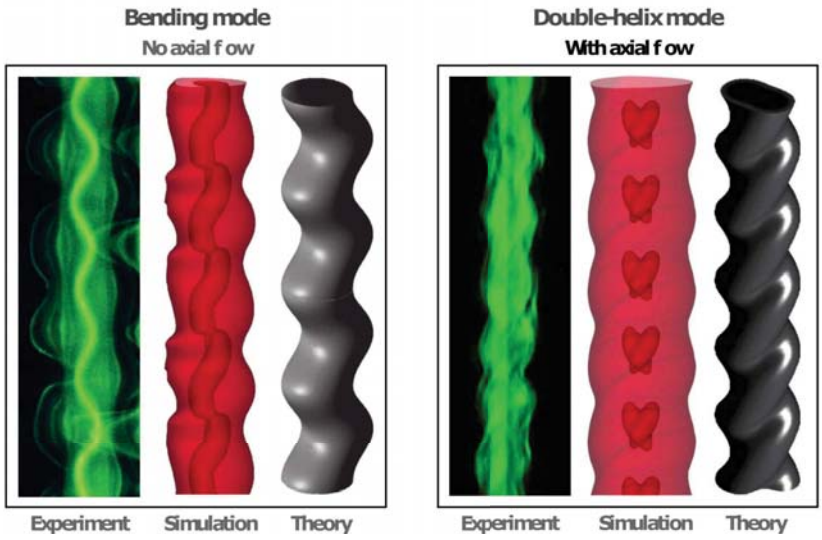

Figure 2.17: Elliptic instability modes for axial and non axial flows. Reproduced with permission from Leweke et.al. [23]

field of the vortex, the mutual induction between the two vortices will cause the elliptic instability to be stronger where the vortex cores are brought closer together by the Crow instability. The elliptic instability then produces secondary structures, which are drawn across between the two vortices, facilitating vortex connection [78].

2.3.3.4 Secondary

In addition to instabilities in the primary vortex pair, instabilities can occur in the previously mentioned secondary vortices which result from ground plane interaction. As this induced vortex now acts as a new counter-rotating pair of unequal strength, very short scale Crow instability can occur. This manifests itself in the form of a short wavelength waviness, as identified by Harris & Williamson's [31] water tunnel experiments. By testing at a Reynolds number of 1260, they found that the secondary instabilities were antisymmetric, as opposed to the primary crow instability, as can be seen in Figure 2.18. It was observed that this mode behaved more as a long wave displacement mode than an elliptic mode within the core. This has be further verified through inviscid analyses and direct numerical simulation [31, 85].

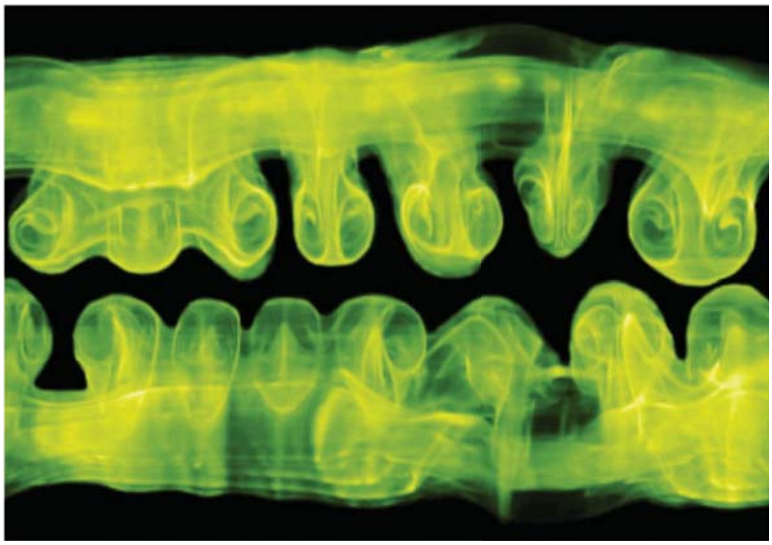

Figure 2.18: Top view of counter rotating pair, showing antisymmetric secondary instability (vortex ring structure) and symmetric Crow instability. Reproduced with permission from Harris et. al. [31]

2.4 Co-Rotating

2.4.1 Structure

In the co-rotating case the base structure formed by the interactions of the two vortices is far more complex than in the counter-rotating condition. It is separated into several regions as identified by Leweke et. al. [23] and seen in Figure 2.19. The inner core regions essentially behave like singular vortices within this structure, while the inner recirculation region contains fluid that travels around both vortices. Outside of these areas there exists the outer recirculation region, which behaves as a secondary pair of vortices as a result of the viscosity of the fluid, and the outer region, which rotates in a singular azimuthal direction.

The induced strain field for a co-rotating pair is the opposite to that of a counter-rotating pair, and consequently the vortex cores will deform in the opposite manner, stretching along a line drawn through the two vortex centres and becoming shorter on the opposite axis.

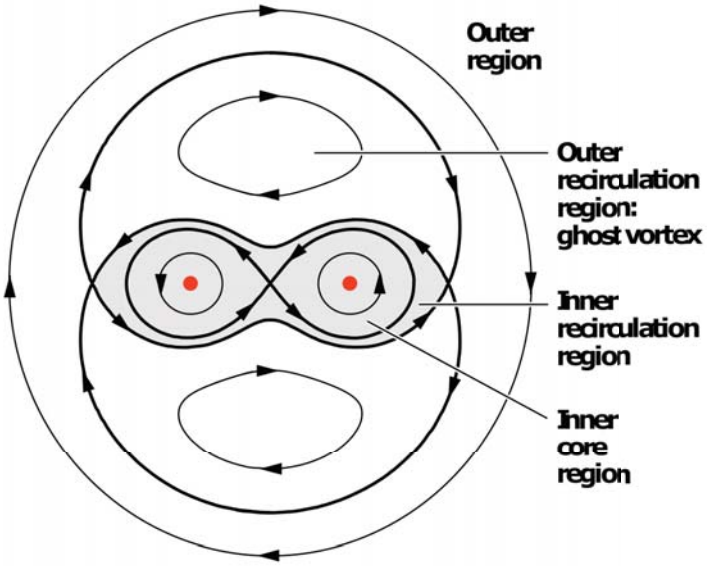

Figure 2.19: Structure of a co-rotating vortex pair, reproduced with permission from Leweke et.al. [23]

2.4.2 Migration Trends

Free Flow Regions If the total circulation of any vortex pair is $\neq 0$, there will be a net rotation of the vortex system [23]. In the case of a co-rotating vortex pair, both circulations are of the same sign, hence they must add to a non-zero amount, causing an orbital motion of the vortex system. If the circulations are equal, this will cause the two cores to orbit at an equal radius around a central point, while if they are unequal the vortices will orbit on different radii. The vortex with more circulation will be closer to the centre point, while the vortex with less circulation will be further out, as can be seen in Figure 2.20.

These migrations can be seen in the water tunnel testing of Rokhsaz and Rebours [8], where dye marker injected into the cores of a pair of co-rotating vortices showed a negligible movement in the centre of orbiting for a pair of co-rotating vortices. As they progressed through the observation domain, they slowly orbited each other in a spiral motion. These vortices were observed to merge within typically one full orbital motion for most cases tested, however as the spacing between vortices, merging distance was shifted further downstream. Increasing vortex swirl decreased merging distance, and also increased the amplitudes of the

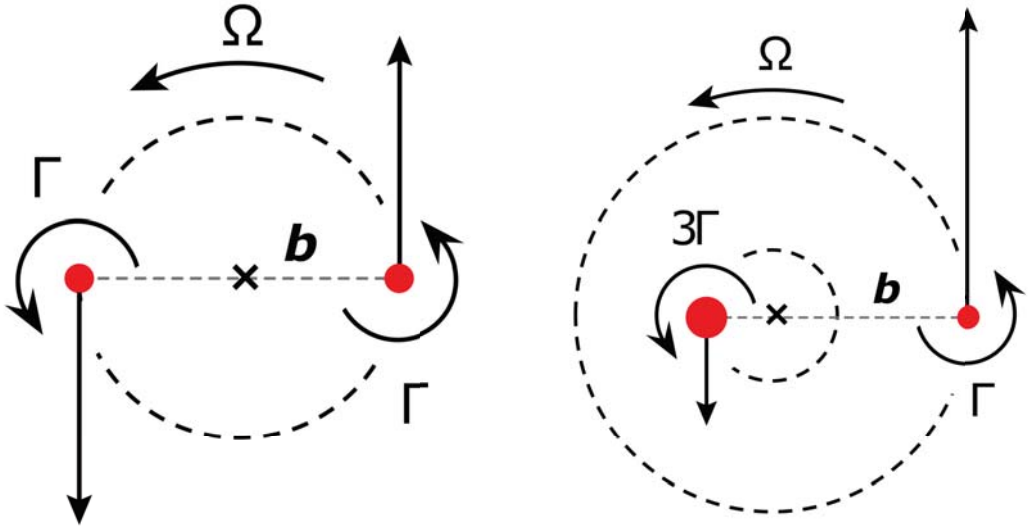

Figure 2.20: Migration trends of a co-rotating vortex pair, reproduced with permission from Leweke et.al. [23]

vortex motion (meandering).

Wall Bounded Regions Interactions between co-rotating pairs and walls are classified into 3 main zones, outside ground effect, near ground effect and inside ground effect [86]. Above 1.5 times the span between the vortices from the ground the vortices are outside ground effect, and between 1.5 times and 0.5 times the vortex span they are in near ground effect. At heights below 0.5 times the vortex span it is considered that a co-rotating vortex pair is in ground effect. Similarly to counter-rotating vortices, in ground effect the induced boundary layer separation from the shear layer on the wall causes vortex rebound, as described by Harvey and Perry [61] and Orlandi [87]. While there has been considerable investigation into the behaviour of counter-rotating vortices in ground effect due to the similarity to the aircraft wake problem, far fewer studies exist for co-rotating vortices.

Kliment and Rokhsaz [86] performed water tunnel testing on a co-rotating pair in close proximity to a wall. They found that the pair underwent a vortex rebound near the surface, as well as a lateral translation resulting from the shear against the wall, similar to a singular vortex. The ground plane also altered the orbital trajectories, with more of a leapfrogging motion occurring than a consistent helical spiral. However, the presence of a ground plane did not significantly change the spiralling rate of the pair.

2.4.3 Instabilities and Merging

As identified previously [88–91], a pair of co-rotating vortices will merge in any viscous flow. The equilibrium states of interacting and merging vortices were first studied by Saffman and Szeto [89] using energy based equations numerically approximated with Newton's method, finding that the vortices will merge in an equilibrium state at a vortex separation to radius ratio of 3.16. This was found to be different from that of an unsteady state, which was predicted at 3.4 by Zabusky et al [92] using contour dynamics, and 3.4-3.8 by Rossow [93] using point vortex methods. All of these evaluations used equal strength and size vortex cores, with two dimensional flow fields and no velocity deficit through the core, limiting their accuracy and resulting in discrepancies between the methods. It is currently accepted that the merging is due to the viscous diffusion causing vorticity to expand from the inner recirculation region to the outer recirculation region [23]. The "ghost vortex" of the outer recirculation region then stretches the vorticity between the two cores, resulting in the production of a singular vortex core.

Merging of equal strength co-rotating vortices can be broken up into four distinct stages, the first diffusive stage, the convective stage, the second diffusive stage and the merged diffusive stage [94–96]. The first diffusive stage consists of the two vortex cores increasing in size through viscous diffusion, and has no change in core separation distance. The convective stage occurs once the two vortices reach a critical size, and the vortices begin to move towards each other at a rapid rate. During this stage, the advection of vorticity away from the cores forces the cores together due to the conservation of angular momentum, causing their merging. The second diffusive stage then involves the diffusion of the two vortex azimuthal velocity peaks to form a singular vortex. In the merged diffusive stage the combined vortices become more axisymmetric, however now have the same core location. The separation distances with respect to time for each stage can be seen in Figure 2.21.

Vortex merging is fundamentally caused by the migration of vorticity from the core to the inner recirculation region, and then into the outer recirculation region. This vorticity is then dispersed in such a way that the vorticity in the outer recirculation region causes the migration of the two vortices towards each other. By dividing the skewed vorticity field into a symmetric vortex field and an antisymmetric field (the total vorticity field minus the symmetric vorticity

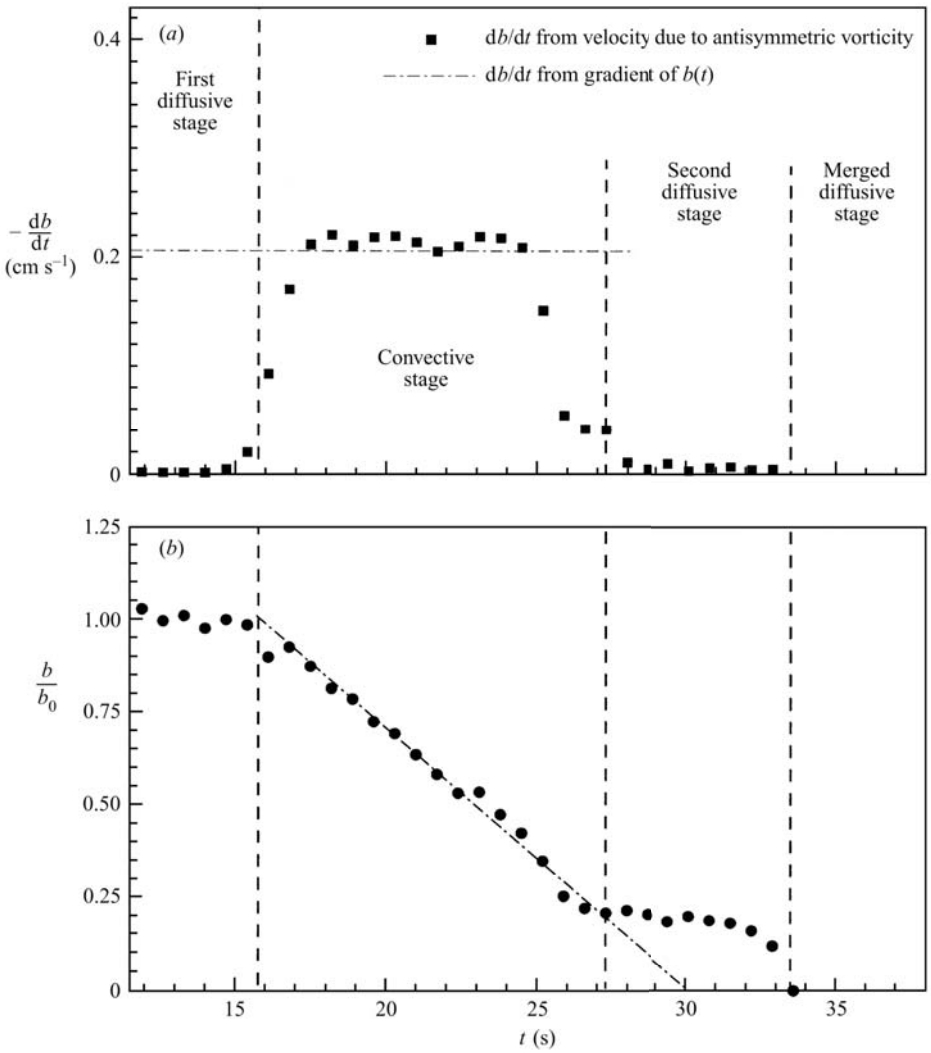

Figure 2.21: Radial velocities of cores (top) and core separation distance (bottom) for different merging phases. Reproduced with permission from Cerretelli & Williamson [96]

field), it can be seen that the asymmetry drives the merger. These distributions can be seen in Figure 2.22.

In the case of vortices of unequal strength the mechanism of merging is notably different if the circulation differential is large. In these cases, the weaker vortex has insufficient circulation to support the strain field induced by the stronger vortex, and as such is strained into a spiral tail structure [23]. This can occur in 3 main ways, partial merger, partial straining and complete straining, with various levels of elongation of the weaker vortex. These structures can be seen in Figure 2.23. The visual difference in these types is subtle and can be characterised by the proximity of the vorticity cores to one another. As can be

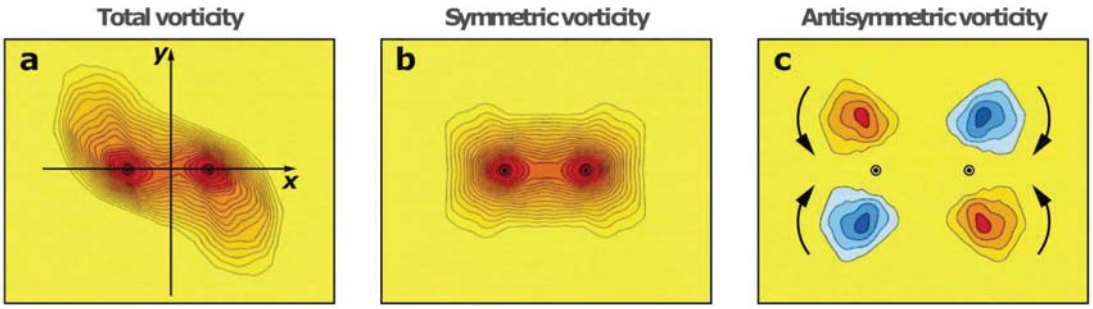

Figure 2.22: Breakdown of co-rotating pair vorticity into symmetric and antisymmetric components. Reproduced with permission from Leweke et.al. [23]

seen in Figure 2.23, the secondary vortex core is kept separate from the primary vortex, causing this vortex to be only affected by the strain field of the primary vortex, but not actually merging with the core. This can cause full vortex dissipation as seen in the complete straining case. In the merger cases however, the vorticity field behaves more like the previously described merging process.

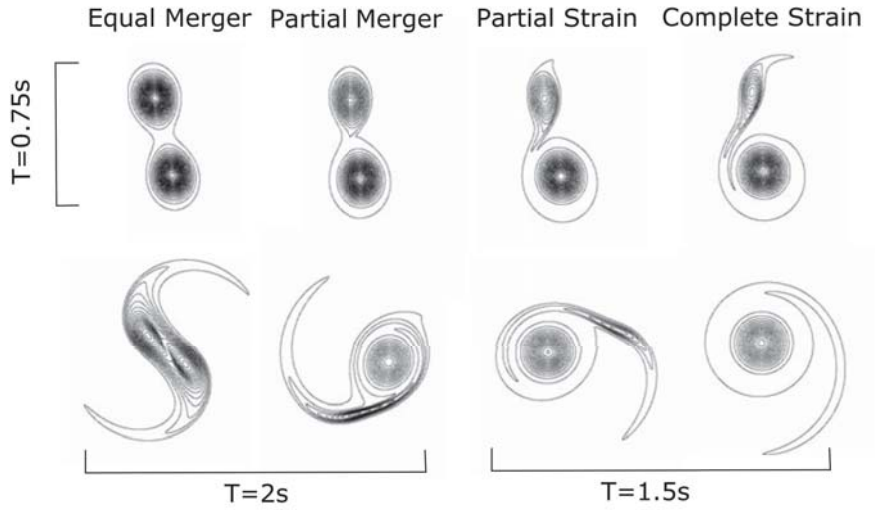

Figure 2.23: Vorticity contours for different types of unequal merger. Reproduced with permission from Brandt and Nomura [97].

Using inviscid contour method calculations, Dritschel and Waugh [98] found that the interaction between two vortices with a large difference in size results in the smaller vortex being torn away, with little increase in size of the larger vortex. This was identified as a regime of either partial or complete straining out. This is in contrast with more closely sized vortices, which often result in total core growth, under a regime they identified as complete merger or partial merger. The merging regimes were defined with respect to the normalised circulation

Table 2.1: Vortex merging regimes for unequal strength vortices

Regime	Γ1	Γ2
Elastic Interaction	1	1
Partial Straining	1	<1
Complete Straining	1	0
Partial Merger	>1	<1
Complete Merger	>1	0

of the two vortices, as can be seen in Table 2.1. In addition to this, equal or similar strength vortex interactions typically produce single vortices, while unequal strength interactions may produce two vortex systems.

A critical ratio of core radius and vorticity was also used by Yasuda and Flierl [99] in their transient contour dynamics calculations to characterise empirically the likely merging state. Numerical studies of such scenarios have also been performed [97], finding similar structures and regimes. The mechanism behind these straining actions is a combination of two causes. Firstly, the weaker vortex is stretched and drawn into the stronger vortex by a process of elongation [100]. Secondly, a continuous erosion of vorticity into the primary vortex is caused by the strong strain field and high shear, in a mechanism analytically observed by Legras and Dritschel [101].

The mechanism behind these straining actions is a combination of two causes. Firstly, the weaker vortex is stretched and drawn into the stronger vortex by a process of elongation, as seen by the water tank experiments of Trieling et al. [100]. Secondly, a continuous erosion of vorticity into the primary vortex is caused by the strong strain field and high shear, in a mechanism analytically observed by Legras and Dritschel [101].

Unlike counter-rotating pairs, co-rotating pairs do not exhibit long wave instabilities and are inherently stable with respect to the Crow instability. However, they still exhibit short wave (elliptic) instabilities. While the elliptic modes behave in the same sense as previously discussed in the counter-rotating section, in co-rotating pairs the growth rate of the instabilities is increased due to the rotation of the entire system [102]. As the Reynolds number is increased, the magnitude of the elliptic perturbations is increased within the vortices, becoming more unstable. When combined with an increased duration of the first diffusive stage at higher Reynolds numbers, this results in an increased contribution of the elliptic instability to the merging of the vortices. As found

through numerical studies by Laporte [103] and Deniau & Nybelen [104], this results in a more rapid merging than would be expected from laminar flow dynamics.

Devenport [7] found by wind tunnel testing of co-rotating vortices deployed from the same upstream location that the unmerged cores of a co-rotating pair were far more turbulent before merging than a single vortex core by itself. It was found that at a Reynolds number of 260000 based off chord length that the two cores continued to spiral around each other for 20 chord lengths after the vanes before merging into a single vortex core. This effect can clearly be seen in Figure 2.24. Once the two cores have merged the final structure was found to be larger and more axisymmetric than a single vane vortex. It is key to note that this study was performed using hot wire anemometry so disturbances in the vortex structure were likely caused. The hot wire measurements showed that post merging, the turbulence of the core was found to decrease, however the induction of a probe into the core would have increased the sensitivity of the vortices to instabilities. As the spacing between vortices increases, the merging distance is shifted further downstream [7, 8]. Increasing vortex swirl decreases merging distance, and also increases the amplitudes of vortex motion (meandering).

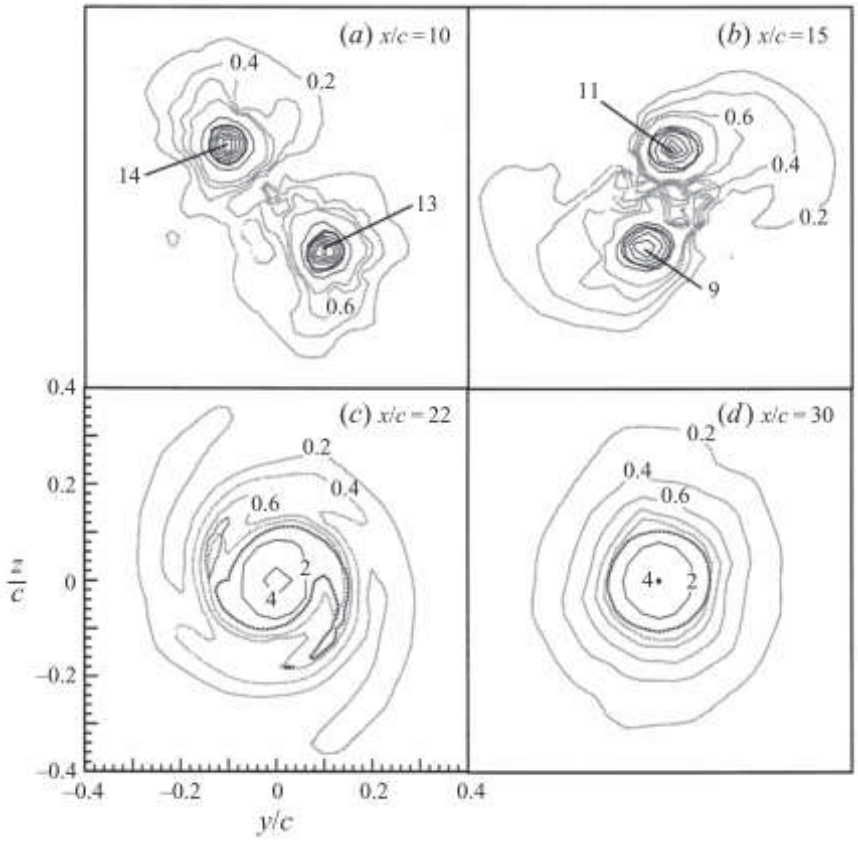

Figure 2.24: Progression of co-rotating vortex interaction, reproduced with permission from Devenport [7]

2.5 Vortex/Structure Interactions

In addition to the interactions between a pair of vortices, vortices may also be exposed to interactions with physical objects. Of particular interest to this study are objects that are producing additional streamwise vortices. As identified by Garmann and Visbal [6], there are considerably fewer studies available on streamwise vortex/structure interactions than either parallel or normal vortex/structure interactions, however a small number of these still exist. Garmann and Visbal [6] computationally investigated the interactions of a streamwise vortex with a wingtip at close range. A plate geometry at α=4 was used to model the wing, with a Reynolds number of 20000 based off chord length. The upstream vortex was imposed on the domain inlet and then shifted to observe the effects of different impingement positions along the wing. The vortices produced were of opposite sign. They found that aligning the incident vortex with the tip increased the energy of the vortex system in the near range,

however causes far more rapid energy attenuation downstream. When the vortex was positioned inboard of the tip, it split into two components above and below the wing, causing small separation bubbles and unloading the outboard section of the wing, reducing the tip vortex. When the vortex was placed outboard of the wingtip its flow enhanced the wingtip vortex strength within their domain. These flow regimes can be seen in Figure 2.25.

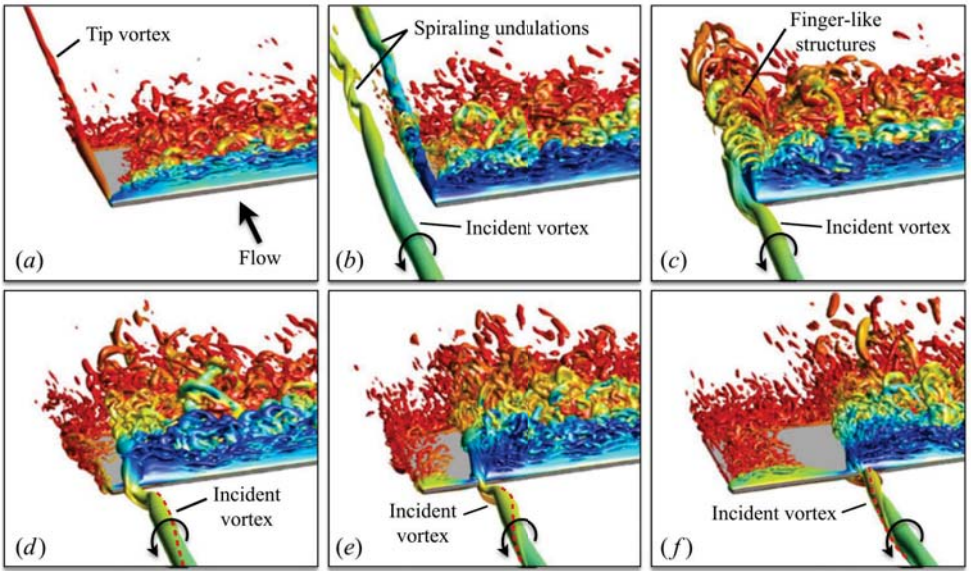

Figure 2.25: Flow structures for different positions of incident tip vortex. Reproduced with permission from Garmann and Visbal [6]

Inasawa et.al. [33] investigated the flowfield around two wings spaced 2.5C apart in the streamwise direction with 5% of the wingspan overlapping. It was found that such positioning notably improved the efficiency of the rearward wing, however it migrated the rear vortex towards the root of the rear wing. It was found that with maximum wing overlap the leading vortex impinged on the trailing wing and split into two smaller vortices, one on the top and one on the bottom. In this case, the leading vortices caused destructive interference with the vortex produced by the trailing wing, reducing total circulation. By raising the height of the leading wing with respect to the trailing wing, they were able direct the lead vortex onto the top near-root surface, where it interacted and produced a separate counter rotating vortex pair as can be seen in Figure 2.26. If this vortex was then directed at the outside edge, smoke visualisation showed that the breakdown point of the leading wing vortex was actually found to be behind that of the trailing wing vortex, as can be seen in Figure 2.26.

Pasche et. al. [32] investigated the effects of a sphere placed in the trajectory of

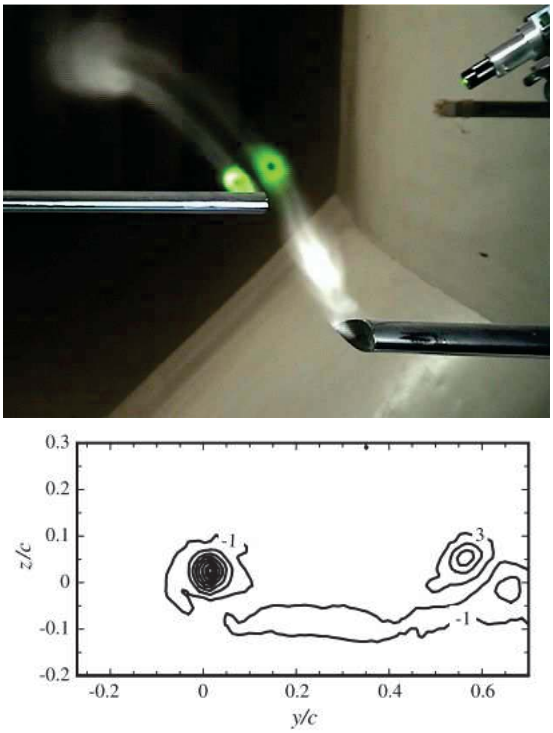

Figure 2.26: Smoke testing of wingtip vortex interactions and LDA of vorticity over rear wing when the vortex was targeted at half span (wing root to the right). Reproduced with permission from Inasawa et. al. [33]

a vortex generated by an elliptical vane in a water tunnel. Microscopic hydrogen bubbles were released from the vane tip to visualise the vortex core and determine the location and type of breakdown mode as illustrated in Figure 2.27. Similarly to other studies, it was found that the vortex breakdown location was dependent on the swirl number (controlled by the angle of incidence of the vane) and the adverse pressure gradient (controlled by the location and size of the obstruction). With no obstacle placed behind the vortex no breakdown was observed, with only slow diffusion of the core observed. It was observed that the short duration adverse pressure gradient generated by the sphere was directly linked to the breakdown location, with larger spheres and moving the sphere upstream causing the breakdown location to move upstream. The authors hypothesised that this may be due to the balance between the centrifugal force generated by the core pressure gradient and the dissipation of pressure through the region of adverse pressure gradient. However, they emphasised that further work needed to be performed on this.

Figure 2.27: Interaction of elliptical wingtip vortex with sphere in the wake, reproduced with permission from Pasche et. al. [32]

2.6 Summary

This thesis will address two primary gaps in literature. While the mechanism of vortex merging in the co-rotating case has been substantially investigated, there is a distinct gap regarding the behaviour of vortex merging when a vortex is induced into a flow downstream of a pre-existing vortex. While it is expected that these vortices will behave like an unequal strength vortex pair and merge, it is not known what the effects will be of the structure which generates the second vortex, such as wing wakes and how this affects the merging process. Also, this scenario has only been significantly investigated with ideal vorticity distributions, instead of vortex shapes indicative of real-world wing-tip vortices, as used in flow control vanes. Axial velocity components have not previously been modelled in analytical evaluations of partially strained and uneven vortex merger. As such, it is important to experimentally and computationally observe the energy and merging properties of realistic vortices under varying conditions. Such a condition that has not been investigated is that of offset, which is equivalent to a yaw or a crosswind in a real world case. This is a scenario that may prove beneficial in the re-energisation of vortices as they travel downstream, as in some flow control applications the vortex breakdown distance is desired to be lengthened and its position better controlled, as well as circulation increased downstream of initial vortex generation.

The final identified gap in the literature is that investigating the premature

breakdown of a pre-existing vortex. Again, the various instabilities in vortex pairs have been thoroughly investigated, as well as instabilities in unequal counter-rotating vortex pairs. However, whether or not the vorticity of a pre-existing vortex can be significantly reduced by a downstream vane through either direct action with the vane or interactions between the subsequent pair has not been studied. An indication of the transition offset at which the vortex interaction changes would be of use to the design of flow control devices, as well as the advancement of aircraft wake vortex breakdown. Additionally, characterisation of the circulation properties of the subsequent vortex pairs at different proximities is distinctly missing from the literature, and would be of use to the aforementioned fields.

Chapter 3

Experimental Facilities

Experimental testing allows a large number of cases to be tested quickly, and facilitates the capture of precise vortex positions, paths and energy transfer. Experimental measurements of flow characteristics can be performed by either intrusive methods such as pitot rakes, hot wire anemometry and cobra probes or non-intrusive methods such as Laser Doppler Anemometry (LDA) or Particle Image Velocimetry (PIV). While intrusive methods allow direct measurement of flow parameters such as pressure and velocity fields, the presence of the probe causes the flowfield to be affected. While often acceptable for wake measurements, in the case of vortices, an induced gradient in the freestream will be substantially increased at the vortex core [35]. This can cause issues such as increased vortex meandering or reduced breakdown distance, and as such non-intrusive measurements must be used to ensure accurate results in flow fields dominated by vortex interactions and instabilities. Of these non intrusive methods, LDA is only a point measurement, whilst PIV is a field measurement. Consequently, PIV can measure instantaneous flow fields while LDA is only capable of resolving the instantaneous flow at a point or a time averaged field. As it was desired to measure the quantitative paths, circulation transfer and magnitude of vortex meandering, PIV was selected as the measurement method. The primary component of vortex motion is across the streamwise direction, and consequently two component PIV was used with planes across the primary direction of motion. This produced a unique set of challenges due to the large out of plane component of motion, and these will be discussed in this chapter.

3.1 Wind Tunnel

Experiments were performed in the Macquarie University open return, closed section wind tunnel. This tunnel has a 610 x 610 mm (24 x 24 inch) octagonal test section with a 1900 mm (6' 3") length. Optical access is through a glass window on the top of the test section and removable windows on the side. The contraction ratio is 5:1 over an inlet length of 1524mm. The tunnel is capable of speeds between 10m/s and 40m/s, however vibrations become significant at speeds exceeding 17 m/s, as will be discussed in later in this chapter. Images of the tunnel can be seen in Figure 3.1.

Figure 3.1: Images of wind tunnel exterior.

One of the key features of this tunnel is it's long diffuser section with a total length of 2.5 times the test section length. This allows a camera to be placed in the diffuser section well downstream of the test section, minimising flow disturbances. The fan housing is connected to the diffuser via means of a flexible coupling, reducing the vibrations passed directly through to the tunnel by the fan. The expansion ratio of the diffuser is 4:1.

3.1.1 Flow Characterisation

The test section was characterised using a Turbulent Flow Instrumentation 100 Series Cobra probe, giving a peak turbulence intensity of 0.35% outside the boundary layer and average of 0.25%. Velocity uniformity was measured as better than 1% variance outside of the boundary layer. Flow angularity was found to vary by a total of less than 1 degree across the test section inlet. The results of this characterisation can be seen in figs. 3.2 to 3.5.

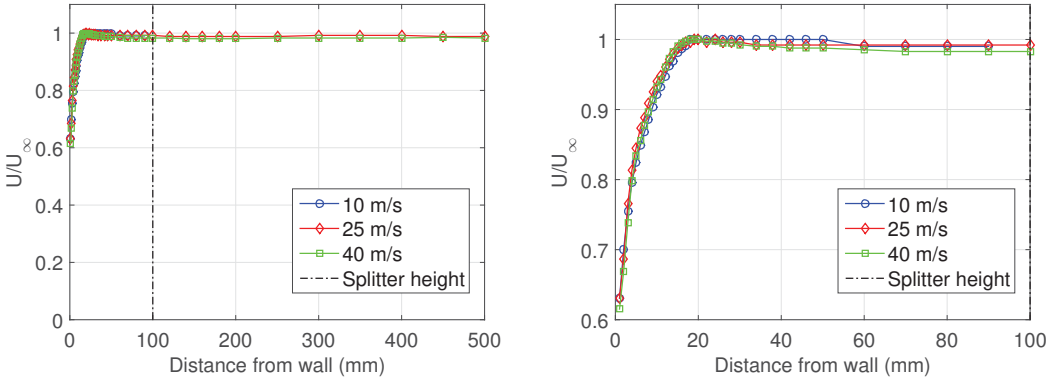

Figure 3.2: Normalised velocity across the test section inlet, right view zoomed.

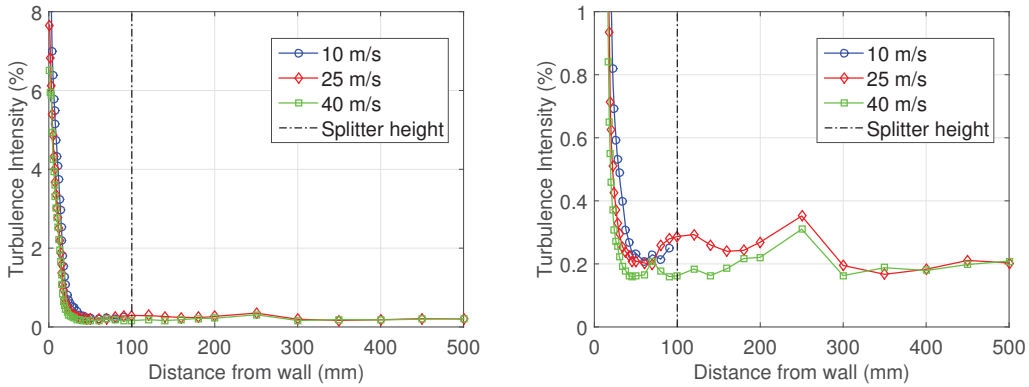

Figure 3.3: Turbulence intensity across the test section inlet, right view zoomed.

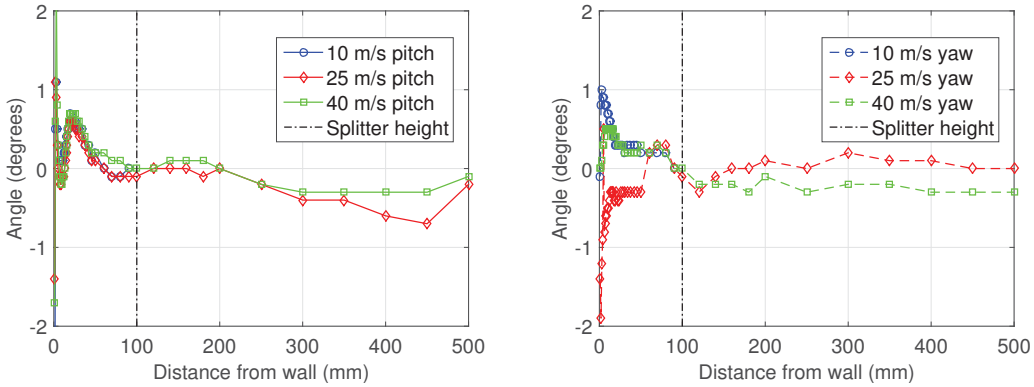

Figure 3.4: Pitch (left) and yaw (right) flow angle across the test section inlet.

3.1.2 Tunnel Control Accuracy

The wind tunnel speed was electronically controlled through a National Instruments MyRIO, with the pressure sensors calibrated against a temperature controlled Baratron 120AD Differential Capacitance Manometer. Streamwise

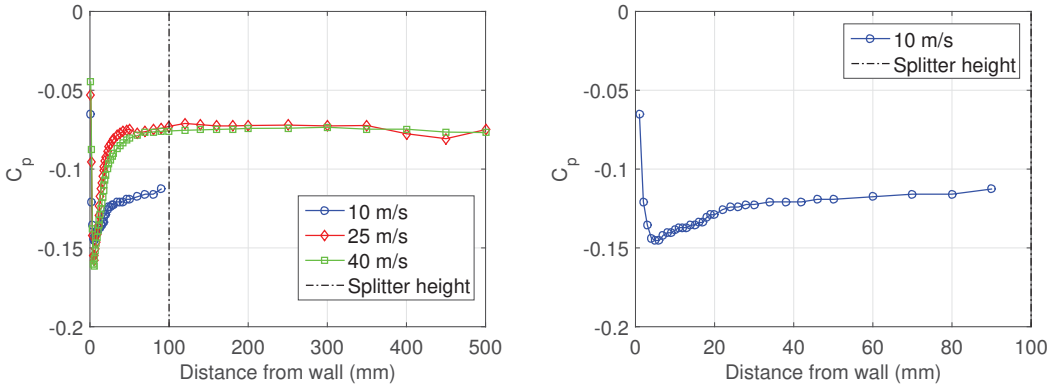

Figure 3.5: Pressure across the test section inlet, right view zoomed.

velocity variance was held to within 0.38% during tunnel operation by a PID control system. The air humidity, barometric pressure and temperature were all monitored continuously to ensure Reynolds number consistency. While the large variance in atmospheric conditions during the period the experiments were conducted over caused a significant variance in Reynolds numbers of 6×10^3, the Reynolds number never fell below 6.5×10^4, hence the shedding regime was consistent as discussed below.

3.1.3 Reynolds Number and Dimensions

The experiment was performed at a Reynolds number of approximately 7×10^4 based on chord length. Huang et. al. [105] found that above 6×10^4 the vortex shedding from a NACA0012 airfoil at 8 degrees angle of attack is within the supercritical region, and therefore any Reynolds number lower than at this angle of attack will result in a shedding regime that is not indicative of higher Reynolds number scenarios, and may result in undesirable transitional effects. Running the tunnel as slow as possible within the acceptable Reynolds number range minimised vibration of the diffuser expansion, camera mounting and test section caused by the operation of the fan, thus minimising imaging error. This Reynolds number also correlated with that of the LES, which will be discussed further in the next chapter.

3.2 Experimental Rig

3.2.1 Overview

In order to investigate the upstream/downstream interactions of two vortices, an experimental rig capable of mounting two vanes in adjustable positions and measuring the resultant flowfields needed to be produced. In order to resolve the domain in three dimensions to track vortex energy levels and paths, a system utilising a traversing laser sheet was devised, as seen in figs. 3.6 and 3.7. A laser arm carried the beam from the stationary laser to the movable sheet optics, allowing rapid repositioning of the laser sheet. The camera was mounted in the expansion section of the tunnel, far from the model, to minimise projection error and aerodynamic disturbance.

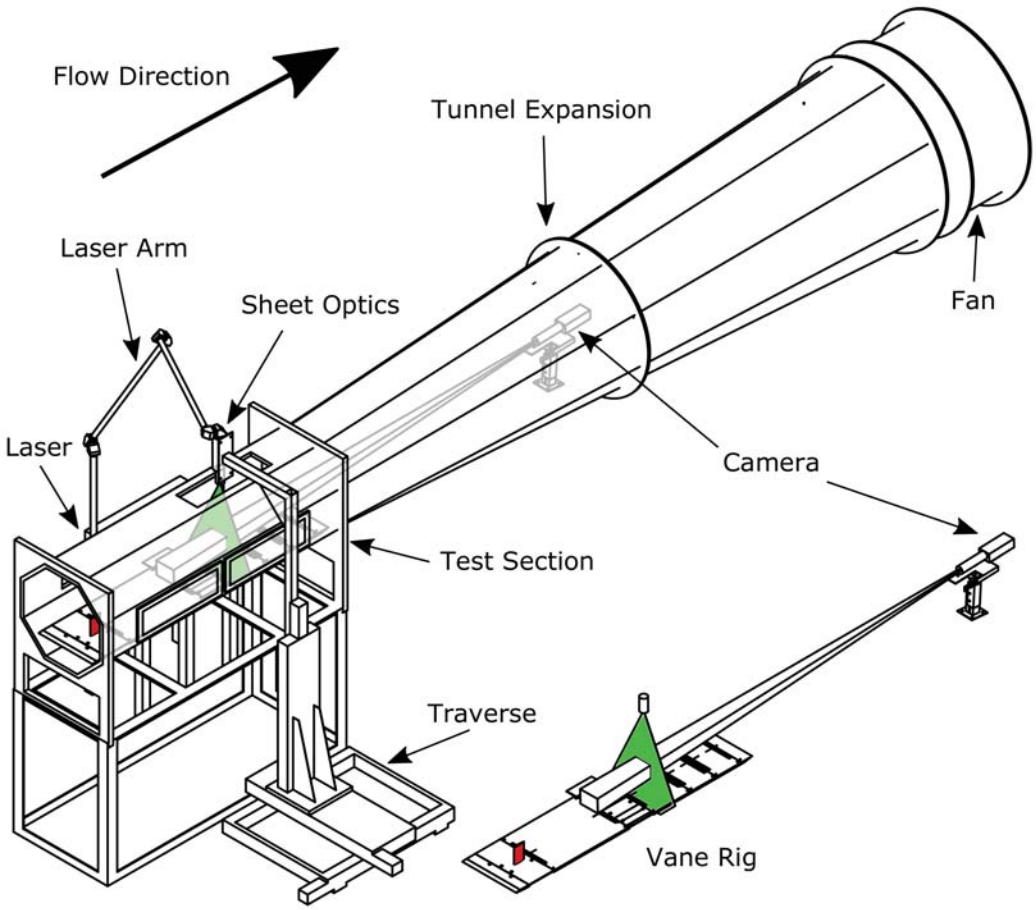

Figure 3.6: Overall experiment layout.

The vane rig itself had to cover a number of design constraints:

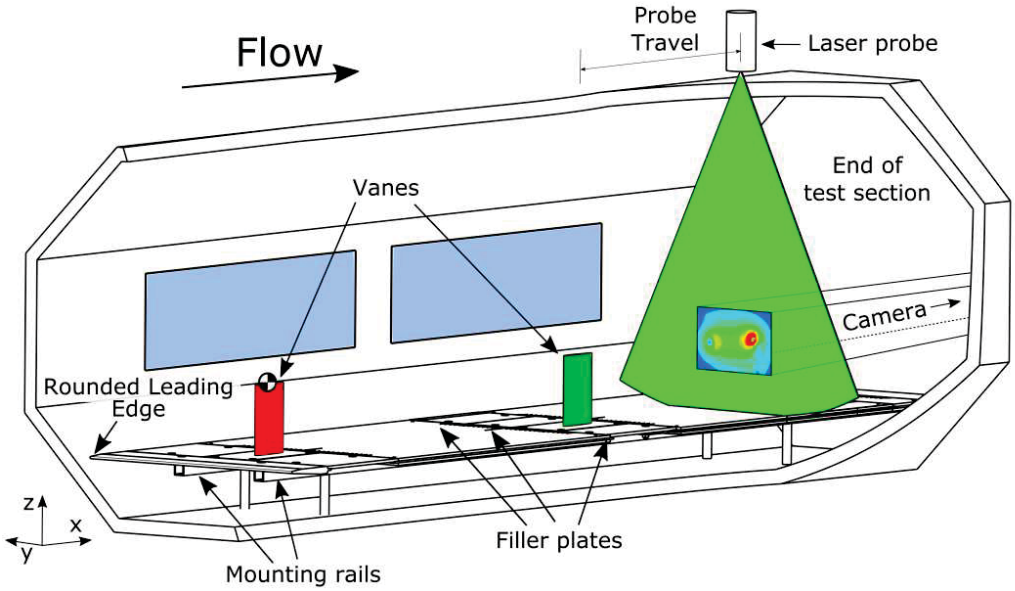

Figure 3.7: Cutaway of test section. Origin is on quarter chord tip of the leading vane, as shown.

- Fit through the tunnel side window
- Allow quick and accurate adjustment of vane position
- Allow rear vane displacement whilst maintaining a continuous floor profile
- Allow reconfiguration to different offset spacings and vane configurations if required in the future
- Minimise boundary layer thickness at the vanes

To fulfil these goals, a system of matte black acrylic plates mounted on steel rails with aluminium filler plates was devised, and can be seen in Figure 3.8. The rails are suspended above the tunnel floor by support posts, with the primary splitter plates being bolted to the rails. A splitter with a rounded leading edge is at the front, as will be discussed in the following section, with a slotted rear edge to allow the vane plate to be fitted flush. The rear vane location is adjusted by sliding the rear vane plate from side to side, with measurement performed via a laser etched ruler embedded in the acrylic plate. This gave an error in lateral vane offset adjustment of $\pm$ 0.005C (10% of the smallest offset change). The gaps at the side of the rear vane plate were then filled with aluminium filler plates of various sizes, and all bolt holes were covered in tape to minimise flow interference. The rear acrylic plates were slotted and mated together such that

they created a continuous surface whilst still being able to be inserted through the constraints of the 610mm x 165mm side window size. Further details of the experimental rig can be seen in Appendix A.

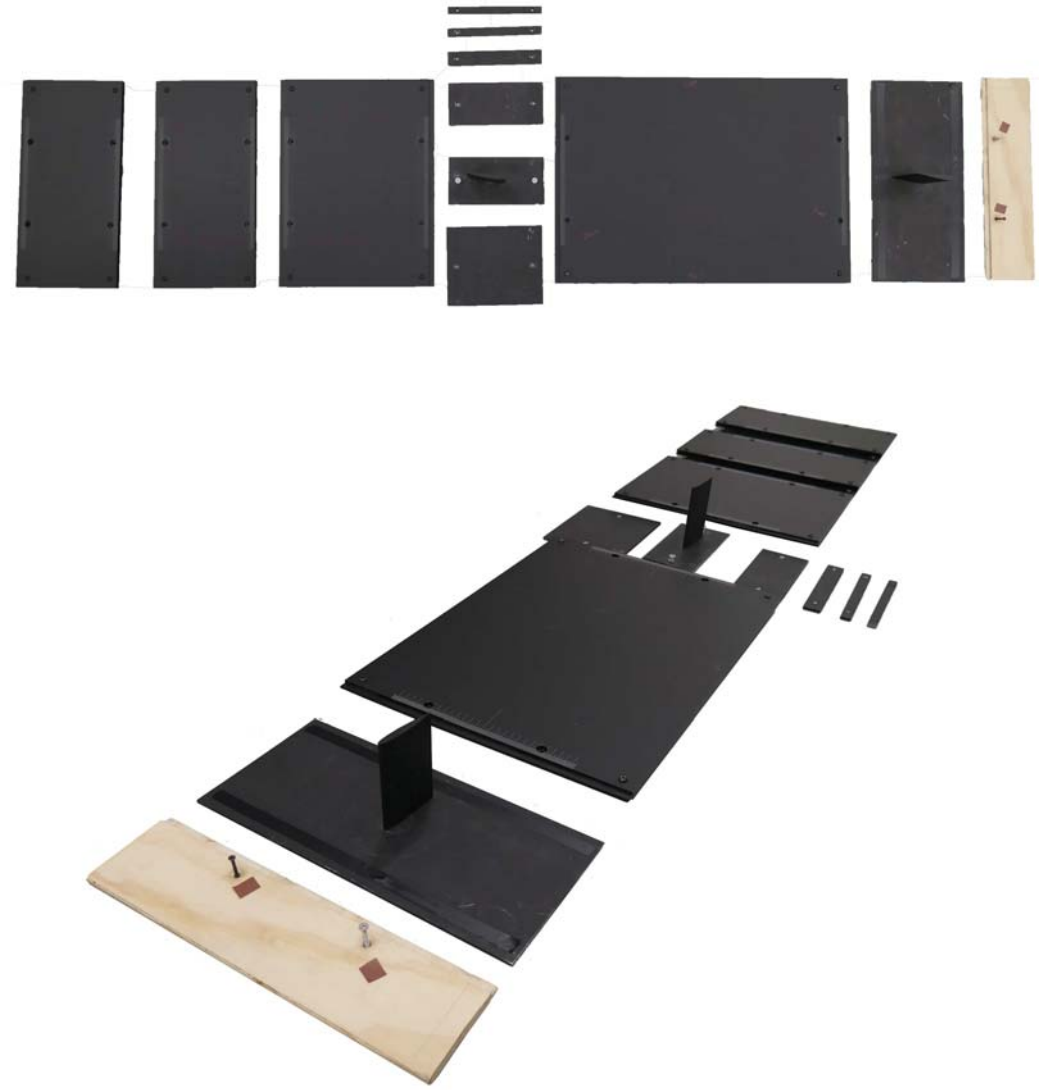

Figure 3.8: Rig plates disassembled

The strength of a vortex produced by a wing for a given planform area is related to the aspect ratio and angle of incidence of the wing, as per Prandtl's Lifting Line Theory [106]. However, for the purposes of these experiments it was desired that the vortices would be sufficiently clear of any boundary layer formed, thus necessitating a higher aspect ratio than commonly used vortex generators. These boundary layer interactions can produce secondary structures from both the stripping of the boundary layer by the primary vortex and the horseshoe vortices produced by the front of the vane [107]. An aspect ratio of 1.5 was selected to allow a strong vortex for the total area to be produced,

whilst still keeping the vortex clear of the boundary layer. The same aspect ratio has been previously used by Igarashi [108], with similar ratios used by others [109–111]. Preliminary CFD and Lifting-line calculations showed that the maximum force predicted on the vanes was in the range of 0.457N for the front vane and 0.635N for the rear vane. These low forces meant no structural issues were expected for 3D printed vanes, and vane deflection would not be a concern.

A NACA0012 profile was chosen due to the abundance of data on it and it's vortices for non interacting cases [108, 109, 112, 113], as well as it's symmetry which allowed quick changes of co and counter-rotating configurations. The vanes were originally produced from extrusion formed 3D printed PLA, with a tolerance of ± 0.05 mm, with profile accuracy verified by a shadowgraph. These were painted with a matte black paint to reduce reflections. An aluminium vane was CNC machined at a later date for comparison, with no observable difference seen between the two in wind tunnel measurements of single vane characteristics. Both sets of vanes were threaded with a single M6 hole underneath at the quarter chord to allow fitment to the experimental rig, as can be seen in Figure 3.9. Vane angle was adjusted using a digital protractor, before the bolt was tightened and the angle was verified.

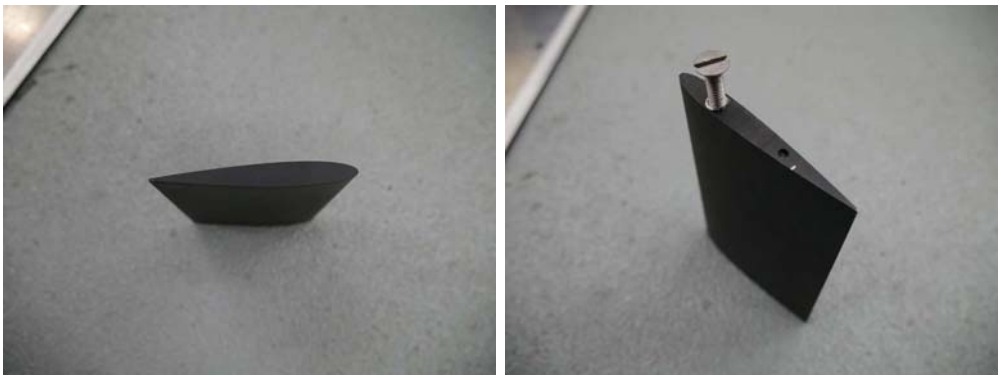

Figure 3.9: Vane profile and mounting detail.

Angles of attack of 2-14 degrees at 2 degree increments for the single upstream vane were investigated to see where the location of breakdown would occur. At 14 degree incidence, breakdown was severe, with 50% lower initial peak velocities than the 12 degree case, and a drop in peak velocity of 17% across the measurement domain. Inspecting the circulation values in Figure 3.10 showed that there was an approximately linear rise in circulation as angle of attack increased, with negligible circulation loss through the domain. However, at the

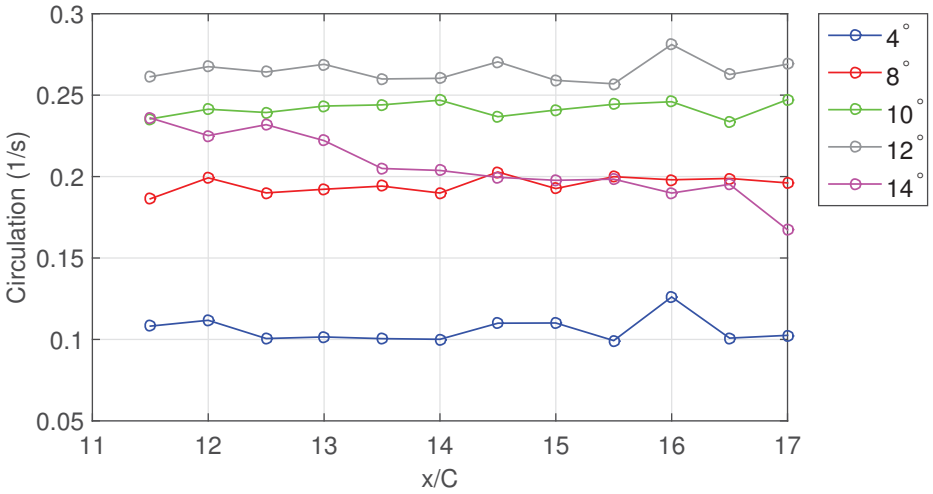

Figure 3.10: Circulation values for different single vane angles of attack.

14 degree angle of attack there was a significant reduction in initial circulation of 10% compared to the 12 degree case, followed by a significant dissipation rate. When the RMS values were inspected, it was found that both the 14 degree and 12 degree cases were substantially higher than the other cases at RMS peaks of 1.8m/s and 1.7m/s respectively, consistent with the high levels of meandering observable in the image capture. Both the 8 degree and 10 degree cases had RMS peaks below 0.6m/s, indicating significantly smaller meandering and transient breakdown. As such, either of these angles would be suitable for testing, however as discussed before 8 degrees is a conservative angle for stall and places the vanes in a suitable vortex shedding regime.

The entire rig mounted in the tunnel can be seen in Figure 3.11.

3.2.2 Splitter Design

The wind tunnel inlet and test section produces a boundary layer, which reduces the average velocity the vane sees, thus lowering the strength of the vortices and potentially introducing secondary effects that are outside of the primary vortex cores we wish to observe. As such, it is desirable to have the boundary layer thickness at a minimum at the location of the vanes. In order to achieve this, a raised splitter plane was used in the tunnel. Multiple splitter designs were tested using 3D CFD of the tunnel section, to ensure minimal interference of the splitter with the net tunnel flow, and the thinnest boundary layer possible. These CFD

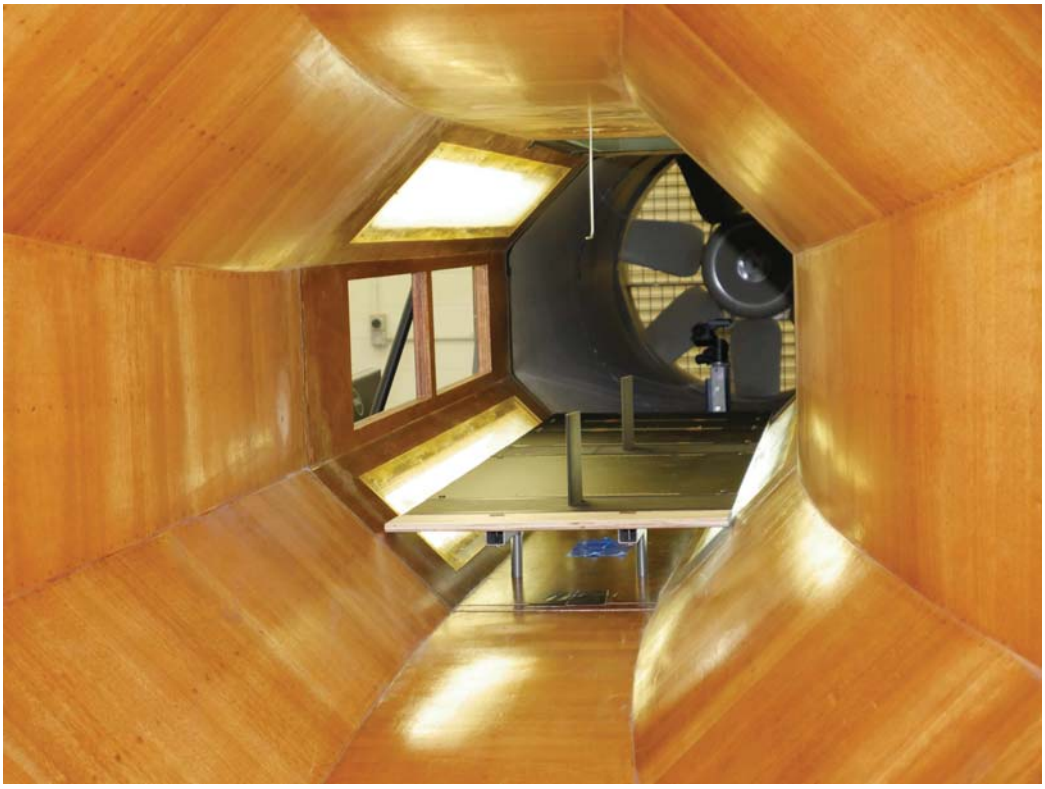

Figure 3.11: Rig assembled in tunnel.

results can be seen in figure Figure 3.12. It was found that the rounded splitter profile provided the best performance, with an equally rounded splitter profile being the easiest to manufacture.

The boundary layer above the experimental rig was characterised using the previously discussed 5 hole cobra probe. The results of the characterisation can be seen in figs. 3.13 to 3.15. This gave a boundary layer height at the location of the rear vane of 5mm thick at 80% of the freestream velocity and 20mm thick at 95% of the freestream velocity. The variations in the plots with the front vane present near the vane tip height are the result of the probe measuring the vortex form the upstream vane.

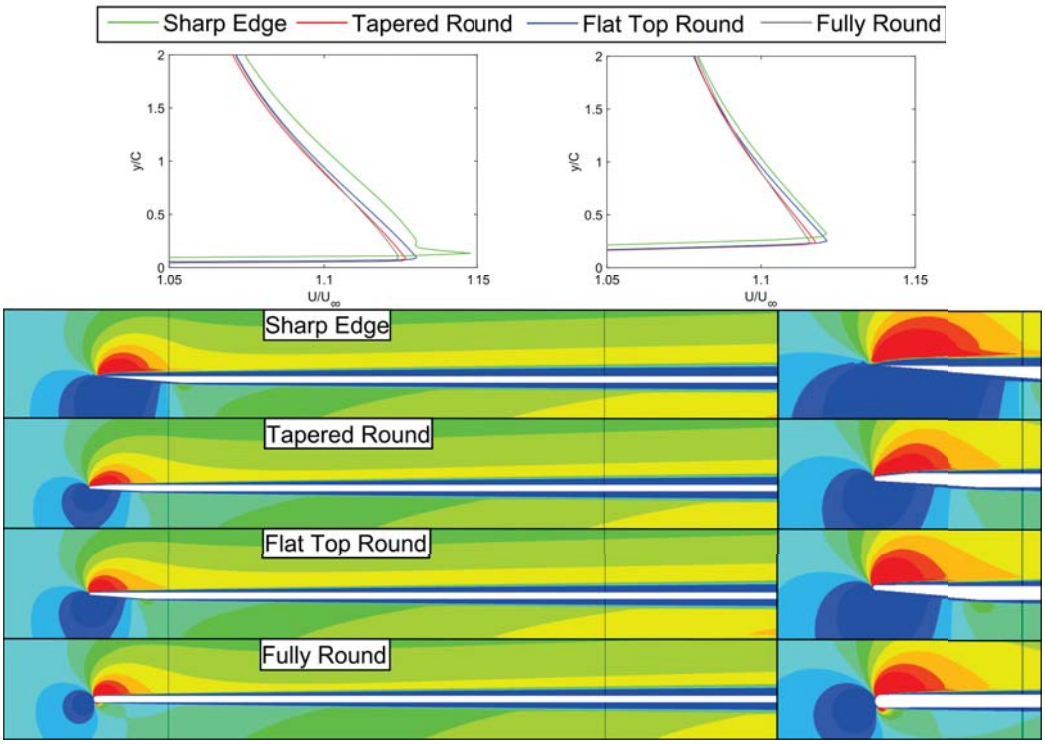

Figure 3.12: Splitter leading edges and resultant velocity profiles in CFD. Note the thickened boundary layer and increased upper flow velocities in the sharp case.

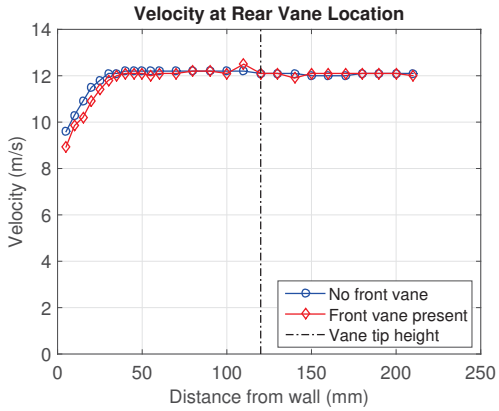

Figure 3.13: Velocity profiles at rear vane location with splitter in tunnel.

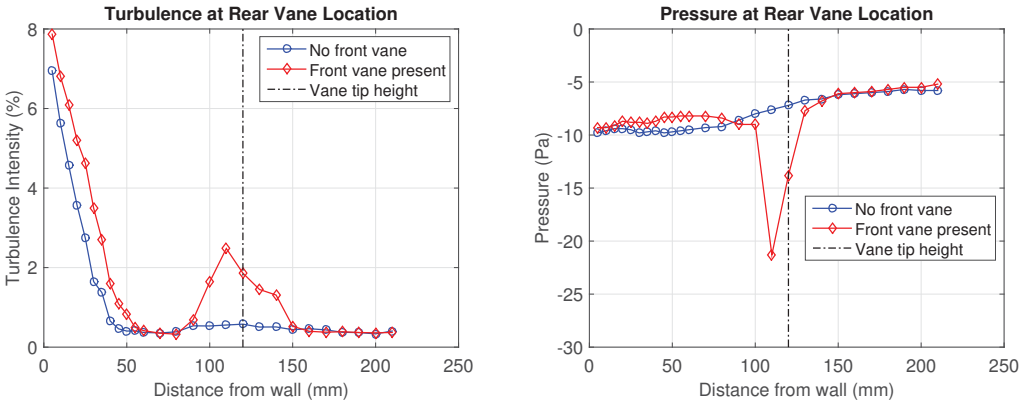

Figure 3.14: Turbulence (left) and pressure (right) profiles at rear vane location with splitter in tunnel.

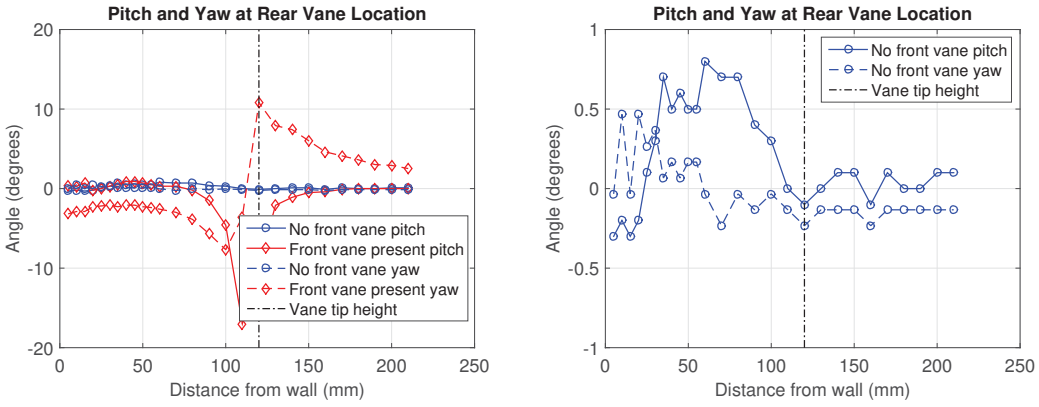

Figure 3.15: Pitch and yaw profiles at rear vane location with splitter in tunnel.

3.3 PIV Setup

3.3.1 Camera Setup

Scattered laser light was captured by a monochrome cooled CCD pco.1600 camera with 1GB of RAM. Images were digitised at 14 bits, with a resolution of 1600x1200 pixels. The camera was fitted with a 120mm lens. The CCD size on the camera was 12.5mm wide x 9.38mm high, giving a field of view at the most downstream plane of approximately 100x133mm. While the tunnel was in operation the camera was not accessible, so in order to focus the camera a remote focussing system was devised. This consisted of a servo actuating a pushrod connected to the focus ring on the lens, and can be seen in Figure 3.16. The camera mount was adjustable to allow for camera positioning up and down to keep it in line with the rear vane tip.

Figure 3.16: Camera mounting detail.

3.3.2 Particle Seeding

Seeding was performed with a PIVtech generator using Di-Ethyl-Hexyl-Sebacat (DEHS) air soluble particles of 0.2-0.3μm typical diameter. The seeder was aimed at the outlet of the tunnel to promote maximum mixing throughout the room, as can be seen in Figure 3.17. This minimised erroneous peaks caused by regions of uneven seeding that were identified through initial testing. The ability of a particle to follow a flow is defined by its Stokes Number, with details of this calculation seen in eqs. (3.1) and (3.2).

$$S_{tk} = \frac{\tau_0 * u_0}{l_0} \tag{3.1}$$

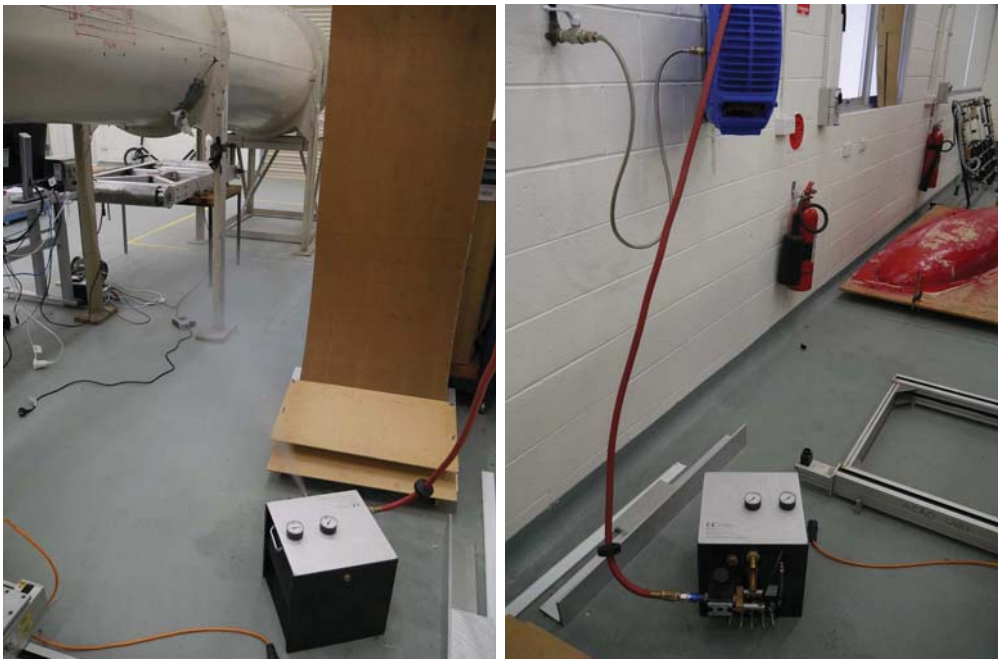

Figure 3.17: Particle seeder and location.

Where u_0 is the flow velocity of 12m/s, l_0 is the length of the object (0.08m), and t_0 is represented by eq. (3.2).

$$\tau_0 = \frac{\rho_p * d_p^2}{18 * \mu_g} \tag{3.2}$$

where ρ_p is the particle density of $912 kg/m^3$ for DEHS, d_p is the particle diameter of $0.25 * 10^{-}6$m, and μ_g is the dynamic gas viscosity of air, $1.983 * 10^{-}5$. This gives a τ_0 of $1.597 * 10^{-}7$. Substituting these values in gives a Stokes number of $2.396 * 10^{-}5$ for the DEHS particles used. If the Stokes number is greater than 1, particles will detach from a flow especially where it decelerates abruptly, if it is below 1 particles will follow fluid streamlines closely [114]. If the Stokes number is less than 0.1 the particle tracing errors are below 1%, as such the DEHS particles will track the flow very effectively.

Due to the rotating nature of vortex particles are displaced from the core due to centripetal effects. In order to maximise the number of particles inside the vortex core, significant premixing of the particles with the mean flow was desired. This was performed by aiming the seeder at the outlet of the tunnel, allowing the seeding to fill the entire room. Seeding levels were monitored on the live images and compared to the existing reference images to ensure they

were above the critical level. By varying the dynamic range selected from the image, a minimum of 5 particles per 32x32px interrogation window was maintained, keeping the probability of a valid vector detection above 90% as can be seen in Figure 3.18.

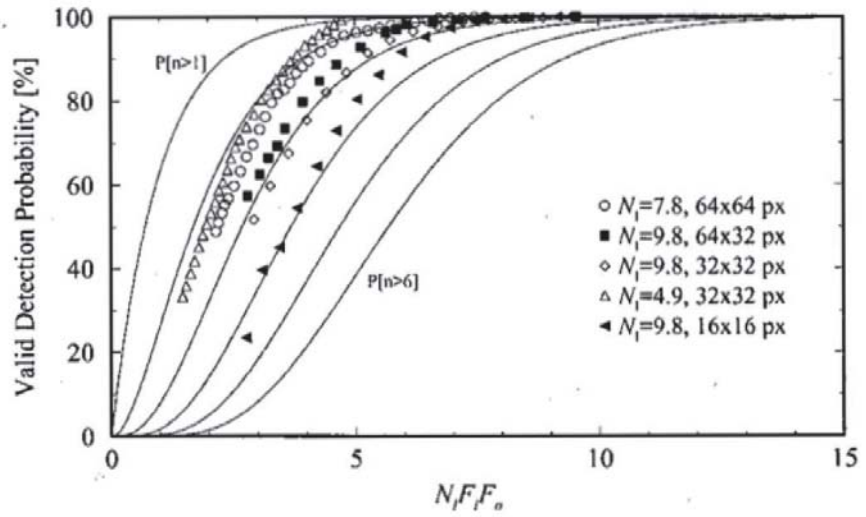

Figure 3.18: Vector detection probability as a function of the product of image density, in-plane loss of pairs and out of plane loss-of-pairs on the x-axis. The solid line represents the probability of having at least a given number of particle images in the interrogation spot. Figure originally from Raffel et.al. [115]

The seeding levels of the room were also evaluated to ensure convergence of values, with the results in Figure 3.19. From these results it was clear that the minimum seeding resulted in a bias towards less circulation, caused by the reduction in magnitude of the velocity vectors. The seeding was maintained above 5 particles per interrogation window within the vortex core for the experiments to ensure minimal seeding errors.

3.3.3 Traverse

The laser beam periscope was connected to a Dantec 3-axis computer controlled traverse. This traverse was restricted to only allow laser sheet movement along the axis of the tunnel. The traverse and laser setup can be seen in Figure 3.20. To minimise the impact of vibrations on imaging plane location the traverse was allowed to come to rest for 10 seconds before imaging was commenced after a planar location change. The imaging planes used for the experiment can be seen in Figure 3.21.

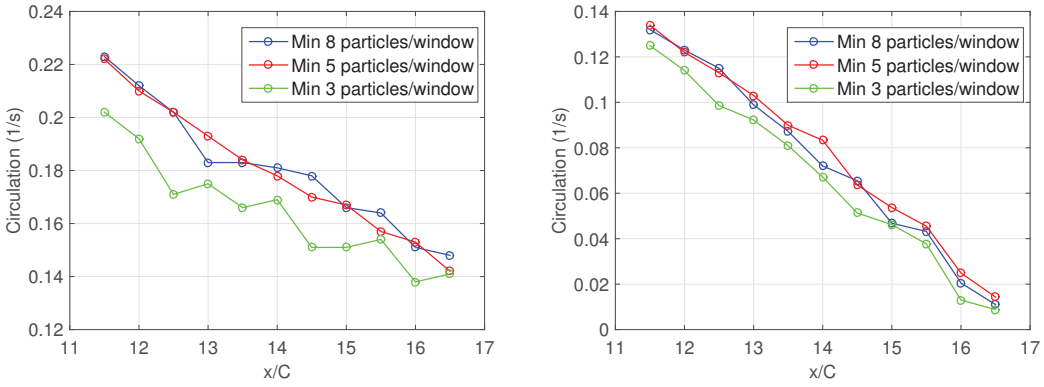

Figure 3.19: Positive (left) and negative (right) circulation decay plots for various seeding levels.

Figure 3.20: Laser (left) and traverse (right) setup.

3.3.4 Laser

Laser access to the tunnel was through a glass window in the top of the test section. The laser beam was sent to this location via a periscope. The laser used was a dual-cavity Nd:YAG laser (Quantel EverGreen) with an output of 200mJ per pulse at 532nm wavelength and a repetition rate of 15hz. Synchronisation between laser and camera was performed with an ILA synchroniser. Laser pulses were delivered at 55μs apart as any higher resulted

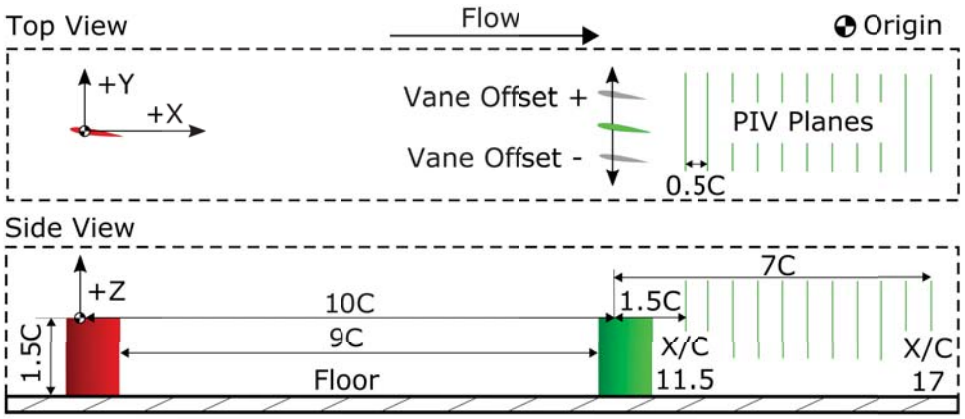

Figure 3.21: Schematic of vane and laser sheet locations.

in significant out of plane migration of particles. The laser sheet thickness varies throughout the observation window as a result of the focus, with an average thickness of approximately 4mm through the region of interest.

3.3.5 Calibration

Calibration of the camera was performed using a grid that was photographed at all analysis plane locations, compensating for the increase in plane size due to perspective. The plane was located using the laser sheet, and then photographed to give an accurate scale.

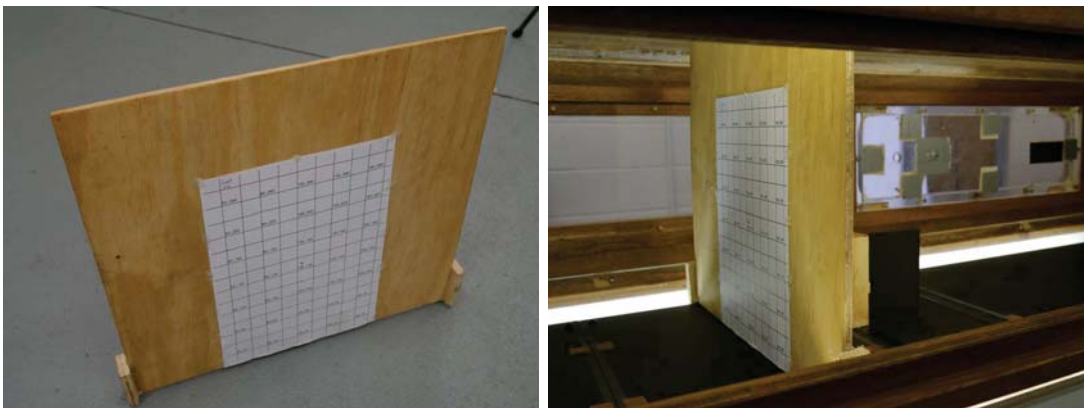

Figure 3.22: Calibration plate and stand.

3.3.6 Analysis Configuration

Image analysis was performed with PIVView software. Multi grid interpolation was used, starting at a coarse grid size of 128px x 128px windows and finishing with refinement to 32px x 32px over 3 passes. Standard FFT correlation was used, with two repeated correlations on 16px offset grids being performed. Subpixel shifting was enabled on all passes with b-spline interpolation and peak detection by a Gaussian least squares fit from 3 points. The final grid size was 99 x 74 nodes. The vectors were validated over 5 passes, with a maximum displacement threshold of 10px and a maximum displacement gradient of 3.0px.

3.4 Experimental Uncertainty

Due to the nature of the manual focussing system there were induced errors, with differences in focus able to produce up to 0.04C error in core location. By implementing a particle pixel size threshold of no more than 2px at a brightness level of 4.5% of the total dynamic range, this error was reduced to 0.0015C in core location. Total error due to the calibration plane procedure was found to be a maximum of 0.18% in location and 0.22% in scale, due to minute differences in lateral calibration plane location. The particle size was measured at an average of 1.5px, giving an uncertainty in position of 0.03px [115]. Quantization errors were negligible due to 14 bit quantization. Any biases inherent in each run were minimised by having the each set of 400 images taken with one forward run of 200 images (plane moving from X17 to X11.5) and one backward run in the opposite direction; this way any errors in seeding or focus would be minimised. The total error in core location was found to be $\pm$ 0.006C. The error in lateral vane offset adjustment is $\pm$ 0.005C (10% of the smallest offset change).

Table 3.1: Experimental error sources

Error Source	Circulation	Position
Calibration	0.22%	$0.0025C$
Focus	3.1%	$0.0015C$
Particle Tracking	≈ 0	≈ 0
Projection	≈ 0	≈ 0
Temporal	3.7%	$< 0.001C$
Vibration	≈ 0	$< 0.001C$

3.4.1 Temporal Convergence and Repeatability

In order to determine the temporal convergence of the image pairs in the time averaged case, a sample of 1000 image pairs was captured in the Counter 0C case, and then analysed in batches of 50, 100, 200, 350, 500, 750 and 1000. The results of this testing can be seen in Figure 3.23. Below 200 image pairs the variation in circulation is significant, while the core location remains relatively constant for all cases. Final sampling error for averaged results was determined to be a maximum of 3.7% in circulation for the 400 total shots taken against a multiple representative sample of 2000 image pairs.

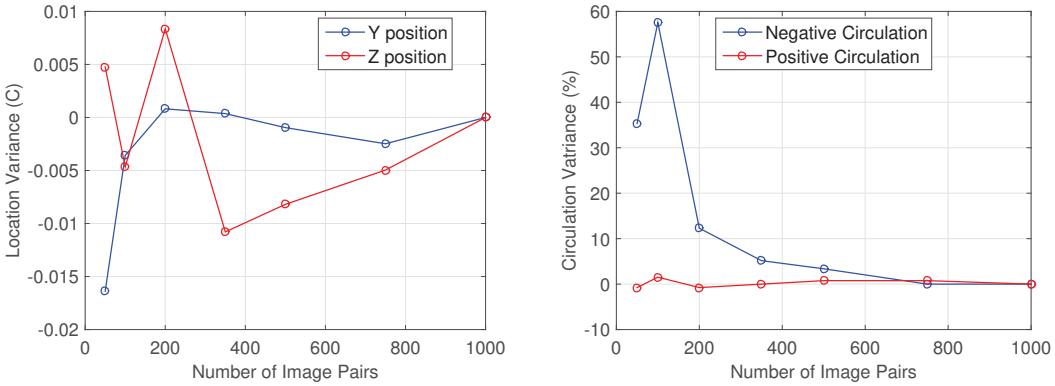

Figure 3.23: Core location (left) and circulation (right) vs. number of image pairs taken.

3.4.2 Projection

The camera was positioned 2100mm downstream of the test section and 2380mm to the nearest image plane, giving a maximum perspective bias of 1.6 degrees per side on a 133mm wide observation plane with a 120mm lens. Planar PIV can produce projection errors when the out of plane motion is dominant [116] However, this can be substantially reduced by lowering the perspective error from the camera, reducing the motion to as close to the in-plane component as possible. For the comparison setup 2D and stereoscopic PIV of Yoon and Lee [116], it was found that a camera with an effective perspective angle of 5.71 degrees per side could produce an absolute maximum error of 20.8% in instantaneous in-plane velocity where the out-of-plane component was proportionally large in a vortex driven flow. By reducing this angle to 1.6 degrees through placing the camera much further away and using a zoom lens, the maximum projection error is

reduced to 5.8% under the same conditions. It should be noted that this error is at the edges of the observation window, and is not indicative of the errors near the centre, which will approach zero projection error as the centre is reached.

While the maximum error in the velocity field is 5.8%, the substantially higher velocity gradient in the vortex core compared to the projection error reduces the vorticity errors to near zero. To demonstrate this phenomenon a sample perspective bias representative of a streamwise aligned freestream flow was imposed on one of the PIV captured flowfields. The original velocity field can be seen in Figure 3.24A, with the velocity field resulting form the projection error seen in Figure 3.24B. Performing the vector sum of these two fields produces the velocity field in Figure 3.24C, as per Equation 3.3.

$$\overrightarrow{C} = \overrightarrow{A} + \overrightarrow{B} \tag{3.3}$$

Performing a scalar subtraction of the velocity magnitudes from these two fields (A - C) produces the velocity differential contour in Figure 3.24D. Note that the velocity magnitude differential (D) does not directly correlate with the projected velocity field (B), as the projected field is radially expanding in a uniform direction, while the velocity field direction is more randomised. When a vector addition and scalar subtraction is performed this leads to the differential result.

The resultant differences in the horizontal and vertical velocities can be seen in Figure 3.24E and F, with the initial velocity indicated by the contour bands and the velocity with the influence of projection error shown by the contour lines. Clear magnitude differences can be seen between the two, with the bands shifting. However, as the velocity gradients have not significantly changed the vorticity field shown in Figure 3.24G and H shows negligible variance between the original field (colours) and field with projected error (lines). The calculated total circulation of the original case was $0.3324786 m^2 s^{-1}$, with the circulation of the projected case being $0.3324786 m^2 s^{-1}$, resulting in a maximum projection error in circulation of $1 * 10^{-7} m^2 s^{-1}$. As such, the projection error influence on vortex core location and circulation is negligible.

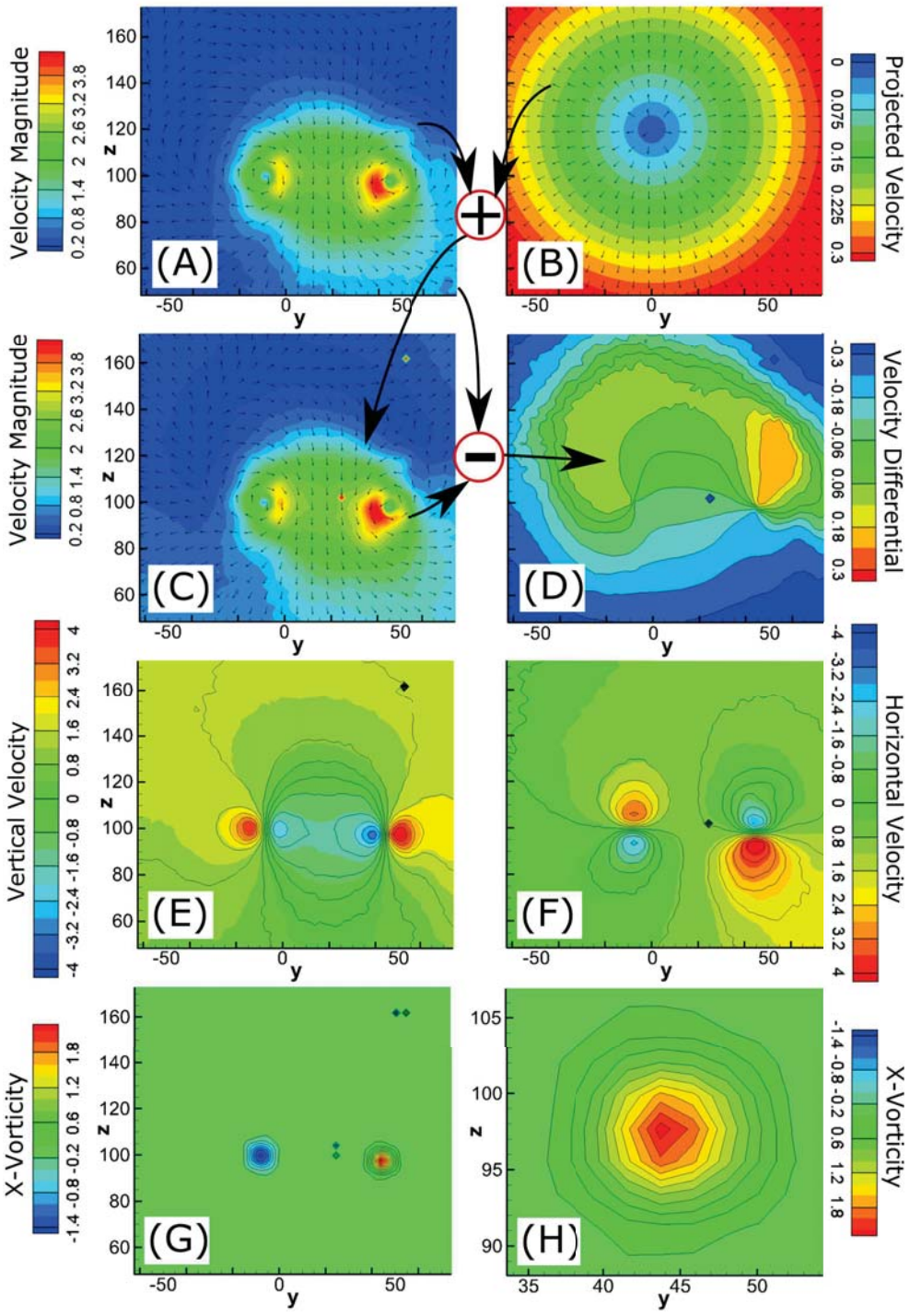

Figure 3.24: Projection error calculation plots. A) Initial velocity field b)Imposed projected velocity C) Velocity field after projection error applied D) Differential between original velocity field and velocity field after projected error applied E) and F) Vertical and horizontal velocity before error applied (lines) and after error applied (bands). G) and H) Vorticity before error applied (lines) and after error applied (bands). Arrows indicate the calculation process of each field.

3.4.3 Vibration

Tracking of camera vibrations between images of an image pair was performed through a Gaussian fit tracking of the illuminated wingtip while the tunnel was running. This was achieved using the PIV analysis technique with the all of the observation window blanked off and no seeding in the tunnel, thus tracking the tip as a single particle as can be seen in Figure 3.25. This yielded a vibrational displacement maximum of 0.0471px between the two images of a pair, which is within the margin of error of Gaussian subpixel tracking of just below 0.1px at low signal to noise ratio as identified by Saunter [117]. Over a test of 200 image pairs, the tip of the rear vane was found to have a maximum displacement change of less than 1 pixel during the entire sampling time. At 17m/s the maximum displacement of the vane tip was found to be 3 pixels over the course of an imaging run, with 0.0497px between pairs. While the in pair variance would not affect the velocity field magnitudes, the variance of 3px over the course of the run would lead to the velocity fields varying in location by up to 3px, giving artificial meandering. As such, it was required to run the tunnel below 17m/s.

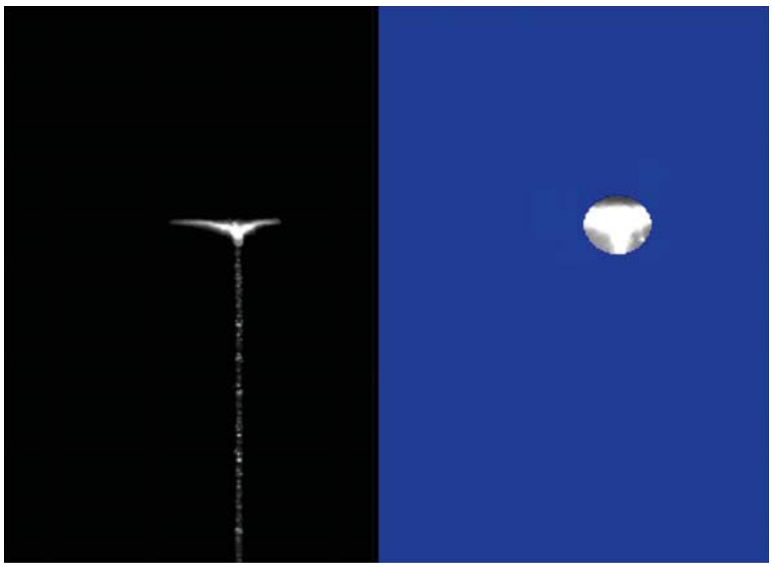

Figure 3.25: Vane tip illumination (left) and mask (right) for camera vibration tracking.

3.4.4 Focus

As previously discussed, in order to track the particle locations a three point Gaussian peak approximator was used. This relies on the particle image diameter

being of the appropriate size to minimise error. As identified by Raffel et al. [115] the ideal particles size for cross correlation PIV is 2 pixels, with a corresponding RMS uncertainty of 0.02px for a 32x32px interrogation window. However, due to the long focal length and subsequently low aperture, at coarser focus settings the light sheet intensity became low to the point where background noise could be observed in the imaging. As such the focus of the camera was convergence tested, with the results shown in Figure 3.26. For the focus test presented in this plot, a full sweep from focussed nearer than the sheet to focused further than the sheet was performed, thus resulting in multiple values for the same particle size. As can be seen, the smaller particle sizes and resultant sheet intensities were maintained within 3.1% total circulation error as long as the maximum particle threshold was kept below 3px diameter. To allow for consistent and repeatable focus results a particle pixel size threshold of no more than 2px at a brightness level of 4.5% of the total dynamic range was implemented. As the mean particle size was maintained above 1 pixel, bias error due to peak locking was maintained below 0.01px.

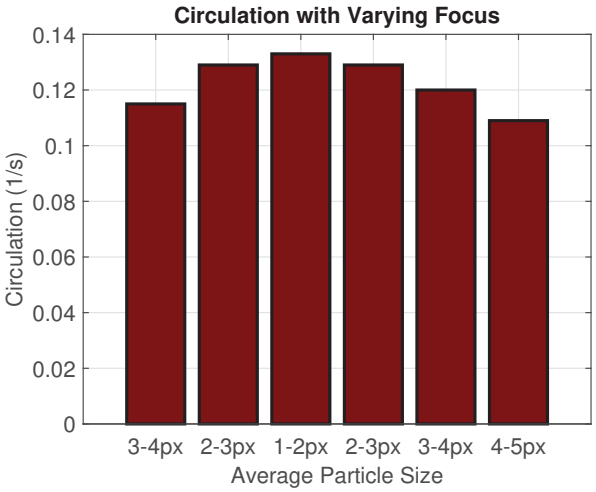

Figure 3.26: Circulation for various particle sizes resulting from focus changes.

3.5 Vortex Calculation Methodology

Vortex radii can vary by up to 35% if time averaged results are used due to vortex meandering and local fluctuations in velocity [118]. In addition to this, the velocity field will be smoothed, resulting in significant deviations in circulation and core size if time averaged results are used. However, it is still desired to have average values for core location, size and strength, and as such

the results were analysed by a script based evaluation of each individual pair of images. These images were sequentially analysed in Matlab, with peak noise filtered by vorticity gradient as previously mentioned. To eliminate the influence of weak secondary vortex structures, vortex shedding and low level noise on the calculation of tip vortex properties, all vorticity constructs except the tip vortex were filtered out. This was performed by computing contours at 10% of the peak vorticity and calculating the area enclosed by each individual structure. These data points were then exported to Matlab, where they were then combined and analysed for average values and variances. This allowed for an accurate calculation of real world core size, as well as time-averaged values that could be used to represent the core characteristics and allow comparison between cases. A graphical representation of the extraction and averaging process can be seen in Figure 3.27.

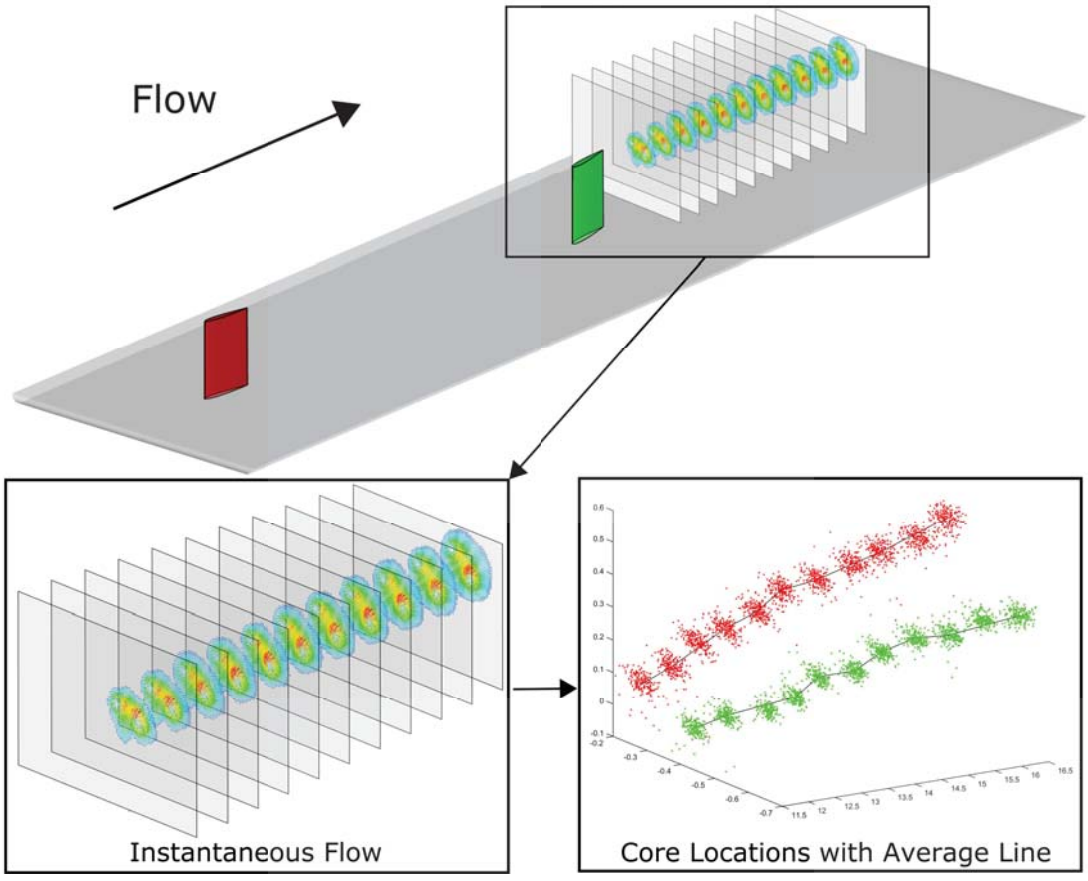

Figure 3.27: Stages of automated PIV data interpretation.

The vortex centre within a plane is defined as the integral of the vorticity (ω) multiplied by the displacement (X or Y value, depending on the axis being calculated), divided by the circulation (Γ) [23]. This can be seen in eqs. (3.4)

and (3.5).

$$X_c = \frac{1}{\Gamma} \int X \omega dS \tag{3.4}$$

$$Y_c = \frac{1}{\Gamma} \int Y \omega dS \tag{3.5}$$

While this does not always align with the location of zero in-plane velocity, it allows for consistent prediction of the centre of circulation intensity even when the vortex pair is migrating with an in plane motion, which would otherwise skew the core location significantly. It is also more robust than simply using the value of peak vorticity, as it is not significantly skewed by asymmetrical vortices or vorticity peaks in the result.

For the co-rotating vortices, they both have the same signed vorticity. This means that identifying the centre of vorticity within a plane will be ineffective as it will only find the centre point between the two vortices. An automated script was used to identify the two separated vorticity peaks and construct a contour line at 0.1 of the peak vorticity and 0.3 of the peak vorticity on a given plane, giving enclosed areas of $A_{0.1}$ and $A_{0.3}$ respectively. In the case that the smaller $A_{0.3}$ was less than a quarter of the larger $A_{0.3}$, the vortices were considered merged. This 1:4 ratio was selected based on the graphical results, which correlated with the observable vortex cores while minimising the influence of signal noise on the results. The area represented by $A_{0.3}$ can be used to track the vortices though the initial stages of the merging process, as it allows for better detection of the secondary peak in a merging and partially strained vortex structure. The single $A_{0.1}$ and two $A_{0.3}$ areas are considered as the vortex core regions for the merging vortex system and individual vortices respectively. Consequently, for path tracking the weighted centroid of eqs. (3.6) and (3.7) was used.

$$X_c = \frac{1}{\Gamma_{A_{0.3}}} \int X_{A_{0.3}} \omega dS \tag{3.6}$$

$$Y_c = \frac{1}{\Gamma_{A_{0.3}}} \int Y_{A_{0.3}} \omega dS \tag{3.7}$$

While the vortices remain near a uniform Lamb-Oseen distribution at the far offsets, at nearer offsets significant partial straining occurs from the influence of

the vortex interaction. This causes a skew in the shape of the vortex core that changes its primary axis as the vortex pair rotates downstream. This prevents the fitting of a Lamb-Oseen distribution of vorticity to the results. Consequently, the radius of the vortices was calculated using the vortex areas and assuming vortex circularity to give an effective radius. These were $R_{0.1}$ and $R_{0.3}$ for $A_{0.1}$ and $A_{0.3}$ respectively.

The vortex circulation was calculated by the integral of the vorticity within the identified core region. For when there are individual vortices identified, this is taken at an $A_{0.3}$ cutoff, as this allows the continued identification of vortex peaks through the merging case. When the vortex is merged, this is evaluated at $A_{0.1}$ to capture the entire vortex. If $A_{0.3}$ is used to characterise the merged vortex it excludes the merging tail region of the vortex, causing a significant drop in effective vortex circulation. This is not an issue for the unmerged vortex cases, as the vortices are still approximately circular in shape so there is no vorticity lost to the tail region. This will however cause an effective circulation reduction for the unmerged cases, so should be noted for the results of this section. This reduction was found to be 10.5% as calculated from the single vortex case.

By comparing this method to a Lamb-Oseen approximation on a uniform, circular vortex, it was found that the sampling resolution could result in a 15% maximum error in peak vorticity. This translated to a 1.5% maximum error in the 10% peak vorticity, giving a maximum core radius error of 5% per image pair, which was considered acceptable for this analysis.

The stages of this data interpretation process can be seen graphically in Figure 3.28.

Given the large and effectively random sample of image pairs taken, the statistics of the variance of both circulation and core location can be used for analysis of the meandering magnitudes. While the period, frequencies and amplitudes of small oscillations cannot be evaluated with non-temporally resolved data, the total magnitudes of displacements and the location distribution of the meandering can be determined with non temporally resolved data and a sufficiently large sample size. Such methodology has been used by Miller et al [119] and Rokhsaz [8] at 30Hz, as well as Heyes et. al [120] at 5Hz. The core variance was calculated as the standard deviation of the radial distance from the average core location, while the circulation variance was calculated from the standard deviation of the difference from instantaneous circulation to average circulation, divided by the

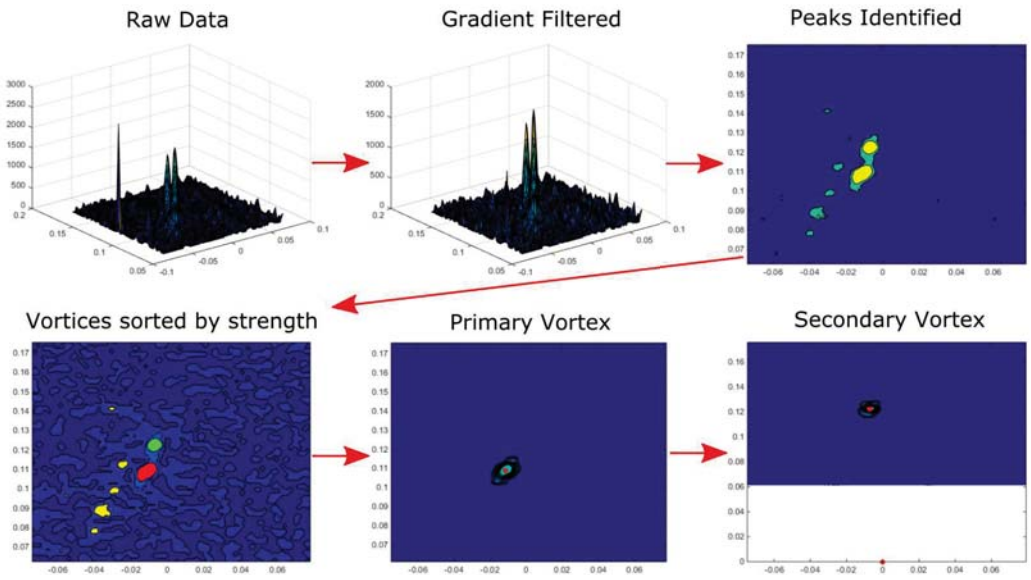

Figure 3.28: Stages of automated PIV data interpretation.

average circulation on the plane. The division by the average circulation was used to remove bias caused by low circulation cases and planes, as this would lead to low circulation cases seemingly having less fluctuation magnitude.

3.6 Water Tunnel

To allow for initial qualitative visualisation and characterisation of the vortex properties a Rolling Hills Research Corporation 0710 water tunnel was used, with a schematic in Figure 3.29. This tunnel allows test sections from 1 to 5.8 inches per second to be tested, which correlated to Reynolds numbers of 1000 to 5800 based off vane chord. The vanes used for this configuration were sized at half the size of the wind tunnel vanes, with a 40mm chord. The tunnel utilised a honeycomb and flow screen for turbulence control and flow uniformity, with a 6:1 contraction ratio. Manufacturer prescribed turbulence intensity was rated at 0.5% RMS. Due to the constraints of the test section length the vanes were spaced closer together than in the wind tunnel testing, with a distance between vanes of 3C (distance between quarter chords of 4C). Dye was injected into the hollow cavities of the vanes, with a hole drilled in the vane tips to enable the dye to escape into the freestream flow. Three camera positions were used to capture the dye motions, with the side and top being used for conventional capture of the dye paths while the rear was used to capture plane by plane images. This

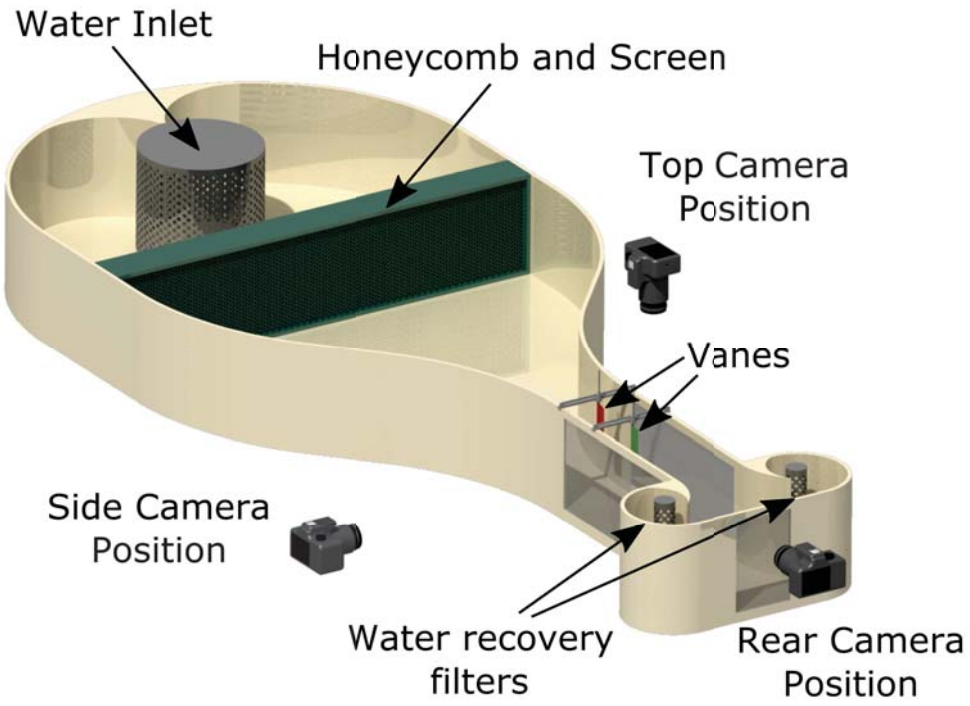

Figure 3.29: Schematic of water tunnel setup

was performed by forming a light sheet with a slit configuration which could illuminate a mixture of coloured dye and milk. By moving the light sheet in the streamwise direction different planar locations could be captured. Ten second videos were taken from each camera location at an imaging rate of 30Hz, allowing for transient capture of the flow effects, as well as time averaged post processing from averaging the video frames. Different coloured dyes were used for the front and rear vanes to identify the path of each vortex.

Chapter 4

Numerical Modelling

While the experimental testing regime allows a large number of offsets to be tested quickly, the planar PIV presented is unable to provide the level of detail that CFD investigations can. Characteristics such as transient vortex behaviour, frequencies, pressure fields and far field effects can be better characterised and visualised using computational methods and post processing. As discussed in the previous chapter, introducing a probe into a vortex driven flow can substantially modify the vortex characteristics such as breakdown length and meandering. Laser Doppler Anemometry (LDA) or Particle Image Velocimetry (PIV) solve this problem, however they cannot measure pressure fields directly. LDA also cannot time resolve meandering vortices. Consequently, Computational Fluid Dynamics (CFD) is a very useful tool for in depth vortex analysis. Both Large Eddy Simulations (LES) and Reynolds Averaged Navier Stokes (RANS) simulations were used for this study, with the RANS simulations being used to investigate the initial flowfield properties and LES being used for subsequent, in depth analysis of the effects seen in the experimental work.

The vane configuration tested is identical to that of the experimental setup, with 8 degrees angle of attack on both vanes. As discussed in the experimental section, eight degrees angle of attack was selected as it gives a high swirl number while being below the stall point of the vanes, reducing any risk of further complicating the flow by introducing flow separation. Six configurations were tested, with counter-rotating and co-rotating vanes at a lateral offset of 0C, 0.2C and -0.2C. These offsets were chosen to observe the effects of the front vortex impacting and

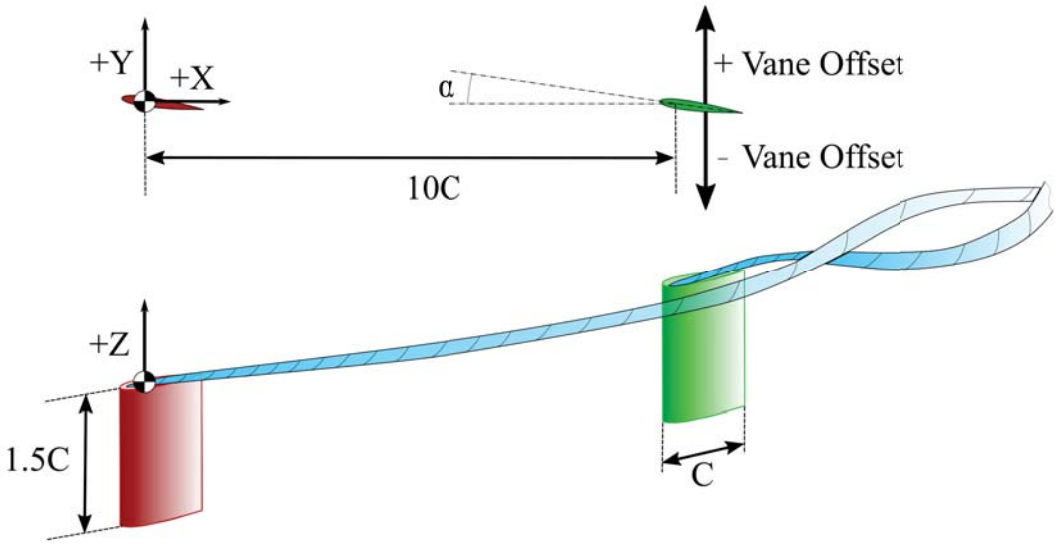

Figure 4.1: Computational vane setup and origin.

passing to either side of the rear vane, thus allowing the interaction effects in the near field on both sides of the vane to be observed. The square tip geometry of the vanes facilitates a high quality mesh in that region while still producing a well-defined vortex. Runs were conducted at a Reynolds number of 7×10^4 as per the previous chapter.

Due to the low velocities of the cases considered the flow was assumed incompressible and isothermal, reducing the equations for conservation of mass and momentum to:

$$\overrightarrow{\nabla} \cdot (\overrightarrow{u}) = 0 \tag{4.1}$$

$$\frac{\partial(\rho \overrightarrow{u})}{\partial t} + [\nabla \cdot \overrightarrow{u}]\rho \overrightarrow{u} = -\nabla p + \nabla \cdot \overline{\overline{\tau}} \tag{4.2}$$

Where p is the pressure, $\overrightarrow{u}$ is the velocity vector, and τ is the shear stress tensor. The equations were solved using the finite volume code ANSYS FLUENT 14.5.

The primary techniques used to numerically evaluate three dimensional flowfields are RANS, LES and DNS. RANS modelling separates the time dependent turbulent velocity fluctuations from the mean flow, solving these components through the application of a turbulence model. LES resolves these fluctuations, however has the provision of a subgrid scale model to approximate

the eddies that are not resolved by the grid. All scales larger than the subgrid filter are solved as per the Navier Stokes equations, whereas all below the filter must be modelled. DNS involves directly solving the Navier-Stokes equations, with no turbulence modelling.

The majority of vortex driven industrial flowfields are currently modelled using RANS, often applied to unstructured grids [121]. This is primarily due to the immense computational expense of high Reynolds number simulations performed in either LES or Direct Numerical Simulations (DNS), stemming from the need to resolve the geometry dominant turbulence structures (LES) down to the Kolmogorov length scale (DNS) [122]. However, numerical dissipation is significantly higher for RANS solutions than LES solutions, resulting in reduced vortex lengths and energies and significant impacts on the interactions of the vortices. Despite this, many recent research studies have still been performed using $k-\omega$ Shear Stress Transport (SST) and Reynolds Stress Models (RSM) [123–126].

Initial studies of the flowfield to determine baseline flow properties were performed with SST RANS simulations, consistent with the methodology used by Wik and Shaw [123] and Dudek [125]. SST was selected over Linear Pressure/Strain RSM due to its stability and superior prediction of lift around the airfoil, which results in more accurate initial vortex strength, however the dissipation rates are significantly higher. While these results were useful for initial determination of key flowfield properties and cases of interest, as discussed in chapter five, their high dissipation rates resulted in unrealistic vortex fields that did not correlate well with the experimental validation work. This was improved upon by the use of a LES solution, resolving the larger turbulent structures and the vortices more effectively. The significantly lower dissipation rates of the LES solutions achieved results far more consistent with the experimental work, predicting longer and consistently stronger vortices. In extreme cases, this resulted in a reversal of interactions from the upstream vortex being weaker and absorbed by the downstream vortex to the upstream vortex being stronger and absorbing the downstream vortex. It was found that the strength of the upstream vortex significantly affects the production of the downstream vortex, and as such modelling the dissipation of this vortex effectively was critical to the final result accuracy.

From initial experimental studies, the circulation based Reynolds numbers of the

vortices was in the vicinity of $8 * 10^4$, with variances occurring depending on the state of vortex interaction. This indicated that a portion of the vortex would be laminar, however instabilities in the vortices can be triggered by such events as shear layer fluctuations resulting in turbulence. As such, a laminar model would not be appropriate to model the problem, despite laminar flows present in both the boundary layer prior to transition and within the vortex core post-rollup. While using LES modelling will dissipate the vortex more rapidly than a laminar model, it is essential that these turbulent flow features are modelled in order to correctly characterise the instabilities present in the flow.

4.1 Subgrid Scale Modelling

In LES a subgrid scale model is applied to approximate the energy dissipation from turbulent viscosity due to isotropic subgrid eddies, and the energy transfer between the resolved and unresolved scales. In the original Smagorinsky-Lilly model the eddy viscosity is modelled as proportional to the subgrid characteristic length scale and a characteristic turbulent velocity. However a consequence of its modelling strategy is that the local strain rate defines the velocity scale [127]. This relates the subgrid dissipation to the rates of strain at the smallest resolved scale, ineffectively resolving regions where the vorticity field is more significant than the strain field. The assumption of fully isotropic turbulence in the inertial subrange also creates issues with wall bounded flows, where the Smagorinsky constant must be reduced and additional damping at the wall must be applied to ensure the eddy viscosity approaches zero at the wall [128]. This causes difficulties with complex geometries, which can be solved by the application of the Wall Adapting Local Eddy Viscosity (WALE) model. This model relates the modelling of the eddy viscosity to the square of the velocity gradient tensor, ensuring the correct asymptotic wall bounded behaviour of y^3 instead of y^2 in the Van Driest modified Smagorinsky-Lilly model. This model has been shown to have effective modelling of boundary layer transition and free vortex problems [129], with superior performance to the standard and dynamic Smagorinsky-Lilly models for free vortex performance [130]. The formulation for the eddy viscosity in the WALE model

is shown below in Equation 4.3.

$$v_t = (C_w \Delta)^2 \frac{(S_{ij}^d S_{ij}^d)^{3/2}}{(\overline{S}_{ij}\overline{S}_{ij})^{5/2} + (S_{ij}^d S_{ij}^d)^{5/4}} \tag{4.3}$$

Where C_w is the WALE constant, $\overline{S}_{ij}$ is the symmetric component of the velocity gradient tensor (also the strain, or deformation tensor of the resolved velocity field), Δ is the characteristic subgrid length scale and S_{ij}^d is the traceless symmetric part of the square of the velocity gradient tensor.

Both the Smagorinsky-Lilly and WALE models were tested against a reference experimental case for co-rotating at 0.2C offset to further confirm the most appropriate model for this study. It was found that the increased dissipation of the Smagorinsky-Lilly model compared to WALE on the grid tested resulted in the upstream vortex having 8.3% lower peak azimuthal velocity at the point of the rear vane, consequently shifting the merging mechanism from the upstream being the stronger vortex into the downstream being significantly stronger. This produced poor validation results in comparison to the WALE modelling, and as such WALE was selected for further evaluations.

The most commonly used WALE constant of 0.325 [131–133] and the value originally recommended by by Nicoud and Ducros of 0.5 [127] were tested to observe the effects of varying the constant on the vortex dissipation and merging length. It was found that the change in vortex merging distance and vortex paths was negligible between these tests. However, the dissipation rate did change with the varying values, with higher vortex dissipation observed at higher C_w. Experimental validation as discussed later in this chapter confirmed that lower numerical dissipation was required. As such, $C_w = 0.325$ was used for the remainder of testing.

4.2 Discretisation Schemes

The equations were solved with an implicit pressure-based solver. A segregated solver was used for pressure/velocity coupling, with the Semi Implicit Method for Pressure Linked Equations - Consistent (SIMPLEC) algorithm [134]. As the vortex flow is dominantly swirling and involves steep pressure gradients, a

second order PRESTO algorithm was selected for pressure discretization. This second order scheme creates a staggered control volume around the cell faces to calculate the face pressure, and is recommended for flows with high swirl number [135, 136].

When first-order methods are used for solving the momentum equations they typically damp out resolved eddies and turbulence in LES solutions due to increased numerical diffusion. Central differencing provides a far more accurate approach, however induces additional instabilities into the solution which may cause convergence issues or non-physical oscillations in the flowfield. By applying a first order scheme when the convection boundness criterion is violated, the stability of the solution can be maintained without significantly adversely affecting results, and its numerical diffusion will remain second order as long as the solution is sufficiently stable. As such, bounded central differencing was utilised for all LES runs.

An iterative time advancement scheme was used, solving for convergence within the SIMPLEC algorithm on each time step using backwards time differencing before advancing. Bounded second order implicit methods were used for time stepping, with an implicit time integration algorithm. To ensure stability for the relatively undamped LES solution, two bounding factors are calculated from the previous solution which limit current timestep parameters.

For RANS solutions Third-Order MUSCL was used to discretize the equations for turbulent kinetic energy and dissipation rate. This scheme blends central differencing and second order upwinding, reducing numerical diffusion for three dimensional flows thus improving the dissipation rates of the RANS solutions.

Least Squares Cell Based methods were used for the gradient evaluation, however due to the structured nature of the mesh it was unlikely that the accuracy differential would be significant from Green-Gauss Node or Cell based evaluations. The increased instability of the Least Squares Cell Based method was not found to be an issue in computational runs.

4.3 Computational Domain and Boundaries

While there is an inherent dependence between the boundary distances and the grid resolution, evaluating all grid resolutions at all possible boundary conditions is extremely computationally expensive and inefficient. By evaluating the conditions sequentially and ensuring conservative conditions are chosen, confidence in the results can be established without the need for excessive computations. The distances were evaluated at each boundary individually to ensure boundary independence, with the finest grid density used to ensure maximum propagation of any boundary related effects. The final boundary distances will be shown at the end of this section. With the boundary distances determined, the mesh convergence and spatial requirements study could then be performed. Grid topology choices and structure will be discussed later in this chapter.

A constant velocity inlet with no boundary layer was specified as the inflow for the CFD modelling. For the RANS cases, a low turbulence value of 0.1% was used, comparable to the wind tunnel testing, with a length scale of 0.03C. To eliminate floor boundary layer influence on the vortices, symmetry (free-slip) conditions were used for all domain walls, with a no slip wall being employed on the vanes themselves. This meant secondary structures and horseshoe vortices that alter the primary vortex interactions, as identified by Velte [107], could not form. This also removed the presence of boundary layer Von-Karmann sheets along the base of the model, and the subsequent need for increased grid resolution away from the vortex. For the outlet a zero normal diffusion flux condition was used, as it was found to provide minimal disturbance to the vortices. Testing of alternative configurations had shown that pressure outlets had caused non-physical necking and upstream disturbances along the vortex core, while the outflow condition replicated vortex behaviour present in a longer domain.

To ensure the boundary conditions were sufficiently spaced to have negligible impact on the vanes and vortices, three configurations each of inlet, outlet and side lengths were tested. The counter-rotating 0.2C offset was selected for boundary testing, as it provided a complex, interacting vortex flowfield with persistent vortices present to the end of the domain. RANS solutions were used to reduce computational expense, thus allowing the testing of more boundary distances. It was found that all the outlets tested were sufficiently far

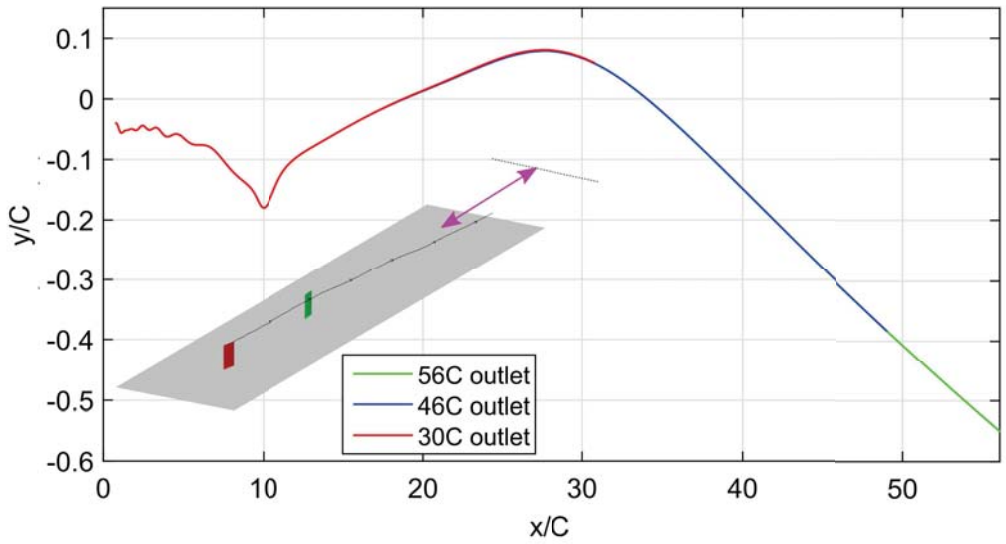

Figure 4.2: Vortex core streamline Y-value with varying outlet lengths. x/C = 0 is at the quarter chord of the front vane.

downstream to not cause variation in the paths of the vortices, and as such boundary selection became an issue of desired observation window and mesh size constraints. The results of the outlet testing for position can be seen in Figure 4.2, with the pressure and velocity in figs. 4.3 and 4.4. There was no position differential in the 30C to 56C cases as any discrepancy was below the mesh resolution. In order to determine the window for observing the vortex path, the gradients and variances in the paths were investigated. Beyond 30C after the vortex generator, it was found that the gradient of the vortex path, pressure and velocity was largely linear, and in the vertical axis the deviation in vortex path was only 0.02C.

Reducing the inlet length to 3C was found to influence the velocity field, with the inlet being within the deceleration region of the upstream vane flowfield, as can be seen in Figure 4.5. This imposed a higher initial velocity on the frontal vane, resulting in a higher vortex velocity which propagated downstream, resulting in 0.3% higher velocity for the length of the centreline at the end of the domain, despite only a 0.1% change in velocity at the start. While these changes are small, the computational expense to expand the inlet to 6C was minimal, and resulted in negligible value deviation from a 10C length.

Modification of the side boundary distance produced the most significant effects on vortex trajectory and flow properties. The velocities in the region of the second vane became significantly reduced by decreasing the side spacing to 2C,

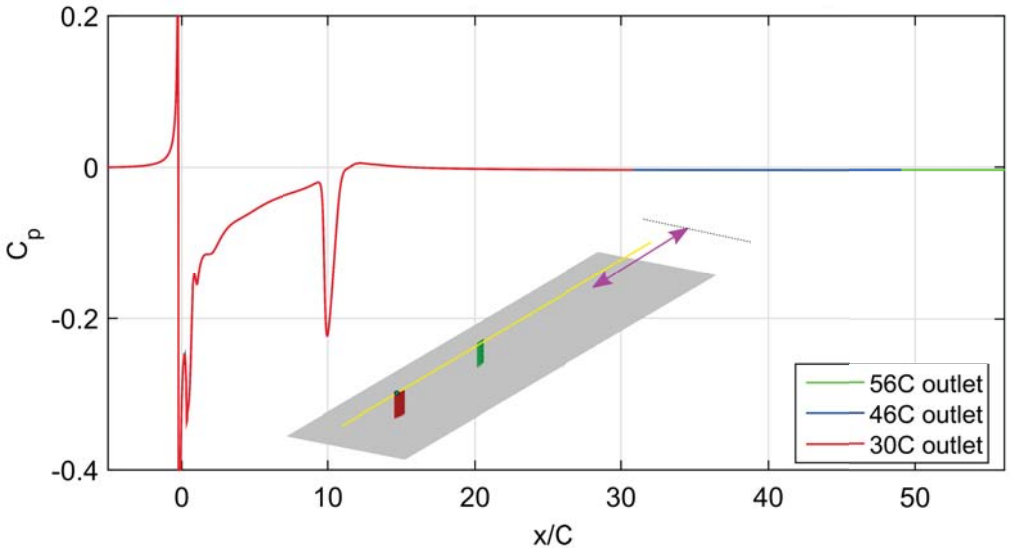

Figure 4.3: Pressure coefficient along line aligned with front vane tip with varying outlet lengths. x/C = 0 is at the quarter chord of the front vane.

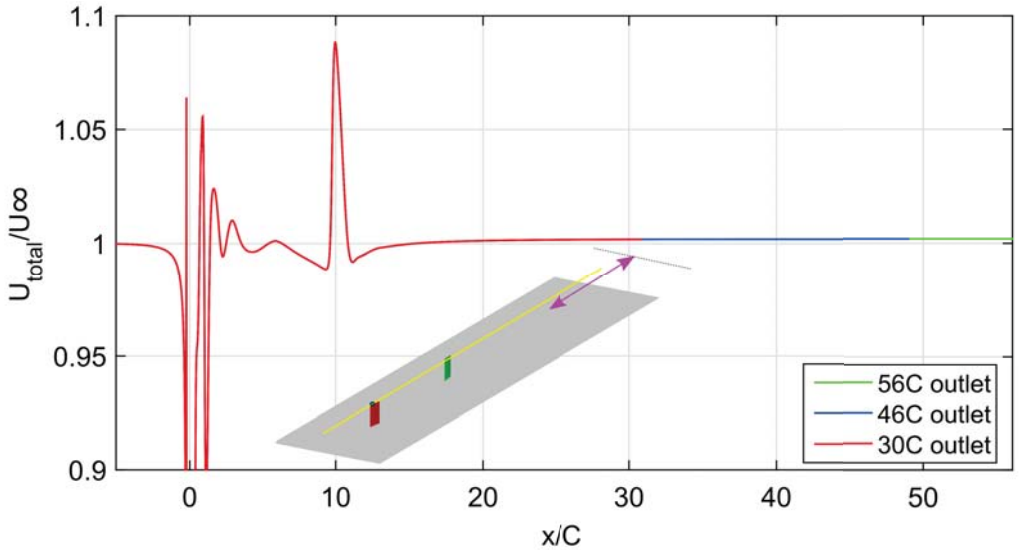

Figure 4.4: Normalised velocity along line aligned with front vane tip with varying outlet lengths. x/C = 0 is at the quarter chord of the front vane.

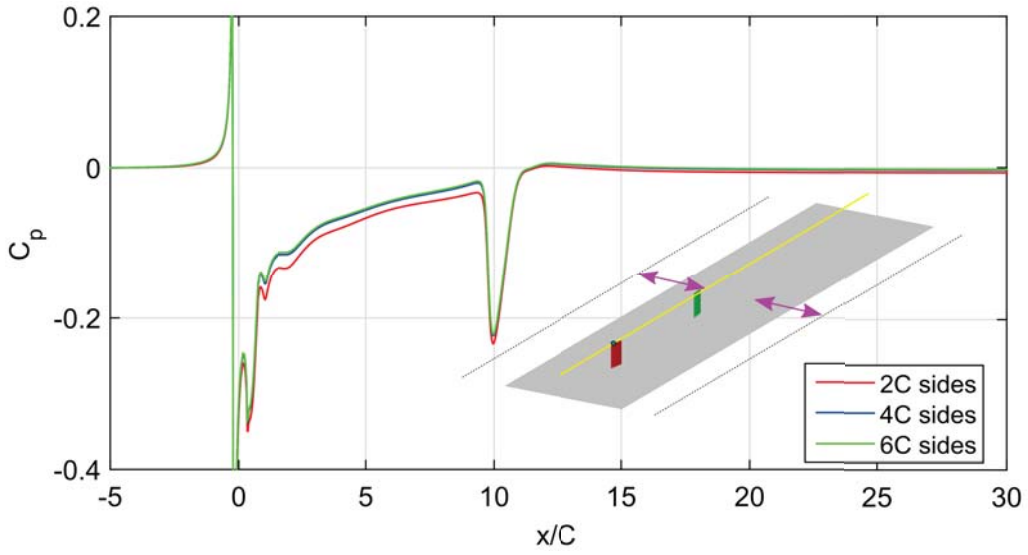

Figure 4.5: Pressure coefficient along line aligned with front vane tip with varying side distances. x/C = 0 is at the quarter chord of the front vane.

with peak reductions of 1%, seen in Figure 4.6. More significant was the increase in y/C for the entire post vane trajectory, seen in Figure 4.7. This is clearly due to the sides restricting vortex motion and tending to restore the vortex towards y/C = 0, as there is convergence from a peak differential of 0.05719 at x/C = 15 down to 0.018 by the end of the domain. Increasing this spacing to 4C showed much closer correlation with the results obtained at a 6C spacing.

The final boundary conditions can be seen in Figure 4.8. The final blockage ratio was 0.6%.

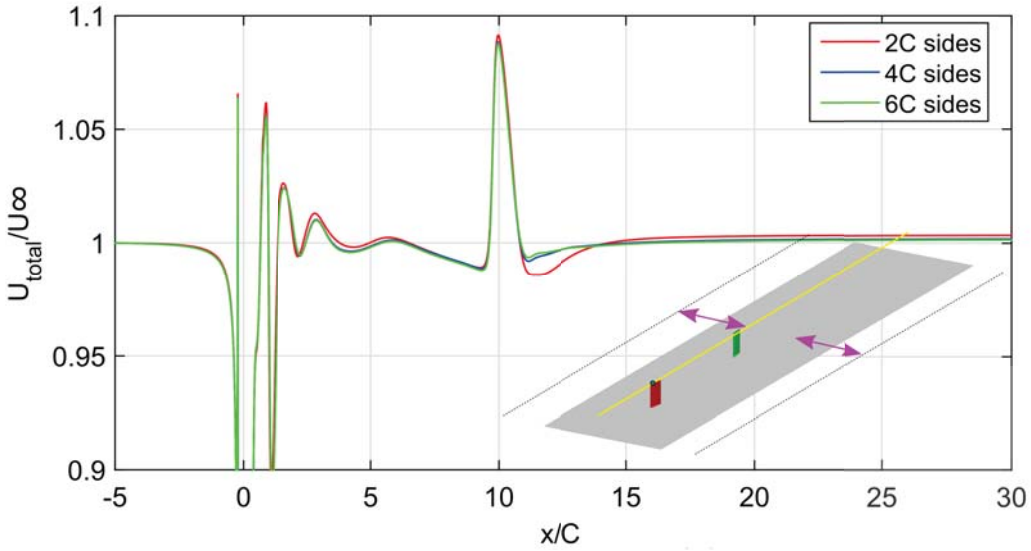

Figure 4.6: Normalised velocity along line aligned with front vane tip with varying side distances. x/C = 0 is at the quarter chord of the front vane.

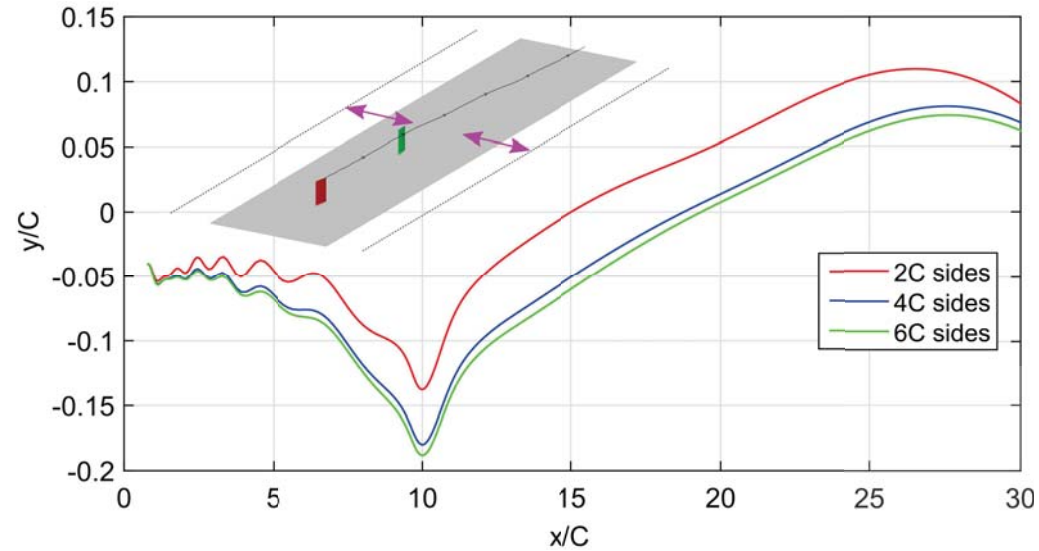

Figure 4.7: Vortex core streamline Y-value with varying varying side distances. x/C = 0 is at the quarter chord of the front vane.

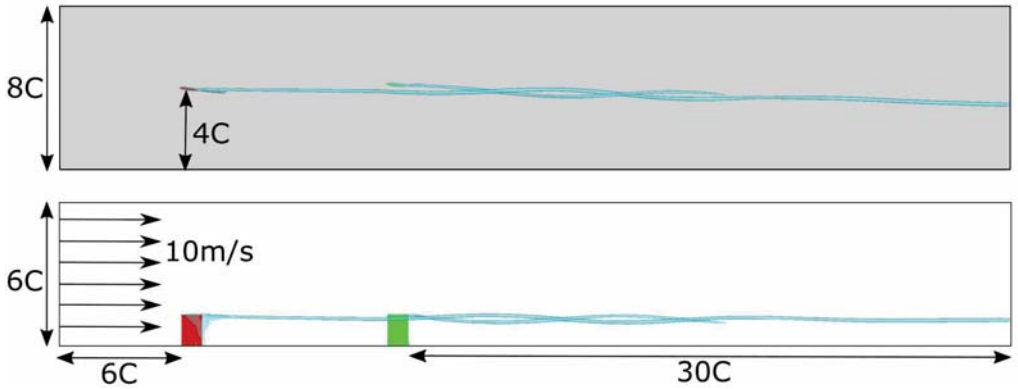

Figure 4.8: Final boundary conditions and spacing.

4.4 Spatial requirements

LES grid generation is significantly more difficult than RANS as cells must maintain low growth rates and anisotropy. Pope [137] recommended that 80% of the turbulent kinetic energy within the domain be resolved by the grid, with the remaining 20% computed by the subgrid model.

In order to accurately represent the structures in the near wall region, y^+ must be less than 2, with Δx^+ between 50 and 150 and Δz^+ between 15 and 40 [138]. This y^+ value choice is to place the first cell within the viscous sublayer (up to $y^+ = 5$) of the boundary layer, allowing resolution of this region. The stretching ratio of the elements moving away from the wall must also be considered, with a ratio of approximately 1.25 to ensure accurate resolution of the log layer [139]. Fulfilling these mesh requirements leads to a mesh of $2.5 * 10^7$ elements simply for the first vane of the configuration at the desired Reynolds number, rendering a full domain computation with two vanes and a lengthy vortex interaction region impractical given computational resources. The high y^+ requirements also give rise to considerable mesh anisotropy in the far wake regions, with high aspect ratio elements that would compromise the fidelity of the vortex interaction mesh region. However, if wall modelling is used, these values can be relaxed to y^+ between 30 and 150, with Δx^+ between 100 and 600 and Δz^+ between 100 and 300. The enhanced wall function of FLUENT uses a blending function between the laminar and turbulent laws of the wall, as suggested by Kader [140]. It is capable of a reasonable representation of the wall velocity profile where y^+ falls between 3 and 10, as well as deactivating for resolved sublayers where $y^+ < 3$. Most importantly, it generates the correct asymptotic behaviour for $y+ > 30$,

thus allowing the first cell to be placed in the logarithmic region of the boundary layer, significantly reducing near wall mesh requirements. As the primary field of interest was the resolution of the vortex interactions rather than fine flow features on the vanes, the first cell height was set at 0.6mm, giving a y^+ range of 20-30. However, the strength of the vortex produced is dependent on such phenomena as boundary layer development and total lift on the vane, which are dependent on the wall modelling. Consequently it is necessary to ensure that total vortex circulation is not modified by the altering of the wall modelling.

To perform this the $y^+ = 20 - 30$ mesh was compared to a $y^+ = 1$ mesh on the single frontal vane to ensure the vortex strength and location were consistent, with the results visible in Figure 4.9. While the vortex shedding off the main span of the vane is under-resolved in the coarser y^+, the net effect on the vane force, vortex strength and far wake eddy dissipation are negligible. Comparing the circulation values in Figure 4.9 it can be seen that the time averaged circulation varies by less than 1.9% after x/C = 6, less than 3% after x/C = 4 and less than 6.6% after x/C = 1. The fluctuation magnitudes and frequencies in the instantaneous cases are also similar. The primary difference between the cases is an increase in circulation on the vane (up to 39.8% at x/C = 0), however this is due to the increased production of vorticity in the three dimensional boundary layer shedding. This vorticity dissipates downstream and does not significantly affect vortex production, rollup or dissipation rates, as evidenced through the circulation values discussed earlier. The mechanism of vortex formation also remained unchanged between the two cases. As the $y^+ = 1$ case required a grid of $2.0\text{x}10^7$ cells for the front vane, and the $y^+ = 30$ case only needed $8.5\text{x}10^6$ cells, the high y^+, wall modelled strategy was employed for the present work.

Grid generation was performed in ANSYS ICEM, using a fully structured multi-block meshing strategy. All elements were generated as hexahedral, with a Y-grid strategy employed at the trailing edge of each vane and a double Y-grid at the leading edge. Mesh density was progressively increased at the leading edge of the rear vane to resolve the near-field vortex interaction, particularly in the case of impact. The elements were stretched in the far regions of the domain where predominantly freestream flow was expected. The final mesh consisted of 58 elements along the length of each vane, with 400 elements along the length of the wake behind the rear vane, and 200 between the vanes. 50 cells were used along the height of the vane, with the majority concentrated at the tip as the base area was of little interest. The significant bias of the mesh to the wake regions resulted

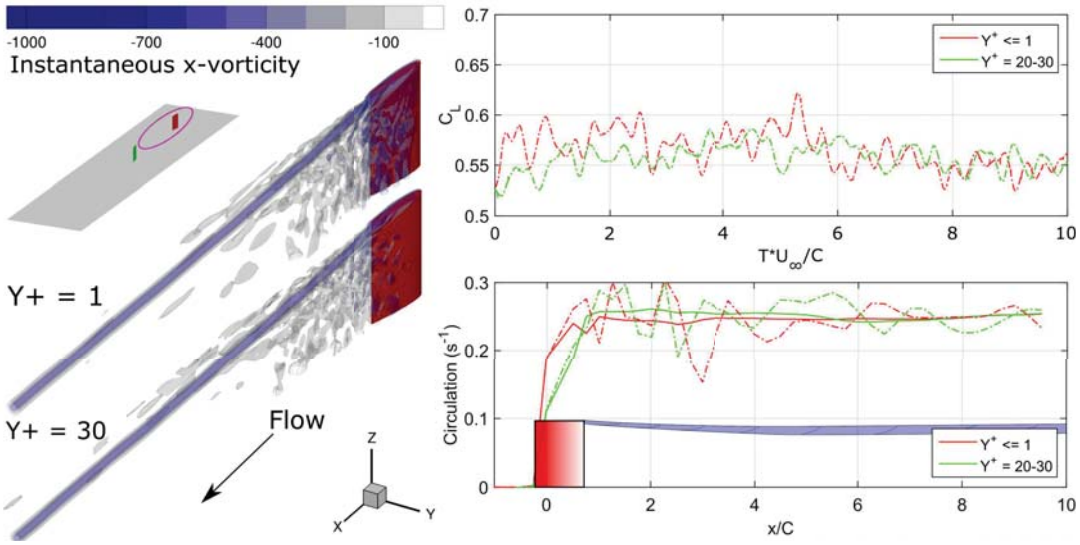

Figure 4.9: Isosurfaces of vorticity (left), vane lift coefficient (top right) and vortex circulation through domain (bottom right, dotted lines indicate instantaneous values, with solid for time averaged values) for $y^+ = 1$ and $y^+ = 20 - 30$ cases

in a comparatively coarse mesh on the vanes, reflective of the key focus of the study on the vortices, vortex formation and vortex interaction rather than the vane surface characteristics. For validation runs mesh density was increased at the vane root to model the boundary layer and horseshoe vortices associated with the ground plane more effectively. This grid can be seen in Figure 4.10.

The final mesh maintained between 25-30 elements across the viscous vortex core behind the vane, notably above the 15-20 elements for correct core capturing recommended by Dacles-Mariani et. al. [141]. However, as a consequence of the need to balance elements between the freestream vortices and the on-tip vortices, this results in the on vane tip vortices having 6-10 elements across the vortex, and as such the specific numbers within these local vortices should be inspected with care.

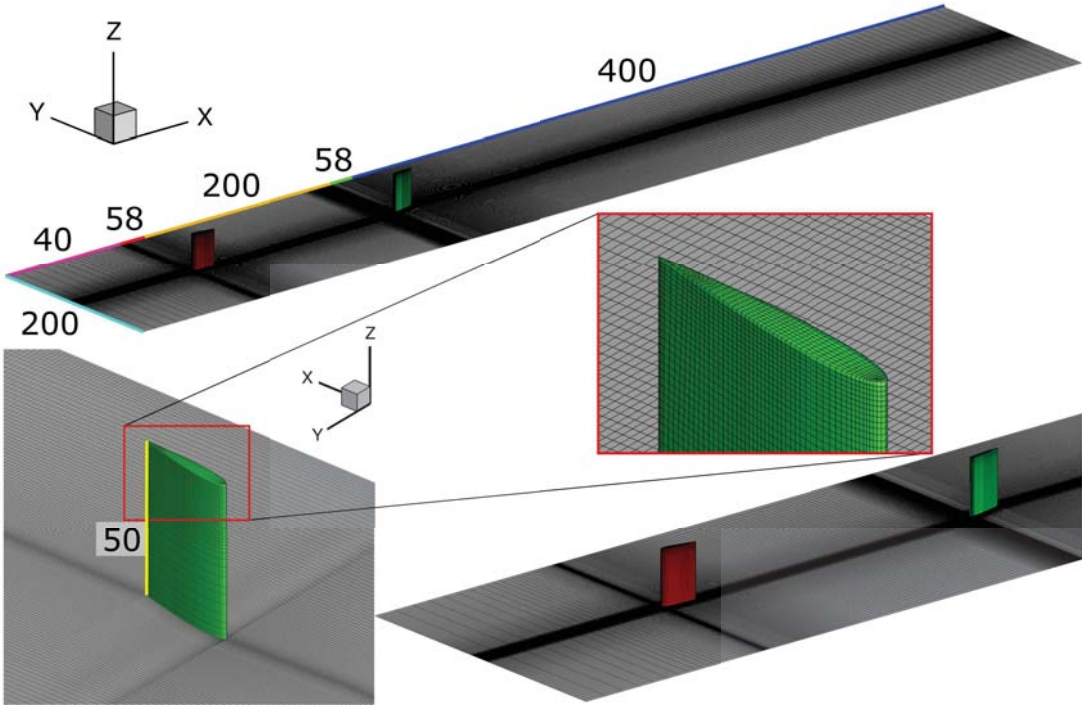

Figure 4.10: Meshing strategy with final cell counts.

4.5 Convergence Evaluation

For the initial RANS evaluation cases, three mesh densities were evaluated at $4x10^5$, $3x10^6$ and $2.6x10^7$ cells respectively, with the dominant increase being in the wake and vortex paths of the two generators. It was found that for RANS solutions, the vortex paths were very similar, with total deviation at the end of the domain being only 0.23C across all cases. Pressure and velocity plots along the centreline showed similar trends, as can be seen in Figure 4.11. The primary difference was noted in the pressure values for the far field conditions on the coarser mesh, with a 0.03 drop in pressure coefficient along a line through the vortex core by the end of the domain. There was a marked increase in the diffusion rates of vorticity in the lower meshes, with vortex length to a peak Q-criterion value of $9000s^{-2}$ varying by 4.8C between the cases. Consequently the $2.6x10^7$ cell mesh was used for RANS evaluations as the solution time for a steady state run was inconsequential and minimal vortex diffusion was desired.

Due to the inherent numerical dissipation in the RANS simulations and the time averaged nature of the solution, it was expected to achieve mesh convergence easier than the LES runs. Consequently, the LES was evaluated at mesh resolutions of $1.2 * 10^7$, $1.6 * 10^7$ and $2.6 * 10^7$. These runs were performed

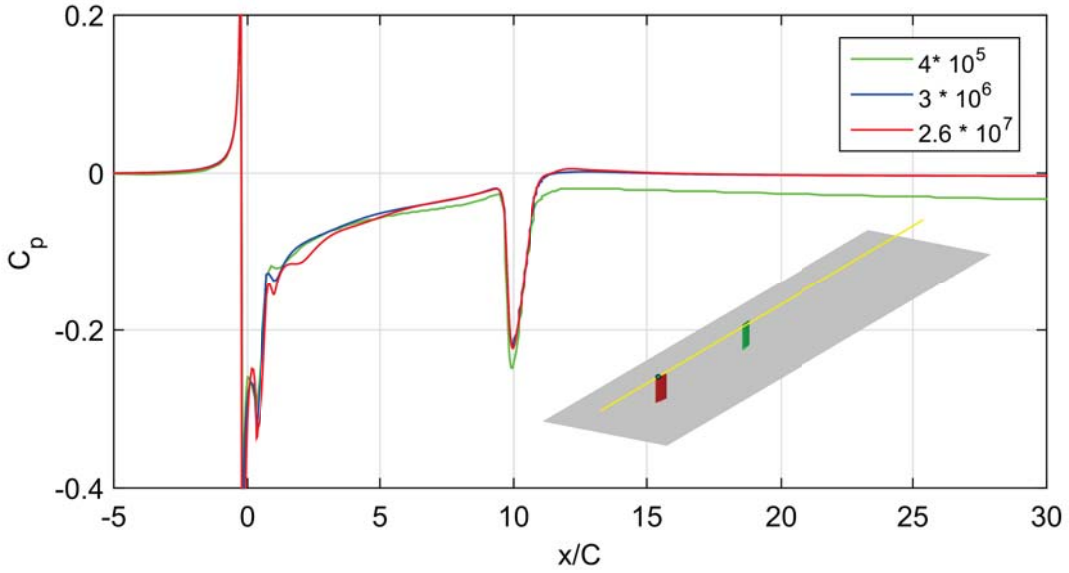

Figure 4.11: RANS pressure coefficient along line aligned with front vane tip with varying mesh densities.

on the co-rotating 0.2C offset case, as mesh density variance within the wake region was expected to modify the elliptic instability within the vortices, with subsequent effects on merging length and energy. The mesh density modification for these runs was entirely in the wake region, increasing the mesh density in the streamwise direction and thus improving cell aspect ratio. All meshes were run at a constant timestep of $3 * 10^{-5}$s as per the following section.

Initial inspection of the forces on the front vane showed a very close correlation for all cases with the forces expected from theory. From Prandtls lifting line theory, the 3D lift coefficient on a wing can be approximated by:

$$C_{L3D} = C_{L2D} * \frac{AR}{AR + 2} \tag{4.4}$$

Where C_{L3D} and C_{L2D} are the three dimensional and two dimensional lift and drag coefficients, and AR is the aspect ratio (adapted from Anderson [142]). A C_{L2D} of 0.9 was calculated using Javafoil [143], giving a C_{L3D} of 0.54. It was found that the LES solutions predicted averages of 0.5508, 0.556 and 0.546 on the front vane for the increasing mesh densities respectively. All of these forces were within 3% of the theoretical force calculation, with the finest mesh within 1%. Tracing the forces on the rear vane as seen in Figure 4.12 and Figure 4.13 found again that all three mesh configurations showed similar trends for force

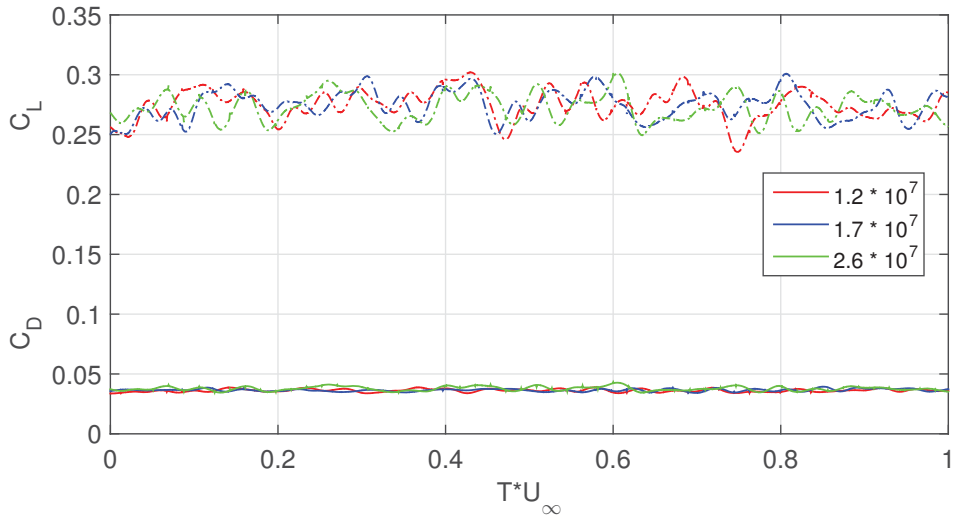

Figure 4.12: Force coefficients of rear vane with varying LES mesh densities.

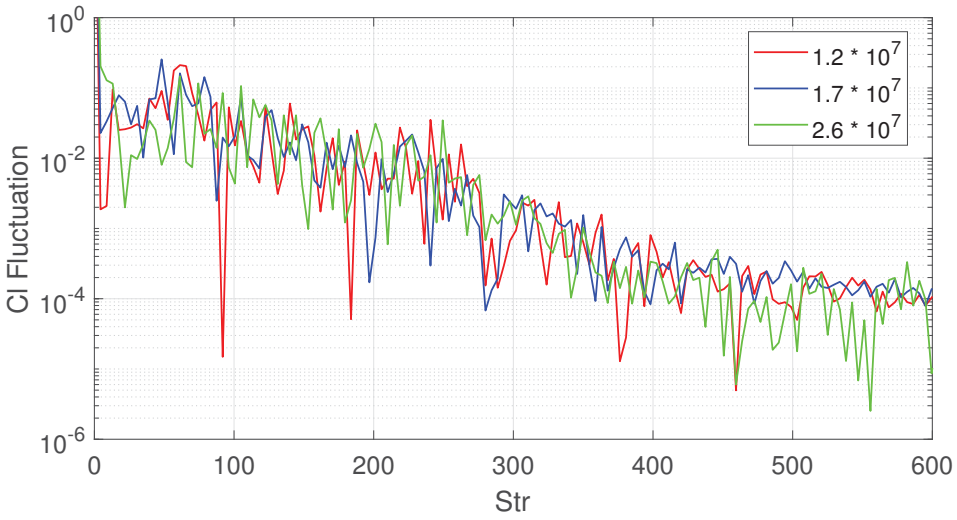

Figure 4.13: FFT of rear vane lift coefficient for varying LES mesh densities.

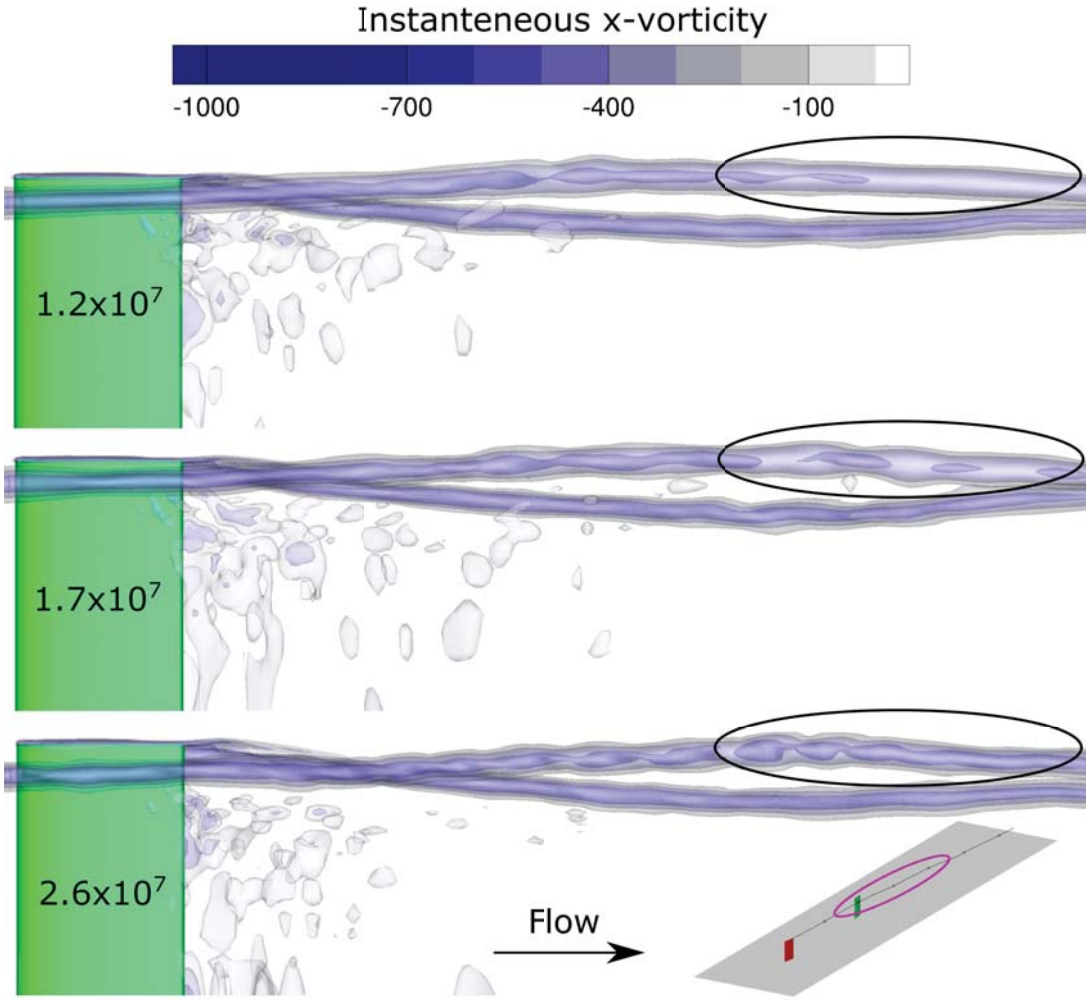

Figure 4.14: X-vorticity isosurfaces for various LES mesh densities.

values and frequencies, and as such any of them would be suitable for resolving the region in between the vortex generators. However, forces can only determine convergence of the flowfield properties on the vane, and may mask flow field issues further downstream. As such, further inspection of the far field vortex flow properties was desired.

As can be seen in Figure 4.14, while the structures near the vane remained similar irrespective of mesh density, the higher energy vortex structures in the far field dissipated faster under the lower resolution meshes. This was particularly evident in the manifestation of the elliptic instability in the vortex core, with more significant fluctuations visible in the densest mesh. The net result of these mesh changes was a faster dissipation in the high energy vortical structures, with an associated loss in high frequency flow features further in the wake. The lower energy, larger radius vorticity levels remained far less affected by the mesh

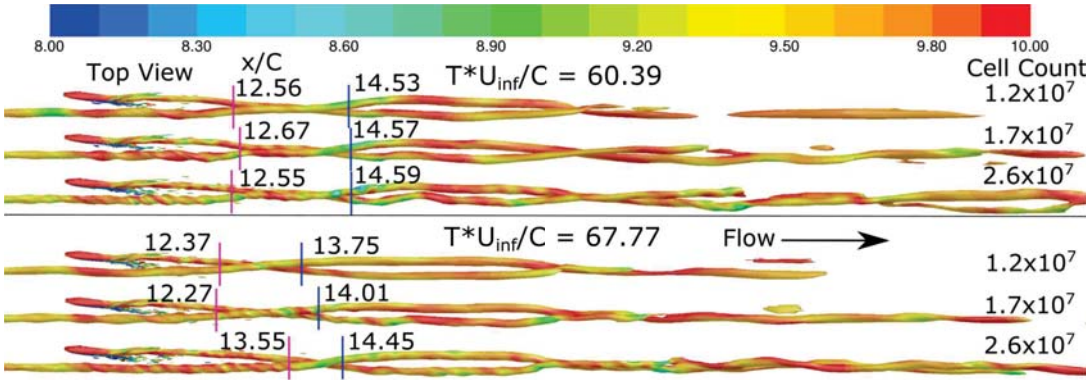

Figure 4.15: Isosurfaces of x-vorticity coloured by x-velocity for multiple LES mesh densities at $T * U_\infty/C = 60.39$ (top) and $T * U_\infty/C = 67.77$ (bottom)

density, with similar diameters and vortex lengths seen for the majority of the domain in all cases.

Whilst the flow structures were conceptually similar between the meshes, with a helical pattern and the downstream vortex merging into the upstream vortex, the transient fluctuation rates varied, as can be seen in Figure 4.15. In the first state the vortex crossover points are near identical between the cases, with 0.06C variance in the rear of the upstream crossover and 0.12C in the front upstream crossover. In the second state the front upstream crossover point varies by 1.28C between the three conditions, with the downstream crossover remaining near constant. This is due to the increasing instabilities with the higher mesh resolutions forcing a higher meandering magnitude on the upstream vortex, resulting in a larger shift in the instantaneous crossover point. The differential in far field dissipation rates can also be observed here, with the 2.6x10^7 cell mesh showing a far longer continuation of the vorticity isosurface than the 1.2x10^7 cell mesh. However, the long range dissipation difference is far less significant between the 1.7x10^7 and 2.6x10^7 cell grid. All three meshes produced an uneven vortex merger, with the downstream vortex merging into the upstream vortex, which was identical to that achieved with experimental results as will be discussed later in this chapter.

Between these meshes the global trends for vortex circulation and in plane kinetic energy remained very similar, with the results shown in Figure 4.16. As the results presented are instantaneous, there will inherently be transient variance due to effective time differences, however the trends can be effectively compared, especially when the time averaged result of the finest mesh is considered. Consistent with the previous observations of instabilities in the

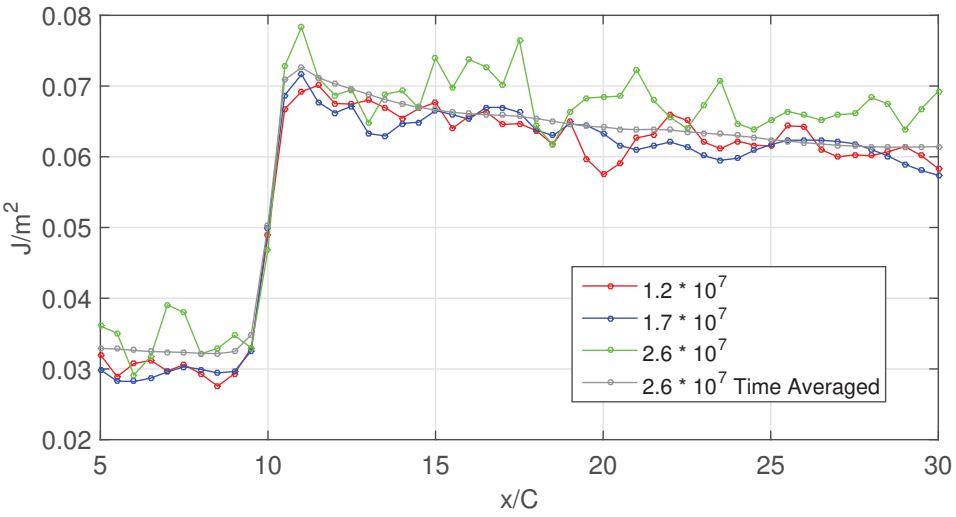

Figure 4.16: In-plane kinetic energy of vortices throughout domain for various LES mesh densities. Both the time averaged and instantaneous values are shown for the finest mesh.

visualisations of Figure 4.14, the magnitude of energy fluctuated at a maximum far wake peak-peak variance of 20.1% for the 2.6x10^7 case, with fluctuation of 9.53% in the 1.7x10^7 case and 12.3% in the 1.2x10^7 case. The RMS values of the fluctuations were $5.351 * 10^{-3} J/m^2$, $2.560 * 10^{-3} J/m^2$ and $2.233 * 10^{-3} J/m^2$, for the fine, medium and coarse meshes respectively. Despite this, the trendline, particularly in the time averaged case, matched closely with the coarser meshes. It should be noted from the time averaged results of the 2.6x10^7 cell case that the more significant instabilities and oscillations present in the finer mesh have caused the particular instantaneous case considered to have a higher than average kinetic energy. However the visualisations of the cases from Figure 4.14 previously showed that the higher mesh resolutions resulted in reduced dissipation, and as such a higher kinetic energy would be expected. This is offset in the time averaged condition by the effects of velocity smearing as the vortex meanders, which dissipates velocity peaks and consequently lowers kinetic energy, as it is a function of velocity squared.

While further mesh resolution may be able to reveal more information about the elliptic instabilities present and reduce dissipation rates further, all three meshes were able to produce similar trends for circulation and kinetic energy, as well as predict very similar merging distances and forces as discussed in the previous paragraphs. Consequently, all the LES meshes tested would have been useful for analysing general trends of the flowfield. As LES tends to DNS as the

mesh size is reduced and the Kolmogorov scale approaches resolution, LES cannot truly achieve grid independence [122, 144, 145]. The $2.6\text{x}10^7$ cell mesh successfully converged on the vane force and frequency characteristics, and downstream kinetic energy properties, demonstrating its suitability for the analysis of this flowfield. While all meshes successfully resolved the global flow structure and large scale instabilities, the $2.6\text{x}10^7$ cell mesh showed the best resolution of transient elliptic instabilities and the least dissipation at high vorticity levels, and therefore was used for the LES analysis.

4.6 Temporal Requirements

Following from the Courant-Friedrichs-Lewy condition, in order to compute a field moving across a discrete spatial grid, the time stepping of a solution must be sufficiently small that the flow features do not fully travel to the next grid point within a single time step, resulting in a CFL number below 1 [146]. Consequently, as mesh density is increased the time must be reduced in order to capture high frequency flow features as they move through. While the timestep must be sufficiently small to resolve the motion of all flow structures, due to the relative sizing of the vanes and the wake region and the resulting mesh densities the overall time step was critical on the vane regions. A timestep of $3 * 10^{-5}$s was used, resulting in the maximum CFL number being maintained at below 1 for all simulations. This is equivalent to a non-dimensionalised timestep $\Delta t^* = 0.003$, which is well below the recommended estimate of Cummings et. al. [147] of $\Delta t^* = 0.01$, and below the $\Delta t^* = 0.006$ vortex breakdown cutoff of Görtz [148].

For each LES case the solution was initialised with a k-ω SST model, followed by two complete flowthroughs of the domain with the WALE LES model. This initialisation period was utilised to ensure that a fully developed transient flow on both vanes had developed and the resulting disturbances from the upstream vane had propagated to, and interacted with, the downstream flow structures. Initial monitoring of forces on the vanes proved ineffective due to the fluctuations in forces being largely caused by the localised vortex shedding, which gives a poor indication of the initialisation and effects on the vortex interaction. Point monitors also shed minimal information on the initialisation due to the meandering nature of the vortices causing the values to artificially

fluctuate by large values, even when sufficient initialisation had been completed. As such, isosurfaces of x-vorticity at $400s^{-1}$ were used to determine when interaction initialisation had occurred, as they could be simply monitored with graphical output. Once these isosurfaces had stabilisied their lateral oscillations to within 0.25C at x/C = 13 and 0.33C at x/C = 17, and had demonstrated consistent periodicity the solution was deemed to have reached a developed state. This, combined with a factor of safety of a full domain cycle after observing graphical convergence and periodicity, ensured that the correct flow state had been obtained prior to time averaging.

To determine the averaging period the forces on the vanes and vortex characteristics were monitored. Investigation of the lift and drag forces on the vanes found that force convergence could be achieved to within 1% in as little as $T * U_\infty/C = 2$, as can be seen in Figure 4.17, with <0.5% convergence within $T * U_\infty/C = 5$. However, the meandering motions and fluctuations of the vortices occur at a considerably lower frequency than the vortex shedding of the vanes, indicating the need for a larger averaging period. To determine this period the vorticity field at X15 was output for each timestep, and analysed as per the automated methodology previously discussed in the previous chapter. This gave a transient history of vortex cores that could be averaged over time to determine the accuracy of the averaging process, as can be seen in Figure 4.18.

For the stronger vortex, circulation convergence was achieved to within 0.5% within $T * U_\infty/C = 1.2$, consistent with the rapid convergence of the rear vane forces that would be reflected in the circulation production. The weaker vortex is only marginally slower to converge at 0.8% at $T * U_\infty/C = 1$. Maximum Z position displacement of 0.0126C was present at $T * U_\infty/C = 4.5$ in comparison to a maximum instantaneous value fluctuation of 0.0726C, indicating a slower fluctuation in vortex location requiring a longer time averaging interval. This was significantly worse for the positive vortex than the negative vortex, which had a maximum fluctuation of 0.072C for an averaging displacement of 0.0056C from $T * U_\infty/C = 4.5$. As such, time averaging error is acceptable from periods exceeding $T * U_\infty/C = 4.5$. However as multiple cycles of key frequencies were desired for the purposes of the transient analysis discussed later in this chapter, the minimum available number of timesteps to average over was 4000. This was equivalent to $T * U_\infty/C = 12$, indicating the time averaging period is sufficient to ensure temporal convergence of values, and ensuring at least 3 low frequency

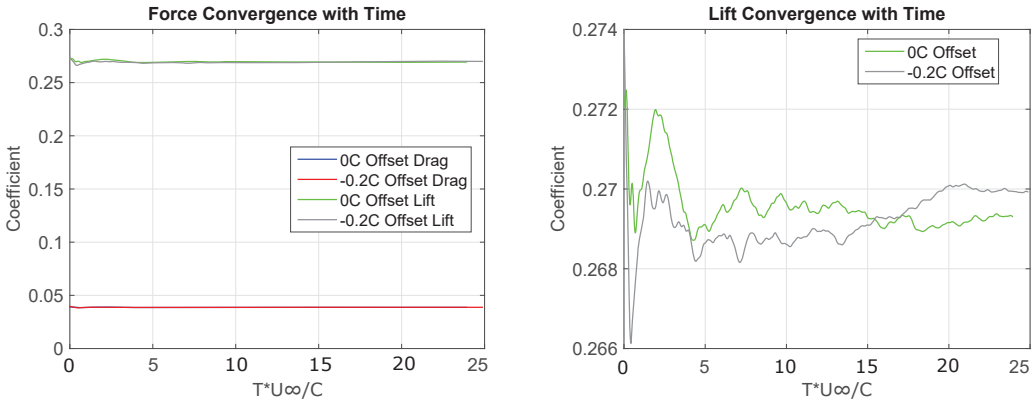

Figure 4.17: Force convergence on rear vane with time for 0C and -0.2C offset counter-rotating conditions.

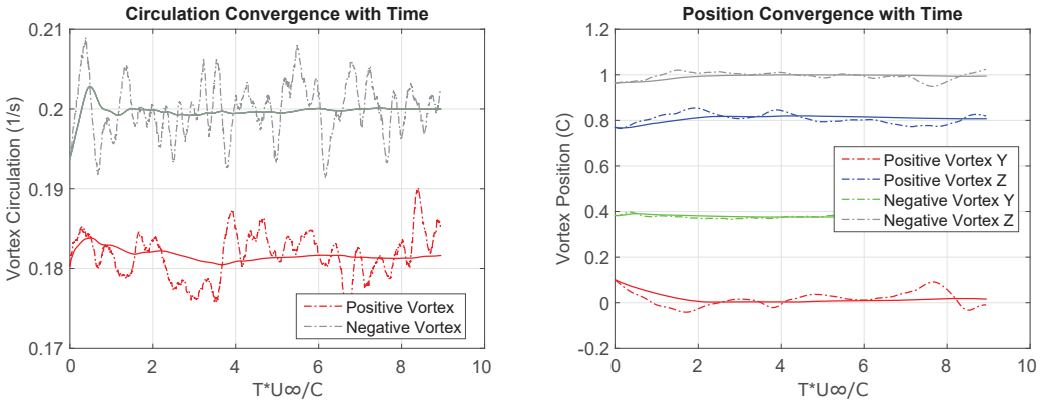

Figure 4.18: Positive and negative vortex time averaging convergence for circulation (left) and position (right). Instantaneous values are given by the dotted lines, with moving averages on solid lines.

cycles were captured.

4.7 Vortex Parameters and Metrics

As discussed in the literature review, there are various methodologies to define and characterise a vortex. In the present work, to ascertain the strength of the vortex and monitor the different ways in which the energy dissipates, a number of parameters will be used. The primary method of determining vortex strength will be through vorticity and circulation, as used by Lewecke et al [23] and others [1, 91, 107]. This can be expressed below as:

For an X plane

$$\Omega_x = \frac{dv}{dz} - \frac{dw}{dy} \tag{4.5}$$

$$\Gamma_x = \int \Omega_x dA \tag{4.6}$$

where Ω_x is the x-vorticity, and Γ_x is the circulation.

The vortices are in a flow free of the complex geometry and the motion in the axial direction is significantly higher than the motion of the vortices in either the horizontal or vertical directions. As such x-vorticity is more useful than other parameters such as Q-criterion as it eliminates influences from outside the plane of interest. This is in contrast to other situations with complex geometry where the complexity of flow may limit meaningful results to Q-criterion or Lambda-2 due to the mis-identification of shear layers as vortices [124]. The low dissipation experienced in the LES results also reduces the need for more unorthodox criterion's such as trimmed tangential velocity.

For many high lift applications a useful metric is the pressure and total pressure in the flowfield. As the flow is dominated by the vortices in the CFD and there are minimal external artefacts, these pressure coefficients can be computed by integrating across a planar slice through the whole domain, as per below:

$$C_{p,x} = \int C_p dA \tag{4.7}$$

$$C_{pt,x} = \int C_{pt} dA \tag{4.8}$$

Where C_p is the pressure coefficient, given by the instantaneous pressure differential from static pressure at the inlet, divided by $1/2 * \rho * u_\infty^2 = 61.25$. C_{pt} is the total pressure coefficient, given by the pressure coefficient plus the local velocity squared divided by u_∞

Again in high lift scenarios it is common to require the total kinetic energy and momentum of the flow to determine its suitability for overcoming regions of adverse pressure gradient. As before, these parameters can be integrated across planar slices to track the variance in these quantities as the vortices move

downstream. By separating these out into planar (subscript p) and total (subscript t) components, the proportion of the flow energy contained in the vortex and the transfer of flow energy to vortex energy can be better monitored, as per below for kinetic energy:

$$K_t = \int u^2 + v^2 + w^2 \, dA \tag{4.9}$$

$$K_p = \int v^2 + w^2 \, dA \tag{4.10}$$

For momentum:

$$P_t = \int \sqrt{u^2 + v^2 + w^2} \, dA \tag{4.11}$$

$$P_p = \int \sqrt{v^2 + w^2} \, dA \tag{4.12}$$

4.8 Transient Vortex Analysis

While point monitors can be used to monitor frequencies and amplitudes in transient flows, their usefulness in unsteady vortex fields is limited. This is primarily due to the meandering motions of vortices, as any point monitor placed within the core of the vortex shifts from monitoring the core to the periphery as a result of the vortex motion, an effect seen in Figure 4.19. The result of this is erratic tangential velocities and pressure readings that are not indicative of the vortex core instantaneous properties. As such, planar data is needed for each timestep to calculate the characteristics of the vortex.

The computational storage expense of such data is very significant, with each plane captured being just under 3MB in size. To capture planes from directly behind the vane down to x/C = 26 at 0.5C spacing for 4000 timesteps produces just under 1 Terrabyte of processed data. As such, this transient behaviour was only recorded for three cases of interest, the 0.2C co-rotating case, the -0.2C counter-rotating case, and the 0.2C counter-rotating case. The singular co-rotating case was selected as it was representative of the merging condition for all cases, while the counter rotating case was selected to investigate the effect

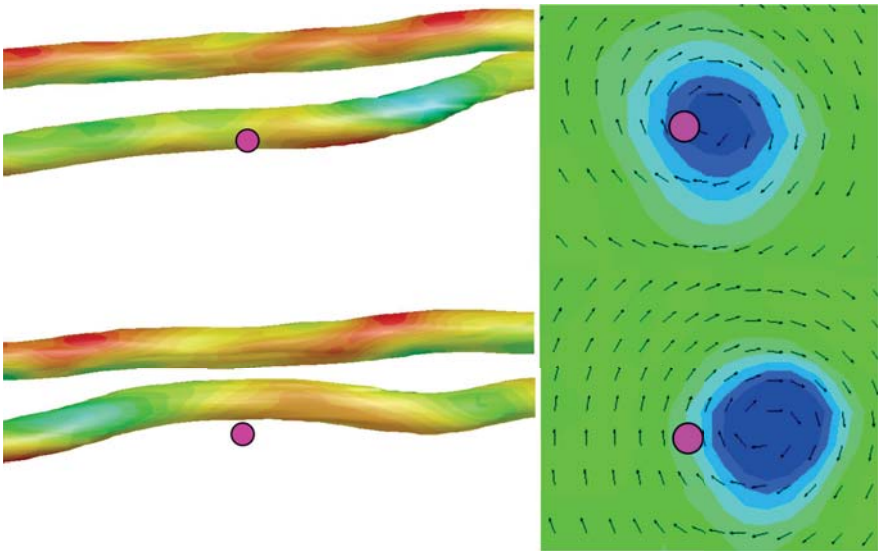

Figure 4.19: Diagram of vortex meandering around a point monitor.

of direct impact on the front of the vane and the near field interaction instabilities, as will be discussed in chapter seven.

Once these planes were extracted, it was desired to track the properties of the vortex cores present for each timestep. A modified version of the vortex extraction code used for the experimental results as discussed in the previous chapter was employed, with additional tracking of pressure peaks and streamwise velocity. As these results were calculated for each timestep, the output could be evaluated in a transient manner, allowing for investigation of the frequencies of each parameter. If later desired, point monitors could be placed on the planes to track point properties.

4.9 Validation of Numerical Model

As previously discussed, good correlation between the model and lifting line theory on the single frontal vane was observed, however the successful prediction of a multiple vortex interaction is far more complex than predicting lift on a common wing profile. As such, the entire double vane system was evaluated against experimental results from the wind tunnel. For these purposes the LES modelling previously described was applied to a representation of the test section used for wind tunnel testing. This representation included the splitter geometry within the test section, and resolved the full domain of the tunnel. No-slip smooth

walls were used on all faces, with a specified inlet velocity profile as measured from the previous experimental characterisation of conditions at the tunnel inlet. All mesh densities around and in between the vanes were maintained as per the previous meshing strategy, with additional elements used to resolve the walls of the wind tunnel and splitter. Results were initialised and time averaged using the previously discussed strategy. As there are two fundamental conditions being evaluated, with two unique vortex interactions, it was necessary to validate the modelling against both the co-rotating and counter-rotating experimental results. For the counter rotating condition the 0.5C offset was used as it maintained the highest vortex energy throughout the domain. In the co-rotating condition, the 0.2C offset was evaluated as it demonstrated multiple stages of merger and had a long merging distance that was still within the tunnel test section.

4.9.1 Counter-Rotating

Inspection of the velocity fields in Figure 4.20 showed good qualitative agreement between the experimental and numerical flowfields. As indicated by the purple arrows, all dominant flow structures maintained the same paths between the two, with a continuous downwards movement of the vortex pair. The lower energy structures showed migration in the same direction. However due to the error limitations of the PIV system at lower velocity magnitudes the velocity field is more poorly resolved and becomes dominated by noise. This can be seen in the top left kink in the velocity field, which has a very clear migration in the CFD case. This is seen as more of an increasing dent in the flowfield in the PIV. Between x/C=13 and x/C=17 the expansion of the low swirl velocity region at the bottom left is also clearly matched in both conditions.

The higher strength downstream vortices both follow the same pattern of rotation counter-clockwise from the point of formation, however the LES predicts the initial velocity horseshoe at x/C=12 to be located higher than the horizontally centred location in the experiment. This is reflected in the final location of the horseshoe, with LES being slightly below horizontal and the experiment being significantly lower at x/C = 17. The subsequent rotational rate for the two cases for the single vortex formation was near identical, with 0.744°/C for the LES and 0.268°/C for the experimental. Total movement of the vortices in the CFD was -0.293C and -0.332C for the upstream and downstream vortices respectively, with -0.260C and -0.293C for the experimental condition. Vortex separation was

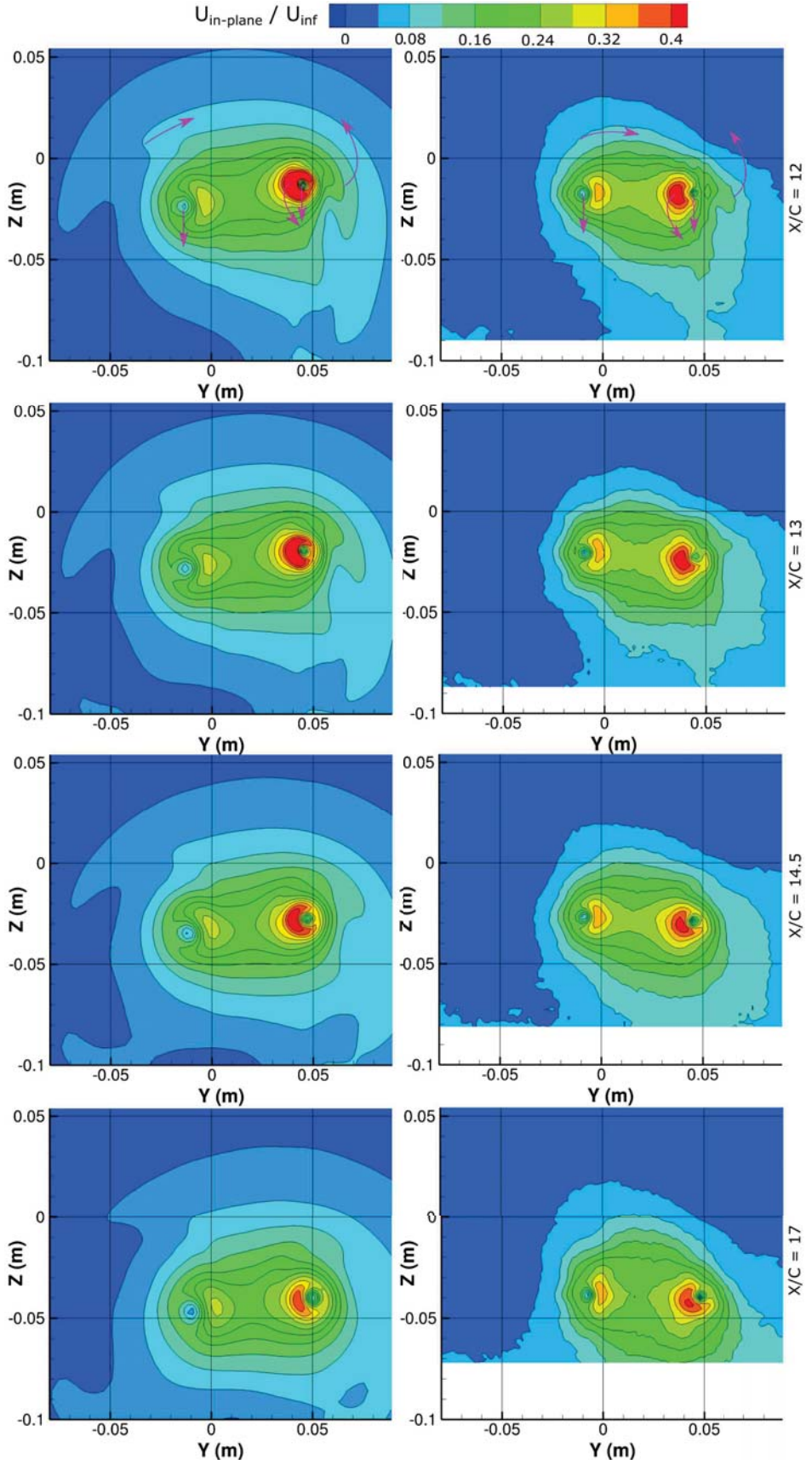

Figure 4.20: Velocity field for counter-rotating validation LES (left) and -0.5C offset PIV (right) at multiple downstream positions. Both data sets are time averaged.

0.612C in the CFD and 0.666C in the experiment, leading to a difference of 0.054C.

The initial peak velocity at the point of vortex generation is higher in the computational model, with a 87.5% larger area at 0.4 U_{ip}/U_{∞} at x/C = 12. However, the computational model displays a higher level of dissipation than the experiments, with the stronger downstream vortex core dissipating to a peak velocity 10% lower than the experimental by x/C=17. The upstream vortex maintains a lower peak velocity in the CFD for the entire length of the observation window, with it showing a lower peak and average velocity at the start of the domain. This is consistent with the higher dissipation rates observed in the downstream vortex, as these are likely also increasing the dissipation of the upstream vortex prior to interaction.

The most significant difference between the two models is the location of the upstream vortex, with the Z value at x/C = 12 being 0.065C lower in the CFD modelling, inverting the slope of the line between the two vortex cores. This is accompanied by a 0.05C lateral shift in the y direction, indicating that the model has over-predicted the migration of the upstream vortex both laterally and vertically. This is further evidenced by the higher vertical rate of migration of the vortices observed when compared to the experiment. While these changes are small, they have a more significant effect in the closer interaction cases, where the effective offset is altered. This will be discussed in more detail in the following subsection. However, the over-prediction of this migration is unlikely to affect the key mechanisms behind the vortex interaction.

4.9.2 Co-Rotating

The primary intent of the co-rotating validation was to determine the accuracy of the modelling of the vortex attraction and merger. Testing with RANS SST and RSM modelling, as well as to a lesser extent Smagorinsky-Lilly LES, had identified issues with high vortex dissipation causing incorrect measurement of the vortex interaction. Specifically, these earlier simulations had found that the upstream vortex had dissipated sufficiently by the point of the rear vane to become the weaker of the two, and the resultant interaction caused the downstream vortex to absorb the upstream vortex. The WALE modelling disagreed with this, showing less dissipation and the downstream vortex being

weakened by the upstream, resulting in it merging into the stronger upstream vortex. As such it was deemed critical to validate the accuracy of the modelling strategy in this condition.

Initial validation of the co-rotating condition proved difficult, as correlation with the 0.2C offset case remained purely qualitative. After finding the upstream vortex had migrated towards a more negative y value, the 0.3C offset experimental case was also investigated to determine the correlation properties, as can be seen in Figure 4.21. Very close correlation was observed to the 0.3C offset case on rotation, separation and vorticity levels, with the same increased CFD dissipation observed as the counter-rotating condition. The average rotational rate in the CFD was 27.088°/C, compared to 26.464°/C in the 0.3C offset experimental condition. This indicated that the model was over-predicting the total downwash from the vanes, which explains how the initial vortex ended up being -0.05C to the left in the counter-rotating condition and -0.1C in the co-rotating condition. The presence of the rear vane produces a downwash in the +y direction for the counter rotating case, shifting the vortex 0.025C from an unobstructed -0.075C location to -0.05C from the expected location. In the co rotating condition the downwash from the rear vane is in the same direction as the initial vane downwash, causing the vortex to shift -0.025C to -0.1C from the expected position, resulting in the correlation with the greater offset case observed. This is consistent with the observation of both vortices being skewed to the -y in the CFD when compared to either experimental case.

More important than the specifics of the vortex positions was the accurate prediction of the merging mechanism. While the increased effective spacing of the validation case meant that it could not be directly compared to the experimental data, by inspecting the vortex characteristics further downstream the merging mechanisms could be validated, as per Figure 4.22. Three distinct stages of merger are visible in both cases, with initially reaching a critical proximity at approximately $B_v/r_v = 2$, followed by an asymmetry developing in the vortex shape and a rapid transfer of vorticity. This is followed by the formation of a spiral tail from the remnants of the second vortex. Most importantly is that the downstream vortex is absorbed into the upstream vortex, as this validates the selection of the WALE model over the other RANS models tested and the Smagorinsky-Lilly LES model.

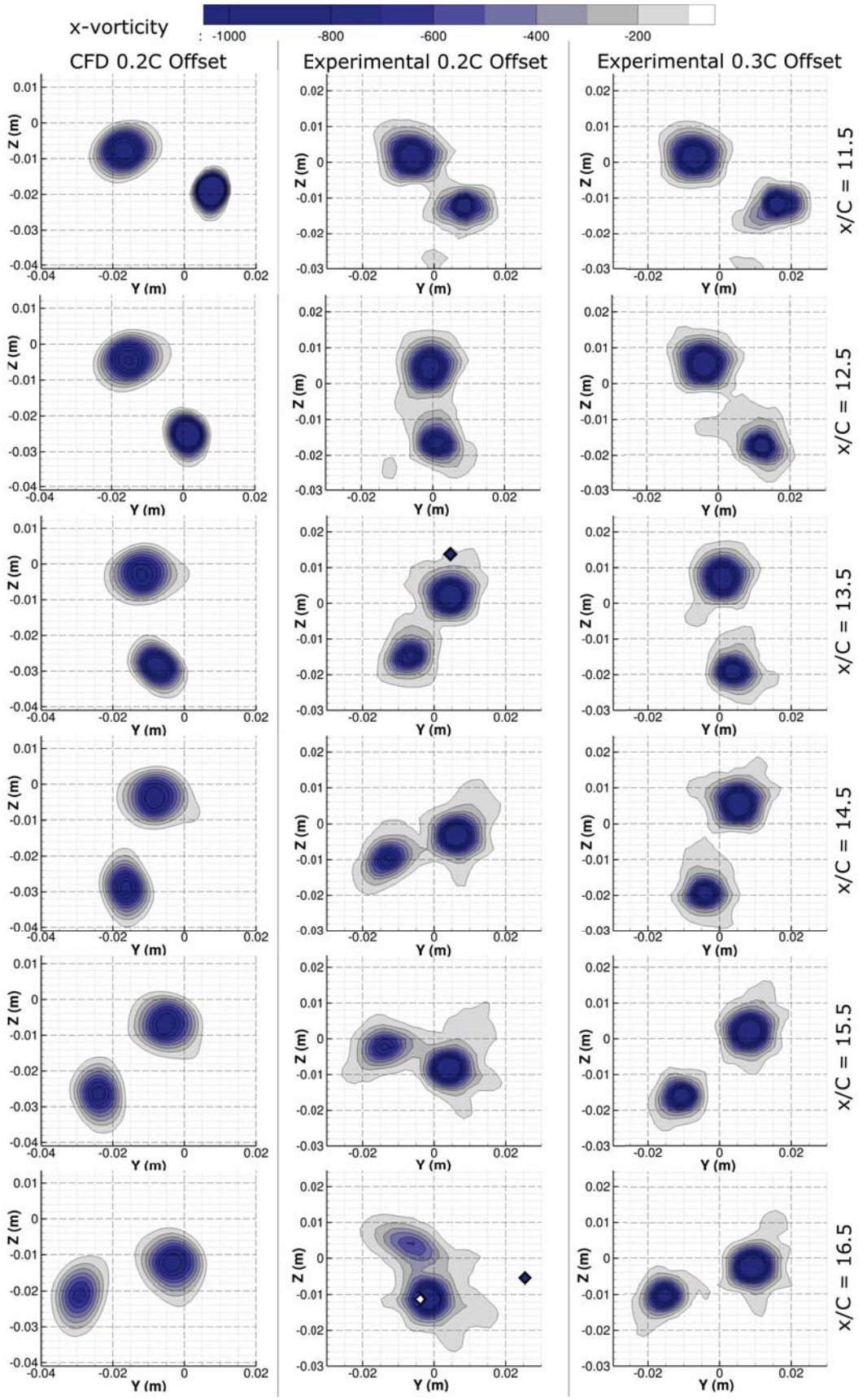

Figure 4.21: Vorticity fields for validation CFD (left), 0.2C offset experimental (centre) and 0.3C offset experimental (right) at multiple downstream positions. All data sets are time averaged.

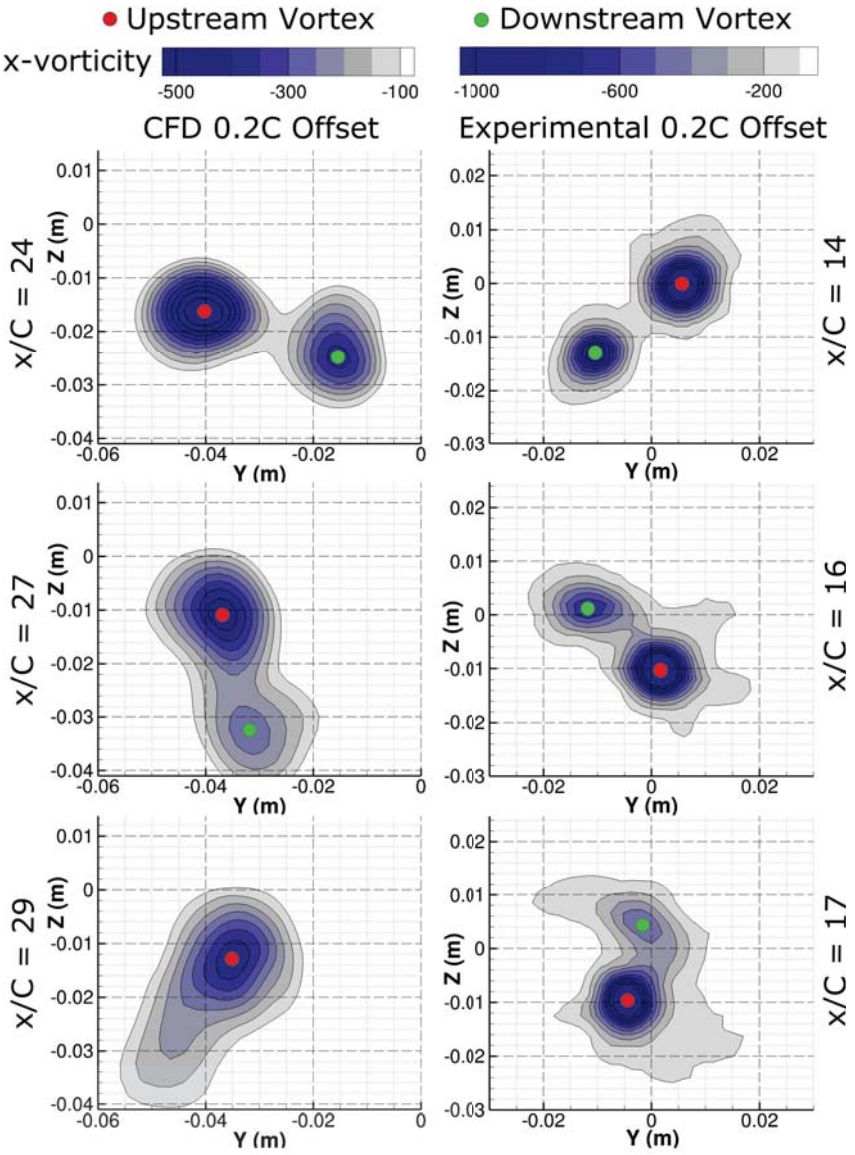

Figure 4.22: Vorticity fields for validation CFD (left) and 0.2C offset experimental (right) with vortex centroids indicated, at multiple downstream positions. Both data sets are time averaged.

Chapter 5

Identification of Key Flowfield Properties

In order to focus the design of the experimental and CFD regime it was desired to understand the qualitative characteristics of the flowfield. By performing initial analysis with techniques such as RANS and flow visualisation the two vane setup was evaluated with minimal resources. The findings of this testing, such as migration patterns and transient behaviour were then used to define the scope and parameters tested in the deeper PIV and LES studies.

5.1 Water Tunnel

Flow visualisation is useful for identifying the paths of the vortices, how steady these paths are, and how Reynolds number can affect the problem. While dye traces are incapable of measuring vorticity values, vortex strength or velocities, the ability to quickly capture position states in both a transient and time averaged manner make the technique invaluable for initial flowfield characterisation. For this visualisation the water tunnel described in chapter three was used. Evaluations were performed at -0.2C, 0C, 0.2C and 0.4C offsets for both the co-rotating and counter-rotating condition.

5.1.1 Co-Rotating

Initial tracing of the vortices showed the two paths forming a helical shape downstream of the rear vane, seen in Figure 5.1. At lower Re the tracer was still clearly visible in the time averaged condition, however instabilities within the vortex core, combined with vortex merging resulted in the upstream vortex being difficult to track for Re >3000. Of note is the fact that the overall path of the downstream vortex straightens more as Reynolds number increases, indicating the point of merger has shifted upstream. The total path in all scenarios also has minimal vertical deviation, remaining relatively flat until the end of the domain.

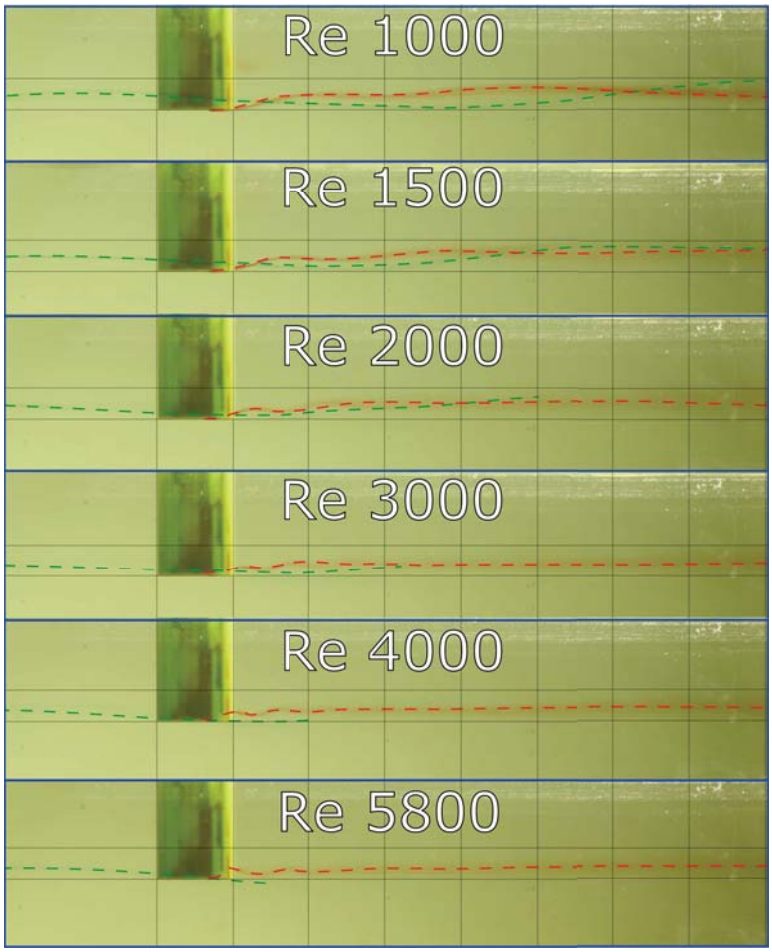

Figure 5.1: Side view of vortex paths of co-rotating vortices at 0.2C vane offset for varying Reynolds numbers.

Some Reynolds number-dependent effects were noticeable with visual inspection of the dye paths, for example in the 0C offset case the vortex was consistently on the pressure side of the rear vane up to Re=3000. However for the higher Re

cases it switched to bi-modal meandering between the two sides of the vane and eventually settling on the suction side of the vane as Re was further increased to 5800. At very low Re (<=1500) the vortex meandering amplitude increased significantly, with long wavelengths and slow motions. At these numbers the small scale instabilities within the vortex core were also reduced, likely due to decreased turbulence, and this made the tracer dye much easier to track as it was not unevenly displaced around the core. The Reynolds number also had an effect on merging distance, with lower Reynolds numbers delaying the point of vortex merger, as seen in Figure 5.1. With Re>=3000, stable merger was observed in all cases by the end of the domain, except for the 0.4C offset which only demonstrated an unstable merger, biased towards unmerged. Such an unsteady merger can be seen in figs. 5.2 and 5.3. Merging in the 0C offset condition was near immediate.

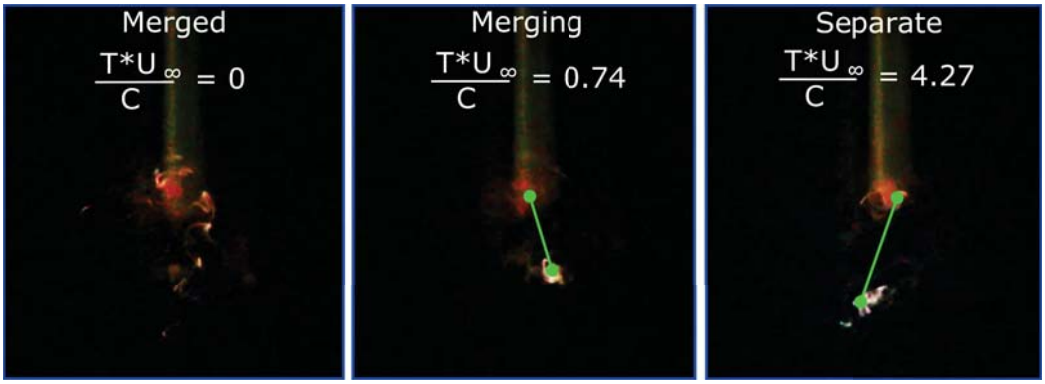

Figure 5.2: Rear view of vortices at Re5800, Co0.2, 5C downstream of rear vane quarter chord. Average recorded vortex separation at this position was 0.22C

Figure 5.2 shows the time history of a transient vortex unmerging. Both the 0.2C and 0.4C offsets experienced this phenomena, with the location downstream varying based off Re as discussed previously. The initial vortex swirls together as one mass at $T * U_\infty / C = 0$, before rapidly separating into two defined vortices within 0.2s. While these vortices are separate, the vortex merging into the other (white dye) oscillates with a substantial magnitude, while the red vortex remains comparatively stable. This can be seen by the difference in position between $T * U_\infty / C = 0.74$ and $T * U_\infty / C = 04.27$. This oscillation occurs at an angle approximately between 30 and 45 degrees from the line between the vortices, and significantly modifies the separation distance by 40%. When separated, the two vortices stay at the large separation for approximately 2s, with minimal oscillation, however once they meander closer together the oscillation magnitudes become substantial, ending in merger. For this offset and distance downstream,

the interaction was biased towards separation rather than merger, with 35% of time spent merged.

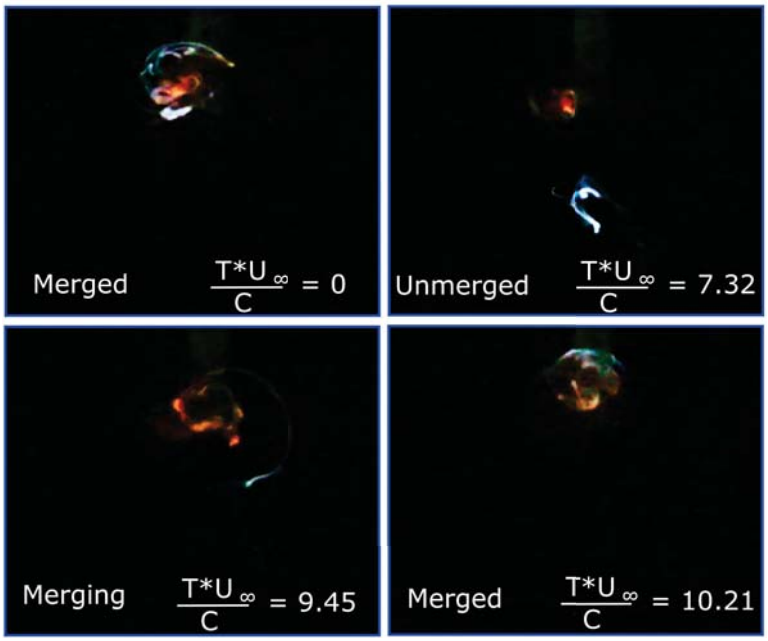

Figure 5.3: Rear view of vortices at Re3000, Co0.2, 7C downstream of rear vane quarter chord

The transient merging/unmerging process can also be seen at lower Re, as evidenced in Figure 5.3. As the Re is lower, the merging distance has been pushed downstream, however again the red vortex remains stable and the white vortex is seen to merge/unmerge with it. At this lower Re, the transition between the two states becomes very clearly visualised, with this position biased more to merger than separation (73% spent merged). When in the merged state, it can be seen that the fluid from the weaker vortex becomes entrained around the outside of the stronger, red vortex, however this transition happens near instantaneously, with the shift of the tracer visible at $T * U_\infty / C = 9.45$. Detailed numerics of this merger will be discussed in Chapter 6, with the fundamental mechanism discussed further in Chapter 7.

5.1.2 Counter-Rotating

The vortex paths of the counter-rotating cases displayed far more vertical movement, with a significant kink in the path of the upstream vortex seen in Figure 5.4. While there was a slight rotation, evidenced in the increase of horizontal path line separation towards the end of the domain, it was far less

significant that the helical pattern observed in the co-rotating condition. While the counter-rotating condition suffered the same dissipative issues observed in the co-rotating condition related to instabilities in the vortex core, the lack of vortex merging meant the cores could be tracked for further downstream through the domain. Ignoring minor changes in vortex separation and path, all of the counter-rotating cases maintained a similar flowfield independent of Re. Passing the vortex on the suction side of the vane resulted in the vortex pair migrating towards the root of the vanes.

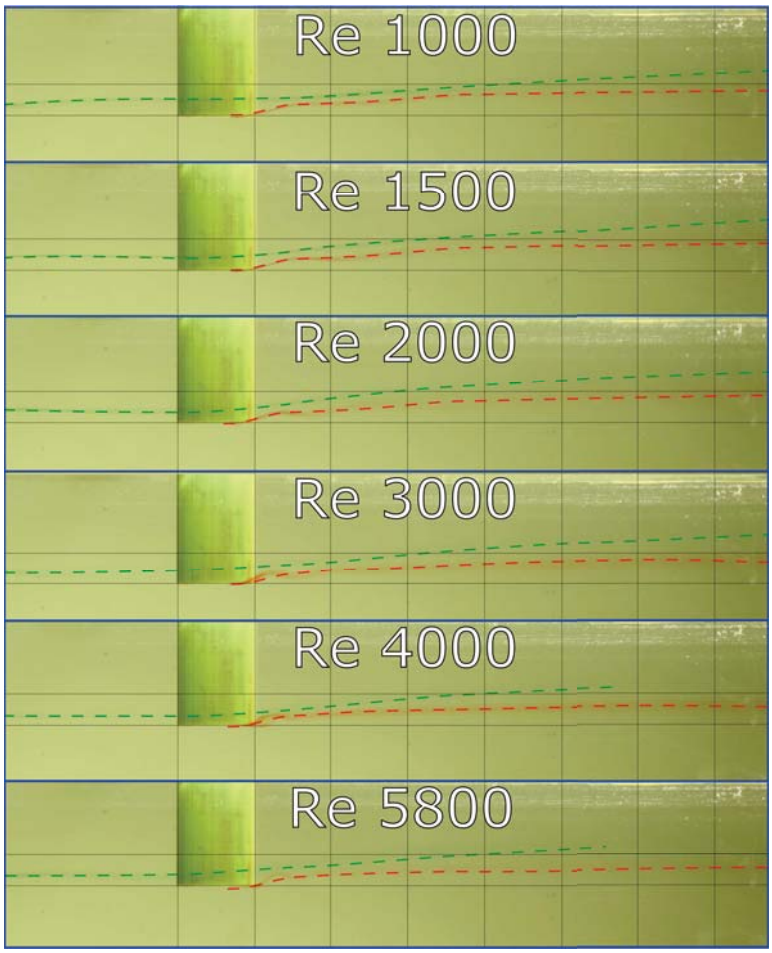

Figure 5.4: Side view of vortex paths of counter-rotating vortices at 0.2C vane offset for varying Reynolds numbers.

The transient oscillations in the counter-rotating cases were very substantial, as can be seen in Figure 5.5. The 0.4C case was selected to demonstrate these oscillations as the nearer offset cases exhibited significant instabilities within the vortex cores, resulting in the transfer of dye marker between vortices that rendered them difficult to distinguish in still images. As with the co-rotating cases, increasing Re typically stabilised the large scale oscillations, however it

also increased the magnitude of fluctuations and marker dispersion within the core. Both vortices were seen to oscillate, with the upstream vortex (white) having significantly larger oscillations as seen in Figure 5.5. These oscillations caused substantial variance in the angle of the line between the vortices and the vortex separation, with the difference in separation between $T * U_\infty/C = 22.10$ and $T * U_\infty/C = 26.66$ visually apparent. The separation changes were primarily driven by a relatively high frequency, small amplitude fluctuation that would occur over the course of a second, while the angle change was much slower, showing only one cycle between $T * U_\infty/C = 3.09$ and $T * U_\infty/C = 64.67$.

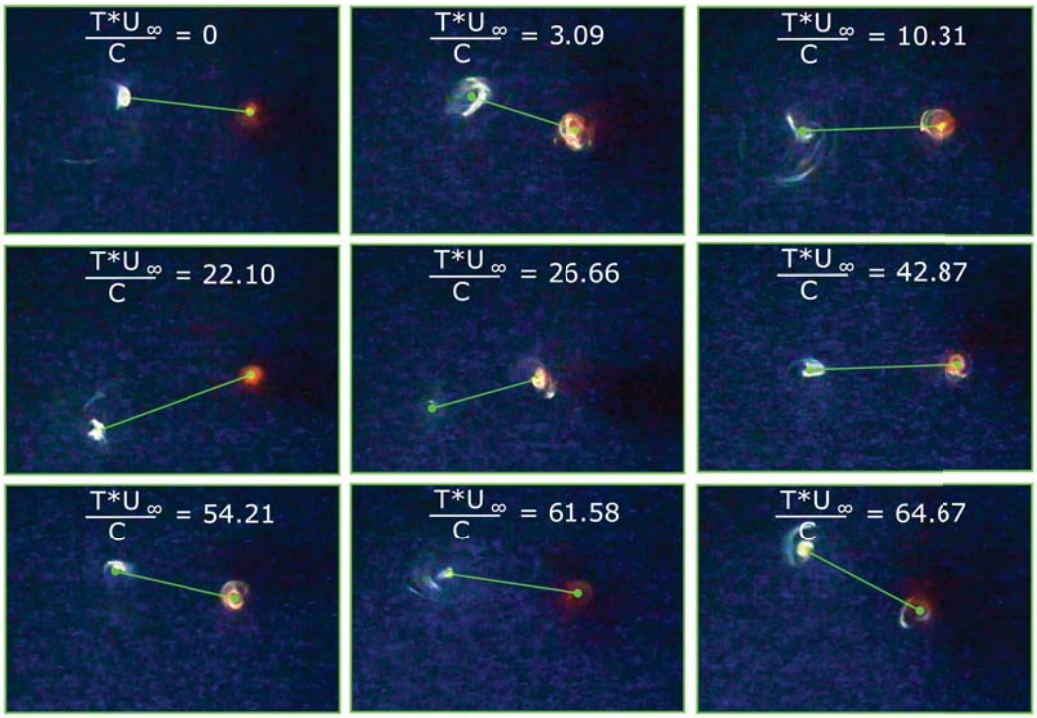

Figure 5.5: Images of counter-rotating vortices at 0.4C vane offset, taken at 5C downstream of rear vane quarter chord

5.2 RANS CFD

The primary objectives of the RANS analyses were to understand some of the velocity and vorticity based properties of passing the vortex to the pressure and suction sides of the vanes at near and far ranges. This would better direct the experimental and LES studies on what areas to look at and what effects to expect. It was also desired to have a baseline with which to observe the limitations of RANS in computing vortex interactions.

5.2.1 Co-Rotating

Results from the analysis of the co-rotating vanes indicated that regardless of the offset of the rear vane, a similar flow structure was formed in all cases. This consisted of the vortex produced from the upstream vane being drawn into a spiral like structure around the vortex produced by the downstream vane. The offset of the downstream vane varied the rate at which this structure formed into a single coherent vortex, as can be seen in Figure 5.6; however it appeared to have a relatively minor effect of the vortex dissipation rate with final energy differences of less than 3.6% observed between cases. This spiral tail appears to be constructed of the initial vortex being stretched into an ellipsoid shape by the downstream vortex at early stages. As it progresses downstream, the upstream vortex transfers its vorticity to the downstream vortex, reducing the vorticity magnitude of the tail. Eventually this results in the dissipation of the tail and the formation of a coherent vortex with a circular structure. It should be noted that after the detailed experimental analysis and LES was performed that it was found for this Reynolds number the dissipation of the first vortex is lowered. This effect, combined with increased reduction of the magnitude of the second vortex resulted in the merging changing to the downstream vortex merging into the upstream one. However, the spiral tail structure was still present in time averaged CFD and experimental results.

The magnitude of in-plane velocity in a plane across direction of flow produces an isosurface that, when trimmed by the Q-criterion [13], is very effective in tracking vortex cores [124]. Inspecting this isosurface at 1m/s swirl velocity provided an effective visualization of the vortex merging (Figure 5.7). Inspecting the vortex paths near the downstream vane showed that the close proximity of the vortex to the vane in the -0.2C offset condition resulted in the vortex impacting the vane just below the tip on the suction side. From here it almost immediately merged with the second vortex, with negligible presence of the core continuing. The increased vortex/vane spacing of the 0.2C offset condition resulted in the upstream vortex passing on the pressure side of the vane without approaching the surface. The initial vortex then appeared to be entrained and pulled around by the downstream vortex, forming the spiral tail seen earlier.

The normalised in-plane momentum was plotted in Figure 5.8 to ascertain the characteristics of the velocity dissipation. From these values it can be seen that the energy state of the vortex structure between offsets is very similar directly

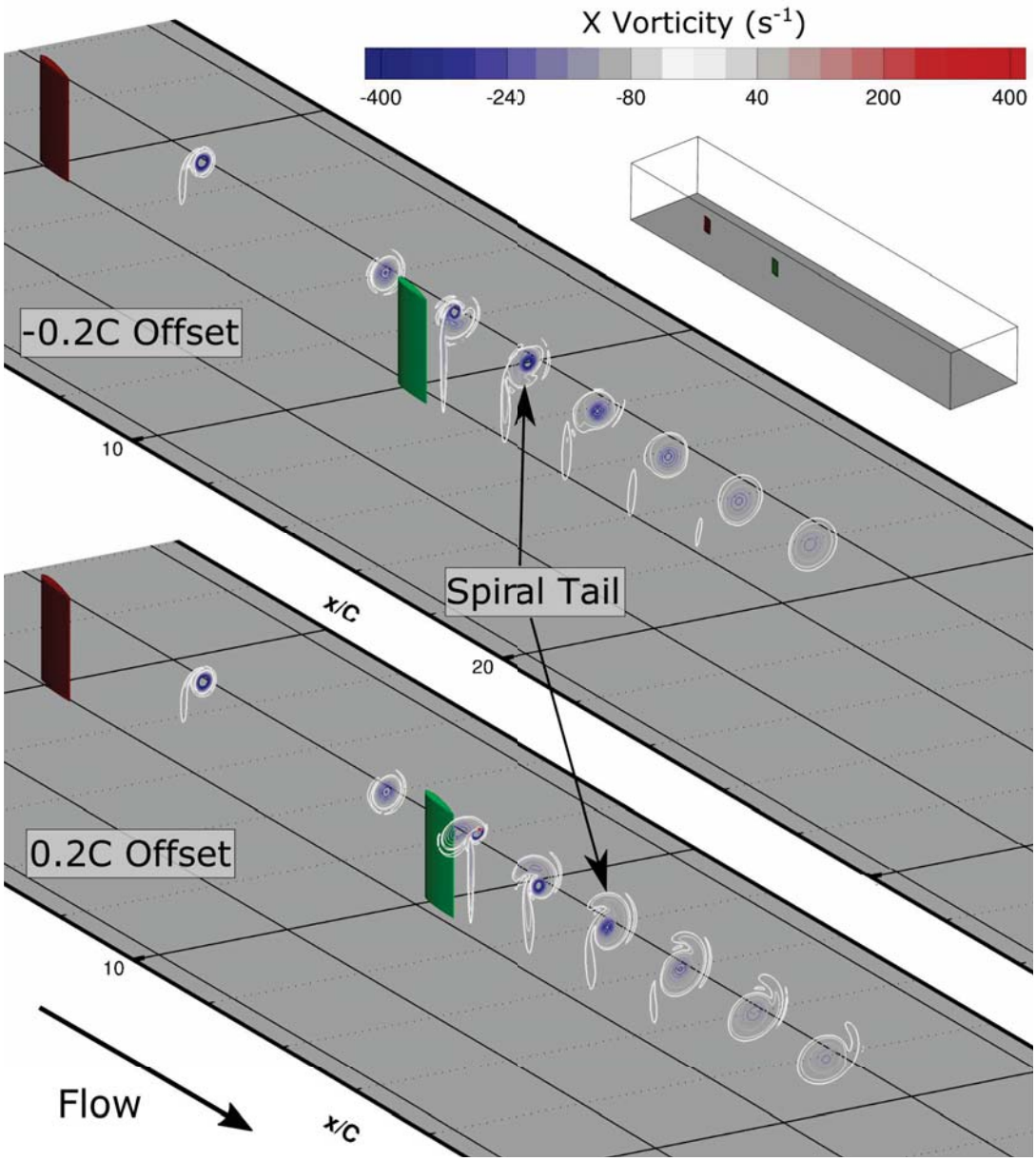

Figure 5.6: Contours of streamwise vorticity for co-rotating cases

behind the vane (x/C = 11), with only 1.5% variance between the 3 co-rotating cases. The total momentum in the co-rotating condition is substantially higher than in a single vane case; with a 29% increase in momentum at the 12C location, and 26% more momentum at 35C. However, the momentum decrease of the co-rotating cases is noticeably higher than the single vane case, at 24-27% for co-rotating compared to 21% for the single vane case. This suggests the momentum dissipation rate of the uneven vortex formed at the second vane is higher than a more coherent singular vane vortex structure, and that there may be a loss of energy in the merging process. The variance of momentum decrease between the

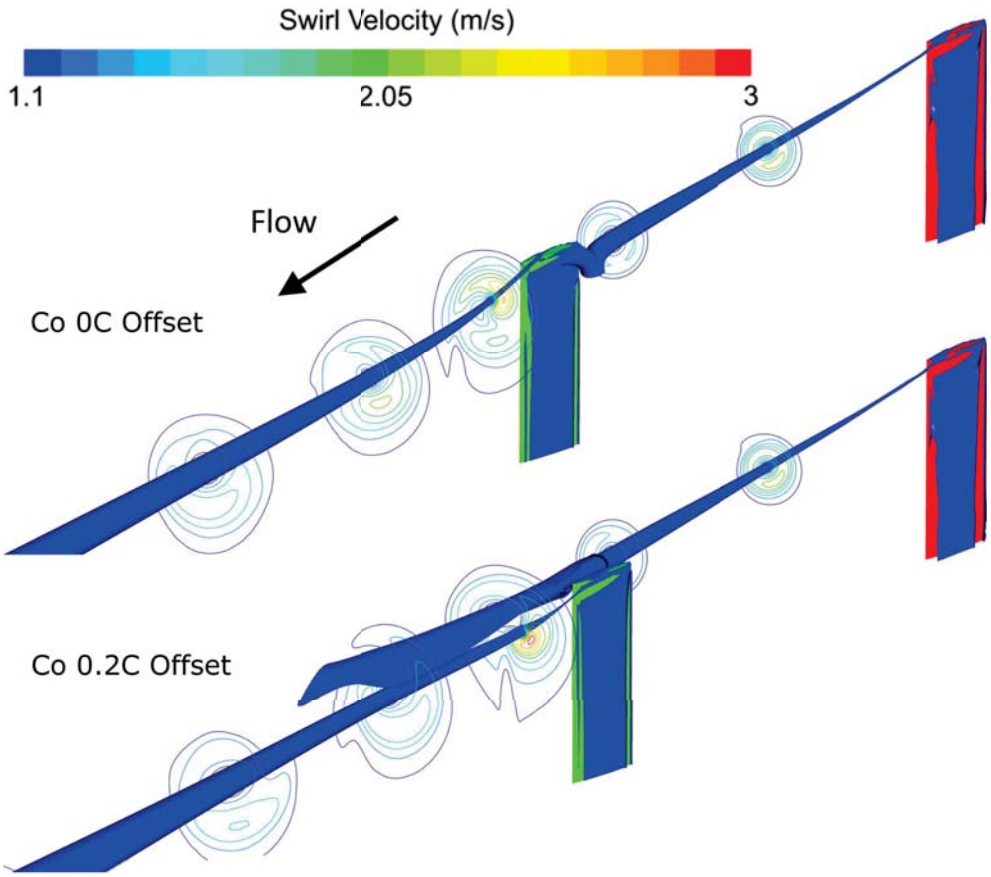

Figure 5.7: Isosurface of trimmed tangential velocity for co-rotating cases, with contours of in-plane velocity.

different offsets is also small but notable, with 1.5% variance in momentum at 12C, but 3.2% variance by the 35C mark. The 0C offset shows the most rapid decrease, with the vortex impacting on the pressure side of the vane. 0.2C offset, with the vortex passing by the pressure side, shows the slowest total momentum dissipation at 24%; however the initial momentum is lower, resulting in a lower final momentum than the -0.2C offset case.

The varying of the vane offset also altered the path of the final vortex slightly, with a vortex path offset equal to 28.4% of the vane offset. This deviation means that the offset of the vanes can modify the location of the final vortex while not significantly altering the re-energization level. As a result, it would be expected that over a wide sweep of offsets the energy levels of the co-rotating vane flowfield would remain relatively unchanged.

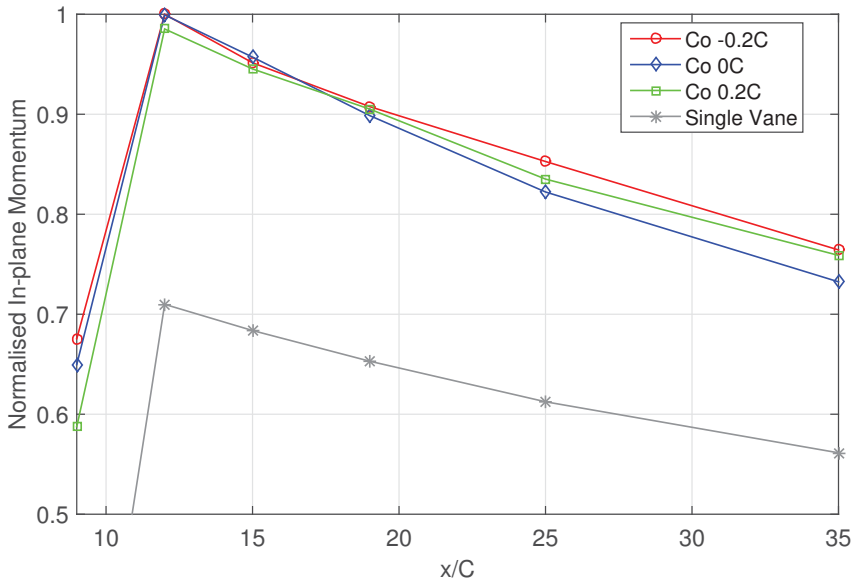

Figure 5.8: Normalised in-plane momentum for co-rotating cases and reference single vane.

5.2.2 Counter-Rotating

Contrary to the co-rotating cases, the counter-rotating scenarios showed significant differences in vortex structure and dissipation rates. Moving the downstream vane immediately in the path of the vortex (-0.2C offset) caused a rapid destruction of the initial vortex, as well as significantly reducing the strength of the secondary vortex, as can be seen in the vorticity contours of Figure 5.9. The remnants of the upstream vortex were forced downwards by the downstream vortex, remaining located directly below the downstream vortex for the remainder of the domain. Moving the vane such that the vortex passed alongside it at a distance instead of near impact (0.2C offset) caused the vortex produced by the downstream vane to equal the strength of the merged vortex of the co-rotating case (-0.2C offset co-rotating). This is related to energy transfer between the vortices, as the downstream vortex could be seen to form with higher vorticity from the contour plots, however dissipated at a more significant rate than the single vane case.

The total momentum for the counter rotating cases in Figure 5.10 confirms this energy dissipation. Ahead of the second vane (x/C = 9) the variation between cases is only 1%, however behind the vane there is a substantial difference in momentum of 47%. -0.2C offset shows the most substantial drop, with a 52%

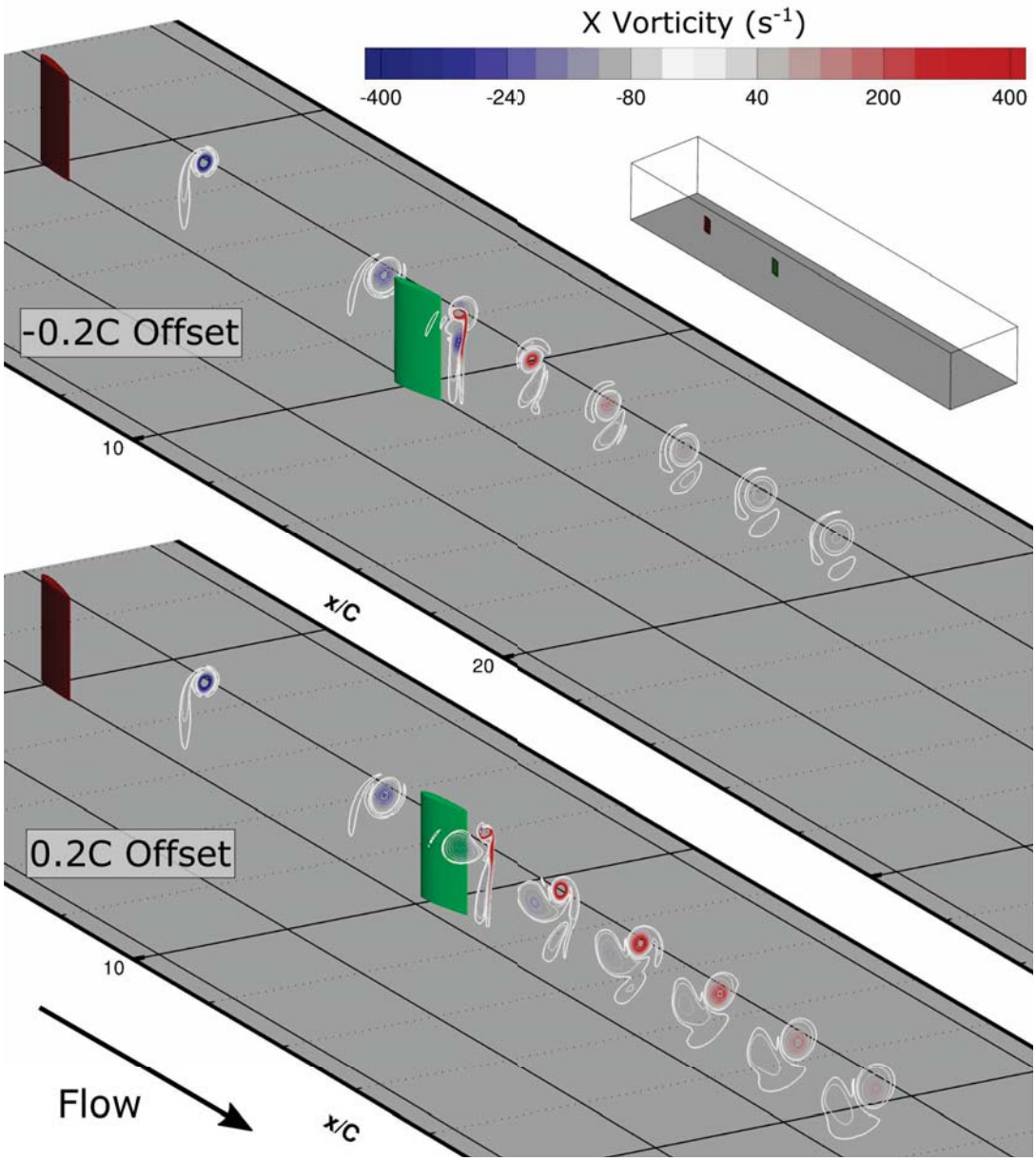

Figure 5.9: Contours of streamwise vorticity for counter-rotating cases

decrease in momentum by x/C = 12. This is due to the very direct leading edge impact of the primary vortex on the rear vane, as was seen in Figure 8. Moving the vane further away from the path of the vortex increased the total momentum; however these values were still substantially lower than the co-rotating cases, with an average 82% lower momentum at the x/C = 35 mark. Some of this is due to the vane downwash, as in the counter-rotating condition the opposed vanes will cancel their downwashes, reducing total in-plane momentum.

The dissipation rates of the counter-rotating configurations were also more significant than that of the co-rotating. 0.2C offset exhibited a dissipation of

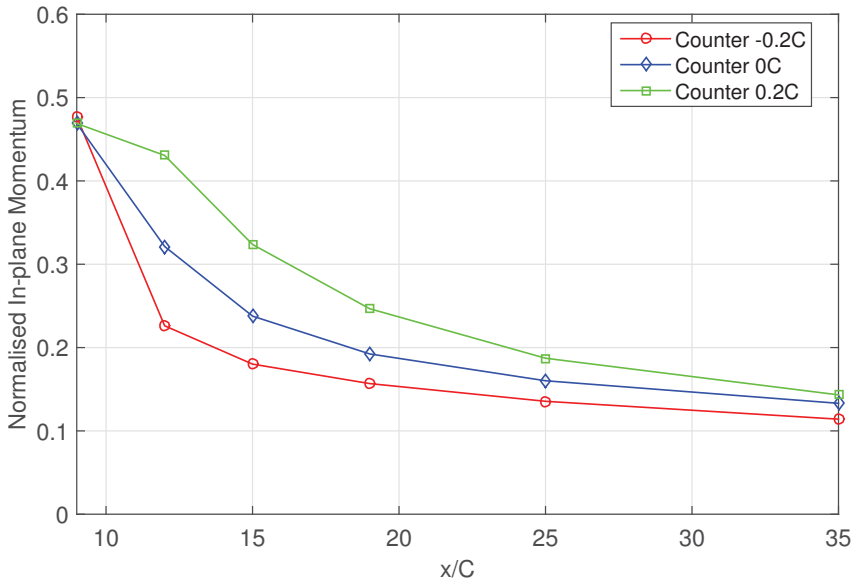

Figure 5.10: Normalized total in-plane momentum for counter-rotating cases

69% from 10C to 35C, while the 0C and -0.2C offset achieved 72% and 77% respectively. The largest discrepancy between offsets is the location of maximum dissipation rate, with the close impact -0.2C offset experiencing very significant drops in momentum immediately after the vane (x/C = 9C to x/C = 12). This decrease was 52%, compared to the other cases 8.5% and 32% in the same region. Consequently it can be seen that the counter-rotating case is highly sensitive to vane offset.

5.3 Cases and Points of Interest

The initial water tunnel and RANS studies identified several key features for later investigation in the experimental and LES testing. The most significant finding from the water tunnel testing was the transience of the vortex flowfield. The oscillations in vortex position and separation, as well as the presence of the merging transience indicated that the subsequent work would need to have the capability of resolving these features. Of particular interest was that the merging was biased to either the merged or unmerged state depending on location downstream and offset. This led to the coding of instantaneous vortex tracking discussed in both the experimental and numerical methods. By tracking the vortices in each image pair for the PIV case a statistical spread of these locations

could be obtained, as well as the resulting variance in core circulation and radius. In the case of LES the position, circulation and pressure could be time resolved through the evaluation of the vortices at each timestep, allowing for a great depth of measurement into these transient characteristics for both the vortex merger and counter-rotating oscillations. The limited variance in the fundamental mechanisms over the sweep of Re presented indicated that sweeping over multiple Re may not yield significant information, and as such one Re as selected for the correct vane shedding regime would be appropriate.

The RANS studies demonstrated very significant offset related variance in the flow structures and energy variance for the counter-rotating cases. As such it could be seen that a wide variety of offsets would need to be evaluated for both vortex paths and circulation, with the experimental investigation tracking from the extremes of offsets with near zero vortex rotation. From the results of this offset testing the LES cases of key interest could then be decided. For the co-rotating condition the RANS showed that similar flow structures were to be expected, however slight differences in near-vane vortex interaction and resultant minor changes in circulation were deemed worth investigation. The combination of the circulation values and need to investigate the transient merging meant that again a wide experimental sweep would be needed for the co-rotating case, however the similarity of the merging mechanism resulted in only one LES case being selected for LES transient vortex analysis. This was the co-rotating 0.2C offset case, as this condition exhibited both the helical spiral and transient merger within the CFD domain, covering the key flowfield features identified in this chapter. Consequently the initial analysis of key flowfield properties was very useful for focussing the scope and intent of the wind tunnel and LES testing programs.

Chapter 6

Experimental Analysis of Vortex Interactions

As discussed in the previous chapters, the primary intent of the experimental work was to ascertain the circulation, radius and position of the vortices as they travelled downstream. The ability to measure the velocity field in the experiment allows the derivation of the vorticity field, thus allowing for determinate vortex centres and circulation to be calculated. The wind tunnel testing allowed for results to be produced for both the co and counter-rotating cases for circulation, core paths and instantaneous core locations.

6.1 Counter-Rotating Condition

6.1.1 Core Paths

The core locations at each plane were calculated using the methodology previously discussed in Chapter 3, with the location on each PIV plane constructed into a core path for both upstream and downstream vortices. Inspecting a selection of paths from across the cases investigated, as seen in Figure 6.1, a basic migration trend emerges. At the far ends of the range (-0.6C and 0.5C) the migration is near linear, and predominantly vertical. At the negative end of the spectrum, the paths move upwards, while at the positive end they move downwards, similar to the theoretical predictions of Lewecke et

al [23]. As discussed in the literature review, this vortex self-advection is due to the shear between the pair being minimal due to complimentary rotation, while at the periphery of the pairs there is no such rotation. This causes a shear between the vortex pair and the freestream flow, resulting in the migration of the vortex pair in the opposite direction to the outer velocity of the vortices, as can be seen in Figure 6.2. At closer offsets, the motion is less vertically dominated, and takes on a more significant lateral component, as well as a significant rotational motion between the vortex pairs. As the configuration transitions between predominantly vertical motion to predominantly lateral motion, the magnitude of the migration increases significantly, as can be seen by the 80.5% difference between the 0.5 and 0.2 case. This is followed by a significant drop of 27.2% in the total migration between the 0.2 and -0.05 cases as the vortices interact more closely. The same effects can be seen on the negative side as it approaches the point of interaction, from -0.5 to -0.25.

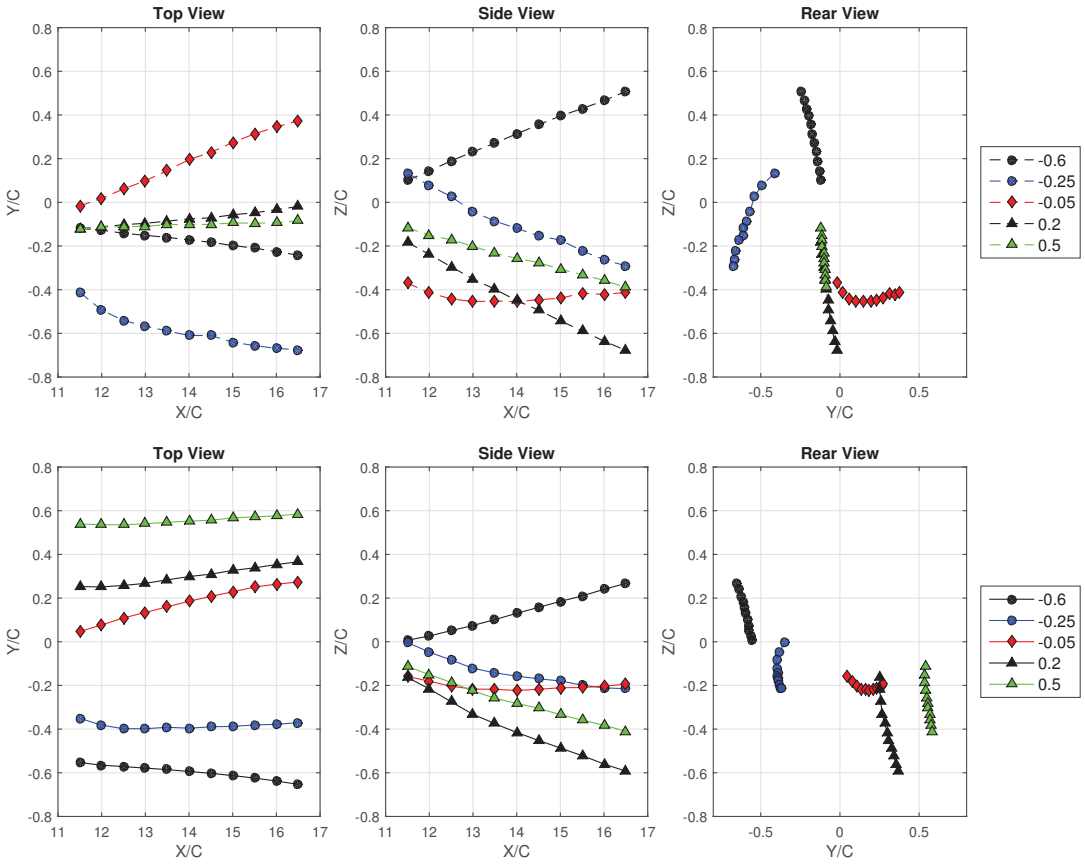

Figure 6.1: Paths of upstream (dotted) and downstream (solid) vortices. Error in core location is ± 0.008C.

The positive offset case vortex paths are shown in Figure 6.3. At the maximum offset (0.5C), the vortex pairs have little interaction, with minimal deviation in

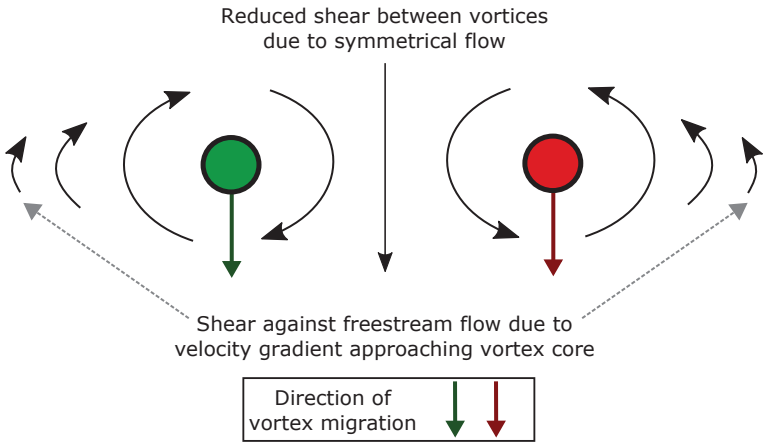

Figure 6.2: Schematic of vortex core migrations for equal circulation counter-rotating cases.

their paths. The separation between the vortex pair alters approximately linearly in the same amount as the variation in offset between the vanes. For this range of offsets the vortex pair separation does not significantly vary from the start to end of the domain, with the spacing increasing by an average of 0.024C. The progressive increase in vortex pair migration as the vortices are brought together can also be seen in this figure, with a progressive increase in vertical migration from the 0.5C to 0.1C cases of 0.19C (101%).

At the 0.1C case, a rotation of the vortex pair has become evident, with significant curvature apparent to both the upstream and downstream vortex paths. This curvature occurs as a result of a differential in vortex strengths in the pair. As the circulation is higher on the downstream vortex, the weaker vortex is drawn into a rotational path around it. This results in a direction of rotation in the direction of the stronger vortex, despite the fact that its downwards shear is higher than that of the weaker vortex due to its increased circulation. Consequently, the path of the weaker (upstream vortex) is significantly longer than the stronger vortex, with a total migration of 0.660C as opposed to 0.522C for the downstream vortex. This can only occur when a combination of conditions are met, both the vortex proximity being sufficiently close to produce significant interactions of the high vorticity core regions, and the differential in strengths between the vortices being sufficient to promote rotation. With both cores having an average $R_{0.1}$ of 0.146C and the vortex separation distance between the cores being 0.274C, this would indicate that significant vortex interactions which affect the strength of the upstream vortex begin to occur at a vortex spacing approximately equivalent to $2\text{x}R_{0.1}$. This is

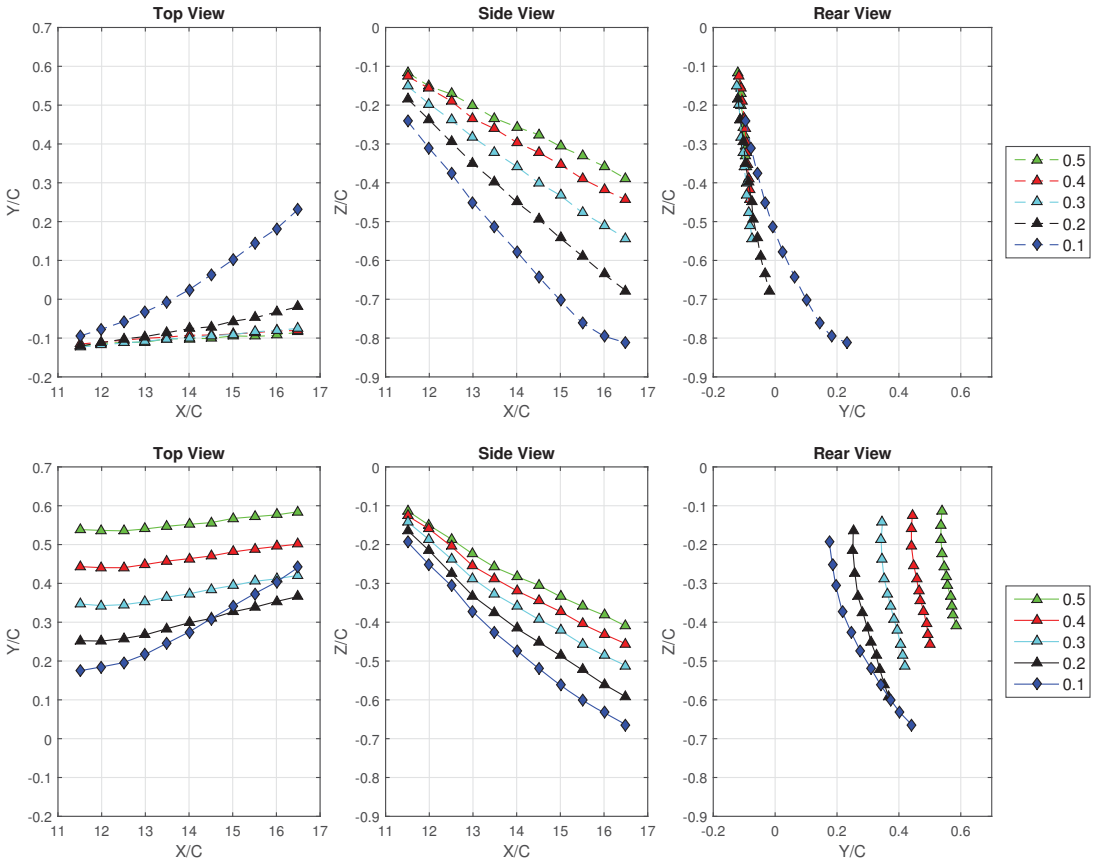

Figure 6.3: Paths of upstream (dotted) and downstream (solid) vortices. Note the scale difference between the top and side views. Error in core location is ± 0.008C.

the spacing where the two vortex radii would just be intersecting.

As the upstream vortex passes closer to the rear vane, the rotational and horizontal migration of the vortex pair significantly increases. This can be seen in Figure 6.4. With no rear vane the upstream vane's vortex core was located at approximately -0.1C. This means the upstream vortex would pass by the downstream vane without direct impingement in the -0.3C and -0.25C cases. However, as the offset is further reduced (-0.15C and -0.1C) the upstream vortex will impinge on the downstream vane. This causes a reduction in the path lengths of both vortices, and increases the separations. At the -0.2C offset the $R_{0.1}$ of the upstream vortex marginally impinges on the suction surface of the downstream vane. This has caused a reduction in downstream path length from 0.216C to 0.128C. As such, the interaction between the downstream and upstream vortices post vane must be strongest at -0.25C, while the point of impingement is located at -0.1C.

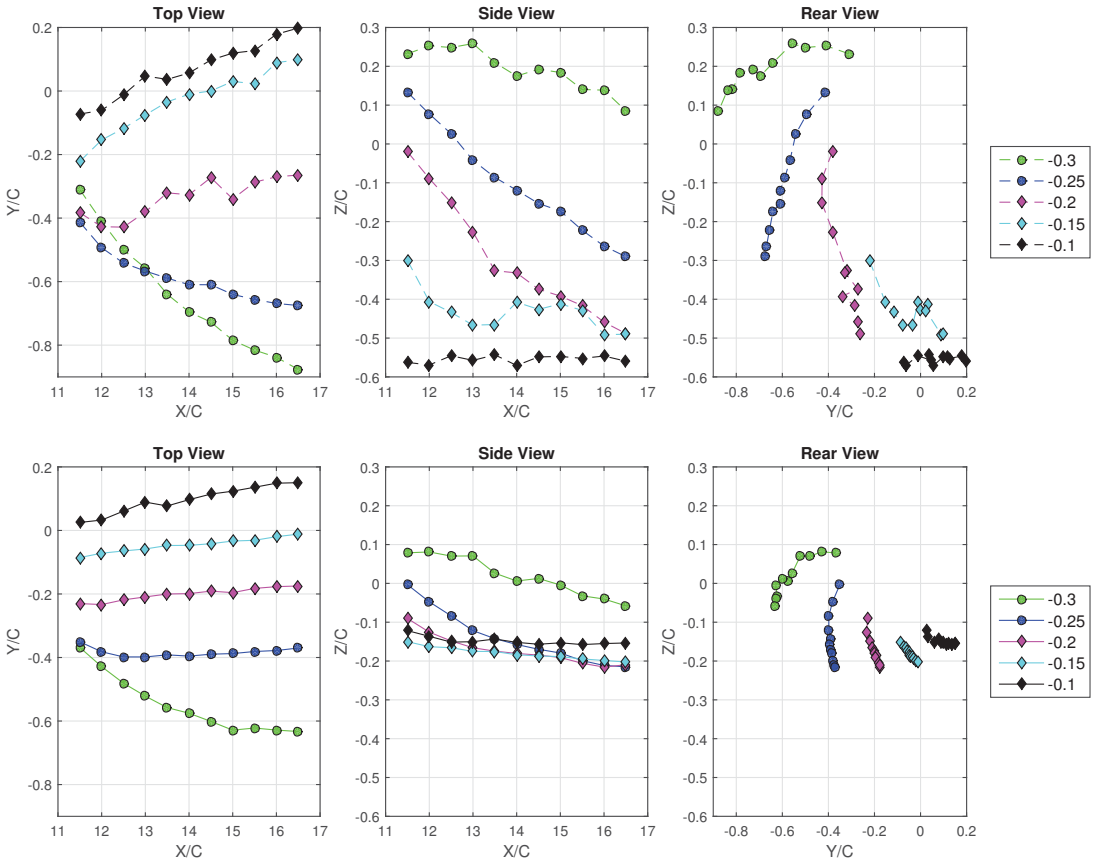

Figure 6.4: Paths of upstream (dotted) and downstream (solid) vortices. Note the scale difference between the top and side views. Error in core location is ± 0.008C.

The rate of rotation by which the two vortices orbit each other was calculated through a linear approximation of the change in angle of the line drawn between the two vortex cores. This can be seen diagrammatically in Figure 6.5. By looking at these rotational rates in Figure 6.6, it can be seen that the lowest angular core velocities are achieved at -0.1C, the point where the upstream core would impact the quarter chord of the downstream vane if no deviations occurred as a result of the presence of the second vane. Rotational rate peaks occur at -0.2C and 0C, at peaks of 19.57 and 17.74 degrees/C respectively. The peaks are caused by a combination of high strength interaction and close vortex proximity. Of interest is the increased rotational rate of the -0.2C case compared to the stronger interacting -0.25C case. Closer inspection revealed that the -0.2C rotation was high at the start of the domain, however rapidly reduced after x/C = 14, while the -0.25C case remained near constant. As such, the partially impinged interaction of the -0.2C offset causes a strong initial interaction as it affects the vortex formation. However, the -0.2C interaction causes a more rapid reduction of the

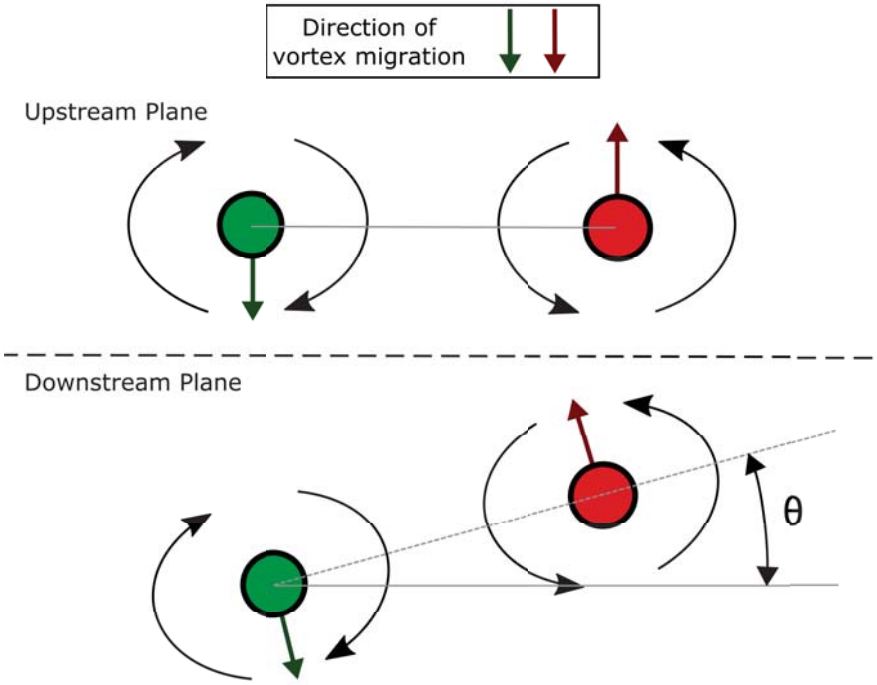

Figure 6.5: Schematic of rotation angle calculation for vortex pairs. In-plane vortex trajectory is shown via the red (upstream vortex) and green (downstream vortex) arrows. The viewing plane is normal to the freestream velocity, with the view seen from downstream of the vanes.

vortex strengths as they progress downstream, with a subsequent reduction in rotational rate, while the -0.25C interaction shows far less reduction. Between -0.35C and 0C there are the most significant gradients of rotational rate due to the transition of the upstream vortex location around the vane. On the negative side of this rotational peak the rotation rates trend towards the values seen on the far positive regions, as would be expected as the vortex separations become significant again.

The initial vortex separations between the vortex pairs remain relatively consistent through the range of near field interactions from -0.35C to -0.2C, however dip slowly, and then drop to their lowest separation at -0.25C. While the initial separations decrease towards the -0.25C offset, the final separations remain far more constant until -0.15C offset. This indicates that for interactions with vortex spacings initially less than $1.8R_{0.1}$ apart the vortices will rapidly separate towards a minimum separation distance, in this case approximately $1.6R_{0.1}$. Further separation of the cores may occur from there, as seen in the far separation cases. The initial core spacing in the -0.25C case is the smallest, at approximately one core radius. Bringing the vortices closer

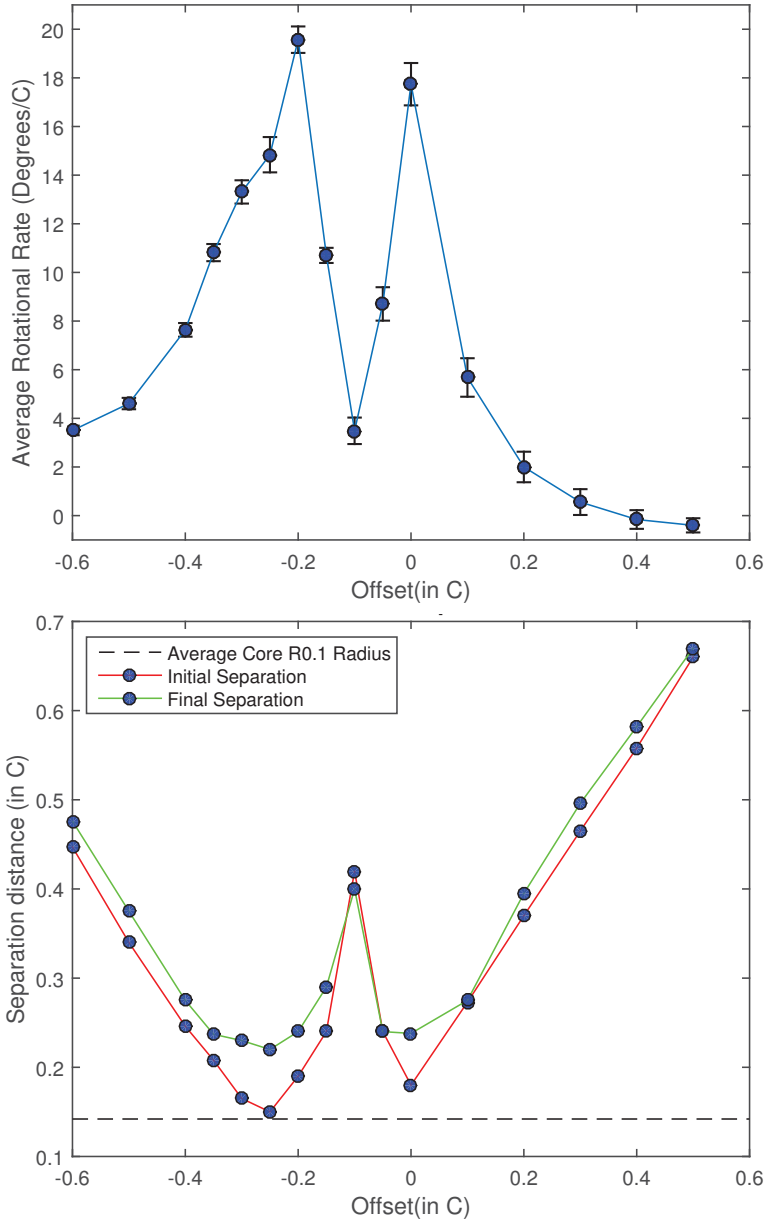

Figure 6.6: Rotational rates of the vortex pairs (top) and average vortex separations (bottom). Error in vortex separation is ± 0.005C. Initial separation is at x/C = 11.5 with final separation at x/C = 16.5.

than this will begin to dissipate the upstream vortex significantly. As the upstream vortex impinges on the vane it causes the vortices to increase both their initial and final separation distances, as can be seen in the points from -0.2C to -0.1C. At the point of complete impingement the separation has become largest, and the rotation smallest, indicating that this is no longer a point of significant interaction, but rather the downstream vane has significantly reduced the strength of the upstream vortex during the direct

vane/vortex interaction. This configuration also displays a smaller difference between the initial and final separations than the surrounding points on the negative side as the vortices have reached a steady equilibrium state in the flow and the subsequent interactions are weak.

6.1.2 Core Sizes

While the vortices remain near a uniform Lamb-Oseen distribution at the far offsets, at nearer offsets significant partial straining occurs from the influence of the vortex interaction. This causes a skew in the shape of the vortex core that changes its primary axis as the vortex pair rotates downstream, preventing the fitting of a Lamb-Oseen distribution of vorticity to the results. Consequently, to calculate the core radius, the area bounded by the isoline of 10% of the peak vorticity within the plane has been used in both the positive and negative circulations, as used by Manolesos [1]. While this area can vary significantly from a circle, an effective radius can be calculated from Equation 6.1 by assuming approximate circularity, thus facilitating quick comparison of the relative vortex sizes.

$$R_{0.1} = \sqrt{\frac{A_{0.1}}{\pi}} \tag{6.1}$$

The removal of noise from the data via the filtering previously discussed in Chapter 3 ensures that only the area of the core itself is processed, and not the surrounding flow features or noise outside the core. By comparing this method to a Lamb-Oseen approximation, it was found that the spatial sampling resolution could result in a 15% maximum error in peak vorticity. This translated to a 1.5% maximum error in the 10% peak vorticity, giving a maximum core radius error of 5% per image pair, which was considered acceptable for this analysis. This was confirmed by evaluating the -0.2C offset case at double the spatial resolution as previously mentioned, yielding errors of $\pm 2.7\%$ in core radius across the averaged sample size.

Initial and final values for core radius were calculated by linearly approximating the gradients of core radius across the domain, reducing the effect of statistical variance on the measured sizes. These core radii can be seen below in Figure 6.7.

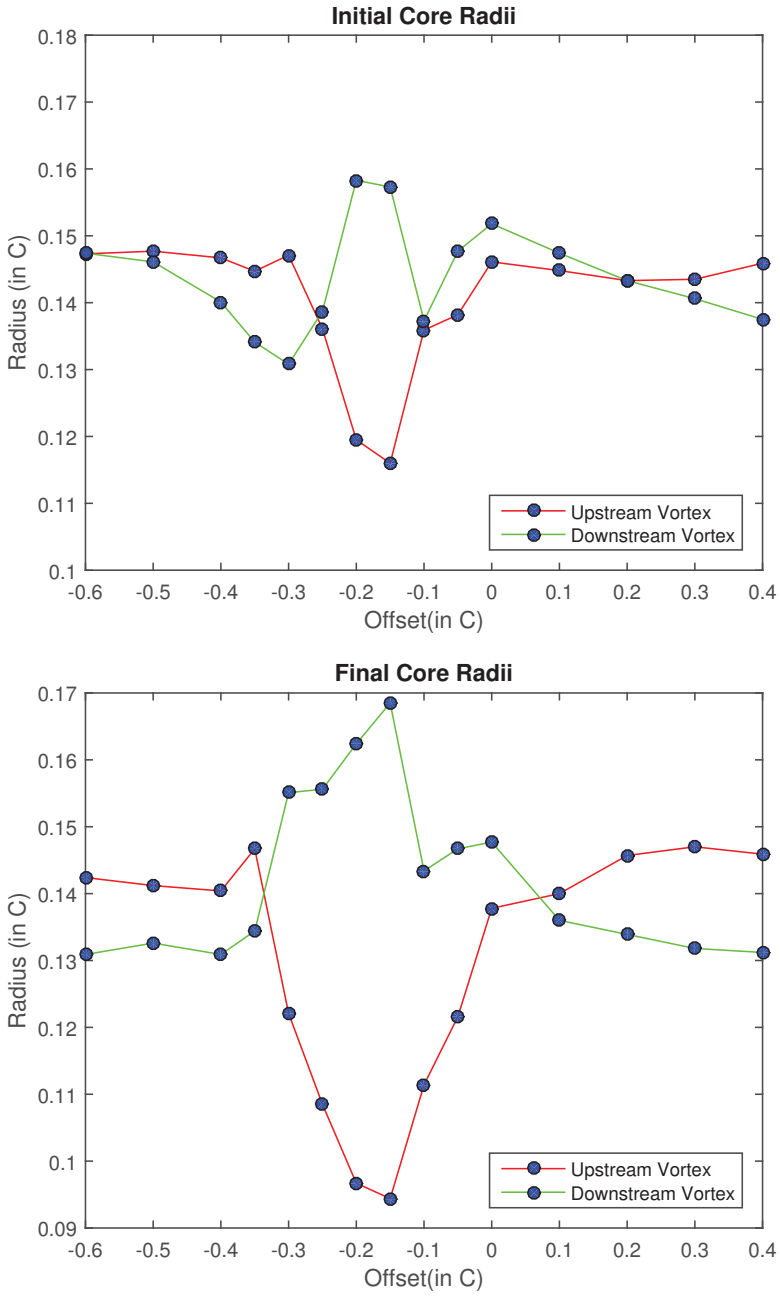

Figure 6.7: Core radii for all cases at x/C = 11.5 (Initial, top) and x/C = 16.5 (Final, bottom).

At the -0.3C offset a significant reduction in initial core radius can be seen for the downstream vortex. However, as these progress through the domain the downstream vortex grows in size by 0.024C, while the upstream vortex radius decreases by 0.025C. This is the only near-field interaction case observed to have a significant trend of growth in the downstream vortex, and is also a local minima before the increase in initial downstream vortex size to the peak at

-0.2C offset. Between -0.25C to -0.2C, the previously identified peak of vortex interaction, there is a transition from a larger initial upstream radius to a larger initial downstream radius. While this change is small in magnitude, the final downstream vortex size peak at the -0.25C case has a more significant change, indicating that the strong interaction has resulted in the transfer of energy from the upstream vortex to the downstream vortex throughout the domain, causing an increase in the size of the downstream vorticity field.

As the interaction approaches the point of impingement, the final size of the upstream vortex decreases to a minima at -0.15C. As the upstream vortex moves closer to the tip, its strength is significantly reduced by the counter-acting vorticity, resulting in these decreases in core size. At the point of impingement (-0.1C) there is a marked decrease in downstream vortex cores size. However, the upstream vortex size has increased by 17% at this point from the -0.15C case. The reason for this was not apparent from the results, however it is likely related to the downstream vortex stripping vorticity from the upstream vortex when slightly offset, while in the direct impingement case the downstream vortex itself is significantly weakened, and as such cannot draw energy from the upstream vortex as successfully. As the offset increases towards the positive side, there is a steady increase in the final core radii for both the upstream and negative vortices, with less clear trends in the initial size.

6.1.3 Vortex Meandering

In addition to the circulation and core location changing as the vortices pass through the domain, they also vary with respect to time. Vortex meandering is the phenomenon of random vortex motions and oscillations that can result from turbulent flow, vortex shedding or other flow disturbances. While the origins of meandering are disagreed upon [6, 149–151], it is still important to characterise, as it changes the predictability of the flowfield, particularly in real world scenarios.

Inspecting the core variances in Figure 6.8, it can be seen that the natural tendency of the cores in the far interacting cases is to maintain a near constant meandering magnitude throughout the domain investigated. From the 0.2C to 0.4C cases it can be seen that the end variance is less than the start variance for the downstream vortices, and very similar for the upstream vortices,

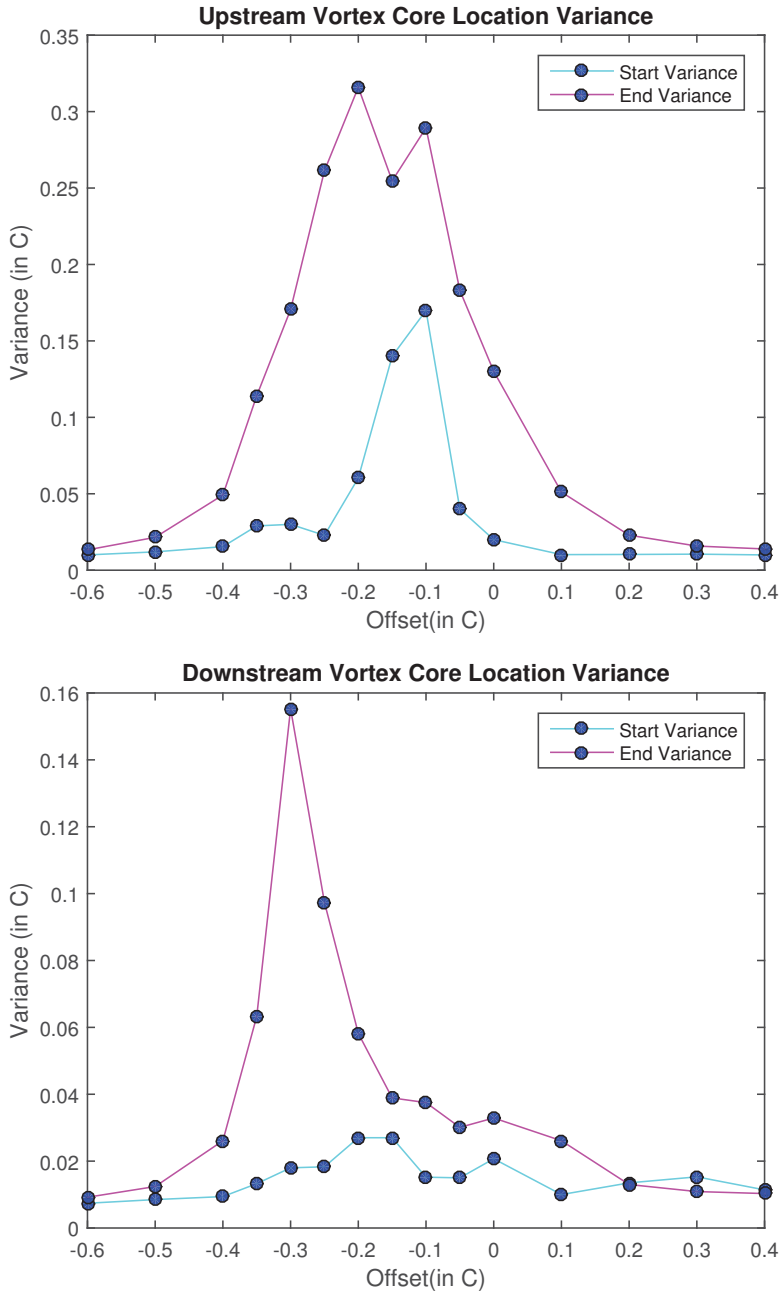

Figure 6.8: Core location standard deviation of upstream vortex (top) and downstream vortex (bottom). Note the scale difference between the two plots. Initial separation is at x/C = 11.5 with final separation at x/C = 16.5.

showing that the initial meandering motion is caused by the formation of the vortices. The shear layers shed off the vanes may provide the initial perturbations, resulting in the fluctuating deviation of the core location. As the flow travels further downstream, these spanwise vortices will be dampened out by viscous effects, as well as flow entrainment into the streamwise vortices. These vortices are too far apart for the Crow instability to have a significant

effect within this domain. This explains the reduction of the meandering magnitudes as the vortices progress.

As the interactions of the vortices become stronger, their meandering magnitudes significantly increase. Between -0.2C and -0.05C the start variance of the upstream vortex significantly increases. This is in the region of the upstream vortex $R_{0.1}$ intersecting the suction side of the downstream vane. At -0.1C offset there is a peak variance of 0.17C, which is greater than $R_{0.1}$. This indicates that in near field interactions the upstream vortex is fluctuating from one side of the vane to the other, creating a large spread of core locations. This increase is co-incident with the reduction in vortex pair rotation angle between -0.2C and 0C. The downstream vortex is far less affected by these variations, with a maximum increase in start variance of 0.0196C over the case with the least variance.

While the start variance is proportional to the proximity of the incident vortex to the downstream vane, the end variance is more dependent on the magnitude of the interaction. This is particularly true for the downstream vortex, which achieves a variance peak of 0.155C at -0.3C offset and a significant increase in meandering from -0.35C to -0.15C. This is accompanied by a wider spread of meandering in the upstream case, with significant increases in meandering once the vortex separation drops below 0.275C (-0.4C and 0.1C offsets). These downstream vortex proximities are sufficiently close to allow for instabilities to be formed between the vortices, creating the meandering observed. In both vortices, the peak in variance at the downstream end of the domain occurs at a more negative offset than either vortices start peak. This indicates that the low pressure region on the suction side of the downstream vane and resultant adverse pressure gradient is enhancing the instabilities of the vortex pair further downstream.

Further investigation of the nature of the meandering shows a clear instability in the upstream vortex, as can be seen in Figure 6.9. At larger offsets (0.3C in figure) the presence of any sinusoidal deviation is minimal, with only a slight skew observed in the upstream vortex. As the offset is brought closer (0.1C) a clear deviation of points at approximately 45 degrees to the line between the vortex centres can be seen. This is indicative of the sinusoidal deviation of an uneven Crow instability. The deviation is far more prominent for the upstream vortex than the downstream vortex, which has an approximately circular distribution of

locations. The reason for this inconsistency was not apparent from the results, however it is likely due to the longer path of the upstream vortex, in addition to reduced vortex strength from the initial vane/vortex interaction. As the offset is further reduced, the upstream vortex is drawn into the velocity field of the downstream vortex, resulting in a curvature of its sinusoidal deviations. This can be seen in the 0C offset of Figure 6.9. The same trends were seen when approaching the vortex impingement from negative offsets.

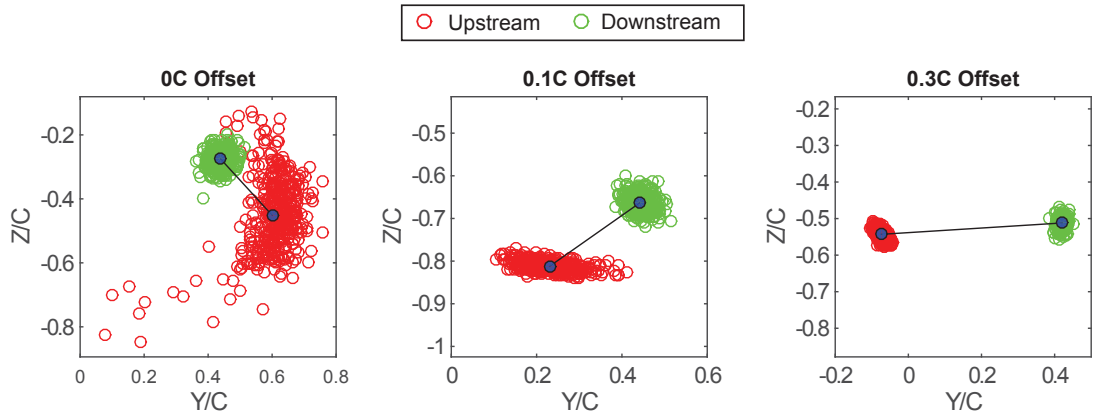

Figure 6.9: Core locations of upstream (red) and downstream (green) vortices for 0C, 0.1C and 0.3C offset cases at X/C = 16.5.

The variances in circulation followed similar trends to that of the core location, so are not presented here. The consistency in these trends indicates that the damping mechanisms which smoothen out the location meandering in the far offset cases also calm the fluctuations of the vortex strength. As the increased swirl velocities of high circulation will be reduced more rapidly by shear than the lower velocities associated with low circulation, it is expected that these fluctuations would be reduced as the vortices pass through the flowfield, as long as there is not a significant instability present. Of more interest is the increase in circulation variance near the points of higher interaction.

In the near field, the normalised circulation variances were increased by 0.078 (75%) and 0.428 (471%) for the downstream and upstream cases respectively. In the far field, these variances were increased by 0.20 (171%) and 0.4551 (932%) for the downstream and upstream cases respectively. This indicates that the close interactions are influential in the magnitude of the circulation fluctuations well downstream from the initial interaction of the vortex with the vane. As such, the interactions of the vortices with one another can be observed to destabilise the cores and enhance the energy transfer between the vortices.

6.2 Co-Rotating Condition

6.2.1 Vortex Migration

In all un-merged cases the vortices followed a helical path as can be seen in Figure 6.10, similar to the water tunnel visualisation results. Downstream vortex positioning at the start of the domain varied linearly with offset, however between 0.2C and -0.25C the vortices were merged. This merging can be seen in the 0.1C offset case, where the downstream vortex disappears after x/C = 12.5 due to it merging into the upstream vortex. As the offset approached the point of vortex merging the path length of both the upstream and downstream vortices increased, with the downstream vortex experiencing the most migration. Total path length at 0.6C offset was 0.308C and 0.186C for the upstream and downstream vortices respectively. At 0.2C offset this increased to 0.511C (66% increase) and 0.330C (77%).

While the paths retained their helical migration pattern with a linear orbital rate independently of which side of the vane the vortex passed on, the total circularity of the path varied. When comparing the -0.3C case to the positive 0.3C case, the non-circularities of the -0.3C case can clearly be seen, with a near horizontal movement of the downstream vortex for the first four data points. There is a translation of 0.1926C in the lateral direction for a total movement of only 0.0542C in the vertical direction for the upstream vortex across these data points. This is due to the non-linearities associated with the vortices being drawn closer in from the initial stages of the merging process, as well as the influence from the wake of the rear vane. The -0.3C offset case is the only case presented in this figure where the vortex paths pass both above and below where the merged vortex is located in the -0.1C offset case. This means that until Z/C drops below -0.025 the vortex is not being affected by the rear vane downwash, and once it is below this value it will be, thus causing the path non-linearity. This can only occur when the upstream vortex passes on the suction side of the vane, as this will cause orbiting motion induced by the downstream vane to draw it through this region. This effect will dissipate as the downstream vane wake dissipates further downstream.

As opposed to the laterally spaced test configuration of Rokhsaz [57] where negligible centre of rotation migration was observed, the migration of the centre

of rotation of the vortices was found to be significant. Total vertical migrations of up to 0.06C and lateral migrations of 0.07C were observed in the centre of rotation. This was as high as 35% of the total vortex migration at an offset of -0.3. The absolute magnitude of the centroid migration remained roughly constant across the offset range measured, however it was a significantly higher percentage of the total migration at the nearer offsets of the vortices. The analytical, inviscid results presented by Lewecke [23] also show a static core rotation centre, demonstrating the differences induced by the realistic vane vortices. The differences observed can be attributed to the downwash produced by the vane in the creation of the second vortex. This downwash causes a change in the migration of the pair, something not previously observed due to the vortices being created at the same upstream location (in the case of Rokhsaz) or not having any vane influence (Leweke).

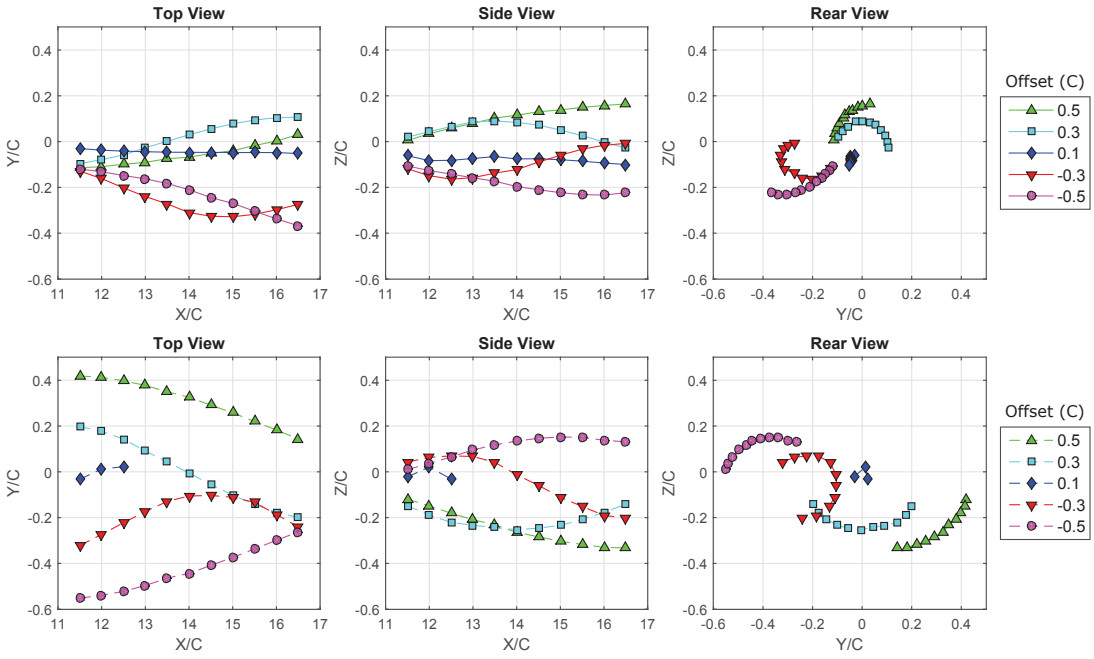

Figure 6.10: Paths of upstream (solid) and downstream (dotted) vortices for various lateral vane offsets. Error in core location is ± 0.006C.

The spiralling rate of the vortices was calculated through the same method as the counter-rotating condition. Decreasing the offset increased the spiralling rate until the point of merging, as can be seen in the rotational rate in Figure 6.11. This rotation had a non-linear trend as the point of merging was reached, peaking at approximately 44 degrees per chord length. This is distinctly less than the 1200 degrees per chord length effective rotational rate of the peak azimuthal velocity region of a single vortex, attained at a radius of .075C and velocity of

37.5C/s (3m/s). While an inverse relationship cannot be explicitly confirmed from the offset range investigated, the rotational rate will tend to zero as the vane separation goes to infinity, indicating the continuance of non-linearity with increasing offset in the rotation trends. The rotation rate remained constant throughout the domain. The separation linearly varied at the same rate as the offset change until the point of vortex merging.

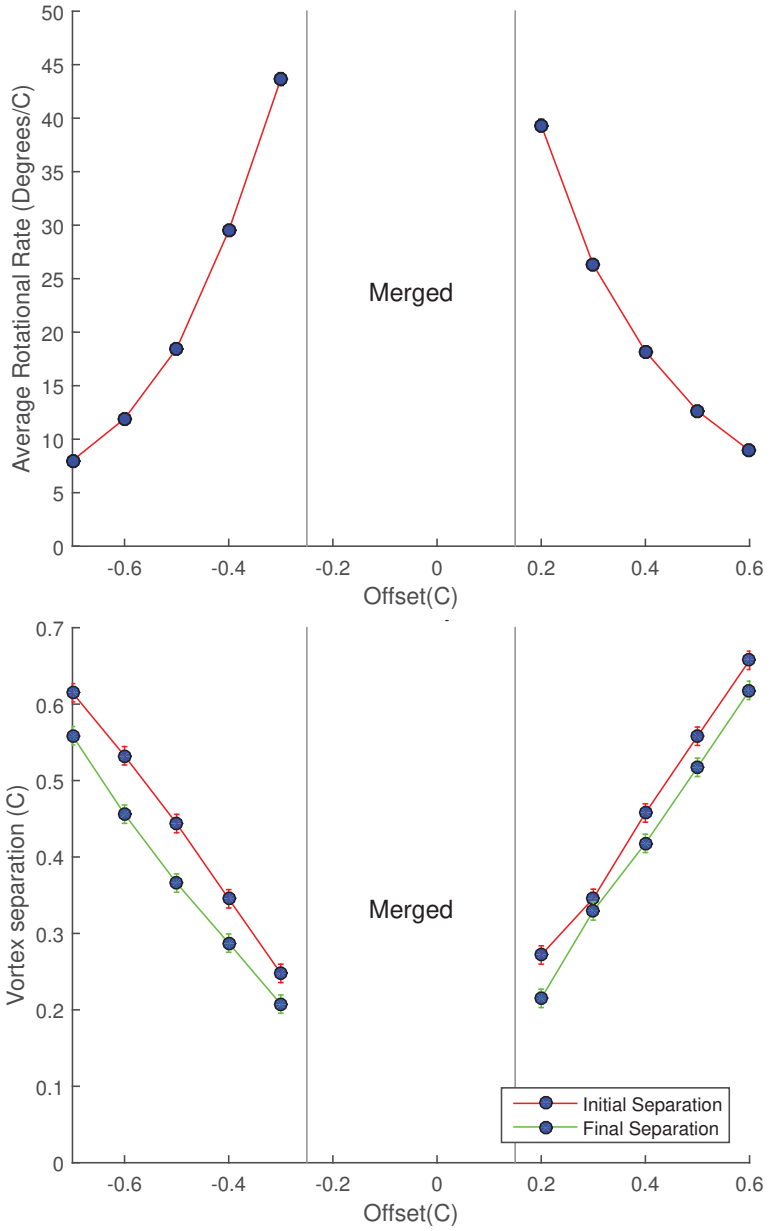

Figure 6.11: Vortex pair rotational rate (top) and vortex pair separation (bottom). Initial separation is at x/C = 11.5 with final separation at x/C = 16.5.

By combining the separation distance curves from each unmerged case, the trends

of separation distance for the vortex pair can be extrapolated to cover a much longer effective distance. This allows us to simulate how a vortex pair deployed at an initial separation width of $B_v/R_{0.3} \approx 7$ would behave further downstream, as can be seen in Figure 6.12. The separation data shows that there are two different separation rate trends depending on which side of the vane the vortex is passed on. If the vortex passes on the pressure side of the vane, for every chord length travelled downstream the vortices move together approximately 0.154 of the core radius. However, if the vortex passes on the suction side of the vane, this is decreased to 0.110 core radii, giving a 28% differential in separation rate. This suggests that the wake region of the vane significantly affects the speed of the merger, causing the vortices to be forced together faster. This happened independently of the circulation within the vortex core, which showed similar trends regardless of which side of the vane the vortex approached from.

As the vortices approach merger, the trend deviates from linear. The -0.25C offset case exhibits all the merging regimes discussed in the merging section up to single vortex, combining the second diffusive and convective merging states. However, it does not show the clear levelling off or core separations as observed by Cerretelli and Williamson [96], instead demonstrating a reduced, but still significant gradient. As the separation between the cores reaches two core radii apart, the sepatrices of the two vortices connect and rapid merging occurs, resulting in the transformation to a singular vortex. The asymmetric mechanism behind these separation trends will be discussed further in the merging section.

In the merged condition the single vortex path only was tracked, as can be seen in Figure 6.13. The path of the merged vortex was laterally shifted by approximately half the offset change of the rear vane, demonstrating the influence of the rear vane on vortex trajectory. This indicated that the downstream vortex contributes to approximately half of the vortex total location, despite the fact that the vortices were merged prior to the window of observation. As the downstream vane is angled to direct the flow towards -Y, it was anticipated that the merged vortex would be located towards -Y due to the vane downwash, but as can be seen from the -0.15C offset case the vortex initially starts at a greater Y/C, peaking at -0.11C. This is of note as the quarter chord of the vane is located to the negative side of the initial vortex core. When the downstream vane was located at -0.1C the resultant merged vortex starts at -0.09C, peaking at -0.08C before dropping to -0.12C by the end

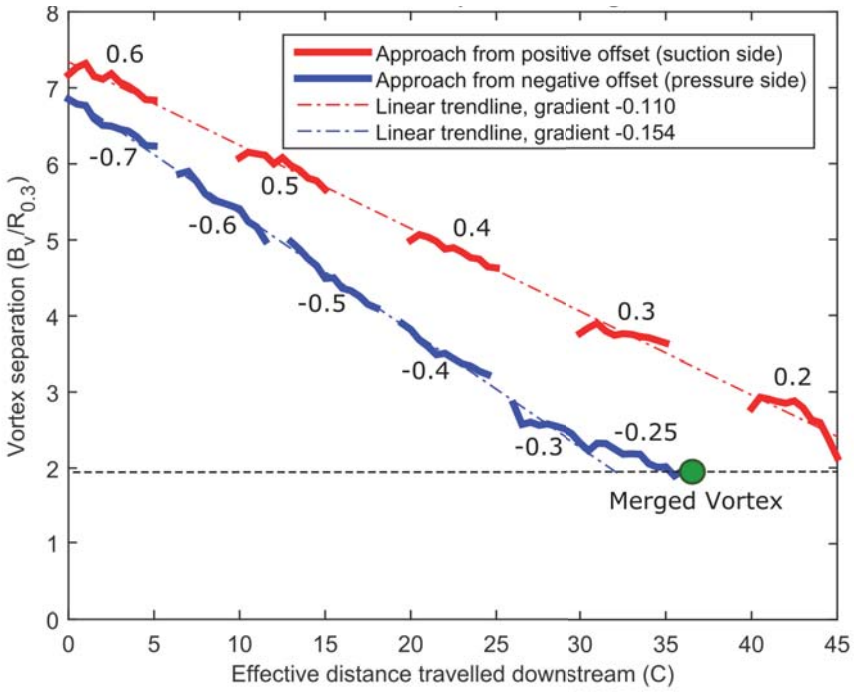

Figure 6.12: Vortex pair separations for all unmerged cases. Each offset case is indicated by the annotations on the line segments.

of the domain. This is significantly more positive than the single vortex case for the entire observation domain. The curvilinear path is due to the tail of the merged vortex produced by the drawing in of the downstream vortex, as will be discussed in the vortex merging section. A component of the curvature is also due to the vortex passing slightly inboard and offset of the wingtip. There is a considerable downwards shift imposed by the presence of the rear vane, as can be seen compared to the path of the single vortex. In all cases the downwards travel was approximately 0.075C, with all paths being within error bars of each other.

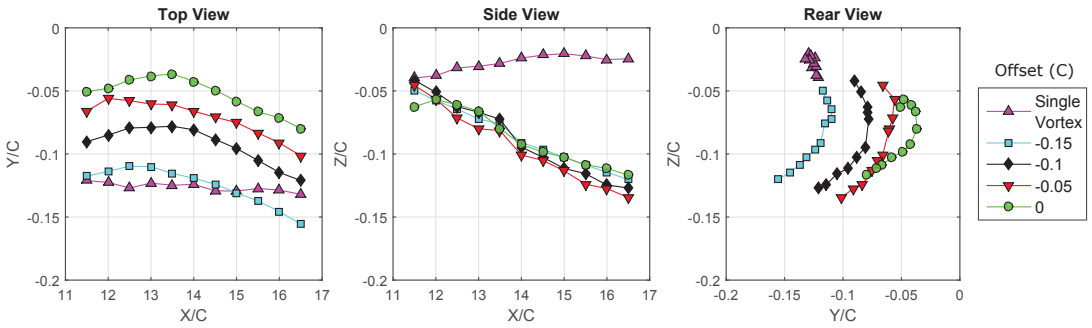

Figure 6.13: Paths of merged vortex for various lateral vane offsets. Error in core location is ± 0.006C.

Vortex path meandering was evaluated through the vortex tracking and analysis of each individual set of image pairs. Uniform meandering on both axes with a circular core location distribution was observed at the far range of the offsets investigated. A maximum radius of displacement of 0.020C was measured at 0.6C offset. As the offset was decreased, there was no observable shift in meandering until 0.2C offset, where partial merging was present towards the end of the domain. The secondary vortex was drawn around the primary at this point, creating a bias in the meandering. This bias predominantly affected the weaker vortex, with a maximum amplitude of 0.066C measured on the axis of bias. This instability was at an average angle of 25 degrees to the line between the two vortex cores. The stronger, upstream vortex was also marginally affected by this instability, with with a maximum meandering amplitude along the axis of bias of 0.029C at 0.2C offset. This gives meandering bias ratios of 3.22 and 1.38 for the downstream and upstream vortices respectively, indicating an instability with stronger effects on the downstream vortex. The same meandering trends were seen on the negative offsets. The magnitude of the instabilities was increased as the vortices travelled downstream and the vortex proximity was reduced through either offset change or drawing in of the vortex paths.

6.2.2 Vortex Merging

Time averaged results were inspected to identify the merging pattern. The stronger and weaker vortices were selected from their circulation, with the upstream vortex (red) being the stronger and downstream vortex (green) being the weaker. The evolution of a typical merging pattern can be seen in the planar slices of the -0.25C offset case in Figure 6.14. Individual vortex identification was performed using the contour lines at 30% of the peak vorticity on the plane ($A_{0.3}$) as discussed in Chapter 3. The stronger and weaker vortices were selected from their circulation, with the upstream vortex (red) being the stronger and downstream vortex (green) being the weaker. The yellow band shown in the figure is the $A_{0.1}$ contour line, with the other contours showing lower levels of vorticity. The scale has been selected to maintain a proportional X and Y axis for visualisation of circularity.

At the start of the domain the vortices have similar circularity, however as they travel downstream they are drawn closer together and partial straining of the

weaker vortex occurs. This process starts at x/C = 14, with the secondary peak being completely dissipated by x/C = 16.5. Throughout the process the upstream vortex $A_{0.3}$ does not significantly increase in area, however the $A_{0.1}$ surrounding it does significantly increase. This is from the vorticity of the weaker vortex being diffused and spread around the stronger vortex. Of note is the fact that the upstream vortex is the stronger, while the downstream vortex is weaker. This indicates the presence of the upstream vortex has caused the strength of the downstream vortex to be weakened. This results in the merger of the downstream vortex into the upstream vortex as the pair progesses downstream, as the upstream vortex is the stronger of the two at the location just behind the rear vane (x/C = 11.5). As a consequence, the downstream vane is effectively re-energising the existing upstream vortex after the vortex pair has merged.

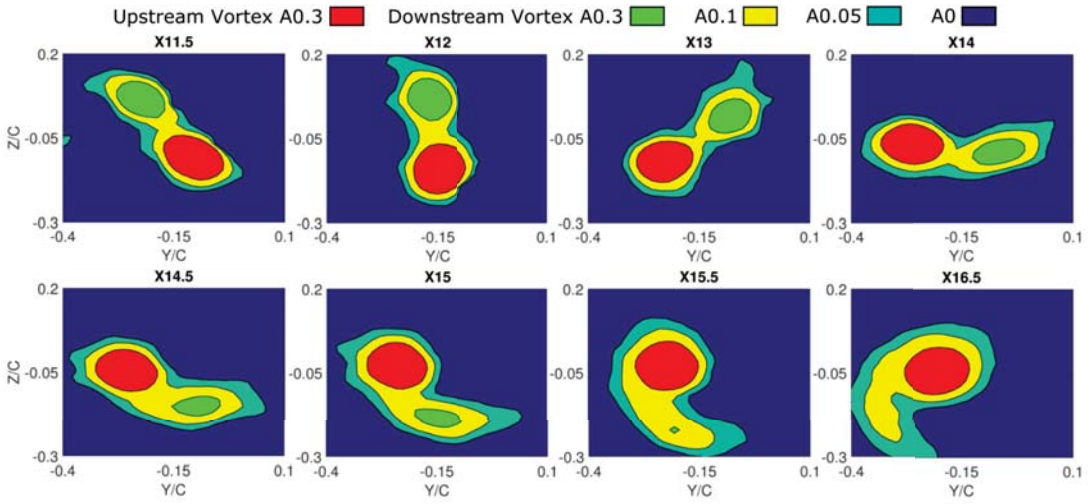

Figure 6.14: Vortex merging pattern for -0.25C offset, with upstream vortex in red and downstream vortex in green. Note the non-uniform spacing of the planes.

The transition of the vortex from a shape with a spiral tail to a circular structure can be better investigated at the -0.2C offset in Figure 6.15. Moving the vane offset -0.05C closer causes a significant upstream shift in the merging location, with no existence of secondary peaks from the x/C = 11.5 plane onwards. As the merged vortices travel downstream the vorticity is transferred from the tail to the circular vortex core. Eventually the tail is completely dissipated, with the final core achieving circularity and a larger size than one individual vortex, as can be seen at the x/C = 16.5 plane.

The initial stages of the merging can be visualised through the inspection of the -0.3C offset as seen in Figure 6.16. While this case did not merge within

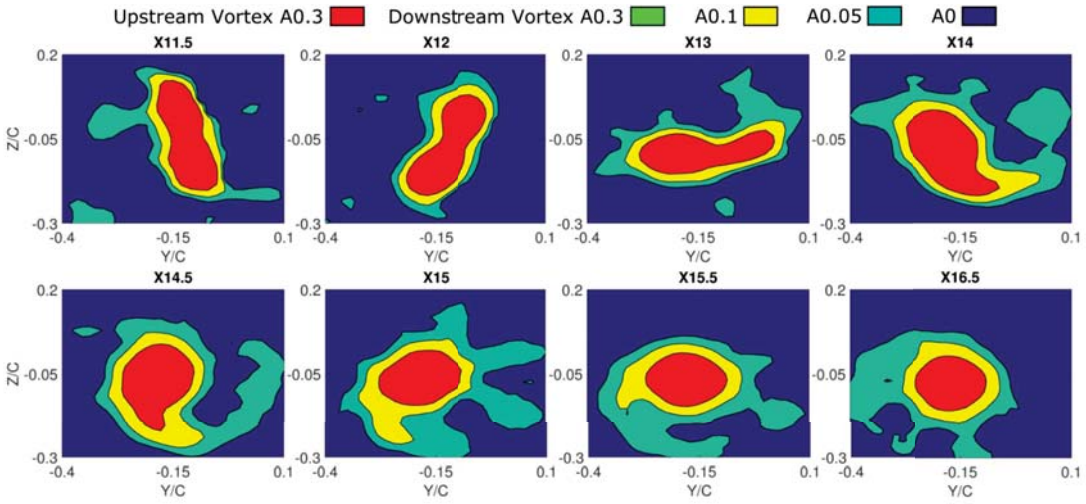

Figure 6.15: Vortex merging pattern for -0.2C offset, with upstream vortex in red and downstream vortex in green. Note the non-uniform spacing of the planes.

the observation window, the initial drawing in and vorticity transfer was clearly occurring. The lower rotational rate of the vortex cores observed at this further offset significantly slows the rate of merging when compared to the -0.25C case. Initially the two vortices are separate, both at the $A_{0.3}$ and $A_{0.1}$ levels. As they travel downstream their separations move closer by approximately 0.007C per chord length downstream. This equates to approximately 6% of the the $R_{0.3}$ per chord length travelled downstream.

From the x/C = 15 to x/C = 16 planes there is a distinct change in the circularity of the weaker vortex, with the x/C = 16 plane showing partial straining and an oval shape occurring at a vortex separation of 0.021C. Between x/C = 16 and x/C = 16.5 there is also an observable reduction in the size of the weaker $A_{0.3}$, however the $A_{0.1}$ has largely remained unchanged. This indicates the vorticity transfer between the two vortices is caused by the diffusion of high level vorticity from the second vortex into the lower energy level $A_{0.1}$. From here it is drawn around the stronger vortex, as was demonstrated in the previous cases. This case also demonstrates the need for tracking the vortex core $A_{0.3}$, as the $A_{0.1}$ indicates the vortices are merged from x/C = 12.5, while $A_{0.3}$ can clearly track distinct vortices until the final plane.

These observations of asymmetric merger show similarities to the two dimensional numerical simulations of Brandt and Nomura [97], with partial straining of the weaker vortex followed by the diffusion of vorticity and absorption into the stronger vortex were observed at similar circulation ratios.

However the very high vortex eccentricities and aspect ratios observed in the weaker vortex by Brandt and Nomura were not observed before complete merging. This is likely reflecting the increased vorticity transfer in the turbulent, three dimensional experimental flow, resulting in faster merging.

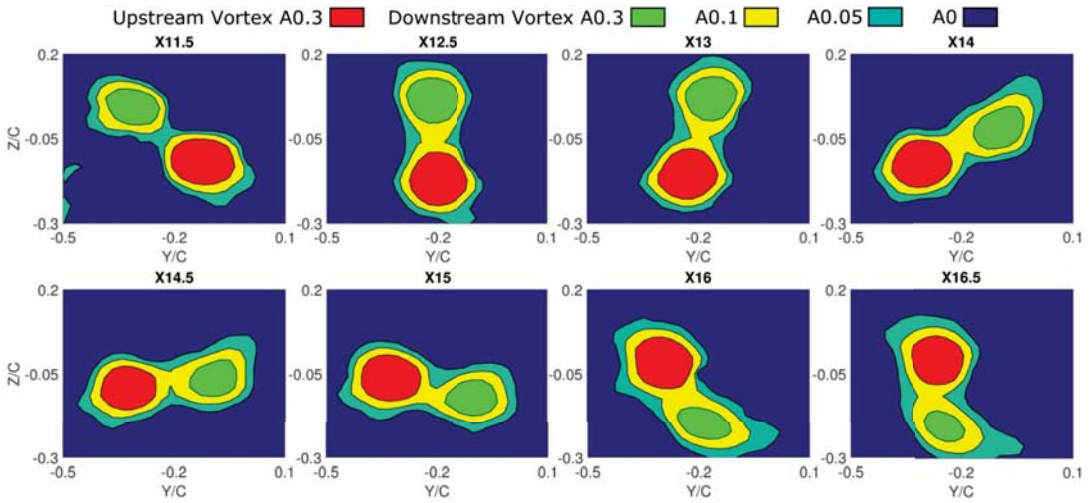

Figure 6.16: Vortex merging pattern for -0.3C offset, with upstream vortex in red and downstream vortex in green. Note the non-uniform spacing of the planes.

Inspecting the pathlines in the co-rotating reference frame as seen in Figure 6.17 allows for further understanding of the uneven merging mechanism. To calculate the rate of rotation of the co-rotating reference frame, the average rotation rate across the entire domain sweep as previously calculated was used. At large separations the vorticity fields of the two primary vortices are significantly separated ($B_v/R_{0.3} > 2.3$), with the streamlines of the two vortices being clearly separated by an inner recirculation region. This inner recirculation region appears to be the origin of the two "ghost vortices" of the outer recirculation region. While not observed in the offset range investigated, it is anticipated that the two ghost vortices will merge at larger offsets, forming a singular recirculation region. As the vortices are drawn closer together, they divide this recirculation region into the two ghost vortices of the outer recirculation region. At this point ($B_v/R_{0.3} \approx 2.3$) the two vortices streamlines connect, as well as their vorticity field.

Unlike the stages of Cerretelli and Williamson [96] the unequal three dimensional merger does not appear to enter the well defined diffusive and convective stages, as from this point onwards the vortex separations do not significantly change, however there is a significant transfer of vorticity from the

weaker to stronger vortices. Once the streamlines of the two vortices have joined and the ghost vortices are fully separated ($B_v/R_{0.3} < 2.3$) the flow begins to become significantly asymmetric in the horizontal axis, as opposed to the relative symmetry present in the further separated condition. Once this asymmetry occurs, the transfer of vorticity and modification of the pathline patterns occurs rapidly. As the merger progresses the rotating pathlines of the weaker vortex are strained out, leaving the previously discussed vorticity tail. After the remnants of the secondary vortex have been strained out, the ghost vortices rapidly migrate to the other side of the vortex configuration and merge into a singular recirculation region. This recirculation region expands and reduces in strength as the vortex slowly normalises itself towards circularity in the merged diffusive state.

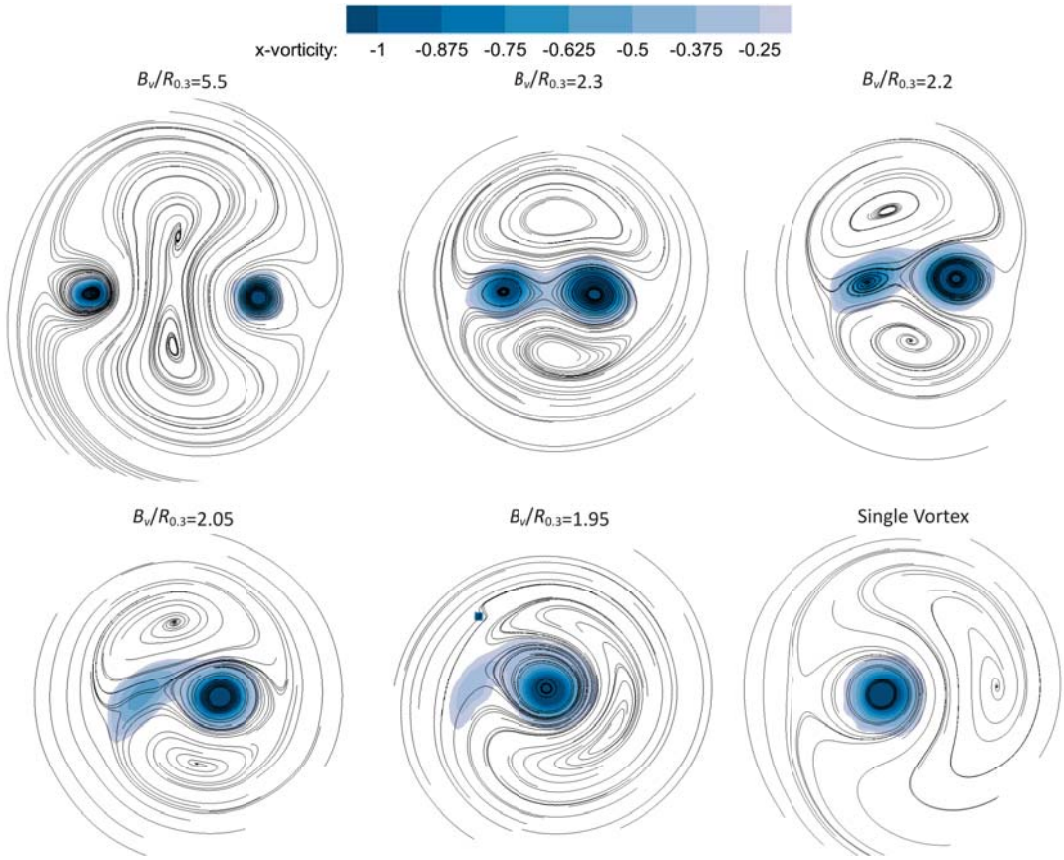

Figure 6.17: Pathlines in the co-rotating reference frame and vorticity for different stages of vortex merger.

The merging lengths identified from the analysis of the time averaged cases can be seen in Figure 6.18. These are only given for cases where merging was observed within the domain. It can be seen that the offset for merging at the start of the domain is skewed to the positive side of the vortex (passing inherently at -0.12C).

This shows that passing the vortex on the pressure side of the downstream vane facilitates more rapid merging then passing it on the suction side. The vortex merging length showed a highly non-linear trend with respect to offset, with the merge length rapidly exceeding the 5C domain length over just 0.15C offset change. This trend and the observed results of the merging pattern indicate that there may be a link between merging length and rotational rate.

While the analysis of the merging patterns was taken from time averaged data, each individual image pair was analysed to detect the vortices. It was found that the vortex merging location in the transition regions was probabilistic rather than deterministic, as seen on the right side of Figure 6.18. The probability of the vortex being merged is simply the percentage of image pairs without a secondary vortex. These probabilities were also tested with a random sample of 200 image pairs and found to be within 5% of the values from the full 400 image pairs, indicating an error in probability of less than $\pm$ 5%. In the -0.2C case there was a 66% occurrence of merging in the first plane, with 100% of image pairs being merged with no secondary peaks by x/C = 15.5. The time averaged point of merge at x/C = 13 lies approximately halfway between these points. Similarly, in the -0.25C case, the probability of merging linearly decreases throughout the domain, with a 44% probability of merging at the time averaged merge location. This indicates the presence of a side to side fluctuation of the vortices, similar to that identified in the water tunnel testing of the vortices. This produces a sinusoidal fluctuation in the merging point. The meandering of the singular vortices causes them to move towards and away from each other, with a resultant fluctuation in vortex separation. As previously identified, the merging location is very sensitive to offset, and consequently any variance in vortex separation will cause a significant difference in the presence of secondary vortex peaks.

Two interesting findings are apparent from these results. The first is the near linear rate of the probability decay with distance. This rate appears to have minimal skew from the samples taken, and minimal non-linearity. However, when considering the probability distribution for a regular sine wave, there is a quasi-constant region that shows similarity. From -50% to +50% of a sine wave amplitude, all sample bins of a frequency histogram are within 2%, and at $\pm$75% of the waves amplitude the samples all fall within a maximum variance of 10%. This means that a sine wave displacement change will appear linear up to 75% of its maximum amplitude. Consequently, the merge is following the sinusoidal oscillation previously discussed in both Chapter 4 and in the previous

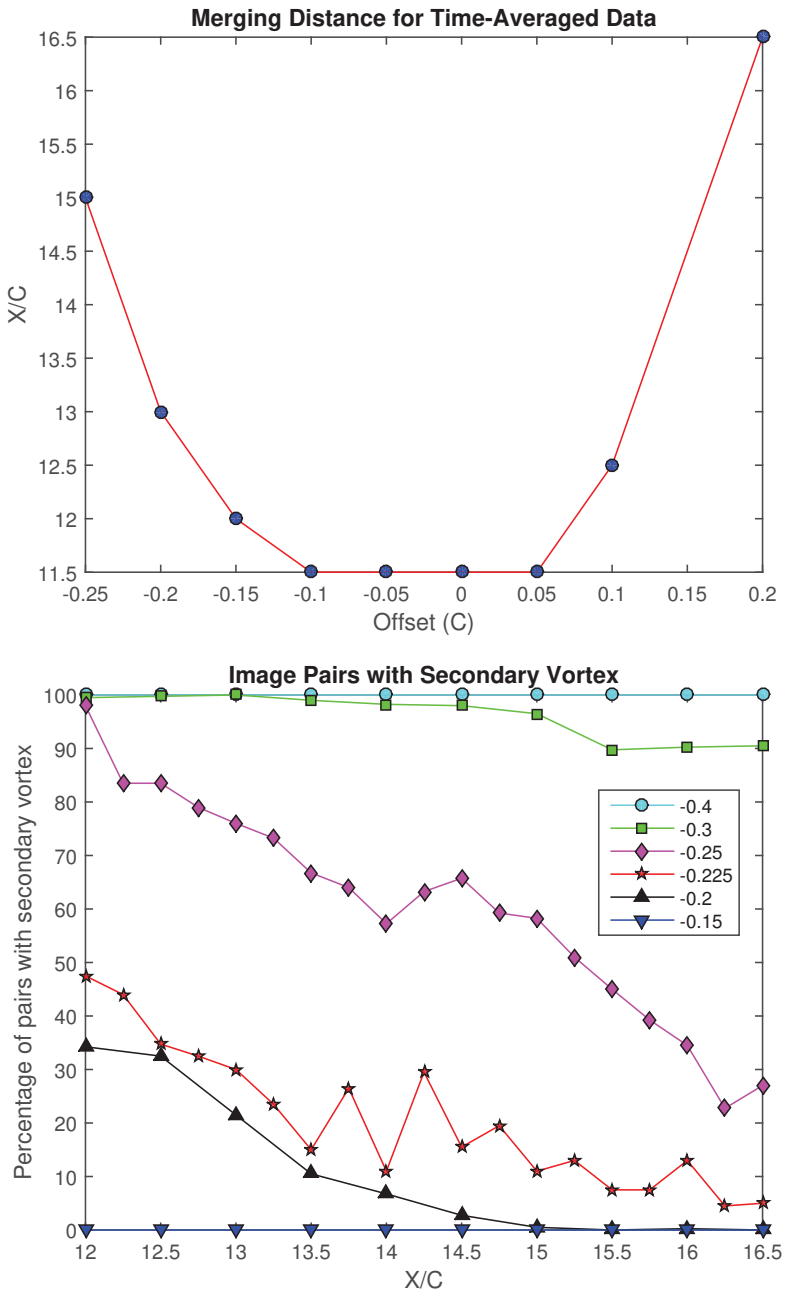

Figure 6.18: Distance to vortex merging for time averaged cases (top), and probability distribution for instantaneous measurements at various lateral vane offsets (bottom)

paragraph, likely caused by a sinusodial instability in one or both of the vortices. This causes a sinusoidal change in vortex spacings, resulting in the observed merging statistics. The second finding is that the time averaged merge location does not necessarily coincide with the point of 50% merging probability. This is clear in the -0.2 case, where the time averaged case merges at x/C = 13, while the probability of merging at this point is 89%. However, in

the -0.15 case the time averaged merge at x/C = 12 is reflected in the 100% merging probability from x/C = 12 onwards. This indicates the the variances in vortex meandering, as well as the change in energy distributions and vortex shapes accounts for significant changes in the transient fluctations of the vortex merger.

6.2.3 Circulations and Core Radii

The radius results of Figure 6.19 show the initial $R_{0.3}$ as remaining relatively constant for the unmerged cases, with the downstream vortex radius approximately 9% smaller than the upstream at the start of the domain. The radius of the upstream vortex does not significantly drop throughout the domain, with drops in radius of approximately 3%. The downstream vortex has a similar trend for its size in far offset cases, however as the offset is reduced its interaction with the upstream vortex causes a reduction in size of up to 13% over the domain. For the merged case it can be seen that the initial $R_{0.3}$ is significantly higher than the single vortex case, however by the end of the domain it has reduced to within the error of the single vortex case. This is due to the dispersion of vorticity from the weaker vortex core to the $A_{0.1}$, as identified in the merging section of this paper.

When inspecting the $R_{0.1}$ this can be seen through the significantly higher radii for both the initial and final cores. The core radius in this merged region is also affected by how merged the vortices are. The $R_{0.3}$ in the -0.2C offset case is the largest of the merged cases at the start of the domain, coinciding with the irregular, non-circular shape seen in Figure 6.15. As the vortex travels downstream, it forms a circular and uniform $A_{0.3}$, and this coincides with the final radius observed in the single vane condition. The nearer offset cases have more significant vortex core relaxation by the initial plane, resulting in their comparatively smaller radii. Applying the same principles to the $R_{0.1}$ it would be expected that over the course of a longer domain the merged $R_{0.1}$ would trend towards the single vortex as the vorticity is drawn in from $A_{0.1}$.

The circulation figures seen in Figure 6.20 show similar trends to the radius, however there is a greater discrepancy between the upstream and downstream vortices. The loss in circulation from the downstream vortex is very apparent, with drops of 28% along the length of the domain observed for the cases nearest

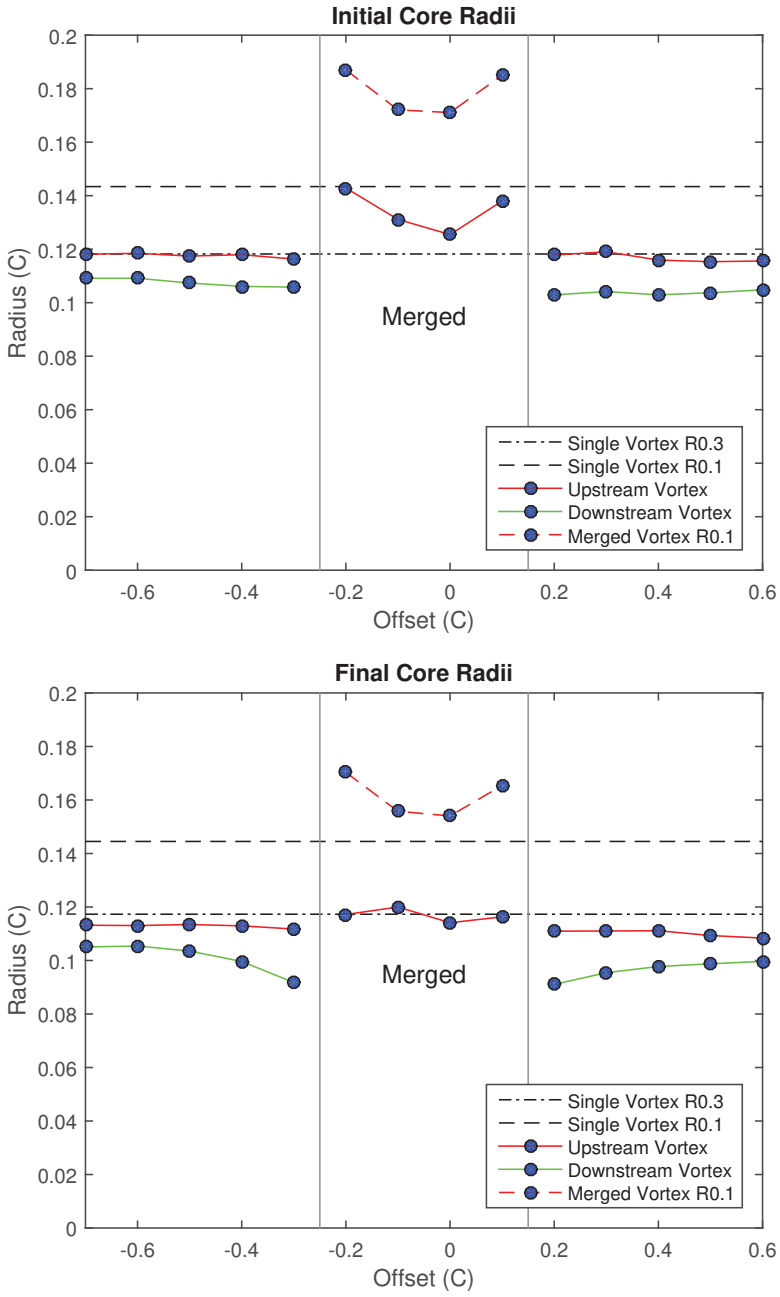

Figure 6.19: Initial vortex radii (top, x/C = 11.5) and final vortex radii (bottom, x/C = 16.5).

to merging. This was a non-linear trend, showing far more significant decreases than core radius changes. This is indicative of the dissipation of the secondary vorticity peak into the $A_{0.1}$ as part of the energy transfer mechanism. Of note is that the energy transfer out from the secondary vortex is occurring at a far greater offset than the merged cases, with it being clearly observable at the -0.4C and 0.4C offsets. The drop in downstream vortex circulation is 4.7% at

the 0.4C offset and 7.3% at the -0.4C offset. This drop is also skewed to the positive offset, similarly to the merging distance. It is hypothesised that this is due to the low pressure core of the upstream vortex passing on the pressure side of the downstream vane, reducing the magnitude of the high pressure here. This reduces the pressure differential across the downstream vane's tip, thus reducing the strength of the resultant tip vortex. It is also a cause of the skew in vortex merging to positive offset, as the lower strength downstream vortex is more rapidly merged.

While the radius of the upstream vortex remained constant as the vanes approached merging offset, the upstream vortex circulation can be seen to reduce at nearer offsets. At the 0.2C offset for example, the upstream circulation drops by 9%, as opposed to the 0.5C offset where it drops by only 3.7%. As such, the diffusion of vorticity from both vortex peaks becomes more significant as their proximities are reduced. This circulation has diffused into the $A_{0.1}$ region as part of the secondary diffusive stage of vortex merging.

Inspecting the initial circulation for the merged case, it can be seen that the outer regions of the merged offsets trend towards the sum of the two individual vortex circulations. At -0.3C offset the initial sum of the upstream and downstream vortex circulations is 0.222 m^2/s, and at 0.2C offset it is 0.227 m^2/s, which compares similarly to the 0.220 m^2/s and 0.236 m^2/s measured at -0.2C and 0.1C offset respectively. However, at the end of the domain the merging process has levelled the circulation to closer to that of the 0C and -0.1C offsets. This indicates the shift towards circularity involves a penalty in circulation, although the final circulation of the merged vortex is still significantly higher than a single vortex case. It is important that this is not necessarily considered as a loss of flow energy, as the circulation is proportional to vorticity, which is not a direct measure of flow energy.

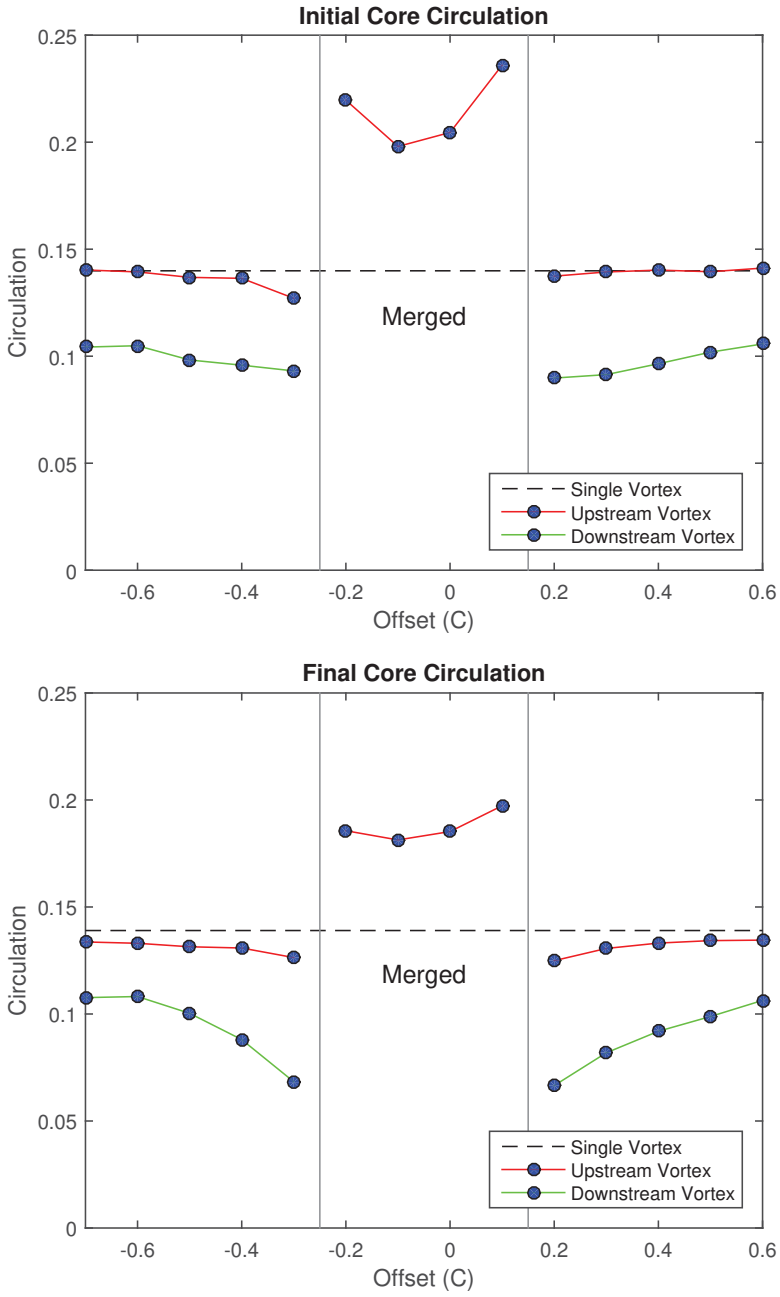

Figure 6.20: Initial vortex circulation (top, x/C = 11.5) and final vortex circulation (bottom, x/C = 16.5).

6.3 Experimental Conclusions

6.3.1 Counter-rotating

The wind tunnel testing provided significant quantitative insight into the precise vortex paths and energy trends of the vortex interactions over a wide range of offsets. For the counter-rotating case no vortex rebound was observed within the domain, indicating the vanes were sufficiently high above the floor to be free of ground effect.

At close offset cases, the motions of the vortex pairs shifted from predominantly vertical to predominantly lateral, with increased rotation of the pairs. The rotational rate of the vortex pair had two peaks at -0.20C offset and 0C, with a minima at -0.1C, the point of core impingement. This is consistent with the location of the core with no downstream vane present. At this point the size and strength of both vortices has been significantly reduced as a result of the destructive interference in the formation stage of the downstream vortex. -0.25C produced the strongest interactions, with the second highest rotational rate and highest vortex size changes, combined with closest vortex pair proximity. The separation between the vortices in this condition was approximately $R_{0.1}$. This indicated that placing a vortex one core radius from the suction side of a vane is preferable for maximum interaction strength, while impacting the vortex on the quarter chord causes the most significant vortex destruction.

The vortex meandering was found to be dependent on the proximity of the interaction, with closer proximities producing higher meandering levels. The strength of the shear layer shedding and instabilities introduced by the unequal strength interaction were found to be significant factors. The meandering magnitudes were found to be more closely related to the strength of the interaction than the destruction of the vortices, with the -0.25C case having the largest meandering magnitude and steady decreases on either side of this. Downstream vortex meandering was found to be more sensitive to the strength of interaction than the upstream vortex, with a typically lower meandering growth at further offset cases. Near offset cases produced a clearly observable instability in the upstream vortex only, with the 45 degree deviations being drawn around the stronger vortex in a curved manner as the separation

distance was reduced. Circulation fluctuations followed similar trends, demonstrating a link between circulation and core location in meandering.

The rich dynamics observed and large changes in vortex state resulting from small offset changes near the point of impingement indicate that the traditional method of exploring only 3 or 4 offsets may not be sufficient when predicting the paths of a counter rotating pair produced in this manner. The presence of vortex meandering over longer distances would further amplify this problem, as the transient changes in location of the initial vortex prior to interaction with the downstream structure will result in large changes of the resultant pair's location and size. As such, in systems where consistent vortex behaviour is required, the counter-rotating pair should be spaced at as high an offset as feasible.

6.3.2 Co-rotating

For all unmerged co-rotating cases the two vortices migrated in a helical pattern. Vortex merging was observed from -0.25C to 0.2C offset, equivalent to -0.15C to +0.3C offset from the unobstructed path of the downstream vortex. This demonstrated a bias to faster vortex merging when the upstream vortex passed on the pressure surface of the downstream vane. As the offset was decreased towards the point of merging, the orbital rate of the vortices increased non-linearly to a maximum of 44 degrees/chord length travelled downstream. Vortex separation varied linearly with offset, with the vortices consistently moving closer together throughout the domain for all offsets investigated. As the vortices moved closer together and further downstream, an instability was identified in the meandering of the vortices. For the merged cases, it was found that the merging process imparted a downwards motion and shifted the vortex path to the positive side. Passing the vortex on the pressure side of the vane resulted in the vortices moving towards each other approximately 28% slower than if it was to be passed on the suction side of the vane.

The vortex merging distance was found to be highly sensitive to offset, with a non-linear trend. An unequal merging process was observed, with the downstream vortex diffusing its vorticity to a lower energy level. This diffuse vorticity was then drawn around the stronger upstream vortex, eventually forming a circular structure. Similar patterns were observed for all offsets where merging occurred. The symmetry of the vortex structure was found to change rapidly once the

vortices came with a core separation 2.3 times the core radius, resulting in rapid merging by the time the vortices where 2 core radii apart. The location of merging could not be determined deterministically, but was instead a statistical phenomena. This was due to the meandering of the vortex location and energy levels shifting the merging location upstream and downstream in a sinusoidal oscillation.

From the circulations, it was found that the presence of the upstream vortex weakened the downstream vortex. As the vortices approached merging, their vorticity peaks were diffused into a larger, lower energy vorticity level. For the fully merged cases, a circulation loss was found to result from transitioning from an irregular shape to a circular one. Despite this penalty, the merged circulation remained higher than that of a single vortex.

While the merging distance is sensitive to offset, these results indicate the fundamental effects and mechanisms of the merging process remain the same regardless of vortex separation. As such, the re-energisation of an upstream vortex can be performed with a relative insensitivity to offset.

Chapter 7

LES Analysis of Vortex Interactions

The ability of LES simulations to accurately model dissipation rates and transient effects encountered by the vortices makes it a far more useful tool than RANS for vortex analysis. This time-resolved nature allows the causes behind the migration, energy and circulation trends discovered in the experimental work to be investigated in more detail. In addition to this, the LES analysis can resolve and visualise volume fields and pressure successfully. Careful selection of these LES cases was of critical importance to investigating the mechanisms behind the results seen in the prior experimental work.

In the far offset counter-rotating cases studied in the experiments, few notable features were present. Circulation rates remained near constant through the domain, with minimal migration and rotation, and vortex meandering was found to be minimal. As such, they were not considered as cases of interest for the LES investigations. In the nearer field the interactions were far more significant, with large changes in rotation rates, meandering and circulation transfer. Three conditions of the near field interactions were considered for further investigation, the first being vortex impact on the front of the vane. This was expected to be at -0.2C offset as identified by the experiments and RANS modelling, with a correction added for the previously described vortex drift over-prediction The second case was a near pass of the upstream vortex, with the complete vortex radius being outside of contact with the downstream vane, this occurred at 0.2C offset. The final case chosen was an intermediate

between these two, with partial impingement of the vortex on the downstream vane, at 0C offset. It was known from the experimental work that the transient migrations of both vortices in the near pass condition was significant, so transient vortex tracking was applied to the 0.2C offset case. It was also expected that the impingement and resultant destruction of the upstream vortex on the rear vane would have significant consequences on the meandering and circulation of the downstream vortex, as such transient vortex tracking was also applied to the -0.2C offset condition.

For the co-rotating cases, three more conditions of interest were identified. The experimental work had shown a difference in vortex merging rates depending on which side of the vane the vortex was passed on. As such, two near field passes of the vortex on the vane were desired, one on each side of the vane. This occurred at -0.2C and 0C offset. It was also desired to investigate the mechanisms present in a longer merging distance case, and for this purpose the 0.2C offset case offered the longest merging length still within the CFD domain. It was not anticipated for the nearer offset, short merging length cases to yield interesting transient meandering data, so only the 0.2C offset was monitored with transient vortex tracking. The locations of these key cases meant the same geometries as the RANS could be used, with the LES modelling applied and the implementation of the transient vortex tracking on the counter-rotating -0.2C and 0.2C offsets, and the co-rotating 0.2C offset.

7.1 Co-Rotating Condition

7.1.1 Mechanism Visualisation

The presence of the upstream vortex caused significant changes in the formation mechanism of the downstream vortex. In the case of the single upstream vane, two separate vortices are initially formed, as can be seen in Figure 7.1. These two vortices both have their own distinct regions of concentrated vorticity, as well as a low pressure core. The merger of these vortices occurs just prior to the trailing edge of the vane, forming a slightly non-uniform vortex core shape that rapidly relaxes into a circular profile by a chord length downstream. Introducing a vortex near to the suction side of the vane significantly modifies this formation process, as seen in the -0.2C offset condition presented in

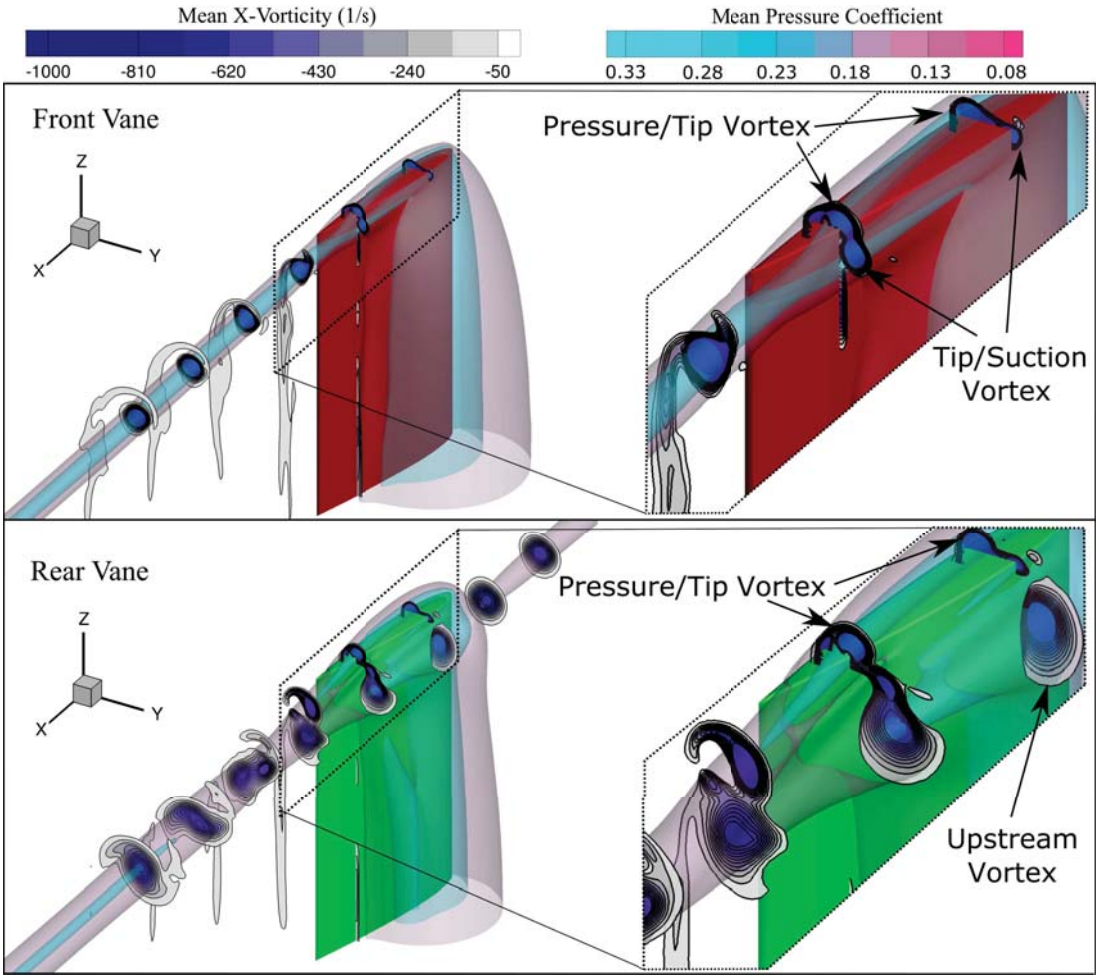

Figure 7.1: Contours of x-vorticity, with isosurfaces of pressure at $C_p = -0.4$ and $C_p = -0.16$ for front vane (top) and rear vane at -0.2C offset (bottom).

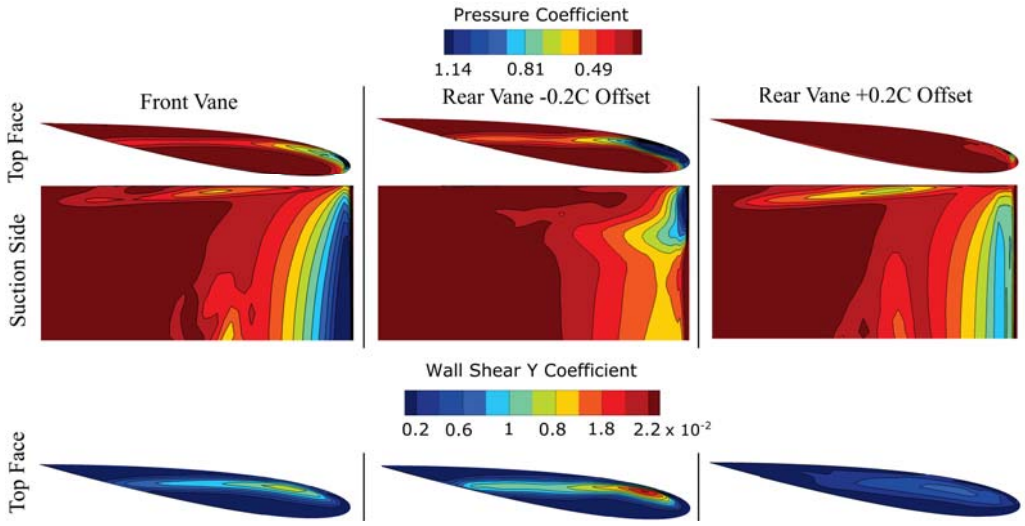

Figure 7.2: Pressure coefficient on vane surfaces (top) with wall shear (bottom) for various offsets

Figure 7.1. The upstream vortex is seen to merge with the suction side vortex, producing a distinct vortex that is separate from the vortex produced from the pressure surface/tip surface bleed. The initially merged vortex has a larger core of both vorticity and pressure deficit than the tip surface/suction surface bleed vortex in the front vane only case, however the pressure reaches a lower peak, with no -0.4 C_p isosurface seen. When the vorticity downstream of the vane is inspected, only two vortices are distinguishable, the partially merged upstream vortex and the pressure/tip vortex. This would appear as a weaker vortex produced by the downstream vane if only the off vane vortices were observed, due to the re-energisation of the upstream vortex by the tip/suction side vortex. As the flow moves further downstream these two vortices merge, eventually forming one coherent structure which relaxes into a uniform vortex. The relaxation to circular takes considerably longer than the single vane case, with significant non-uniformities present at 1.5C downstream. The resultant low pressure core of the merged vortices is larger at -0.16 C_p, however the low pressure peaks have been reduced, with the -0.4 C_p isosurface being considerably smaller in diameter. More interesting is the disappearance of the -0.4 C_p isosurface while the two vortices are in the merging process, however after merging and during the relaxation stage it returns. This indicates that the relaxation back to vortex circularity also coincides with an increase in peak pressure drop within the vortex.

Inspecting the on-surface pressures and wall shears presented in Figure 7.2 can

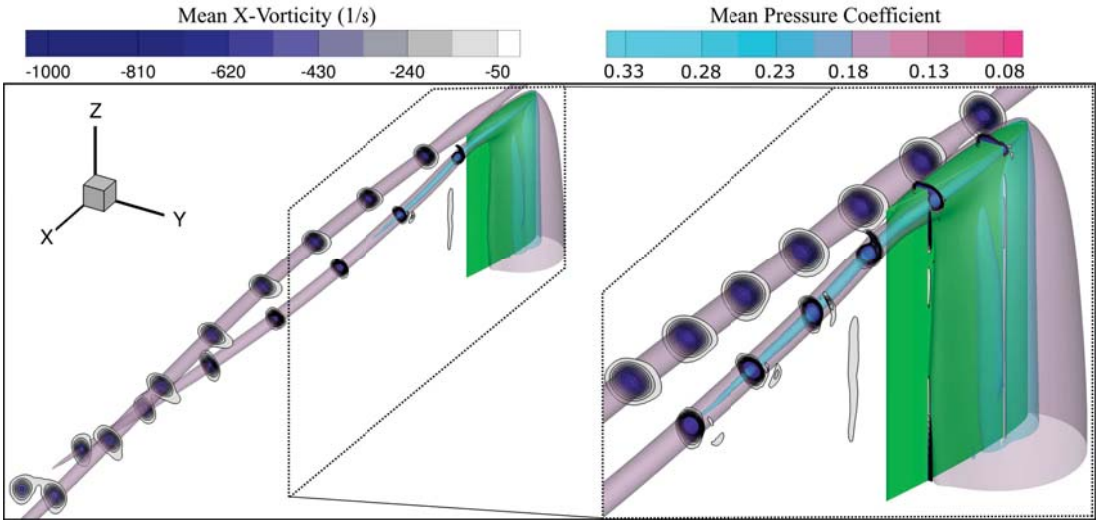

Figure 7.3: Contours of x-vorticity, with isosurfaces of pressure at $C_p = -0.4$ and $C_p = -0.16$ at 0.2C offset.

further highlight the differences in vortex suppression and enhancement between the offsets. As previously discussed, passing the vortex on the suction side of the vane suppressed the tip/suction vortex, pulling the vortex off the surface. This caused the pressure of the core to be indistinguishable on the surface in the -0.2C offset condition, whilst the upstream vortex showed a clear enhancement of the suction peak at the tip. The pressure/tip vortex also produced a more significant low pressure region than in the front vane, with a clear enhancement despite the downstream vane producing less lift than the upstream due to downwash and unfavourable vortex interactions. This was also reflected in the wall shear, with the pressure/tip vortex having 275% higher peak cross plane shear, indicating the vortex generated on the tip surface of the vane was both stronger and forced closer to the surface than in the single vane condition. With the offset modified to positive 0.2C and the upstream vortex passing on the pressure side, the enhancement and suppression of the two tip vortices was effectively reversed. Through the presence of the low pressure core on the suction side of the vane reducing the magnitude of the local pressure differential, in addition to the downwards flow induced by the swirling vortex core, the pressure/tip vortex is suppressed. This can be seen in the nearly non-existent tip pressure reduction and low wall shear. Passing the vortex on the pressure side also enhanced the tip/suction surface vortex, with an increase in peak suction of 0.16 against the single vane case clearly visible.

The results of the vortex suppression on the positive offset case can be seen in

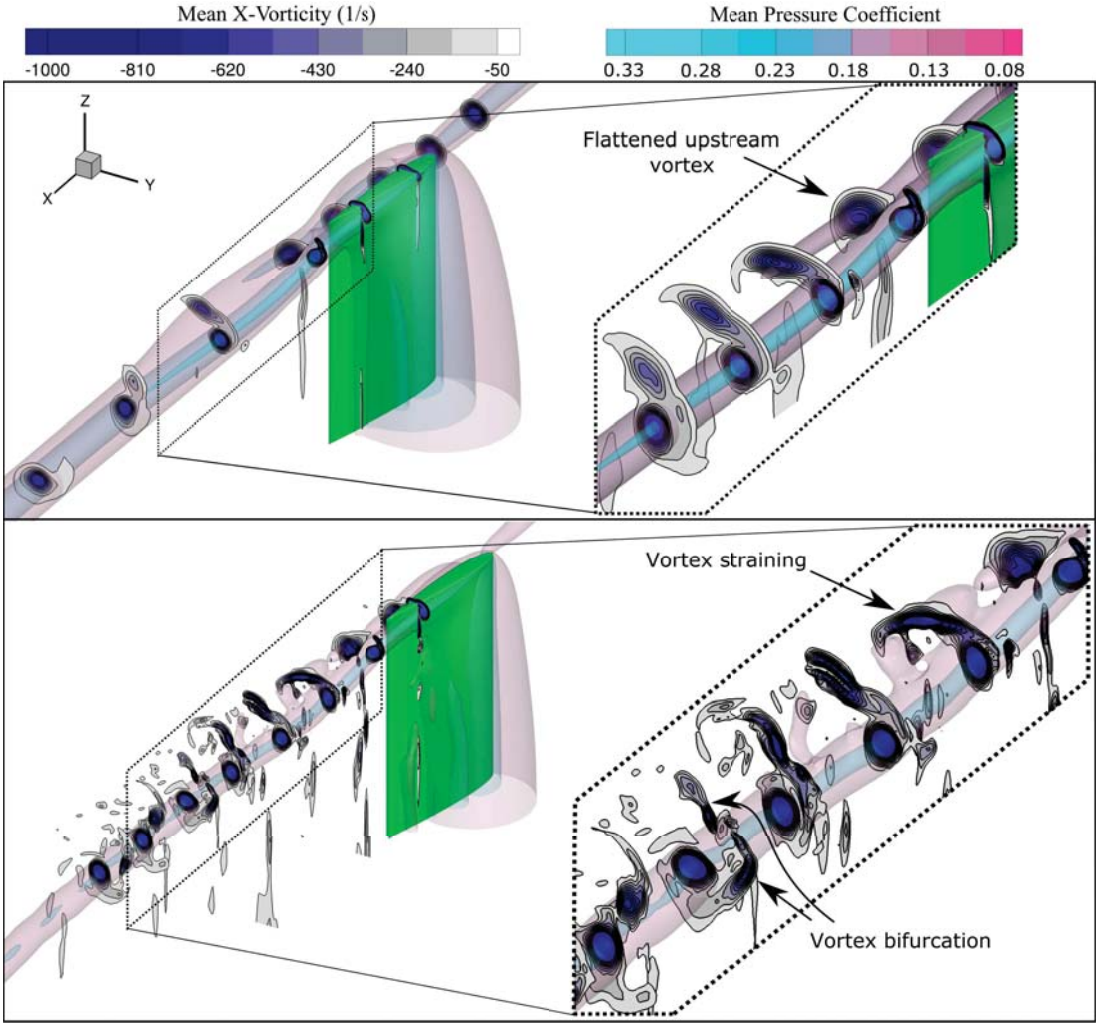

Figure 7.4: Time averaged (left) and instantaneous (right) contours of x-vorticity, with isosurfaces of pressure at $C_p = -0.4$ and $C_p = -0.16$ at 0C offset.

Figure 7.3. Suppression of the pressure/tip vortex results in only a small tail of vorticity forming on the end of the dominant tip/suction vortex, resulting in rapid vortex relaxation. This causes the low pressure -0.4 C_p isosurface to extend for a longer distance and at a larger diameter than in the -0.2C offset. Despite the lower pressure core than the upstream vortex, the dissipation rate of the vorticity and the pressure is larger for the downstream vortex, resulting in its eventual merger into the upstream vortex. The suppressing effect of the upstream vortex on the pressure/tip vortex weakens the strength and radius of vorticity of the final downstream vortex, making it the weaker vortex, thus resulting in its merger with the upstream vortex through the asymmetric merger process previously identified in the experimental work.

When the upstream vortex was kept on the pressure side of the vane, but the

offset reduced, the same pressure/tip vortex suppression was observed, seen in Figure 7.4. However, the contact between the upstream vortex and the surface resulted in the flattening of the vorticity profile on the vane. This caused a loss in total vortex circulation, making the upstream vortex the weaker of the two. Consequently, it was found to merge into the downstream vortex, an effect not seen in the experimental results as the near offset cases were all merged through the observation domain. This merger did however produce the asymmetric merger and vorticity tail observed in the experimental merging mechanism. When the instantaneous results were analysed it was found the merger was a highly unsteady process, with significant fluctuations of 14.2% in core radius at C_p = -0.16, and peak vorticity reaching 61% more than time averaged at x/C = 13. In the instantaneous condition the upstream vortex became more strained by the downstream vortex, forming an elongated structure that split into two separate structures further downstream. Due to the presence of both bifurcated and singular upstream vortices it could be seen that this was a transient fluctuation between the bifurcated and singular state.

7.1.2 Transient Trend Analysis

As discussed previously, only the far offset 0.2C co-rotating condition was evaluated with the transient vortex tracking methodology, over a time period of $T * U_\infty / C = 12$. The key properties tracked by this process were vortex position and circulation, with vortex separation and circulation differential calculated from these parameters. The positions of the upstream and downstream vortices in the horizontal (y) and vertical (z) directions can be seen in Figure 7.5. To interpret these plots, one can think of a horizontal line drawn through the domain indicating the state of the vortices at any given time, while a vertical line gives a time history of the vortices on a given plane. As the vortices travel through the domain they rotate in a helical manner, resulting in a long duration spatial fluctuation. An example of this can be seen in the transition of the upstream Z position from an average value around -0.05C at x/C = 15 to -0.45C at x/C = 23. What is more interesting from these graphs is the nature of the fluctuations in position and their propagation downstream. A clear periodicity can be seen in all of the position traces, visible from the start of the domain in the upstream vortex and developing more towards the end of the downstream vortex domain. Approximately two and a half primary fluctuation

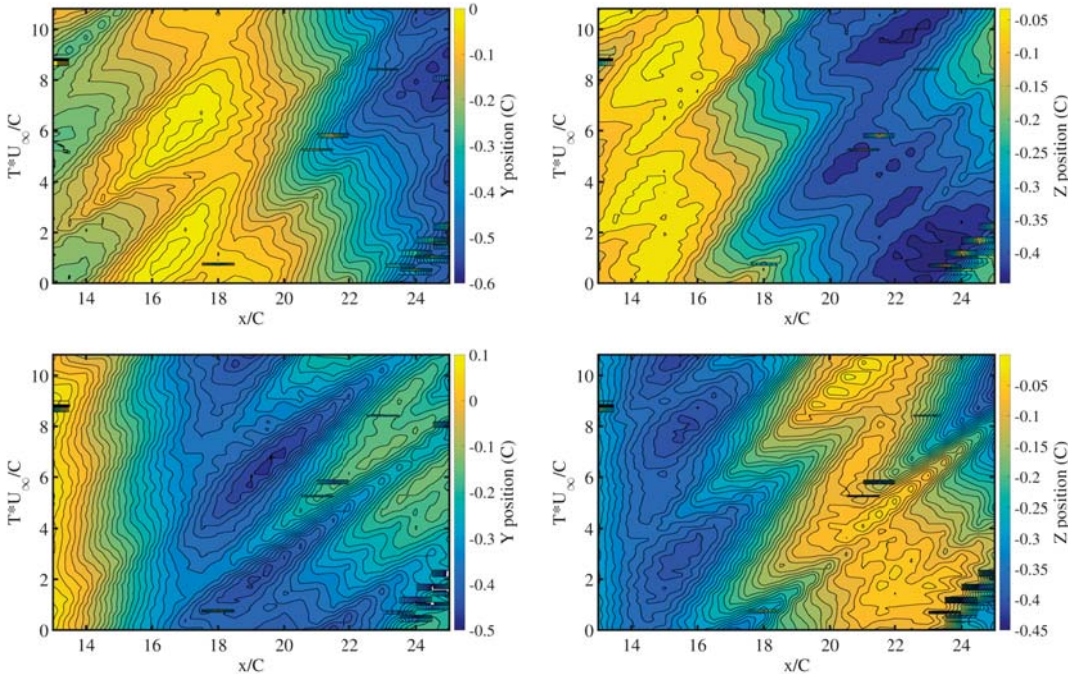

Figure 7.5: Y and Z positions of upstream (top) and downstream (bottom) vortices with respect to time (vertical axis) and distance travelled downstream (horizontal axis) for the 0.2C offset condition. Rapid changes in position from x/C = 20 onwards caused by detection of a merged state. Diagonal variations in the contour plot are indicative of path disturbances travelling downstream.

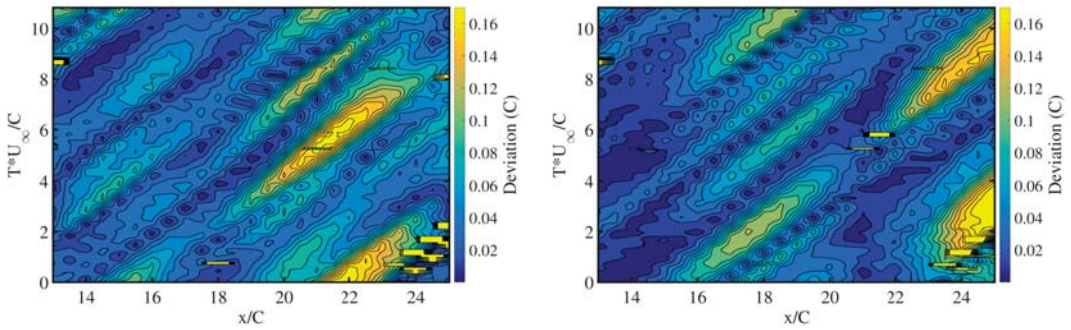

Figure 7.6: Deviation from average position of upstream (left) and downstream (right) vortices with respect to time (vertical axis) and distance travelled downstream (horizontal axis) for the 0.2C offset condition. Diagonal variations in the contour plot are indicative of path disturbances travelling downstream.

periods can be seen within the domain, indicating a dominant fluctuation frequency approaching Str = 25. This fluctuation frequency is similar between the two vortices, and will be discussed in more detail later in this section. It is also evident from the plots of the downstream vortex that the magnitude of the fluctuation increases significantly with motion downstream.

By inspecting the deviation from the averaged vortex location on a given plane the magnitude of the fluctuations could be more clearly analysed (Figure 7.6). The near zero deviation in the downstream vortex just behind the rear vane is expected due to it's proximity to its formation location, however as the vortex progresses downstream its amplitude of deviation grows to match that of the upstream vortex at 0.17C. The deviation of the upstream vortex is also seen to grow with distance downstream, peaking at x/C = 22. The peaks in deviation occur over a relatively short downstream, and propagate downstream, however there is clear interaction between he peaks of the upstream and downstream vortex. along the diagonal peaks line starting at x/C = 16, it can be seen that initially this manifests as a peak in the downstream vortex before switching to the largest peak of the upstream vortex and then returning to the downstream vortex peaking. Whilst one vortex is at peak deviation, the other is closest to its average values, showing a clear in phase motion.

However, the separation changes are not directly reflective of these deviation changes, with results seen in Figure 7.7. Following the same diagonal fluctuation as previously discussed from x/C = 16 it can be seen that the vortex separation remains within 0.02C consistency until x/C = 22, at which point it starts to rapidly increase by 0.06C to 0.4C by x/C = 24. This pattern

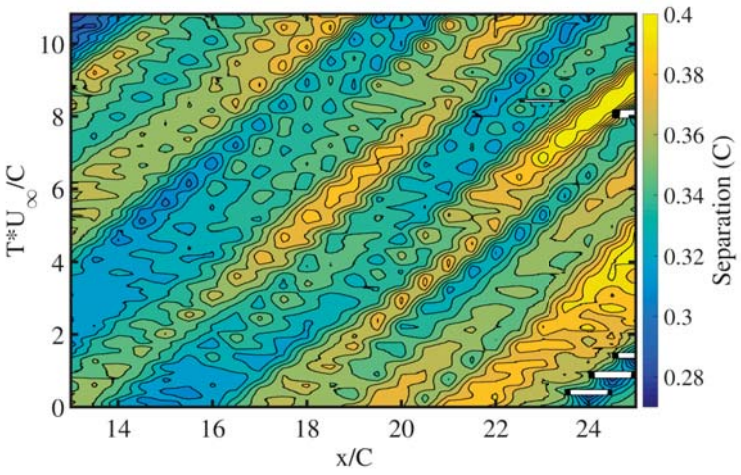

Figure 7.7: Separation between vortices with respect to time (vertical axis) and distance travelled downstream (horizontal axis) for the 0.2C offset condition. Diagonal variations in the contour plot are indicative of separation disturbances travelling downstream.

is similarly reflected in the cycle starting at x/C = 12, which encounters a similar step at x/C = 20, indicating that despite significant cycle to cycle variance there is still a fundamental pattern in the vortex meandering which is followed. Another significant observation is that when the instantaneous results are considered the fluctuations can result in the downstream vortex separation being larger than the upstream separation, despite the tendencies of the vortices to migrate towards each other. From the fluctuations observed, it appears that a degree of separation trend reversal also occurs, causing the vortices to meander back together after an extended separation. In the bottom right corner (as well as further up the right side) a number of blanked out values can be seen, these correlate with locations of vortex merger. This merger in the instantaneous sense clearly happens when the separation distances fluctuate to a minima at the critical merging distance, as identified in the experimental work. These fluctuations happens just before a point of local maxima, and produces a merger which propagates downstream. The presence of this merger which can form well upstream of the time averaged point of merger before propagating downstream explains the statistical merging properties observed in the experiments.

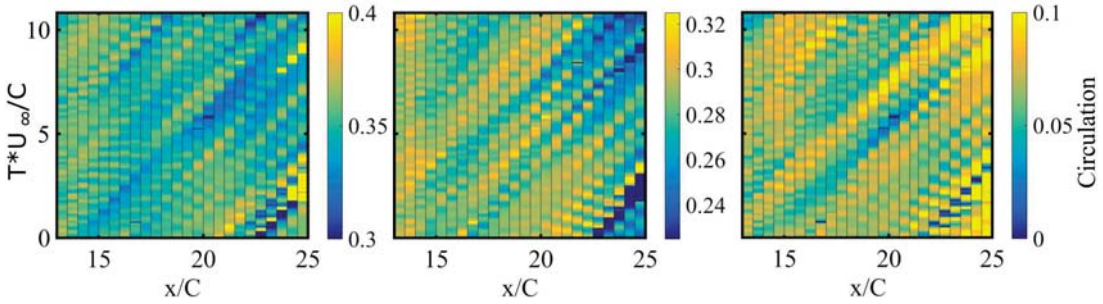

Figure 7.8: Nondimensionalised circulation variation with respect to time (vertical axis) and distance travelled downstream (horizontal axis) for the 0.2C offset condition. Upstream vortex left, downstream vortex centre, differential between vortices on right. Diagonal variations in the plot are indicative of circulation disturbances travelling downstream.

7.1.3 Frequency Analysis

While contour plots can be used effectively for the separations and vortex core locations, this is primarily due to the dominant forcing of the low frequency fluctuations overwhelming the higher frequency, smaller amplitude oscillations in core location. In the case of circulation however, the fluctuations occur at a far higher frequency, and often with a less consistent direction than location, and as such contour plots, while clear for location, become very unclear for circulation. As such the circulation of the two vortices, as well as the circulation difference between the two, is represented in the contoured lines of Figure 7.8. At the start of vortex interaction the fluctuations are small, random and high frequency, however as the vortices progress through the domain they become more coherent and traceable changes. In the bottom right corner the high upstream circulation, low downstream circulation and large circulation difference can be seen at the point of vortex merger. In both the upstream vortex and the first 10C downstream of the downstream vortex there is very little variation in the average value of circulation. However after x/C = 20 in the downstream vortex there is a significant drop-off in the circulation from 0.3 m^2s^{-1} to 0.25 m^2s^{-1} as the asymmetric merging mechanism initiates. This is accompanied by a significant differential in circulation, as the variation in the upstream vortex circulation is comparatively small. Inspecting the deviation starting at x/C = 14 The lowest circulation values in the upstream vortex correlate with the smallest separation values experienced by the vortex pairs, with larger circulation typically associated with larger separations. The smallest differential between circulations is also located along the lines of closest

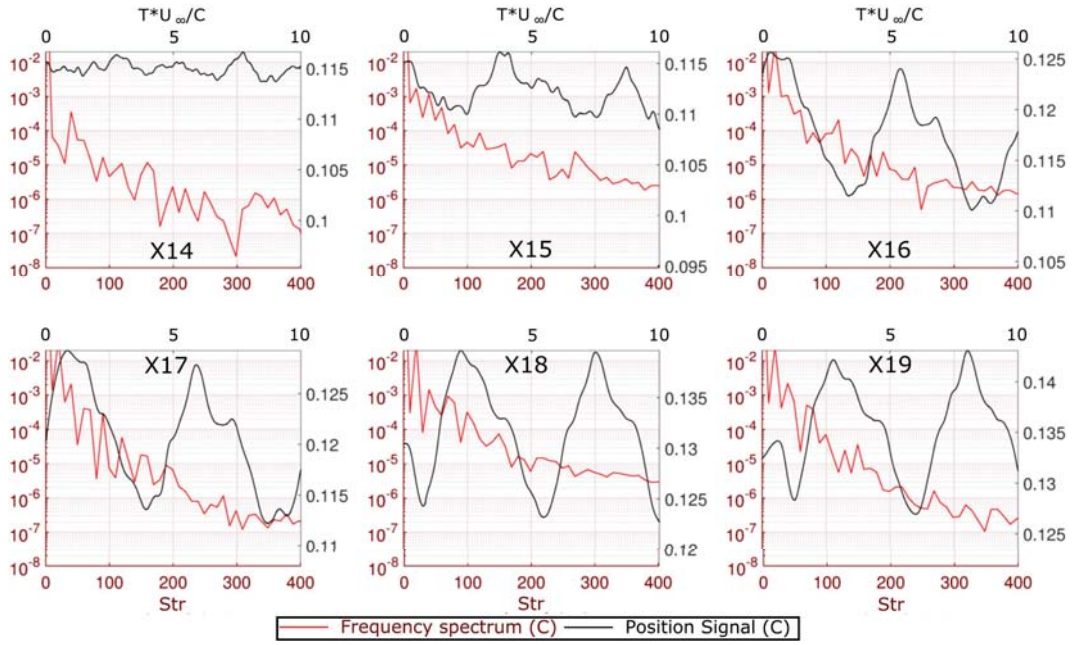

Figure 7.9: Z position (C) evolution with time for the downstream vortex at multiple locations (black), with frequency spectra (C) in red. Position signals are all plotted on axes with the same range magnitude.

separations.

To gain a better understanding of the rate and growth of the transience of the vortex positions, the frequency spectra of the position signals at various locations downstream were analysed, with the downstream Z variance presented in Figure 7.9 and the upstream variance presented in Figure 7.10. The previously discussed growth in the downstream vortex signal can be clearly seen, with 22.9% less fluctuation magnitude at x/C = 14 than x/C = 19. For the downstream vortex at x/C = 14, the small scale, high frequency fluctuations are still significant with respect to the larger fluctuations, as evidenced by the lack of a consistent low frequency response above $2 * 10^{-4}$ at frequencies below Str = 50. As the vortex progresses downstream the amplitude of oscillations increases by a factor of four, with a significant bias to increasing the lower frequency magnitudes. The range of frequencies above 10^{-4}C magnitude increases from Str = 0-10 to Str = 0-100 by x/C = 18, with little consistent variation in the higher frequency magnitudes from x/C = 15 onwards. As such the bias of the downstream vortex strongly shifts from high frequency, lower amplitude oscillations to a longer wavelength instability as the flow moves downstream.

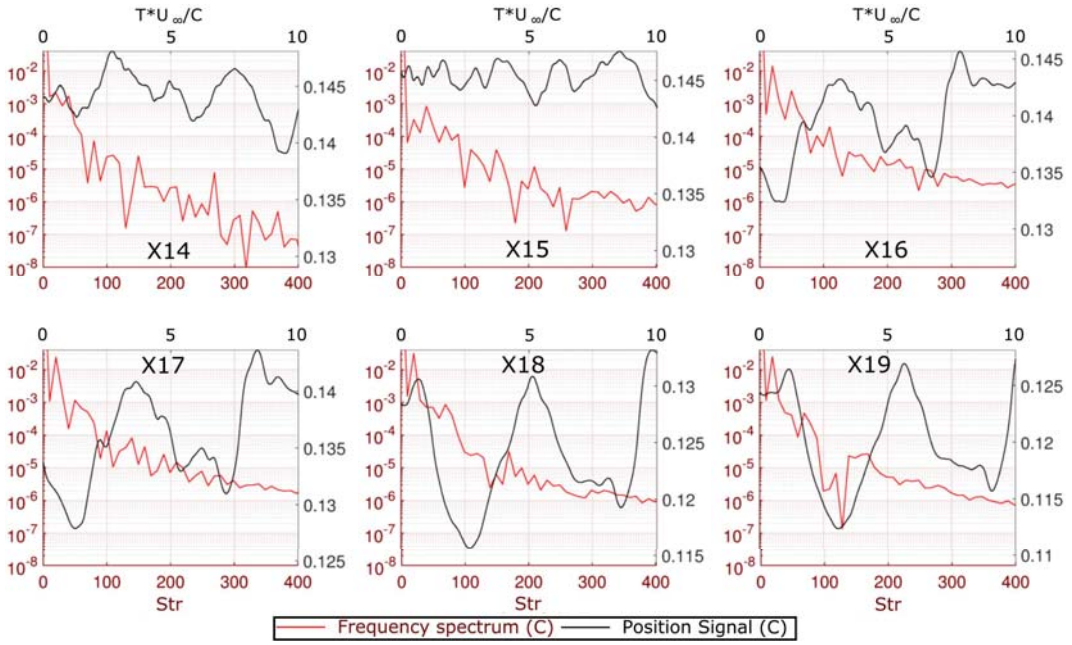

Figure 7.10: Z position (C) evolution with time for the upstream vortex at multiple locations (black), with frequency spectra (C) in red. Position signals are all plotted on axes with the same range magnitude.

Inspecting the upstream vortex, it could be seen that the initial fluctuations were significantly higher, in the order of 2.5 times that of the downstream vortex at x/C = 14. Growth is also seen in the upstream vortex, although to a lesser extent, with the x/C = 19 fluctuation magnitude being 217% larger than the fluctuation at x/C = 14. The fluctuation magnitudes trend towards convergence between the upstream and downstream vortices, with a difference in magnitude by the x/C = 19 of 23.7% as opposed to 148% at x/C = 14. Observing the frequency trends reveals that the upstream vortex behaves slightly differently to the downstream vortex with respect to the magnitude of its lower frequencies, with the 10^{-4}C intensity band stretching from Str = 0-50 at x/C = 14, five times wider than the downstream vortex. However this band does not exhibit the same level of growth, with lesser intensities observed downstream at Str = 100, as well as a slightly faster frequency drop-off. However, it appears that the interaction of these vortices causes them to both equalise their instabilities to the same magnitudes and frequencies of oscillation.

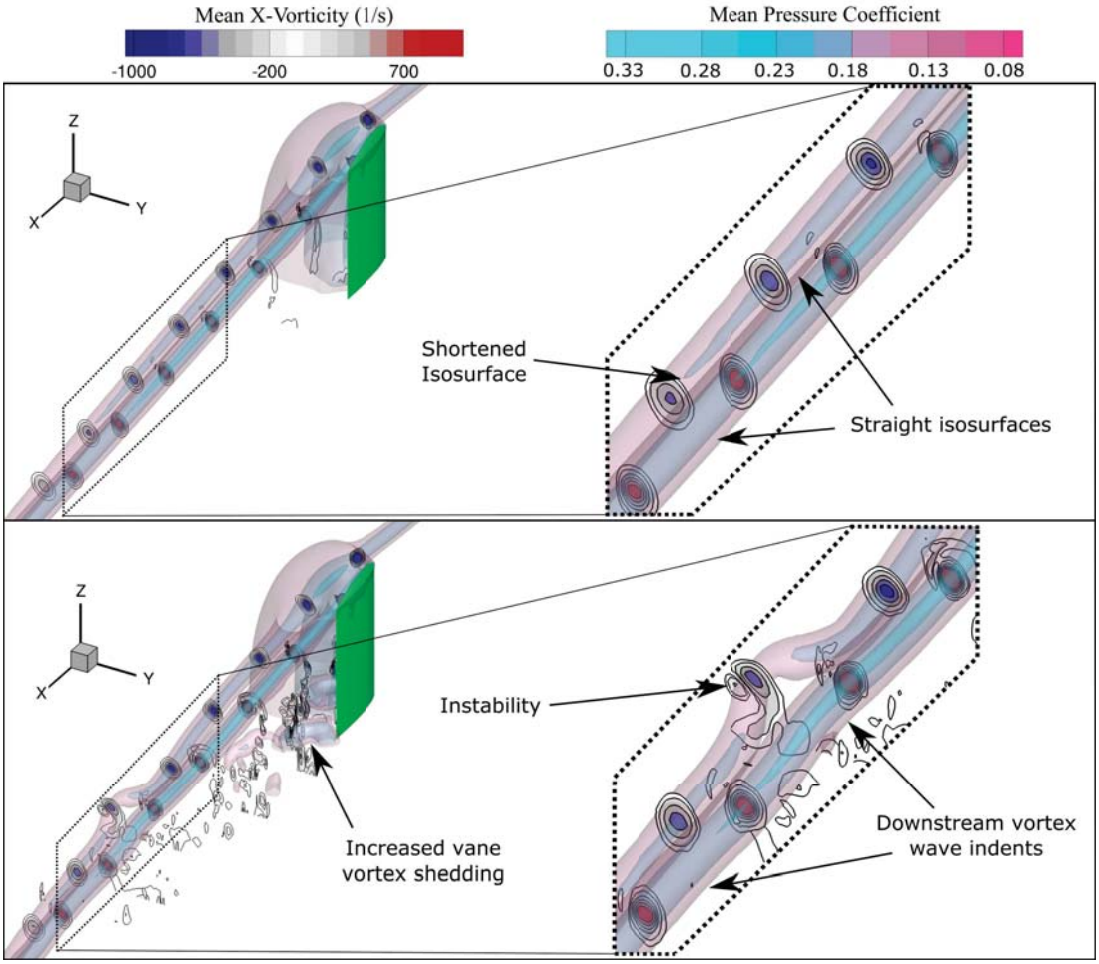

Figure 7.11: Contours of x-vorticity, with isosurfaces of pressure at $C_p = -0.4$, $C_p = -0.16$ and $C_p = -0.08$ for rear vane at 0.2C offset in time averaged (top) and instantaneous (bottom) conditions.

7.2 Counter-Rotating Condition

7.2.1 Suction Side Pass-by

The counter-rotating conditions had the highest dissipation rates and instabilities observed in the experimental results, and as such it was expected that the LES analysis would show very significant transience. This was particularly true for the 0.2C offset condition presented in Figure 7.11, which showed a large difference between the time averaged and instantaneous results. In addition to the small deviation waviness in both vortex cores there was a periodic shedding of a large deviation instability resembling a vortex ring. This was not the dominant flow feature, hence was not observed in the time averaged

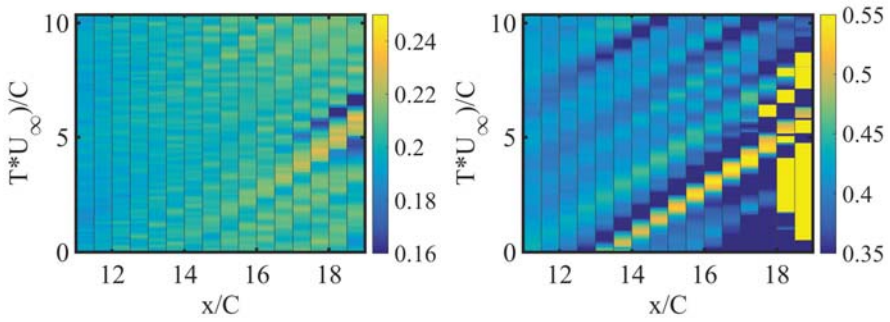

Figure 7.12: Nondimensionalised circulation evolution with time for downstream vortex (left) over an extended downstream range, with vortex separation (C) right. Diagonal variations in the plot are indicative of circulation and separation disturbances travelling downstream.

results, however animations of the solution output during the simulation were inspected and these confirmed this as a periodic feature with a shedding frequency of Str = 7. This frequency is near the Str = 8 for trailing edge vortex shedding and Str = 8-10 for shear layer instabilities identified by Schiavetta et. al. [152], indicating that this phenomenon may be triggered by these vortex shedding phenomena. While the vorticity strength and pressure deficit within the core was reduced by this deviation, it still maintained a circular vortex profile. Within this kinked vortex segment the -0.4 C_p isosurface ended, indicating less pressure deficit, however this same isosurface also extended 0.75C longer in the upstream vortex in the instantaneous condition than the time averaged case. The large vortex deviation produced a region of pressure higher than -0.4 C_p that when averaged would have the effect of a lower average pressure deficit, highlighting the modification of the time-averaged results from the meandering-based vortex smearing.

Closer inspection of the transience of the interaction showed a strong link between the magnitude of the vortex separation and circulation, seen in Figure 7.12. A clear diagonal line of exceptionally high separation (greater than 0.5C) can be seen starting from x/C = 13.5, propagating through the domain. This is indicative of the wave instability seen in Figure 7.11. It can be seen that this instability grows through the domain, reaching a peak value around 0.55C before tracking of the secondary vortex is lost (indicated by the yellowed-out areas after x/C = 18). This correlates directly with the circulation trends, with the circulation of the downstream vortex being up to 0.03 m^2s^{-1} higher than average at peak separation, and dropping considerably once the separation is reduced. This correlated with the inverse of the upstream vortex circulation,

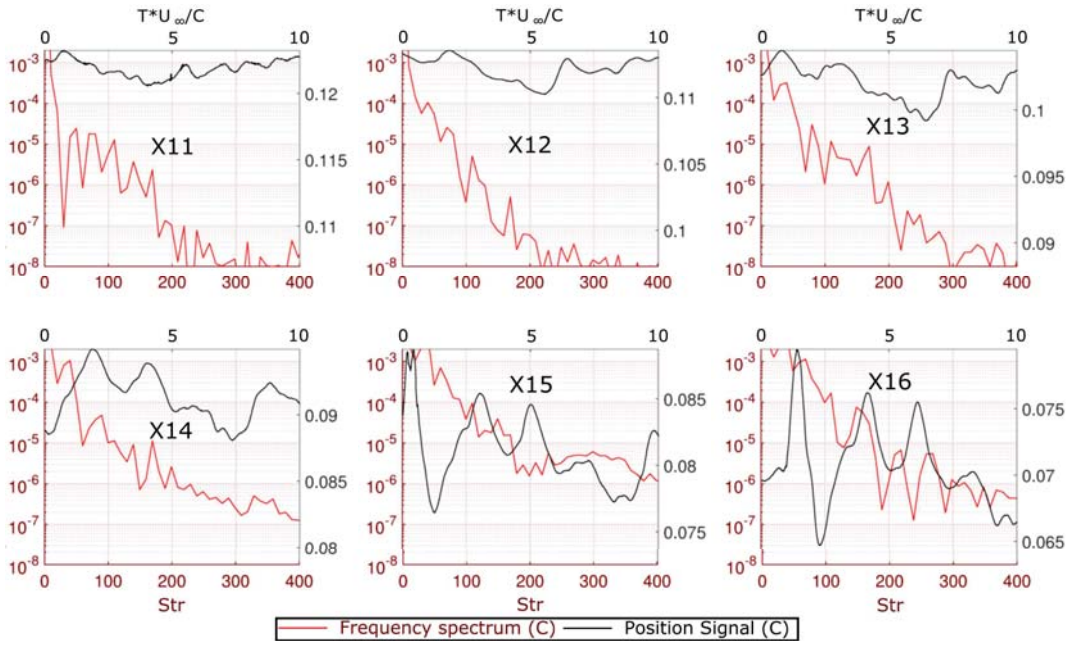

Figure 7.13: Z position (C) evolution with time for the upstream vortex at multiple locations (black), with frequency spectra (C) in red. Position signals are all plotted on axes with the same range magnitude.

with the upstream vortex having reduced circulation at higher offsets. As such, the coupling between the vortices resulted in the upstream vortex imparting its circulation to the downstream one whilst moving apart, while when the instability brought the vortices close together the energy was more evenly spread between the two.

The position signals and frequency spectra of the upstream vortex are presented in Figure 7.13 and Figure 7.14. Unlike the co-rotating case there is a monotonic increasing of the entire frequency range across the domain, with the entire frequency spectra translating upwards from x/C = 11 to x/C = 16. This is due to the counter-rotating case being able to manifest both the elliptic and long wave instabilities, with a bias to the larger long wave/Crow instabilities. The fluctuation magnitudes of both the y and z position values increase substantially through the domain presented, with a starting magnitude of $1.75 * 10^{-3}$ and $2.60 * 10^{-3}$ at x/C = 11 and finishing magnitude of $2.61 * 10^{-2}$ and $14.7 * 10^{-2}$ at x/C = 16. The respective gains in fluctuation magnitude are 14.9 and 5.65 times respectively, showing a far more significant fluctuation gain in y than z. These oscillation magnitudes at x/C = 16 are over 77.5% greater than for the co-rotating case at x/C = 19, showing a considerably higher magnitude of deviation. This is consistent with the presence of the wave

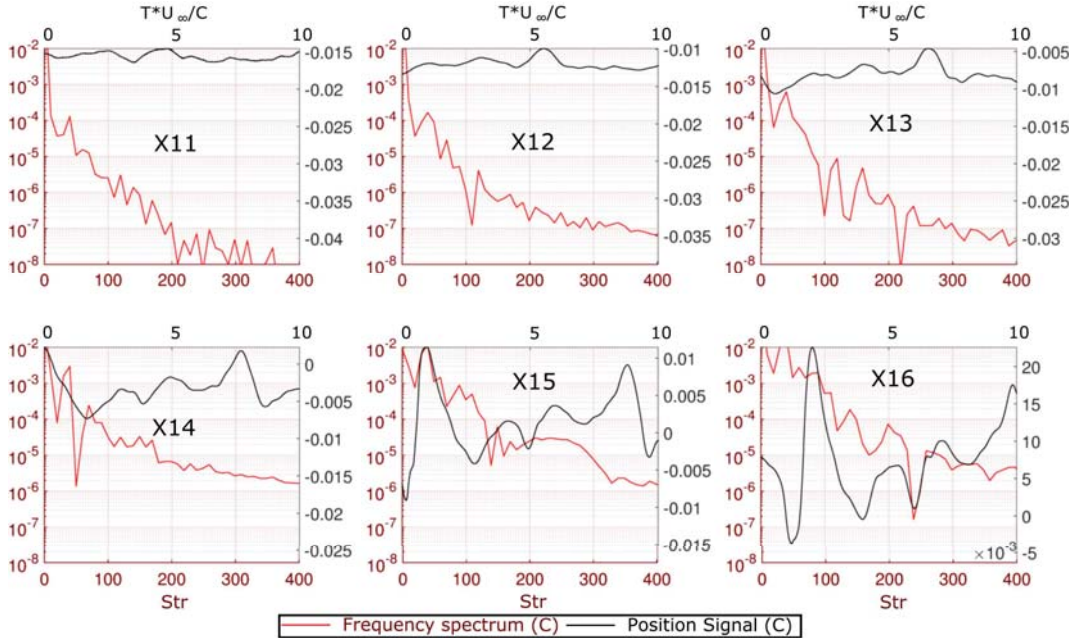

Figure 7.14: Y position (C) evolution with time for the upstream vortex at multiple locations (black), with frequency spectra (C) in red. Position signals are all plotted on axes with the same range magnitude.

instability noted in the visualisation, which contributes to the much faster dissipation of energy in the counter-rotating case than the co-rotating case noted in the experimental section and discussed further in the next chapter.

Similar trends are seen in the oscillation of the downstream vortex, presented in Figure 7.15 and Figure 7.16. For this condition the fluctuation magnitudes of the y and z position values are $5.5 * 10^{-4}$ and $9.0 * 10^{-4}$ at x/C = 11 and finishing magnitude of $2.61 * 10^{-2}$ and $4.96 * 10^{-3}$ at x/C = 16. Again this vortex exhibited a far higher growth in instability on the y axis than the z axis, showing that this was not just a simple consequence of vortex pair rotation of a 45 degree crow instability, as this would cause one vortex to grow in Y instability and the other to reduce. Peak y value correlated approximately with minimum z value by x/C = 16, however the correlation was far less defined prior to x/C = 14. As such, the instabilities could be seen to develop more clearly downstream into long wave, while closer to the vane they were being driven more by on-vane characteristics such as vortex shedding at the tip.

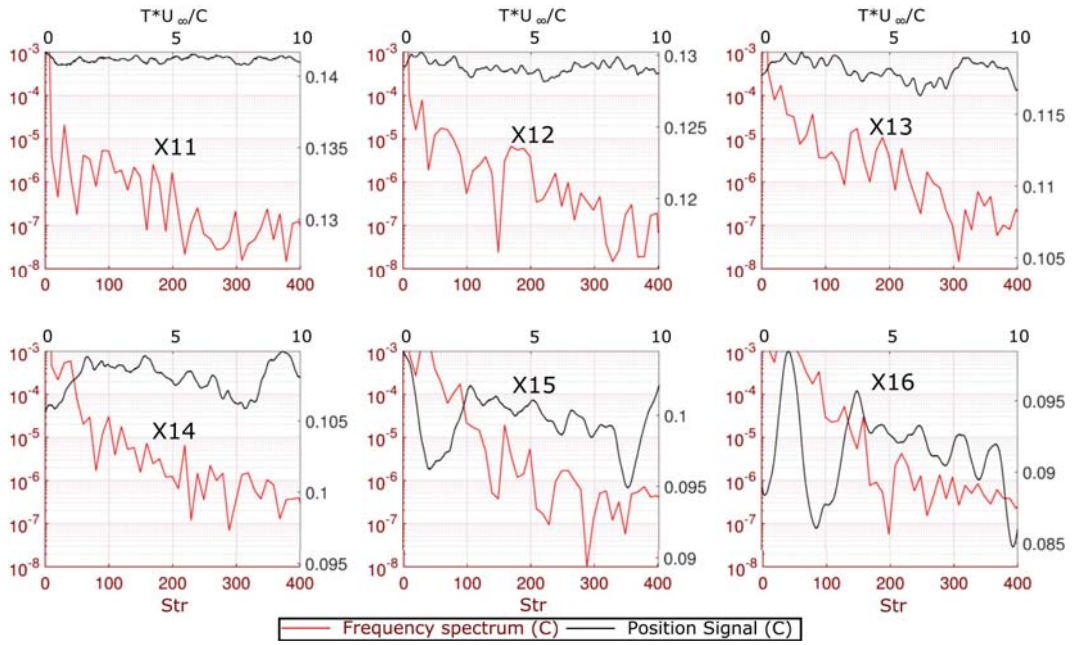

Figure 7.15: Z position (C) evolution with time for the downstream vortex at multiple locations (black), with frequency spectra (C) in red. Position signals are all plotted on axes with the same range magnitude.

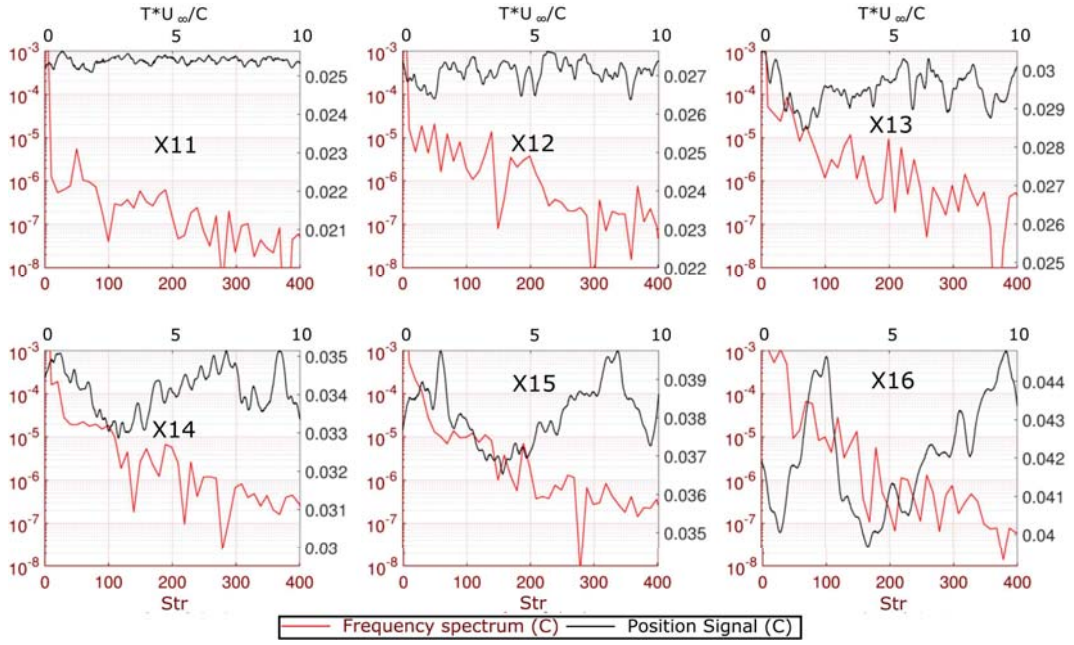

Figure 7.16: Y position (C) evolution with time for the downstream vortex at multiple locations (black), with frequency spectra (C) in red. Position signals are all plotted on axes with the same range magnitude.

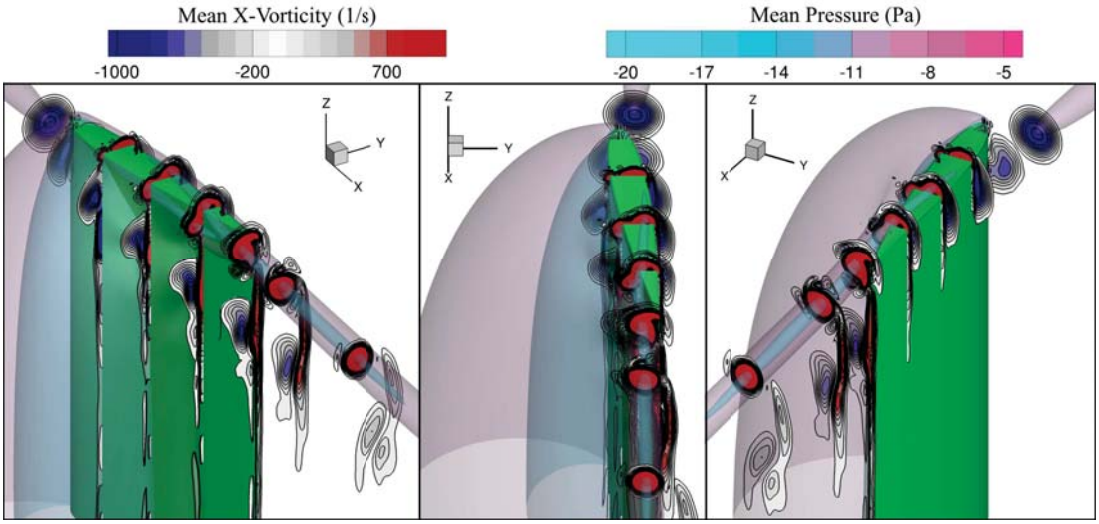

Figure 7.17: Contours of x-vorticity, with isosurfaces of pressure at $C_p = -0.4$ and $C_p = -0.16$ for rear vane at -0.2C offset (right).

7.2.2 Direct Impingement

In the direct impingement condition (-0.2C offset) far less unsteadiness and instability was seen, with a stable downstream vortex and largely destroyed upstream vortex. The impingement of the upstream vortex on the downstream vane did not cause breakdown of the upstream vortex, instead forcing the vortex to bifurcate. This is due to the pressure gradient on the front of the vane being of insufficient magnitude and distance to force a full vortex breakdown. The vortex segment on the pressure side of the downstream vane is drawn towards the tip by the spanwise movement of the flow. This process forces the direct interaction with the tip vortex and rapid dissipation of the vorticity from the upstream core, completely eliminating the vortex by the trailing edge of the vane. On the suction side of the vane the bifurcated vortex is forced downwards along the vane surface by the spanwise flow. This causes a significant increase in vortex spacing, similar to what was seen in the initial RANS study and the experimental work.

The reduced strength of the upstream vortex in conjunction with the high separation results in the significantly reduced rotational rate of the vortex pair at this offset as observed in the experimental work. By forcing the rotating vortex into such close proximity with the vane, the shear within the boundary layer is increased. This creates an enhanced region of positive vorticity on the surface of the vane, inboard of the tip. This region is of similar circulation

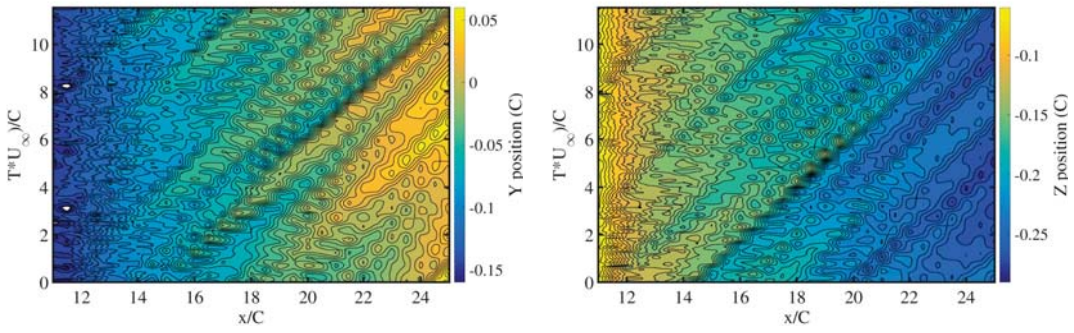

Figure 7.18: Y position (left) and Z position (right) for downstream vortex. Diagonal variations in the contour plot are indicative of path disturbances travelling downstream.

magnitude to the remaining upstream vortex, however is highly strained, with little circularity. This causes it to break down into two separate vortices once off the vane body, with one interacting with the upstream vortex remnant forming a rotating vortex pair. The other vortex moves towards the downstream tip vortex, however dissipates rapidly. The drawn out tail structure of this upper vortex pair shows behaviour similar to that of the asymmetric co-rotating merging process, with a rapid transfer of vorticity into the primary vortex. At the same time, the lower counter-rotating pair then behaves like the counter-rotating 0.2C offset case, with a high rate of circulation dissipation and a high local rotation rate. The final outcome of these interactions in the far field is a singular downstream vortex, with minimal remnants of the upstream vortex.

The evolution of the downstream vortex position with respect to time can be seen in Figure 7.18. Similar to the downstream vortex in the co-rotating case, immediately behind the downstream vane the oscillations in position are small, with increased growth throughout the domain. However the fluctuation rates are far less significant than the other transient cases. The peak y position amplitude of 0.06C at x/C = 16 is less than half of the equivalent amplitude in the co-rotating 0.2C offset case, and 40% of the counter-rotating 0.2C offset case. This is due to the lack of a strong secondary vortex structure, which cannot introduce elliptic or long-wavelength instabilities into the downstream vortex. As such the primary mechanism for fluctuation growth is the downstream amplification of instabilities caused by the initial vortex interaction and vortex shedding previously discussed. The progressive migration of the vortex towards +y and -z can also be seen, driven by the downwash of the

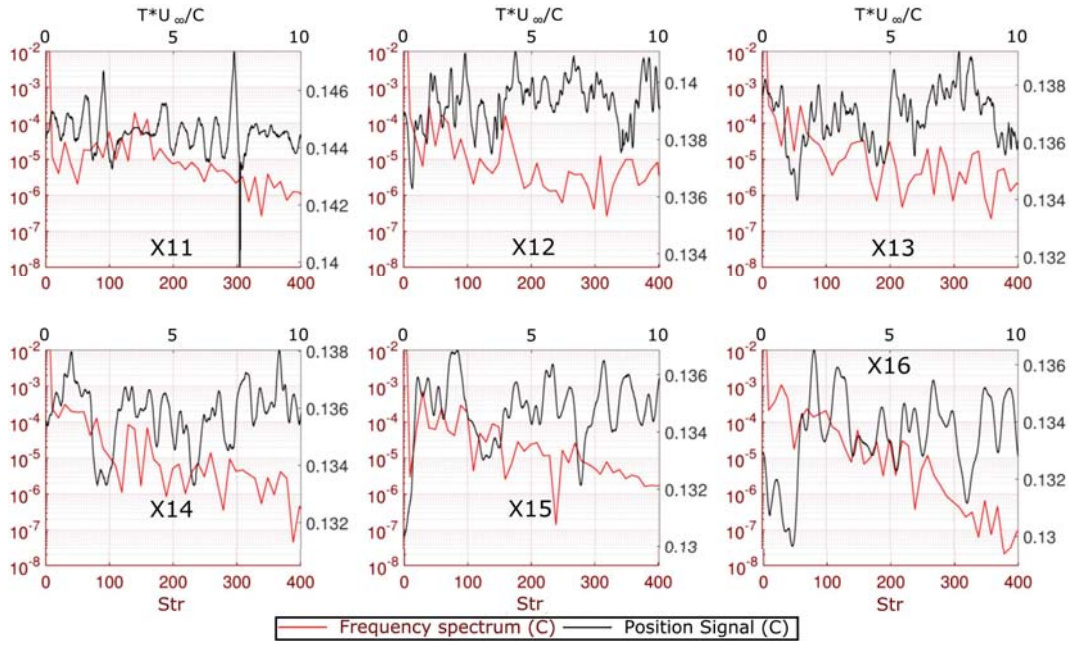

Figure 7.19: Z position (C) evolution with time for the downstream vortex at multiple locations (black), with frequency spectra (C) in red. Position signals are all plotted on axes with the same range magnitude.

vane.

A more complete picture of the instability growth can be seen when the individual position signals and frequency spectra in Figure 7.19 and Figure 7.20. The comparative lack of meandering growth to the other transient cases can be seen by the high starting and low finishing oscillation magnitudes, with $3.5 * 10^{-3}$ at x/C = 12 being higher than either of the starting magnitudes for the counter-rotating 0.2C offset case. At x/C = 16 the magnitude is $8.5 * 10^{-3}$, which is significantly lower than the $1.18 * 10^{-2}$ seen in the counter-rotating 0.2C offset case, demonstrating this low instability growth rate. However, inspecting the frequency spectra shows that the majority of the oscillations in the -0.2C offset case are higher frequency than the other cases, with significant fluctuations in the Str = 300-400 frequency band above 10^{-6} up to x/C = 16. This is a direct result of the increased interactions on the vane body causing high frequency changes in on-vane characteristics, and subsequently minimal downstream vortex interaction due to the largely destroyed upstream vortex core.

These fluctuations in position showed a far less clear correlation with circulation than in the other transient cases presented. The circulation values

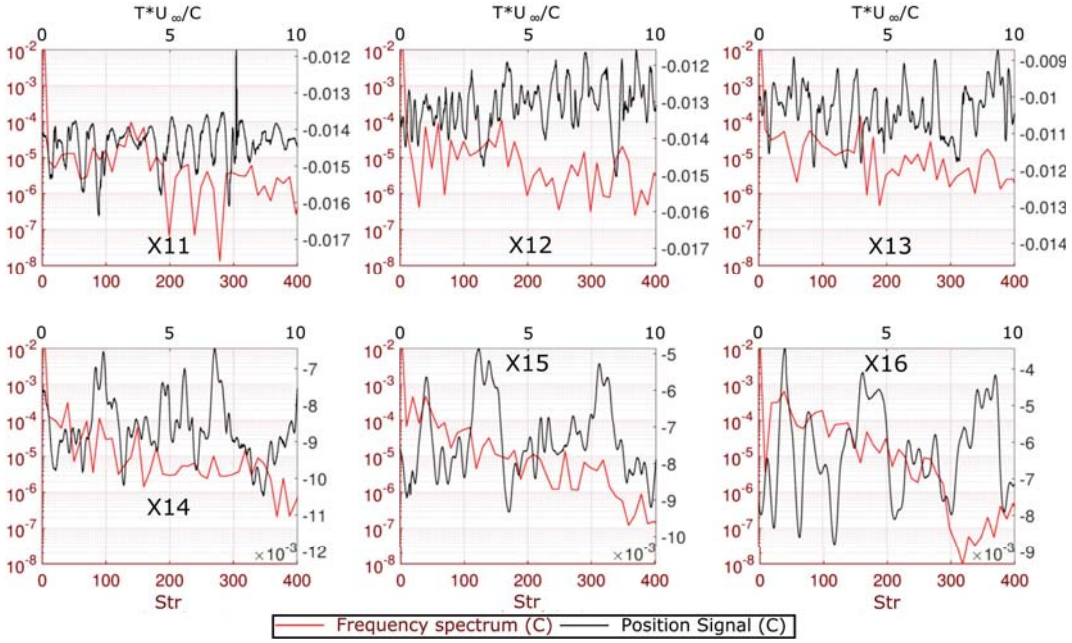

Figure 7.20: Y position (C) evolution with time for the downstream vortex at multiple locations (black), with frequency spectra (C) in red. Position signals are all plotted on axes with the same range magnitude.

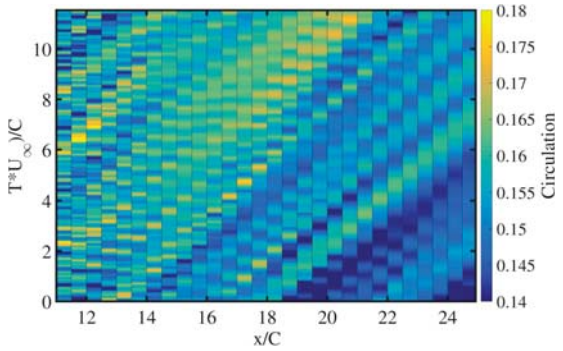

Figure 7.21: Nondimensionalised circulation evolution with time for downstream vortex. Diagonal variations in the plot are indicative of circulation disturbances travelling downstream.

presented in Figure 7.21 showed an average reduction in circulation throughout the domain, with an uneven periodicity with time. The fluctuations in circulation closer to the rear vane occurred with a significantly higher primary frequency, and less of a smooth periodicity. This was a result of the transience of the suction side bifurcated upstream vortex modifying the shear layer and consequently altering whether or not the secondary positive vortex had merged with the primary, as discussed earlier and seen in Figure 7.17. As the flow progresses downstream these fluctuations diffuse and spread out in space, leading them to bleed into the surrounding time regions. These results in the smoother fluctuations in circulation seen by the end of the domain. While the correlation with position was generally weak as previously mentioned, trends could be seen when compared to y position, with peaks in y position fluctuation associated with higher circulation values. It is likely that this has resulted from the interactions on the vane producing varying levels of vane downwash, the higher this downwash the more kinetic energy available to be rolled into the vortex. Higher y values result from a more significant downwash, hence the correlation between y value and circulation is understandable.

7.3 Conclusions

The LES analysis allowed considerably more information to be identified regarding the mechanisms behind the quantitative values observed in the wind tunnel testing. Key cases in both the co-rotating and counter-rotating regimes were identified from the experimental work, and were analysed with both instantaneous and time averaged methods to ascertain the key flow mechanisms behind the effects observed in the experiments.

It was found that the tendency of the downstream vortex to merge with the upstream in the co-rotating condition was driven by the suppression of one of the two tip vortices created at the downstream vane, resulting in a much weaker vane vortex. This, in conjunction with a lift reduction from the presence of the upstream vortex, resulted in the merger trend observed. However, at extremely close proximities on the pressure side, the vane elongated the shape of the upstream vortex, ultimately resulting in it being the weaker of the two and merging into the downstream vortex. This produced a highly strained vortex, with transient production of bifurcated vortices in the wake region. The

instabilities produced by the vortices interacting at far ranges were found to tend towards equalisation between the two vortices rather than one dominating over the other, despite the difference in vortex formation length. The instabilities and meandering between the two vortices was found to be responsible for the statistical merging phenomenon seen in the experimental work, with the vortices merging once the meander caused the separation between the vortices to reach the critical spacing.

The counter-rotating far offset condition was found to produce instabilities of a greater magnitude than the co-rotating condition, with a periodic large sinusoidal deviation forming. However this deviation was very unsteady in its shedding, and did not form continuously. It was found that the circulation transfer between the vortices was linked to the magnitude of their separation, with high separation fluctuations weakening the upstream vortex and strengthening the downstream vortex. The magnitude of both the small scale, high frequency and large scale, low frequency oscillations was found to increase with distance downstream. In the case of upstream vortex impingement, the upstream vortex was found to bifurcate instead of break down, with the pressure side bifurcation rapidly dissipating. The suction side vortex was forced downwards, creating the vortex remnant identified in the experimental work. A four vortex system was created in the process by the interactions with the shear layer, exhibiting all the interaction mechanisms previously investigated. The result of these interactions was a single dominant vortex, which did not magnify its amplitudes of oscillation significantly as it travelled downstream due to the destruction of all interacting vortices.

Chapter 8

Comparison of Vortex Systems

Despite the fundamental similarity of the flowfield in terms of the presence and proximity of two vortices, significant differences were observed in both the vortex paths and the energy transfer between the two vortices. However, many of these characteristics are comparable, and as such differences between the vortex configurations can be evaluated. As scenarios in both aircraft flight and flow control where these interactions may be present in either configuration, it is important to know the differential effects between the two, and as such target the desired interaction for a given scenario. This chapter takes the previous results of the experimental and numerical work and compares the trends and flow features of the co-rotating and counter-rotating vortices.

8.1 Comparison

The separation between the two vortices at the start and end of the measurement domain can be seen as the initial and final separations respectively in Figure 8.1. In the far offset ranges the vortex separations varied linearly for both the co and counter-rotating conditions. However, in the counter-rotating condition the vortex proximities shifted further apart by approximately 0.026C as the vortex pair travelled downstream, while in the co-rotating cases they were drawn together by between 0.077C in the negative offsets and 0.043C in the positive offsets. This consequently led to the merging of the vortices as the vane offset decreased due to their same sign vorticity. In this same near field offset range, the counter-rotating vortex proximities were

actually separated further up to 0.41C due to the destruction of the initial vortex, leaving only the remnants of this vortex to propagate downstream at a location towards the root of the vane.

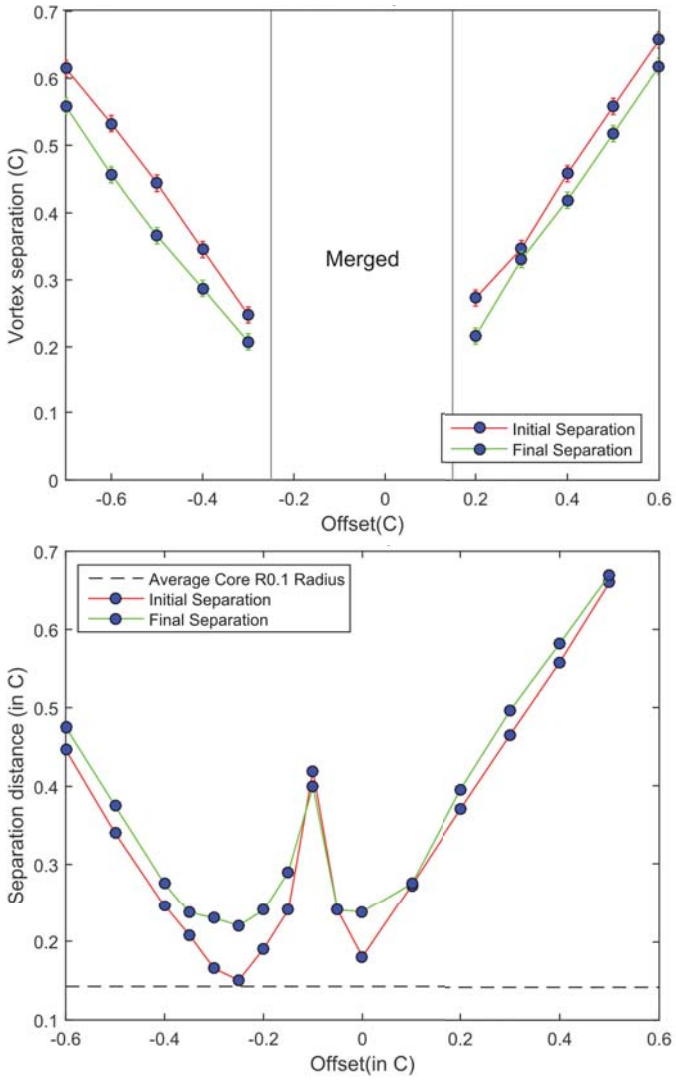

Figure 8.1: Vortex pair separations plotted against offset for all unmerged cases for co-rotating (top) and counter-rotating (bottom) experimental configurations.

While there is symmetry in the far offset separations, the centre of vortex interactions is offset depending on whether the scenario is co-rotating or counter-rotating. The merging range for the co-rotating case is -0.25C to 0.15C, while the points of closest separation for the counter-rotating case are at -0.25C and 0C. There is also a visibly clear skew of the separations to being reduced at the negative offsets in the counter-rotating condition, as evidenced by 0.25C separation at -0.4C offset as opposed to 0.37C separation at 0.2C offset.

In both cases, a critical point was present where the nature of the interaction

significantly changed. Once the vortex separation in the co-rotating case reached double the vortex radius, the vortices rapidly merged. For the counter-rotating case it was found that the vortices could be brought much closer to approximately one core radius separation before the initial separations started to diverge. The counter-rotating condition also contains 3 distinct separation regimes instead of the co-rotating's merged and unmerged state. In the far field ($B_v < -0.4C$, $B_v > 0.1C$) counter-rotating condition, the separations are near constant, in the near field ($-0.4C < B_v < -0.25C$, $0C < B_v < 0.1C$) they continue to decrease in initial separation while remaining constant in final separation, and in the very near field ($-0.25C < B_v < 0C$) they markedly increase in both initial and final separation.

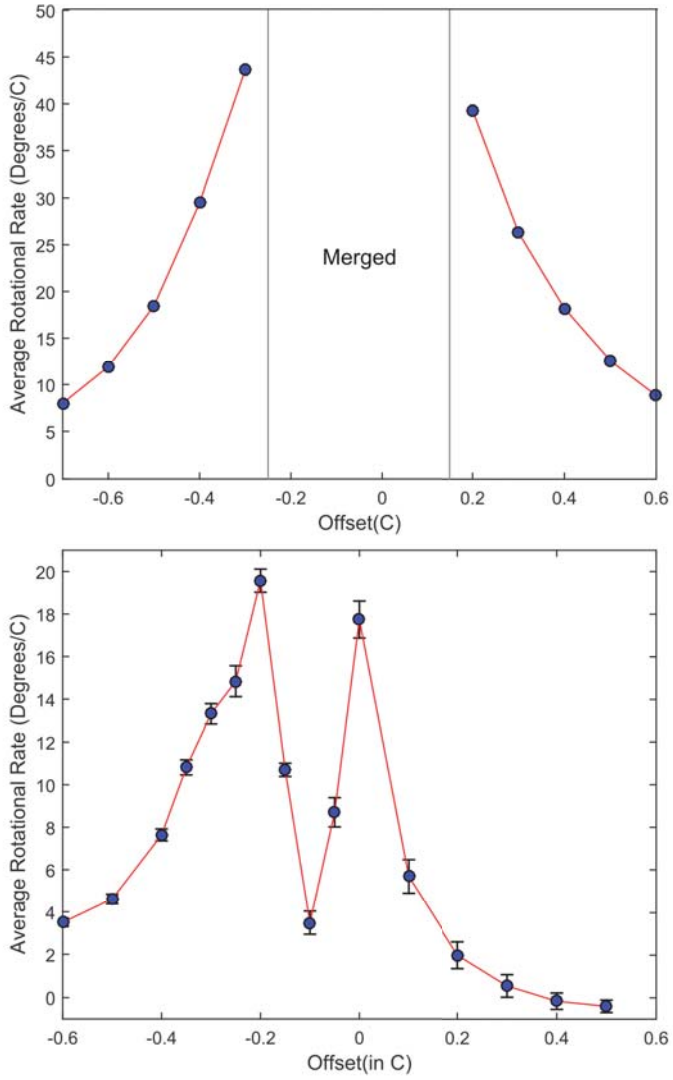

Figure 8.2: Vortex pair rotations plotted against offset for all unmerged cases for co-rotating (top) and counter-rotating (bottom) experimental configurations.

The rotation rates presented in Figure 8.2 showed similar trends in the offset skew and the strength of interaction as the proximities were reduced. For the counter-rotating case, peaks can be seen at -0.2C and 0C, while for the co-rotating cases the rotational rate increased until the point of vortex merging. Both cases showed a non-linear trend in rotational rate as separations were reduced. The co-rotating condition had a substantially higher rotational rate than the counter-rotating case, with peaks over twice as high. This is due to the co-rotating condition's vortices orbiting around a central point between the vortices whereas the counter-rotating condition's orbital centre was located to the outside of the two vortices.

Inspecting the circulation trends of the two conditions shows significant differences in the total energy available and the rates of energy dissipation. The counter-rotating circulations seen in Figure 8.3 show that as the offset increases between the vanes at the far edges of the range investigated the circulation between the two vortices becomes more equal. As they are drawn closer from -0.6C to -0.4C, the circulation of the upstream vortex is decreased by 4.7% with a corresponding increase in the circulation of the downstream vortex of 8.6%. This shows an energy transfer from the upstream vortex to the downstream vortex. The transfer of energy in these far offset cases happens during the initial stages of vortex formation, as negligible circulation decrease is noted after this point. As the offsets are brought within the previously identified near-field range, there is a transition from relatively little circulation loss through the domain to a downwards trends in the circulation, with the -0.4C offset having a loss of 5.6% in the downstream vortex and the -0.35C having a 17.9% equivalent loss. As the offset is further decreased, the initial circulation destruction in the upstream vortex increases, with the strength being reduced from $0.147 m^2 s^{-1}$ at x/C = 11.5 in the -0.6C case to $0.0439 m^2 s^{-1}$ in the -0.15C case. As such, the counter-rotating condition decreases in the duration of its strength as the offset decreases and the vortices interact. It should be noted that using the time averaged results smears the vorticity field resulting from the highly meandering upstream vortex in these low energy scenarios. This shows the vortex as completely disappearing in the time averaged case, whereas weak coherent vortex structures were observed in the instantaneous results. This is represented by the circulation from x/C = 15 to x/C = 16.5 in the very near field circulation results.

The co-rotating results showed that there was less total circulation present in

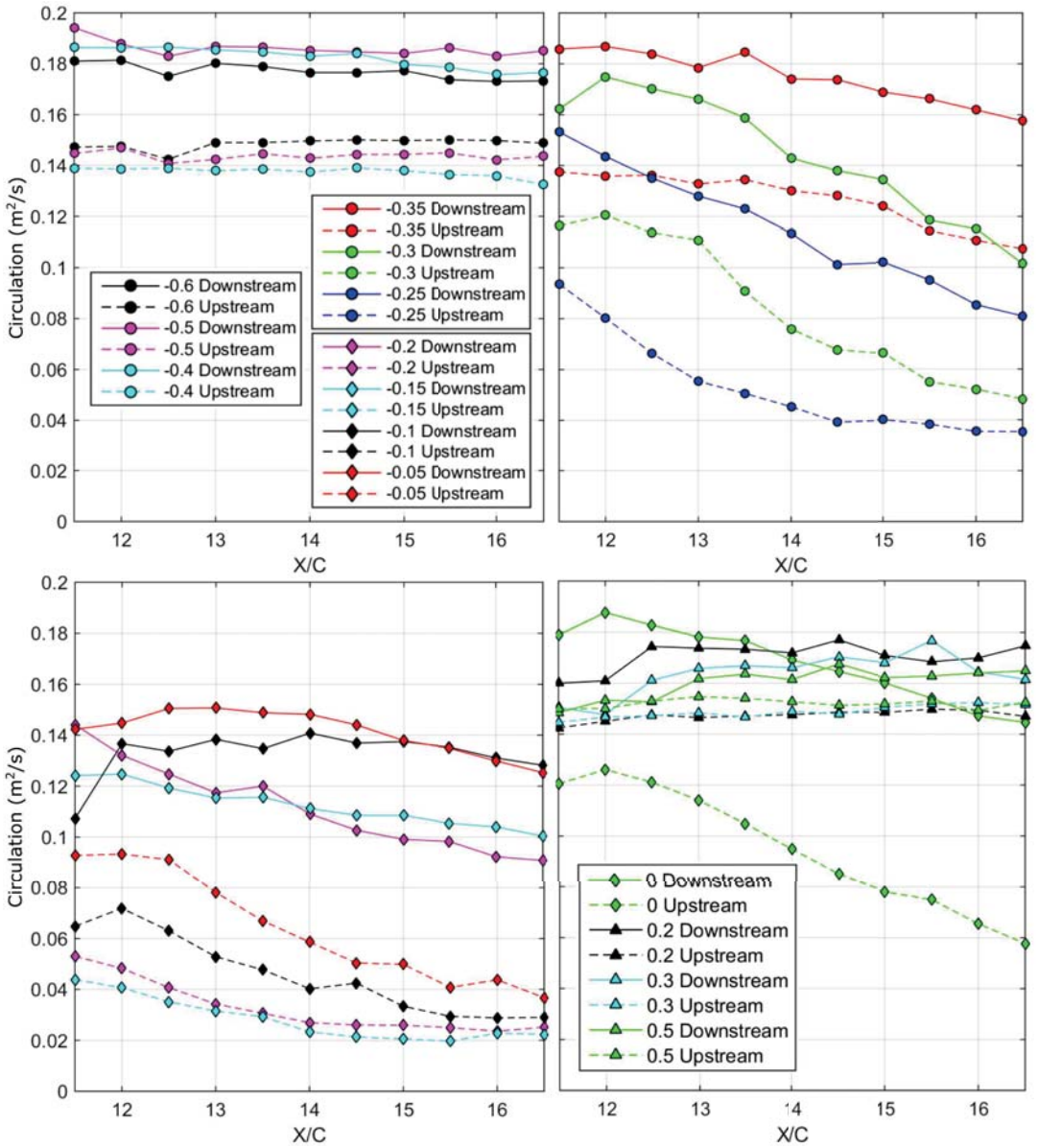

Figure 8.3: Experimental circulation values for various counter-rotating vortex cases.

all far offset cases than the counter-rotating condition, with approximately 26% less total circulation from -0.6C offset to -0.4C offset, as can be seen in Figure 8.4. In contrast to the counter-rotating case where the downstream vortex is dominant, the upstream vortex is the dominant vortex. This is due to the presence of the upstream vortex reducing the strength of the downstream vortex in its production, instead of enhancing it with a counter-rotating field. Some of this strength reduction is due to the local change in angle of attack of the vane due to the presence of the upstream vortex. This was found to change the local angle of attack by up to 3 degrees, modifying the total circulation

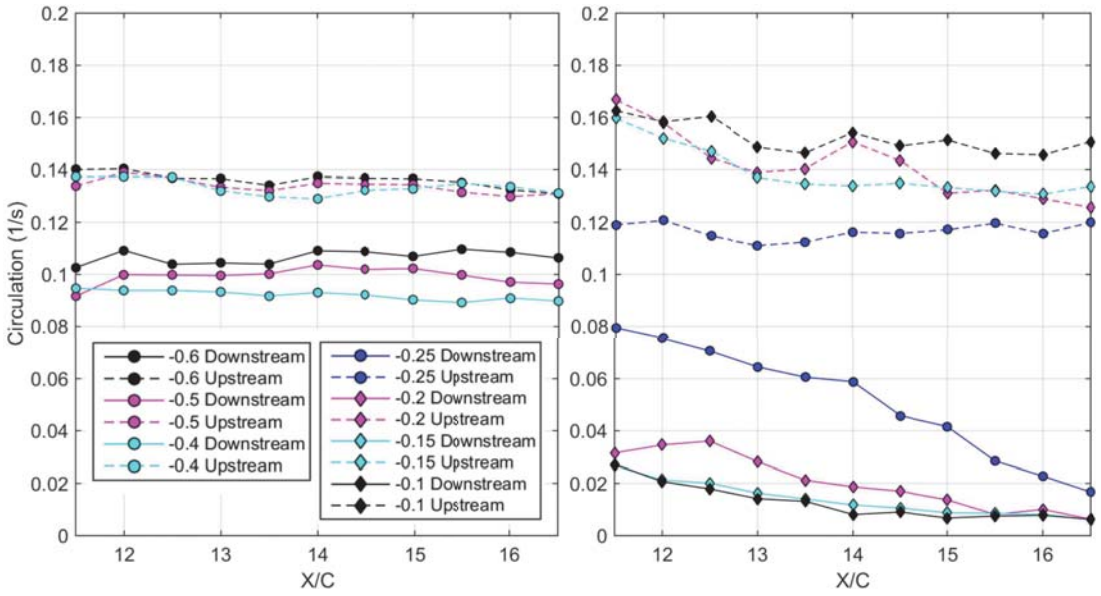

Figure 8.4: Experimental circulation values for various co-rotating vortex cases.

produced by the rear vane. However this does not affect the resultant energy dissipation and transfer rates further downstream, only the starting energies.

As the total offset decreases from -0.6C to -0.4C the strength of the downstream vortex decreases from an average of $0.108 m^2 s^{-1}$ to $0.093 m^2 s^{-1}$, with negligible strength observed in the upstream vortex. The strength of the upstream vortex in the far offset cases is very similar between both the co-rotating and counter-rotating cases, with an average value of approximately $0.14 m^2 s^{-1}$. This demonstrates how significant the vortex direction is on the production strength of the downstream vortex from the rearward vane, with substantial enhancement seen in the counter-rotating case and a loss of circulation in the co-rotating condition. From this it can be seen that the counter-rotating condition will produce a higher circulation initial vortex system than the co-rotating condition. As the offset is further reduced and the merged state is approached there is circulation transfer from the downstream vortex to the upstream vortex. This results in the circulation of the upstream vortex rising to a level up to 16% above that attained by the counter-rotating upstream vortex, at the cost of the strength of the downstream vortex. As the offsets are moved closer together the vortices became merged from the start of the domain, resulting in the highest upstream vortex circulation in the -0.1C offset case.

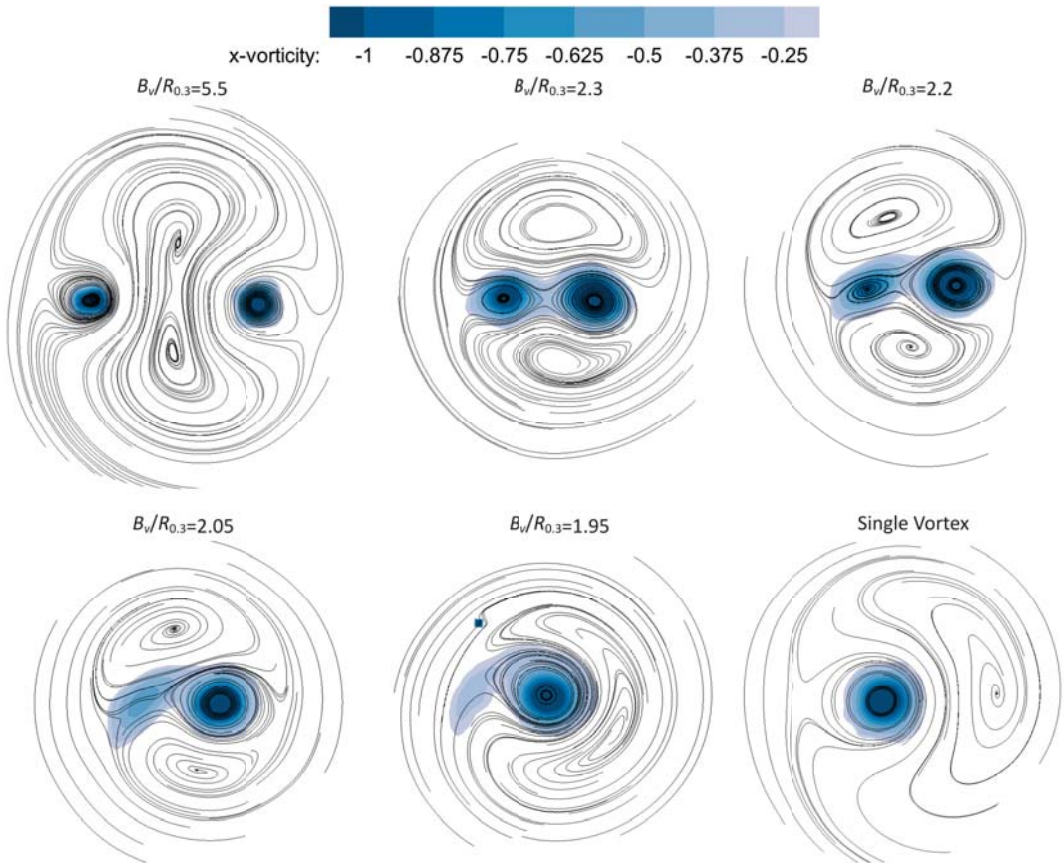

Figure 8.5: Pathlines in the co-rotating reference frame and vorticity for different stages of vortex merger, taken from experimental results.

The differences between the mechanisms of the vortex interactions can be seen clearly by plotting the two dimensional pathlines over contours of vorticity. As identified earlier in this chapter, in the co-rotating condition the vortices rotate at a far more rapid rate, with the slowest rotating case being faster than all but five of the counter-rotating cases, and peak rotational rate differences of 2.31 times. In order to observe the merging mechanisms responsible for the merger, it was necessary to translate the velocity into the co-rotating reference frame. As the mechanism was noted as being the same regardless of offset, the data from multiple offsets could be combined to show the different stages of vortex merger, as can be seen in Figure 8.5. This showed that as the vortices approached a separation of two core radii, a significant asymmetry in the flow fields formed, followed by a rapid transmission of vorticity from the weaker vortex to the stronger vortex without a large change in vortex separation. This was accompanied by a movement of the ghost vortex regions (the outer recirculation regions with little vorticity) from one side of the primary vortex to the other, before they merged together and normalised.

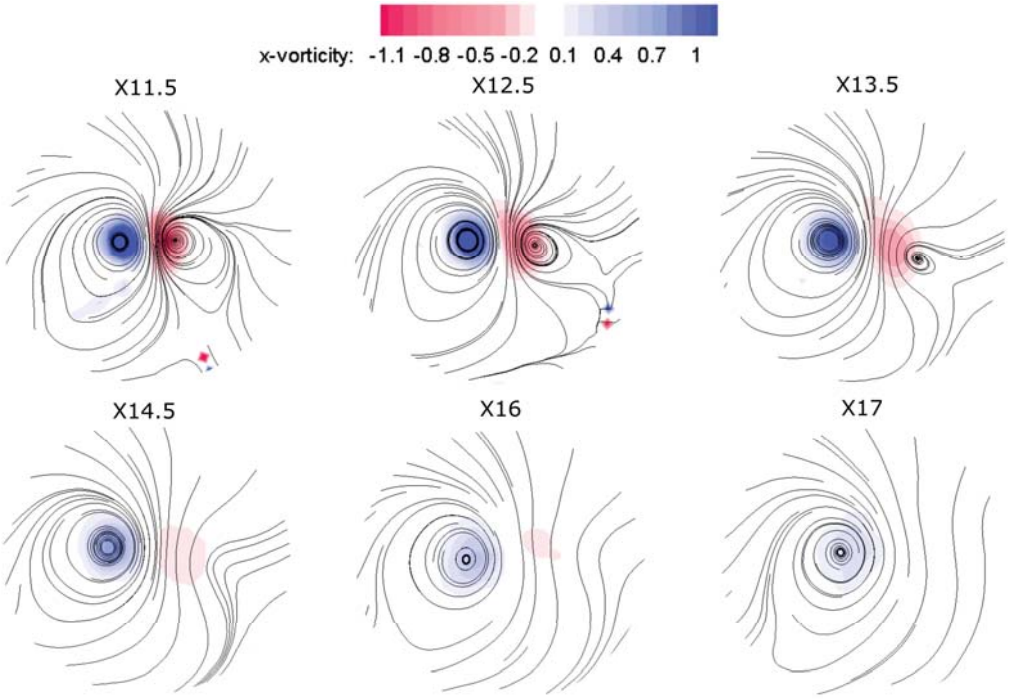

Figure 8.6: Pathlines in the stationary reference frame and vorticity for different stages of vortex merger in counter-rotating -0.3C offset condition, taken from experimental results. Vortex locations are reframed to be consistent in alignment.

While the co-rotating condition could be extrapolated across the cases into a consistent merging process, the mechanism behind the counter rotating interaction was far more variable, resulting in substantial differences depending on offset. At very near field offsets the mechanism for destruction appeared to be from direct impact on the front of the vane causing and vorticity interaction and vortex breakdown, leaving only remnants of the initial vortex and a weak downstream vortex. For larger offsets in the near field and far field, this shifted to the vortices inducing instabilities in each other, causing the long term loss in circulation. As can be seen in Figure 8.6 the -0.3C case started with the vortices spaced at a very close proximity before drifting apart by x/C = 12.5. The upstream vortex then undergoes a rapid reduction in vorticity, with its limit streamline completely destroyed by x/C = 14.5. Following this the downstream vortex proceeded to dissipate. The process can be broken up into four main pathline states. Initially, the limit cycle of the pathlines for both vortices is at a similar radius. This then separates as the vorticity of the upstream vortex reduces in magnitude, with the stronger vortex retaining similar streamlines but the weaker moving away and decreasing in size. The limit cycle is then broken down into kinked pathlines, as observed at x/C = 14.5. These pathlines are

straightened out, leaving just the remains of the stronger vortex. In other near field offset cases the process remained similar, however the rate of the process increased, with the -0.25C offset case having moved to the 4th stage by x/C = 14.5, leaving a reduction in stage length of 2.5C for an offset change of only 0.5C. In the very near field the second vortex was nearly indistinguishable in the time averaged results, with the 4th stage present from x/C = 11.5.

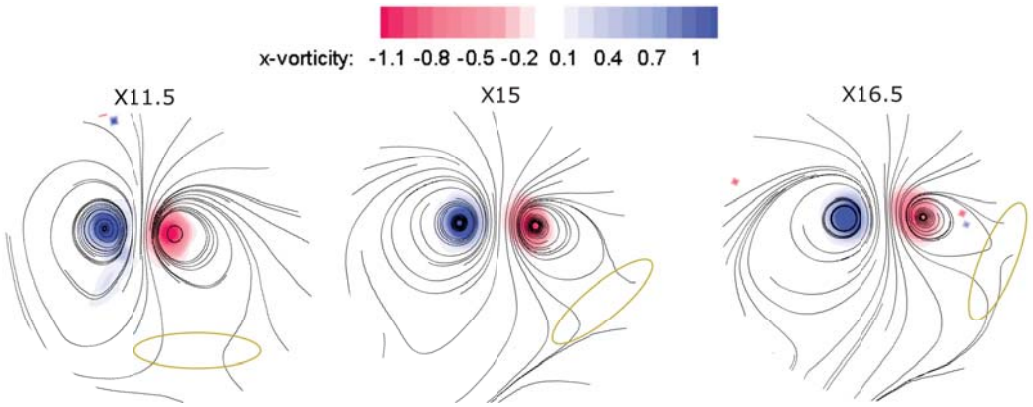

Figure 8.7: Pathlines in the stationary reference frame and vorticity for different stages of vortex merger in counter-rotating -0.4C offset condition, taken from experimental results. The base of the limit cycle of the weaker vortex highlighted by the orange ovals. Vortex locations are reframed to be consistent in alignment.

At far offsets the destruction of the vorticity and reduction of circulation was far less pronounced, however the shifting of the streamlines was still significant, as seen in Figure 8.7. This shifting of streamlines from a downwards position to a more uniform vortex shape indicates that this structure may be a consequence of the formation of the downstream vortex by the vane, even though the structure is observed in the upstream vortex. From the figure, the movement of the streamlines both around and towards the vortex can clearly be seen, as highlighted by the orange ovals in the figure. It is anticipated that if the vortex spacing is sufficiently large that the strength of the vortices does not dissipate, with a long enough distance downstream this will normalise to form a more uniform and symmetric vortex structure.

Both the co-rotating and counter-rotating scenarios produced instabilities in the vortices, traceable by analysing the instantaneous positions of the vortex cores from the image pairs as previously discussed in Chapter 6. The instability observed in the counter-rotating case was typically dominant in the weaker vortex at nearer offsets, with a 45 degree angle observed between the weaker vortex instability and the vortex centreline. This indicated the presence of an

uneven crow instability. In the co-rotating condition the instabilities were of lower magnitude and shallower angle closer to 30 degrees in the weaker vortex. The magnitude of oscillation of the weaker vortex did not substantially increase as vortex proximity reduced until the point of merging, unlike the counter-rotating condition. This instability shared some similarities such as deviation angle with that of equal co-rotating vortices identified by Miller et al. [119].

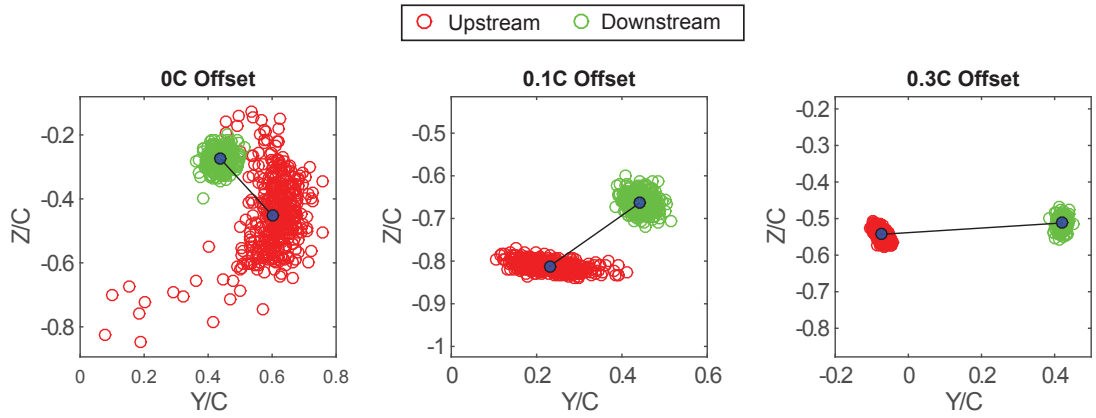

Figure 8.8: Core locations of upstream (red) and downstream (green) counter-rotating vortices for 0C, 0.1C and 0.3C offset cases at x/C = 16.5.

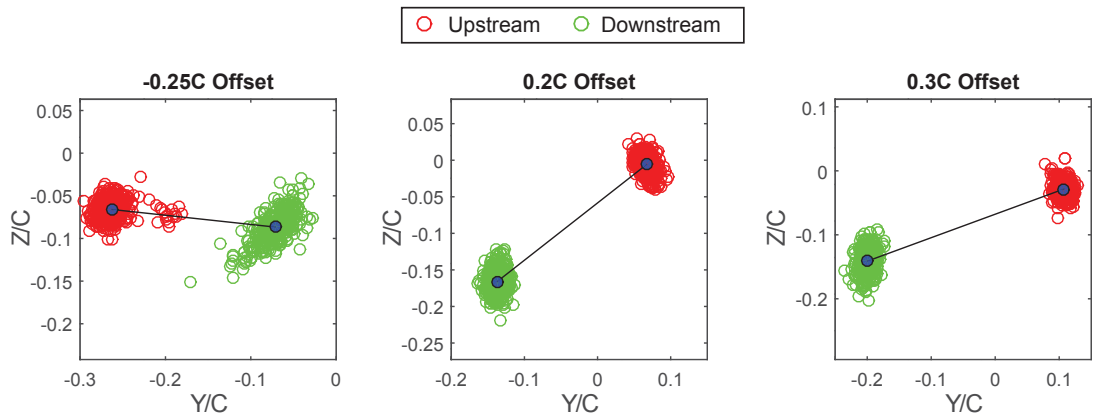

Figure 8.9: Core locations of upstream (red) and downstream (green) co-rotating vortices for -0.25C and 0.2C offset cases at x/C = 14 and 0.3C offset at x/C = 16.5.

The increased meandering of the counter rotating cases was quantitatively assessed against the co-rotating case in the previous chapter, however by inspecting instantaneous isosurfaces of pressure the magnitude difference becomes visually clear, seen in Figure 8.10. The instabilities in the counter-rotating case are far more pronounced than that of the co-rotating case, with both a clear gentle sinusoidal oscillation and occasional large deviations

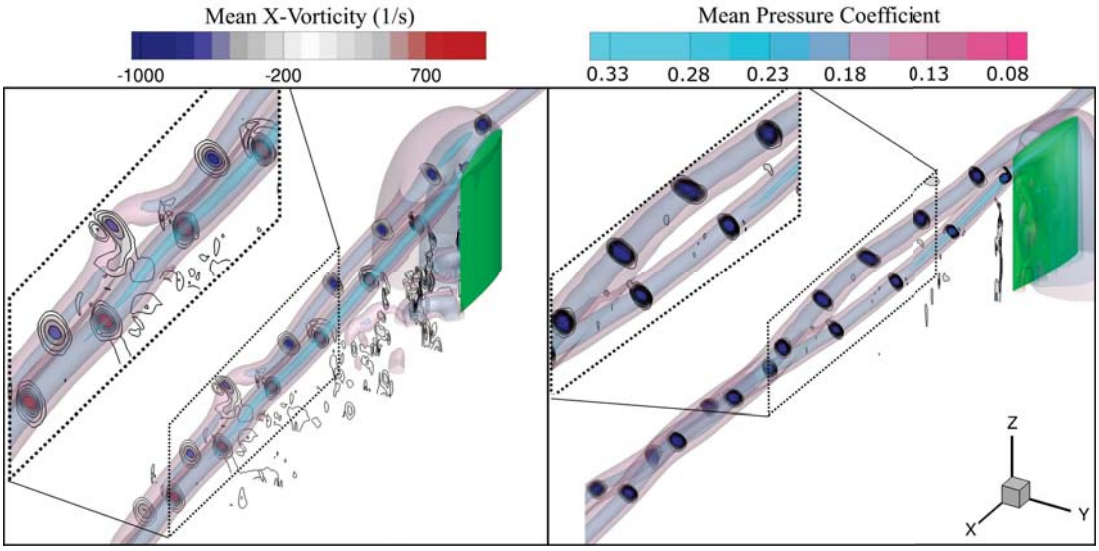

Figure 8.10: Contours of x-vorticity, with isosurfaces of pressure at $C_p = -0.4$, $C_p = -0.16$ and $C_p = -0.08$ for counter-rotating (left) and co-rotating (right) at 0.2C offset.

present. In the co-rotating case a more subtle deviation in core location and size can be seen, with larger waviness observed in the far wake. The subtlety of these deviations demonstrates why the quantitative analysis of the previously chapter was essential for monitoring and comparing the vortex fluctuations. The difference in vortex shedding magnitude off the rear vane driven by the presence of the upstream vortex can also be clearly seen in the wake region of the downstream vane, with significantly more shedding in the counter-rotating condition. This is from a combination of the additional low pressure induced by the upstream vortex on the suction side of the wing, as well as the effective upwash from the vortex over the central portion of the span.

The planar integrals of pressure, vorticity and in-plane kinetic energy can be seen in Figure 8.11. Two pressure traces are presented, one with the integral restricted to a vortex core of at least 5pa drop from the static pressure, and the other with the integral restricted to 2pa static pressure drop. By using these static pressure thresholds it can be ensured that only the core is captured and not any slight wake effects propagating downstream. While these wake regions may only have small pressure drops, they can occur over larger areas, and hence significantly skew the integrals. At the higher intensity 5pa cut-off it can be seen that the counter-rotating 0.2C offset produces the most significant initial pressure field, however suffers the highest dissipation rate of any case. A substantial portion of this dissipation is the increasing scale of the downstream instabilities causing smearing

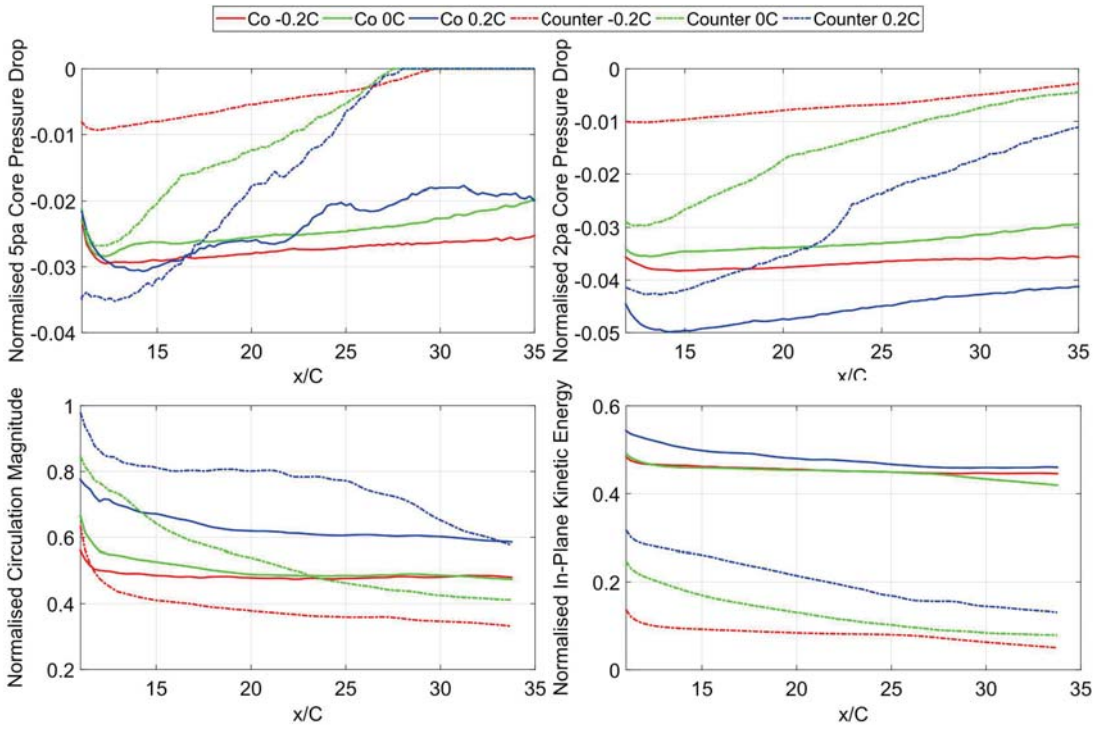

Figure 8.11: LES traces of pressure drop at 5pa core cut-off (top left), 2pa core cut-off (top right), total circulation (bottom left) and in-plane kinetic energy (bottom right).

of the high intensity pressure field when time averaged. The direct impingement counter-rotating -0.2C offset produces the least intense pressure drop behind the rear vane of all the cases, however it also has the lowest pressure dissipation due to the lack of a secondary interacting vortex and consequently reduced instabilities. The dissipation rate at the lower 2pa pressure cut-off is very similar to that of the co-rotating cases in total magnitude. In comparison to the counter-rotating cases the co-rotating condition has very limited dissipation of pressure, kinetic energy and circulation, with only 10.8% the pressure dissipation for the equivalent 0C offset condition. All co rotating cases follow much closer dissipation rates for pressure, however at the higher level cut-off a waviness in pressure is observed due to the fluctuation of pressure intensities during the merging and relaxation process of the vortices, as discussed in the previous chapter.

The trend of higher initial energies with faster dissipation rates for the counter-rotating condition is again displayed in the circulation values. Both the 0C and 0.2C counter-rotating cases display circulation values above any of the co-rotating cases, however these rapidly dissipate, with the 0C offset falling below the 0.2C co-rotating case at x/C = 14 and below the 0C co-rotating case at X/C = 24.

The initial destruction present in the direct impingement counter-rotating case results in it having the lowest circulation and kinetic energy values of any of the vortex arrangements. The kinetic energy values for the counter-rotating cases are all considerably lower than the co-rotating cases due to the cancellation of downwash by the opposite angled downstream vane. However dissipation rates further downstream can be related to the results of the vortex interactions, with the counter-rotating cases again showing the highest dissipation rates. Again, the increased instabilities in the 0.2C offset condition cause the highest dissipation rates of any case. In both conditions, having the vanes spaced at impact or near-impact offsets causes a reduction in all measurable vortex parameters in comparison to allowing the vortices to interact off-body.

8.2 Conclusion

While the flow fields are very similar conceptually, many pronounced differences were observed in both the formation of the downstream vortex and the mechanisms observed in the evolution of the system. While both systems underwent rotation, the counter-rotating system was driven by a differential in strength between the vortices, and the co-rotating system rotated due to shear at the periphery of the same signed vorticity. This resulted in the co-rotating pair having a much higher rotational rate due to the centre of rotation being inside the vortex pair, as opposed to being outside in the counter case.

The separations between the co-rotating pair followed a consistent trend of moving together regardless of offset, while the counter-rotating pair moved further apart, with a substantial increase in motion in the near field range to an equilibrium distance of approximately 0.23C. The direction of the vortex interaction considerably affected the strength of downstream vortex production, with counter-rotating configurations enhancing downstream vortex strength by 30% and co-rotating conditions reducing it by 28%. The co-rotating vortex merger showed similar levels of energy transfer in all cases, while the counter-rotating condition saw vortex dissipation rates substantially increase as the offset was reduced. It was found that the mechanism responsible for energy transfer remained the same, regardless of vortex offset in the co-rotating condition, with only the distance to merger changing. In the counter-rotating condition the mechanism was found to vary significantly between the far, near

and very near field, with the resulting instabilities increasing as the vortices were shifted closer together.

As such, these results indicate that where a short duration, high circulation vortex system is required a counter-rotating upstream/downstream configuration would be best, while a co-rotating configuration will be superior for cases requiring a vortex system that is more stable in the long term.

Chapter 9

Conclusions and Future Work

9.1 Conclusions

An investigation of the interactions of a pair of streamwise vortices at various offsets was performed, inspecting both time averaged and instantaneous conditions. Two NACA 0012 vanes were used for the purposes of vortex generation, separated in the streamwise direction, with lateral offset of the rear vane used to vary the relative vortex positioning. Initial testing was performed using water tunnel dye visualisation and RANS modelling to determine the baseline flow characteristics, with wind tunnel experimentation used to cover a wide sweep of cases and LES for a select number of cases.

Initial flowfield visualisations showed substantial oscillations in vortex position and separation, as well as a transience in vortex merger for co-rotating cases. This indicated an instantaneous and transient analysis would be required for later studies. It was also found that over a sweep of Reynolds number that the variance in the fundamental characteristics of the interactions was minimal. The RANS studies found very significant variances in the flow structures, energy levels and dissipation rates for the counter-rotating cases. However, in the co-rotating cases similar flow structures and energy trends were found between the offsets.

Further evaluation of the quantative values of the vortices at multiple offsets was performed through the use of a cross-flow, two dimensional planar PIV setup employed within a wind tunnel. Reducing the offset of the

counter-rotating vortices increased the rotation of the resultant pair until the vortex separation was reduced below 0.1C, at which point rapid vortex destruction and a reduction of orbital rate ensued, with the upstream vortex remnants being forced towards the root of the downstream vane. Passing the upstream vortex just over one core radius offset from the downstream vane caused the strongest vortex interactions, with the highest rotational rates. Closer vortex proximities were found to increase the magnitudes of the vortex meandering, with the meandering being proportional to the strength of the interaction and subsequently dissipating with upstream vortex destruction. A 45 degree, unequal instability was noted in the vortex cores, with the weaker upstream vortex showing a higher deviation. Circulation levels were also found to fluctuate proportionally with position fluctuations. These evaluations showed that the counter-rotating cases had a high sensitivity to offset, demonstrating that real world scenarios such as yaw and crosswind may cause issues for vortex systems reliant on counter-rotating vortex pairs.

All co-rotating cases were observed to follow a pattern of steady helical motion, ultimately resulting in merger at near offsets. This merger was found to be biased to the vortex passing on the pressure side of the vane. When the vortex separation dropped below 2.3 core radii, significant asymmetry formed in the vortex structure, followed by rapid merger once the vortices were two core radii apart. The length travelled downstream prior to vortex merger was highly sensitive to offset, with a strongly nonlinear trend. At a given location, the merger was found to be transient, resulting in a statistical merging location resulting from vortex meandering. The vortices were found to move towards each other at all offsets, with a faster motion when the upstream vortex was passed on the suction side of the downstream vane. The direction of movement of the vortices towards each other was found to be opposite from the counter-rotating cases, which drifted apart. The rotational rate of the co-rotating cases was found to be considerably higher than that of the equivalent counter-rotating condition, resulting from enhanced periphery shear. The presence of the upstream vortex weakened the downstream vortex in all cases, resulting in the downstream vortex merging with the upstream vortex. The merging process resulted in a total circulation loss, however the two merged vortices maintained higher circulation than a single vortex from one vane, hence re-energisation of the initial vortex was successfully achieved. Due to the insensitivity of the final result of the merging process to offset, a vortex-energisation system could be successfully implemented in real world

scenarios with minimal regard for conditions such as yaw and crosswind.

Large Eddy Simulations with a Wall Adapting Local Eddy Viscosity subgrid model were then performed on a select number of cases from the experimental testing, allowing deeper analysis of the transient flow features and better visualisation. This modelling strategy was evaluated against the experimental results, showing good correlation on both qualitative and quantitative properties.

The LES found that the tendency of the downstream vortex to merge into the upstream vortex at near offsets in the co-rotating condition was due to the suppression of one of the two downstream vane tip vortices, resulting in a weaker total downstream vortex. If the upstream vortex impinged on the downstream vane it weakened the strength of the vortex, resulting in a reversal of this merging order. This was not observed in the experiment as it occurred more rapidly than the experimental measurement domain could capture. An unstable free wake vortex bifurcation was observed in the remnants of the upstream vortex, resulting from significant straining and elongation from impact on the vane body. The LES confirmed the meandering of the vortices was responsible for the statistical merging phenomenon, with merging occurring once the vortex meander caused the separation between the vortices to reach the critical spacing for asymmetric merger.

The instabilities in the near offset counter-rotating condition were found to be higher in magnitude, with less even periodicity. The circulation transfer between the vortices was linked to the magnitude of their separation, with fluctuations in position and circulation seen to increase with distance travelled downstream. When the upstream vortex impinged upon the downstream vane it was found to bifurcate instead of break down. The result of this bifurcation was a four vortex system off the rear of the vane, with rapid dissipation of all upstream vortex remnants resulting. Consequently, interaction between the remnants of the upstream vortex and the newly formed downstream vortex were minimal, and the growth of instabilities in the downstream vortex was consequently limited. In all cases it was found the dissipation rates of circulation, kinetic energy and pressure drop were higher for counter-rotating cases than co-rotating, with the non-impingement counter-rotating condition demonstrating the strongest initial metrics of all cases.

It was found that a counter-rotating vane could be used to successfully destroy

an upstream vortex rapidly, however such a configuration is highly sensitive to offset. If a short duration, high circulation vortex system with rapid vortex breakdown is required, a near impingement counter rotating case would be ideal, with high instabilities and interactions rapidly weakening the vortex pair with distance travelled downstream. If consistent vortex system behaviour is required in varying conditions and a counter-rotating vortex system is necessary, it is recommended that the vortex offset be kept as high as feasible. In a situation where a stable, long duration vortex system is required, a co-rotating multiple vane setup can be utilised. This would be superior for cases requiring a vortex system to be insensitive to yaw, displacement variance and crosswind, as the similarity in outcomes of the merging mechanism mean a similar vortex for these conditions. The results presented indicate that there is no limit to the number of times such a vortex could be re-energised within a flow with no adverse pressure gradient.

9.2 Future Work

A number of areas have been identified for further investigation regarding these interacting vortex systems.

The effects of the vortex interactions at a number of angles of attack on the vanes would be of interest for future study. For example, increasing the angle of attack on the front vane to the point where vortex breakdown would occur naturally at the location of the rear vane would allow the effects of the rear vane on the breakdown location to be observed. Specifically, this would answer the question of if a series of co-rotating vanes could suppress vortex breakdown, rather than just adding energy and circulation to the vortex.

Testing of different angles on the front and rear vanes would allow a more comprehensive evaluation of different interaction types. This could be used to evaluate what minimum angle, and consequently minimum drag penalty, on the rear vane is required to ensure fastest vortex dissipation in the counter-rotating case, and how the mechanism varies with said angle change.

Modification of the tip geometry would allow the investigation of the dependency of the near field merging mechanism on relative tip vortex strength, and if the single vortex suppression effect observed in the present work for the co-rotating

condition would extend to various tip geometries.

A more practical implementation of this vortex interaction knowledge would also be of great interest. Creating an adverse pressure scenario such as that experienced on an aircraft wing or automotive diffuser would allow the effects of these vortex systems on aerodynamic performance. By using multiple, smaller generators in a streamwise line and comparing to a singular, larger generator, the relative performance trade-offs of each could be ascertained, and recommendations made for real world scenarios.

Appendix A

Additional Experimental Rig Material

This appendix presents additional images of the experimental rig components.

Figure A.1: Detail of mounting rail, with plate mounting holes shown.

Figure A.2: Mounting rail, with camera mounting in background.

Figure A.3: Mounting rail, with camera mounting in background.

Figure A.4: Detail of rear vane filler plates.

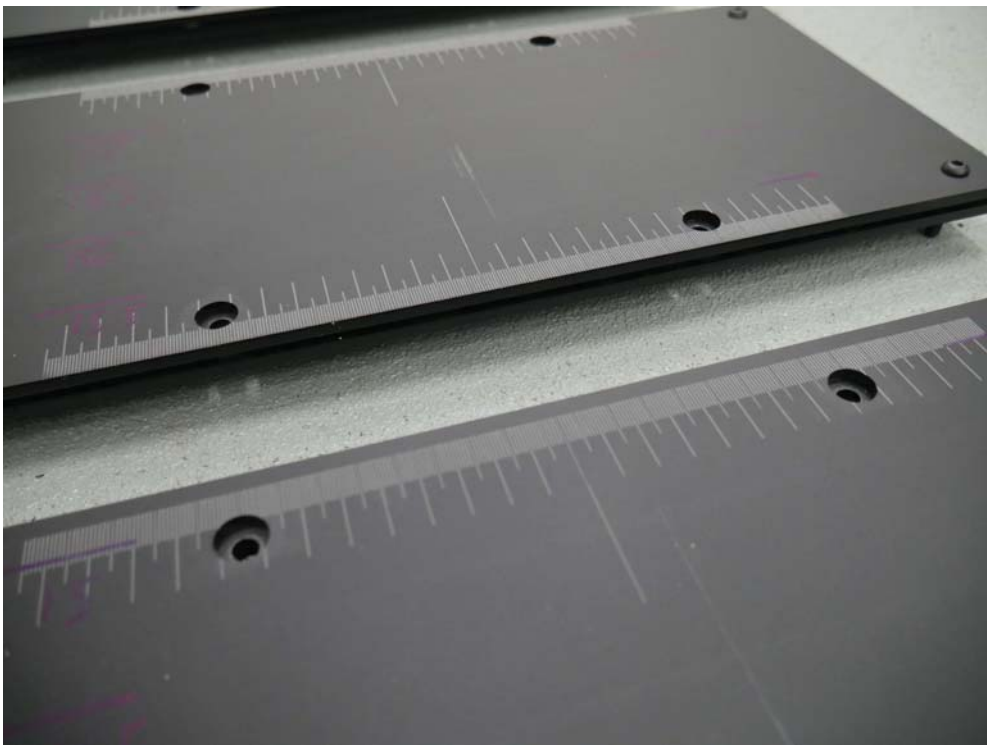

Figure A.5: Laser etched ruler inscription on plates.

Figure A.6: Plate slot system.

Figure A.7: Plates in tunnel.

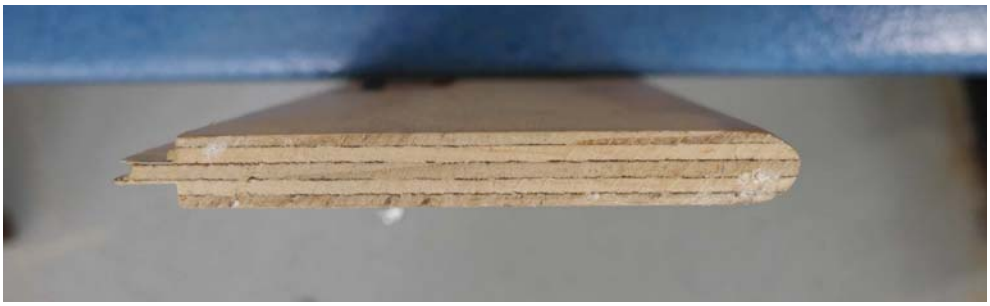

Figure A.8: Splitter leading edge.

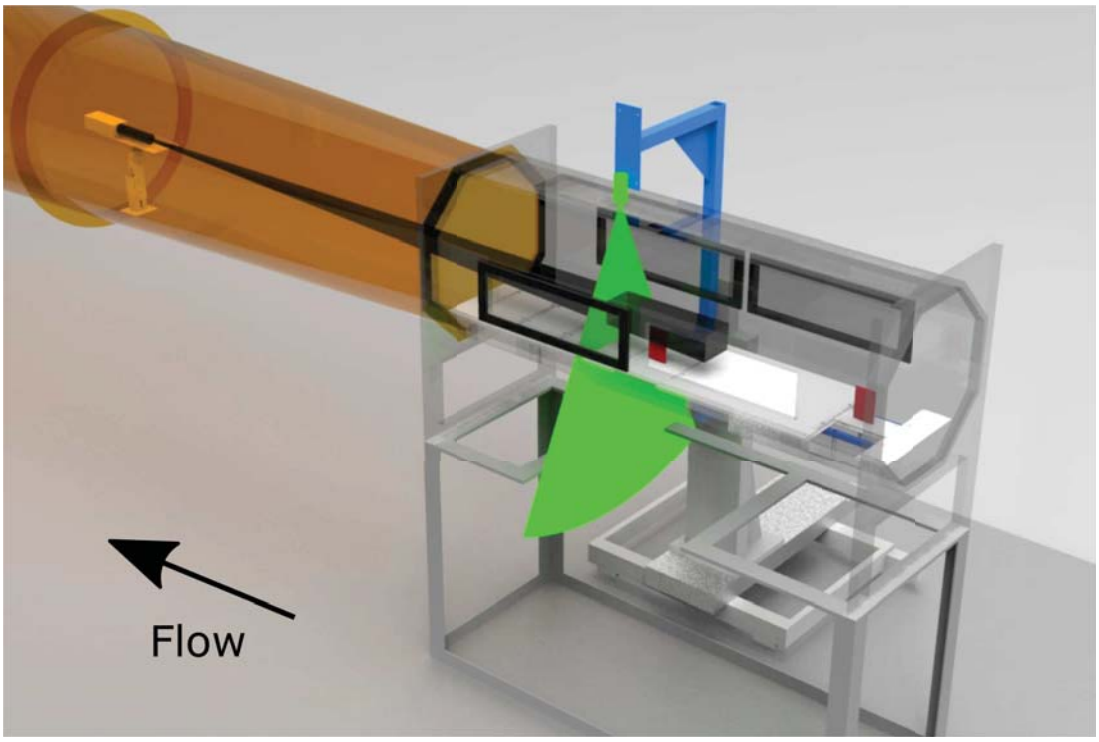

Figure A.9: Overall rig layout.

Figure A.10: Rapid prototyped Cobra probe holder (left) fitted to streamline tube in tunnel (right).

Figure A.11: Pitot tube arrangement for characterisation of tunnel flow, with traverse up (left) and midway through tunnel (right).

Appendix B

Published Papers

Interactions of a co-rotating vortex pair at multiple offsets

Kyle J. Forster, Tracie J. Barber, Sammy Diasinos, and Graham Doig

Citation: Physics of Fluids **29**, 057102 (2017); doi: 10.1063/1.4982217
View online: http://dx.doi.org/10.1063/1.4982217
View Table of Contents: http://aip.scitation.org/toc/phf/29/5
Published by the American Institute of Physics

Interactions of a co-rotating vortex pair at multiple offsets

Kyle J. Forster,[1] Tracie J. Barber,[1] Sammy Diasinos,[2] and Graham Doig[1,3]
[1]*School of Mechanical and Manufacturing Engineering, University of New South Wales, Kensington, NSW 2052, Australia*
[2]*Department of Engineering, Macquarie University, North Ryde, NSW 2109, Australia*
[3]*Aerospace Engineering Department, California Polytechnic State University, San Luis Obispo, California 93407, USA*

(Received 16 November 2016; accepted 12 April 2017; published online 4 May 2017)

Two NACA0012 vanes at various lateral offsets were investigated by wind tunnel testing to observe the interactions between the streamwise vortices. The vanes were separated by nine chord lengths in the streamwise direction to allow the upstream vortex to impact on the downstream geometry. These vanes were evaluated at an angle of incidence of 8° and a Reynolds number of 7×10^4 using particle image velocimetry. A helical motion of the vortices was observed, with rotational rate increasing as the offset was reduced to the point of vortex merging. Downstream meandering of the weaker vortex was found to increase in magnitude near the point of vortex merging. The merging process occurred more rapidly when the upstream vortex was passed on the pressure side of the vane, with the downstream vortex being produced with less circulation and consequently merging into the upstream vortex. The merging distance was found to be statistical rather than deterministic quantity, indicating that the meandering of the vortices affected their separations and energies. This resulted in a fluctuation of the merging location. A loss of circulation associated with the merging process was identified, with the process of achieving vortex circularity causing vorticity diffusion, however all merged cases maintained higher circulation than a single vortex condition. The presence of the upstream vortex was found to reduce the strength of the downstream vortex in all offsets evaluated. *Published by AIP Publishing.* [http://dx.doi.org/10.1063/1.4982217]

NOMENCLATURE

$R_{0.1}$	Average radius of vortex at 0.1 vorticity threshold
$R_{0.3}$	Average radius of vortex at 0.3 vorticity threshold
$A_{0.1}$	Area of vortex at 0.1 vorticity threshold
$A_{0.3}$	Area of vortex at 0.3 vorticity threshold
Γ	Circulation
X_c	X core location
Y_c	Y core location
C	Chord length
R_e	Reynolds number, based off chord length
B_v	Vortex separation.

I. INTRODUCTION

Turbomachinery blade interactions, aircraft taking off in succession, wind turbines, and vortex generators can all produce vortex interactions with multiple streamwise vortices in close proximity to each other.[9,12,16,20,26] These vortices may be desirable (flow control, heat transfer) or undesirable (aircraft wake vortices). In previous work, both vortices of a vortex pair have been typically deployed from the same streamwise location,[5,22] limiting the study of their interactions at extremely close core spacings. These close interactions are important conditions to understand in order to provide a knowledge base for practical vortex applications, where upstream vortices may move in locations on either side of a vortex producing obstacle, such as a wing or vane.

As identified previously,[6,19,21,25] a pair of co-rotating vortices will merge in any viscous flow. The equilibrium states of interacting and merging vortices were first studied by Saffman and Szeto[25] using energy based equations numerically approximated with Newton's method, finding that the vortices will merge in an equilibrium state at a vortex separation to a radius ratio of 3.16. This was found to be different from that of an unsteady state, which was predicted at a ratio of 3.4 by Zabusky *et al.*[30] using contour dynamics, and a ratio of 3.4-3.8 by Rossow[24] using point vortex methods. All of these evaluations used equal strength and size vortex cores, with two dimensional flow fields and no velocity deficit through the core, limiting their accuracy and resulting in the discrepancies between the methods. It is currently accepted that merging is due to the viscous diffusion causing vorticity to expand from the inner recirculation region to the outer recirculation region.[14] The ghost vortex of the outer recirculation region then stretches the vorticity between the two cores, resulting in the production of a singular vortex core.

Merging of equal strength co-rotating vortices can be broken up into four distinct stages, the first diffusive stage, the convective stage, the second diffusive stage, and the merged diffusive stage.[3,17,18] The first diffusive stage consists of the two vortex cores increasing in size through viscous diffusion and has no change in core separation distance. The convective stage occurs once the two vortices reach a critical size, and the vortices begin to move towards each other at a rapid rate. During this stage, the advection of vorticity away from the cores forces the cores together due to the conservation of angular momentum, causing their merging. The second diffusive stage then involves the diffusion of the two vortex azimuthal velocity

peaks to form a singular vortex. In the merged diffusive stage, the combined vortices become more axisymmetric; however, now they have the same core location.

Devenport[5] found by wind tunnel testing of co-rotating vortices deployed from the same upstream location that the unmerged cores of a co-rotating pair were far more turbulent before merging than a single vortex core by itself. Once the two cores have merged, the final structure was found to be larger and more axisymmetric than a single vane vortex. The hot wire measurements showed that post merging, the turbulence of the core was found to decrease; however, the induction of a probe into the core would have increased the sensitivity of the vortices to instabilities. As the spacing between vortices increases, the merging distance is shifted further downstream.[5,22] Increasing vortex swirl decreases merging distance and also increases the amplitudes of vortex motion (meandering).

In the case of vortices of unequal strength, the mechanism of merging is notably different if the circulation differential is large. In these cases, the weaker vortex has insufficient circulation to support the strain field induced by the stronger vortex, and as such is strained into a spiral tail structure.[14] Using inviscid contour method calculations, Dritschel and Waugh[7] found that the interaction between two vortices with a large difference in size results in the smaller vortex being torn away, with little increase in the size of the larger vortex. This was identified as a regime of either partial or complete straining out. This is in contrast with more closely sized vortices, which often result in total core growth, under a regime they identified as complete merger or partial merger. In addition to this, equal or similar strength vortex interactions typically produce single vortices, while unequal strength interactions may produce two vortex systems. A critical ratio of core radius and vorticity was also used by Yasuda and Flierl[28] in their transient contour dynamics calculations to characterise empirically the likely merging state. Numerical studies of such scenarios have also been performed,[1] finding similar structures and regimes. The mechanism behind these straining actions is a combination of two causes. First, the weaker vortex is stretched and drawn into the stronger vortex by a process of elongation.[27] Second, a continuous erosion of vorticity into the primary vortex is caused by the strong strain field and high shear, in a mechanism analytically observed by Legras and Dritschel.[13]

If the total circulation of any vortex pair is non-zero, there will be a net rotation of the vortex system.[14] In the case of a co-rotating vortex pair, both circulations are of the same sign, hence they must add to a non-zero amount, causing an orbital motion of the vortex system. If the circulations are equal, this will cause the two cores to orbit at an equal radius around a central point, while if they are unequal, the vortices will orbit on different radii. These migrations have been seen in the water tunnel testing of Rokhsaz,[22] where dye marker injected into the cores of a pair of co-rotating vortices showed negligible change in the location of the orbital centre. While the dye marker can show the location of the core streamline, it cannot predict vorticity strength or the centre of vorticity, making it difficult to ascertain the mechanisms behind merging.

Vortices act as pressure gradient amplifiers, increasing an induced pressure gradient in the freestream at the vortex core.[10] As such, a probe placed near a vortex causes substantial upstream migration of the breakdown location.[2] Consequently either Laser Doppler Anemometry (LDA) or Particle Image Velocimetry (PIV) must be used for accurate experimental results. Due to vortex meandering, averaging point measurements can result in errors of up to 35% in tangential velocity, emphasising the importance of a global measurement technique for vortex analysis.[29]

The work described in this paper investigates the near field interactions of a vortex produced by an upstream vortex with a downstream vane. PIV analyses have been performed for a wide variety of vane offsets at multiple downstream locations, allowing inspection of both the paths of the vortices and the meandering of the vortex pairs. Vortex interactions at very close core spacings have not been previously experimentally observed, as the vortices have been typically 2D or deployed at the same streamwise location. The studies that have deployed vortices from an upstream location have either focussed on the flow characteristics on the downstream wing itself, and/or have been limited in the number of vortex positions run, making trend analysis difficult. The aim of this work is to achieve a better characterisation of near-field co-rotating vortex interactions than has been previously available and to determine the effects of generating a vortex in a flow field with a pre-existing vortex structure. This will facilitate a better understanding of the vortex fields produced by multiple arrays of vortex generators or aircraft in following flight.

II. EXPERIMENTAL SETUP

The present study considers the interaction of two streamwise vortices produced by two NACA 0012 vanes. One vane was located 10 chord lengths (C) downstream of the other, as can be seen in Figure 1. This configuration was chosen as it allows interactions between vortices to occur at close proximities that cannot be observed if the vortices are deployed at the same location. This is also the representative of the effects of a pre-existing vortex in a flow interacting with a vortex producing device. An angle of attack of 8° on each vane has been used for all cases, with a square-edged tip. Higher angles of attack decreased the vortex stability, with unsteady breakdown becoming observable for a single vortex case at 12°. Multiple offsets were tested from −0.7C to 0.6C in an increments of 0.1C, with a finer spacing of 0.05C between −0.3C and 0.05C.

The X axis is in the direction of the flow, with positive downstream, the Y axis is across the tunnel, and the Z axis is in the vertical direction. As such, the rear vane quarter chord was located at X = 10C, with the vane root at Z = −1.5C.

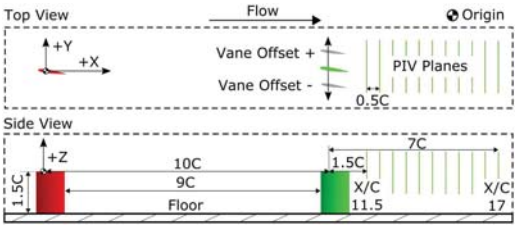

FIG. 1. Vane layout diagram, origin is at the quarter chord tip of front vane.

Planar slices of the flowfield were captured using PIV at 0.5C intervals from 1.5C back from the quarter chord of the trailing vane to 7C back. These correspond to 11.5C and 17C from the leading vane, respectively. The laser sheet was not moved closer than 11.5C as the reflections from the vanes began to distort the results. The experiment was performed at a Reynolds number of approximately 7×10^4 based on the chord length. At 7×10^4 the vortex shedding from a NACA0012 airfoil at 8° angle of attack is within the supercritical region[11] and therefore any Reynolds number lower than 6×10^4 at this angle of attack will result in a shedding regime that is not indicative of higher Reynolds number scenarios. Running the tunnel as slow as possible within the acceptable Reynolds number range minimised vibration of the diffuser expansion, camera mounting, and test section caused by the operation of the fan, thus minimising imaging errors. It is expected that at higher Reynolds numbers, the merging distance and number of rotations to merger will increase, as identified by Cerretelli and Williamson,[3] however the mechanism studied here will be representative of a broader range of flow conditions.

A. Wind tunnel

Experiments were performed in the Macquarie University open return, closed section wind tunnel. This tunnel has a 610 × 610 mm (24 × 24 in.) octagonal test section with a 1900 mm (6′3″) length. Optical access is through a glass window on the top of the test section and removable windows on the side. The test section was characterised using a Turbulent Flow Instrumentation 100 Series Cobra probe, giving a peak turbulence intensity of 0.35% and an average of 0.25%. Velocity uniformity was measured as better than 1% variance, and flow angularity was found to vary by 1° across the test section inlet. The wind tunnel speed was electronically controlled through a National Instruments MyRIO, with the pressure sensors calibrated against a temperature controlled Baratron 120AD Differential Capacitance Manometer. Streamwise velocity variance was held to within 0.38%.

A separate elevated ground is mounted to the floor of the tunnel with a rounded front splitter to minimise the effects of the pre-existing boundary layer in the test section. This ground is mounted 100 mm above the tunnel floor on two steel rails. The vanes have a chord of 80 mm and a span of 120 mm and are painted matte black to minimise reflections. A schematic of this setup can be seen in Figure 2. The boundary layer at the location of the rear vane was experimentally measured to be 5 mm thick at 80% of the freestream velocity and 20 mm thick at 95% of the freestream velocity.

B. PIV setup

A planar two component PIV system was used to capture the vortex dynamics. Due to the large expansion length of the Macquarie University wind tunnel, the camera was placed inside the expansion itself rather than using a mirror system. This allowed the camera to be positioned 2.1 m downstream of the test section, giving a maximum perspective bias of 6.25° (0.21 mm at furthest edge or 0.0027C) with a 120 mm lens. Focus was controlled remotely. By placing the camera this far downstream of the test section, there was no observable difference to the flow in characterisation measurements obtained through the tunnel section. The expansion section of the tunnel was on isolated mounts from the tunnel fan, minimising vibration. Over 200 image pairs, the tip of the rear vane was found to have a maximum displacement change of 1 pixel during operation, with no observable change between images of an image pair.

Laser access to the tunnel was through a glass window in the top of the test section. The laser beam was sent to this location via a periscope connected to a Dantec 3-axis computer controlled traverse. This traverse was restricted to only allow laser sheet movement along the axis of the tunnel. The laser used was a dual-cavity Nd:YAG laser (Quantel EverGreen) with an output of 200 mJ per pulse at 532 nm wavelength and a repetition rate of 15 Hz. Synchronisation between the laser and camera was performed with an ILA synchroniser. Laser pulses were delivered at 55 μs apart as any higher resulted in significant out of plane migration of particles. The laser sheet thickness varies throughout the observation window as a result of the focus, with an average thickness of approximately 4 mm through the region of interest. Seeding was performed with a PIVtech generator using Di-Ethyl-Hexyl-Sebacat (DEHS) air soluble particles of 0.2-0.3 μm typical diameter. This gives a Stokes number of approximately 2×10^{-5}, indicating that the particle size is sufficiently low to follow all flow streamlines accurately.[4]

Scattered laser light was captured by a monochrome cooled CCD pco.1600 camera with 1 GB of RAM. Images were digitised at 14 bits, with a resolution of 1600 × 1200 pixels. The camera was fitted with a 120 mm lens. The CCD size on the camera was 12.5 mm wide × 9.38 mm high, giving a field of view at the most downstream plane of approximately 100 × 133 mm. Image analysis was performed with PIVView software. Multi grid interpolation was used, starting at a coarse grid size of 128 pixels × 128 pixels windows and finishing with refinement to 32 pixels × 32 pixels over 3 passes. Standard FFT correlation was used, with two repeated

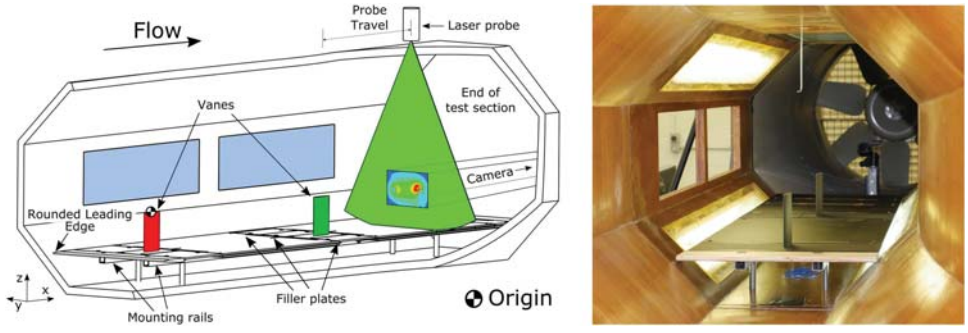

FIG. 2. Cutaway diagram of tunnel test section (left) and image of in-tunnel setup (right).

correlations on 16 pixels offset grids being performed. Subpixel shifting was enabled on all passes with b-spline interpolation and peak detection by a Gaussian least squares fit from 3 points. The final grid size was 99 × 74 nodes.

Calibration of the camera was performed using a grid that was photographed at all analysis plane locations, compensating for the increase in the plane size due to perspective. The plane was located using the laser sheet and then photographed to give an accurate scale.

C. Sources of error

The sampling error for averaged results was determined to be 3.7% in circulation and 0.0035C in location for the 400 total shots taken against a multiple representative sample of 2000 image pairs. Due to the nature of the manual focussing system, there were induced errors, with differences in focus able to produce up to 0.04C error in core location. By implementing a particle pixel size threshold of no more than 2 pixels at a brightness level of 4.5% of the total dynamic range, this error was reduced to 0.0015C in core location. Total error due to the calibration plane procedure was found to be a maximum of 0.18% in location and 0.22% in scale, due to minute differences in lateral calibration plane location. Seeding levels in the room were convergence tested such that the error from the seeding was not discernible from the randomness induced by the other errors. Camera vibration was not observed at an appreciable level, with a maximum image migration of 0.06% measured over the course of an imaging run. The particle size was measured at an average of 1.5 pixels, giving an uncertainty in position of 0.03 pixels.[15] Quantization errors were negligible due to 14 bit quantization. Any biases inherent in each run were minimised by having the each set of 400 images taken with one forward run of 200 images (plane moving from X17 to X11.5) and one backward run in the opposite direction; this way any errors in seeding or focus would be minimised. The total error in core location was found to be ±0.006C. The error in lateral vane offset adjustment is ±0.005C (10% of the smallest offset change).

D. Vortex analysis methodology

Vortex radii can vary by up to 35% if time averaged results are used due to vortex meandering and local fluctuations in velocity.[29] In addition to this, the velocity field will be smoothed, resulting in significant deviations in circulation and core size if time averaged results are used. However, it is still desired to have average values for core location, size, and strength, and as such the results were analysed by a script based evaluation of each individual pair of images. These images were sequentially analysed in Matlab, with peak noise filtered by vorticity gradient as previously mentioned. To eliminate the influence of weak secondary vortex structures, vortex shedding, and low level noise on the calculation of tip vortex properties, all vorticity constructs except the tip vortex were filtered out. This was performed by computing contours at 10% of the peak vorticity and calculating the area enclosed by each individual structure. These data points were then exported to Matlab, where they were then combined and analysed for average values and variances. This allowed for an accurate calculation of real world core size, as well as time-averaged values that could be used to represent the core characteristics and allow comparison between cases.

The vortex centre within a plane is defined as the integral of the vorticity (ω) multiplied by the displacement (X or Y value, depending on the axis being calculated) divided by the circulation (Γ).[14] This can be seen in Eqs. (1) and (2),

$$X_c = \frac{1}{\Gamma}\int X\omega dS, \tag{1}$$

$$Y_c = \frac{1}{\Gamma}\int Y\omega dS. \tag{2}$$

While this does not always align with the location of zero in-plane velocity, it allows for consistent prediction of the centre of circulation intensity even when the vortex pair is migrating with an in-plane motion, which would otherwise skew the core location significantly. It is also more robust than simply using the value of peak vorticity, as it is not significantly skewed by asymmetrical vortices or vorticity peaks in the result.

As the vortices are co-rotating, they both have the same signed vorticity. This means that identifying the centre of vorticity within a plane will be ineffective as it will only find the centre point between the two vortices. An automated script was used to identify the two separated vorticity peaks and construct a contour line at 0.1 of the peak vorticity and 0.3 of the peak vorticity on a given plane, giving enclosed areas of $A_{0.1}$ and $A_{0.3}$, respectively. In the case that the smaller $A_{0.3}$ was less than a quarter of the larger $A_{0.3}$, the vortices were considered merged. This 1:4 ratio was selected based on the graphical results, which correlated with the observable vortex cores while minimising the influence of signal noise on the results. The area represented by $A_{0.3}$ can be used to track the vortices though the initial stages of the merging process, as it allows for better detection of the secondary peak in a merging and partially strained vortex structure. The single $A_{0.1}$ and two $A_{0.3}$ areas are considered as the vortex core regions for the merging vortex system and individual vortices, respectively. Consequently, for path tracking the weighted centroid of Eqs. (3) and (4) was used,

$$X_c = \frac{1}{\Gamma_{A_{0.3}}}\int X_{A_{0.3}}\omega dS, \tag{3}$$

$$Y_c = \frac{1}{\Gamma_{A_{0.3}}}\int Y_{A_{0.3}}\omega dS. \tag{4}$$

While the vortices remain near a uniform Lamb-Oseen distribution at the far offsets, at nearer offsets significant partial straining occurs from the influence of the vortex interaction. This causes a skew in the shape of the vortex core that changes its primary axis as the vortex pair rotates downstream. This prevents the fitting of a Lamb-Oseen distribution of vorticity to the results. Consequently, the radius of the vortices was calculated using the vortex areas and assuming vortex circularity to give an effective radius. These were $R_{0.1}$ and $R_{0.3}$ for $A_{0.1}$ and $A_{0.3}$, respectively. The vortex circulation was calculated by the integral of the vorticity within the identified core region. For when there are individual vortices identified, this is taken at an $A_{0.3}$ cutoff, as this allows the continued identification of vortex peaks through the merging case. When the vortex is merged,

this is evaluated at $A_{0.1}$ to capture the entire vortex. If $A_{0.3}$ is used to characterise the merged vortex, it excludes the merging tail region of the vortex, causing a significant drop in effective vortex circulation. This is not an issue for the unmerged vortex cases, as the vortices are still approximately circular in shape so there is no vorticity lost to the tail region. This will however cause an effective circulation reduction for the unmerged cases, so should be noted for the results of this section. This reduction was found to be 10.5% as calculated from the single vortex case.

By comparing this method to a Lamb-Oseen approximation on a uniform, circular vortex, it was found that the sampling resolution could result in a 15% maximum error in peak vorticity. This translated to a 1.5% maximum error in the 10% peak vorticity, giving a maximum core radius error of 5% per image pair, which was considered acceptable for this analysis.

III. RESULTS AND DISCUSSION

A. Vortex migration

In all un-merged cases, the vortices followed a helical path as can be seen in Figure 3. Downstream vortex positioning at the start of the domain varied linearly with offset; however, between 0.2C and −0.25C the vortices were merged. This merging can be seen in the 0.1C offset case, where the downstream vortex disappears after X12.5 due to it merging into the upstream vortex. As the offset approached the point of vortex merging, the path length of both the upstream and downstream vortices increased, with the downstream vortex experiencing the most migration. Total path length at 0.6C offset was 0.308C and 0.186C for the upstream and downstream vortices, respectively. At 0.2C offset, this increased to 0.511C (66% increase) and 0.330C (77%).

While the paths retained their helical migration pattern with a linear orbital rate independently of which side of the vane the vortex passed on, the total circularity of the path varied. When comparing the −0.3C case to the positive 0.3C case, the non-circularities of the −0.3C case can clearly be seen, with a near horizontal movement of the downstream vortex for the first 4 data points. There is a translation of 0.1926C in the lateral direction for a total movement of only 0.0542C in the vertical direction for the upstream vortex across these data points. This is due to the non-linearities associated with the vortices being drawn closer from the initial stages of the merging process, as well as the influence from the wake of the rear vane. The −0.3C offset case is the only case presented in this figure where the vortex paths pass both above and below where the merged vortex is located in the −0.1C offset case. This means that until Z/C drops below −0.025, the vortex is not being affected by the rear vane downwash, and once it is below this value it will be, thus causing the path non-linearity. This can only occur when the upstream vortex passes on the suction side of the vane, as this will cause orbiting motion induced by the downstream vane to draw it through this region. This effect will dissipate as the downstream vane wake dissipates further downstream.

As opposed to the laterally spaced test configuration of Rokhsaz[23] where negligible centre of rotation migration was observed, the migration of the centre of rotation of the vortices was found to be significant. Total vertical migrations of up to 0.06C and lateral migrations of 0.07C were observed in the centre of rotation. This was as high as 35% of the total vortex

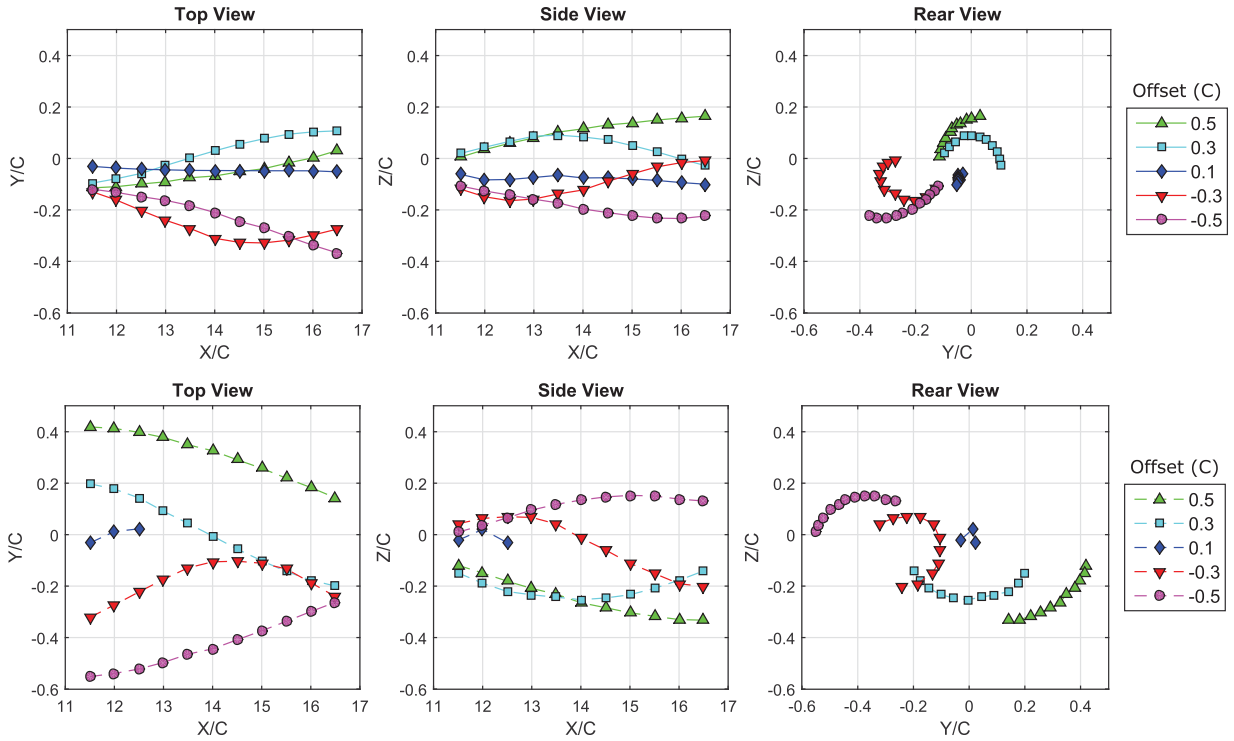

FIG. 3. Paths of upstream (solid) and downstream (dotted) vortices for various lateral vane offsets. Error in core location is ±0.006C.

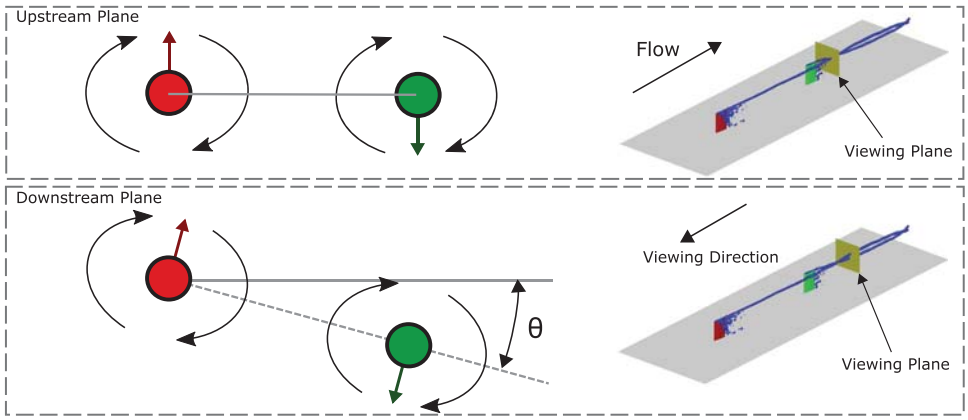

FIG. 4. Schematic of rotation angle calculation for vortex pairs. In-plane vortex trajectory is shown via the red (upstream vortex) and green (downstream vortex) arrows. The viewing plane is normal to the freestream velocity, with the view seen from downstream of the vanes.

migration at an offset of −0.3. The absolute magnitude of the centroid migration remained roughly constant across the offset range measured; however, it was a significantly higher percentage of the total migration at the nearer offsets of the vortices. The analytical, inviscid results presented by Leweke[14] also show a static core rotation centre. The differences observed can be attributed to the downwash produced by the vane in the creation of the second vortex. This downwash causes a change in the migration of the pair, something not previously observed due to the vortices being created at the same upstream location (in the case of Rokhsaz) or not having any vane influence (Leweke).

The spiralling rate of the vortices was calculated through a linear approximation of the change in the angle of the line drawn between the two vortex cores, as can be seen in Figure 4. Decreasing the offset increased the spiralling rate until the point of merging, as can be seen in the rotational rate in Figure 5. This rotation had a non-linear trend as the point of merging was reached, peaking at approximately 44° per chord length. This is distinctly less than the 1200° per chord length effective rotational rate of the peak azimuthal velocity region of a single vortex, attained at a radius of 0.075C and velocity of 37.5 C/s (3 m/s). While an inverse relationship cannot be explicitly confirmed from the offset range investigated, the rotational rate will trend to zero as the vane separation goes to infinity, indicating an extension of the non-linearity observed in the rotation trends. The rotation rate remained constant throughout the domain. The separation linearly varied at the same rate as the offset changed until the point of vortex merging.

By combining the separation distance curves from each unmerged case, the trends of separation distance for the vortex pair can be extrapolated to cover a much longer effective distance. This allows us to simulate how a vortex pair deployed at an initial separation width of $B_v/R_{0.3} \approx 7$ would behave further downstream, as can be seen in Figure 6. The separation data show that there are two different separation rate trends depending on which side of the vane the vortex is passed on. If the vortex passes on the pressure side of the vane, for every chord length travelled downstream, the vortices move together approximately 0.154 of the core radius. However, if the vortex passes on the suction side of the vane, this is decreased to 0.110 core radii, giving a 28% differential in separation rate. This suggests that the wake region of the vane significantly affects the speed of the merger, causing the vortices to be forced together faster. This happened independently of the circulation within the vortex core, which showed similar trends regardless of which side of the vane the vortex approached from.

As the vortices approach merger, the trend deviates from linear. The −0.25C offset case exhibits all the merging regimes discussed in the merging section up to single vortex, combining the second diffusive and convective merging states. However, it does not show the clear levelling off or core separations as observed by Cerretelli and Williamson,[3] instead demonstrating a reduced but still significant gradient. As the separation between the cores reaches two core radii apart, the separatrices of the two vortices connect and rapid merging occurs, resulting in the transformation to a singular vortex. The asymmetric mechanism behind these separation trends will be discussed further in the merging section.

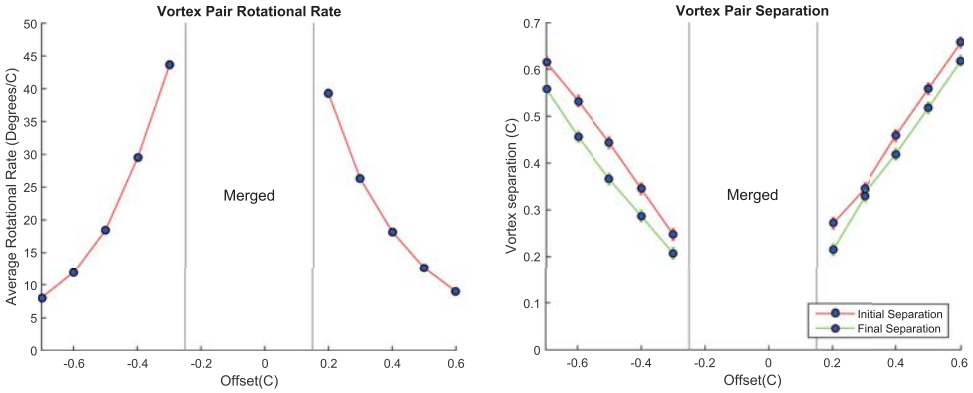

FIG. 5. Vortex pair rotational rate (left) and vortex pair separation (right).

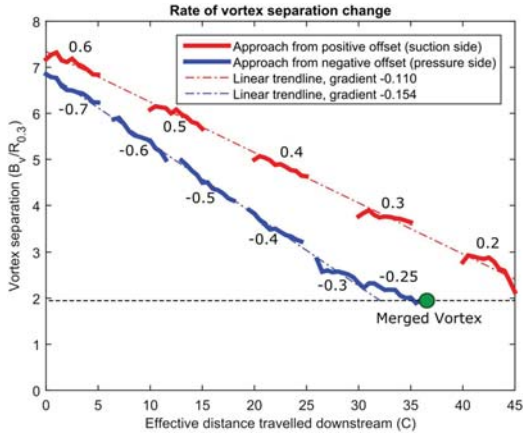

FIG. 6. Vortex pair separations for all unmerged cases. Each offset case is indicated by the annotations on the line segments.

In the merged condition, the single vortex path only was tracked, as can be seen in Figure 7. The path of the merged vortex was laterally shifted by approximately half the offset change of the rear vane, demonstrating the influence of the rear vane on vortex trajectory. This indicated that the downstream vortex contributes to approximately half of the vortex total location, despite the fact that the vortices were merged prior to the window of observation. As the downstream vane is angled to direct the flow towards −Y, it was anticipated that the merged vortex would be located towards −Y due to the vane downwash, but as can be seen from the −0.15C offset case, the vortex initially starts at a greater Y/C, peaking at −0.11C. This is of note as the quarter chord of the vane is located to the negative side of the initial vortex core. When the downstream vane was located at −0.1C, the resultant merged vortex starts at −0.09C, peaking at −0.08C before dropping to −0.12C by the end of the domain. This is significantly more positive than the single vortex case for the entire observation domain. The curvilinear path is due to the tail of the merged vortex produced by the drawing in of the downstream vortex, as will be discussed in Sec. III B. A component of the curvature is also due to the vortex passing slightly inboard and offset of the wingtip. There is a considerable downwards shift imposed by the presence of the rear vane, as can be seen compared to the path of the single vortex. In all cases, the downwards travel was approximately 0.075C, with all paths being within error bars of each other.

Vortex path meandering was evaluated through the vortex tracking and analysis of each individual set of image pairs. Uniform circular meandering was observed at the far range of the offsets investigated. A maximum radius of displacement of 0.020C was measured at 0.6C offset. As the offset was decreased, there was no observable shift in meandering until 0.2C offset, where partial merging was present towards the end of the domain. The secondary vortex was drawn around the primary at this point, creating a bias in the meandering. This bias predominantly affected the weaker vortex, with a maximum amplitude of 0.066C measured on the axis of bias. This instability was at an average angle of 25° to the line between the two vortex cores. The stronger, upstream vortex was also marginally affected by this instability, with a maximum meandering amplitude along the axis of bias of 0.029C at 0.2C offset. This gives meandering bias ratios of 3.22 and 1.38 for the downstream and upstream vortices, respectively, indicating an instability with stronger effects on the downstream vortex. The same meandering trends were seen on the negative offsets. The magnitude of the instabilities was increased as the vortices travelled downstream and the vortex proximity was reduced through either offset change or drawing in of the vortex paths.

B. Vortex merging

Time averaged results were inspected to identify the merging pattern. The stronger and weaker vortices were selected from their circulation, with the upstream vortex (red) being the stronger and downstream vortex (green) being the weaker. The evolution of a typical merging pattern can be seen in the planar slices of the −0.25C offset case in Figure 8. Individual vortex identification was performed using the contour lines at 30% of the peak vorticity on the plane ($A_{0.3}$). The stronger and weaker vortices were selected from their circulation, with the upstream vortex (red) being the stronger and downstream vortex (green) being the weaker. The yellow band shown in the figure is the $A_{0.1}$ contour line, with the other contours showing lower levels of vorticity. The scale has been selected to maintain a proportional X and Y axis for visualisation of circularity.

At the start of the domain, the vortices have similar circularity; however, as they travel downstream they are drawn closer together and partial straining of the weaker vortex occurs. This process starts at X14, with the secondary peak

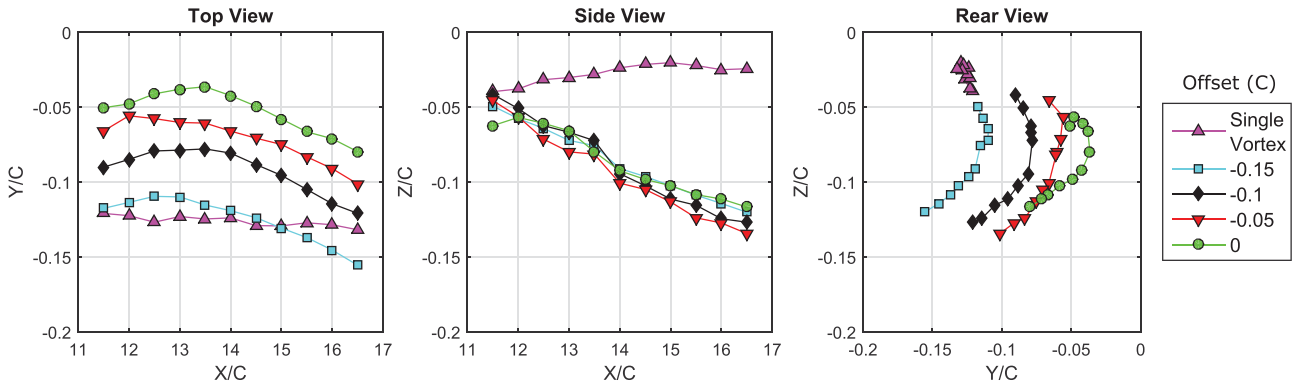

FIG. 7. Paths of merged vortex for various lateral vane offsets. Error in core location is ±0.006C.

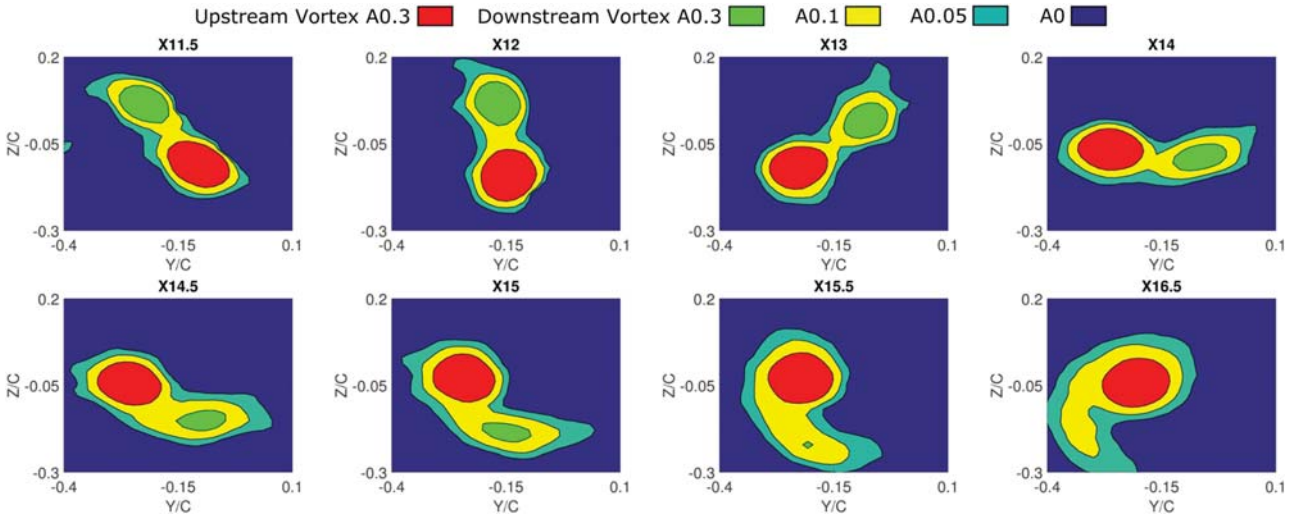

FIG. 8. Vortex merging pattern for –0.25C offset, with upstream vortex in red and downstream vortex in green. Note the non-uniform spacing of the planes.

being completely dissipated by X16.5. Throughout the process, the upstream vortex $A_{0.3}$ does not significantly increase in area; however, the $A_{0.1}$ surrounding it does significantly increase. This is from the vorticity of the weaker vortex being diffused and spread around the stronger vortex. Of note is the fact that the upstream vortex is the stronger, while the downstream vortex is weaker. This indicates that the presence of the upstream vortex has caused the strength of the downstream vortex to be weakened. This results in the merger of the downstream vortex into the upstream vortex as the pair progesses downstream, as the upstream vortex is the stronger of the two at the location just behind the rear vane (X11.5). As a consequence, the downstream vane is effectively re-energising the existing upstream vortex after the vortex pair has merged.

The transition of the vortex from a shape with a spiral tail to a circular structure can be better investigated at the −0.2C offset in Figure 9. Moving the vane offset −0.05C closer causes a significant upstream shift in the merging location, with no existence of secondary peaks from the X11.5 plane onwards. As the merged vortices travel downstream, the vorticity is transferred from the tail to the circular vortex core. Eventually the tail is completely dissipated, with the final core achieving circularity and a larger size than one individual vortex, as can be seen at the X16.5 plane.

The initial stages of the merging can be visualised through the inspection of the −0.3C offset as seen in Figure 10. While this case did not merge within the observation window, the initial drawing in and vorticity transfer was clearly occurring. The lower rotational rate of the vortex cores observed at this further offset significantly slows the rate of merging when compared to the −0.25C case. Initially the two vortices are separate, both at the $A_{0.3}$ and $A_{0.1}$ levels. As they travel downstream, their separations move closer by approximately 0.007C per chord length downstream. This equates to approximately 6% of the $R_{0.3}$ per chord length travelled downstream. From the X15 to X16 planes, there is a distinct change in the circularity of the weaker vortex, with the X16 plane showing partial straining and an oval shape occurring at a vortex separation of 0.021C. Between X16 and X16.5, there is also an observable reduction in the size of the weaker $A_{0.3}$; however,

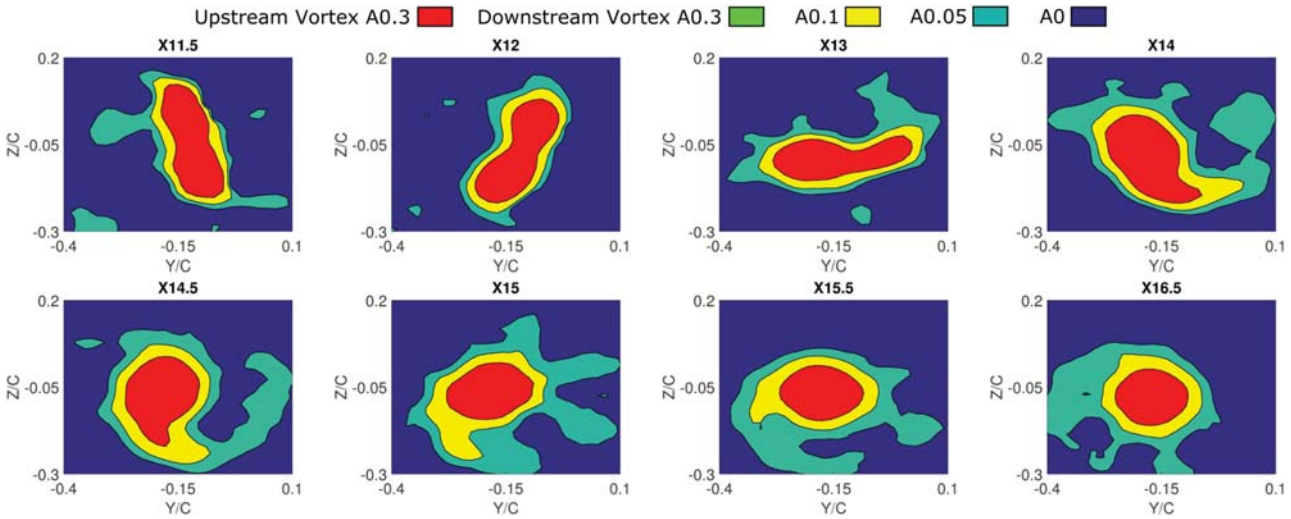

FIG. 9. Vortex merging pattern for –0.2C offset, with upstream vortex in red and downstream vortex in green. Note the non-uniform spacing of the planes.

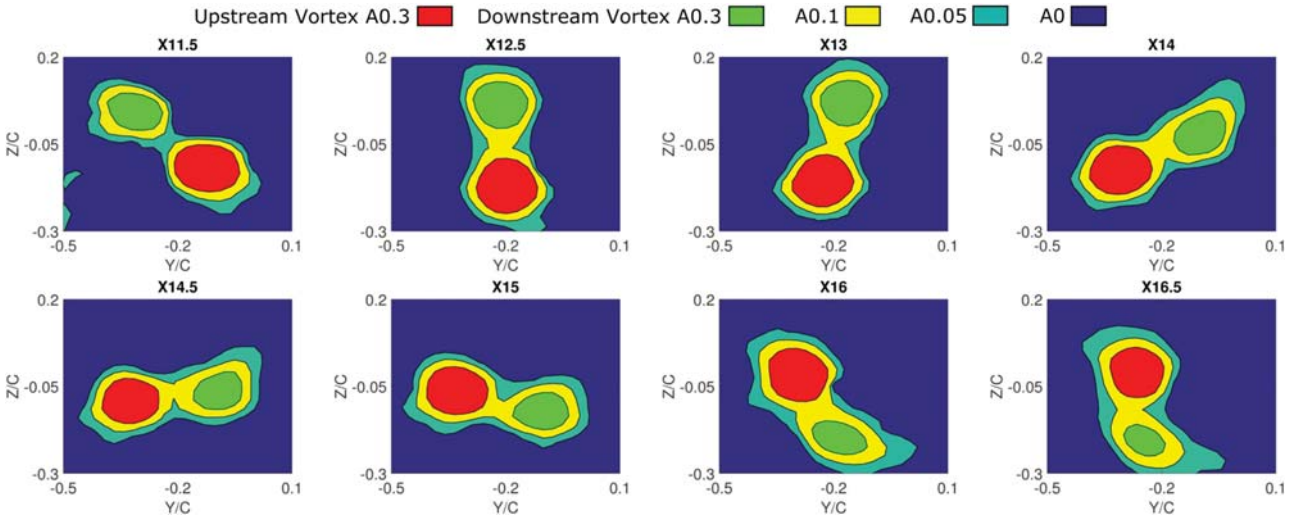

FIG. 10. Vortex merging pattern for –0.3C offset, with upstream vortex in red and downstream vortex in green. Note the non-uniform spacing of the planes.

$A_{0.1}$ has largely remained unchanged. This indicates that the vorticity transfer between the two vortices is caused by the diffusion of high level vorticity from the second vortex into the lower energy level $A_{0.1}$. From here it is drawn around the stronger vortex, as was demonstrated in the previous cases. This case also demonstrates the need for tracking the vortex core $A_{0.3}$, as $A_{0.1}$ indicates that the vortices are merged from X12.5, while $A_{0.3}$ can clearly track distinct vortices until the final plane.

These observations of asymmetric merger show similarities to the two dimensional numerical simulations of Brandt and Nomura.[1] Partial straining of the weaker vortex followed by the diffusion of vorticity and absorption into the stronger vortex were observed at similar circulation ratios. However, the very high vortex eccentricities and aspect ratios observed in the weaker vortex by Brandt and Nomura were not observed before complete merging. This is likely reflecting the increased vorticity transfer in the turbulent, three-dimensional experimental flow, resulting in faster merging.

Inspecting the pathlines in the co-rotating reference frame as seen in Figure 11 allows for further understanding of the uneven merging mechanism. To calculate the rate of rotation of the co-rotating reference frame, the average rotation rate across the entire domain sweep as previously calculated was used. At large separations, the vorticity fields of the two primary vortices are significantly separated ($B_v/R_{0.3} > 2.3$), with

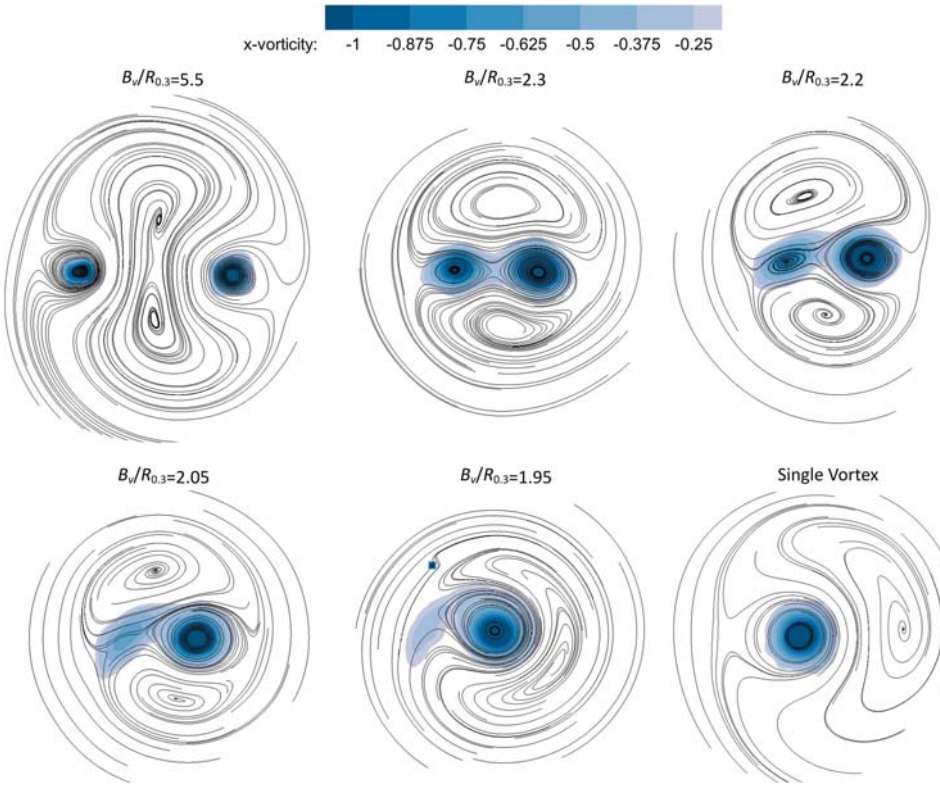

FIG. 11. Pathlines in the co-rotating reference frame and vorticity for different stages of vortex merger.

the streamlines of the two vortices being clearly separated by an inner recirculation region. This inner recirculation region appears to be the origin of the two "ghost vortices" of the outer recirculation region. While not observed in the offset range investigated, it is anticipated that the two ghost vortices will merge at larger offsets, forming a singular recirculation region. As the vortices are drawn closer together, they divide this recirculation region into the two ghost vortices of the outer recirculation region. At this point ($B_v/R_{0.3} \approx 2.3$), the two vortex streamlines connect, as well as their vorticity field. Unlike the stages of Cerretelli and Williamson,[3] the unequal three dimensional merger does not appear to enter the well defined diffusive and convective stages, as from this point onwards the vortex separations do not significantly change; however, there is a significant transfer of vorticity from the weaker to stronger vortices. Once the streamlines of the two vortices have joined and the ghost vortices are fully separated ($B_v/R_{0.3} < 2.3$), the flow begins to become significantly asymmetric in the horizontal axis, as opposed to the relative symmetry present in the further separated condition. Once this asymmetry occurs, the transfer of vorticity and modification of the pathline patterns occurs rapidly. As the merger progresses that the rotating pathlines of the weaker vortex are strained out, leaving the previously discussed vorticity tail. After the remnants of the secondary vortex have been strained out, the ghost vortices rapidly migrate to the other side of the vortex configuration and merge into a singular recirculation region. This recirculation region expands and reduces in strength as the vortex slowly normalises itself towards circularity in the merged diffusive state.

The merging lengths identified from the analysis of the time averaged cases can be seen in Figure 12. These are only given for cases where merging was observed within the domain. It can be seen that the offset for merging at the start of the domain is skewed to the positive side of the vortex (passing inherently at −0.12C). This shows that passing the vortex on the pressure side of the downstream vane facilitates more rapid merging then passing it on the suction side. The vortex merging length showed a highly non-linear trend with respect to offset, with the merge length rapidly exceeding the 5C domain length over just 0.15C offset change. This trend and the observed results of the merging pattern indicate that there may be a link between the merging length and rotational rate.

While the analysis of the merging patterns was taken from time averaged data, each individual image pair was analysed to detect the vortices. It was found that the vortex merging location in the transition regions was probabilistic rather than deterministic, as seen on the right side of Figure 12. The probability of the vortex being merged is simply the percentage of image pairs without a secondary vortex. These probabilities were also tested with a random sample of 200 image pairs and found to be within 5% of the values from the full 400 image pairs, indicating an error in probability of less than ±5%. In the −0.2C case there was a 66% occurrence of merging in the first plane, with 100% of image pairs being merged with no secondary peaks by X15.5. The time averaged point of merge at X13 lies approximately halfway between these points. Similarly, in the −0.25C case, the probability of merging linearly decreases throughout the domain, with a 44% probability of merging at the time averaged merge location. This indicates the presence of a fluctuation side to side of the vortices, similar to that identified in a previous computational study by the authors[8] producing a sinusoidal fluctuation in the merging point. This meandering of the singular vortices causes them to move towards and away from each other, with a resultant fluctuation in vortex separation. As previously identified, the merging location is very sensitive to offset, and consequently any variance in vortex separation will cause a significant difference in the presence of secondary vortex peaks.

Two interesting findings are apparent from these results. The first is the near linear rate of the probability decay with distance. This rate appears to have minimal skew from the samples taken, and minimal non-linearity. However, when considering the probability distribution for a regular sine wave, there is a quasi-constant region that shows similarity. From −50% to +50% of a sine wave amplitude, all sample bins of a frequency histogram are within 2%, and at ±75% of the waves amplitude, the samples all fall within a maximum variance of 10%. This means that a sine wave displacement change will appear linear up to 75% of its maximum amplitude. Consequently, the merge is following the sinusoidal oscillation previously discussed, likely caused by a sinusoidal instability in one or both of the vortices. This causes a sinusoidal change in vortex spacings, resulting in the observed merging statistics. The second finding is that the time averaged merge location does not necessarily coincide with the point of 50% merging probability. This is clear in the −0.2 case, where the time averaged case merges at X13, while the probability of merging at this point is 89%. However, in the −0.15 case, the time averaged merge

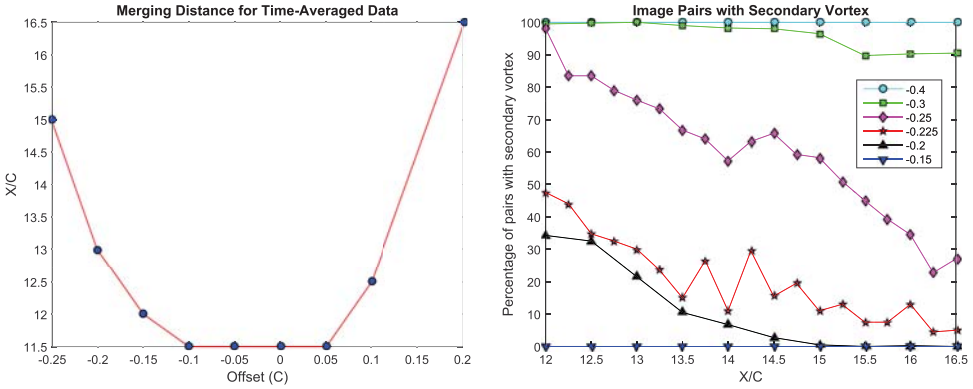

FIG. 12. Distance to vortex merging for time averaged cases (left) and probability distribution for instantaneous measurements at various lateral vane offsets (right).

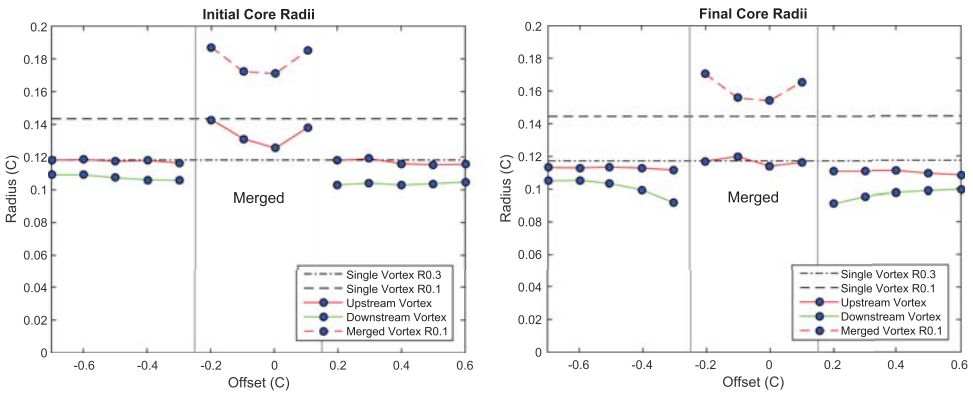

FIG. 13. Initial vortex radii (left) and final vortex radii (right).

at X12 is reflected in the 100% merging probability from X12 onwards. This indicates the variances in vortex meandering, as well as the change in energy distributions and vortex shapes accounts for significant changes in the transient fluctuations of the vortex merger.

C. Circulations and core radii

The radius results of Figure 13 show the initial $R_{0.3}$ as remaining relatively constant for the unmerged cases, with the downstream vortex radius approximately 9% smaller than the upstream at the start of the domain. The radius of the upstream vortex does not significantly drop throughout the domain, with drops in radius of approximately 3%. The downstream vortex has a similar trend for its size in far offset cases; however, as the offset is reduced, its interaction with the upstream vortex causes a reduction in size of up to 13% over the domain. For the merged case it can be seen that the initial $R_{0.3}$ is significantly higher than the single vortex case; however, by the end of the domain, it has reduced to within the error of the single vortex case. This is due to the dispersion of vorticity from the weaker vortex core to the $A_{0.1}$, as identified in the merging section of this paper.

When inspecting the $R_{0.1}$ this can be seen through the significantly higher radii for both the initial and final cores. The core radius in this merged region is also affected by how merged the vortices are. $R_{0.3}$ in the −0.2C offset case is the largest of the merged cases at the start of the domain, coinciding with the irregular, non-circular shape seen in Figure 9. As the vortex travels downstream, it forms circular and uniform $A_{0.3}$, and this coincides with the final radius observed in the single vane condition. The nearer offset cases have more significant vortex core relaxation by the initial plane, resulting in their comparatively smaller radii. Applying the same principles to $R_{0.1}$, it would be expected that over the course of a longer domain, merged $R_{0.1}$ would trend towards the single vortex as the vorticity is drawn in from $A_{0.1}$.

The circulation figures seen in Figure 14 show similar trends to the radius; however, there is a greater discrepancy between the upstream and downstream vortices. The loss in circulation from the downstream vortex is very apparent, with drops of 28% along the length of the domain observed for the cases nearest to merging. This was a non-linear trend, showing far more significant decreases then core radius changes. This is indicative of the dissipation of the secondary vorticity peak into the $A_{0.1}$ as part of the energy transfer mechanism. Of note is that the energy transfer out from the secondary vortex is occurring at a far greater offset than the merged cases, with it being clearly observable at the −0.4C and 0.4C offsets. The drop in downstream vortex circulation is 4.7% at the 0.4C offset and 7.3% at the −0.4C offset. This drop is also skewed to the positive offset, similarly to the merging distance. It is hypothesised that this is due to the low pressure core of the upstream vortex passing on the pressure side of the downstream vane, reducing the magnitude of the high pressure here. This reduces the pressure differential across the downstream vane's tip, thus reducing the strength of the resultant tip vortex. It is also a cause of the skew in vortex merging to positive offset, as the lower strength downstream vortex is more rapidly merged.

While the radius of the upstream vortex remained constant as the vanes approached merging offset, the upstream vortex circulation can be seen to reduce at nearer offsets. At the 0.2C

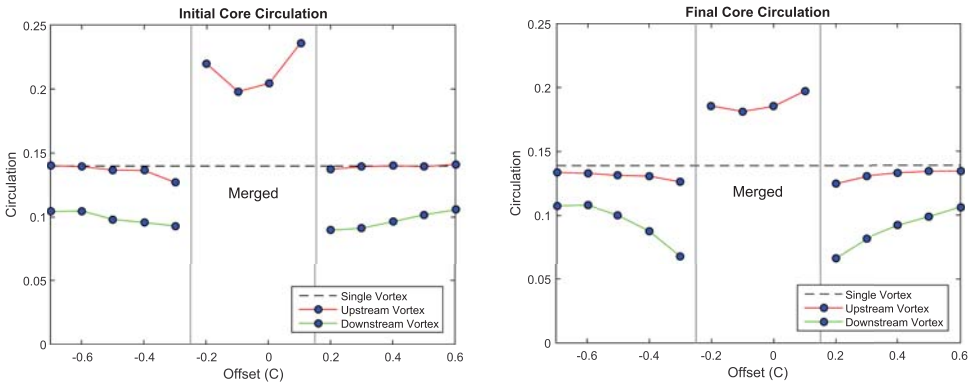

FIG. 14. Initial vortex circulation (left) and final vortex circulation (right).

offset, for example, the upstream circulation drops by 9%, as opposed to the 0.5C offset where it drops by only 3.7%. As such, the diffusion of vorticity from both vortex peaks becomes more significant as their proximities are reduced. This circulation has diffused into the $A_{0.1}$ region as part of the secondary diffusive stage of vortex merging.

Inspecting the initial circulation for the merged case, it can be seen that the outer regions of the merged offsets trend towards the sum of the two individual vortex circulations. At −0.3C offset, the initial sum of the upstream and downstream vortex circulations is 0.222 m^2/s, and at 0.2C offset it is 0.227 m^2/s, which compares similarly to 0.220 m^2/s and 0.236 m^2/s measured at −0.2C and 0.1C offset, respectively. However, at the end of the domain, the merging process has levelled the circulation to closer to that of the 0C and −0.1C offsets. This indicates that the shift towards circularity involves a penalty in circulation, although the final circulation of the merged vortex is still significantly higher than a single vortex case. It is important that this is not necessarily considered as a loss of flow energy, as the circulation is proportional to vorticity, which is not a direct measure of flow energy.

IV. CONCLUSION

Wind tunnel experimentation was performed to investigate the behaviour of the interactions between a co-rotating vortex pair produced by two offset vanes. NACA0012 wings of 1.5 aspect ratio, at 8° angle of attack and a Reynolds number of 70 000 were used for this study, spaced 10C apart in the streamwise direction. Lateral offsets from −0.7C to 0.6C were studied to examine the effects of vortex proximity on the resulting vortex sizes and paths.

For all unmerged cases, the two vortices migrated in a helical pattern. Vortex merging was observed from −0.25C to 0.2C offset, equivalent to −0.15C to +0.3C offset from the unobstructed path of the downstream vortex. This demonstrated a bias to faster vortex merging when the upstream vortex passed on the pressure surface of the downstream vane. As the offset was decreased towards the point of merging, the orbital rate of the vortices increased non-linearly to a maximum of 44°/chord length travelled downstream. Vortex separation varied linearly with offset, with the vortices consistently moving closer together throughout the domain for all offsets investigated. As the vortices moved closer together and further downstream, an instability was identified in the meandering of the vortices. For the merged cases, it was found that the merging process imparted a downwards motion and shifted the vortex path to the positive side. Passing the vortex on the pressure side of the vane resulted in the vortices moving towards each other approximately 28% slower than if it was to be passed on the suction side of the vane.

The vortex merging distance was found to be highly sensitive to offset, with a non-linear trend. An unequal merging process was observed, with the downstream vortex diffusing its vorticity to a lower energy level. This diffuse vorticity was then drawn around the stronger upstream vortex, eventually forming a circular structure. Similar patterns were observed for all offsets where merging occurred. The symmetry of the vortex structure was found to change rapidly once the vortices came with a core separation 2.3 times the core radius, resulting in rapid merging by the time the vortices were 2 core radii apart. The location of merging could not be determined deterministically but was instead statistical phenomena. This was due to the meandering of the vortex location and energy levels shifting the merging location upstream and downstream in a sinusoidal oscillation.

From the circulations, it was found that the presence of the upstream vortex weakened the downstream vortex. As the vortices approached merging, their vorticity peaks were diffused into a larger, lower energy vorticity level. For the fully merged cases, a circulation loss was found to result from transitioning from an irregular shape to a circular one. Despite this penalty, the merged circulation remained higher than that of a single vortex.

While the merging distance is sensitive to offset, these results indicate that the fundamental effects and mechanisms of the merging process remain the same regardless of vortex separation. As such, the re-energisation of an upstream vortex can be performed with a relative insensitivity to offset.

[1]L. K. Brandt and K. K. Nomura, "Characterization of the interactions of two unequal co-rotating vortices," J. Fluid Mech. **646**, 233–253 (2010).
[2]J. J. Cassidy and H. T. Falvey, "Observations of unsteady flow arising after vortex breakdown," J. Fluid Mech. **41**(04), 727 (1970).
[3]C. Cerretelli and C. H. K. Williamson, "The physical mechanism for vortex merging," J. Fluid Mech. **475**, 41–77 (2003).
[4]C. A. Cruz, *Experimental and Numerical Characterization of Turbulent Slot Film Cooling* (ProQuest, 2008).
[5]W. Devenport, J. S. Zsoldos, and C. M. Vogel, "The structure and development of a counter-rotating wing-tip vortex pair," J. Fluid Mech. **332**, 71 (1997).
[6]D. G. Dritschel, "The stability and energetics of corotating uniform vortices," J. Fluid Mech. **157**, 95–134 (1985).
[7]D. G. Dritschel and D. W. Waugh, "Quantification of the inelastic interaction of unequal vortices in two-dimensional vortex dynamics," Phys. Fluids A **4**(8), 1737 (1992).
[8]K. J. Forster, T. Barber, S. Diasinos, and G. Doig, "Numerical investigation of streamwise vortex interaction," in *SAE Technical Paper* (SAE International, 2015), Vol. 09.
[9]K. J. Forster and T. R. White,"Numerical investigation into vortex generators on heavily cambered wings," AIAA J. **52**(5), 1059–1071 (2014).
[10]M. Hall, "A new approach to vortex breakdown," in *Proceedings of the Heat Transfer and Fluid Mechanics Institute* (The Stanford University Press for the Heat Transfer and Fluid Mechanics Institute, 1967), pp. 319–340.
[11]R. F. Huang and C. L. Lin, "Vortex shedding and shear-layer instability of wing at low-Reynolds numbers," AIAA J. **33**(8), 1398–1403 (1995).
[12]D. Hummel, "Formation flight as an energy-saving mechanism," Isr. J. Zool. **41**(3), 261–278 (1995).
[13]B. Legras and D. Dritschel, "Vortex stripping and the generation of high vorticity gradients in two-dimensional flows," Appl. Sci. Res. **51**, 445–455 (1993).
[14]T. Leweke, S. Le Dizès, and C. H. K. Williamson, "Dynamics and instabilities of vortex pairs," Annu. Rev. Fluid Mech. **48**, 507–541 (2016).
[15]C. W. M. Raffel and J. Kompenhas, *Particle Image Velocimetry, A Practical Guide* (Springer, Berlin, Germany, 1998).
[16]M. Manolesos and S. G. Voutsinas, "Experimental investigation of the flow past passive vortex generators on an airfoil experiencing three-dimensional separation," J. Wind Eng. Ind. Aerodyn. **142**, 130–148 (2015).
[17]M. V. Melander, N. J. Zabusky, and J. C. Mcwilliams, "Symmetric vortex merger in two dimensions: Causes and conditions," J. Fluid Mech. **195**, 303 (1988).
[18]P. Meunier, U. Ehrenstein, T. Leweke, and M. Rossi, "A merging criterion for two-dimensional co-rotating vortices," Phys. Fluids **14**(8), 2757–2766 (2002).
[19]E. A. Overman and N. J. Zabusky, "Evolution and merger of isolated vortex structures," Phys. Fluids **25**(8), 1297 (1982).

[20]L. A. A. Pereira, M. H. Hirata, and N. M. Filho, "Wake and aerodynamics loads in multiple bodies-application to turbomachinery blade rows," J. Wind Eng. Ind. Aerodyn. **92**, 477–491 (2004).
[21]K. Roberts and J. Christiansen, "Topics in computational fluid dynamics," Comput. Phys. Commun. **3**, 14–32 (1972).
[22]K. Rokhsaz and L. K. Kliment, "Experimental investigation of co-rotating vortex filaments in a water tunnel," in 32nd AIAA Fluid Dynamics Conference and Exhibit, June 2002.
[23]K. Rokhsaz, R. Rebours, and S. R. Foster, "Quantitative measurements of wake vortex motion in a water tunnel," in 39 Aerospace Sciences Meeting and Exhibit, January 2001.
[24]V. J. Rossow, "Convective merging of vortex cores in liftgenerated wakes," J. Aircr. **14**(3), 283–290 (1977).
[25]P. G. Saffman and R. Szeto, "Equilibrium shapes of a pair of equal uniform vortices," Phys. Fluids **23**(12), 2339–2342 (1980).
[26]M. Toloui, L. P. Chamorro, and J. Hong, "Detection of tip-vortex signatures behind a 2.5 MW wind turbine," J. Wind Eng. Ind. Aerodyn. **143**, 105–112 (2015).
[27]R. R. Trieling and G. J. F. V. Heijst, "Kinematic properties of monopolar vortices in a strain flow," Fluid Dyn. Res. **23**, 319–341 (1998).
[28]I. Yasuda and G. R. Flierl, "Two-dimensional asymmetric vortex merger: Contour dynamics experiment," J. Oceanogr. **51**(2), 145–170 (1995).
[29]A. F. K. Yeung and B. H. K. Lee, "Particle image velocimetry study of wing-tip vortices," J. Aircr. **36**(2), 482–484 (1999).
[30]N. J. Zabusky, M. H. Hughes, and K. V. Roberts, "Contour dynamics for the Euler equations in two dimensions," J. Comput. Phys. **30**, 96–106 (1979).

Experimental Thermal and Fluid Science 86 (2017) 63–74

Contents lists available at ScienceDirect

Experimental Thermal and Fluid Science

journal homepage: www.elsevier.com/locate/etfs

Interactions of a counter-rotating vortex pair at multiple offsets

Kyle J. Forster [a,*], Tracie J. Barber [a], Sammy Diasinos [b], Graham Doig [c,a]

[a] School of Mechanical and Manufacturing Engineering UNSW Australia, NSW 2052, Australia
[b] Department of Engineering, Macquarie University, North Ryde, NSW 2109, Australia
[c] Aerospace Engineering Department, California Polytechnic State University, CA 93407, USA

ARTICLE INFO

Article history:
Received 27 September 2016
Received in revised form 3 April 2017
Accepted 3 April 2017
Available online 5 April 2017

Keywords:
Aerodynamics
Particle Image Velocimetry
Vortex interaction
Streamwise vortices
Counter-rotating vortices
Vortex instability

ABSTRACT

The interactions between two streamwise vortices were investigated by wind tunnel testing of two NACA0012 vanes at various lateral offsets. One vane was spaced 10 chord lengths (C) downstream of the other, with both at an angle of incidence of 8 degrees and a Reynolds number of 7×10^4. The evolution of the vortex pair was observed until 6.5C behind the downstream vane using Particle Image Velocimetry (PIV). It was found that proximity of the upstream vortex to the downstream vane had a significant effect on the rotational rate of the subsequent vortex pair, with far offset cases having little rotation, and near field cases having angle changes of 19.6 degrees per chord length travelled downstream. At the point of vortex impingement on the downstream vane, the rotational rate dropped to near zero due to a significant strength reduction of both vortices. The point of strongest interaction was found to be laterally offset from the point of closest vortex proximity to the downstream vane by −0.15C, with the vortex on the suction side of the vane. In the offset range investigated, a significant instability was observed in only the upstream vortex. These instabilities increased as the proximity between the vortices decreased, peaking where the vortex interaction was strongest.

1. Introduction

Vortex generators operating in boundary layers, turbomachinery blade interactions, wind turbines and aircraft flying in formation can all produce vortex interactions with multiple streamwise vortices in close proximity to each other [1–6]. Streamwise vortex/structure interactions have been studied considerably less than either parallel or normal vortex/structure interactions [7], particularly relating to the effects of the upstream vortex migration. Vortices of a vortex pair have been typically deployed from the same streamwise location, limiting their proximity. However, close interactions are important conditions to understand in order to provide a knowledge base for practical vortex applications, where upstream vortices may move in locations on either side of a vortex producing obstacle, such as a wing or vane.

Interacting pairs of streamwise vortices can be classified into either counter-rotating or co-rotating configurations. Counter-rotating pairs exhibit a number of instabilities when placed in close proximity to one another, including long wavelength (Crow [8]), short wavelength (elliptic [9]) and spiral [10,11]. The Crow instability is described through a solution to a linear wave system, which describes the deviations of counter-rotating vortex pairs [8]. Once the vortex cores reach a certain proximity or cutoff distance the two wakes unify into vortex rings and rapidly breakdown. Vortices that break down or dissipate in short distances and timeframes do not have a long enough duration for waves to form, and as such are not subject to the Crow instability. Using these models, it has been found that all counter-rotating pairs are inherently unstable regarding the long wave Crow instability [12–14]. For vortices of unequal strength, the Crow instability can manifest itself at much shorter wavelengths than for an equal strength case. This has been simulated numerically using Computational Fluid Dynamics (CFD), and it has been found that a medium length instability is present where the weaker vortex is drawn around the primary vortex [15].

The short wave (elliptic) instability is identified in counter and co-rotating pairs by a streamtube in the core of the vortex with a diameter approximately half that of the instabilities wavelength. This instability is caused fundamentally by a resonance of two Kelvin waves (a sinusoidal deformation) within the vortex core as driven by the strain field induced by the other vortex [16]. Like the Crow instability, it is modified by differing axial velocity components and vortex strengths. The effect of these instabilities on migration and core size in practical upstream/downstream vortex layouts is currently unknown.

* Corresponding author.
E-mail address: kyle@forsters.com.au (K.J. Forster).

http://dx.doi.org/10.1016/j.expthermflusci.2017.04.007
0894-1777/

Nomenclature

$R_{0.1}$	average radius of vortex at 0.1 vorticity threshold	C	chord length
$A_{0.1}$	total area of vortex at 0.1 vorticity threshold	R_e	Reynolds number, based off chord length
Γ	circulation		
X_c	X core location		
Y_c	Y core location		

For free flow (unbounded) inviscid cases any vortex pair will maintain a constant core separation distance due to the conservation of angular momentum [9]. For a symmetric (equal circulation), counter-rotating case, this will mean that the pair will translate along the vortex pair centre axis, while for a case with unequal circulations there will be an orbital motion [9]. These migrations have also been observed in water tunnel testing [17], where dye marker injected into the cores of a pair of counter-rotating vortices showed a near linear trend in downwards motion of an equal strength pair. This motion increases in magnitude as vortex swirl is increased through varying the angle of attack of the vortex generation blades.

The interactions of a streamwise vortex with a wingtip at close range have also been computationally investigated [7,11]. By aligning an incident vortex with the tip of a downstream vane, the energy of the vortex system is increased in the near range, however more rapid energy attenuation occurs downstream. When the vortex is positioned inboard of the tip, it reduces the tip vortex size and strength, while placing it outboard of the wingtip enhances the wingtip vortex [7]. Reducing the distance of the incident vortex to the wingtip has been found to increase the magnitude of the turbulence production from the resultant vortex interaction [11]. It has experimentally been found that a counter-rotating wing configuration with a 2.5C streamwise wing spacing can substantially improve rear wing L/D by up to 24% at an overlap of 5% of the wingspan [18]. Such a configuration causes migration of the rear vortex towards the root of the rear wing, however the downstream consequences of these interactions have not been characterised for more than one chord length downstream. These effects have also not been evaluated at different vortex distances from the suction and pressure sides of the downstream vane.

Adverse pressure gradients produced by downstream geometries can interact with and disrupt the path of an existing vortex. A significant obstruction in the path of a vortex will cause the vortex to transition into either a spiral or bubble breakdown mode [19]. This vortex breakdown location is dependent on the swirl number (controlled by the angle of incidence of the upstream vane) and the adverse pressure gradient. If the adverse pressure gradient is not sufficient to cause breakdown, only slow diffusion of the core through viscous mechanisms will occur.

Due to the swirling nature of vortices, they act as pressure gradient amplifiers in the sense that an induced pressure gradient in the freestream will be substantially increased at the vortex core [20]. A probe placed near a vortex causes substantial upstream migration of the breakdown location [21]. As such, either Laser Doppler Anemometry (LDA) or Particle Image Velocimetry (PIV) must be used for accurate experimental results for steady vortices. However averaging point measurements can result in errors of up to 35% in tangential velocity in meandering vortex cases, emphasising the importance of a global measurement technique for meandering or unstable vortex analysis [22,23].

The work described in this paper investigates the near field interactions of a vortex produced by an upstream vortex with a downstream vane. PIV analyses have been performed for a wide variety of vane offsets at multiple downstream locations, allowing inspection of both the paths of the vortices and the meandering of the vortex pairs. Characterisation of near-field counter-rotating vortex interactions has been achieved, and the effects of generating a vortex in a flow field with a pre-existing vortex structure are found.

2. Experimental setup

The present study considers the interaction of two streamwise vortices produced by two NACA 0012 vanes. One vane was located 10 chord lengths (C) downstream of the other, as can be seen in Fig. 1. This configuration was chosen as it allows interactions between vortices to occur at extremely close proximities that cannot be observed if the vortices are deployed at the same locations. This is also representative of the effects of a pre-existing vortex in a flow interacting with a vortex producing device. An angle of attack of 8 degrees on each vane has been used for all cases, with a square-edged tip. Higher angles of attack decreased the vortex stability, with unsteady breakdown becoming observable for a single vortex case at 12 degrees. Multiple offsets were tested from −0.6C to 0.5C in increments of 0.1C, with a finer spacing of 0.05C between −0.4C and 0C.

The x-axis is in the direction of the flow, with positive downstream, the Y axis is across the tunnel and the Z axis is in the vertical direction. As such, the rear vane quarter chord was located at $X = 10C$, with the vane root at $Z = -1.5C$.

Planar slices of the flowfield were captured using PIV at 0.5C intervals from 1.5C back from the quarter chord of the trailing vane to 7C back. These correspond to 11.5C and 17C from the leading vane respectively. The laser sheet was not moved closer than 11.5C as the reflections from the vanes began to distort the results. The experiment was performed at a Reynolds number of approximately 7×10^4 based on chord length. At 7×10^4 the vortex shedding from a NACA0012 airfoil at 8 degrees angle of attack is within the supercritical region [24] and therefore any Reynolds number lower than 6×10^4 at this angle of attack will result in a shedding regime that is not indicative of higher Reynolds number scenarios. Running the tunnel as slow as possible within the acceptable Reynolds number range minimised vibration of the diffuser expansion, camera mounting and test section caused by the operation of the fan, thus minimising imaging errors.

2.1. Wind tunnel

Experiments were performed in the Macquarie University open return, closed section wind tunnel. This tunnel has a 610×610 mm (24×24 in.) octagonal test section with a 1900 mm (6′ 3″) length. Optical access is through a glass window on the top of the test section and removable windows on the side. The test section was characterised using a Turbulent Flow Instrumentation 100 Series Cobra probe, giving a peak turbulence intensity of 0.35% and average of 0.25%. Velocity uniformity was measured as better than 1% variance, and flow angularity was found to vary by 1 degree across the test section inlet. The wind tunnel speed was electronically controlled through a National Instruments MyRIO, with the pressure sensors calibrated against a temperature

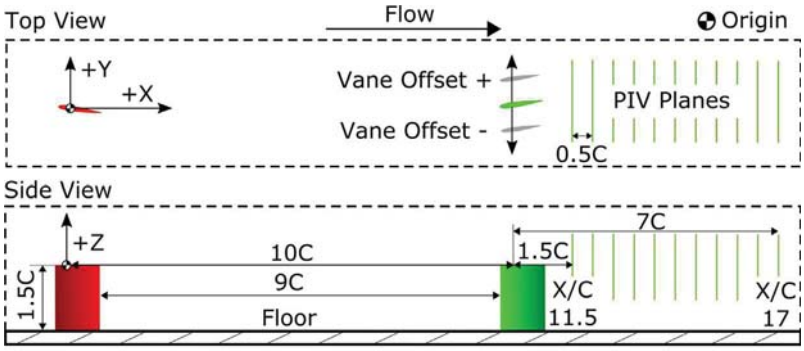

Fig. 1. Vane layout diagram, origin is at quarter chord tip of front vane.

controlled Baratron 120AD Differential Capacitance Manometer. Streamwise velocity variance was held to within 0.38%.

A separate elevated ground is mounted to the floor of the tunnel with a rounded front splitter to minimise the effects of the pre-existing layer in the test section. This ground is mounted 100 mm above the tunnel floor on two steel rails. To reduce the influence of secondary structures resulting from horseshoe vortices or boundary layer stripping, the vanes were sized to be significantly taller than the boundary layer. This prevents strong interactions with these secondary structures, allowing the study to focus on the interactions of the two tip vortices. The vanes have a chord of 80 mm and a span of 120 mm, and are painted matte black to minimise reflections.The boundary layer at the location of the rear vane was experimentally measured to be 5 mm thick at 80% of the freestream velocity and 20 mm thick at 95% of the freestream velocity. A schematic of this setup can be seen in Fig. 2.

2.2. PIV setup

A planar two component PIV system was used to capture the vortex dynamics. Due to the large expansion length of the Macquarie University wind tunnel, the camera was placed inside the expansion itself rather than using a mirror system. This allowed the camera to be positioned 2100 mm downstream of the test section and 2380 mm to the nearest image plane, giving a maximum perspective bias of 1.6 degrees per side on a 133 mm wide observation plane with a 120 mm lens. Planar PIV can produce projection errors when the out of plane motion is dominant [25]. However, this can be substantially reduced by lowering the perspective error from the camera, reducing the motion to as close to the in-plane component as possible. For the comparison setup 2D and stereoscopic PIV of Yoon and Lee [25], it was found that a camera with an effective perspective angle of 5.71 degrees per side could produce an absolute maximum error of 20.8% in instantaneous in-plane velocity where the out-of-plane component was proportionally large in a vortex driven flow. By reducing this angle to 1.6 degrees through placing the camera much further away and using a zoom lens, as per the setup described in this paper, the maximum projection error is reduced to 5.8% under the same conditions. It should be noted that this error is at the edges of the observation window, and is not indicative of the errors near the centre, which will approach zero projection error as the centre is reached. The resultant vorticity field is consequently less affected due to the steepness of the velocity gradients in the core of the vortex as opposed to the shallow gradient of projection error induced velocities. By superimposing the calculated projection error of a uniform streamwise velocity field on the captured time-resolved PIV data, the error in peak vortex core velocity was found to be below 4% against the absolute velocity field, with an imperceptible change in the vorticity field. This resulted in a negligible change in the calculated core location and circulation. Focus was controlled remotely. By placing the camera this far downstream of the test section, there was no observable difference to the flow in characterisation measurements obtained through the tunnel section. The expansion section of the tunnel was on isolated mounts from the tunnel fan, minimising vibration. Over a test of 200 image pairs, the tip of the rear vane was found to have a maximum displacement change of 1 pixel during the entire sampling time.

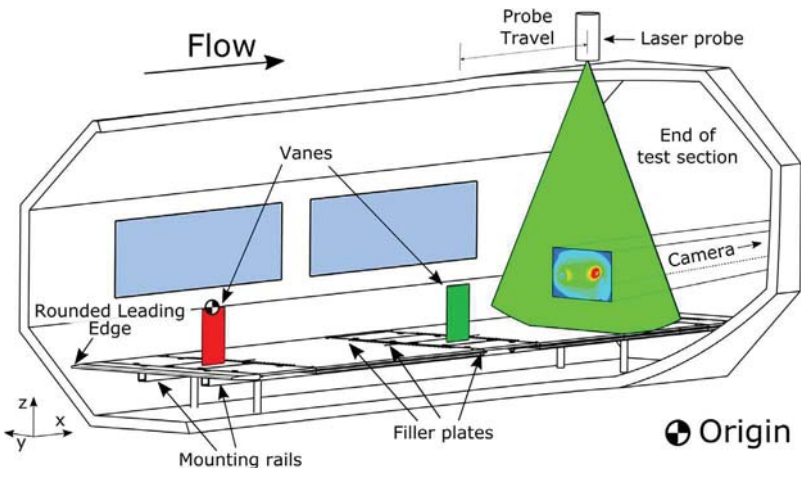

Fig. 2. Cutaway diagram of tunnel test section.

Tracking of camera vibrations between images of an image pair was performed through a Gaussian fit tracking of the illuminated wingtip while the tunnel was running. This yielded a vibrational displacement maximum of 0.0471px between the two images of a pair, which is within the margin of error of Gaussian subpixel tracking of just below 0.1px at low signal to noise ratio as identified by Saunter [26].

Laser access to the tunnel was through a glass window in the top of the test section. The laser beam was sent to this location via a periscope connected to a Dantec 3-axis computer controlled traverse. This traverse was restricted to only allow laser sheet movement along the axis of the tunnel. The laser used was a dual-cavity Nd:YAG laser (Quantel EverGreen) with an output of 200 mJ per pulse at 532 nm wavelength and a repetition rate of 15 Hz. Synchronisation between laser and camera was performed with an ILA synchroniser. Laser pulses were delivered at 55 μs apart as any higher resulted in significant out of plane migration of particles. This is equivalent to a downstream movement of 0.665 mm per particle at the freestream velocity. The laser sheet thickness varies throughout the observation window as a result of the focus, with an average thickness of approximately 4 mm through the region of interest. This large thickness was selected to minimise the amount of out-of-plane pair loss [27], with the laser being run at maximum power to compensate for the reduced sheet intensity. By combining this thickness with the short pulse separation of 55 μs and a high particle seeding density the effective number of particle image pairs in the interrogation window was kept above 10, giving a greater than 98% valid detection probability [27], thus being sufficient to compensate for the predominately out of plane flow component. Validation of post-processed data was performed by excluding points with vorticity gradients from the surrounds greater than 500 $\frac{1}{s.mm}$.

Seeding was performed with a PIVtech generator using Di-Ethyl-Hexyl-Sebacat (DEHS) air soluble particles of 0.2–0.3 μm typical diameter. This gives a Stokes number of approximately 2×10^{-5}, indicating the particle size is sufficiently low to follow all flow streamlines accurately [28].

Scattered laser light was captured by a monochrome cooled CCD pco.1600 camera with 1 GB of RAM. Images were digitised at 14 bits, with a resolution of 1600x1200 pixels. The camera was fitted with a 120 mm lens. The CCD size on the camera was 12.5 mm wide × 9.38 mm high, giving a field of view at the most downstream plane of approximately 100 × 133 mm.

Image analysis was performed with PIVView software. Multi grid interpolation was used, starting at a coarse grid size of 128px × 128px windows and finishing with refinement to 32px × 32px over 3 passes. Standard FFT correlation was used, with two repeated correlations on 16px offset grids being performed resulting in minimal in-plane loss of pairs. Subpixel shifting was enabled on all passes with b-spline interpolation and peak detection by a Gaussian least squares fit from 3 points. The final grid size was 99 × 74 nodes.

Calibration of the camera was performed using a grid that was photographed at all analysis plane locations, compensating for the increase in plane size due to perspective. The plane was located using the laser sheet, and then photographed to give an accurate scale.

2.3. Sources of error

Sampling error for averaged results was determined to be 3.7% in circulation and 0.0035C in location for the 400 total shots taken against a multiple representative sample of 2000 image pairs. Due to the nature of the manual focussing system there were induced errors, with differences in focus able to produce up to 0.04C error in core location. By implementing a particle pixel size threshold of no more than 2 px at a brightness level of 4.5% of the total dynamic range, this error was reduced to 0.0015C in core location. Total error due to the calibration plane procedure was found to be a maximum of 0.18% in location and 0.22% in scale, due to minute differences in lateral calibration plane location. Seeding levels in the room were convergence tested such that the error from the seeding were not discernible from the randomness induced by the other errors. Spatial convergence was ensured by evaluating the −0.2C offset case at half the interrogation window size, effectively doubling the spatial resolution. This yielded errors of ±2.7% in core radius and ±0.0026C in location across the averaged sample size for the zoomed out condition used. As previously discussed, camera vibration was not observed at an appreciable level, with a maximum image migration of 0.06% measured over the course of an imaging run. The particle size was measured at an average of 1.5 px, giving an uncertainty in position of 0.03 px [27]. Quantization errors were negligible due to 14 bit quantization. Any biases inherent in each run were minimised by having the each set of 400 images taken with one forward run of 200 images (plane moving from X17 to X11.5) and one backward run in the opposite direction; this way any errors in seeding or focus would be minimised. The total error in core location was found to be ±0.008C.

3. Results and discussion

Vortex radii can vary by up to 35% from instantaneous results if time averaged results are used due to vortex meandering and local fluctuations in velocity [22]. In addition to this, the velocity field will be smoothed, resulting in significant deviations in circulation and core size if time averaged results are used. However, it is still desired to have average values for core location, size and strength, and as such the results were analysed by a script based evaluation of each individual pair of images. These images were sequentially analysed in Matlab, with peak noise filtered by vorticity gradient as previously mentioned. To eliminate the influence of vortex shedding and low level noise on the calculation of tip vortex properties, all vorticity constructs except the tip vortex were filtered out. This was performed by computing contours at 10% of the peak vorticity and calculating the area enclosed by each individual structure. All structures except the largest were then eliminated, leaving only the tip vortex. The positive and negative vortices were evaluated separately, giving the positive and negative circulation magnitudes, location of the positive and negative vortex cores, and core radii. These data points were then combined and analysed for average values and variances. This allowed for an accurate calculation of instantaneous core size, as well as time-averaged values that could be used to represent the core characteristics and allow comparison between cases.

3.1. Core paths

The vortex centre within a plane is defined as the integral of the vorticity multiplied by the displacement, divided by the circulation [9]. This can be seen in Eqs. (1) and (2).

$$X_c = \frac{1}{\Gamma} \int X \omega dS \tag{1}$$

$$Y_c = \frac{1}{\Gamma} \int Y \omega dS \tag{2}$$

While this does not always align with the location of zero in-plane velocity, it allows for consistent prediction of the centre of circulation intensity even when the vortex pair is migrating with an in plane motion, which would otherwise skew the core location

significantly. It is also more robust than simply using the value of peak vorticity, as it is not significantly skewed by asymmetrical vortices or vorticity peaks in the result. As previously mentioned, these values were calculated at all image pairs, then averaged in Matlab. An example of the averaging is given below in Fig. 3. From this data, the core paths can be compared between cases.

Inspecting a selection of paths from across the cases investigated, as seen in Fig. 4, a basic migration trend emerges. At the far ends of the range (−0.6C and 0.5C) the migration is near linear, and predominantly vertical. At the negative end of the spectrum, the paths move upwards, while at the positive end they move downwards, similar to the theoretical predictions of Lewecke et al. [9]. This is due to the shear between the pair being minimal due to complimentary rotation, while at the periphery of the pairs there is no such rotation. This causes a shear between the vortex pair and the freestream flow, resulting in the migration of the vortex pair in the opposite direction to the outer velocity of the vortices, as can be seen in Fig. 5. At closer offsets, the motion is less vertically dominated, and takes on a more significant lateral component, as well as a significant rotational motion between the vortex pairs. As the configuration transitions between predominantly vertical motion to predominantly lateral motion, the magnitude of the migration increases significantly, as can be seen by the 80.5% difference between the 0.5 and 0.2 case. This is followed by a significant drop of 27.2% in the total migration between the 0.2 and −0.05 cases as the vortices interact more closely. The same effects can be seen on the negative side as it approaches the point of interaction, from −0.5 to −0.25.

The positive offset case vortex paths are shown in Fig. 6. At the maximum offset (0.5C), the vortex pairs have little interaction, with minimal deviation in their paths. The separation between the vortex pair alters approximately linearly in the same amount as the variation in offset between the vanes. For this range of offsets the vortex pair separation does not significantly vary from the start to end of the domain, with the spacing increasing by an average of 0.024C. The progressive increase in vortex pair migration as the vortices are brought together can also be seen in this figure, with a progressive increase in vertical migration from the 0.5C to 0.1C cases of 0.19C (101%).

At the 0.1C case, a rotation of the vortex pair has become evident, with significant curvature apparent to both the upstream and downstream vortex paths. This curvature occurs as a result of a differential in vortex strengths in the pair. As the circulation is higher on the downstream vortex, the weaker vortex is drawn into a rotational path around it. This results in a direction of rotation in the direction of the stronger vortex, despite the fact that its downwards shear is higher than that of the weaker vortex due to its increased circulation. Consequently, the path of the weaker (upstream vortex) is significantly longer than the stronger vortex, with a total migration of 0.660C as opposed to 0.522C for the downstream vortex. This can only occur when a combination of conditions are met, both the vortex proximity being sufficiently close to produce significant interactions of the high vorticity core regions, and the differential in strengths between the vortices being sufficient to promote rotation. With both cores having an average $R_{0.1}$ of 0.146C and the vortex separation distance between the cores being 0.274C, this would indicate that significant vortex interactions which affect the strength of the upstream vortex begin to occur at a vortex spacing approximately equivalent to $2xR_{0.1}$. This is the spacing where the two vortex radii would just be intersecting.

As the upstream vortex passes closer to the rear vane, the rotational and horizontal migration of the vortex pair significantly increases. This can be seen in Fig. 7. With no rear vane the upstream vane's vortex core was located at approximately −0.1C. This means the upstream vortex would pass by the downstream vane without direct impingement in the −0.3C and −0.25C cases. However, as the offset is further reduced (−0.15C and −0.1C) the upstream vortex will impinge on the downstream vane. This causes a reduction in the path lengths of both vortices, and

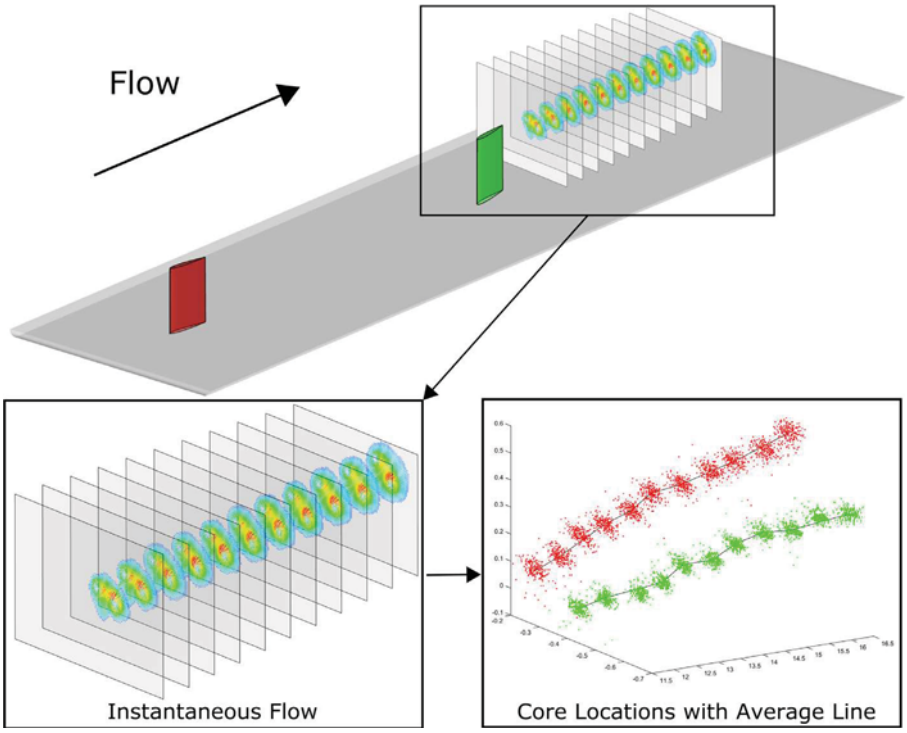

Fig. 3. Velocity vectors coloured by velocity magnitude (left), converted to vortex core locations for all planes and image pairs (right) with black line through core average locations.

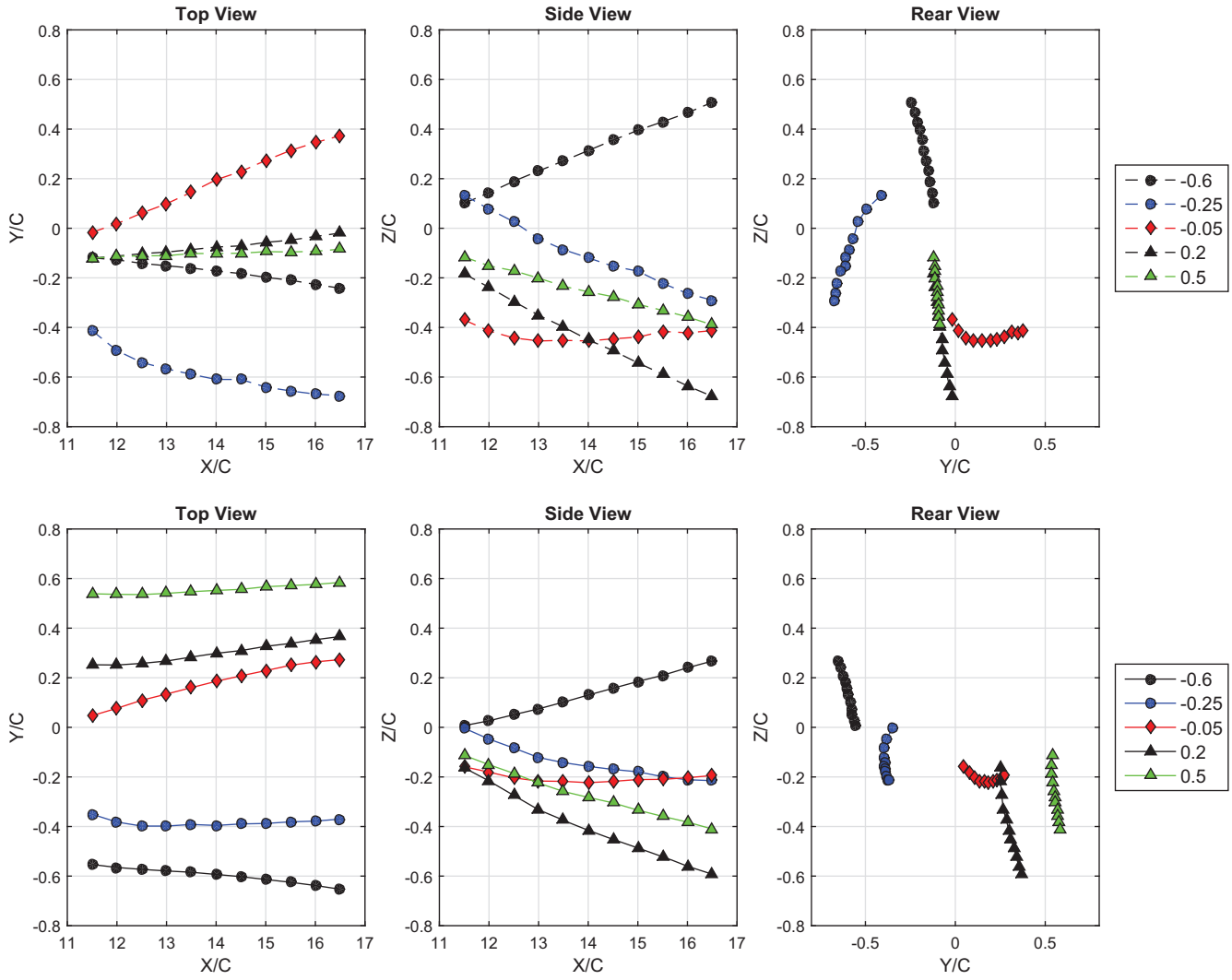

Fig. 4. Paths of upstream (dotted) and downstream (solid) vortices. Note the scale difference between the top and side views. Error in core location is ±0.008C.

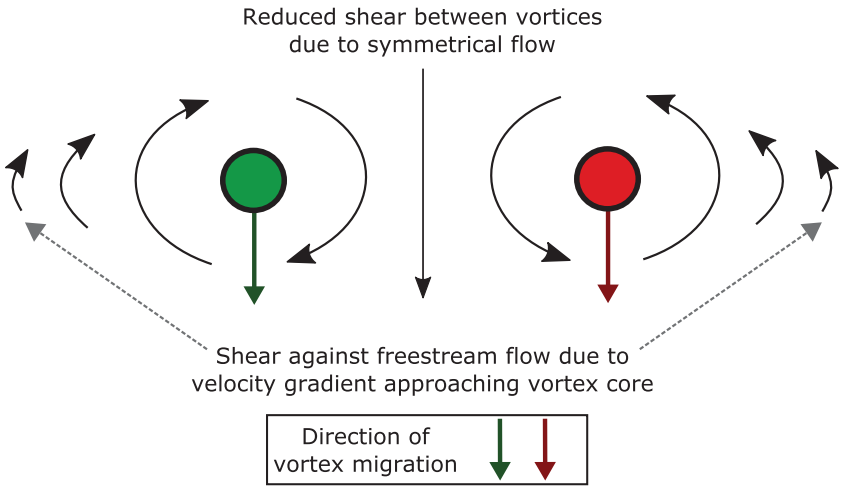

Fig. 5. Schematic of vortex core migrations for equal circulation counter-rotating cases.

increases the separations. At the −0.2C offset the $R_{0.1}$ of the upstream vortex marginally impinges on the suction surface of the downstream vane. This has caused a reduction in downstream path length from 0.216C to 0.128C. As such, the interaction between the downstream and upstream vortices post vane must

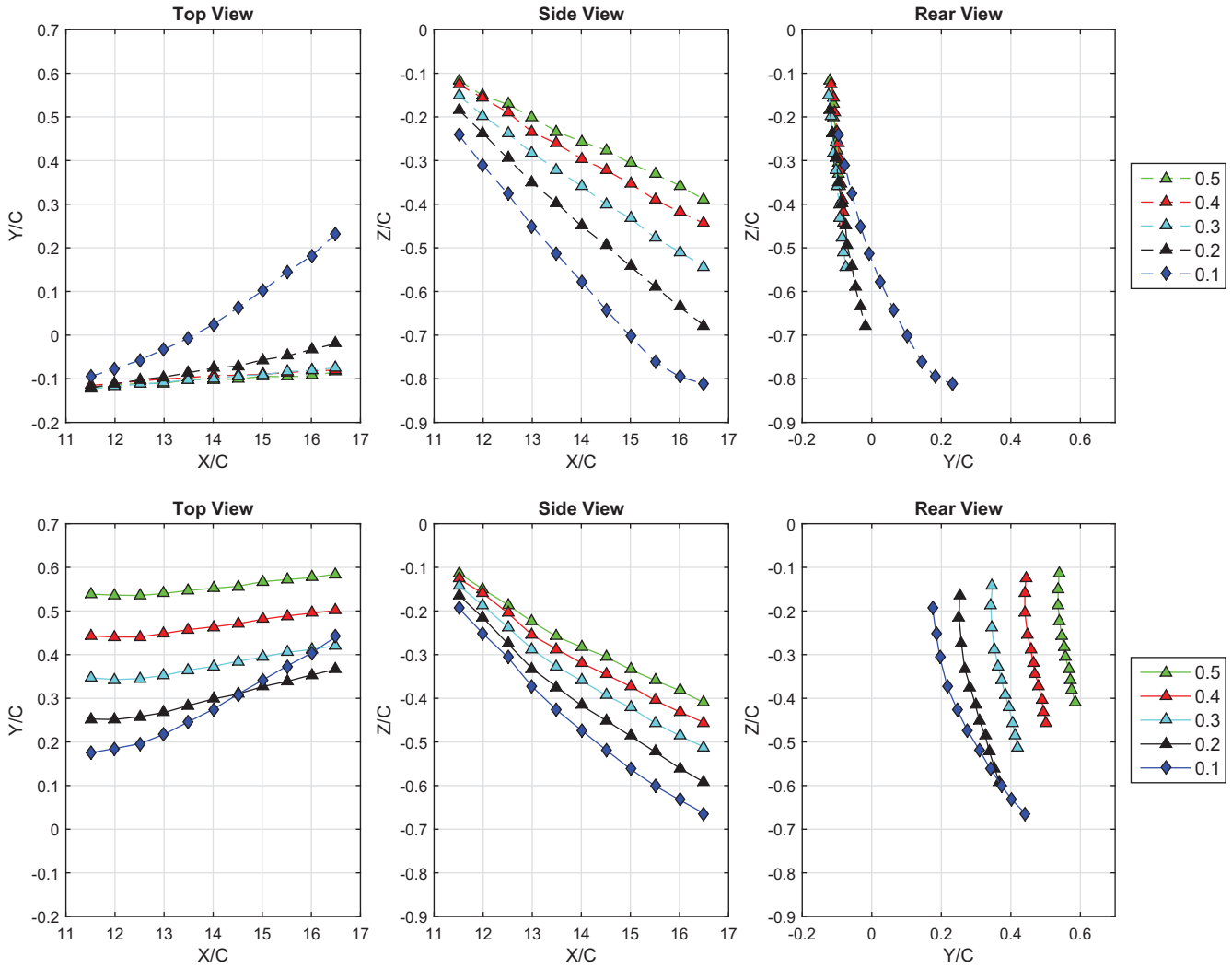

Fig. 6. Paths of upstream (dotted) and downstream (solid) vortices. Note the scale difference between the top and side views. Error in core location is ±0.008C.

be strongest at −0.25C, while the point of impingement is located at −0.1C.

The rate of rotation by which the two vortices orbit each other was calculated through a linear approximation of the change in angle of the line drawn between the two vortex cores. This can be seen diagrammatically in Fig. 8. By looking at these rotational rates in Fig. 9, it can be seen that the lowest angular core velocities are achieved at −0.1C, the point where the upstream core would impact the quarter chord of the downstream vane if no deviations occurred as a result of the presence of the second vane. Rotational rate peaks occur at −0.2C and 0C, at peaks of 19.57 and 17.74 degrees/C respectively. The peaks are caused by a combination of high strength interaction and close vortex proximity. Of interest is the increased rotational rate of the −0.2C case compared to the stronger interacting −0.25C case. Closer inspection revealed that the −0.2C rotation was high at the start of the domain, however rapidly reduced after X14, while the −0.25C case remained near constant. As such, the partially impinged interaction of the −0.2C offset causes a strong initial interaction as it affects the vortex formation. However, the −0.2C interaction causes a more rapid reduction of the vortex strengths as they progress downstream, with a subsequent reduction in rotational rate, while the −0.25C interaction shows far less reduction. Between −0.35C and 0C there are the most significant gradients of rotational rate due to the transition of the upstream vortex location around the vane. On the negative side of this rotational peak the rotation rates trend towards the values seen on the far positive regions, as would be expected as the vortex separations become significant again.

The initial vortex separations between the vortex pairs remain relatively consistent through the range of near field interactions from −0.35C to −0.2C, however dip slowly, and then drop to their lowest separation at −0.25C. While the initial separations decrease towards the −0.25C offset, the final separations remain far more constant until −0.15C offset. This indicates that for a given vortex core size the vortices will attempt to reach an equilibrium separation distance, in this case approximately $1.6R_{0.1}$. The initial core spacing in the −0.25C case is the smallest, at approximately 1 core radius. Bringing the vortices closer than this will begin to destroy the upstream vortex significantly. As the upstream vortex impinges on the vane it causes the vortices to increase both their initial and final separation distances, as can be seen in the points from −0.2C to −0.1C. At the point of complete impingement the separation has become largest, and the rotation smallest, indicating that this is no longer a point of significant interaction, but rather the downstream vane has significantly reduced the strength of the upstream vortex during the direct vane/vortex interaction. This configuration also displays a smaller difference between the initial and final separations than the surrounding points on the

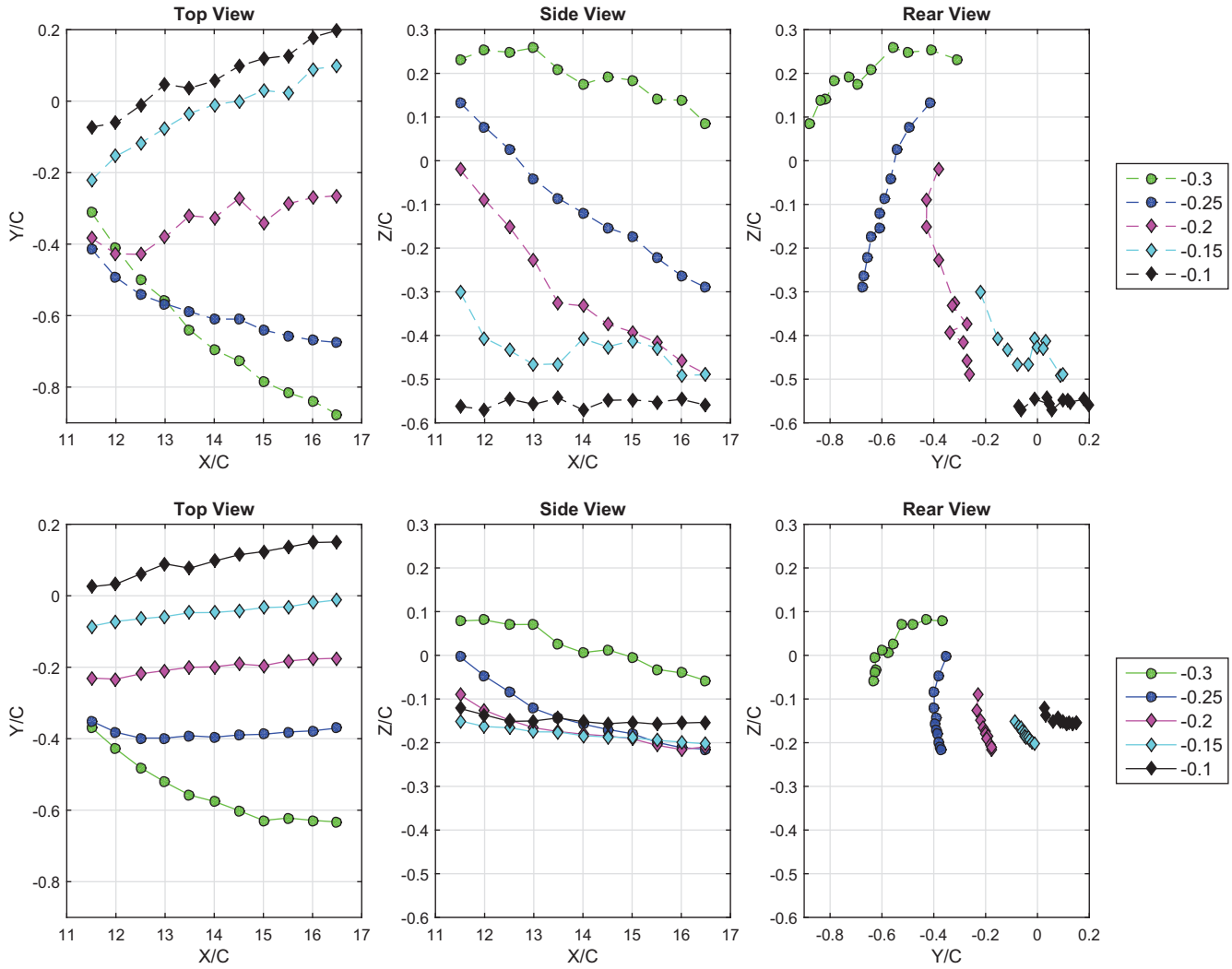

Fig. 7. Paths of upstream (dotted) and downstream (solid) vortices. Note the scale difference between the top and side views. Error in core location is ±0.008C.

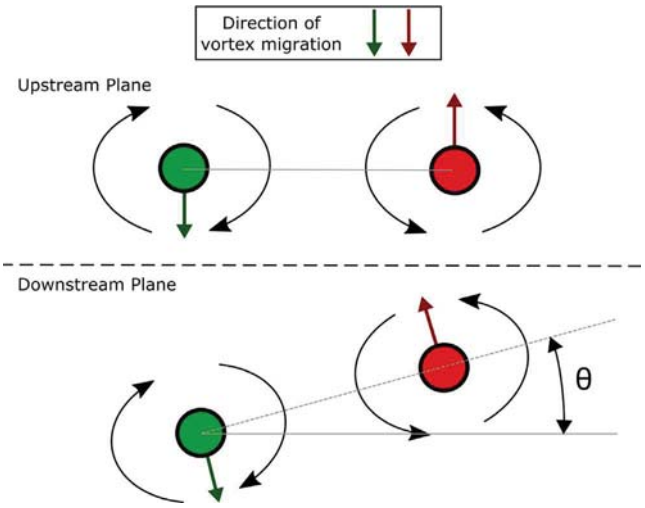

Fig. 8. Schematic of rotation angle calculation for vortex pairs.

negative side as the vortices have reached a steady equilibrium state in the flow and the subsequent interactions are weak.

3.2. Core sizes

While the vortices remain near a uniform Lamb-Oseen distribution at the far offsets, at nearer offsets significant partial straining occurs from the influence of the vortex interaction. This causes a skew in the shape of the vortex core that changes its primary axis as the vortex pair rotates downstream. This prevents the fitting of a Lamb-Oseen distribution of vorticity to the results. Consequently, to calculate the core radius, the area bounded by the isoline of 10% of the peak vorticity within the plane has been used in both the positive and negative circulations, as used by Manolesos [29]. While this area can vary significantly from a circle, an effective radius can be calculated from Eq. (3) by assuming approximate circularity.

$$R_{0.1} = \sqrt{\frac{A_{0.1}}{\pi}} \tag{3}$$

The removal of noise from the data via the previously mentioned filtering ensures that only the area of the core itself is processed, and not the surrounding flow features or noise outside the core. By comparing this method to a Lamb-Oseen approximation, it was found that the spatial sampling resolution could result in a 15% maximum error in peak vorticity. This translated to a 1.5% maximum error in the 10% peak vorticity, giving a maximum core

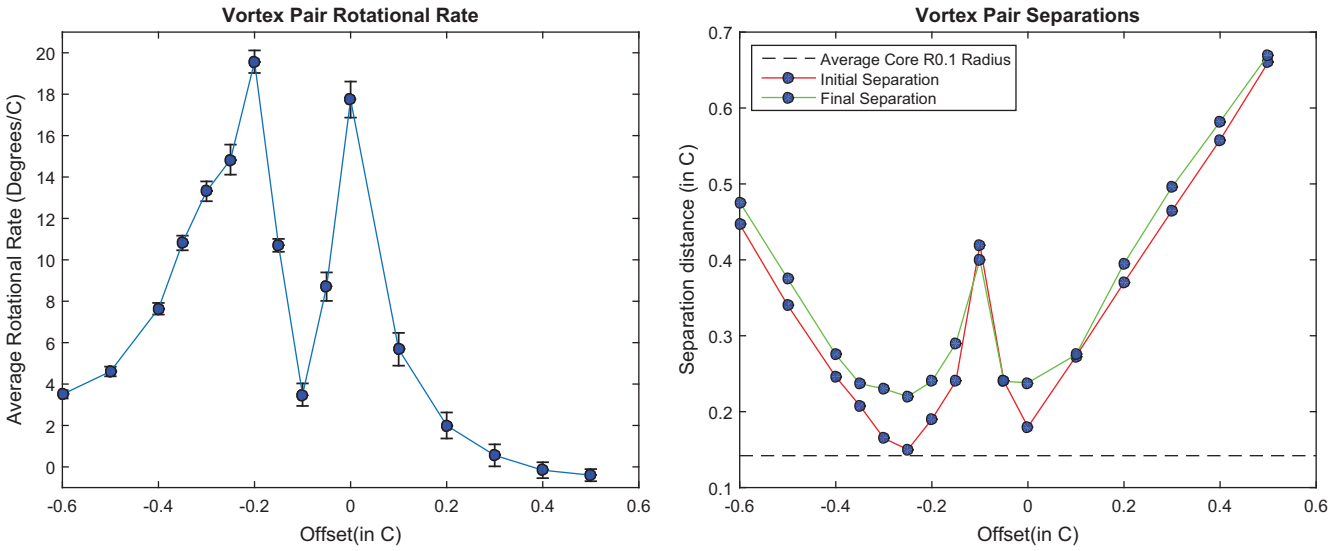

Fig. 9. Rotational rates of the vortex pairs (left) and average vortex separations (right). Error in vortex separation is ±0.005C.

radius error of 5% per image pair, which was considered acceptable for this analysis. This was confirmed by evaluating the −0.2C offset case at double the spatial resolution as previously mentioned, yielding errors of ±2.7% in core radius across the averaged sample size.

Initial and final values for core radius were calculated by linearly approximating the gradients of core radius across the domain, reducing the effect of statistical variance on the measured sizes. These core radii can be seen below in Fig. 10.

At the −0.3C offset a significant reduction in initial core radius can be seen for the downstream vortex. However, as these progress through the domain the downstream vortex grows in size by 0.024C, while the upstream vortex radius decreases by 0.025C. This is the only near-field interaction case observed to have a significant trend of growth in the downstream vortex, and is also a local minima before the increase in initial downstream vortex size to the peak at −0.2C offset. Between −0.25C to −0.2C, the previously identified peak of vortex interaction, there is a transition from a larger initial upstream radius to a larger initial downstream radius. While this change is small in magnitude, the final downstream vortex size peak at the −0.25C case has a more significant change, indicating that the strong interaction has resulted in the transfer of energy from the upstream vortex to the downstream vortex throughout the domain, causing an increase in the size of the downstream vorticity field.

As the interaction approaches the point of impingement, the final size of the upstream vortex decreases to a minima at −0.15C. As the upstream vortex moves closer to the tip, its strength is significantly reduced by the counter-acting vorticity, resulting in these decreases in core size. At the point of impingement (−0.1C) there is a marked decrease in downstream vortex cores size. However, the upstream vortex size has increased by 17% at this point from the −0.15C case. The reason for this was not apparent from the results, however it is likely related to the downstream vortex stripping vorticity from the upstream vortex when slightly offset, while in the direct impingement case the downstream vortex itself is significantly weakened, and as such cannot draw energy from the upstream vortex as successfully. As the offset increases towards the positive side, there is a steady increase in the final core

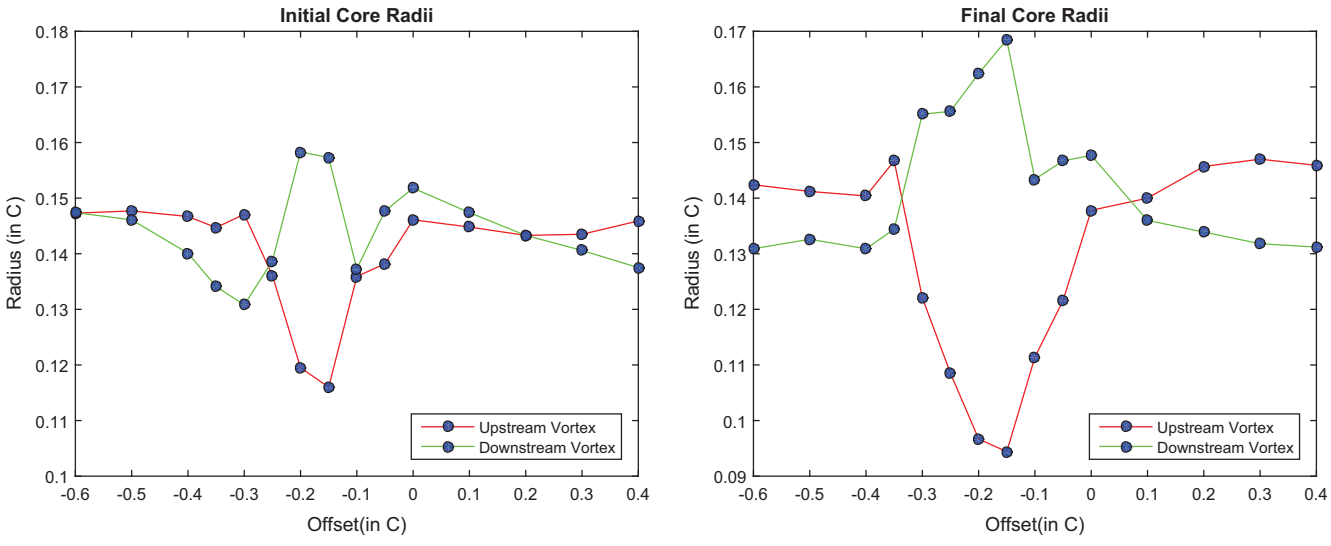

Fig. 10. Core radii for all cases at X11.5 (Initial, left) and X16.5 (Final, right).

radii for both the upstream and negative vortices, with less clear trends in the initial size.

3.3. Vortex meandering

In addition to the circulation and core location changing as the vortices pass through the domain, they also vary with respect to time. Vortex meandering is the phenomenon of random vortex motions and oscillations that result from any turbulent vortex flow. While the origins of meandering are disagreed upon [7,30–32], it is still important to characterise, as it changes the predictability of the flowfield, particularly in real world scenarios. Given the large and effectively random sample of image pairs taken, the statistics of the variance of both circulation and core location can be used for analysis of the meandering magnitudes. While the period, frequencies and amplitudes of small oscillations cannot be evaluated with non-temporally resolved data, the total magnitudes of displacements and the location distribution of the meandering can be determined with non temporally resolved data and a sufficiently large sample size. Such methodology has been used by Miller et al. [33] and Rokhsaz [34] at 30 Hz, as well as Heyes et al. [35] at 5 Hz. The core variance was calculated as the standard deviation of the radial distance from the average core location, while the circulation variance was calculated from the standard deviation of the difference from instantaneous circulation to average circulation, divided by the average circulation on the plane. The division by the average circulation was used to remove bias caused by low circulation cases and planes, as this would lead to low circulation cases seemingly having less fluctuation magnitude.

Inspecting the core variances in Fig. 11, it can be seen that the natural tendency of the cores in the far interacting cases is to maintain a near constant meandering magnitude throughout the domain investigated. From the 0.2C to 0.4C cases it can be seen that the end variance is less than the start variance for the downstream vortices, and very similar for the upstream vortices, showing that the initial meandering motion is be caused by the formation of the vortices. The shear layers shed off the vanes may provide the initial perturbations, resulting in the fluctuating deviation of the core location. As the flow travels further downstream, these spanwise vortices will be dampened out by viscous effects, as well as flow entrainment into the streamwise vortices. These vortices are too far apart for the Crow instability to have a significant effect within this domain. This explains the reduction of the meandering magnitudes as the vortices progress.

As the interactions of the vortices become stronger, their meandering magnitudes significantly increase. Between −0.2C and −0.05C the start variance of the upstream vortex significantly increases. This is in the region of the upstream vortex $R_{0.1}$ intersecting the suction side of the downstream vane. At −0.1C offset there is a peak variance of 0.17C, which is greater than $R_{0.1}$. This indicates that in near field interactions the upstream vortex is fluctuating from one side of the vane to the other, creating a large spread of core locations. This increase is co-incident with the reduction in vortex pair rotation angle between −0.2C and 0C. The downstream vortex is far less affected by these variations, with a maximum increase in start variance of 0.0196C over the case with the least variance.

While the start variance is proportional to the proximity of the incident vortex to the downstream vane, the end variance is more dependent on the magnitude of the interaction. This is particularly true for the downstream vortex, which achieves a variance peak of 0.155C at −0.3C offset and a significant increase in meandering from −0.35C to −0.15C. This is accompanied with a wider spread of meandering in the upstream case, with significant increases in meandering once the vortex separation drops below 0.275C (-0.4C and 0.1C offsets). These downstream vortex proximities are sufficiently close to allow for instabilities to be formed between the vortices, creating the meandering observed. In both vortices, the peak in variance at the downstream end of the domain occurs at a more negative offset than either vortices start peak. This indicates that the low pressure region on the suction side of the downstream vane and resultant adverse pressure gradient is enhancing the instabilities of the vortex pair further downstream.

Further investigation of the nature of the meandering shows a clear instability in the upstream vortex, as can be seen in Fig. 12. At larger offsets (0.3C in figure) the presence of any sinusoidal deviation is minimal, with only a slight skew observed in the upstream vortex. As the offset is brought closer (0.1C) a clear deviation of points at approximately 45 degrees to the line between the vortex centres can be seen. This is indicative of a sinusoidal deviation, similar to the uneven Crow instability previously identified in computational work by the authors [11]. The deviation is far more prominent for the upstream vortex than the downstream vortex, which has an approximately circular distribution of locations. The reason for this inconsistency was not apparent from the

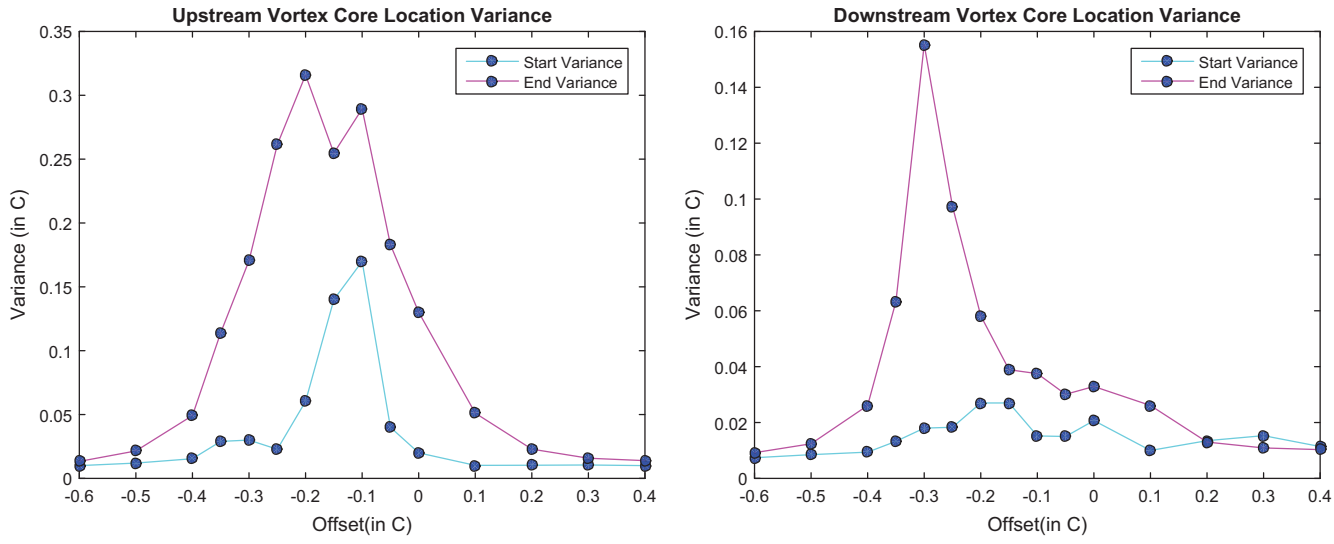

Fig. 11. Core location standard deviation of upstream vortex (left) and downstream vortex (right). Note the scale difference between the two plots.

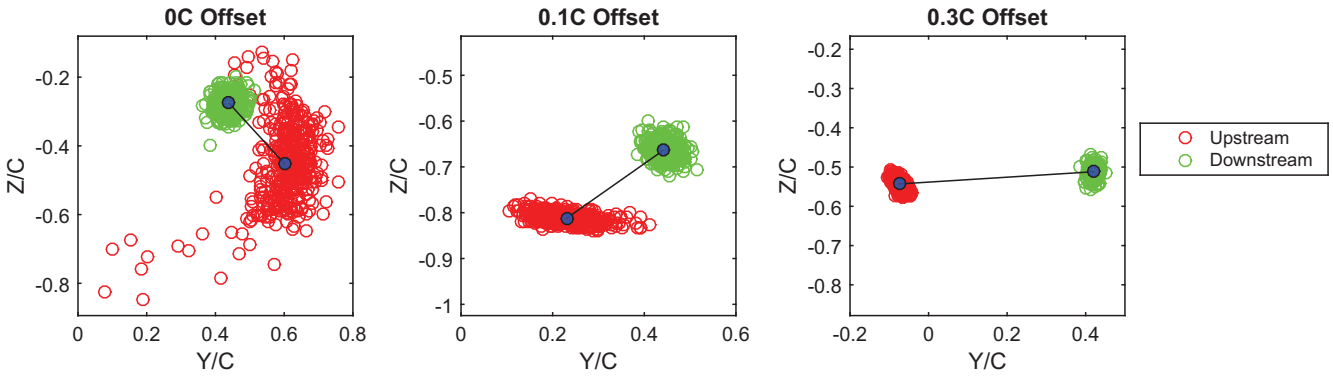

Fig. 12. Core locations of upstream (red) and downstream (green) vortices for 0C, 0.1C and 0.3C offset cases at X/C = 16.5. (For interpretation of the references to colour in this figure legend, the reader is referred to the web version of this article.)

results, however it is likely due to the longer path of the upstream vortex, in addition to reduced vortex strength from the initial vane/vortex interaction. As the offset is further reduced, the upstream vortex is drawn into the velocity field of the downstream vortex, resulting in a curvature of its sinusoidal deviations. This can be seen in the 0C offset of Fig. 12. The same trends were seen when approaching the vortex impingement from negative offsets.

The variances in circulation followed similar trends to that of the core location, so are not presented here. The consistency in these trends indicates that the damping mechanisms which smoothen out the location meandering in the far offset cases also calm the fluctuations of the vortex strength. As the increased swirl velocities of high circulation will be reduced more rapidly by shear than the lower velocities associated with low circulation, it is expected that these fluctuations would be reduced as the vortices pass through the flowfield, as long as there is not a significant instability present. Of more interest is the increase in circulation variance near the points of higher interaction. In the near field, the normalised circulation variances were increased by 0.078 (75%) and 0.428 (471%) for the downstream and upstream cases respectively. In the far field, these variances were increased by 0.20 (171%) and 0.4551 (932%) for the downstream and upstream cases respectively. This indicates that the close interactions are influential in the magnitude of the circulation fluctuations well downstream from the initial interaction of the vortex with the vane. As such, the interactions of the vortices with one another can be observed to destabilise the cores and enhance the energy transfer between the vortices.

4. Conclusion

Wind tunnel experimentation has been performed to characterise the behaviour of the downstream interactions of the vortex pair produced by two offset vanes, spaced 10C apart in the streamwise direction. 1.5 aspect ratio NACA0012 wings at 8 degrees angle of attack and a Reynolds number of 70000 were used for this study. Several lateral offsets were used to examine the effects of vortex proximity on the resulting vortex sizes and paths.

For far positive offset cases, the vortex pair migrated downwards, while for far negative offsets the pair migrated upwards. No vortex rebound was observed within the domain, indicating the vanes were sufficiently high above the floor to be free of ground effect. At close offset cases, the motions of the vortex pairs shifted from predominantly vertical to predominantly lateral, with increased rotation of the pairs. The rotational rate of the vortex pair had two peaks at −0.20C offset and 0C, with a minima at −0.1C, the point of core impingement. This is consistent with the location of the core with no downstream vane present. At this point the size and strength of both vortices has been significantly reduced as a result of the destructive interference in the formation stage of the downstream vortex. This is responsible for the low rotational rate. −0.25C produced the strongest interactions, with the second highest rotational rate and highest vortex size changes, combined with closest vortex pair proximity. The separation between the vortices in this condition was approximately $R_{0.1}$. This indicated that placing a vortex one core radius from the suction side of a vane is preferable for maximum interaction strength, while impacting the vortex on the quarter chord causes the most significant vortex destruction.

The vortex meandering was found to be dependent on the proximity of the interaction, with closer proximities producing higher meandering levels. The strength of the shear layer shedding and instabilities introduced by the unequal strength interaction were found to be significant factors. The meandering magnitudes were found to be more closely related to the strength of the interaction than the destruction of the vortices, with the −0.25C case having the largest meandering magnitude and steady decreases on either side of this. Downstream vortex meandering was found to be more sensitive to the strength of interaction than the upstream vortex, with a typically lower meandering growth at further offset cases. Near offset cases produced a clearly observable instability in the upstream vortex only, with the 45 degree deviations being drawn around the stronger vortex in a curved manner as the separation distance was reduced. Circulation fluctuations followed similar trends, demonstrating a link between circulation and core location in meandering.

The rich dynamics observed and large changes in vortex state resulting from small offset changes near the point of impingement indicate that the traditional method of exploring only 3 or 4 offsets may not be sufficient when predicting the paths of a counter rotating pair produced in this manner. The presence of vortex meandering over longer distances would further amplify this problem, as the transient changes in location of the initial vortex prior to interaction with the downstream structure will result in large changes of the resultant pair's location and size. As such, in systems where consistent vortex behaviour is required, the counter-rotating pair should be spaced at as high an offset as feasible.

References

[1] K.J. Forster, T.R. White, Numerical investigation into vortex generators on heavily cambered wings, AIAA J. 52 (5) (2014) 1059–1071, http://dx.doi.org/10.2514/1.J052529. <http://arc.aiaa.org/doi/abs/10.2514/1.J052529>.

[2] K.J. Forster, S. Diasinos, T.J. Barber, G. Doig, Computational analysis of backwards facing vortex generators for boundary layer mixing applications, in: 19th Australasian Fluid Mechanics Conference (December), 2014, p. 341.

[3] L.A.A. Pereira, M.H. Hirata, N.M. Filho, Wake and aerodynamics loads in multiple bodies-application to turbomachinery blade rows, J. Wind Eng. Ind. Aerodyn. 92 (2004) 477–491, http://dx.doi.org/10.1016/j.jweia.2004.02.001.
[4] M. Toloui, L.P. Chamorro, J. Hong, Detection of tip-vortex signatures behind a 2.5 MW wind turbine, J. Wind Eng. Ind. Aerodyn. 143 (2015) 105–112, http://dx.doi.org/10.1016/j.jweia.2015.05.001.
[5] D. Hummel, Formation flight as an energy-saving mechanism, Israel J. Zool. 41 (3) (1995) 261–278.
[6] C.M. Velte, M.O. Hansen, V.L. Okulov, Multiple vortex structures in the wake of a rectangular winglet in ground effect, Exp. Thermal Fluid Sci. 72 (2016) 31–39, http://dx.doi.org/10.1016/j.expthermflusci.2015.10.026. <http://www.sciencedirect.com/science/article/pii/S0894177715003027>.
[7] D. Garmann, M. Visbal, Interactions of a streamwise-oriented vortex with a finite wing, J. Fluid Mech. 767 (2015) 782–810, http://dx.doi.org/10.1017/jfm.2015.51. <http://www.journals.cambridge.org/abstract_S0022112015000518>.
[8] S. Crow, Stability theory for a pair of trailing vortices, 1970. doi:http://dx.doi.org/10.2514/3.6083. <http://arc.aiaa.org/doi/abs/10.2514/3.6083>.
[9] T. Leweke, S. Le Dizès, C.H.K. Williamson, Dynamics and instabilities of vortex pairs, Annu. Rev. Fluid Mech. 48 (2016) 507–541, http://dx.doi.org/10.1146/annurev-fluid-122414-034558.
[10] R.E. Gordnier, M.R. Visbal, Numerical simulation of the impingement of a streamwise vortex on a plate, Int. J. Comput. Fluid Dynam. 12 (1) (1999) 49–66.
[11] K.J. Forster, T. Barber, S. Diasinos, G. Doig, Numerical investigation of streamwise vortex interaction, SAE Technical Paper.
[12] R. Klein, Simplified equations for the interaction of nearly parallel vortex filaments, J. Fluid Mech. 288 (1995) 201–248. <http://journals.cambridge.org/abstract_S0022112095001121>.
[13] D. Fabre, L. Jacquin, A. Loof, Optimal perturbations in a four-vortex aircraft wake in counter-rotating configuration, J. Fluid Mech. 451 (2002) 319–328, http://dx.doi.org/10.1017/S0022112001006954.
[14] S.E. Widnall, The structure and dynamics of vortex filaments, Annu. Rev. Fluid Mech. 7 (1975) 141–165, http://dx.doi.org/10.1146/annurev.fl.07.010175.001041.
[15] P. Chatelain, A. Curioni, M. Bergdorf, D. Rossinelli, W. Andreoni, P. Koumoutsakos, Billion vortex particle direct numerical simulations of aircraft wakes, Comput. Methods Appl. Mech. Eng. 197 (2008) 1296–1304, http://dx.doi.org/10.1016/j.cma.2007.11.016.
[16] C.-Y. Tsai, S.E. Widnall, The stability of short waves on a straight vortex filament in a weak externally imposed strain field, J. Fluid Mech. 73 (1976) 721, http://dx.doi.org/10.1017/S0022112076001584.
[17] K. Rokhsaz, R. Rebours, S.R. Foster, Quantitative measurements of wake vortex motion in a water tunnel, in: 39 Aerospace Sciences Meeting and Exhibit, no. January, 2001. doi:http://dx.doi.org/10.2514/6.2001-111.
[18] A. Inasawa, F. Mori, M. Asai, Detailed observations of interactions of Wingtip vortices in close-formation flight, J. Aircraft 49 (1) (2012) 206–213, http://dx.doi.org/10.2514/1.C031480. <http://arc.aiaa.org/doi/abs/10.2514/1.C031480>.
[19] S. Pasche, F. Gallaire, M. Dreyer, M. Farhat, Obstacle-induced spiral vortex breakdown, Exp. Fluids 55 (8) (2014) 1784, http://dx.doi.org/10.1007/s00348-014-1784-7. <http://link.springer.com/10.1007/s00348-014-1784-7>.
[20] M. Hall, A new approach to vortex breakdown, Proc. Heat Transfer Fluid Mech. Inst. (1967) 319–340.
[21] J.J. Cassidy, H.T. Falvey, Observations of unsteady flow arising after vortex breakdown, J. Fluid Mech. 41 (04) (1970) 727, http://dx.doi.org/10.1017/S0022112070000873. <http://www.journals.cambridge.org/abstract_S0022112070000873>.
[22] A.F.K. Yeung, B.H.K. Lee, Particle image velocimetry study of wing-tip vortices, J. Aircraft 36 (2) (1999) 482–484, http://dx.doi.org/10.2514/2.2460.
[23] T. Barber, P. Kurts, Downstream evolution of wingtip vortices produced from an inverted wing, Aeronaut. J. 119 (January) (2015) 747–763, http://dx.doi.org/10.1017/S0001924000010800. <http://www.journals.cambridge.org/abstract_S0001924000010800>.
[24] R.F. Huang, C.L. Lin, Vortex shedding and shear-layer instability of wing at low-Reynolds numbers, AIAA J. 33 (8) (1995) 1398–1403, http://dx.doi.org/10.2514/3.12561.
[25] J.-H. Yoon, S.-J. Lee, Direct comparison of 2D PIV and stereoscopic PIV measurements, Meas. Sci. Technol. 13 (2002) 1631–1642, http://dx.doi.org/10.1088/0957-0233/13/10/317.
[26] C.D. Saunter, Quantifying subpixel accuracy: an experimental method for measuring accuracy in image-correlation-based, single-particle tracking, Biophys. J . 98 (8) (2010) 1566–1570, http://dx.doi.org/10.1016/j.bpj.2009.12.4297.
[27] C.W.M. Raffel, J. Kompenhas, Particle Image Velocimetry, A Practical Guide, Springer, Berlin, Germany, 1998.
[28] C.A. Cruz, Experimental and numerical characterization of turbulent slot film cooling, ProQuest, 2008.
[29] M. Manolesos, S.G. Voutsinas, Experimental investigation of the flow past passive vortex generators on an airfoil experiencing three-dimensional separation, J. Wind Eng. Ind. Aerodyn. 142 (2015) 130–148, http://dx.doi.org/10.1016/j.jweia.2015.03.020.
[30] L. Jacquin, D. Fabre, P. Geffroy, E. Coustols, The properties of a transport aircraft extended near field: an experimental study, in: AIAA conference proceedings, vol. 1038, 2001.
[31] S.J. Beresh, J.F. Henfling, R.W. Spillers, Meander of a fin trailing vortex measured using particle image velocimetry, in: 47th AIAA Aerospace Sciences Meeting Including The New Horizons Forum and Aerospace Exposition, no. January, 2009.
[32] K. Rokhsaz, T.S. Miller, Theoretical and experimental investigation of the self-induced oscillations of a single vortex filament, in: 32nd AIAA Fluid Dynamics Conference and Exhibit, no. June, 2002. doi:http://dx.doi.org/10.2514/6.2002-3304.
[33] T.S. Miller, L.K. Kliment, K. Rokhsaz, Analytical investigation of co-rotating vortex filaments with experimental verification, in: 33rd AIAA Fluid Dynamics COnference and Exhibit, no. June, 2003. doi:http://dx.doi.org/10.2514/6.20033601.
[34] K. Rokhsaz, L.K. Kliment, Experimental investigation of co-rotating vortex filaments in a water tunnel, in: 32nd AIAA FLuid Dynamics Conference and Exhibit, no. June, 2002. doi:http://dx.doi.org/10.2514/6.2002-3303.
[35] A. L. Heyes, R.F. Jones, D.A. Smith, Wandering of wing-tip vortices, in: 12th International Symposium on Applications of Laser Techniques to Fluid Mechanics, 2004, p. 35-3.

AIAA AVIATION Forum
5-9 June 2017, Denver, Colorado
47th AIAA Fluid Dynamics Conference

The Variation in Co and Counter-Rotating Upstream-Downstream Vortex Interactions

Kyle Forster*

Tracie Barber †

School of Mechanical and Maunfacturing Engineering, UNSW Australia, NSW, 2053, Australia

Sammy Diasinos‡

Department of Engineering, Macquarie University, North Ryde, NSW, 2109, Australia

Graham Doig§

Aerospace Engineering Department, California Polytechnic State University, CA 93407, USA

The interactions between two streamwise vortices at various lateral offsets were investigated by the wind tunnel testing of two NACA0012 vanes. The vanes were separated by nine chord lengths in the streamwise direction such that the upstream vortex impacted on the downstream geometry. These vanes were evaluated at an angle of incidence of 8 degrees and a Reynolds number of 70,000, with Particle Image Velocimetry (PIV) used for data collection. To produce a co-rotating pair, both vane angles were orientated in the same direction, while to produce a counter-rotating pair the angle of the rear vane was reversed. Despite the fundamental similarity of the flowfield in terms of the presence and proximity of two vortices, pronounced differences were observed in both the vortex paths and the energy transfer between the two vortices. Circulation enhancement of the upstream vortex occurred at all lateral offsets for the co-rotating case. The counter-rotating condition was far more sensitive to offset, with far offsets causing vortex enhancement and near offsets causing vortex destruction. The presence of the upstream vortex was found to increase the production strength of the downstream vortex in the counter-rotating condition, and decrease it in the co-rotating condition. However, the counter rotating condition was found to have more rapid energy loss than the co-rotating condition, which did not significantly lose circulation across the domain observed.

Nomenclature

$A_{0.1}$	Area of vortex at 0.1 vorticity threshold
$A_{0.3}$	Area of vortex at 0.3 vorticity threshold
$R_{0.1}$	Average radius of vortex at 0.1 vorticity threshold
$R_{0.3}$	Average radius of vortex at 0.3 vorticity threshold
B_v	Vortex separation
C	Chord length
Γ	Circulation
R_e	Reynolds number, based off chord length
X_c	X core location
Y_c	Y core location

*PhD Candidate, School of Mechanical and Maunfacturing Engineering, UNSW Australia
†Associate Professor, School of Mechanical and Maunfacturing Engineering, UNSW Australia
‡Lecturer, Department of Engineering, Macquarie University
§Assistant Professor, Aerospace Engineering Department, California Polytechnic State University

I. Introduction

Turbomachinery blade interactions, aircraft taking off in succession, wind turbines and vortex generators can all produce vortex interactions with multiple streamwise vortices in close proximity to each other[1,2,3] . These vortices may be desirable (flow control, heat transfer) or undesirable (aircraft wake vortices). There are considerably fewer studies available on streamwise vortex/structure interactions than either parallel or normal vortex/structure interactions.[4] Vortex interactions at extremely close core spacings have not been studied extensively, as in previous work both vortices of a vortex pair have been typically deployed from the same streamwise location.[5,6] These close interactions are important conditions to understand in order to provide a knowledge base for practical vortex applications, where upstream vortices may move in locations on either side of a vortex producing obstacle, such as a wing or vane. This study considers the interaction of an initial vortex which travels downstream before interacting with a downstream vane, and the resultant downstream flowfield.

Two fundamental types of streamwise vortex interactions can occur between vortex pairs; co-rotating and counter-rotating. Despite the relative conceptual similarity of a flowfield with two interacting vortices, the change in relative rotational direction alters the instabilities and paths of a vortex pair.[7] This can have a significant effect on the strength of the vortices, as well as the rates of energy decay, leading to some scenarios being well suited to vortex destruction, while others are more effective at the re-energisation of the initial vortex.

If the total circulation of any vortex pair is non-zero, there will be a net rotation of the vortex system.[7] In the case of a co-rotating vortex pair, both circulations are of the same sign, hence they must add to a non-zero amount, causing an orbital motion of the vortex system. If the circulations are equal, this will cause the two cores to orbit at an equal radius around a central point, while if they are unequal the vortices will orbit on different radii. For a symmetric (equal circulation), counter-rotating case, the pair will translate along the vortex pair centre axis with no rotation, while for a case with unequal circulations there will be an orbital motion. These migrations have been seen in water tunnel testing at a reynolds number of 20000,[8] where dye marker injected into the cores of a pair of co-rotating vortices showed negligible change in the location of the orbital centre. While the dye marker can show the location of the core streamline, it cannot predict vorticity strength, the centre of vorticity or the vorticity and velocity fields, making it difficult to ascertain the mechanisms behind merging.

A pair of co-rotating vortices will merge in any viscous flow,[9,10,11] however the majority of experimentation and analysis surrounding this subject has used equal strength and size vortex cores, with two dimensional flow fields and no velocity deficit through the core, limiting their applicability to real world interaction scenarios. The authors[5,6] have previously investigated these interactions in upstream/downstream scenarios with unequal strength cores, however the differences between the co and counter-rotating cases have not been directly compared.

Both co-rotating and counter-rotating vortex pairs exhibit instabilities when placed in close proximity. These include long wavelength (Crow[12]) for counter-rotating systems, and short wavelength (elliptic[7] and spiral[13,14]) for counter-rotating and co-rotating pairs. All counter-rotating pairs are inherently unstable regarding the Crow instability, however may be found to break down in too short a distance for the instability to manifest significantly[15,16] . The elliptic instability is caused in both types of interactions by a resonance of two Kelvin waves (a sinusoidal deformation) within the vortex core as driven by the strain field induced by the other vortex[17] . The behaviour of both the short wave and long wave instabilities can be modified by altering the axial velocity components and vortex strengths.

II. Experimental Setup

The present study considers the interaction of two streamwise vortices produced by two NACA 0012 vanes. One vane was located 10 chord lengths (C) downstream of the other, as can be seen in Figure 1. This configuration was chosen as it allows interactions between vortices to occur at extremely close proximities that cannot be observed if the vortices are deployed at the same locations. An angle of attack of 8 degrees on each vane has been used for all cases, with a square-edged tip. Higher angles of attack decreased the vortex stability, with unsteady breakdown becoming observable for a single vortex case at 12 degrees. Multiple offsets were tested from -0.6C to 0.5C in increments of 0.1C, with a finer spacing of 0.05C between -0.4C and 0C.

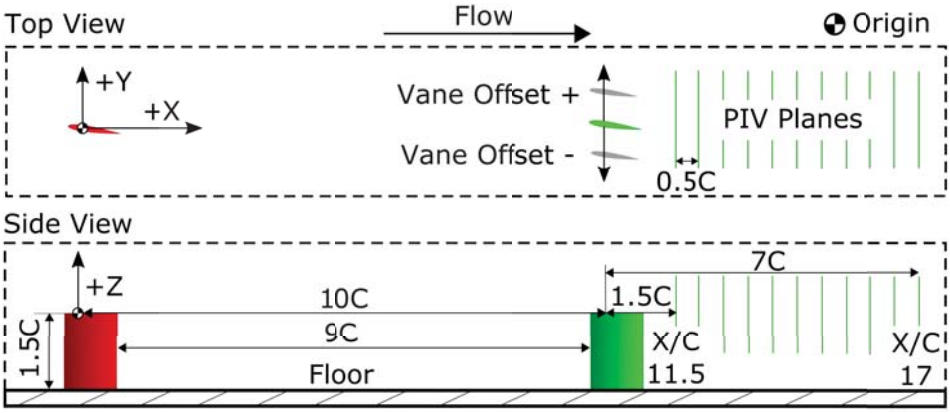

Figure 1: Vane layout diagram. Reproduced with permission from "Interactions of a Counter-Rotating Vortex Pair at Multiple Offsets".[5]

The x-axis is in the direction of the flow, with positive downstream, the Y axis is across the tunnel and the Z axis is in the vertical direction. As such, the rear vane quarter chord was located at X = 10C, with the vane root at Z = -1.5C.

Planar slices of the flowfield were captured using PIV at 0.5C intervals from 1.5C back from the quarter chord of the trailing vane to 7C back. These correspond to 11.5C and 17C from the leading vane respectively. The laser sheet was not moved closer than 11.5C as the reflections from the vanes began to distort the results. The experiment was performed at a Reynolds number of approximately 7×10^4 based on chord length. At 7×10^4 the vortex shedding from a NACA0012 airfoil at 8 degrees angle of attack is within the supercritical region[18] and therefore any Reynolds number lower than 6×10^4 at this angle of attack will result in a shedding regime that is not indicative of higher Reynolds number scenarios.

A. Wind Tunnel

Experiments were performed in the Macquarie University open return, closed section wind tunnel. This tunnel has a 610 x 610 mm (24 x 24 inch) octagonal test section with a 1900 mm (6' 3") length. The test section has a peak turbulence intensity of 0.35% and average turbulence intensity of 0.25%, with velocity uniformity better than 1% variance, and flow angularity less than 1 degree across the test section inlet. Streamwise velocity variance was held to within 0.38%.

A separate elevated ground 100mm tall was mounted to the floor of the tunnel with a rounded front splitter to minimise the effects of the pre-existing boundary layer in the test section. To reduce ground plane interactions the vanes were sized to be considerably taller than the boundary layer. The vanes have a chord of 80mm and a span of 120mm, and are painted matte black to minimise reflections.The boundary layer at the location of the rear vane was experimentally measured to be 5mm thick at 80% of the freestream velocity and 20mm thick at 95% of the freestream velocity. A schematic of this setup can be seen in Figure 2.

B. PIV Setup

A planar two component PIV system was used to capture the vortex dynamics. Due to the large expansion length of the Macquarie University wind tunnel, the camera was placed inside the expansion itself rather than using a mirror system. This allowed the camera to be positioned 2100mm downstream of the test section and 2380mm to the nearest image plane, giving a maximum perspective bias of 1.6 degrees per side on a 133mm wide observation plane with a 120mm lens. Focus was controlled remotely. By comparing to the setup of 2D and stereoscopic PIV of Yoon and Lee,[19] the setup described in this paper was found to have maximum projection error of 5.8% under the same conditions. It should be noted that this error is at the edges of the observation window, and is not indicative of the errors near the centre, which will approach zero projection error as the centre is reached. By superimposing the calculated projection error of a uniform streamwise velocity field on the captured time-resolved PIV data, the error in peak vortex core velocity was found to be below 4% against the absolute velocity field, with an imperceptible change in the vorticity field

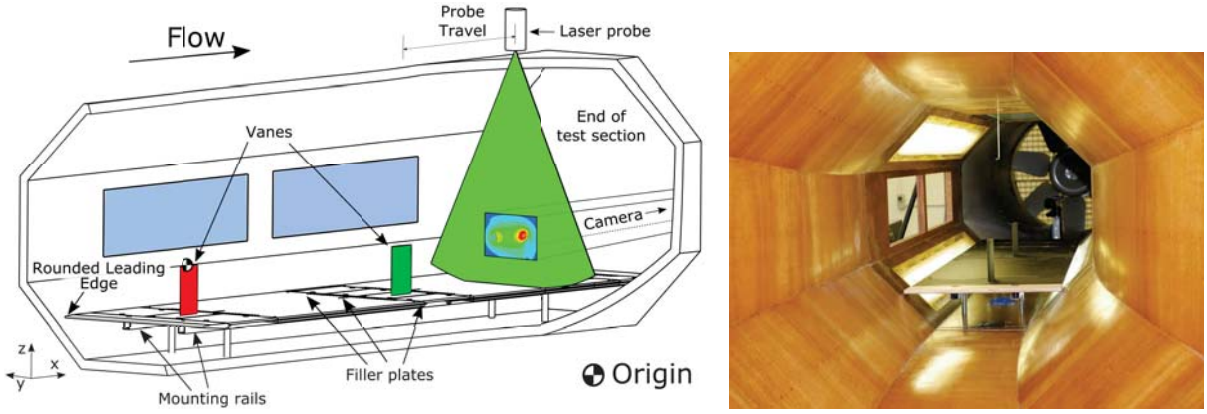

Figure 2: Cutaway diagram of tunnel test section, reproduced with permission from "Interactions of a Counter-Rotating Vortex Pair at Multiple Offsets".[5]

with a negligible change in the calculated core location and circulation. The expansion section of the tunnel was on isolated mounts from the tunnel fan, minimising vibration. Over a test of 200 image pairs, the tip of the rear vane was found to have a maximum displacement change of 1 pixel during the entire sampling time. Tracking of camera vibrations between images of an image pair was performed through a Gaussian fit tracking of the illuminated wingtip while the tunnel was running. This yielded a vibrational displacement maximum of 0.0471px between the two images of a pair, which is within the margin of error of Gaussian subpixel tracking.

The laser probe was mounted on top of a traverse to allow laser sheet movement along the axis of the tunnel. The laser used was a dual-cavity Nd:YAG laser (Quantel EverGreen) with an output of 200mJ per pulse at 532nm wavelength and a repetition rate of 15hz. Laser pulses were delivered 55μs apart. The laser sheet thickness varies throughout the observation window as a result of the focus, with an average thickness of approximately 4mm through the region of interest. This large thickness was selected to minimise the amount of out-of-plane pair loss.[20] Validation of post-processed data was performed by excluding points with vorticity gradients from the surrounds greater than 500 $\frac{1}{s.mm}$.

Seeding was performed with a PIVtech generator using Di-Ethyl-Hexyl-Sebacat (DEHS) air soluble particles of 0.2-0.3μm typical diameter. This gives a Stokes number of approximately 2×10^{-5}, indicating the particle size is sufficiently low to follow all flow streamlines accurately.[21]

Scattered laser light was captured by a monochrome cooled CCD pco.1600 camera with 1GB of RAM. Images were digitised at 14 bits, with a resolution of 1600x1200 pixels. The camera was fitted with a 120mm lens. The CCD size on the camera was 12.5mm wide x 9.38mm high, giving a field of view at the most downstream plane of approximately 100x133mm.

Image analysis was performed with PIVView software. Multi grid interpolation was used, starting at a coarse grid size of 128px x 128px windows and finishing with refinement to 32px x 32px over 3 passes. Standard FFT correlation was used, with two repeated correlations on 16px offset grids being performed resulting in minimal in-plane loss of pairs. Subpixel shifting was enabled on all passes with b-spline interpolation and peak detection by a Gaussian least squares fit from 3 points. The final grid size was 99 x 74 nodes.

C. Sources of Error

Sampling error for averaged results was determined to be 3.7% in circulation and 0.0035C in location for the 400 total shots taken against a multiple representative sample of 2000 image pairs. Due to the nature of the manual focussing system there were induced errors, with differences in focus able to produce up to 0.04C error in core location. By implementing a particle pixel size threshold of no more than 2px at a brightness level of 4.5% of the total dynamic range, this error was reduced to 0.0015C in core location. Total error due to the calibration plane procedure was found to be a maximum of 0.18% in location and 0.22% in scale, due to minute differences in lateral calibration plane location. Seeding levels in the room were convergence tested such that the error from the seeding were not discernible from the randomness induced by the other errors. Spatial convergence was ensured by evaluating the -0.2C offset case at half the interrogation window

size, effectively doubling the spatial resolution. This yielded errors of ±2.7% in core radius and ±0.0026C in location across the averaged sample size for the zoomed out condition used. As previously discussed, camera vibration was not observed at an appreciable level, with a maximum image migration of 0.06% measured over the course of an imaging run. The particle size was measured at an average of 1.5px, giving an uncertainty in position of 0.03px.[20] Quantization errors were negligible due to 14 bit quantization. Any biases inherent in each run were minimised by having the each set of 400 images taken with one forward run of 200 images (plane moving from X17 to X11.5) and one backward run in the opposite direction; this way any errors in seeding or focus would be minimised. The total error in core location was found to be ± 0.008C.

D. Vortex Analysis Methodology

Vortex radii can vary by up to 35% if time averaged results are used due to vortex meandering and local fluctuations in velocity.[22] In addition to this, the velocity field will be smoothed, resulting in deviations in circulation and core size if time averaged results are used. This particularly affects the tracking of strongly meandering vortices, such as those present after vortex breakdown. However, it is still desired to have average values for core location, size and strength. As such the results were analysed by a script based evaluation of each individual pair of images. To eliminate the influence of vortex shedding and low level noise on the calculation of tip vortex properties, all vorticity constructs except the tip vortex were filtered out. This was performed by computing contours at 10% of the peak vorticity and calculating the area enclosed by each individual structure. These data points were then combined and analysed for average values and variances.

The vortex centre within a plane is defined as the integral of the vorticity (ω) multiplied by the displacement (X or Y value, depending on the axis being calculated), divided by the circulation (Γ),[7] as shown in eqs. (1) and (2).

$$X_c = \frac{1}{\Gamma}\int X\omega dS \tag{1}$$

$$Y_c = \frac{1}{\Gamma}\int Y\omega dS \tag{2}$$

While this does not always align with the location of zero in-plane velocity, it allows for consistent prediction of the centre of circulation intensity even when the vortex pair is migrating with an in plane motion, which would otherwise skew the core location. It is also more robust than simply using the value of peak vorticity, as it is not significantly skewed by asymmetrical vortices or vorticity peaks in the result.

For the co-rotating vortices, vorticity is of the same sign. This means that identifying the centre of vorticity within a plane will be ineffective as it will only find the centre point between the two vortices. An automated script was used to identify the two separated vorticity peaks and construct a contour line at 0.1 of the peak vorticity and 0.3 of the peak vorticity on a given plane, giving enclosed areas of $A_{0.1}$ and $A_{0.3}$ respectively. In the case that the smaller $A_{0.3}$ was less than a quarter of the larger $A_{0.3}$, the vortices were considered merged. This 1:4 ratio was selected based on the graphical results, which correlated with the observable vortex cores while minimising the influence of signal noise on the results. The single $A_{0.1}$ and two $A_{0.3}$ areas are considered as the vortex core regions for the merging vortex system and individual vortices respectively. Consequently, for path tracking the weighted centroid of eqs. (3) and (4) was used.

$$X_c = \frac{1}{\Gamma_{A_{0.3}}}\int X_{A_{0.3}}\omega dS \tag{3}$$

$$Y_c = \frac{1}{\Gamma_{A_{0.3}}}\int Y_{A_{0.3}}\omega dS \tag{4}$$

Due to the skew towards non-circularity at near offsets, the radius of the vortices was calculated using the vortex areas and assuming vortex circularity to give an effective radius. These were $R_{0.1}$ and $R_{0.3}$ for $A_{0.1}$ and $A_{0.3}$ respectively. The vortex circulation was calculated by the integral of the vorticity within the identified core region. When there are individual vortices identified, this is taken at an $A_{0.3}$ cutoff, as this allows the continued identification of vortex peaks through the merging case. When the vortex is merged, this is evaluated at $A_{0.1}$ to capture the entire vortex. If $A_{0.3}$ is used to characterise the merged vortex it excludes the merging tail region of the vortex, causing a significant drop in effective vortex circulation. This is not an issue for the unmerged vortex cases, as the vortices are still approximately circular in shape so

there is no vorticity lost to the tail region. This will however cause an effective circulation reduction for the unmerged cases, so should be noted for the results of this section. This reduction was found to be 10.5% as calculated from the single vortex case.

III. Results

The separation between the two vortices at the start and end of the measurement domain can be seen as the initial and final separations respectively in Figure 3. In the far offset ranges the vortex separations varied linearly for both the co and counter-rotating conditions. However, in the counter-rotating condition the vortex proximities shifted further apart by approximately 0.026C as the vortex pair travelled downstream, while in the co-rotating cases they were drawn together by between 0.077C in the negative offsets and 0.043C in the positive offsets. This consequently led to the merging of the vortices as the vane offset decreased due to their same sign vorticity. In this same near field offset range, the counter-rotating vortex proximities were actually separated further up to 0.41C due to the destruction of the initial vortex, leaving only the remnants of this vortex to propagate downstream at a location towards the root of the vane.

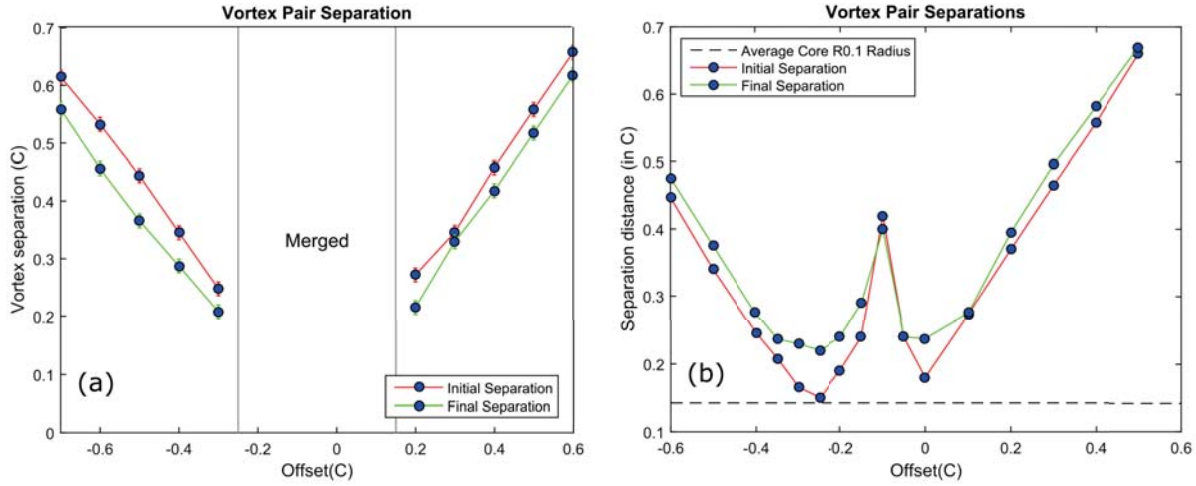

Figure 3: Vortex pair separations plotted against offset for all unmerged cases for co-rotating (a) and counter-rotating (b) configurations. Reproduced with permission from "Interactions of a Counter-Rotating Vortex Pair at Multiple Offsets" and "Interactions of a Co-Rotating Vortex Pair at Multiple Offsets".[5,6]

While there is symmetry in the far offset separations, the centre of vortex interactions is offset depending on whether the scenario is co-rotating or counter-rotating. The merging range for the co-rotating case is -0.25C to 0.15C, while the points of closest separation for the counter-rotating case are at -0.25C and 0C. There is also a visibly clear skew of the separations to being reduced at the negative offsets in the counter-rotating condition, as evidenced by 0.25C separation at -0.4C offset as opposed to 0.37C separation at 0.2C offset. It is hypothesised that this is due to the low pressure field of the upstream vortex affecting the formation of the downstream vortex via the reduction in pressure on the pressure or suction surface of the downstream vane.

In both cases, a critical point was present where the nature of the interaction significantly changed. Once the vortex separation in the co-rotating case reached double the vortex radius, the vortices rapidly merged through the merging mechanism discussed later in this paper. For the counter-rotating case it was found that the vortices could be brought much closer to approximately one core radius separation before the initial separations started to diverge. The counter-rotating condition also contains 3 distinct separation regimes instead of the co-rotating's merged and unmerged state. In the far field ($B_v < -0.4C$, $B_v > 0.1C$) counter-rotating condition, the separations are near constant, in the near field ($-0.4C < B_v < -0.25C$, $0C < B_v < 0.1C$) they continue to decrease in initial separation while remaining constant in final separation, and in the very near field ($-0.25C < B_v < 0C$) they markedly increase in both initial and final separation.

As the co-rotating vortices continually decrease in spacing, their separation behaviours across all the individual cases can be extrapolated to simulate the behaviour of a single vortex pair deployed at an initial

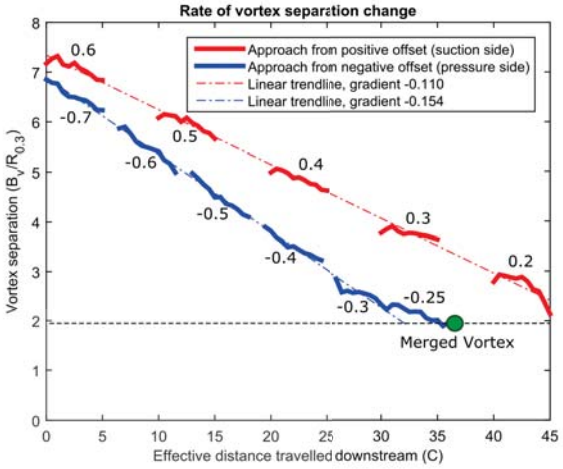

Figure 4: Vortex pair separations for all unmerged cases. Each offset case is indicated by the annotations on the line segments. Reproduced with permission from "Interactions of a Co-Rotating Vortex Pair at Multiple Offsets".[6]

spacing of $B_v/R_{0.3} \approx 7$. These results can be seen in Figure 4, demonstrating that the speed of the drawing together process of the vortices was dependent on which side of the vane the upstream vortex was passed on. If the vortex passed on the pressure side of the vane, for every chord length travelled downstream the vortices move together approximately 0.154 of the core radius. However, if the vortex passes on the suction side of the vane, this is decreased to 0.110 core radii, giving a 28% differential in separation rate. This suggests that the wake region of the vane significantly affects the speed of the merger, causing the vortices to be forced together faster. Despite this differential in the separation changes the merging mechanism observed was the same for all co-rotating cases, while for the counter rotating cases it was substantially different depending on offset.

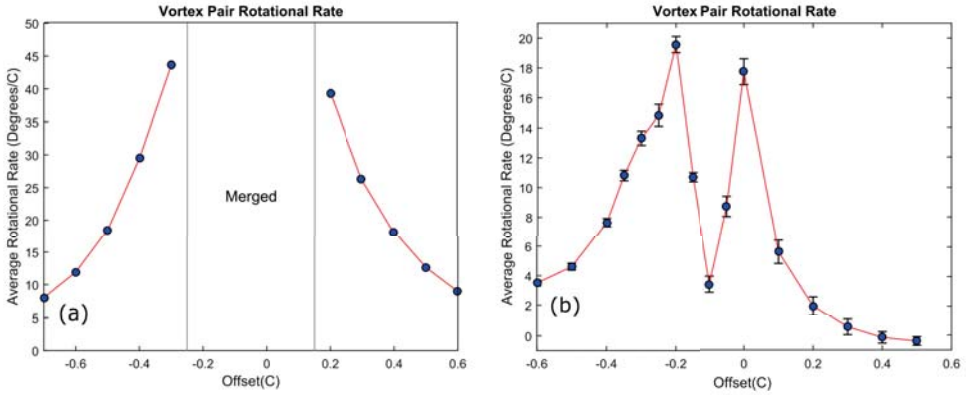

Figure 5: Vortex pair rotations plotted against offset for all unmerged cases for co-rotating (a) and counter-rotating (b) configurations. Reproduced with permission from "Interactions of a Counter-Rotating Vortex Pair at Multiple Offsets" and "Interactions of a Co-Rotating Vortex Pair at Multiple Offsets".[5,6]

The rotation rates presented in Figure 5 showed similar trends in the offset skew and the strength of interaction as the proximities were reduced. For the counter-rotating case, peaks can be seen at -0.2C and 0C, while for the co-rotating cases the rotational rate increased until the point of vortex merging. Both cases showed a non-linear trend in rotational rate as separations were reduced. The co-rotating condition had a substantially higher rotational rate than the counter-rotating case, with peaks over twice as high. This is due to the co-rotating condition's vortices orbiting around a central point between the vortices whereas the counter-rotating condition's orbital centre was located to the outside of the two vortices.

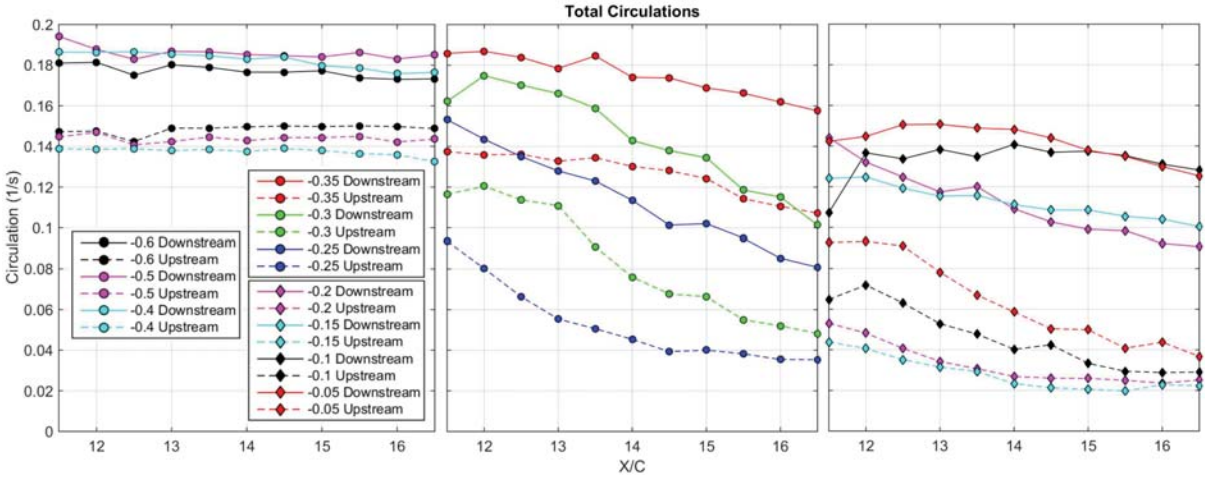

Figure 6: Circulation values for various counter-rotating vortex cases.

Inspecting the circulation trends of the two conditions shows significant differences in the total energy available and the rates of energy dissipation. The counter-rotating circulations seen in Figure 6 show that as the offset increases between the vanes at the far edges of the range investigated the circulation between the two vortices becomes more equal. As they are drawn closer from -0.6C to -0.4C, the circulation of the upstream vortex is decreased by 4.7% with a corresponding increase in the circulation of the downstream vortex of 8.6%. This shows an energy transfer from the upstream vortex to the downstream vortex. The transfer of energy in these far offset cases happens during the initial stages of vortex formation, as negligible circulation decrease is noted after this point. As the offsets are brought within the previously identified near-field range, there is a transition from relatively little circulation loss through the domain to a downwards trends in the circulation, with the -0.4C offset having a loss of 5.6% in the downstream vortex and the -0.35C having a 17.9% equivalent loss. As the offset is further decreased, the initial circulation destruction in the upstream vortex increases, with the strength being reduced from $0.147s^{-1}$ at X11.5 in the -0.6C case to $0.0439s^{-1}$ in the -0.15C case. As such, the counter-rotating condition decreases in the duration of its strength as the offset decreases and the vortices interact. It should be noted that using the time averaged results smears the vorticity field resulting from the highly meandering upstream vortex in these low energy scenarios. This shows the vortex as completely disappearing in the time averaged case, whereas weak coherent vortex structures were observed in the instantaneous results. This is represented by the circulation from X15 to X16.5 in the very near field circulation results.

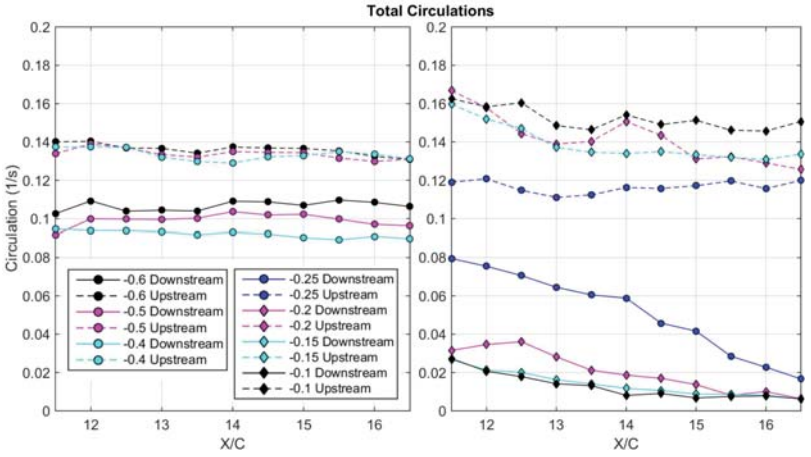

Figure 7: Circulation values for various co-rotating vortex cases.

The co-rotating results showed that there was less total circulation present in all far offset cases than the counter-rotating condition, with approximately 26% less total circulation from -0.6C offset to -0.4C offset, as can be seen in Figure 7. In contrast to the counter-rotating case where the downstream vortex is dominant, the upstream vortex is the dominant vortex. This is due to the presence of the upstream vortex reducing the strength of the downstream vortex in its production, instead of enhancing it with a counter-rotating field. As the total offset decreases from -0.6C to -0.4C the strength of the downstream vortex decreases from an average of $0.108s^{-1}$ to $0.093s^{-1}$, with negligible strength observed in the upstream vortex. The strength of the upstream vortex in the far offset cases is very similar between both the co-rotating and counter-rotating cases, with an average value of approximately $0.14s^{-1}$. This demonstrates how significant the vortex direction is on the production strength of the downstream vortex from the rearward vane, with substantial enhancement seen in the counter-rotating case and a loss of circulation in the co-rotating condition.From this it can be seen that the counter-rotating condition will produce a higher circulation initial vortex system than the co-rotating condition. As the offset is further reduced and the merged state is approached there is circulation transfer from the downstream vortex to the upstream vortex. This results in the circulation of the upstream vortex rising to a level up to 16% above that attained by the counter-rotating upstream vortex, at the cost of the strength of the downstream vortex. As the offsets are moved closer together the vortices became merged from the start of the domain, resulting in the highest upstream vortex circulation in the -0.1C offset case.

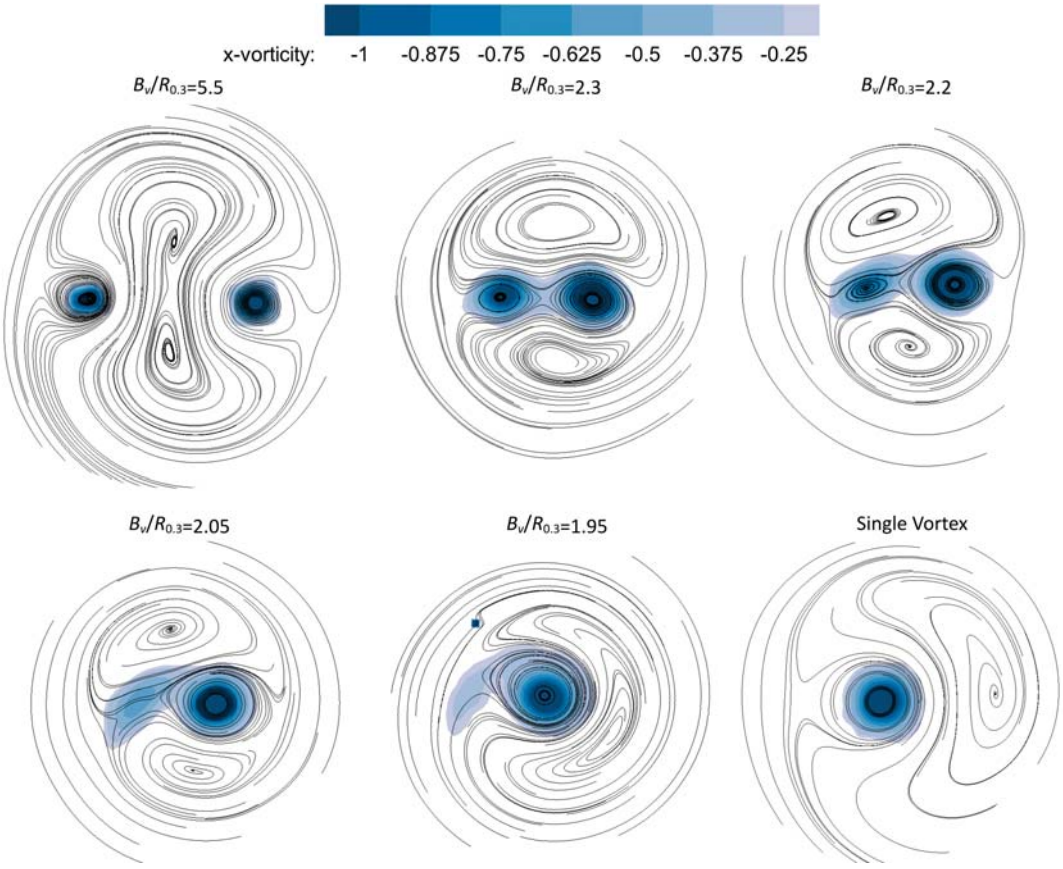

Figure 8: Pathlines in the co-rotating reference frame and vorticity for different stages of vortex merger. Reproduced with permission from "Interactions of a Co-Rotating Vortex Pair at Multiple Offsets".[6]

The differences between the mechanisms of the vortex interactions can be seen clearly by plotting the two dimensional pathlines over contours of vorticity. As previously identified, in the co-rotating condition the vortices rotate at a far more rapid rate, with the slowest rotating case being faster than all but five of the counter-rotating cases. In order to observe the merging mechanisms responsible forthe merger, it was necessary to translate the velocity into the co-rotating reference frame. As the mechanism was noted as being

the same regardless of offset, the data from multiple offsets could be combined to show the different stages of vortex merger, as can be seen in Figure 8. This showed that as the vortices approached a separation of two core radii a significant asymmetry in the flow fields formed, followed by a rapid transmission of vorticity from the weaker vortex to the stronger vortex without a large change in vortex separation. This was accompanied by a movement of the ghost vortex regions (the outer recirculation regions with little vorticity) from one side of the primary vortex to the other, before they merged together and normalised.

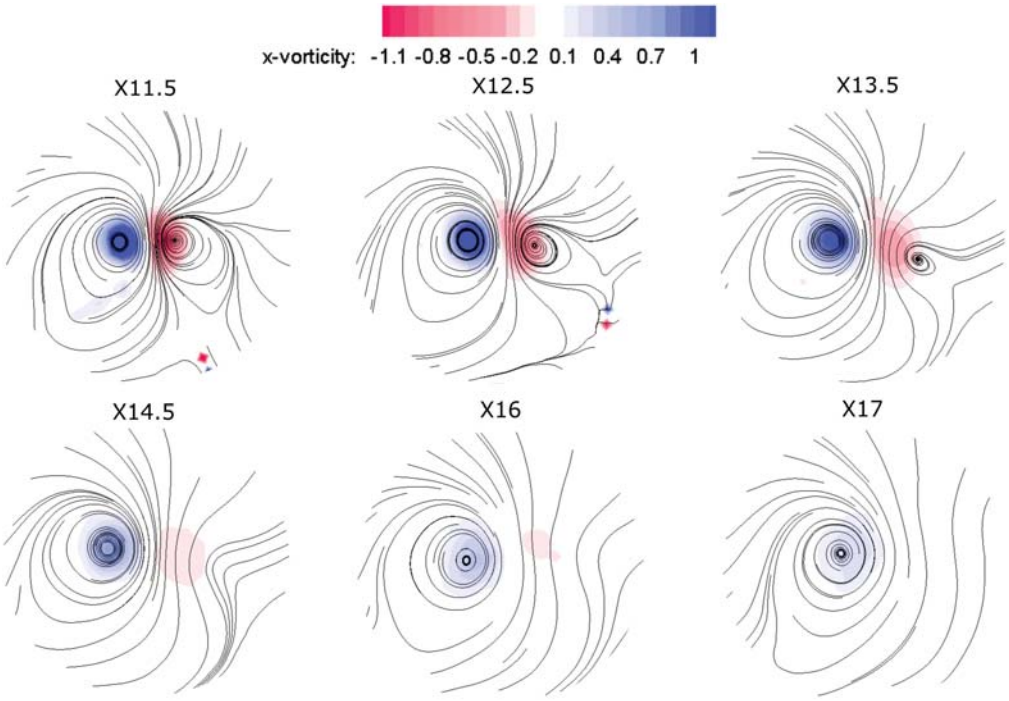

Figure 9: Pathlines in the stationary reference frame and vorticity for different stages of vortex merger in counter-rotating -0.3C offset condition. Vortex locations are reframed to be consistent in alignment.

While the co-rotating condition could be extrapolated across the cases into a consistent merging process, the mechanism behind the counter rotating interaction was far more variable, resulting in substantial differences depending on offset. At very near field offsets the the mechanism for destruction appeared to be from direct impact on the front of the vane causing and vorticity interaction and vortex breakdown, leaving only remnants of the initial vortex and a weak downstream vortex. For larger offsets in the near field and far field, this shifted to a mutual instability inductance, which caused the long term loss in circulation. As can be seen in Figure 9 the -0.3C case started with the vortices spaced at a very close proximity before drifting apart by X12.5. The upstream vortex then undergoes a rapid reduction in vorticity, with its limit streamline completely destroyed by X14.5. Following this the downstream vortex proceeded to dissipate. The process can be broken up into four main pathline states. Initially, the limit cycle of the pathlines for both vortices is at a similar radius. This then separates as the vorticity of the upstream vortex reduces in magnitude, with the stronger vortex retaining similar streamlines but the weaker moving away and decreasing in size. The limit cycle is then broken down into kinked pathlines, as observed at X14.5. These pathlines are straightened out, leaving just the remains of the stronger vortex. In other near field offset cases the process remained similar, however the rate of the process increased, with the -0.25C offset case having moved to the 4th stage by X14.5, leaving a reduction in stage length of 2.5C for an offset change of only 0.5C. In the very near field the second vortex was nearly indistinguishable in the time averaged results, with the 4th stage present from X11.5.

At far offsets the destruction of the vorticity and reduction of circulation was far less pronounced, however the shifting of the streamlines was still significant, as seen in Figure 10. This shifting of streamlines from a downwards position to a more uniform vortex shape indicates that this structure may be a consequence of the formation of the downstream vortex by the vane, even though the structure is observed in the upstream

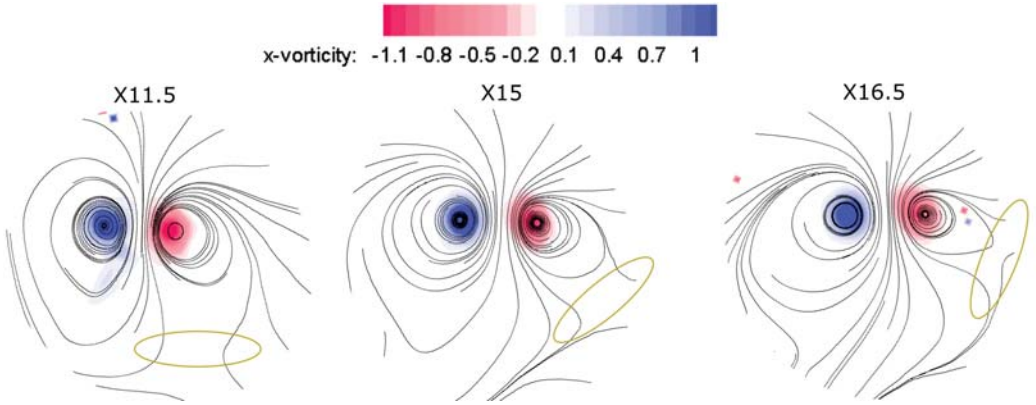

Figure 10: Pathlines in the stationary reference frame and vorticity for different stages of vortex merger in counter-rotating -0.4C offset condition, with the base of the limit cycle of the weaker vortex highlighted by the orange ovals. Vortex locations are reframed to be consistent in alignment.

vortex. From the figure, the movement of the streamlines both around and towards the vortex can clearly be seen, as highlighted by the orange ovals in the figure. It is anticipated that if the vortex spacing is sufficiently large that the strength of the vortices does not dissipate, with a long enough distance downstream this will normalise to form a more uniform and symmetric vortex structure.

Both the co-rotating and counter-rotating scenarios produced instabilities in the vortices, traceable by analysing the instantaneous positions of the vortex cores from the image pairs as previously discussed. The instability observed in the counter-rotating case was typically dominant in the weaker vortex at nearer offsets, with a 45 degree angle observed between the weaker vortex instability and the vortex centreline. This indicated the presence of an uneven crow instability, similar to that identified by the authors.[14] In the co-rotating condition the instabilities were of lower magnitude and shallower angle closer to 30 degrees in the weaker vortex. The magnitude of oscillation of the weaker vortex did not substantially increase as vortex proximity reduced until the point of merging, unlike the counter-rotating condition. This instability shared some similarities such as deviation angle with that of equal co-rotating vortices identified by Miller et al.[23]

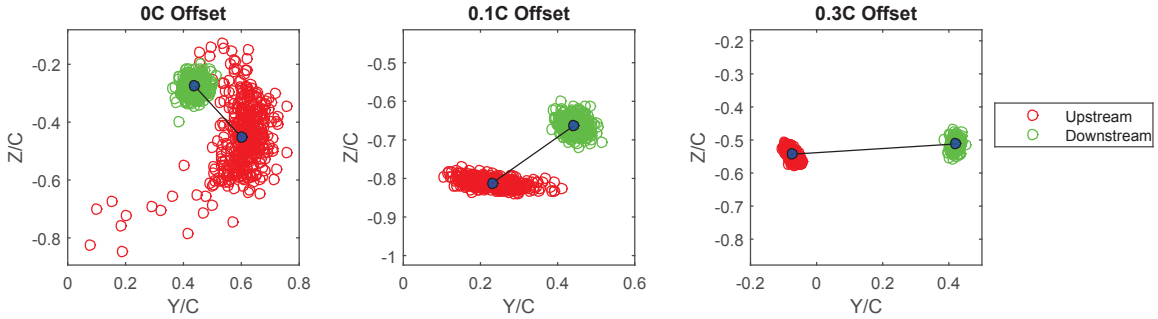

Figure 11: Core locations of upstream (red) and downstream (green) counter-rotating vortices for 0C, 0.1C and 0.3C offset cases at X/C = 16.5. Reproduced with permission from "Interactions of a Counter-Rotating Vortex Pair at Multiple Offsets".[5]

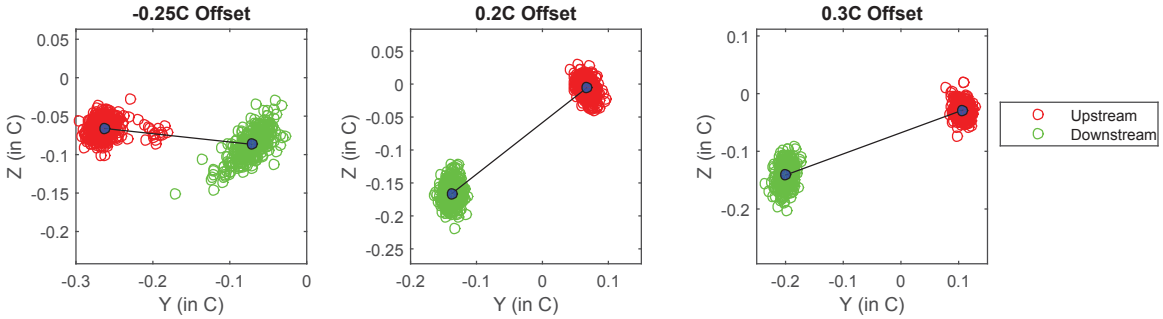

Figure 12: Core locations of upstream (red) and downstream (green) co-rotating vortices for -0.25C and 0.2C offset cases at X/C = 14 and 0.3C offset at X/C = 16.5.

IV. Conclusion

Wind tunnel experimentation was performed to investigate the behaviour of the interactions between both co-rotating and counter-rotating vortex pairs produced by two offset vanes. NACA0012 wings of 1.5 aspect ratio, at 8 degrees angle of attack and a Reynolds number of 70000 were used for this study, spaced 10C apart in the streamwise direction. Lateral offsets from -0.7C to 0.6C were studied to examine the effects of vortex proximity on the resulting vortex sizes, paths circulations and instabilities.

While the flow fields are very similar conceptually, many pronounced differences were observed in both the formation of the downstream vortex and the mechanisms observed in the evolution of the system. While both systems underwent rotation, the counter-rotating system was driven by a differential in strength between the vortices, and the co-rotating system rotated due to shear at the periphery of the same signed vorticity. This resulted in the co-rotating pair having a much higher rotational rate due to the centre of rotation being inside the vortex pair, as opposed to being outside in the counter case.

The separations between the co-rotating pair followed a consistent trend of moving together regardless of offset, while the counter-rotating pair moved further apart, with a substantial increase in motion in the near field range to an equilibrium distance of approximately 0.23C. The direction of the vortex interaction considerably affected the strength of downstream vortex production, with counter-rotating configurations enhancing downstream vortex strength by 30% and co-rotating conditions reducing it by 28%. The co-rotating vortex merger showed similar levels of energy transfer in all cases, while the counter-rotating condition saw vortex dissipation rates substantially increase as the offset was reduced. It was found that the mechanism responsible for energy transfer remained the same, regardless of vortex offset in the co-rotating condition, with only the distance to merger changing. In the counter-rotating condition the mechanism was found to vary significantly between the far, near and very near field, with the resulting instabilities increasing as the vortices were shifted closer together.

As such, these results indicate that where a short duration, high circulation vortex system is required a counter-rotating upstream/downstream configuration would be best, while a co-rotating configuration will be superior for cases requiring a vortex system that is more stable in the long term.

References

[1]M. Manolesos and S. G. Voutsinas, "Experimental investigation of the flow past passive vortex generators on an airfoil experiencing three-dimensional separation," *Journal of Wind Engineering and Industrial Aerodynamics*, vol. 142, pp. 130–148, 2015.

[2]L. A. A. Pereira, M. H. Hirata, and N. M. Filho, "Wake and aerodynamics loads in multiple bodies-application to turbomachinery blade rows," *Journal of Wind Engineering and Industrial Aerodynamics*, vol. 92, pp. 477–491, 2004.

[3]K. J. Forster and T. R. White, "Numerical Investigation into Vortex Generators on Heavily Cambered Wings," *AIAA Journal*, vol. 52, pp. 1059–1071, May 2014.

[4]D. Garmann and M. Visbal, "Interactions of a streamwise-oriented vortex with a finite wing," *Journal of Fluid Mechanics*, vol. 767, pp. 782–810, 2015.

[5]K. J. Forster, T. J. Barber, S. Diasinos, and G. Doig, "Interactions of a Counter-Rotating Vortex Pair at Multiple Offsets," *Experimental Thermal and Fluid Science*, vol. 86, pp. 63–74, 2017.

[6]K. J. Forster, T. J. Barber, S. Diasinos, and G. Doig, "Interactions of a Co-Rotating Vortex Pair at Multiple Offsets (in print)," *Physics of Fluids*, 2017.

[7]T. Leweke, S. Le Dizès, and C. H. K. Williamson, "Dynamics and Instabilities of Vortex Pairs," *Annual Review of Fluid Mechanics*, vol. 48, pp. 507–541, 2016.

[8]K. Rokhsaz and L. K. Kliment, "Experimental Investigation of Co-Rotating Vortex Filaments in a Water Tunnel," in *32nd AIAA Fluid Dynamics Conference and Exhibit*, vol. 40, 2002.

[9]D. G. Dritschel, "The stability and energetics of corotating uniform vortices," *Journal of Fluid Mechanics*, vol. 157, pp. 95–134, 1985.

[10]E. A. Overman, "Evolution and merger of isolated vortex structures," *Physics of Fluids*, vol. 25, no. 1982, p. 1297, 1982.

[11]K. Roberts and J. Christiansen, "Topics in Computational Fluid Dynamics," *Computational Physics Communications*, vol. 3, no. I 972, pp. 14–32, 1972.

[12]S. Crow, "Stability theory for a pair of trailing vortices," *AIAA Journal*, vol. 8, no. 12, pp. 2172–2179, 1970.

[13]R. E. Gordnier and M. R. Visbal, "Numerical simulation of the impingement of a streamwise vortex on a plate," *International Journal of Computational Fluid Dynamics*, vol. 12, no. 1, pp. 49–66, 1999.

[14]K. J. Forster, T. Barber, S. Diasinos, and G. Doig, "Numerical investigation of streamwise vortex interaction," in *SAE Technical Paper*, SAE International, 09 2015.

[15]R. Klein, "Simplified equations for the interaction of nearly parallel vortex filaments," *Journal of Fluid Mechanics*, vol. 288, pp. 201–248, 1995.

[16]D. Fabre, L. Jacquin, and A. Loof, "Optimal perturbations in a four-vortex aircraft wake in counter-rotating configuration," *Journal of Fluid Mechanics*, vol. 451, pp. 319–328, 2002.

[17]C.-Y. Tsai and S. E. Widnall, "The stability of short waves on a straight vortex filament in a weak externally imposed strain field," *Journal of Fluid Mechanics*, vol. 73, p. 721, 1976.

[18]R. F. Huang and C. L. Lin, "Vortex shedding and shear-layer instability of wing at low-Reynolds numbers," *AIAA Journal*, vol. 33, no. 8, pp. 1398–1403, 1995.

[19]J.-H. Yoon and S.-J. Lee, "Direct comparison of 2D PIV and stereoscopic PIV measurements," *Measurement Science and Technology*, vol. 13, pp. 1631–1642.

[20]C. W. M. Raffel and J. Kompenhas, *Particle Image Velocimetry, a practical guide*. Berlin, Germany: Springer, 1998.

[21]C. A. Cruz, *Experimental and numerical characterization of turbulent slot film cooling*. ProQuest, 2008.

[22]A. F. K. Yeung and B. H. K. Lee, "Particle Image Velocimetry Study of Wing-Tip Vortices," *Journal of Aircraft*, vol. 36, no. 2, pp. 482–484, 1999.

[23]T. S. Miller, L. K. Kliment, and K. Rokhsaz, "Analytical Investigation of Co-Rotating Vortex Filaments with Experimental Verification," in *33rd AIAA Fluid Dynamics Conference and Exhibit*, no. June, 2003.

Numerical Investigation of Streamwise Vortex Interaction

2015-01-2573
Published 09/15/2015

Kyle J. Forster and Tracie Barber
UNSW Australia

Sammy Diasinos
Macquarie University

Graham Doig
California Polytechnic State University, UNSW Australia

CITATION: Forster, K., Barber, T., Diasinos, S., and Doig, G., "Numerical Investigation of Streamwise Vortex Interaction," SAE Technical Paper 2015-01-2573, 2015, doi:10.4271/2015-01-2573.

Abstract

Streamwise vortices can be observed to interact in a number of real world scenarios. Vortex generators operating in boundary layers, as well as aircraft flying in formation can produce vortex interactions with multiple streamwise vortices in close proximity to each other. The tracking of these vortex paths as well as the location and nature of their breakdown is critical to determining how the structures can be used to aid flow control, and how large scale turbulence develops from them.

Six configurations of two NACA0012 vanes were evaluated computationally to observe the interactions of a pre-existing vortex with a vortex generated downstream. Co and counter-rotating configurations at three different lateral spacings were used to vary vortex position and impingement on the rear vane. RANS testing of all configurations revealed that the strength of the downstream vortex in the co-rotating case was largely unaffected by the presence of the upstream vortex, while the counter-rotating case saw a reduction in vortex strength of up to 30%. LES simulations to better understand the flow mechanisms exhibit the Crow instability in the counter-rotating case and a helical merging pattern in the co-rotating condition.

These findings show that multiple vortex generators can be used to re-energize vortices, allowing far longer vortices than commonly achieved in fields such as flow control. The outcomes indicate that accurate positioning of counter-rotating vortex pairs to cause the premature destruction of undesirable vortices is possible.

Introduction

Boundary layer flow control is often enacted through the use of streamwise vortices, which can delay flow separation by the re-energization of the near-wall region [1,2,3]. This allows wings to operate at higher angles of attack without stall occurring [1], and can keep duct flows from separating around bends [2]. However, the presence of adverse pressure gradients in these flowfields inherently causes the vortex to break down beyond a certain point and be rendered ineffective. To ensure flow remains attached for the desired surface, a vortex used for flow control must persist the length of the required geometry without suffering breakdown.

In contrast, the presence of upstream vortices may produce negative effects on downstream flow devices. An example of this is aircraft wakes, which prevent the closely spaced landings of subsequent aircraft due to the dangerous downwash produced by their vortices [4]. The breakdown of these vortices is a critical factor, allowing safe landings of subsequent aircraft, and is typically due to the Crow instability [5]. Similar negative effects can be seen in race car aerodynamics, where existing vortices may reduce the efficiency of components such as air intakes, radiators and wings [6]. As such, it is important to know how upstream vortices interact with geometries, and to determine methods of producing rapid vortex breakdown where required.

Experimental studies have identified seven types of vortex breakdown falling under 3 primary categories, as classified by Lucca-Negro and O'Doherty [7]. The three primary modes are bubble type, spiral type and helical breakdown, with the other modes typically being combinations of these. Escudier and Zehnder [8] and Leibovich [9] found that increasing the swirl number (the ratio of maximum azimuthal velocity to axial velocity) of a vortex transitioned the breakdown from spiral to bubble, and subsequently moved it further upstream as the swirl number became higher. As such, the swirl number essentially defines the stability of a vortex, as well as its localized strength due to increased flow entrainment from vortices with higher swirl. Pasche, Gallaire and Dreyer [10] demonstrated that the swirl number was linked to the angle of attack of a given vane, and as such selection of angle of attack on a wing or vane will determine the vortex effectiveness and duration.

The simplest method for invoking vortex breakdown is to place a blockage in the flow path of the vortex, producing a steep adverse pressure gradient. Pasche, Gallaire and Dreyer [10] investigated the effects of a sphere placed in the trajectory of a vortex generated by an elliptical vane in a water tunnel. The short duration adverse pressure gradient generated by the sphere was directly linked to the breakdown location, with larger spheres and sphere upstream movement causing the breakdown location to move upstream. While this method is effective in causing vortex breakdown, it will cause significant drag and large flow losses due to the significant blockage and adverse pressure gradient required. A method to perform this vortex breakdown with less drag, such as breaking it down with another vortex, may be greatly beneficial.

Experimental studies have also been performed on co-rotating and counter-rotating vortices produced by vanes. Inasawa, Mori and Asai [11] investigated the flowfield around two wings spaced 2.5C apart in the streamwise direction with 5% of the wingspan overlapping. They were able direct the lead vortex onto the trailing wingtip surface, where it interacted and produced a separate counter rotating vortex pair. Smoke visualization showed that the burst point of the leading wing vortex was behind that of the trailing wing, with some energy transfer occurring. Devenport, Vogel and Zsoldos [12] looked at the interactions of a co-rotating pair, finding at a Reynolds number of 260000 based on chord length that the two cores continued to spiral around each other for 20 chord lengths after the vanes before merging into a single vortex core. This final core structure was found to be larger and more axisymmetric than a vortex produced from a single vane.

Due to the swirling nature of vortices, they act as pressure gradient amplifiers in the sense that an induced gradient in the freestream will be substantially increased at the vortex core [13]. Cassidy and Falvey [14] found that a probe placed near a pure vortex caused a substantial upstream migration of the breakdown location. As such, either Laser Doppler Anemometry (LDA) or Particle Image Velocimetry (PIV) must be used for accurate experimental results; however these methods are time consuming and difficult to construct a full transient picture of all vortex properties. In addition to this, pressure fields cannot be directly measured by either LDA or PIV, and LDA cannot time resolve meandering vortices. Consequently, Computational Fluid Dynamics (CFD) is a very useful tool for in depth vortex analysis.

The work described in this paper investigates the near field interactions of a vortex produced by an upstream vortex with a downstream vane. Steady state RANS solutions have been used for preliminary analysis of a two vane configuration, allowing for approximate flowfields for comparison and cases of interest to be decided. Due to the solution time reduction, using RANS solutions has allowed for more cases to be compared for numerical analysis. Transient LES simulations of three of the six cases have then been run to more accurately observe the flowfield and monitor the dynamics of the vortex motions and interactions. The aim of this work is to determine if vortex re-energization is possible by the introduction of a secondary vortex, and if premature vortex destruction may be promoted through the use of vortices.

This paper details the computational methodology of the analysis, with detailed results from the RANS and LES runs performed, and a comparison of the different configurations as well as the results obtained from the different methods. The suitability of vortex generators for re-energization and destruction of vortices will then be discussed.

Computational Setup

The present study looks into the interaction of two streamwise vortices produced by two NACA 0012 vanes. One vane is located 10 chord lengths (C) downstream of the other, as can be seen in Figure 1. Six configurations were initially tested, with counter and co rotating vanes with a lateral offset of 0C, 0.2C and −0.2C. These were chosen to observe the effects of the front vortex impacting and passing to either side of the rear vortex, thus allowing the effects of the front vortex on the rear vortex's breakdown length to be observed. An angle of attack of 8 degrees on each vane has been used for all cases, with a square edged tip. This tip geometry was selected as it is facilitates a high quality mesh in that region while still producing a well-defined vortex. Eight degrees was selected as it will give a sufficiently high swirl number to observe the vortices while being below the stall point of the vanes, reducing any risk of further complicating the flow by introducing flow separation. The vanes are 1.5C tall, a compromise between larger clearance from the floor boundary and the stronger relative vortex produced by shorter aspect ratios. The configurations for the cases to be evaluated are detailed below in Table 1 and Figure 1.

Table 1. Case Configurations

Lateral Offset	Co-Rotating	Counter-Rotating
0C	A	D
-0.2C	B	E
0.2C	C	F

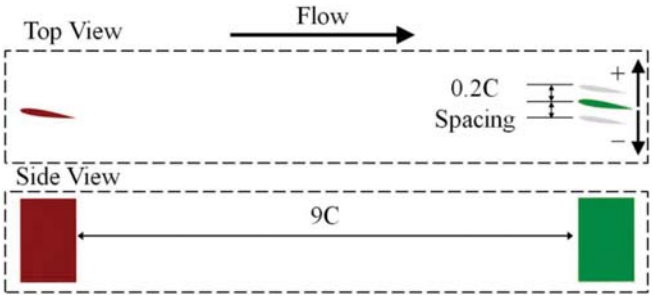

Figure 1. Diagram of vane setup

A constant velocity inlet with no boundary layer was specified as the inflow. As the primary objective was to observe the paths of the vortices with minimal external flow disturbances, a low turbulence value of 0.1% was used, with a length scale of 0.03C. Because a minimised boundary layer influence on the vortices was desired, symmetry (free-slip) conditions were used for all domain walls, with a no slip wall being employed on the vanes themselves. For the outlet an outflow condition was used to provide minimal disturbance to the vortices, as previous tests had shown that pressure outlets had caused necking and upstream disturbances along the vortex core. A Reynolds number of approximately 70000 based on chord length was selected provide a compromise between the shorter vortex breakdown length at high Reynolds numbers and the lessened flow disturbances at low

Reynolds numbers. This is also such a number that the flow can easily be replicated in a wind tunnel at a later point in time. The flow was assumed to be incompressible.

Extensive testing of the boundary distances was carried out on the inlet, outlet and sides, with RANS solutions used to reduce evaluation times. Configuration F was selected for boundary testing. Four positions were tested for outlet length, with three for the inlet and sides. It was found that all the outlets tested were sufficiently far downstream to not cause interference with the paths of the vortices, and as such boundary selection became an issue of desired observation window and mesh size constraints. In outlet cases of 20C, 30C, 38C and 46C the differential in vortex core location as determined by core streamlines was found to be less than 1.3% from the 20C case to the 46C case. There was no differential in the 30C to 46C cases as any discrepancy was below the mesh resolution. In order to determine the window for observing the vortex path, the gradients and variances in the paths were investigated. Beyond 30C after the vortex generator, it was found that the gradient of the vortex path was largely linear, and in the vertical axis the deviation in vortex path was only 0.02C.

In addition to the testing of the outlet length, rigorous checking of the inlet and side boundaries was performed with a similar level of thoroughness, yielding the following results in Figure 2. The final blockage ratio was 0.6%.

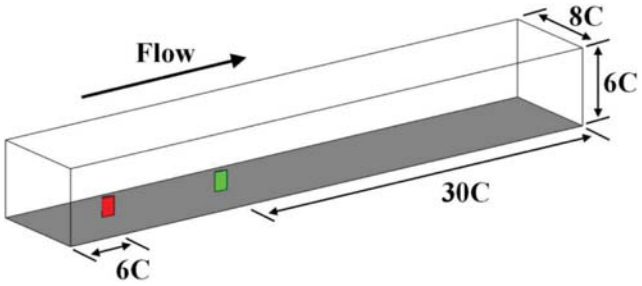

Figure 2. Computational domain and boundary distances.

Grid generation was performed in ANSYS ICEM, with ANSYS FLUENT 14.5 being used to evaluate the model. A fully structured multi-block meshing strategy was employed. Due to the large domain size required to capture the far field flow features, a significant number of cells was required. Three mesh densities were evaluated at 400,000, 3 million and 22million cells respectively, with the dominant increase being in the wake and vortex paths of the two generators. It was found that for RANS solutions, the vortex paths were very similar, with total deviation at the end of the domain being only 0.23C. However there was a marked increase in numerical diffusion rates in the lower meshes, with vortex length at a Q-criterion value of 9000 s^{-2} varying by 4.8C between the cases. This diffusion differential was expected to have a significant impact on the fidelity of the LES results, and as such the 22 million element mesh was selected. This consisted of 58 elements along the length of each vane, with 300 elements along the length of the wake behind the rear vane, and 200 between the vanes. 40 cells were used along the height of the vane, with the majority concentrated at the tip as the base area was of little interest. To ensure a courant number of below 1 on this mesh while still providing timestep convergence, a timestep of 0.00003s was used. The distribution of cells and the meshing strategy around the vane tips can be seen in Figure 3.

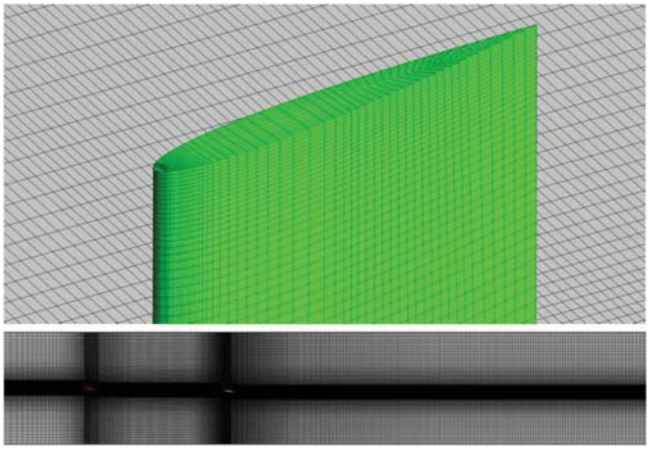

Figure 3. Meshing strategy (top) and distribution of cells around domain (bottom).

Runs were performed on the UNSW Australia School of Mechanical and Manufacturing Engineering Trentino Cluster on one 64 core node running at 2.1GHz. With this configuration, it took two months to run 15000 timesteps on the 22 million element mesh, with 25 iterations per timestep selected to ensure residual convergence after monitoring of residual levelling off. RANS runs were performed in steady state for 3000 iterations to give force and wake velocity convergence of <0.001%. To initialise the flow through the entire domain a flow time of 0.46 seconds is required, which is equivalent to 15333 timesteps.

SIMPLEC pressure-velocity coupling was used as it provides improved convergence over SIMPLE and reduced computational cost compared to a coupled or PISO solver, particularly important for the LES runs. As the dominant flow feature is swirling and involves reasonably steep pressure gradients, a second order PRESTO algorithm was selected for pressure discretization. Bounded central differencing was utilised for momentum to damp out any artefacts the naturally undamped LES solution may create, whilst still retaining solution fidelity. Bounded second order implicit methods were used for time stepping to improve accuracy over first order whilst maintaining stability. For RANS solutions Third-Order MUSCL was used for turbulent kinetic energy and dissipation rate to reduce diffusion in the solution.

The K-ω SST turbulence model was selected for the RANS testing, as it has been proven successful in a variety of wing analyses, and is effective in predicting vortex paths [1,15]. For the LES analysis, the Wall Adapting Local Eddy-Viscosity (WALE) model was used. This model does not have as stringent a mesh requirement for the near wall region as Wall Modelled LES, which allowed for more of the mesh elements to be used in the wake region of interest. It also has superior treatment of laminar regions of flow over the Smagorinsky-Lilly model, such as the leading edges of the vanes [17].

Analysis Results

The primary objectives of the RANS analyses were to compare the effectiveness of each configuration, as well as identify the potential cases of most interest for LES. It was also desired to have a baseline with which to observe the limitations of RANS in computing vortex interactions. The LES simulations were intended to provide a detailed

insight into the specific nature of the transient interactions between the two vortices, as well as the near-field interaction of the upstream vortex with the vane itself.

RANS

Co-Rotating

Results from the analysis of the co-rotating vanes indicated that regardless of the offset of the rear vane, a similar flow structure was formed in all cases. This consisted of the vortex produced from the upstream vane being drawn into a spiral like structure around the vortex produced by the downstream vane. The offset of the downstream vane varied the rate at which this structure formed into a single coherent circle, as can be seen in Cases B and C of Figure 4; however appeared to have a relatively minor effect of the vortex dissipation rate with final energy differences of less than 3.6% observed between cases. This spiral tail appears to be constructed of the initial vortex being stretched into an ellipsoid shape by the downstream vortex at early stages. As it progresses downstream, the upstream vortex transfers it's vorticity to the downstream vortex, reducing the vorticity magnitude of the tail. Eventually this results in the dissipation of the tail and the formation of a coherent vortex with a circular structure.

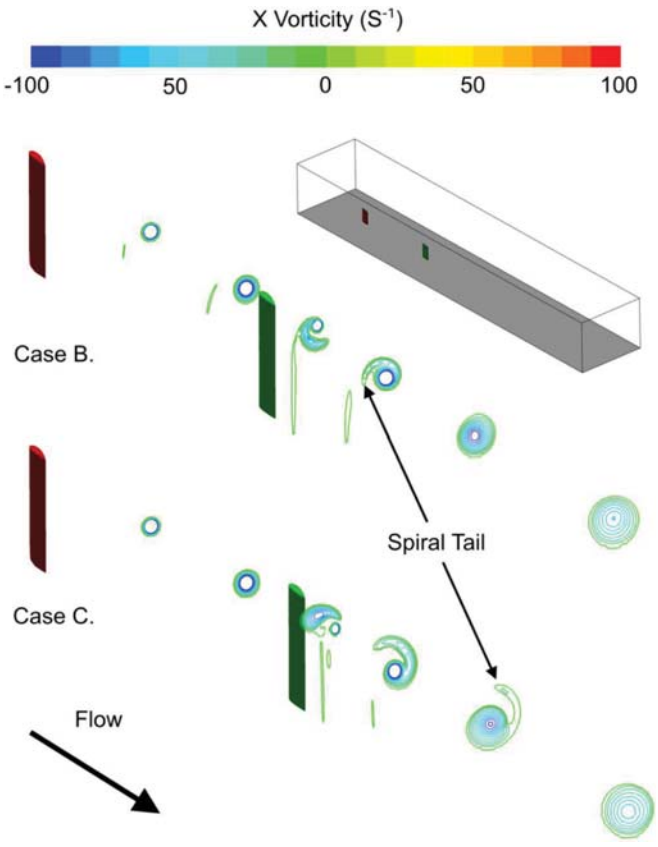

Figure 4. Contours of streamwise vorticity for co-rotating cases.

The magnitude of velocity across the flow direction produces an isosurface that, when trimmed by the Q-criterion [18], is very effective in tracking vortex cores [16]. Inspecting this isosurface at 1m/s swirl velocity provided an effective visualization of the vortex merging (Figure 5). Inspecting the vortex paths rear the downstream vane showed that the close offset of Case B resulted in the vortex impacting the vane just below the tip on the suction side. From here it almost immediately merged with the second vortex, with negligible presence of the core continuing. In the further spaced Case C it was found to pass on the pressure side of the vane without approaching the surface. The initial vortex then appeared to be entrained and pulled around by the downstream vortex, forming the spiral tail seen earlier.

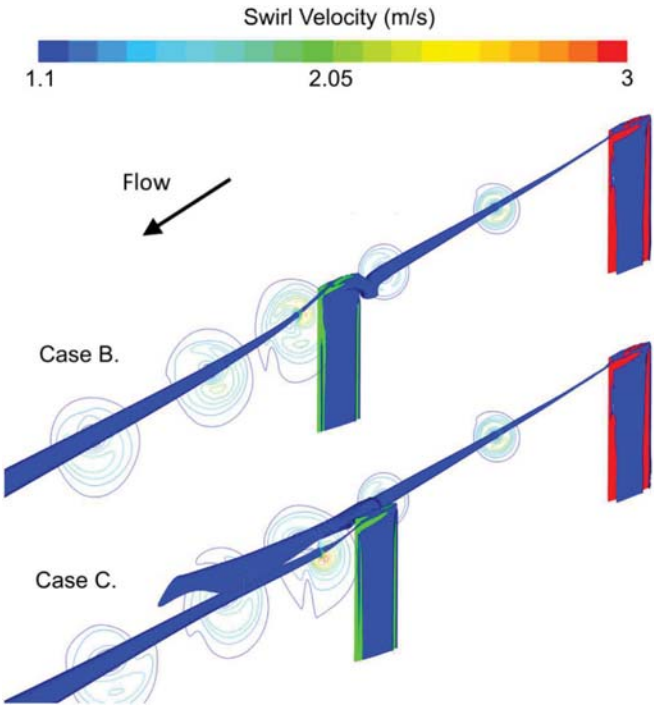

Figure 5. Trimmed tangential velocity isosurface at 1m/s and swirl contours for co-rotating cases.

In order to calculate the strength of the vortices at any given plane, the circulation around the vortex core can be measured. Circulation is typically calculated via a sum of line integrals along circular curves in a field; however this is not practical in many cases due to the non-uniformities of real world vortices. This is due to the different shapes of vortices both between cases and downstream in the same case, as could be seen from the vorticity contours in Figure 4. Due to the nature of the geometries present, a method of calculating the circulation can be performed by measuring the average of the in plane velocities at a slice across the flow. By eliminating the streamwise velocity component, only the vortex swirl and downwash from the vanes remain in-plane. As the downwash is perpendicular to a line drawn out from the vortex core, it is included in the circulation calculation. This would not be the case for more complex geometries with additional flow motion, however is appropriate for the dual vane scenario. As such, the normalized total circulation can be taken as the average value of the in-plane velocities, divided by the maximum total circulation calculated. These results are shown in Figure 6 below. A single vane at the same location as the rear vane is included for comparison. X=0 is referenced from the leading edge of the first vane, and positive X is taken downstream of the vanes.

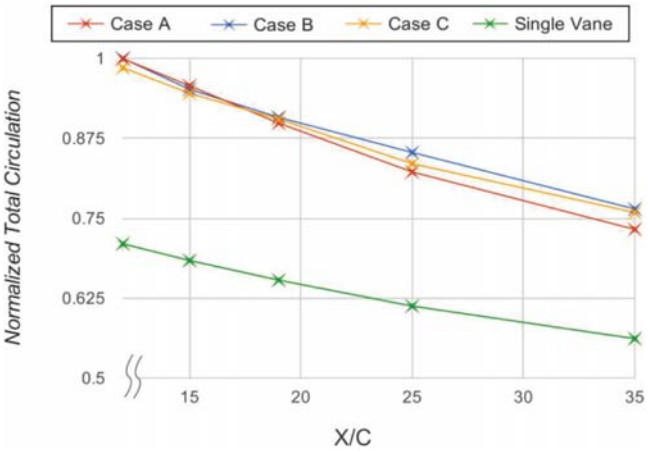

Figure 6. Normalized total circulation for co-rotating cases, estimated error in calculation method ±0.15%

From these values it can be seen that the energy state of the vortex structure is very similar directly behind the vane (12C downstream of first vane), with only 1.5% variance between the 3 co-rotating cases. The total circulation in the co-rotating condition is substantially higher than in a single vane case; with a 29% increase in circulation at the 12C location, and 26% more circulation at 35C. However, the dissipation rate of the co-rotating cases is noticeably higher than the single vane case, with a circulation dissipation of between 24-27% for co-rotating compared to 21% for the single vane case. This suggests the dissipation rate of the uneven vortex formed at the second vane is higher that a more coherent singular vane vortex structure. The variance of dissipation between the different offsets is also small but notable, with 1.5% variance in circulation at 12C, but 3.2% variance by the 35C mark. Case A shows the most rapid dissipation, with the vortex impacting on the pressure side of the vane. Case C, with the vortex passing by the pressure side shows the slowest total dissipation at 24%; however the initial circulation is lower, resulting in a lower final circulation than Case B. While Cases A and C show a fairly consistent trend of decreasing circulation gradient after 15C, Case B has a point of inflexion at the 25C mark. To further investigate this phenomenon, average vortex turbulent kinetic energies (TKE) were plotted, as seen in Figure 7.

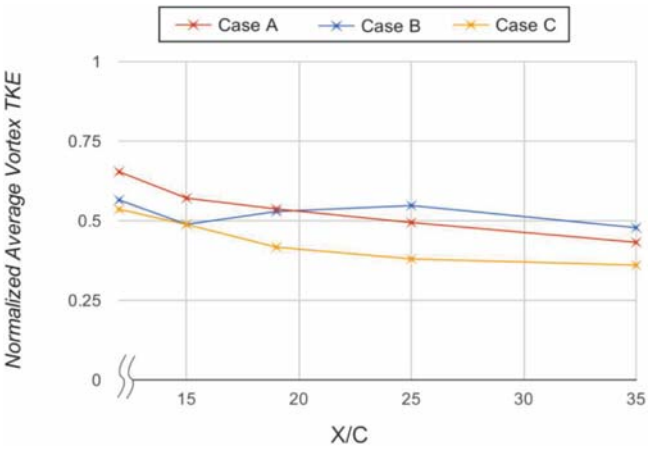

Figure 7. Normalized turbulent kinetic energy for co-rotating cases, estimated error in calculation method ±0.25%

To calculate these values, planar slices were set up at the various downstream locations and the turbulent kinetic energy values were averaged to provide a means of comparing total TKE between cases. Analysis of the values shows that Case B has a peak in the turbulent kinetic energy observed concurrent with the point of inflection in the total circulation at X=25C. As Case B is also the case to most rapidly form into a coherent vortex structure, this indicates that this effect is due to the fully formed vortex itself, and not the combination of the two vortices. Case A and C also exhibit signs of a similar pattern, with Case A exhibiting an inflexion point at 19C and Case C showing a significantly shallower gradient in the 25C to 35C interval. While not as pronounced as the turbulence peak from Case B, both Case A and Case C have longer vortex merging lengths, and this would indicate that there is a relative rise in turbulence post vortex merging. However, in Case A and C the overall turbulence dissipation rate outweighs this effect, hence why the absolute turbulence level does not increase, but only the gradient changes. As such the offset of the secondary vane affects the coherency of the vortex structure in turbulence and velocity distribution, despite not significantly affecting circulation.

The varying of the vane offset also altered the path of the final vortex slightly, with a vortex path offset equal to 28.4% of the vane offset. This deviation means that the offset of the vanes can be used to assist in the direction of the vortex while not altering the re-energization level. As a result, it would be expected that a configuration of multiple co-rotating vanes would be less sensitive to yaw and crossflow conditions than a larger single vane. This would also improve control of the vortex over a longer distance than the single vane configuration.

Counter-Rotating

Contrary to the co-rotating cases, the counter-rotating scenarios showed significant differences in vortex structure and dissipation rates. Moving the downstream vane immediately in the path of the vortex as per Case E. caused a rapid destruction of the initial vortex, as well as significantly reducing the strength of the strength of the secondary vortex. Moving the vane such that the vortex passed alongside it at a distance instead of near impact (Case F) caused the vortex produced by the downstream vane to equal the vortex length of the co-rotating case (Case B). This is related to energy transfer between the vortices, as the primary vortex dissipated at a more significant rate than the single vane case. These features can clearly be seen when the streamwise vorticity was inspected, as in Figure 8.

The total circulation for the counter rotating cases in Figure 9 confirms this energy dissipation. Ahead of the second vane (5C and 10 C) the variation between cases is only 1%, however behind the vane there is a substantial difference in circulation of 47%. Case E shows the most substantial drop, with a 52% decrease in circulation by 12C. This is due to the very direct leading edge impact of the primary vortex on the rear vane, as was seen in Figure 8. Moving the vane further away from the path of the vortex increased the total circulation; however these values were still substantially lower than the co-rotating cases, with an average 82% lower circulation at the 35C mark.

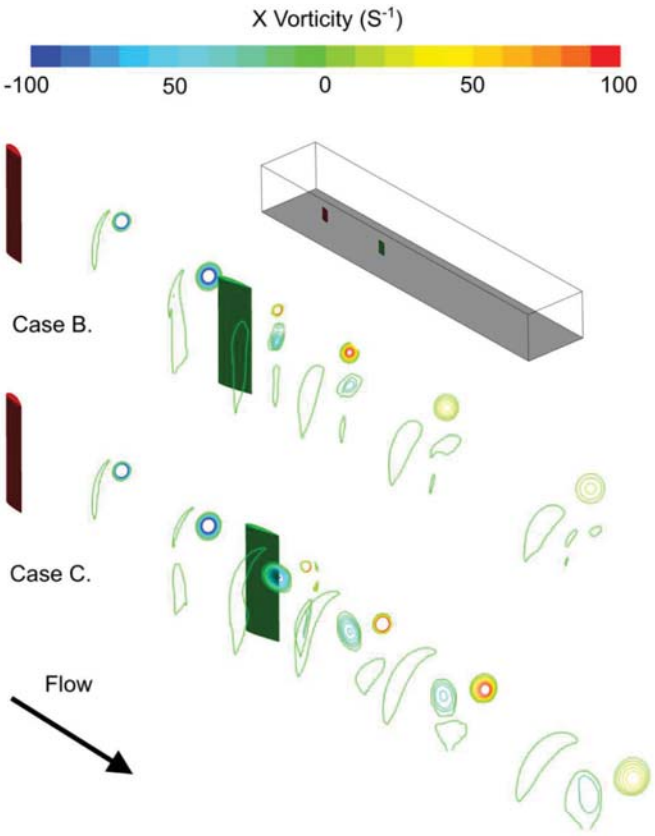

Figure 8. Contours of streamwise vorticity for counter-rotating cases.

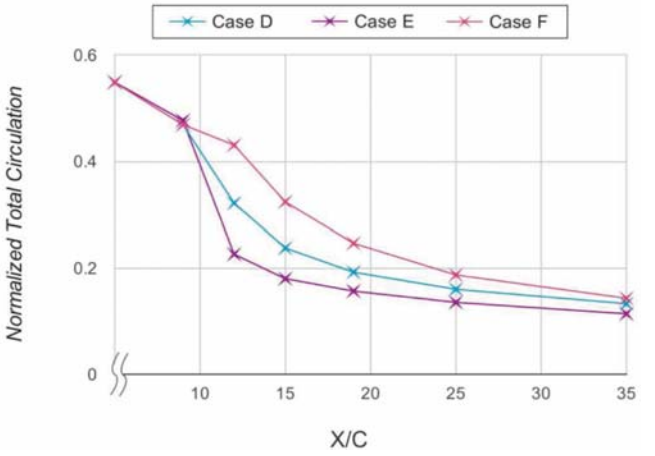

Figure 9. Normalized total circulation for counter-rotating cases, estimated error in calculation method ±0.15%

The dissipation rates of the counter-rotating configurations were also more significant than that of the co-rotating. Case F exhibited a dissipation of 69% from 10C to 35C, while Case D and E achieved 72% and 77% respectively. The largest discrepancy between offsets is the location of maximum dissipation rate, with the close impact Case E experiencing very significant drops in circulation immediately after the vane (9C to 12C). This decrease was 52%, compared to the other cases 8.5% and 32% in the same region. This is consistent with the turbulence production observed, as can be seen in Figure 10.

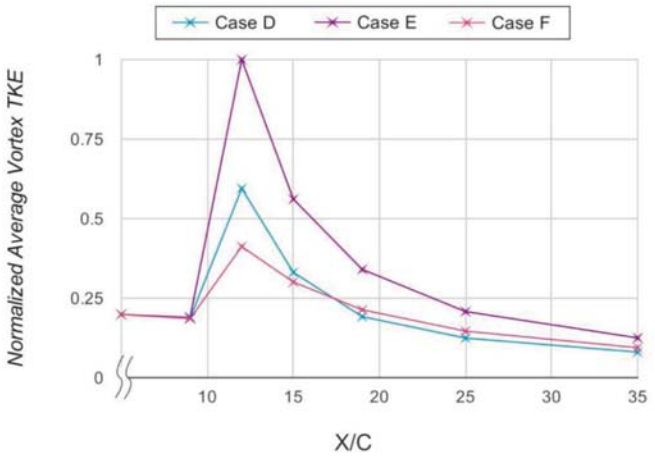

Figure 10. Normalized TKE for counter-rotating cases, estimated error in calculation method ±0.25%

The high level of turbulence production in Case E coincides with the region of very rapid circulation decay, indicating that this configuration has caused the initial vortex to breakdown. Cases D and F both had substantially lower initial turbulence production, with 41% and 59% less respectively. This places the turbulence of Case F below that of all the co-rotating cases as the two vortices have a further separated interaction, while still transferring energy between each other. Consequently it can be seen that the counter-rotating case is highly sensitive to vane offset, leading to the conclusion that it would be a problematic way of rapidly breaking down vortices in conditions involving crossflow or other uncertainty.

Comparison

To allow for simple comparison between the counter and co cases the total pressure deficits and peak in-plane velocities were compared. Analyzing the peak in plane velocities shown in Figure 11 reveals that despite the lower circulations produced by the counter rotating cases; the peak velocities are higher, with a 33% increase between the highest peaks of each configuration. This indicates the non-uniformity of the counter-rotating cases is substantially higher than that of the co-rotating due to the high swirl region at the interface between the two vortices. As mixing and redistribution of azimuthal velocity within the vortex pair occurs, the in-plane velocities drop at a much faster rate than the co-rotating cases, until they are less than the co-rotating cases as the circulation analysis suggests.

From the 25C location onwards, the co-rotating cases all align very closely in peak in-plane velocity, with variances of less than 1%; however the counter-rotating cases show substantial discrepancies of up to 18%. This trend is consistent with the total circulation analysis, and demonstrates the insensitivity to offset of the co-rotating case vs the counter-rotating case. This demonstrates the difficulty of using peak swirl number to characterize non-uniform vortices, as it is dependent on the strength and velocity distribution. As such, a circulation averaging or pressure averaging approach is more useful for a geometry such as the double vane configuration, compared to the swirl number approach often used by other studies [8,9,10].

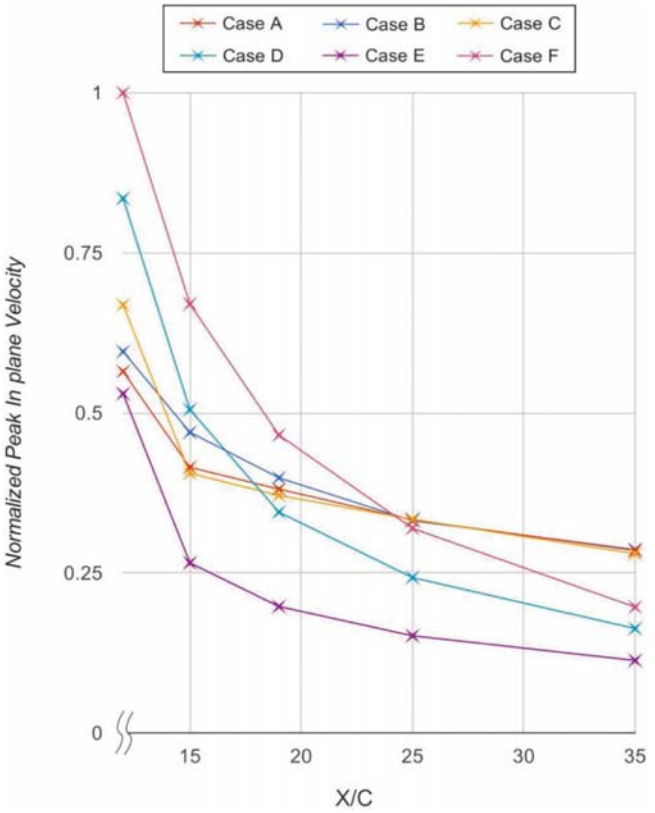

Figure 11. Normalized peak in plane velocities for all cases

A method of measuring vortex strength that is less sensitive to the non-uniformities of the vortex is the total pressure deficit variance. As the pressure deficit in the core of the vortex provides the centripetal force required to hold the vortex in rotation, its magnitude is related to the total intensity of the vortex. These pressure deficits are plotted in Figure 12. The pressure deficits of all co-rotating cases are greater in magnitude that all counter-rotating cases at all points logged, showing the greater strength and coherency of the single vortex structure. However the pressure deficit dissipation is higher in all co-rotating cases, with a maximum of 37% as opposed to a maximum dissipation of 21% in the counter rotating cases. Of interest is that Case F displays a more nonlinear dissipation pattern compared to cases D and E, with this being linked to the persistence of the co-rotating vortex structure. Also of note is the pressure deficit of Case E being more substantial than Case D, despite the far more significant levels of vortex dissipation. This further supports the hypothesis of vortex breakdown being induced by the second vane, as it is common for a vortex breakdown to exhibit a wake behind it similar to a bluff body [19,20], which would result in a larger pressure deficit than expected from the size and strength of the vortex itself.

LES

From the RANS cases it was identified that the extremes of the co-rotating cases could be used to determine the flow features of the vortex re-energization interaction. This led to the selection of Case B (−0.2C) and Case C (0.2C) for LES analysis. For the counter-rotating case, all RANS examples showed similar destructive interactions, and as such only one case was selected. This was chosen to be Case F (0.2C) as it caused dissipation of the primary vortex without any geometrical interference, as well as having a substantial length of the secondary vortex.

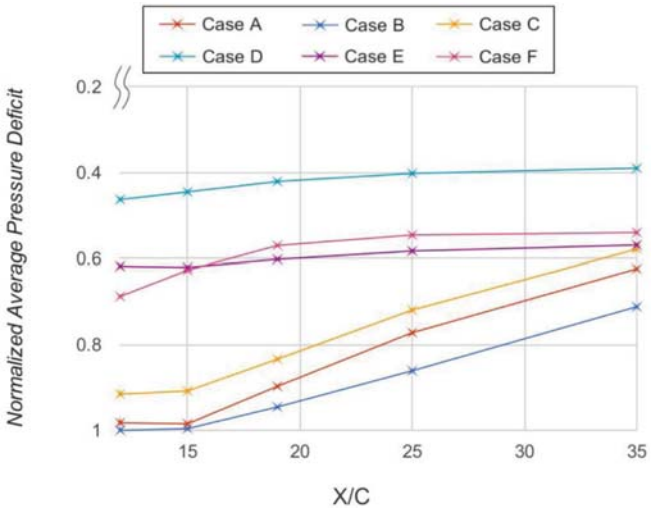

Figure 12. Normalized pressure deficit for all cases

Case B

Observing isosurfaces of streamwise vorticity at 300s^{-2} revealed that the impact of the vortex on the front of the rear vane continued almost directly into another vortical structure, as can be seen in Figure 13. Initially this was thought to be a small scale breakdown due to the increased turbulence around the rear of the vane; however the rotational momentum as observed by the swirl velocity was conserved to the same level as if a new vortex had been formed. This meant a vortex breakdown was not occurring at this location.

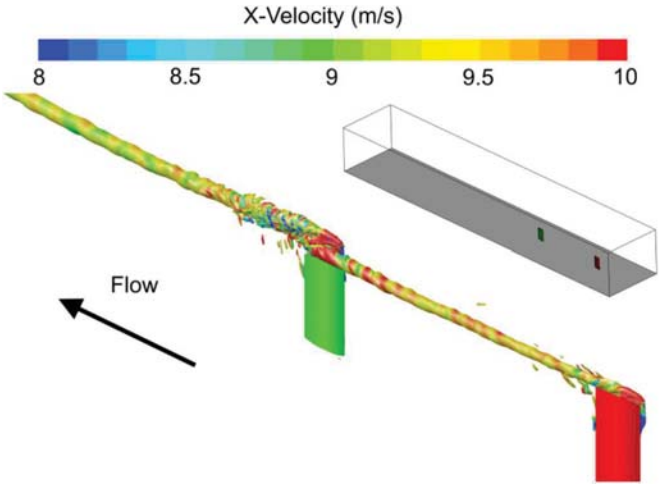

Figure 13. Isosurfaces of streamwise vorticity at 300s^{-2} colored by contours of streamwise velocity for ease of visualization.

In addition to this continuation of the vortex core, it was noted that the rotation direction of the upstream vortex produced improved flow attachment on the downstream vane, reducing noise from vortex shedding on the vane itself. This may be a cause of improved vane vortex generation efficiency.

Looking closely at the vortex structure around the rear vane as in Figure 14, the mechanism by which the vortices merge can be observed. The pre-existing vortex core travels very close to the vane surface, just below the top of the vane. As the high swirl region of the new vortex wraps around the top of the vane, the swirl of the existing vortex draws it around. The low swirl core of the new vortex forms a

deficit in the swirl peak around the existing vortex, resulting in a merge of the two swirl regions and an ellipsoid of low swirl being formed. Around this orbits the two regions of high swirl, one from the existing vortex, and one from the new vortex. As the flow travels further downstream, the disturbances in these high swirl regions equalizes, eventually forming an overall swirl pattern with a very similar structure to a singular vortex core at a merging distance of 3.6C. This final pattern had a swirl peak above that of the initial vortex at the point of interaction, and was similar in peak velocity magnitude to the single vane case, with a decrease of 16%. It should be noted that the swirl distribution at this point was more uniform than in the single vane case due to the reduction in the spiral tail produced by the vane.

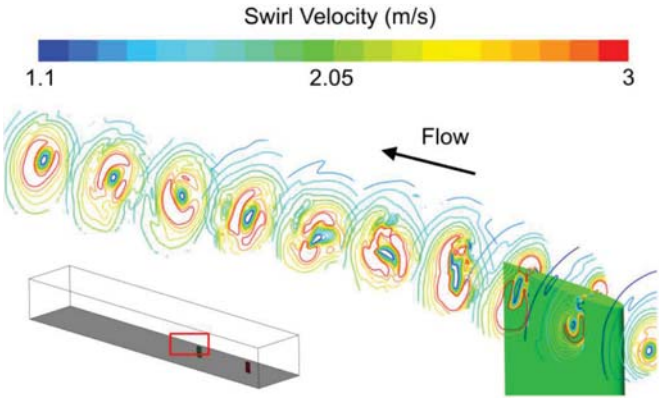

Figure 14. Contours of swirl velocity around rear vane.

Case C

Case C exhibited a superficially very different flow structure to Case B, with a helical path of the two vortex cores culminating in a vortex merge around 20C downstream of the rear vane. Oscillations within each individual vortex resulted in a meandering of the crossover locations of the double helix, as can be seen in Figure 15. However, these oscillations do not pose any instability, as no breakdown was observed before or after the merge. This helical pattern was relatively stable in nature, with no spiraling of core locations or downstream movement of the structure observed.

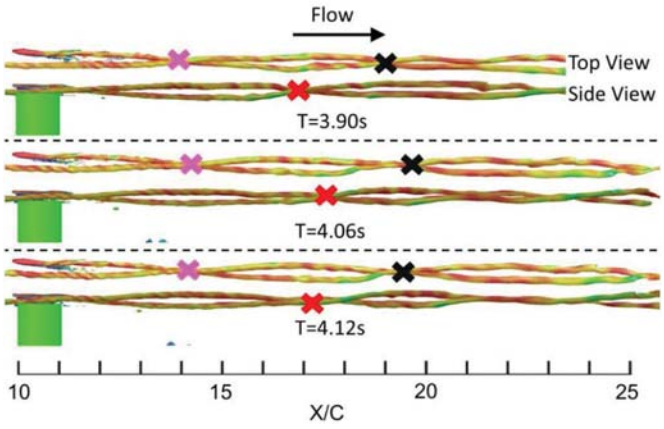

Figure 15. Isosurfaces of streamwise vorticity at $300s^{-2}$ colored by contours of streamwise velocity, with crossover locations indicated.

Upon closer inspection of the trimmed tangential velocity (Figure 16), it could be seen that the vortex merging structure closely resembled that of Case B. While the initial vortex does not intersect with the surface of the vane, it is still entrained into a spiral like formation by the rotation of the secondary vortex downstream of the vane. This rotation produces a low swirl location in the middle of the two vortex cores, with the high swirl vortices themselves orbiting around it. This low swirl center region produced a swirl deficit in the two vortex cores, which allows the central core to expand, merging the two vortices together. The swirl velocity distribution then evens itself out similarly to Case B, forming a coherent single vortex core.

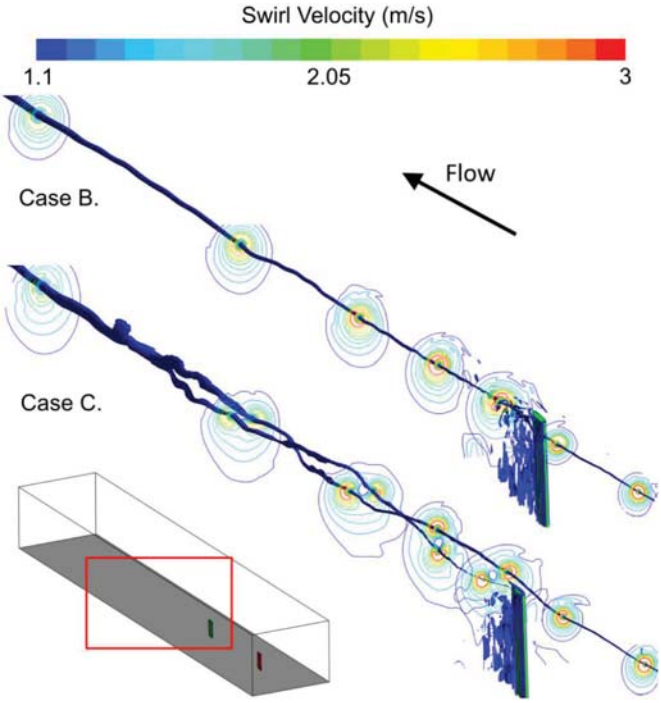

Figure 16. Trimmed tangential velocity isosurface at 1m/s and swirl contours for co-rotating LES cases.

As can be seen from Figure 16, despite the mechanism of merging being fundamentally similar, the length scales these interactions occur on varies substantially. In the scale of the figure, the merging in Case B is almost imperceptible, while the merging of Case C is very clear. As such, the length of vortex merging depends on the proximity of the upstream vortex core to the location of generation of the downstream vortex. Of interest is the fact that the low swirl core and helical vortex path causes the two vortices to essentially act as a single vortex even when they are not merged. This may allow for effective use of this structure as a single vortex, and indicates that the co-rotating vane configuration is reasonably insensitive to crossflow and other flow disturbances for the purposes of vortex re-energization.

Case F

LES analysis of Case F indicated that the predominant cause behind the premature breakdown of the primary vortex was a phenomenon similar to the Crow instability. This could be observed through the presence of a sinusoidal deviation in the path of the primary vortex, as can be seen in Figure 17. Contrary to the lack of instability observed in Case C, this deviation became very severe in the primary vortex, causing a rapid reduction in vortex strength. It also manifested itself in the second vortex, where small deviations began to occur in its bath, increasing in size towards the end of the domain.

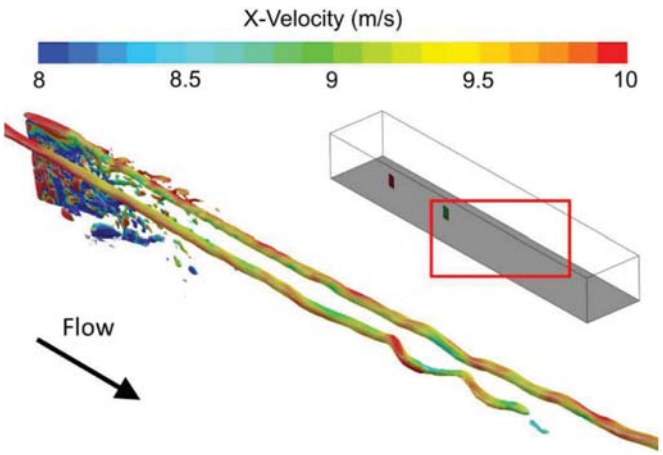

Figure 17. Isosurfaces of vorticity at $300s^{-2}$ colored by contours of streamwise velocity for ease of visualization.

The difference in rotational direction between the vortices resulted in substantially more flow separation from the vane than in the co-rotating case, with the upstream vortex essentially pulling the flow off the surface of the vane. This increased the level of noise in the solution, making it more difficult to analyze. Despite this, use of the trimmed tangential velocity allowed for effective tracking of the core paths and dissipation locations. By observing this in conjunction with the swirl contours in Figure 18, it was clear that the initial vortex does contribute to the strength of the secondary vortex, with a large region of high swirl formed. However, the instability and inherent unsteadiness imparted to the second vortex, in conjunction with the increased swirl, clearly accelerates its dissipation rate, with a far more rapid expansion than the co-rotating cases. This is consistent with the 56% in-plane velocity reduction by 10C downstream observed in the RANS, compared to the 42% of Case C.

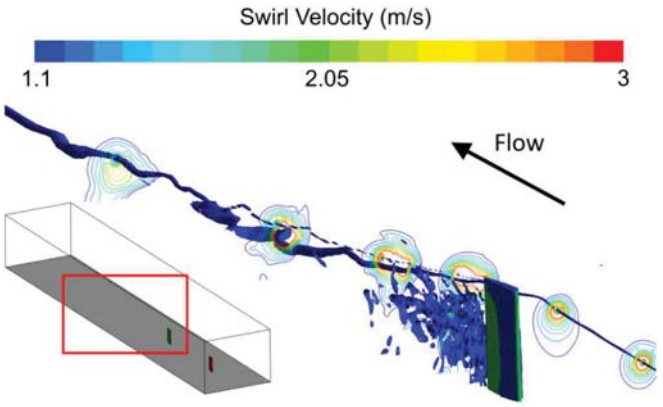

Figure 18. Trimmed tangential velocity isosurface at 1m/s and swirl contours for co-rotating LES cases.

Summary/Conclusions

The analysis of counter and co-rotating vane pairs at different lateral offsets revealed that it is possible to both re-energize and prematurely destroy vortices through the use of a downstream vane. It was found that the re-energization process is insensitive to lateral offset of the downstream vane from the vortex in a range of −0.2C to 0.2C, maintaining similar energy states when the offset was altered. However, the vortex paths substantially changed with offset, resulting in the merging distance of the two vortices increasing as the distance between the vortex core and the vane became larger. Despite the difference in merging length, the mechanism with which the merging occurred remained the same regardless of offset.

This indicates that such a configuration for vortex re-energization would be effective in conditions involving crosswinds and other real-world disturbances. After re-energization of the vortex with a second vane, it was found that the total circulation of the resulting vortex was higher than that produced by a single vane. Such a scenario will have superior control of vortex location over longer distances than a single vane setup.

It was found that while the counter-rotating case was effective at premature vortex destruction, it was very sensitive to offset. Large distances from the vane to the vortex core resulted in energy transfer between the upstream vortex and the downstream vortex, resulting in the destruction of the upstream vortex. However, under this configuration the strength of the downstream vortex was increased and an instability was introduced. This was not the case for when the vortex passed closer to the downstream vane, with an overall reduction in strength of both vortices and an immediate destruction of the upstream vortex in the direct impact case. It was found that this was due to the breakdown of the upstream vortex.

This indicates this configuration is efficient in the destruction of vortices in the ideal case, however is highly sensitive to crosswind and yaw conditions. As such, it may only be employed successfully in scenarios where the vortex location is well known and there is little chance of wandering.

References

1. Forster, K. and White, T., “Numerical Investigation into Vortex Generators on Heavily Cambered Wings”, AIAA Journal, Vol. 52, No. 5, 1059-107, 2014, doi:10.2514/1.J052529
2. Brown, A., Nawrocki, H., and Paley, P., “Subsonic diffusers designed integrally with vortex generators”. Journal of Aircraft, 5(3), 221-229, 1968, doi:10.2514/3.43931
3. Lin, J., “Review of research on low-profile vortex generators to control boundary-layer separation.” Progress in Aerospace Sciences (Vol. 38, pp. 389-420), 2002 doi:10.1016/S0376-0421(02)00010-6
4. Boustead, N., Ryan, K., and Sheard, G., “Short-wave instability growth in closely spaced vortex pairs.” Progress in Computational Fluid Dynamics, An International Journal, 2010, doi:10.1504/PCFD.2010.035360
5. Crow, S., “Stability Theory for a Pair of Trailing vortices,” AIAA journal, vol. 8, no. 12, pp. 2172, 1970, doi:10.2514/3.6083
6. Zhang, X., Toet, W., Zerihan, J., “Ground Effect Aerodynamics of Race Cars.” ASME. Appl. Mech. Rev. 2006;59(1):33-49. doi:10.1115/1.2110263
7. Lucca-Negro, O. and O'Doherty, T., “Vortex Breakdown: a Review,” Progress in Energy and Combustion Science, vol. 27, pp. 431, 2001, doi:10.1016/S0360-1285(00)00022-8
8. Escudier, M. and Zehnder, N., “Vortex-Flow Regimes,” Journal of Fluid Mechanics, vol. 115, pp. 105-121, 1982, doi:10.1017/S0022112082000676

9. Leibovich, S., "The Structure of Vortex Breakdown," Annual Review of Fluid Mechanics, pp. 221-246, 1978.
10. Pasche, S., Gallaire, F., Dreyer, M. and Farhat, M., "Obstacle-Induced Spiral Vortex Breakdown," Experiments in Fluids, vol. 55, p. 1784, 2014, doi:10.1007/s00348-014-1784-7
11. Inasawa, A., Mori, F., and Asai, M., "Detailed Observations of Interactions of Wingtip Vortices in Close-Formation Flight," Journal of Aircraft, vol. 49, pp. 206-213, 2012, doi:10.2514/1.C031480
12. Devenport, W. J., Vogel, C. M., & Zsoldos, J. S., "Flow Structure Produced by the Interaction and Merger of a Pair of Co-rotating Wing-tip Vortices," Journal of Fluid Mechanics, vol 394, 357-377, 1999, doi:10.1017/S0022112099005777
13. Hall, M., "A new approach to vortex breakdown," Proc. Heat Transfer and Fluid Mechanics Institute, pp. 319-340, 1967.
14. Cassidy, J. and Falvey, H., "Observations of Unsteady Flow Arising after Vortex Breakdown," Journal of Fluid Mechanics, vol. 41, no. 04, pp. 727-736, 1970, doi:10.1017/S0022112070000873
15. Wik, E. and Shaw, S., "Numerical Simulation of Micro Vortex Generators. In 2nd AIAA Flow Control Conference, 2004, doi:10.2514/6.2004-2697
16. Forster, K., Diasinos, S., Barber, T.J., and Doig, G., "Computational Analysis of Backwards Facing Vortex Generators for Boundary Layer Mixing Applications", 19th Australasian Fluid Mechanics Conference, 342, 2014.
17. Zhou, Ying, and Wang Z. J.. "Implicit large eddy simulation of transitional flow over a SD7003 wing using high-order spectral difference method." AIAA paper 4442 (2010): 2010, doi:10.2514/6.2010-4442
18. Jeong, J. and Hussain, F., "On the identification of a vortex.", Journal of Fluid Mechanics, vol. 285, no. 69, 1995, 69-94, doi:10.1017/S0022112095000462
19. Leibovich, S., "Vortex stability and breakdown-Survey and extension", AIAA journal, vol. 22, no. 9, pp. 1192-1206, 1984. doi:10.2514/3.8761
20. Faler, J. H. and Leibovich, S., "Disrupted states of vortex flow and vortex breakdown", Physics of Fluids (1958-1988), vol. 20, no. 9, pp. 1385-1400, 1977, doi:10.1063/1.862033

Contact Information

Kyle Forster
k.forster@unsw.edu.au

Definitions/Abbreviations

RANS - Reynolds Averaged Navier Stokes

LES - Large Eddy Simulation

CFD - Computational Fluid Dynamics

LDA - Laser Doppler Anemometry

PIV - Particle Image Velocimetry

C - Chord length

CD - Drag Coefficient

The Engineering Meetings Board has approved this paper for publication. It has successfully completed SAE's peer review process under the supervision of the session organizer. The process requires a minimum of three (3) reviews by industry experts.

ISSN 0148-7191

http://papers.sae.org/2015-01-2573

Large Eddy Simulation of Transient Upstream/Downstream Vortex Interactions

Kyle J. Forster[1]†, Sammy Diasinos[2], Graham Doig[1,3] and Tracie J. Barber[1],

[1]School of Mechanical and Maunfacturing Engineering, UNSW Sydney, NSW, 2053, Australia
[2]Department of Engineering, Macquarie University, North Ryde, NSW, 2109, Australia
[3]Aerospace Engineering Department, California Polytechnic State University, CA 93407, USA

(Received xx; revised xx; accepted xx)

Experimentally validated Large Eddy Simulations were performed on two NACA0012 vanes at various lateral offsets to observe the transient effects of the near field interactions between two streamwise vortices. The vanes were separated in the streamwise direction, allowing the upstream vortex to impact on the downstream geometry. These vanes were evaluated at an angle of incidence of 8 degrees and a Reynolds number of 70,000, with rear vane angle reversed to create a co-rotating or counter-rotating vortex pair. The downstream vortex merged with the upstream in the co-rotating condition, driven by the suppression of one of the tip vortices of the downstream vane. At close proximity to the pressure side, the vane elongated the upstream vortex, resulting in it being the weakened and merging into the downstream vortex. This produced a transient production of bifurcated vortices in the wake region. The downstream vortex of the co-rotating pair experienced faster meandering growth, with oscillations equalising between the vortices. The oscillation was determined to be responsible for statistical variance in merging location, with variation in vortex separation causing the vortices at a single plane to merge and unmerge. In the counter-rotating condition oscillations were found to be larger, with higher growth, but less uniform periodicity. It was found that the circulation transfer between the vortices was linked to the magnitude of their separation, with high separation fluctuations weakening the upstream vortex and strengthening the downstream vortex. In the case of upstream vortex impingement, the upstream vortex was found to bifurcate, with a four vortex system being formed by interactions with the shear layer. This eventually resulted in a single dominant vortex, which did not magnify its oscillation amplitudes as it travelled downstream due to the destruction of the interacting vortices.

Key words:
vortex dynamics, vortex interactions, vortex flows, vortex instabilities

1. Introduction

The successful control of vortex structures is critical in the field of modern aerodynamics, with automotive and aerospace applications becoming increasingly reliant on vortices to improve aerodynamic efficiency. Knowledge of how streamwise vortex interactions

† Email address for correspondence: kyle@forsters.com.au

behave as they propagate downstream is essential to designing systems to control these flow structures. Turbomachinery blade interactions, aircraft taking off in succession, wind turbines and vortex generators can all produce multiple streamwise vortices in close proximity to each other (Manolesos & Voutsinas (2015); Pereira *et al.* (2004); Toloui *et al.* (2015); Hummel (1995); Forster & White (2014)). These vortices may be desirable (flow control, heat transfer) or undesirable (aircraft wake vortices). Streamwise vortex/structure interactions have been studied considerably less than either parallel or normal vortex/structure interactions (Garmann & Visbal (2015)), particularly relating to the effects of the upstream vortex migration. In previous work both vortices of a vortex pair have been typically deployed from the same streamwise location (Devenport *et al.* (1997); Rokhsaz & Kliment (2002)), limiting the study of their interactions at extremely close core spacings. These close interactions are important conditions to understand in order to provide a knowledge base for practical vortex applications, where upstream vortices may move in locations on either side of a vortex producing obstacle, such as a wing or vane.

Interacting pairs of streamwise vortices can be classified into either counter-rotating or co-rotating configurations. Both co-rotating and counter-rotating vortex pairs exhibit instabilities when placed in close proximity including long wavelength (Crow, Crow (1970)) for counter-rotating pairs, short wavelength (elliptic, Leweke *et al.* (2016)) for counter-rotating and co-rotating pairs and spiral (Gordnier & Visbal (1999); Forster *et al.* (2015)) for singular vortices. The Crow instability is described through a solution to a linear wave system, which describes the deviations of counter-rotating vortex pairs (Crow (1970)). Once the vortex cores reach a certain proximity or cutoff distance the two wakes unify into vortex rings and rapidly breakdown. Vortices that break down or dissipate in short distances and timeframes do not have a long enough duration for waves to form, and as such are not subject to the Crow instability. Using these models, it has been found that all counter-rotating pairs are inherently unstable regarding the long wave Crow instability (Klein (1995); Fabre *et al.* (2002); Widnall (1975)). For vortices of unequal strength, the Crow instability can manifest itself at much shorter wavelengths than for an equal strength case. This has been simulated numerically using Computational Fluid Dynamics (CFD), and it has been found that a medium length instability is present where the weaker vortex is drawn around the primary vortex in four vortex systems (Chatelain *et al.* (2008)). However, the mechanisms behind the downstream instabilities of a close proximity, two vortex system are still poorly understood.

The short wave (elliptic) instability is identified in counter and co-rotating pairs by a streamtube in the core of the vortex with a diameter approximately half that of the instabilities wavelength. This instability is caused fundamentally by a resonance of two Kelvin waves (a sinusoidal deformation) within the vortex core as driven by the strain field induced by the other vortex (Tsai & Widnall (1976)). Like the Crow instability, it is modified by differing axial velocity components and vortex strengths.

A pair of co-rotating vortices will merge in any viscous flow (Dritschel (1985); Overman (1982); Roberts & Christiansen (1972)), however the majority of experimentation and analysis surrounding this subject has used equal strength and size vortex cores, with two dimensional flow fields and no velocity deficit through the core, limiting their applicability to real world interaction scenarios. In the case of vortices of unequal strength the mechanism of merging is notably different if the circulation differential is large. In these cases, the weaker vortex has insufficient circulation to support the strain field induced by the stronger vortex, and as such is strained into a spiral tail structure (Leweke *et al.* (2016)). Using inviscid contour method calculations, Dritschel and Waugh (Dritschel & Waugh (1992)) found that the interaction between two vortices with a large difference

in size results in the smaller vortex being torn away, with little increase in size of the larger vortex. This was identified as a regime of either partial or complete straining out. This is in contrast with more closely sized vortices, which often result in total core growth, under a regime they identified as complete merger or partial merger. In addition to this, equal or similar strength vortex interactions typically produce single vortices, while unequal strength interactions may produce two vortex systems. Numerical studies of such scenarios have also been performed Brandt & Nomura (2010), finding similar structures and regimes. The mechanism behind these straining actions is a combination of two causes. Firstly, the weaker vortex is stretched and drawn into the stronger vortex by a process of elongation Trieling & Heijst (1998). Secondly, a continuous erosion of vorticity into the primary vortex is caused by the strong strain field and high shear, in a mechanism analytically observed by Legras and Dritschel Legras & Dritschel (1993). The authors (Forster *et al.* (2017*b*)) have previously experimentally investigated these interactions in upstream/downstream scenarios with unequal strength cores, however the transient mechanisms behind these interactions still require investigation. The merging distance for an upstream/downstream close proximity vortex interaction has been found to be statistical rather than deterministic, and while the mechanism behind this has been proposed (Forster *et al.* (2017*b*)), further investigation and confirmation is yet to be performed.

The interactions of a streamwise vortex with a wingtip at close range have also been computationally investigated (Garmann & Visbal (2015); Forster *et al.* (2015)). By aligning an incident vortex with the tip of a downstream vane, the energy of the vortex system is increased in the near range, however more rapid energy attenuation occurs downstream. When the vortex is positioned inboard of the tip, it reduces the tip vortex size and strength, while placing it outboard of the wingtip enhances the wingtip vortex (Garmann & Visbal (2015)). Reducing the distance of the incident vortex to the wingtip has been found to increase the magnitude of the turbulence production from the resultant vortex interaction (Forster *et al.* (2015)). It has experimentally been found that a counter-rotating wing configuration with a 2.5C streamwise wing spacing can substantially improve rear wing L/D by up to 24% at an overlap of 5% of the wingspan (Inasawa *et al.* (2012)). Such a configuration causes migration of the rear vortex towards the root of the rear wing, however the downstream consequences of these interactions have not been characterised for more than one chord length downstream.

In this work, experimentally validated, Large Eddy Simulations (LES) have been used to investigate the close proximity interactions of two streamwise vortices. Previous experimental work (Forster *et al.* (2017*c*,*b*)) identified that in far offset cases, few notable features were present. Circulation rates remained near constant through the domain, with minimal migration and rotation, and vortex meandering was found to be minimal. As such, they were not considered as cases of interest for the LES investigations. In the nearer field the interactions were far more significant, with large changes in rotation rates, meandering and circulation transfer, resulting in their selection for investigation. An upstream vane is used to produce a realistic vortex that is allowed to travel downstream and interact with a downstream vane, with the downstream vane's lateral offset modified to pass the vortex on either the pressure or suction side, as well as investigate the results of direct vortex impingement. The resulting flowfield has then been analysed in both a time averaged and transient sense to observe the instabilities and flow features present. The focus has been limited to the results of a vane configuration at low Reynolds number and intermediate swirl number, allowing a strong vortex interaction. Through this, a better understanding of the mechanisms behind experimentally observed vortex characteristics can be achieved.

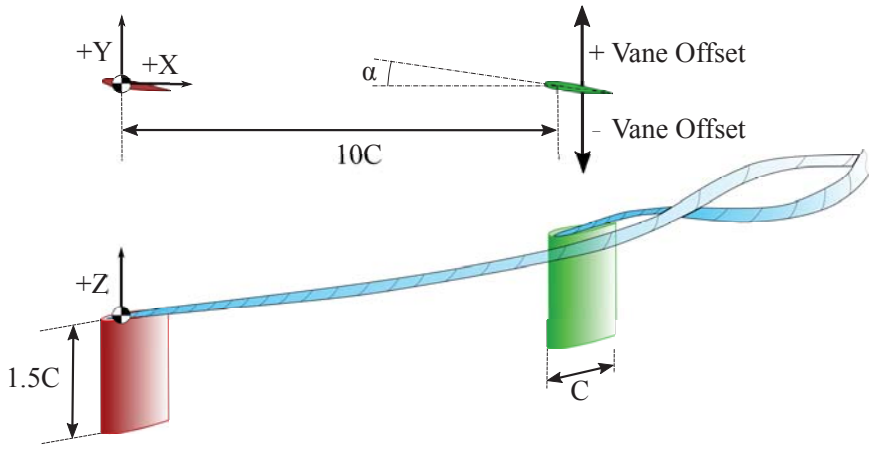

FIGURE 1. Schematic of vane layout.

2. Geometry and Cases Considered

The present study considers the interaction of two streamwise vortices produced by two NACA 0012 vanes, with a similar setup to that used in previous experiments by the authors (Forster *et al.* (2017*c*,*b*)). One vane was located 10 chord lengths (C) downstream of the other, as can be seen in 1. This configuration was chosen as it allows interactions between vortices to occur at close proximities that cannot be observed if the vortices are deployed at the same location. This is also representative of the effects of a pre-existing vortex in a flow interacting with a vortex producing device. An angle of attack of 8 degrees on each vane has been used for all cases, with a square-edged tip. As identified previously higher angles of attack decreased the vortex stability, with unsteady breakdown becoming observable for a single vortex case at 12 degrees. The analysis was performed at a Reynolds number of approximately 7×10^4 based on chord length, within the supercritical region (Huang & Lin (1995)) at this angle of attack. This is also consistent with the previous experimental Reynolds number tested by the authors (Forster *et al.* (2017*c*,*b*)).

While point monitors can be used to monitor frequencies and amplitudes in transient flows, their usefulness in unsteady vortex fields is limited. This is primarily due to the meandering motions of vortices, as any point monitor placed within the core of the vortex shifts from monitoring the core to the periphery as a result of the vortex motion. The result of this is erratic tangential velocities and pressure readings that are not indicative of the vortex core instantaneous properties. As such, planar data is needed for each timestep to calculate the characteristics of the vortex. The computational storage expense of such data is very significant, consequently this transient behaviour was only recorded for three cases where it was expected the transient quantities would be of interest. The properties of the vortex cores present on planes spaced 0.5C apart were extracted for each timestep, applying the previous experimental methodology of the authors (Forster *et al.* (2017*c*,*b*)).

For the counter-rotating case three conditions of the near field interactions were considered for investigation, the first being vortex impact on the front of the vane. This was expected to be at -0.2C offset as identified by prior work (Forster *et al.* (2017*c*,*b*)) The second case was a near pass of the upstream vortex, with the complete vortex radius being outside of contact with the downstream vane, this occurred at 0.2C offset. The final case chosen was an intermediate between these two, with partial impingement of the vortex on the downstream vane, at 0C offset. It was known from previous studies that the transient migrations of both vortices in the near pass condition was significant, so transient vortex tracking was applied to the 0.2C offset case. It was also expected

that the impingement and resultant destruction of the upstream vortex on the rear vane would have significant consequences on the meandering and circulation of the downstream vortex, as such transient vortex tracking was also applied to the -0.2C offset condition.

Three more conditions of interest were identified for the co-rotating case. Previous experimental work (Forster *et al.* (2017*b*)) had shown a difference in vortex merging rates depending on which side of the vane the vortex was passed on. As such, two near field passes of the vortex on the vane were desired, one on each side of the vane. This occurred at -0.2C and 0C offset. It was also desired to investigate the mechanisms present in a longer merging distance case, and for this purpose the 0.2C offset case offered the longest merging length still within the CFD domain. It was not anticipated for the nearer offset, short merging length cases to yield interesting transient meandering data, so only the 0.2C offset was monitored with transient vortex tracking.

3. Numerical Model

A consequence of the original Smagorinsky-Lilly model defining the eddy viscosity proportional to the subgrid characteristic length scale and turbulent velocity is that the local strain rate defines the velocity scale (Nicoud & Ducros (1999)). This inherently relates the subgrid dissipation to the rates of strain at the smallest resolved scale, ineffectively resolving regions where the vorticity field is more significant than the strain field. The assumption of fully isotropic turbulence in the inertial subrange also creates issues with wall bounded flows, where the Smagorinsky constant must be reduced and additional damping at the wall must be applied to ensure the eddy viscosity approaches zero at the wall (Van Driest (1956)). This causes difficulties with complex geometries, which can be solved by the application of the Wall Adapting Local Eddy Viscosity (WALE) model. This model relates the modelling of the eddy viscosity to the square of the velocity gradient tensor, ensuring the correct asymptotic wall bounded behaviour of y^3 instead of y^2 in the Van Driest modified Smagorinsky-Lilly model. This model has been shown to have effective modelling of boundary layer transition and free vortex problems (Ma *et al.* (2009)), with superior performance to the standard and dynamic Smagorinsky-Lilly models for free vortex performance (Yilmaz & Davidson (2015)). The formulation for the eddy viscosity in the WALE model is shown below in equation 3.1.

$$v_t = (C_w \Delta)^2 \frac{(S^d_{ij} S^d_{ij})^{3/2}}{(\overline{S}_{ij}\overline{S}_{ij})^{5/2} + (S^d_{ij} S^d_{ij})^{5/4}} \tag{3.1}$$

Where C_w is the WALE constant, $\overline{S}_{ij}$ is the symmetric component of the velocity gradient tensor (also the strain, or deformation tensor of the resolved velocity field), Δ is the characteristic subgrid length scale and S^d_{ij} is the traceless symmetric part of the square of the velocity gradient tensor.

Both the Smagorinsky-Lilly and WALE models were tested against a reference experimental case for co-rotating at 0.2C offset. It was found that the increased dissipation of the Smagorinsky-Lilly model compared to WALE on the grid tested resulted in the upstream vortex having 8.3% lower peak azimuthal velocity at the point of the rear vane, consequently shifting the merging mechanism from the upstream being the stronger vortex into the downstream being significantly stronger. This produced poor validation results, discussed in the next section, in comparison to the WALE modelling, and as such WALE was selected for further evaluations.

The most commonly used WALE constant of 0.325 (Lehmkuhl *et al.* (2013); Safdari & Kim (2015); Probst & Reuß (2015)) and the value originally recommended by by Nicoud

and Ducros of 0.5 (Nicoud & Ducros (1999)) were tested to observe the effects of varying the constant on the vortex dissipation and merging length. It was found that the change in vortex merging distance and vortex paths was negligible between these tests. However, the dissipation rate did change with the varying values, with higher vortex dissipation observed at higher C_w. Experimental validation as discussed later confirmed that lower numerical dissipation was required. As such, $C_w = 0.325$ was used for the remainder of testing.

An implicit pressure-based solver was used, with segregated pressure/velocity coupling and a SIMPLEC algorithm (Patankar (1971)). To successfully resolve the dominantly swirling vortex flow with steep pressure gradients, a second order PRESTO algorithm was selected for pressure discretization. This scheme has previously proved successful for flows with high swirl number (Peyret (1996); Kaya & Karagoz (2008)). Second order central differencing was used for all other quantities, with bounded second order implicit time stepping. A convection boundness criterion was enforced to maintain solution stability. A timestep of $3 * 10^{-5}$s was used, resulting in the maximum Courant-Friedrichs-Lewy (CFL) number being maintained at below 1 for all simulations, ensuring proper temporal resolution (Courant *et al.* (1967)).

A fully structured multi-block meshing strategy was employed. The final grid consisted of 58 elements along the chord of each vane, with 400 elements along the length of the wake behind the rear vane, and 200 between the vanes. 50 cells were used along the height of the vane, with the majority concentrated at the tip as the base area was of little interest. The significant bias of the mesh to the wake regions resulted in a comparatively coarse mesh on the vanes, reflective of the key focus of the study on the vortices, vortex formation and vortex interaction rather than the vane surface characteristics. For validation runs mesh density was increased at the vane root to model the boundary layer and horseshoe vortices associated with the ground plane more effectively. A constant velocity inlet with no boundary layer placed six chord lengths upstream of the upstream vane. Elimination of floor boundary layer influence on the vortices was performed with symmetry (free-slip) conditions were used for all domain walls, with a no slip wall being employed on the vanes themselves. For the outlet a zero normal diffusion flux condition was placed 30 chord lengths downstream of the rear vane, with behaviour found to be consistent with an outlet length of 56 chord lengths downstream.

The grid was evaluated at resolutions of $1.2 * 10^7$, $1.6 * 10^7$ and $2.6 * 10^7$, with $2.6 * 10^7$ considered the practical grid limit for the computational resources available. These runs were performed on the co-rotating 0.2C offset case, as mesh density variance within the wake region was expected to modify the elliptic instability within the vortices, with subsequent effects on merging length and energy. The mesh density modification for these runs was entirely in the wake region, increasing the mesh density in the streamwise direction and thus improving cell aspect ratio. All meshes were run at a constant timestep of $3 * 10^{-5}$s, with maximum CFL number being maintained below 1.

Initial inspection of the forces on the front vane showed a very close correlation for all cases with the forces expected from theory. From Prandtls lifting line theory, the 3D lift coefficient on the wing was calculated to be 0.54. It was found that the LES solutions predicted averages of 0.5508, 0.556 and 0.546 on the front vane for the increasing mesh densities respectively. All of these forces were within 3% of the theoretical force calculation, with the finest mesh within 1%. Tracing the forces on the rear vane as seen in figure 2 found again that all three mesh configurations showed similar trends for force values and frequencies, and as such any of them would be suitable for resolving the region in between the vortex generators. As such, further inspection of the far field vortex properties was desired.

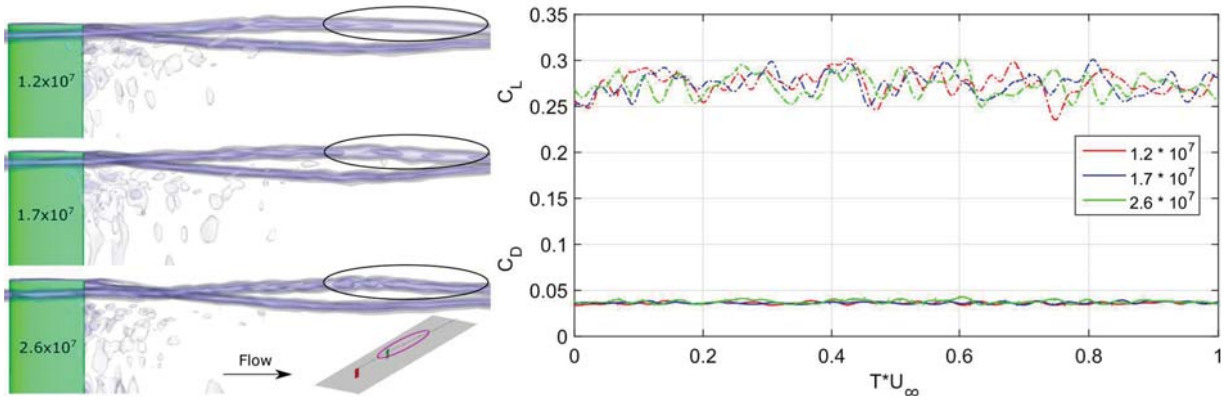

FIGURE 2. Isosurfaces of x-vorticity (left) and force values for rear vane (right) for different mesh resolutions.

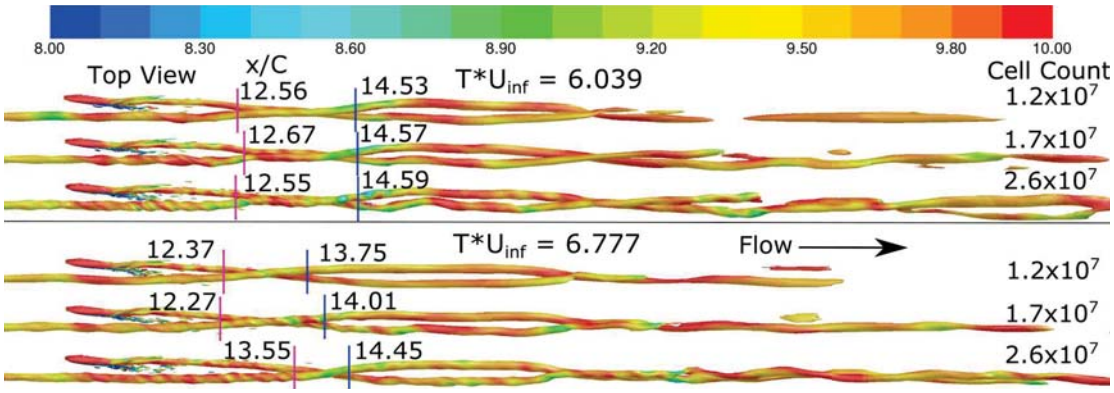

FIGURE 3. Isosurfaces of x-vorticity coloured by x-velocity for multiple LES mesh densities at $T * U_\infty = 6.039$ (top) and $T * U_\infty = 6.777$ (bottom)

As can be seen in figure 2, while the structures near the vane remained similar irrespective of mesh density, the higher energy vortex structures in the far field dissipated faster under the lower resolution meshes. This was particularly evident in the manifestation of the elliptic instability in the vortex core, with more significant fluctuations visible in the densest mesh. The net result of these mesh changes was a faster dissipation in the high energy vortical structures, with an associated loss in high frequency flow features further in the wake. The lower energy, larger radius vorticity levels remained far less affected by the mesh density, with similar diameters and vortex lengths seen for the majority of the domain in all cases.

Whilst the flow structures were conceptually similar between the meshes, with a helical pattern and the downstream vortex merging into the upstream vortex, the transient fluctuation rates varied, as can be seen in figure 3. In the first state the vortex crossover points are near identical between the cases, with 0.06C variance in the rear of the upstream crossover and 0.12C in the front upstream crossover. In the second state the front upstream crossover point varies by 1.28 C between the three conditions, with the downstream crossover remaining near constant. This is due to the increasing instabilities with the higher mesh resolutions forcing a higher meandering magnitude on the upstream vortex, resulting in a larger shift in the instantaneous crossover point. The differential in far field dissipation rates can also be observed here, with the $2.6\text{x}10^7$ cell mesh showing a far longer continuation of the vorticity isosurface than the $1.2\text{x}10^7$ cell mesh. However, the long range dissipation difference is far less significant between the $1.7\text{x}10^7$ and $2.6\text{x}10^7$ cell grid. All three meshes produced an uneven vortex merger, with the downstream vortex merging into the upstream vortex, which was identical to that achieved with

experimental results as will be discussed later in the validation section. As the $2.6\text{x}10^7$ cell mesh successfully converged on the quantities of interest and showed the best resolution of transient instabilities and dissipation within the practical mesh limit, it was therefore was used for the analysis.

4. Model Validation

As previously discussed, good correlation between the model and lifting line theory on the single frontal vane was observed, however the successful prediction of a multiple vortex interaction is far more complex than predicting lift on a common wing profile. As such, the entire double vane system was evaluated against the previous wind tunnel PIV experimental results of the authors (Forster *et al.* (2017*c*,*b*)). For these purposes the LES modelling previously described was applied to a representation of the test section used for wind tunnel testing. No-slip smooth walls were used on all faces, with a specified inlet velocity profile as measured from experimental characterisation of conditions at the tunnel inlet. All mesh densities around and in between the vanes were maintained as per the previous meshing strategy, with additional elements used to resolve the walls of the wind tunnel and splitter. Results were initialised and time averaged using the previously discussed strategy. As there are two fundamental conditions being evaluated, with two unique vortex interactions, it was necessary to validate the modelling against both the co-rotating and counter-rotating experimental results. For the counter rotating condition the 0.5C offset was used as it maintained the highest vortex energy throughout the domain. In the co-rotating condition, the 0.2C offset was evaluated as it demonstrated multiple stages of merger and had a long merging distance that was still within the tunnel test section.

4.1. *Co-Rotating*

The primary intent of the co-rotating validation was to determine the accuracy of the modelling of the vortex attraction and merger. Testing with RANS SST and RSM modelling, as well as to a lesser extent Smagorinsky-Lilly LES, allowed identification of issues with high vortex dissipation causing incorrect measurement of the vortex interaction (Forster *et al.* (2015)). Specifically, these earlier simulations had shown that the upstream vortex had dissipated sufficiently by the point of the rear vane to become the weaker of the two, and the resultant interaction caused the downstream vortex to absorb the upstream vortex. The WALE modelling disagreed with this, showing less dissipation and the downstream vortex being weakened by the upstream, resulting in it merging into the stronger upstream vortex. As such it was deemed critical to validate the accuracy of the modelling strategy in this condition.

Initial validation of the co-rotating condition proved difficult, as correlation with the 0.2C offset case remained purely qualitative. After finding the upstream vortex had migrated towards a more negative y value, the 0.3C offset experimental case was also investigated to determine the correlation properties, as can be seen in figure 4. Very close correlation was observed to the 0.3C offset case on rotation, separation and vorticity levels, with the marginally increased dissipation observed in the LES. The average rotational rate in the CFD was 27.088°/C, compared to 26.464°/C in the 0.3C offset experimental condition. This indicated that the model was over-predicting the total downwash from the vanes, forcing the initial vortex -0.05C to the left in the counter-rotating condition and -0.1C in the co-rotating condition. The presence of the rear vane produces a downwash in the +y direction for the counter rotating case, shifting the vortex 0.025C from an unobstructed -0.075C location to -0.05C from the expected location. In

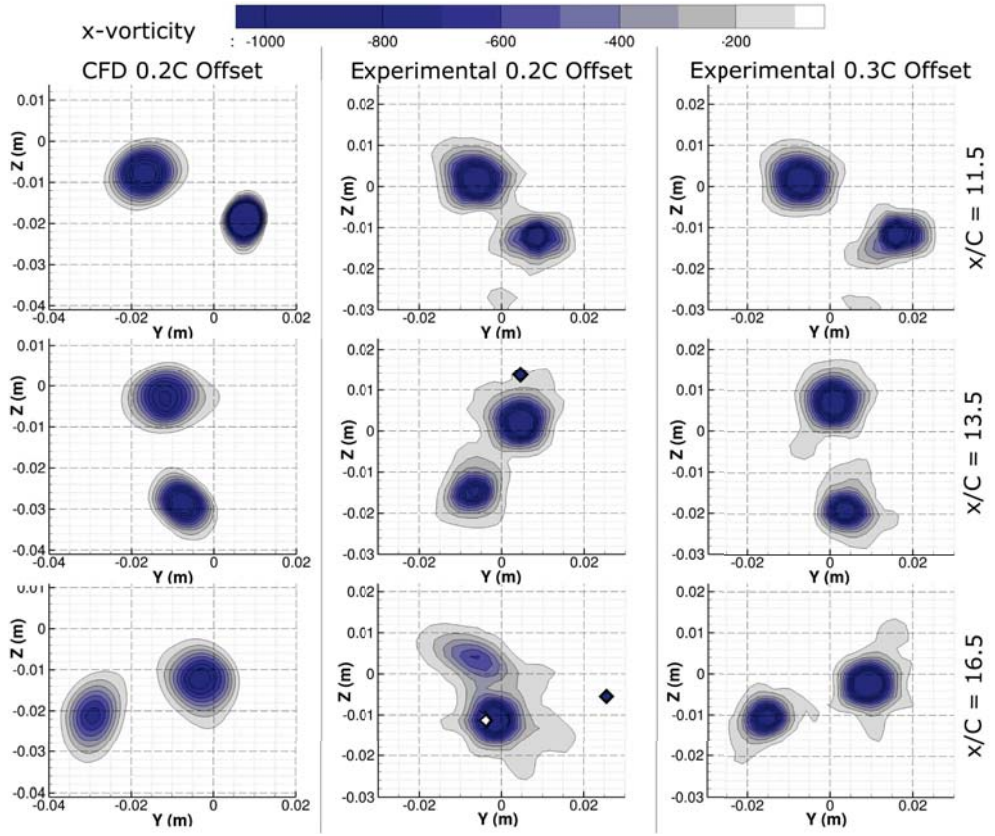

FIGURE 4. x-vorticity results for LES (left) and experimental (centre and right) results for co-rotating condition.

the co rotating condition the downwash from the rear vane is in the same direction as the initial vane downwash, causing the vortex to shift -0.025C to -0.1C from the expected position, resulting in the correlation with the greater offset case observed. This is consistent with the observation of both vortices being skewed to the -y in the CFD when compared to either experimental case.

More important than the specifics of the vortex positions was the accurate prediction of the merging mechanism. Three distinct stages of merger were visible in both the far downstream LES results and the 0.2C experimental results, with the vortices initially reaching a critical proximity at approximately $B_v/r_v = 2$, followed by an asymmetry developing in the vortex shape and a rapid transfer of vorticity. This is followed by the formation of a spiral tail from the remnants of the second vortex. Most importantly is that the downstream vortex is absorbed into the upstream vortex, as this validates the selection of the WALE model over the Smagorinsky-Lilly LES model.

4.2. *Counter-Rotating*

Inspection of the velocity fields in figure 5 showed good qualitative agreement between the experimental and numerical flowfields. As indicated by the purple arrows, all dominant flow structures maintained the same paths between the two, with a continuous downwards movement of the vortex pair. The lower energy structures showed migration in the same direction, however due to the error limitations of the PIV system at lower velocity magnitudes the velocity field is more poorly resolved and becomes dominated by noise. This can be seen in the top left kink in the velocity field, which has a very clear migration in the CFD case, however is seen as more of an increasing dent in the flowfield in the PIV. Between x/C=13 and x/C=17 the expansion of the low swirl velocity region at the bottom left is also clearly matched in both conditions.

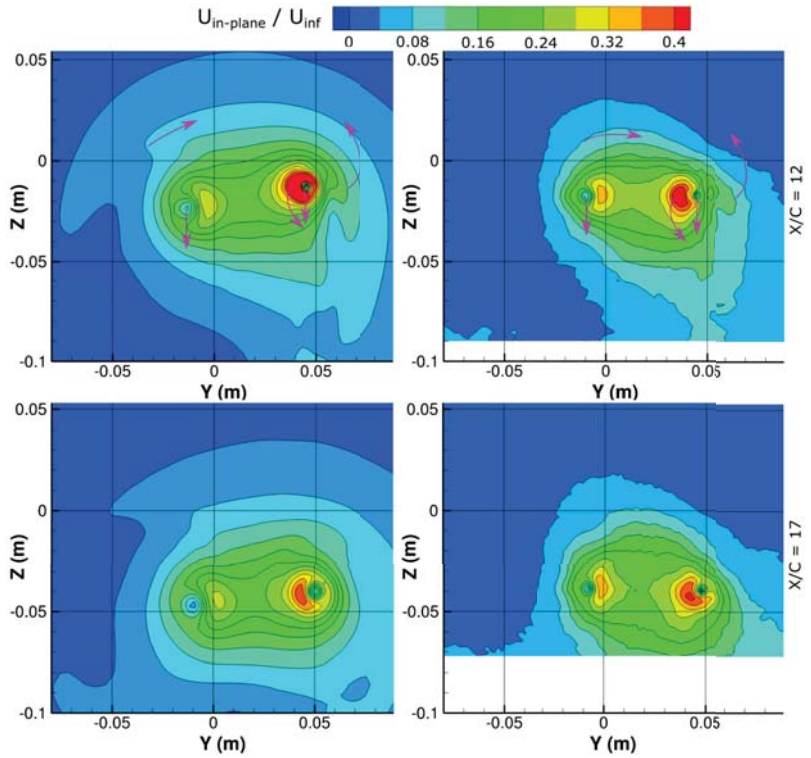

FIGURE 5. In-plane velocity fields for LES (left) and Experimental (right) counter rotating cases at 0.5C offset.

The higher strength downstream vortices both follow the same pattern of rotation counter-clockwise from the point of formation, however the LES predicts the initial velocity horseshoe at x/C=12 to be located higher than the horizontally centred location in the experiment. This is reflected in the final location of the horseshoe, with LES being slightly below horizontal and the experiment being significantly lower at x/C = 17. The subsequent rotational rate for the two cases for the single vortex formation was near identical, with 0.744°/C for the LES and 0.268°/C for the experimental. Total movement of the vortices in the CFD was -0.293C and -0.332C for the upstream and downstream vortices respectively, with -0.260C and -0.293C for the experimental condition. Vortex separation was 0.612C in the CFD and 0.666C in the experiment, leading to a difference of 0.054C.

The initial peak velocity at the point of vortex generation is higher in the computational model, with a 87.5% larger area at 0.4 U_{ip}/U_∞ at x/C = 12. However, the computational model displays a higher level of dissipation than the experiments, with the stronger downstream vortex core dissipating to a peak velocity 10% lower than the experimental by x/C=17. The upstream vortex maintains a lower peak velocity in the CFD for the entire length of the observation window, with it showing a lower peak and average velocity at the start of the domain. This is consistent with the higher dissipation rates observed in the downstream vortex, as these are likely also increasing the dissipation of the upstream vortex prior to interaction.

The most significant difference between the two models is the location of the upstream vortex, with the Z value at x/C = 12 being 0.065C lower in the CFD modelling, inverting the slope of the line between the two vortex cores. This is accompanied by a 0.05C lateral shift in the y direction, indicating that the model has over-predicted the migration of the upstream vortex both laterally and vertically. This is further evidenced by the higher vertical rate of migration of the vortices observed when compared to the experiment. While these changes are small, they have a more significant effect in the closer interaction

cases, where the effective offset is altered. This will be discussed in more detail in the following subsection. However, the over-prediction of this migration is unlikely to affect the key mechanisms behind the vortex interaction.

5. Results

5.1. *Co-Rotating Condition*

The presence of the upstream vortex caused significant changes in the formation mechanism of the downstream vortex. In the case of the single upstream vane, two separate vortices are initially formed, as can be seen in figure 6. These two vortices both have their own distinct regions of concentrated vorticity, as well as a low pressure core. The merger of these vortices occurs just prior to the trailing edge of the vane, forming a slightly non-uniform vortex core shape that rapidly relaxes into a circular profile by a chord length downstream. Introducing a vortex near to the suction side of the vane significantly modifies this formation process, as seen in the -0.2C offset condition presented in figure 6. The upstream vortex is seen to merge with the suction side vortex, producing a distinct vortex that is separate from the vortex produced from the pressure surface/tip surface bleed. The initially merged vortex has a larger core of both vorticity and pressure deficit than the tip surface/suction surface bleed vortex in the front vane only case, however the pressure reaches a lower peak, with no -0.4 C_p isosurface seen. When the vorticity downstream of the vane is inspected, only two vortices are distinguishable, the partially merged upstream vortex and the pressure/tip vortex. This would appear as a weaker vortex produced by the downstream vane if only the off vane vortices were observed, due to the re-energisation of the upstream vortex by the tip/suction side vortex. As the flow moves further downstream these two vortices merge, eventually forming one coherent structure which relaxes into a uniform vortex. The relaxation to circular takes considerably longer than the single vane case, with significant non-uniformities present at 1.5C downstream. The resultant low pressure core of the merged vortices is larger at -0.16 C_p, however the low pressure peaks have been reduced, with the -0.4 C_p isosurface being considerably smaller in diameter. More interesting is the disappearance of the -0.4 C_p isosurface while the two vortices are in the merging process, however after merging and during the relaxation stage it returns. This indicates that the relaxation back to vortex circularity also coincides with an increase in peak pressure drop within the vortex.

Inspecting the on-surface pressures and wall shears presented in figure 7 can further highlight the differences in vortex suppression and enhancement between the offsets. As previously discussed, passing the vortex on the suction side of the vane suppressed the tip/suction vortex, pulling the vortex off the surface. This caused the pressure of the core to be indistinguishable on the surface in the -0.2C offset condition, whilst the upstream vortex showed a clear enhancement of the suction peak at the tip. The pressure/tip vortex also produced a more significant low pressure region than in the front vane, with a clear enhancement despite the downstream vane producing less lift than the upstream due to downwash and unfavourable vortex interactions. This was also reflected in the wall shear, with the 275% of the peak cross plane shear, indicating the vortex generated on the tip surface of the vane was both stronger and forced closer to the surface than in the single vane condition. With the offset modified to positive 0.2C and the upstream vortex passing on the pressure side, the enhancement and suppression of the two tip vortices was effectively reversed. Through the presence of the low pressure core on the suction side of the vane reducing the magnitude of the local pressure differential, in addition

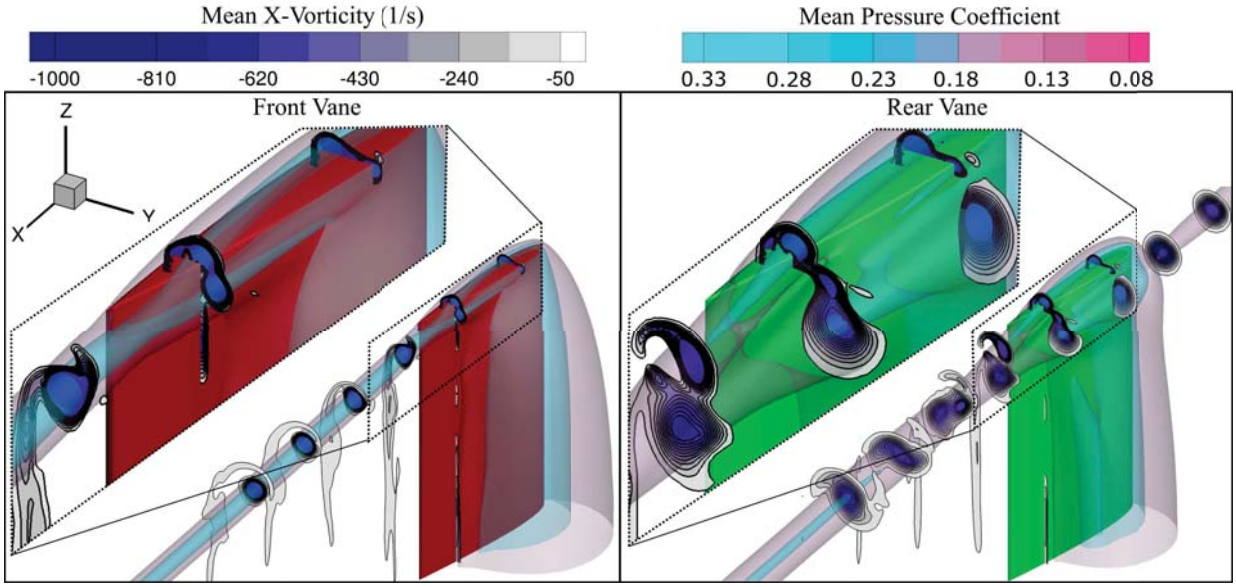

FIGURE 6. Contours of x-vorticity, with isosurfaces of pressure at $C_p = -0.4$ and $C_p = -0.16$ for front vane (top) and rear vane at -0.2C offset (bottom).

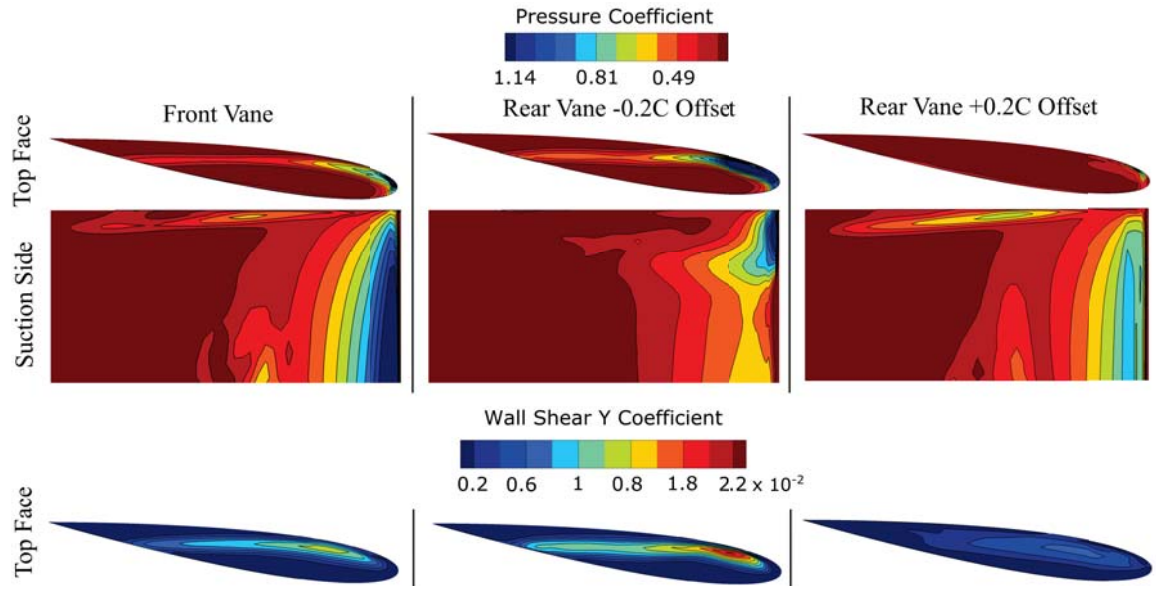

FIGURE 7. Pressure coefficient on vane surfaces (top) with wall shear (bottom) for various offsets

to the downwards flow induced by the swirling vortex core, the pressure/tip vortex is suppressed. This can be seen in the nearly non-existent tip pressure reduction and low wall shear. Passing the vortex on the pressure side also enhanced the tip/suction surface vortex, with an increase in peak suction of 0.16 against the single vane case clearly visible.

The results of the vortex suppression on the positive offset case can be seen in figure 8. Suppression of the pressure/tip vortex results in only a small tail of vorticity forming on the end of the dominant tip/suction vortex, resulting in rapid vortex relaxation. This causes the low pressure -0.4 C_p isosurface to extend for a longer distance and at a larger diameter than in the -0.2C offset. Despite the lower pressure core than the upstream vortex, the dissipation rate of the vorticity and the pressure is larger for the downstream vortex, resulting in its eventual merger into the upstream vortex. The suppressing effect of the upstream vortex on the pressure/tip vortex weakens the strength and radius of vorticity of the final downstream vortex, making it the weaker vortex, thus resulting in

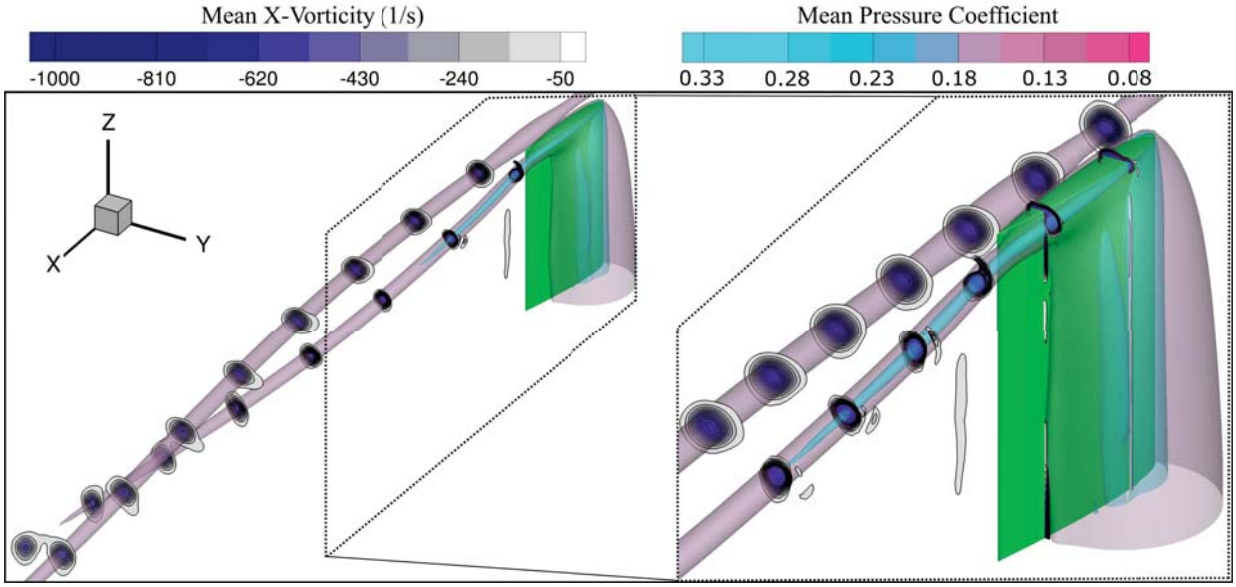

FIGURE 8. Contours of x-vorticity, with isosurfaces of pressure at $C_p = -0.4$ and $C_p = -0.16$ at 0.2C offset.

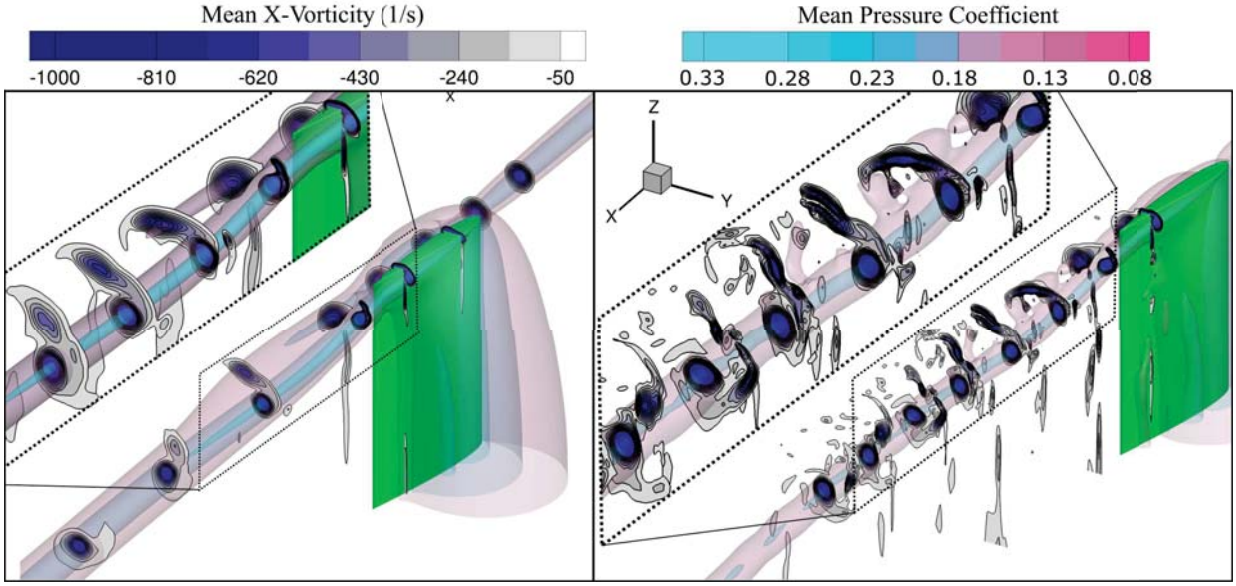

FIGURE 9. Time averaged (left) and instantaneous (right) contours of x-vorticity, with isosurfaces of pressure at $C_p = -0.4$ and $C_p = -0.16$ at 0C offset.

its merger with the upstream vortex through the asymmetric merger process previously identified in the experimental work of the authors (Forster *et al.* (2017*b*)).

When the upstream vortex was kept on the pressure side of the vane, but the offset reduced, the same pressure/tip vortex suppression was observed, seen in figure 9. However, the contact between the upstream vortex and the surface resulted in the flattening of the vorticity profile on the vane. This caused a loss in total vortex circulation, making the upstream vortex the weaker of the two. Consequently, it was found to merge into the downstream vortex, an effect not seen in the experimental results (Forster *et al.* (2017*b*)) as the near offset cases were all merged through the observation domain. This merger did however produce the asymmetric merger and vorticity tail observed in the experimental merging mechanism. When the instantaneous results were analysed it was found the merger was a highly unsteady process, with significant fluctuations of 14.2% in core radius at C_p = -0.16, and peak vorticity reaching 61% more than time averaged

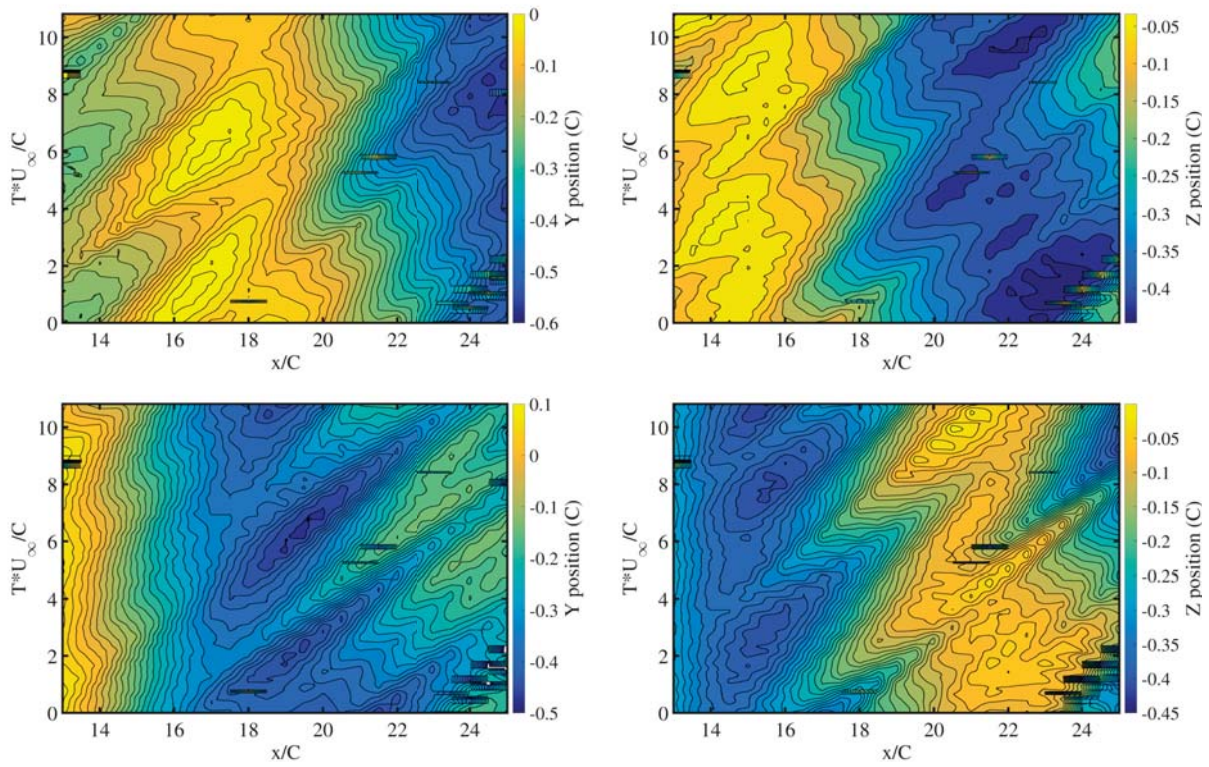

FIGURE 10. Y and Z positions of upstream (top) and downstream (bottom) vortices with respect to time (vertical axis) and distance travelled downstream (horizontal axis) for the 0.2C offset condition. Rapid changes in position from x/C = 20 onwards caused by detection of a merged state.

at x/C = 13. In the instantaneous condition the upstream vortex became more strained by the downstream vortex, forming an elongated structure that split into two separate structures further downstream. Due to the presence of both bifurcated and singular upstream vortices it could be seen that this was a transient fluctuation between the bifurcated and singular state.

As discussed previously, only the far offset 0.2C co-rotating condition was evaluated with the transient vortex tracking methodology, over a time period of $T*U_\infty/C = 12$. The key properties tracked by this process were vortex position and circulation, with vortex separation and circulation differential calculated from these parameters. The positions of the upstream and downstream vortices in the horizontal (y) and vertical (z) directions can be seen in figure 10. To interpret these plots, one can think of a horizontal line drawn through the domain indicating the state of the vortices at any given time, while a vertical line gives a time history of the vortices on a given plane. As the vortices travel through the domain they rotate in a helical manner, resulting in a long duration spatial fluctuation. An example of this can be seen in the transition of the upstream Z position from an average value around -0.05C at x/C = 15 to -0.45C at x/C = 23. What is more interesting from these graphs is the nature of the fluctuations in position and their propagation downstream. A clear periodicity can be seen in all of the position traces, visible from the start of the domain in the upstream vortex and developing more towards the end of the downstream vortex domain.Approximately two and a half primary fluctuation periods can be seen within the domain, indicating a dominant fluctuation frequency approaching Str = 25. This fluctuation frequency is similar between the two vortices, and will be discussed in more detail later in this section. It is also evident from the plots of the downstream vortex that the magnitude of the fluctuation increases significantly with motion downstream.

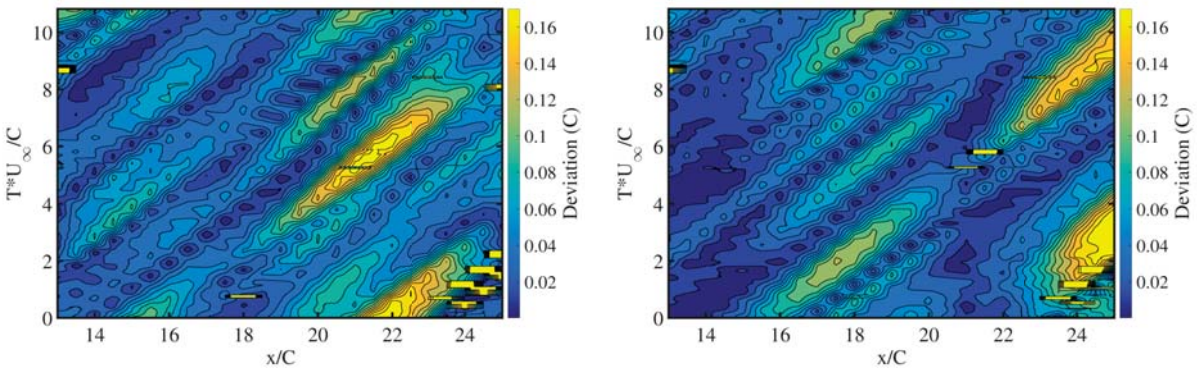

FIGURE 11. Deviation from average position of upstream (left) and downstream (right) vortices with respect to time (vertical axis) and distance travelled downstream (horizontal axis) for the 0.2C offset condition.

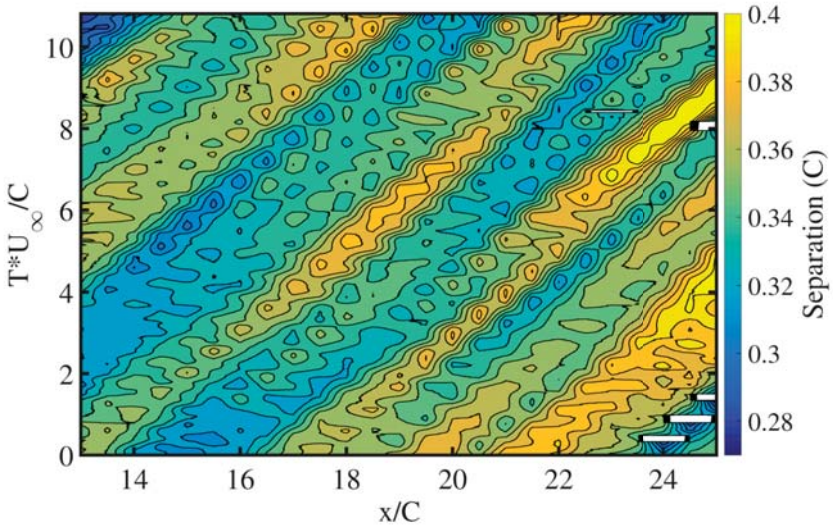

FIGURE 12. Separation between vortices with respect to time (vertical axis) and distance travelled downstream (horizontal axis) for the 0.2C offset condition.

By inspecting the deviation from the averaged vortex location on a given plane the magnitude of the fluctuations could be more clearly analysed (figure 11). The near zero deviation in the downstream vortex just behind the rear vane is expected due to its proximity to its formation location, however as the vortex progresses downstream its amplitude of deviation grows to match that of the upstream vortex at 0.17C. The deviation of the upstream vortex is also seen to grow with distance downstream, peaking at x/C = 22. The peaks in deviation occur over a relatively short downstream, and propagate downstream, however there is clear interaction between he peaks of the upstream and downstream vortex. along the diagonal peaks line starting at x/C = 16, it can be seen that initially this manifests as a peak in the downstream vortex before switching to the largest peak of the upstream vortex and then returning to the downstream vortex peaking. Whilst one vortex is at peak deviation, the other is closest to its average values, showing a clear in phase motion.

However, the separation changes are not directly reflective of these deviation changes, with results seen in figure 12. Following the same diagonal fluctuation as previously discussed from x/C = 16 it can be seen that the vortex separation remains within 0.02C consistency until x/C = 22, at which point it starts to rapidly increase by 0.06C to 0.4C by x/C = 24. This pattern is similarly reflected in the cycle starting at x/C = 12,

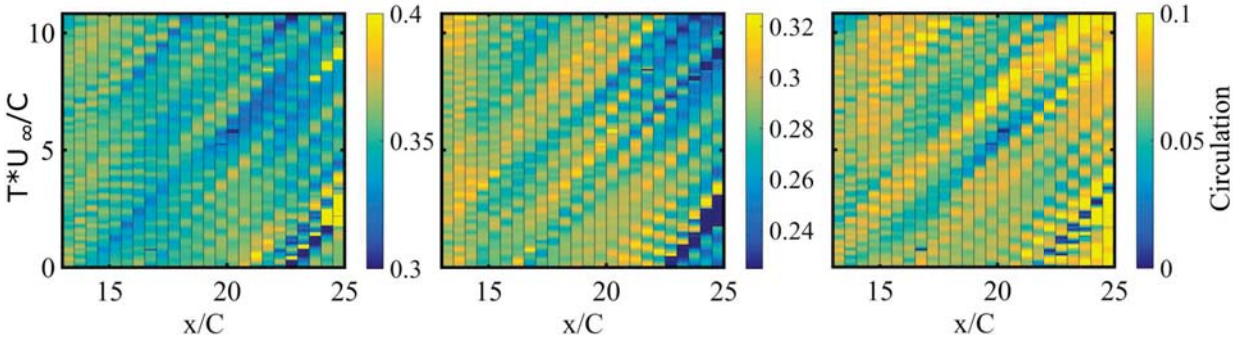

FIGURE 13. Nondimensionalised circulation variation with respect to time (vertical axis) and distance travelled downstream (horizontal axis) for the 0.2C offset condition. Upstream vortex left, downstream vortex centre, differential between vortices on right.

which encounters a similar step at x/C = 20, indicating that despite significant cycle to cycle variance there is still a fundamental pattern in the vortex meandering which is followed. Another significant observation is that when the instantaneous results are considered the fluctuations can result in the downstream vortex separation being larger than the upstream separation, despite the tendencies of the vortices to migrate towards each other. From the fluctuations observed, it appears that a degree of separation trend reversal also occurs, causing the vortices to meander back together after an extended separation. In the bottom right corner (as well as further up the right side) a number of blanked out values can be seen, these correlate with locations of vortex merger. This merger in the instantaneous sense clearly happens when the separation distances fluctuate to a minima at the critical merging distance, as identified in experimental work (Forster *et al.* (2017*b*)). These fluctuations happens just before a point of local maxima, and produces a merger which propagates downstream. The presence of this merger which can form well upstream of the time averaged point of merger before propagating downstream explains the statistical merging properties observed experimentally.

While contour plots can be used effectively for the separations and vortex core locations, this is primarily due to the dominant forcing of the low frequency fluctuations overwhelming the higher frequency, smaller amplitude oscillations in core location. In the case of circulation however, the fluctuations occur at a far higher frequency, and often with a less consistent direction than location, and as such contour plots, while clear for location, become very unclear for circulation. As such the circulation of the two vortices, as well as the circulation difference between the two, is represented in the contoured lines of figure 13. At the start of vortex interaction the fluctuations are small, random and high frequency, however as the vortices progress through the domain they become more coherent and traceable changes. In the bottom right corner the high upstream circulation, low downstream circulation and large circulation difference can be seen at the point of vortex merger. In both the upstream vortex and the first 10C downstream of the downstream vortex there is very little variation in the average value of circulation. However after x/C = 20 in the downstream vortex there is a significant drop-off in the circulation from 0.3 m^2s^{-1} to 0.25 m^2s^{-1} as the asymmetric merging mechanism initiates. This is accompanied by a significant differential in circulation, as the variation in the upstream vortex circulation is comparatively small. The lowest circulation values in the upstream vortex correlate with the smallest separation values experienced by the vortex pairs, with larger circulation typically associated with larger separations. The smallest differential between circulations is also located along the lines of closest separations.

To gain a better understanding of the rate and growth of the transience of the vortex

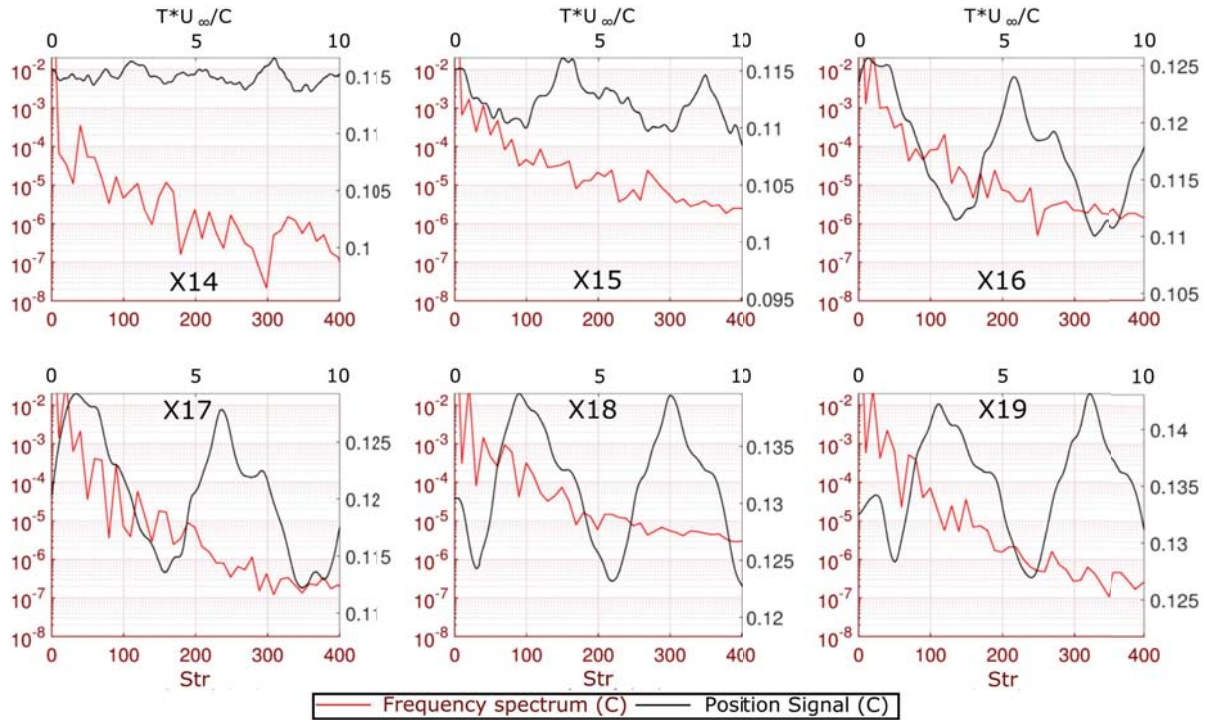

FIGURE 14. Z position (C) evolution with time for downstream vortex at multiple downstream locations (black), with frequency spectra in red. Position signals are all plotted on axes with the same range magnitude.

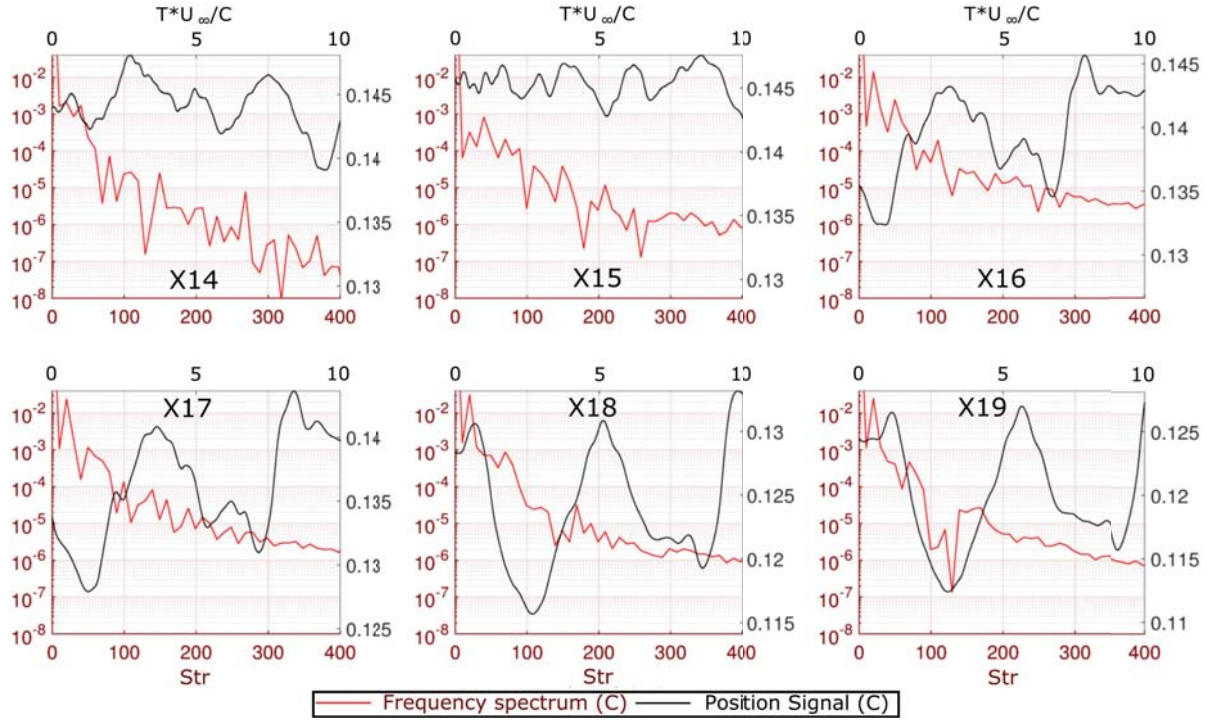

FIGURE 15. Z position (C) evolution with time for upstream vortex at multiple downstream locations (black), with frequency spectra in red. Position signals are all plotted on axes with the same range magnitude.

positions, the frequency spectra of the position signals at various locations downstream were analysed, with the downstream Z variance presented in figure 14 and the upstream variance presented in figure 15. The previously discussed growth in the downstream vortex signal can be clearly seen, with 22.9% less fluctuation magnitude at x/C = 14

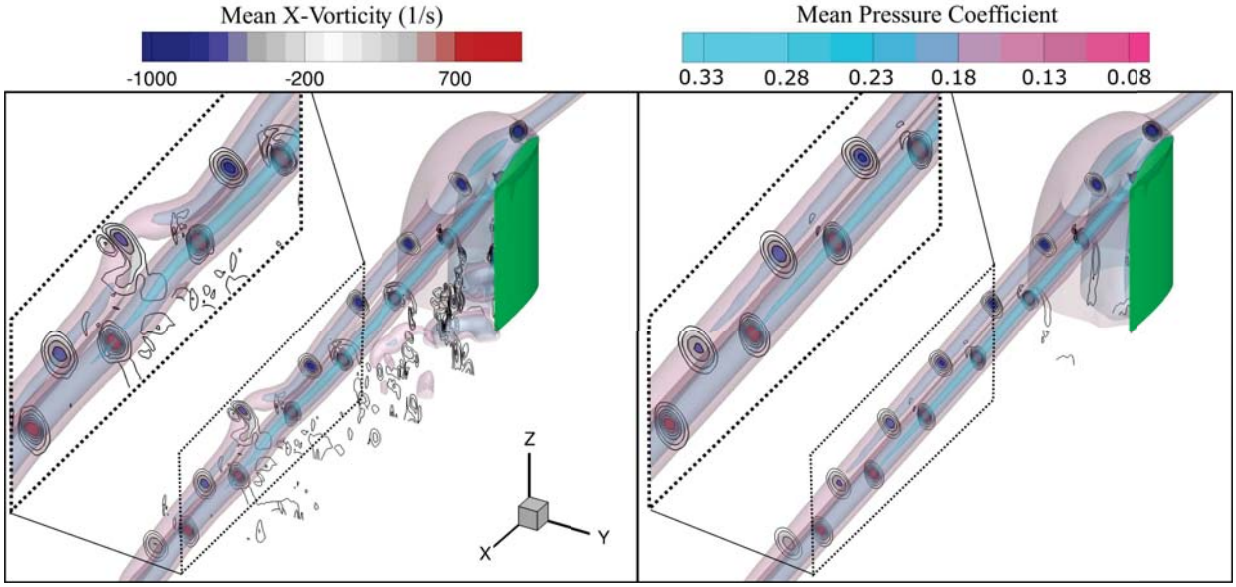

FIGURE 16. Contours of x-vorticity, with isosurfaces of pressure at $C_p = -0.4$, $C_p = -0.16$ and $C_p = -0.08$ for rear vane at 0.2C offset in time averaged (top) and instantaneous (bottom) conditions.

than x/C = 19. For the downstream vortex at x/C = 14, the small scale, high frequency fluctuations are still significant with respect to the larger fluctuations, as evidenced by the lack of a consistent low frequency response above $2 * 10^{-4}$ at frequencies below Str = 50. As the vortex progresses downstream the amplitude of oscillations increases by a factor of four, with a significant bias to increasing the lower frequency magnitudes. The range of frequencies above 10^{-4}C magnitude increases from Str = 0-10 to Str = 0-100 by x/C = 18, with little consistent variation in the higher frequency magnitudes from x/C = 15 onwards. As such the bias of the downstream vortex strongly shifts from high frequency, lower amplitude oscillations to a longer wavelength instability as the flow moves downstream.

Inspecting the upstream vortex, it could be seen that the initial fluctuations were significantly higher, in the order of 2.5 times that of the downstream vortex at x/C = 14. Growth is also seen in the upstream vortex, although to a lesser extent, with the x/C = 19 fluctuation magnitude being 217% larger than the fluctuation at x/C = 14. The fluctuation magnitudes trend towards convergence between the upstream and downstream vortices, with a difference in magnitude by the x/C = 19 of 23.7% as opposed to 148% at x/C = 14. Observing the frequency trends reveals that the upstream vortex behaves slightly differently to the downstream vortex with respect to the magnitude of its lower frequencies, with the 10^{-4}C intensity band stretching from Str = 0-50 at x/C = 14, five times wider than the downstream vortex. However this band does not exhibit the same level of growth, with lesser intensities observed downstream at Str = 100, as well as a slightly faster frequency drop-off. However, it appears that the interaction of these vortices causes them to both equalise their instabilities to the same magnitudes and frequencies of oscillation.

5.2. *Counter-Rotating Condition*

The counter-rotating conditions had the highest dissipation rates and instabilities observed in the experimental results (Forster *et al.* (2017*c*)), and as such it was expected that the LES analysis would show very significant transience. This was particularly true for the 0.2C offset condition presented in figure 16, which showed a large difference

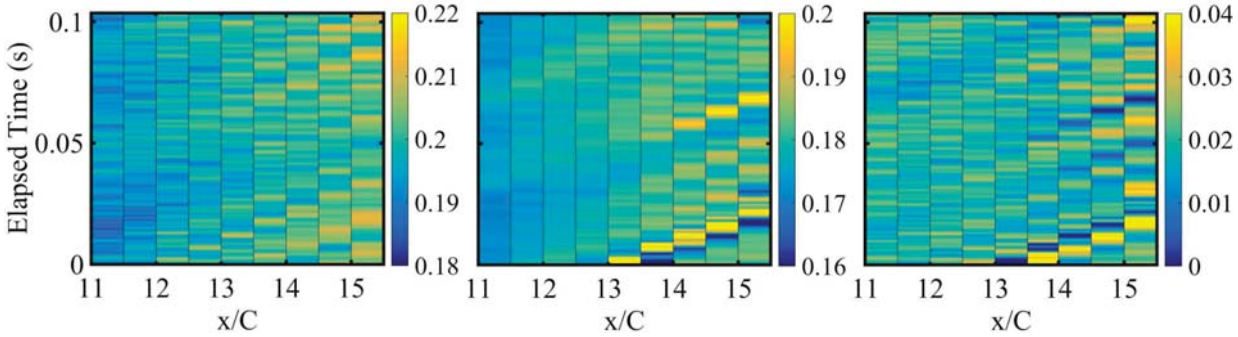

FIGURE 17. Circulation (m^2s^{-1}) evolution with time for downstream vortex (left), upstream vortex (centre) and differential between two vortices (right). All graphs presented on identical axes with scales of equal magnitude range.

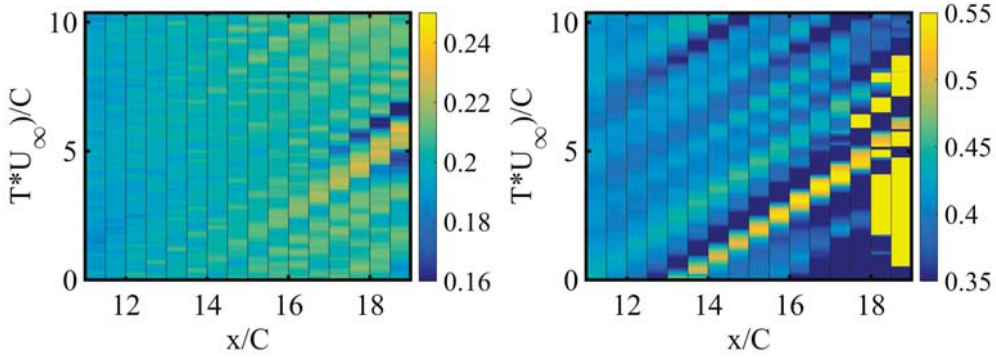

FIGURE 18. Nondimensionalised circulation evolution with time for downstream vortex (left) over an extended downstream range, with vortex separation (C) right.

between the time averaged and instantaneous results. In addition to the small deviation waviness in both vortex cores there was a periodic shedding of a large deviation instability resembling a vortex ring. This was not the dominant flow feature, hence was not observed in the time averaged results, however animations of the solution output during the simulation were inspected and these confirmed this as a periodic feature with a shedding frequency of Str = 7. While the vorticity strength and pressure deficit within the core was reduced by this deviation, it still maintained a circular vortex profile. Within this kinked vortex segment the -0.4 C_p isosurface ended, indicating less pressure deficit, however this same isosurface also extended 0.75C longer in the upstream vortex in the instantaneous condition than the time averaged case. The large vortex deviation produced a region of pressure higher than -0.4 C_p that when averaged would have the effect of a lower average pressure deficit, highlighting the modification of the time-averaged results from the meandering based vortex smearing.

Closer inspection of the transience of the interaction showed a strong link between the magnitude of the vortex separation and circulation, seen in figure 18. A clear diagonal line of exceptionally high separation (greater than 0.5C) can be seen starting from x/C = 13.5, propagating through the domain. This is indicative of the wave instability seen in figure 16. It can be seen that this instability grows through the domain, reaching a peak value around 0.55C before tracking of the secondary vortex is lost (indicated by the yellowed-out areas after x/C = 18). This correlates directly with the circulation trends, with the circulation of the downstream vortex being up to 0.03 m^2s^{-1} higher than average at peak separation, and dropping considerably once the separation is reduced. This correlated with the inverse of the upstream vortex circulation, with the upstream vortex having reduced circulation at higher offsets. As such, the coupling between the

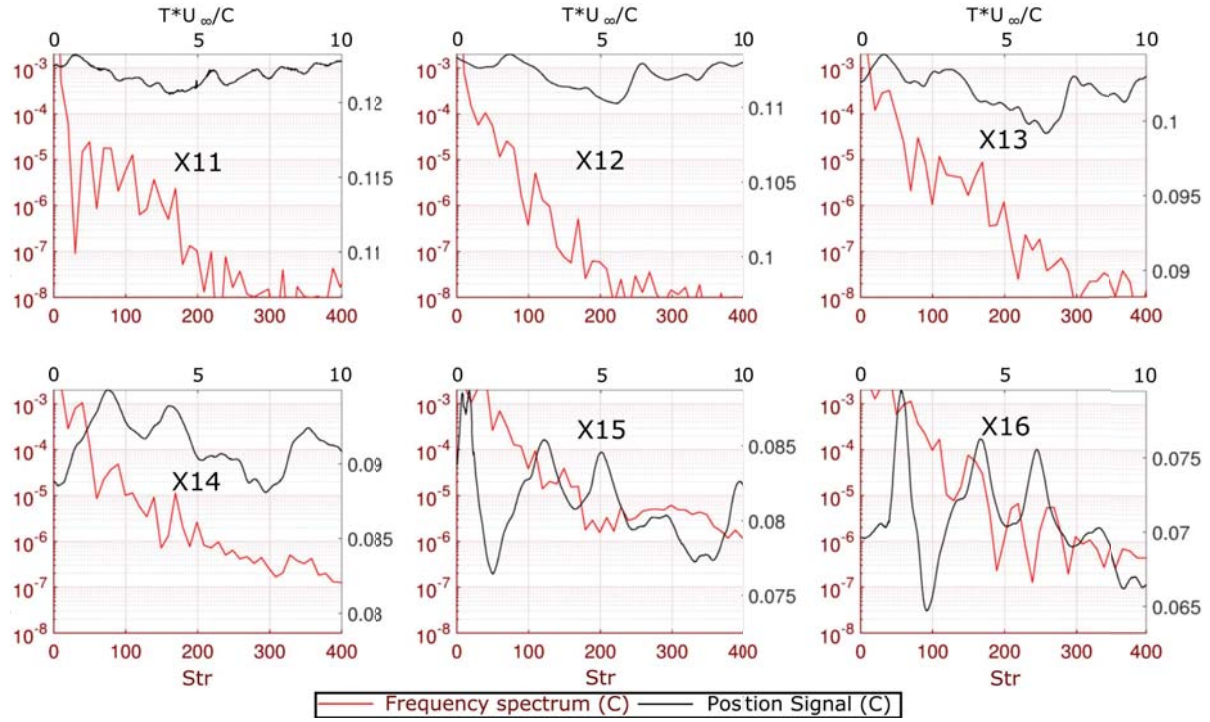

FIGURE 19. Z position (C) evolution with time for upstream vortex at multiple downstream locations (black), with frequency spectra in red. Position signals are all plotted on axes with the same range magnitude.

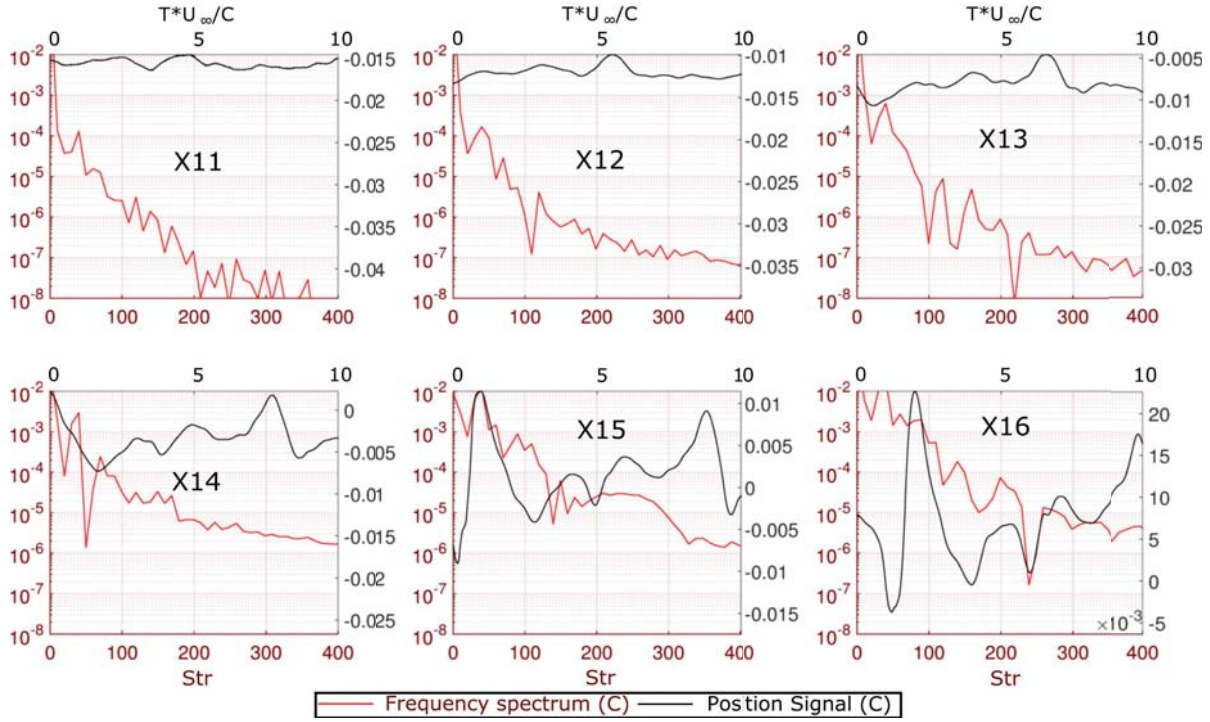

FIGURE 20. Y position (C) evolution with time for upstream vortex at multiple downstream locations (black), with frequency spectra in red. Position signals are all plotted on axes with the same range magnitude.

vortices resulted in the upstream vortex imparting its circulation to the downstream one whilst moving apart, while when the instability brought the vortices close together the energy was more evenly spread between the two.

The position signals and frequency spectra of the upstream vortex are presented in

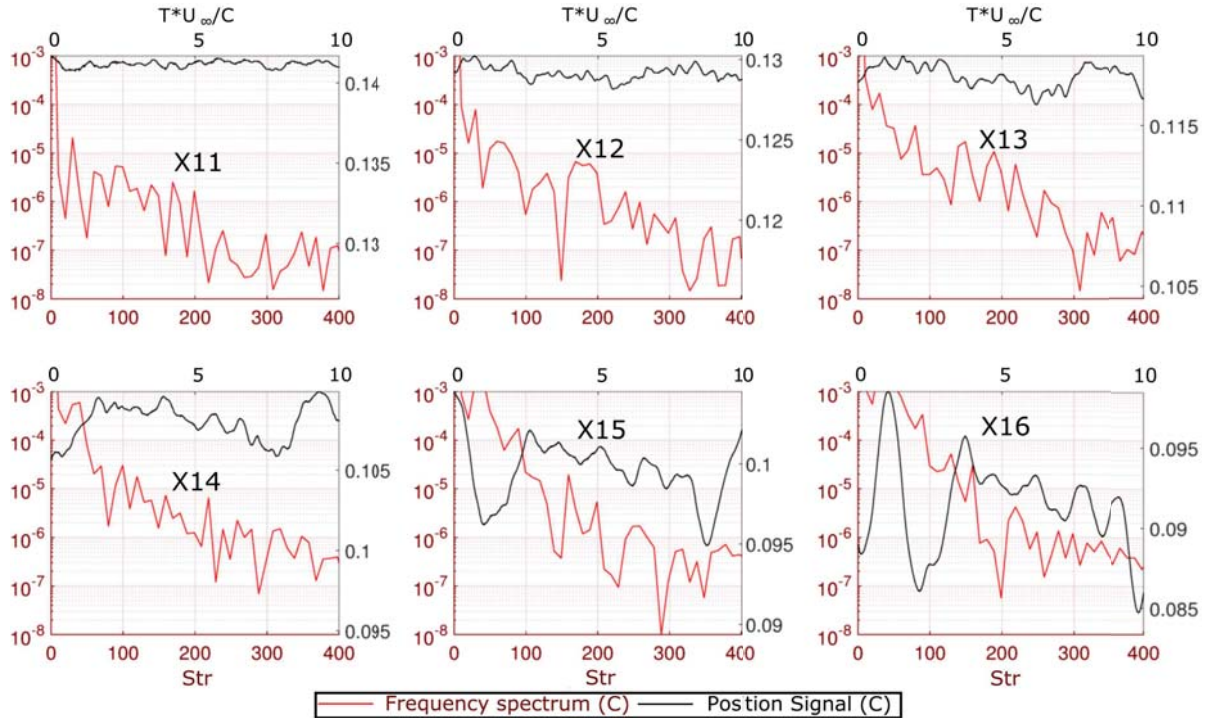

FIGURE 21. Z position (C) evolution with time for downstream vortex at multiple downstream locations (black), with frequency spectra in red. Position signals are all plotted on axes with the same range magnitude.

figure 19 and figure 20. Unlike the co-rotating case there is a monotonic increasing of the entire frequency range across the domain, with the entire frequency spectra translating upwards from x/C = 11 to x/C = 16. This is due to the counter-rotating case being able to manifest both the elliptic and long wave instabilities, with a bias to the larger long wave/Crow instabilities. The fluctuation magnitudes of both the y and z position values increase substantially through the domain presented, with a starting magnitude of $1.75 * 10^{-3}$ and $2.60 * 10^{-3}$ at x/C = 11 and finishing magnitude of $2.61 * 10^{-2}$ and $14.7 * 10^{-2}$ at x/C = 16. The respective gains in fluctuation magnitude are 14.9 and 5.65 times respectively, showing a far more significant fluctuation gain in y than z. These oscillation magnitudes at x/C = 16 are over 77.5% greater than for the co-rotating case at x/C = 19, showing a considerably higher magnitude of deviation. This is consistent with the presence of the wave instability noted in the visualisation, which contributes to the much faster dissipation of energy in the counter-rotating case than the co-rotating case noted in the previous experimental work of the authors (Forster *et al.* (2017*c*)).

Similar trends are seen in the oscillation of the downstream vortex, presented in figure 21 and figure 22. For this condition the fluctuation magnitudes of the y and z position values are $5.5*10^{-4}$ and $9.0*10^{-4}$ at x/C = 11 and finishing magnitude of $2.61*10^{-2}$ and $4.96 * 10^{-3}$ at x/C = 16. Again this vortex exhibited a far higher grown in instability on the y axis than the z axis, showing that this was not just a simple consequence of vortex pair rotation of a 45 degree crow instability, as this would cause one vortex to grow in Y instability and the other to reduce. Peak y value correlated approximately with minimum z value by x/C = 16, however the correlation was far less defined prior to x/C = 14. As such, the instabilities could be seen to develop more clearly downstream into long wave, while closer to the vane they were being driven more by on-vane characteristics such as vortex shedding at the tip.

In the direct impingement condition (-0.2C offset) far less unsteadiness and instability was seen, with a stable downstream vortex and largely destroyed upstream vortex. The

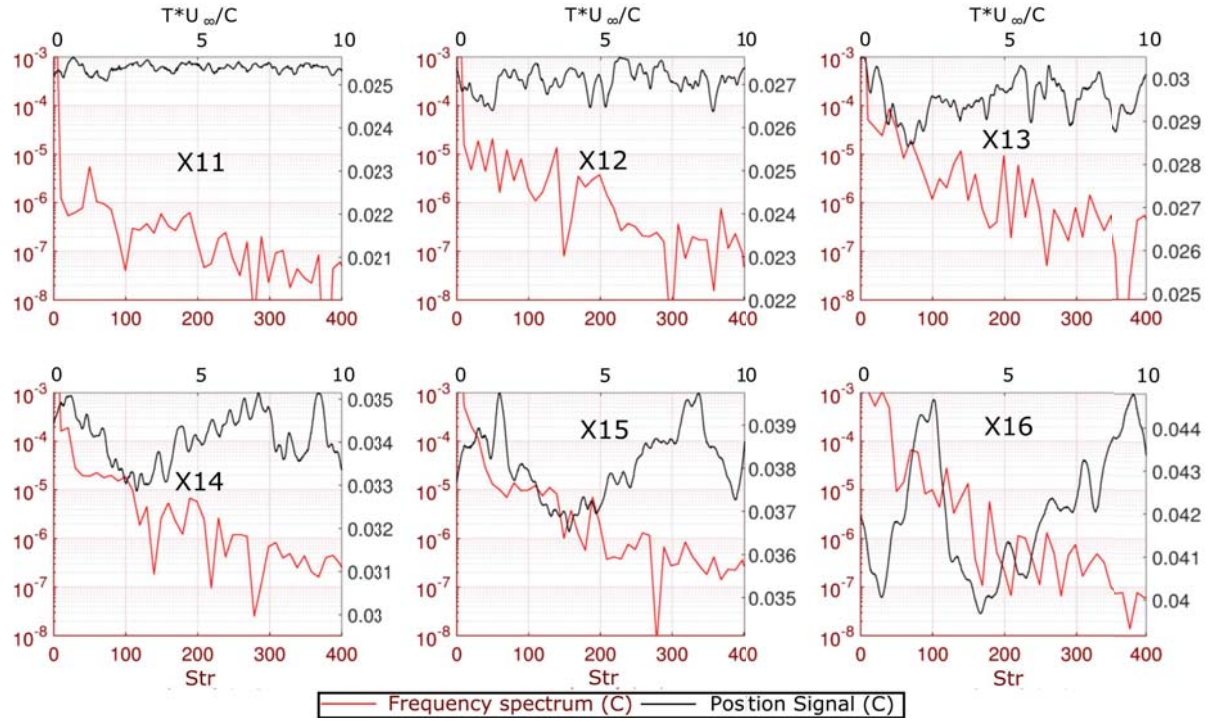

FIGURE 22. Y position (C) evolution with time for downstream vortex at multiple downstream locations (black), with frequency spectra in red. Position signals are all plotted on axes with the same range magnitude.

impingement of the upstream vortex on the downstream vane did not cause breakdown of the upstream vortex, instead forcing the vortex to bifurcate. This is due to the pressure gradient on the front of the vane being of insufficient magnitude and distance to force a full vortex breakdown. The vortex segment on the pressure side of the downstream vane is drawn towards the tip by the spanwise movement of the flow. This process forces the direct interaction with the tip vortex and rapid dissipation of the vorticity from the upstream core, completely eliminating the vortex by the trailing edge of the vane. On the suction side of the vane the bifurcated vortex is forced downwards along the vane surface by the spanwise flow. This causes a significant increase in vortex spacing, similar to what was seen in earlier RANS studies and the experimental work by the authors (Forster *et al.* (2017*c*, 2015)).

The reduced strength of the upstream vortex in conjunction with the high separation results in the significantly reduced rotational rate of the vortex pair at this offset. By forcing the rotating vortex into such close proximity with the vane, the shear within the boundary layer is increased. This creates an enhanced region of positive vorticity on the surface of the vane, inboard of the tip. This region is of similar circulation magnitude to the remaining upstream vortex, however is highly strained, with little circularity. This causes it to break down into two separate vortices once off the vane body, with one interacting with the upstream vortex remnant forming a rotating vortex pair. The other vortex moves towards the downstream tip vortex, however dissipates rapidly. The drawn out tail structure of this upper vortex pair shows behaviour similar to that of the asymmetric co-rotating merging process, with a rapid transfer of vorticity into the primary vortex. At the same time, the lower counter-rotating pair then behaves like the counter-rotating 0.2C offset case, with a high rate of circulation dissipation and a high local rotation rate. The final outcome of these interactions in the far field is a singular downstream vortex, with minimal remnants of the upstream vortex.

The evolution of the downstream vortex position with respect to time can be seen

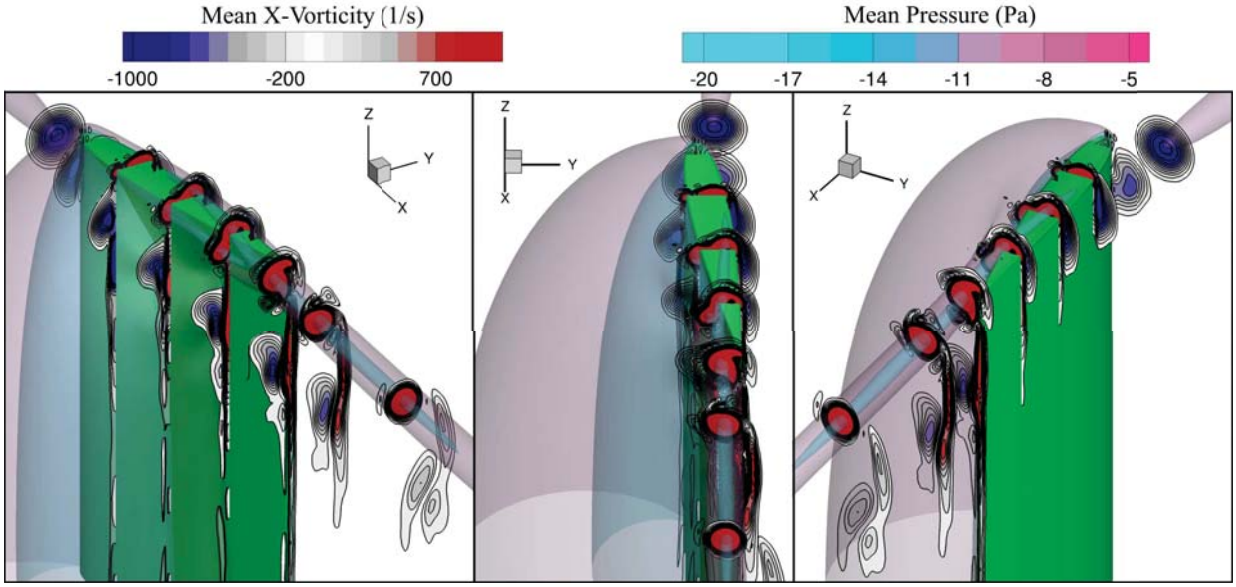

FIGURE 23. Contours of x-vorticity, with isosurfaces of pressure at $C_p = -0.4$ and $C_p = -0.16$ for rear vane at -0.2C offset (right).

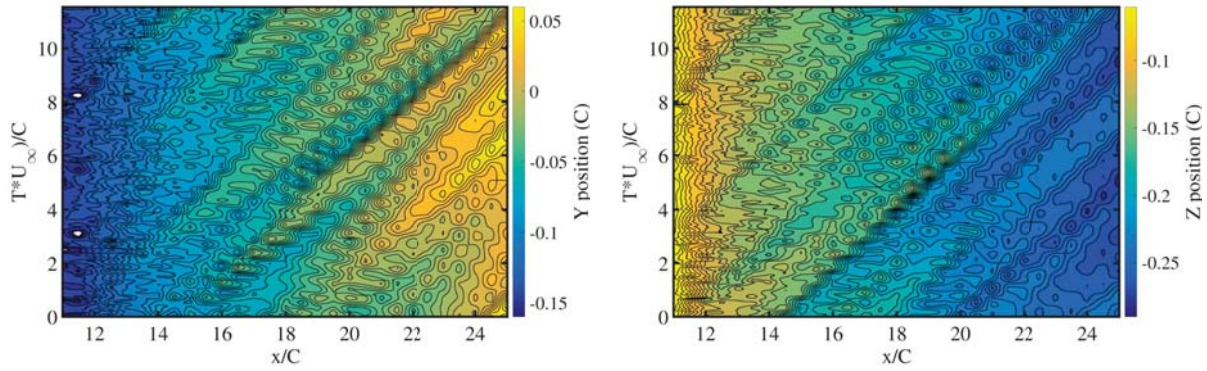

FIGURE 24. Y position (left) and Z position (right) for downstream vortex.

in figure 24. Similar to the downstream vortex in the co-rotating case, immediately behind the downstream vane the oscillations in position are small, with increased growth throughout the domain. However the fluctuation rates are far less significant than the other transient cases. The peak y position amplitude of 0.06C at x/C = 16 is less than half of the equivalent amplitude in the co-rotating 0.2C offset case, and 40% of the counter-rotating 0.2C offset case. This is due to the lack of a strong secondary vortex structure, which cannot introduce elliptic or long-wavelength instabilities into the downstream vortex. As such the primary mechanism for fluctuation growth is the downstream amplification of instabilities caused by the initial vortex interaction and vortex shedding previously discussed. The progressive migration of the vortex towards +y and -z can also be seen, driven by the downwash of the vane.

A more complete picture of the instability growth can be seen when the individual position signals and frequency spectra in figure 25 and figure 26. The comparative lack of meandering growth to the other transient cases can be seen by the high starting and low finishing oscillation magnitudes, with $3.5 * 10^{-3}$ at x/C = 12 being higher than either of the starting magnitudes for the counter-rotating 0.2C offset case. At x/C = 16 the magnitude is $8.5 * 10^{-3}$, which is significantly lower than the $1.18 * 10^{-2}$ seen in the counter-rotating 0.2C offset case, demonstrating this low instability growth rate. However, inspecting the frequency spectra shows that the majority of the

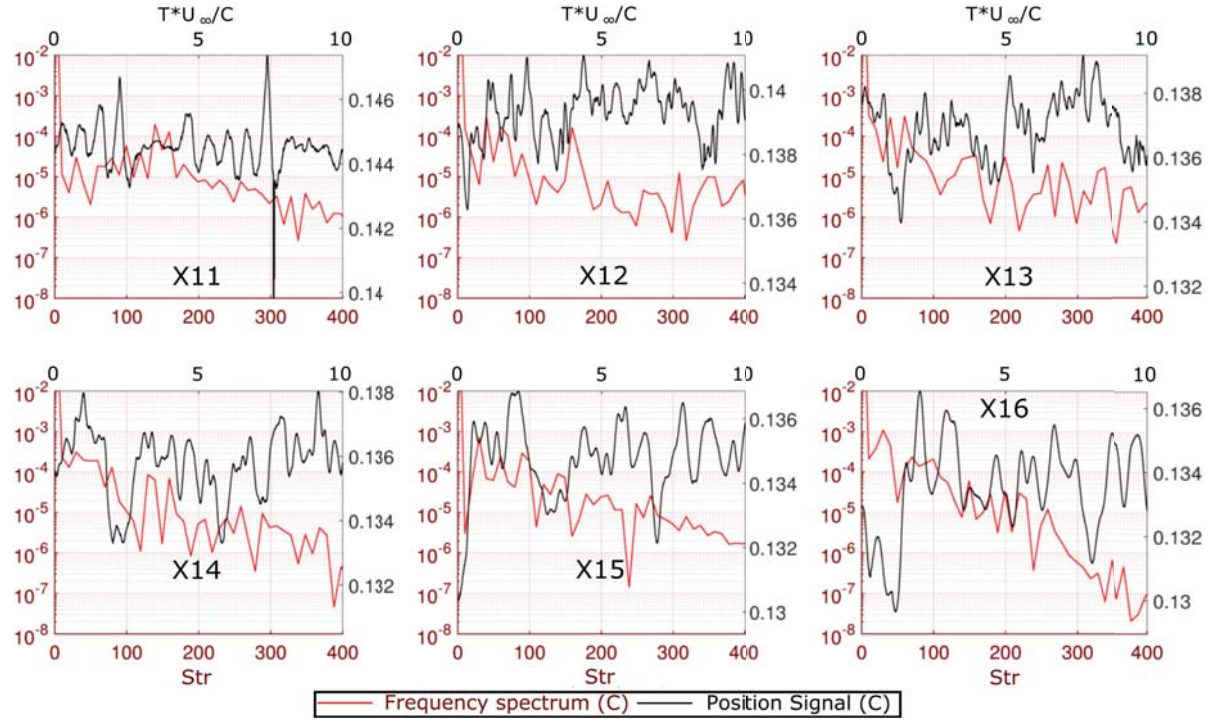

FIGURE 25. Z position (C) evolution with time for downstream vortex at multiple downstream locations (black), with frequency spectra in red. Position signals are all plotted on axes with the same range magnitude.

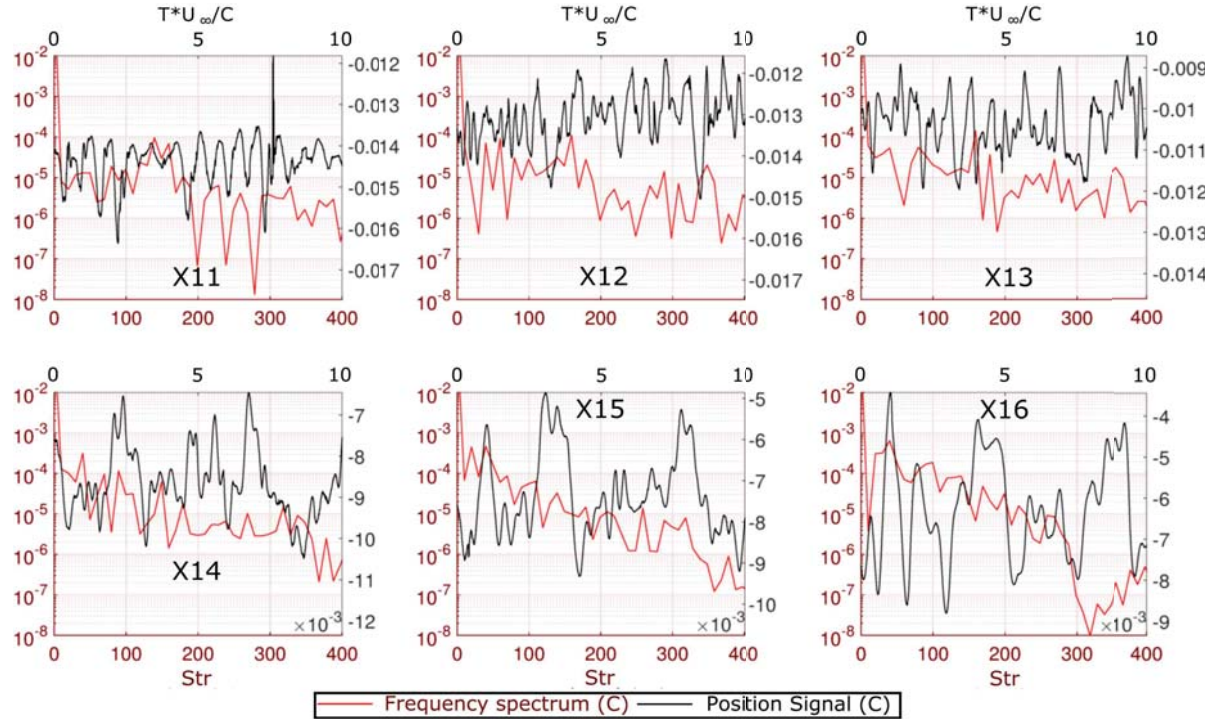

FIGURE 26. Y position (C) evolution with time for downstream vortex at multiple downstream locations (black), with frequency spectra in red. Position signals are all plotted on axes with the same range magnitude.

oscillations in the -0.2C offset case are higher frequency than the other cases, with significant fluctuations in the Str = 300-400 frequency band above 10^{-6} up to x/C = 16. This is a direct result of the increased interactions on the vane body causing

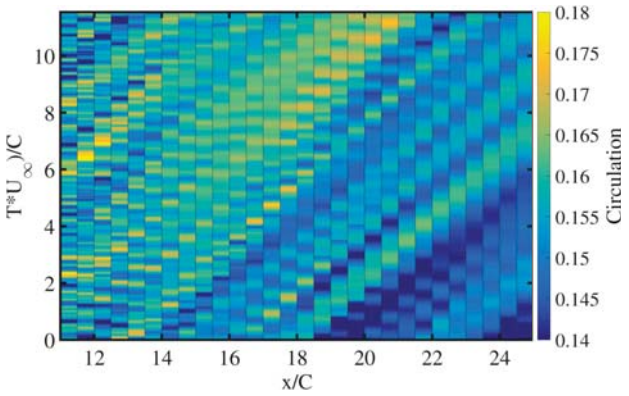

FIGURE 27. Nondimensionalised circulation evolution with time for downstream vortex.

high frequency changes in on-vane characteristics, and subsequently minimal downstream vortex interaction due to the largely destroyed upstream vortex core.

These fluctuations in position showed a far less clear correlation with circulation than in the other transient cases presented. The circulation values presented in figure 27 showed an average reduction in circulation throughout the domain, with an uneven periodicity with time. The fluctuations in circulation closer to the rear vane occurred with a significantly higher primary frequency, and less of a smooth periodicity. This was a result of the transience of the suction side bifurcated upstream vortex modifying the shear layer and consequently altering whether or not the secondary positive vortex had merged with the primary, as discussed earlier and seen in figure 23. As the flow progresses downstream these fluctuations diffuse and spread out in space, leading them to bleed into the surrounding time regions. These results in the smoother fluctuations in circulation seen by the end of the domain. While the correlation with position was generally weak as previously mentioned, trends could be seen when compared to y position, with peaks in y position fluctuation associated with higher circulation values. It is likely that this has resulted from the interactions on the vane producing varying levels of vane downwash, the higher this downwash the more kinetic energy available to be rolled into the vortex. Higher y values result from a more significant downwash, hence the correlation between y value and circulation is understandable.

6. Conclusions

LES was performed to characterise the mechanisms arising from the downstream interactions of the vortex pair produced by two offset vanes. NACA0012 wings of 1.5 aspect ratio, at 8 degrees angle of attack and a Reynolds number of 70000 were used for this study, spaced 10C apart in the streamwise direction. Key cases in both the co-rotating and counter-rotating regimes were identified, and were analysed with both instantaneous and time averaged methods to ascertain the key flow mechanisms behind the effects observed in prior experiments (Forster *et al.* (2017*c*,*b*,*a*)).

It was found that the tendency of the downstream vortex to merge with the upstream in the co-rotating condition was driven by the suppression of one of the two tip vortices created at the downstream vane, resulting in a much weaker vane vortex. This, in conjunction with a lift reduction from the presence of the upstream vortex, resulted in the merger trend observed. However, at extremely close proximities on the pressure side, the vane elongated the shape of the upstream vortex, ultimately resulting in it being the weaker of the two and merging into the downstream vortex. This produced a highly strained vortex, with transient production of bifurcated vortices in the wake region. The

instabilities produced by interacting the vortices at far ranges were found to tend towards equalisation between the two vortices rather than one dominating over the other, despite the difference in vortex formation length. The instabilities and meandering between the two vortices was found to be responsible for the statistical merging phenomenon seen in prior work (Forster *et al.* (2017*b*)), with the vortices merging once the meander caused the separation between the vortices to reach the critical spacing.

The counter-rotating far offset condition was found to produce instabilities of a greater magnitude than the co-rotating condition, with a periodic large sinusoidal deviation forming. However this deviation was very unsteady in its shedding, and did not form continuously. It was found that the circulation transfer between the vortices was linked to the magnitude of their separation, with high separation fluctuations weakening the upstream vortex and strengthening the downstream vortex. The magnitude of both the small scale, high frequency and large scale, low frequency oscillations was found to increase with distance downstream. In the case of upstream vortex impingement, the upstream vortex was found to bifurcate instead of break down, with the pressure side bifurcation rapidly dissipating. The suction side vortex was forced downwards, creating the vortex remnant identified in the prior experimental work (Forster *et al.* (2017*c*)). A four vortex system was created in the process by the interactions with the shear layer, exhibiting all the interaction mechanisms previously investigated. The result of these interactions was a single dominant vortex, which did not magnify its amplitudes of oscillation significantly as it travelled downstream due to the destruction of all interacting vortices.

REFERENCES

Brandt, Laura K. & Nomura, Keiko K. 2010 Characterization of the interactions of two unequal co-rotating vortices. *Journal of Fluid Mechanics* **646**, 233–253.

Chatelain, Philippe, Curioni, Alessandro, Bergdorf, Michael, Rossinelli, Diego, Andreoni, Wanda & Koumoutsakos, Petros 2008 Billion vortex particle direct numerical simulations of aircraft wakes. *Computer Methods in Applied Mechanics and Engineering* **197**, 1296–1304.

Courant, R, Friedrichs, K O & Lewy, H 1967 On the partial difference equation of mathematical physics. *Ibm J.* **11** (March), 32–74, arXiv: AD0832715.

Crow, SC 1970 Stability theory for a pair of trailing vortices. *AIAA Journal* **8** (12), 2172–2179.

Devenport, WJ, Zsoldos, Jeffrey S. & Vogel, Christine M. 1997 The structure and development of a counter-rotating wing-tip vortex pair. *Journal of Fluid Mechanics* .

Dritschel, D G 1985 The stability and energetics of corotating uniform vortices. *Journal of Fluid Mechanics* **157**, 95–134.

Dritschel, D. G. & Waugh, D. W. 1992 Quantification of the inelastic interaction of unequal vortices in two-dimensional vortex dynamics. *Physics of Fluids A: Fluid Dynamics* **4** (1992), 1737.

Fabre, David, Jacquin, Laurent & Loof, Antoine 2002 Optimal perturbations in a four-vortex aircraft wake in counter-rotating configuration. *Journal of Fluid Mechanics* **451**, 319–328.

Forster, Kyle J., Barber, Tracie, Diasinos, Sammy & Doig, Graham 2015 Numerical investigation of streamwise vortex interaction. In *SAE Technical Paper*. SAE International.

Forster, Kyle J., Barber, Tracie, Diasinos, Sammy & Doig, Graham 2017*a* The Variation in Co and Counter-Rotating Upstream-Downstream Vortex Interactions. *47th AIAA Fluid Dynamics Conference* (June), 1–13.

Forster, Kyle J., Barber, Tracie J., Diasinos, Sammy & Doig, Graham 2017*b* Interactions of a Co-Rotating Vortex Pair at Multiple Offsets. *Physics of Fluids* **29**, 057102.

Forster, Kyle J., Barber, Tracie J., Diasinos, Sammy & Doig, Graham 2017*c*

Interactions of a Counter-Rotating Vortex Pair at Multiple Offsets. *Experimental Thermal and Fluid Science* **86**, 63–74.

Forster, K. J. & White, T. R. 2014 Numerical Investigation into Vortex Generators on Heavily Cambered Wings. *AIAA Journal* **52** (5), 1059–1071.

Garmann, D.J. & Visbal, M.R. 2015 Interactions of a streamwise-oriented vortex with a finite wing. *Journal of Fluid Mechanics* **767**, 782–810.

Gordnier, Raymond E & Visbal, Miguel R 1999 Numerical simulation of the impingement of a streamwise vortex on a plate. *International Journal of Computational Fluid Dynamics* **12** (1), 49–66.

Huang, Rong F & Lin, Chih L 1995 Vortex shedding and shear-layer instability of wing at low-Reynolds numbers. *AIAA Journal* **33** (8), 1398–1403.

Hummel, Dietrich 1995 Formation flight as an energy-saving mechanism. *Israel Journal of Zoology* **41** (3), 261–278.

Inasawa, Ayumu, Mori, Fumihide & Asai, Masahito 2012 Detailed Observations of Interactions of Wingtip Vortices in Close-Formation Flight. *Journal of Aircraft* **49** (1), 206–213.

Kaya, F. & Karagoz, I. 2008 Performance analysis of numerical schemes in highly swirling turbulent flows in cyclones. *Current Science* **94** (10), 1273–1278.

Klein, R 1995 Simplified equations for the interaction of nearly parallel vortex filaments. *Journal of Fluid Mechanics* **288**, 201–248.

Legras, B. & Dritschel, D. 1993 Vortex stripping and the generation of high vorticity gradients in two-dimensional flows. *Applied Scientific Research* **51**, 445–455.

Lehmkuhl, O., Rodríguez, I., Baez, a., Oliva, a. & Pérez-Segarra, C. D. 2013 On the large-eddy simulations for the flow around aerodynamic profiles using unstructured grids. *Computers and Fluids* **84**, 176–189.

Leweke, Thomas, Le Dizès, Stéphane & Williamson, Charles H K 2016 Dynamics and Instabilities of Vortex Pairs. *Annual Review of Fluid Mechanics* **48**, 507–541.

Ma, Jiamei, Wang, Fujun & Tang, Xuelin 2009 *Comparison of Several Subgrid-Scale Models for Large-Eddy Simulation of Turbulent Flows in Water Turbine*, pp. 328–334. Berlin, Heidelberg: Springer Berlin Heidelberg.

Manolesos, Marinos & Voutsinas, Spyros G. 2015 Experimental investigation of the flow past passive vortex generators on an airfoil experiencing three-dimensional separation. *Journal of Wind Engineering and Industrial Aerodynamics* **142**, 130–148.

Nicoud, F. & Ducros, F. 1999 Subgrid-scale stress modelling based on the square of the velocity gradient tensor. *Flow, Turbulence and Combustion* **62**, 183–200, arXiv: arXiv:1503.01439v1.

Overman, Edward A. 1982 Evolution and merger of isolated vortex structures. *Physics of Fluids* **25** (1982), 1297.

Patankar, Suhas V. 1971 *Numerical Heat Transfer and Fluid Flow*. New York, New York: McGraw-Hill Book Company.

Pereira, Luiz Antonio Alcântara, Hirata, Miguel Hiroo & Filho, Nelson Manzanares 2004 Wake and aerodynamics loads in multiple bodies-application to turbomachinery blade rows. *Journal of Wind Engineering and Industrial Aerodynamics* **92**, 477–491.

Peyret, R. 1996 *Handbook of Computational Fluid Mechanics,Academic Press*.

Probst, Axel & Reuss, Silvia 2015 *Scale-Resolving Simulations of Wall-Bounded Flows with an Unstructured Compressible Flow Solver*, pp. 481–491. Cham: Springer International Publishing.

Roberts, K.V. & Christiansen, J.P. 1972 Topics in Computational Fluid Dynamics. *Computational Physics Communications* **3** (I 972), 14–32.

Rokhsaz, Kamran & Kliment, Linda K 2002 Experimental Investigation of Co-Rotating Vortex Filaments in a Water Tunnel. In *32nd AIAA Fluid Dynamics Conference and Exhibit*.

Safdari, Arman & Kim, Kyung Chun 2015 Aerodynamic and Structural Evaluation of Horizontal Archimedes Spiral Wind Turbine. *Journal of Clean Energy Technologies* **3** (1), 34–38.

Toloui, Mostafa, Chamorro, Leonardo P. & Hong, Jiarong 2015 Detection of tip-vortex

signatures behind a 2.5MW wind turbine. *Journal of Wind Engineering and Industrial Aerodynamics* **143**, 105–112.

Trieling, R. R. & Heijst, G. J F Van 1998 Kinematic properties of monopolar vortices in a strain flow. *Fluid Dynamics Research* **23**, 319–341.

Tsai, Chon-Yin & Widnall, Sheila E. 1976 The stability of short waves on a straight vortex filament in a weak externally imposed strain field. *Journal of Fluid Mechanics* **73**, 721.

Van Driest, E. R. 1956 On Turbulent Flow Near a Wall. *Journal of the Aeronautical Sciences* **23** (4), 1007–1011.

Widnall, S E 1975 The Structure and Dynamics of Vortex Filaments. *Annual Review of Fluid Mechanics* **7**, 141–165.

Yilmaz, Ilyas & Davidson, Lars 2015 Comparison of SGS Models in Large-Eddy Simulation for Transition to Turbulence in TAYLOR-GREEN Flow. In *The 16th International Conference on Fluid Flow Technologies*.

Bibliography

[1] M. Manolesos and S. G. Voutsinas, "Experimental investigation of the flow past passive vortex generators on an airfoil experiencing three-dimensional separation," *Journal of Wind Engineering and Industrial Aerodynamics*, vol. 142, pp. 130–148, 2015.

[2] L. A. A. Pereira, M. H. Hirata, and N. M. Filho, "Wake and aerodynamics loads in multiple bodies-application to turbomachinery blade rows," *Journal of Wind Engineering and Industrial Aerodynamics*, vol. 92, pp. 477–491, 2004.

[3] M. Toloui, L. P. Chamorro, and J. Hong, "Detection of tip-vortex signatures behind a 2.5MW wind turbine," *Journal of Wind Engineering and Industrial Aerodynamics*, vol. 143, pp. 105–112, 2015.

[4] D. Hummel, "Formation flight as an energy-saving mechanism," *Israel Journal of Zoology*, vol. 41, no. 3, pp. 261–278, 1995.

[5] K. J. Forster and T. R. White, "Numerical investigation into vortex generators on heavily cambered wings," *AIAA Journal*, vol. 52, pp. 1059–1071, May 2014.

[6] D. J. Garmann and M. R. Visbal, "Interactions of a streamwise-oriented vortex with a finite wing," *JFM*, vol. 767, pp. 782–810, 2015.

[7] W. Devenport, J. S. Zsoldos, and C. M. Vogel, "The structure and development of a counter-rotating wing-tip vortex pair," *JFM*, 1997.

[8] K. Rokhsaz and L. K. Kliment, "Experimental investigation of co-rotating vortex filaments in a water tunnel," in *32nd AIAA Fluid Dynamics Conference and Exhibit*, vol. 40, pp. 1115–1122, June 2002.

[9] F. Lu, Q. Li, Y. Shih, A. Pierce, and C. Liu, "Review of micro vortex generators in high-speed flow," *49th AIAA Aerospace Sciences Meeting and Exhibit*, no. January, p. 31, 2011.

[10] H. Lugt, "The dilemma of defining a vortex," in *Recent Developments in Theoretical and Experimental Fluid Mechanics* (U. Müller, K. Roesner, and B. Schmidt, eds.), pp. 309–321, Springer Berlin Heidelberg, 1979.

[11] G. Haller, "An objective definition of a vortex," *JFM*, vol. 525, pp. 1–26, Feb. 2005.

[12] M. Roth, "Automatic extraction of vortex core lines and other line-type features for scientific visualization," *Selected Readings in Vision and Graphics*, vol. 9, no. 13673, 2000.

[13] J. Jeong and F. Hussain, "On the identification of a vortex," *JFM*, vol. 285, pp. 69–94, 1995.

[14] A. Globus, C. Levit, and T. Lasinski, "A tool for visualizing the topology of three-dimensional vector fields," *2nd conference on Visualization*, pp. 33–40, 1991.

[15] M. Hall, "A new approach to vortex breakdown," in *Proc. Heat Transfer Fluid Mech. Inst*, pp. 319–340, 1967.

[16] H. H. Bossel, "Vortex breakdown flowfield," *Physics of Fluids*, vol. 12, pp. 498–508, Mar. 1969.

[17] M. Escudier, "Vortex breakdown: Observations and explanations," *Progress in Aerospace Sciences*, vol. 25, pp. 189–229, jan 1988.

[18] A. Mager, "Dissipation and breakdown of a wing-tip vortex," *JFM*, vol. 55, p. 609, Mar. 2006.

[19] O. Lucca-Negro and T. O'Doherty, "Vortex breakdown: a review," *Progress in Energy and Combustion Science*, vol. 27, pp. 431–481, Jan. 2001.

[20] H. Schlichting and J. Kestin, *Boundary-layer theory*. New York: McGraw-Hill, 7th ed ed., 1979. Translation of Grenzschicht-Theorie.

[21] H. Lamb, "On the uniform motion of a sphere through a viscous fluid," *Katalog BPS*, vol. 33, no. 29, pp. 81–87, 1911.

[22] G. K. Batchelor, *An introduction to fluid dynamics*. Cambridge: Cambridge university press, 1967.

[23] T. Leweke, S. Le Dizès, and C. H. K. Williamson, "Dynamics and instabilities of vortex pairs," *Annual Review of Fluid Mechanics*, vol. 48, pp. 507–541, 2016.

[24] L. Ting and C. Tung, "Motion and decay of a vortex in a nonuniform stream," *Physics of Fluids*, vol. 8, no. 1965, p. 1039, 1965.

[25] P. G. Saffman, *Vortex Dynamics*. Cambridge Monographs on Mechanics, Cambridge: Cambridge University Press, 1993.

[26] D. L. Mathias, J. C. Ross, and R. M. Cummings, "Wake integration to predict wing span loading from a numerical simulation," *Journal of Aircraft*, vol. 32, no. 5, pp. 1165–1167, 1995.

[27] O. Logdberg, "Vortex generators and turbulent boundary layer separation control," *PhD Thesis*, no. October, 2006.

[28] A. Jacobi and R. Shah, "Heat transfer surface enhancement through the use of longitudinal vortices: a review of recent progress," *Experimental Thermal and Fluid Science*, vol. 1777, no. 95, pp. 295–309, 1995.

[29] S. Leibovich, "Vortex stability and breakdown-Survey and extension," *AIAA Journal*, vol. 22, no. 9, pp. 1192–1206, 1984.

[30] T. Leweke and C. H. K. Williamson, "Experiments on long-wavelength instability and reconnection of a vortex pair," *Physics of Fluids*, vol. 23, no. 2011, 2011.

[31] D. M. Harris and C. H. K. Williamson, "Instability of secondary vortices generated by a vortex pair in ground effect," *JFM*, vol. 700, pp. 148–186, 2012.

[32] S. Pasche, F. Gallaire, M. Dreyer, and M. Farhat, "Obstacle-induced spiral vortex breakdown," *Experiments in Fluids*, vol. 55, p. 1784, July 2014.

[33] A. Inasawa, F. Mori, and M. Asai, "Detailed observations of interactions of wingtip vortices in close-formation flight," *Journal of Aircraft*, vol. 49, pp. 206–213, Jan. 2012.

[34] L. K. Kliment and K. Rokhsaz, "Experimental investigation of the forced response of a pair of co-rotating vortex filaments," in *34th AIAA Fluid Dynamics Conference and Exhibit*, p. 2434, American Institute of Aeronautics and Astronautics, July 2004.

[35] J. J. Cassidy and H. T. Falvey, "Observations of unsteady flow arising after vortex breakdown," *JFM*, vol. 41, p. 727, Mar. 1970.

[36] S. Leibovich, "The structure of vortex breakdown," *Annual Review of Fluid Mechanics*, pp. 221–246, 1978.

[37] J. H. Faler and S. Leibovich, "Disrupted states of vortex flow and vortex breakdown," *Physics of Fluids*, vol. 20, no. 9, pp. 1385–1400, 1977.

[38] M. Escudier and N. Zehnder, "Vortex-flow regimes," *JFM*, vol. 115, pp. 105–121, 1982.

[39] R. C. Chanaud, "Observations of oscillatory motion in certain swirling flows," *JFM*, vol. 21, no. 01, pp. 111–127, 1965.

[40] R. C. Chanaud, "Experiments concerning the vortex whistle," *The Journal of the Acoustical Society of America*, vol. 35, no. 7, pp. 953–960, 1963.

[41] T. Sarpkaya, "On stationary and travelling vortex breakdowns," *JFM*, vol. 45, no. 03, pp. 545–559, 1971.

[42] T. Sarpkaya, "Vortex breakdown in swirling conical flows," *AIAA Journal*, vol. 9, no. 9, pp. 1792–1799, 1971.

[43] M. Lowson and A. Riley, "Vortex breakdown control by delta wing geometry," *Journal of Aircraft*, vol. 32, no. 4, pp. 832–838, 1995.

[44] E. Krause, "A contribution to the problem of vortex breakdown," *Computers and Fluids*, vol. 13, no. 3, pp. 375–381, 1985.

[45] A. Kazakov, "Stability of a viscous subsonic swirl flow," *Fluid Dynamics*, vol. 33, pp. 338–345, May 1998.

[46] D. G. Sloan, P. J. Smith, and L. D. Smoot, "Modeling of swirl in turbulent flow systems," *Progress in Energy and Combustion Science*, vol. 12, no. 3, pp. 163–250, 1986.

[47] H. Moet, F. Laporte, G. Chevalier, and T. Poinsot, "Wave propagation in vortices and vortex bursting," *Physics of Fluids*, vol. 17, no. 5, p. 054109, 2005.

[48] K. Oberleithner, M. Sieber, C. N. Nayeri, C. O. Paschereit, C. Petz, H.-C. Hege, B. R. Noack, and I. Wygnanski, "Three-dimensional coherent structures in a swirling jet undergoing vortex breakdown: stability analysis and empirical mode construction," *JFM*, vol. 679, pp. 383–414, May 2011.

[49] C. O. Umeh, Z. Rusak, E. Gutmark, R. Villalva, and D.-J. Cha, "Experimental and computational study of nonreacting vortex breakdown in a swirl-stabilized combustor," *AIAA Journal*, vol. 48, pp. 2576–2585, Nov. 2010.

[50] S. Wang and Z. Rusak, "On the stability of an axisymmetric rotating flow in a pipe," *Physics of Fluids*, vol. 8, no. 4, p. 1007, 1996.

[51] P. Iudiciani and C. Duwig, "Large eddy simulation of the sensitivity of vortex breakdown and flame stabilisation to axial forcing," *Flow, Turbulence and Combustion*, vol. 86, pp. 639–666, Feb. 2011.

[52] D. Sipp, L. Jacquin, and C. Cossu, "Self-adaptation and viscous selection in concentrated two-dimensional vortex dipoles," *Physics of Fluids*, vol. 245, no. 2000, pp. 245–248, 2000.

[53] S. Le Dizès and F. Laporte, "Theoretical predictions for the elliptical instability in a two-vortex flow," *JFM*, vol. 471, pp. 169–201, 2002.

[54] H. Moffatt, S. Kida, and H. Ohkitani, "Stretched vortices –the sinews of turbulence; large-Reynolds-number-asymptotics," *JFM*, vol. 259, pp. 241–264, 1994.

[55] V. J. Rossow, "Classical wing theory and the downward velocity of vortex wakes," *Journal of Aircraft*, vol. 43, pp. 381–385, 2006.

[56] V. J. Rossow, "Application of vortex invariants to roll up of vortex pairs," *Journal of Aircraft*, vol. 41, pp. 1098–1105, 2004.

[57] K. Rokhsaz, R. Rebours, and S. R. Foster, "Quantitative measurements of wake vortex motion in a water tunnel," in *39 Aerospace Sciences Meeting and Exhibit*, p. 0111, Jan. 2001.

[58] S. Crow, "Stability theory for a pair of trailing vortices," *AIAA Journal*, vol. 8, no. 12, pp. 2172–2179, 1970.

[59] H. Lamb, *Hydrodynamics*, vol. 4. Cambridge: Cambridge University Press, 1916.

[60] F. W. Dee and O. Nicholas, "Flight measurements of wing-tip vortex motion near the ground," *Aeronautical Research Council Current Papers*, vol. 1065, 1969.

[61] J. K. Harvey and F. J. Perry, "Flowfield produced by trailing vortices in the vicinity of the ground," *AIAA Journal*, vol. 9, no. August, pp. 1659–1660, 1971.

[62] A. J. Peace and N. Riley, "A viscous vortex pair in ground effect," *JFM*, vol. 129, p. 409, 1983.

[63] L. Kliment and K. Rokhsaz, "Influence of terrain roughness on trailing vortices in ground effect," *37th AIAA Fluid Dynamics Conference and Exhibit*, pp. 1–10, June 2007.

[64] B. Cantwell and N. Rott, "The decay of a viscous vortex pair," *Physics of Fluids*, vol. 31, no. 1988, p. 3213, 1988.

[65] D. J. Asselin and C. H. K. Williamson, "Vortex pair impinging on a horizontal ground plane," *Physics of Fluids*, vol. 25, no. 2013, pp. 2–4, 2013.

[66] S. E. Widnall, D. Bliss, and A. Zalay, *Aircraft Wake Turbulence and Its Detection*, ch. Theoretical and Experimental Study of the Stability of a Vortex Pair, pp. 305–338. Boston, MA: Springer US, 1971.

[67] S. E. Widnall, "The structure and dynamics of vortex filaments," *Annual Review of Fluid Mechanics*, vol. 7, pp. 141–165, 1975.

[68] R. Klein, "Simplified equations for the interaction of nearly parallel vortex filaments," *JFM*, vol. 288, pp. 201–248, 1995.

[69] D. Fabre, L. Jacquin, and A. Loof, "Optimal perturbations in a four-vortex aircraft wake in counter-rotating configuration," *JFM*, vol. 451, pp. 319–328, 2002.

[70] V. J. Rossow, "Prospects for destructive self-induced interactions in a vortex pair," *Journal of Aircraft*, vol. 24, pp. 433–440, 1987.

[71] S. Kida, "Vortex reconnection," *Annual Review of Fluid Mechanics*, vol. 26, pp. 169–189, 1994.

[72] M. R. Dhanak and B. D. Bernardinis, "The evolution of an elliptic vortex ring," *JFM*, vol. 109, pp. 189–216, 1981.

[73] P. Chatelain, A. Curioni, M. Bergdorf, D. Rossinelli, W. Andreoni, and P. Koumoutsakos, "Billion vortex particle direct numerical simulations of aircraft wakes," *Computer Methods in Applied Mechanics and Engineering*, vol. 197, pp. 1296–1304, 2008.

[74] J. M. Ortega, R. L. Bristol, and O. Savas, "Experimental study of the instability of unequal-strength counter-rotating vortex pairs," *JFM*, vol. 474, pp. 35–84, 2003.

[75] D. J. Asselin and C. H. K. Williamson, "Influence of a wall on the three-dimensional dynamics of a vortex pair," *JFM*, vol. 817, pp. 339–373, 2017.

[76] C.-Y. Tsai and S. E. Widnall, "The stability of short waves on a straight vortex filament in a weak externally imposed strain field," *JFM*, vol. 73, p. 721, 1976.

[77] D. Moore and P. Saffman, "The instability of a straight vortex filament in a strain field," *Proceedings of the Royal Society*, no. 346, pp. 413–425, 1975.

[78] T. Leweke and C. H. K. Williamson, "Cooperative elliptic instability of a vortex pair," *JFM*, vol. 360, pp. 85–119, 1998.

[79] P. Meunier, S. Le Dizès, and T. Leweke, "Physics of vortex merging," *Comptes Rendus Physique*, vol. 6, pp. 431–450, 2005.

[80] L. Lacaze, A. L. Birbaud, and S. Le Dizès, "Elliptic instability in a Rankine vortex with axial flow," *Physics of Fluids*, vol. 17, pp. 1–5, 2005.

[81] L. Lacaze, K. Ryan, and S. Le Dizès, "Elliptic instability in a strained Batchelor vortex," *JFM*, vol. 577, p. 341, Apr. 2007.

[82] K. Ryan and G. J. Sheard, "Non-linear growth of short-wave instabilities in a Batchelor vortex pair," in *16th Australasian Fluid Mechanics Conference*, pp. 1463–1469, Dec. 2007.

[83] C. Roy, T. Leweke, M. C. Thompson, and K. Hourigan, "Experiments on the elliptic instability in vortex pairs with axial core flow," *JFM*, vol. 677, pp. 383–416, 2011.

[84] E. W. Mayer and K. G. Powell, "Viscous and inviscid instabilities of a trailing vortex," *JFM*, vol. 245, pp. 91–114, 1992.

[85] G. Winckelmans and R. Cocle, "Direct numerical simulation and large-eddy simulation of wake vortices: going from laboratory conditions to flight conditions," *European Conference on Computational Fluid Dynamics*, pp. 1–20, 2006.

[86] L. K. Kliment and K. Rokhsaz, "Experimental investigation of pairs of vortex filaments in ground effect," *Journal of Aircraft*, vol. 45, no. June, pp. 622–629, 2008.

[87] P. Orlandi, "Vortex dipole rebound from a wall," *Physics of Fluids A: Fluid Dynamics*, vol. 2, no. 1990, p. 1429, 1990.

[88] K. Roberts and J. Christiansen, "Topics in computational fluid dynamics," *Computational Physics Communications*, vol. 3, no. I 972, pp. 14–32, 1972.

[89] P. G. Saffman and R. Szeto, "Equilibrium shapes of a pair of equal uniform vortices," *Physics of Fluids*, vol. 23, no. 1980, pp. 2339–2342, 1980.

[90] E. A. Overman, "Evolution and merger of isolated vortex structures," *Physics of Fluids*, vol. 25, no. 1982, p. 1297, 1982.

[91] D. G. Dritschel, "The stability and energetics of corotating uniform vortices," *JFM*, vol. 157, pp. 95–134, 1985.

[92] N. J. Zabusky, M. H. Hughes, and K. V. Roberts, "Contour dynamics for the Euler equations in two dimensions," *Journal of Computational Physics*, vol. 30, pp. 96–106, 1979.

[93] V. J. Rossow, "Convective merging of vortex cores in lift-generated wakes," *Journal of Aircraft*, vol. 14, no. 3, pp. 283–290, 1977.

[94] M. V. Melander, N. J. Zabusky, and J. C. McWilliams, "Symmetric vortex merger in two dimensions: causes and conditions," *JFM*, vol. 195, p. 303, 1988.

[95] P. Meunier, U. Ehrenstein, T. Leweke, and M. Rossi, "A merging criterion for two-dimensional co-rotating vortices," *Physics of Fluids*, vol. 14, no. 2002, pp. 2757–2766, 2002.

[96] C. Cerretelli and C. H. K. Williamson, "The physical mechanism for vortex merging," *JFM*, vol. 475, pp. 41–77, 2003.

[97] L. K. Brandt and K. K. Nomura, "Characterization of the interactions of two unequal co-rotating vortices," *JFM*, vol. 646, pp. 233–253, 2010.

[98] D. G. Dritschel and D. W. Waugh, "Quantification of the inelastic interaction of unequal vortices in two-dimensional vortex dynamics," *Physics of Fluids A: Fluid Dynamics*, vol. 4, no. 1992, p. 1737, 1992.

[99] I. Yasuda and G. R. Flierl, "Two-dimensional asymmetric vortex merger: Contour dynamics experiment," *Journal of Oceanography*, vol. 51, no. 1984, pp. 145–170, 1995.

[100] R. R. Trieling and G. J. F. V. Heijst, "Kinematic properties of monopolar vortices in a strain flow," *Fluid Dynamics Research*, vol. 23, pp. 319–341, 1998.

[101] B. Legras and D. Dritschel, "Vortex stripping and the generation of high vorticity gradients in two-dimensional flows," *Applied Scientific Research*, vol. 51, pp. 445–455, 1993.

[102] C. Roy, N. Schaeffer, S. Le Dizès, and M. Thompson, "Stability of a pair of co-rotating vortices with axial flow," *Physics of Fluids*, vol. 20, no. 2008, 2008.

[103] F. Laporte and T. Leweke, "Elliptic instability of counter-rotating vortices: experiment and direct numerical simulation," *AIAA Journal*, vol. 40, no. 12, pp. 2483–2494, 2002.

[104] H. Deniau and L. Nybelen, "Strategy for spatial simulation of co-rotating vortices," *International Journal for Numerical Methods in Fluids*, vol. 61, no. 1, pp. 23–56, 2009.

[105] R. F. Huang and C. L. Lin, "Vortex shedding and shear-layer instability of wing at low-Reynolds numbers," *AIAA Journal*, vol. 33, no. 8, pp. 1398–1403, 1995.

[106] L. Prandtl, "Applications of modern hydrodynamics to aeronautics, NACA Report No 116.pdf," tech. rep., Gottingen University, 1921.

[107] C. M. Velte, M. O. Hansen, and V. L. Okulov, "Multiple vortex structures in the wake of a rectangular winglet in ground effect," *Experimental Thermal and Fluid Science*, vol. 72, pp. 31 – 39, 2016.

[108] H. Igarashi, P. a. Durbin, H. Ma, and H. Hu, "A stereoscopic PIV study of a near-field wingtip vortex," *AIAA Journal*, vol. 48, no. January, pp. 1–13, 2010.

[109] J. Cai, P. Xie, H. Wei, and C. Liu, "Verification and validation of LES for interaction of wingtip vortex and wakes," *46th AIAA Aerospace Sciences Meeting and Exhibit*, no. January, p. 673, 2008.

[110] V. Kolář and J. Šístek, "Recent progress in explicit shear-eliminating vortex identification," in *19th Australasian Fluid Mechanics Conference*, pp. 2–5, 2014.

[111] K. Rokhsaz, S. R. Foster, and L. S. Miller, "Exploratory study of aircraft wake vortex filaments in a water tunnel," in *17th Applied Aerodynamics Conference*, vol. 37, pp. 1022–1027, American Institute of Aeronautics and Astronautics, jun 1999.

[112] A. Vogt, P. Baumann, J. Kompenhans, and M. Gharib, "Investigations of a wing tip vortex in air by means of DPIV," *Advanced Measurement and Ground Testing Conference*, no. June, pp. 17–20, 1996.

[113] B. J. Wendt, "The modelling of symmetric vortex generators airfoil vortex generators," *Aerospace Sciences Meeting and Exhibit, 34th, Reno, NV*, no. January, pp. 15–18, 1996.

[114] C. A. Cruz, *Experimental and numerical characterization of turbulent slot film cooling*. PhD thesis, University of Maryland, College Park, 2008.

[115] C. W. M. Raffel and J. Kompenhas, *Particle Image Velocimetry, a practical guide*. Berlin, Germany: Springer, 1998.

[116] J.-H. Yoon and S.-J. Lee, "Direct comparison of 2D PIV and stereoscopic PIV measurements," *Measurement Science and Technology*, vol. 13, pp. 1631–1642, 2002.

[117] C. D. Saunter, "Quantifying subpixel accuracy: An experimental method for measuring accuracy in image-correlation-based, single-particle tracking," *Biophysical Journal*, vol. 98, no. 8, pp. 1566–1570, 2010.

[118] A. F. K. Yeung and B. H. K. Lee, "Particle image velocimetry study of wing-tip vortices," *Journal of Aircraft*, vol. 36, no. 2, pp. 482–484, 1999.

[119] T. S. Miller, L. K. Kliment, and K. Rokhsaz, "Analytical investigation of co-rotating vortex filaments with experimental verification," in *33rd AIAA Fluid Dynamics Conference and Exhibit*, p. 3601, June 2003.

[120] A. L. Heyes, R. F. Jones, and D. A. Smith, "Wandering of wing-tip vortices," *12th International Symposium on Applications of Laser Techniques to Fluid Mechanics*, pp. 35–3, 2004.

[121] J. Slotnick, A. Khodadoust, J. Alonso, D. Darmofal, W. Gropp, E. Lurie, and D. Mavriplis, "CFD vision 2030 study: A path to revolutionary computational aerosciences," *NASA Cr-2014-21878*, no. March 2014, pp. 1–73, 2014.

[122] Y. Addad, U. Gaitonde, D. Laurence, and S. Rolfo, *Optimal Unstructured Meshing for Large Eddy Simulations*. Dordrecht, Germany: Springer, 2008.

[123] Erik Wik and Scott T. Shaw, "Numerical simulation of micro vortex generators," in *2nd AIAA Flow Control Conference*, no. 2697, p. 2004, 2004.

[124] K. J. Forster, S. Diasinos, T. J. Barber, and G. Doig, "Computational analysis of backwards facing vortex generators for boundary layer mixing applications," *19th Australasian Fluid Mechanics Conference*, no. December, p. 341, 2014.

[125] J. C. Dudek, "Modeling vortex generators in a navier-stokes code," *AIAA Journal*, vol. 49, pp. 748–759, Apr. 2011.

[126] C. C. Tseng and Y. E. Cheng, "Numerical investigations of the vortex interactions for a flow over a pitching foil at different stages," *Journal of Fluids and Structures*, vol. 58, pp. 291–318, 2015.

[127] F. Nicoud and F. Ducros, "Subgrid-scale stress modelling based on the square of the velocity gradient tensor," *Flow, Turbulence and Combustion*, vol. 62, pp. 183–200, 1999.

[128] E. R. Van Driest, "On turbulent flow near a wall," *Journal of the Aeronautical Sciences*, vol. 23, no. 4, pp. 1007–1011, 1956.

[129] J. Ma, F. Wang, and X. Tang, *Comparison of Several Subgrid-Scale Models for Large-Eddy Simulation of Turbulent Flows in Water Turbine*, pp. 328–334. Berlin, Heidelberg: Springer Berlin Heidelberg, 2009.

[130] I. Yilmaz and L. Davidson, "Comparison of SGS models in Large-Eddy Simulation for transition to turbulence in TAYLOR-GREEN flow," in *The 16th International Conference on Fluid Flow Technologies*, 2015.

[131] O. Lehmkuhl, I. Rodríguez, a. Baez, a. Oliva, and C. D. Pérez-Segarra, "On the large-eddy simulations for the flow around aerodynamic profiles using unstructured grids," *Computers and Fluids*, vol. 84, pp. 176–189, 2013.

[132] A. Safdari and K. C. Kim, "Aerodynamic and structural evaluation of horizontal archimedes spiral wind turbine," *Journal of Clean Energy Technologies*, vol. 3, no. 1, pp. 34–38, 2015.

[133] A. Probst and S. Reuß, *Scale-Resolving Simulations of Wall-Bounded Flows with an Unstructured Compressible Flow Solver*, pp. 481–491. Cham: Springer International Publishing, 2015.

[134] S. V. Patankar, *Numerical Heat Transfer and Fluid Flow*. New York, New York: McGraw-Hill Book Company, 1971.

[135] R. Peyret, *Handbook of Computational Fluid Mechanics*. Academic Press, 1996.

[136] F. Kaya and I. Karagoz, "Performance analysis of numerical schemes in highly swirling turbulent flows in cyclones," *Current Science*, vol. 94, no. 10, pp. 1273–1278, 2008.

[137] S. B. Pope, *Turbulent Flows*. Cambridge: Cambridge University Press, 2000.

[138] U. Piomelli, "Large-eddy simulation: achievements and challenges," *Progress in Aerospace Sciences*, vol. 35, pp. 335–362, 1999.

[139] P. R. Spalart, "Young-person's guide to detached-eddy simulation grids," tech. rep., NASA Technical Report, 2001.

[140] B. A. Kader, "Temperature and concentration profiles in fully turbulent boundary layers," *International Journal of Heat and Mass Transfer*, vol. 24, no. 9, pp. 1541–1544, 1981.

[141] J. Dacles-Mariani, G. G. Zilliac, J. S. Chow, and P. Bradshaw, "Numerical/experimental study of a wingtip vortex in the near field," *AIAA Journal*, vol. 33, no. 9, pp. 1561–1568, 1995.

[142] J. D. Anderson, *Fundamentals of Aerodynamics*. New York, NY: McGraw-Hill Education, 2011.

[143] M. Hepperle, "Javafoil application," *http://www.mh-aerotools.de/airfoils/javafoil.htm*, 2006.

[144] C. Speziale, "Turbulence modeling for time-dependent RANS and VLES: A review," *AIAA Journal*, vol. 36, no. 2, pp. 173–184, 1998.

[145] R. R. Tirunagari and S. B. Pope, "Les/pdf for premixed combustion in the dns limit," *Combustion Theory and Modelling*, vol. 20, no. 5, pp. 834–865, 2016.

[146] R. Courant, K. O. Friedrichs, and H. Lewy, "On the partial difference equation of mathematical physics," *IBM J.*, vol. 11, no. March, pp. 32–74, 1967.

[147] R. M. Cummings, S. A. Morton, and D. R. McDaniel, "Experiences in accurately predicting time-dependent flows," *Progress in Aerospace Sciences*, vol. 44, pp. 241–257, 2008.

[148] S. Goertz and Y. Le Moigne, "Detached-eddy simulations of a full-Span delta wing at high incidence," *21st AIAA Applied Aerodynamics Conference*, p. 4216, 2003.

[149] L. Jacquin, D. Fabre, P. Geffroy, and E. Coustols, "The properties of a transport aircraft extended near field: an experimental study," in *39th Aerospace Sciences Meeting and Exhibit*, vol. 1038, 2001.

[150] S. J. Beresh, J. F. Henfling, and R. W. Spillers, "Meander of a fin trailing vortex measured using particle image velocimetry," in *47th AIAA Aerospace Sciences Meeting Including The New Horizons Forum and Aerospace Exposition*, p. 53, Jan. 2009.

[151] K. Rokhsaz and T. S. Miller, "Theoretical and experimental investigation of the self-induced oscillations of a single vortex filament," in *32nd AIAA Fluid Dynamics Conference and Exhibit*, p. 3304, June 2002.

[152] L. Schiavetta, K. Badcock, and R. Cummings, "Comparison of DES and URANS for unsteady vortical flows over delta wings," *45th AIAA Aerospace Sciences Meeting and Exhibit*, p. 1085, 2007.